Seismic Behavior, Performance and Design of Steel Concentrically Braced Frame Systems

Keith D. Palmer

A dissertation submitted in partial fulfillment
of the requirements for the degree of

Doctor of Philosophy

University of Washington

2012

Reading Committee:

Charles Roeder, Chair

Dawn Lehman

Jeffrey Berman

Program Authorized to Offer Degree:
Civil & Environmental Engineering

©Copyright 2012
Keith D. Palmer

University of Washington

Abstract

Seismic Behavior, Performance and Design of
Steel Concentrically Braced Frame Systems

Keith D. Palmer

Chair of the Supervisory Committee:
Professor Charles Roeder
Civil & Environmental Engineering

This dissertation describes a research program on special concentrically braced frame (SCBF) and buckling-restrained braced frame (BRBF) systems. The study builds upon previous work performed as part of a research program supported by the George E. Brown Network for Earthquake Engineering Simulation (NEES) entitled "International Hybrid Simulation of Tomorrow's Braced Frame." This program was initiated due to practical and experimental evidence that SCBFs were not performing as intended by current seismic design provisions. The current study includes a comprehensive experimental and analytical program which included two first-of-its-kind, two-story, one-bay by one-bay SCBF and BRBFs experiments. The experiments were performed at the University of Minnesota NEES laboratory to take advantage of its ability to apply large-displacement bi-directional loading.

The two specimens were configured with braces in two orthogonal bays framing into a "shared" column with a floor system designed and constructed to simulate realistic conditions. The first specimen, the SCBF, employed HSS3x3x1/4 braces in a single-story X-configuration with one continuous brace and a pair of spliced braces in the opposing direction. The second test specimen, the BRBF, employed pin-ended, collared BRBs in a single-diagonal configuration.

The analytical study consisted of a large suite of finite element simulations aimed at

identifying the main parameters that influence the damage at the beam-column-gusset connection region in BRBFs and to make recommendations for the design and detailing of this connection region.

This research has resulted in a number of findings including the observation that out-of-plane loading and deformation had little impact on the drift and ductility capacity of the system when compared to planar frame test results. In fact, the drift capacity of the SCBF test frame was only 6% less than that of comparable planar frames while the ductility and cumulative ductility capacities of the BRBF exceeded that of many of the planar BRBF system tests. Based on the experimental and analytical findings, design and detailing recommendations were developed for the connection at the brace splice point in the single-story, X-configured system. Design and detailing recommendations were also made for the corner gusset plate connection region in BRBFs.

TABLE OF CONTENTS

Page

List of Figures v

List of Tables xxiii

Chapter 1: Introduction 1
1.1 General 1
1.2 Research Motivation 2
1.3 NEES CBF Research Program 2
1.4 Organization of Dissertation 4

Chapter 2: Literature Review 9
2.1 Introduction 9
2.2 Conventional Brace Component Research 9
2.3 Buckling-Restrained Brace Component Research 14
2.4 Gusset Plate Research 15
2.5 Braced Frame System Research 19
2.6 Continuum Finite Element Simulations 29

Chapter 3: Experimental Program 59
3.1 Introduction 59
3.2 MAST Facility Description 59
3.3 Specimen Description 60
3.4 Specimen Member and Connection Design 62
3.5 Base and Crosshead Connections 78
3.6 Instrumentation 80
3.7 Loading Protocol 84

Chapter 4: Experimental Results 135
4.1 Introduction 135
4.2 Description of Performance States 135

4.3 Nomenclature . . . 137
4.4 Test 1: Buckling Brace SCBF . . . 138
4.5 Test 2: Buckling-Restrained Braced Frame (BRBF) . . . 156

Chapter 5: Data Analysis . . . 242
5.1 Introduction . . . 242
5.2 SCBF Experimental Data Analysis . . . 242
5.3 BRBF Experimental Data Analysis . . . 255
5.4 Analysis and Comparison of Powell's Tests . . . 268
5.5 Drift and Ductility Capacity Comparison . . . 270

Chapter 6: SCBF Test Frame Simulations . . . 318
6.1 Introduction . . . 318
6.2 Model I Description . . . 318
6.3 Model II Description . . . 319
6.4 Models III and IV Description . . . 319
6.5 Displacement-Based Loading Protocol . . . 323
6.6 Analysis Results . . . 323
6.7 OpenSees Analysis Summary and Conclusions . . . 327

Chapter 7: BRBF Continuum Finite Element Simulations . . . 343
7.1 Introduction . . . 343
7.2 BRBF Test Frame Description . . . 344
7.3 Description of FE Model . . . 344
7.4 FE Model Boundary Conditions . . . 345
7.5 BRB Model . . . 346
7.6 BRB Connection to Gusset Plate . . . 348
7.7 Modeling of Wide-flange and Plates . . . 348
7.8 Modeling of Concrete Slab . . . 348
7.9 Stress and Strain Indices . . . 349
7.10 BRB Material Modeling and Calibration . . . 350
7.11 Wide Flange and Gusset Plate Material Modeling and Calibration . . . 353
7.12 Slab Material Modeling . . . 354
7.13 Mesh Refinement Study . . . 356
7.14 Test Frame Simulation Validation . . . 357
7.15 Gusset plate weld tearing analysis . . . 360

7.16 Conclusions . . . 362

Chapter 8: BRBF Parametric Study . . . 389
8.1 Introduction . . . 389
8.2 Description of Parameters . . . 389
8.3 Results of Parameteric Study . . . 394
8.4 Further Analysis . . . 419
8.5 Summary of Parametric Study . . . 422

Chapter 9: Design Recommendations . . . 475
9.1 Introduction . . . 475
9.2 SCBF Design Recommendations . . . 475
9.3 BRBF Design Recommendations . . . 482

Chapter 10: Summary, Conclusions and Recommendations . . . 492
10.1 Summary . . . 492
10.2 Summary of Experimental Program . . . 493
10.3 Summary of Analytical Program . . . 498
10.4 Conclusions from SCBF Experimental Investigation . . . 500
10.5 Conclusions from the BRBF Experimental Investigation . . . 501
10.6 Conclusions from the SCBF Analytical Investigations . . . 501
10.7 Conclusions from BRBF Simulations and Parametric Study . . . 502
10.8 Recommendations for Future Research . . . 504

References . . . 506

Appendix A: Specimen Design . . . 513
A.1 SCBF Gusset Plate Design . . . 514
A.2 Column Panel Zone Calculations . . . 520

Appendix B: Specimen Drawings . . . 523

Appendix C: Data Reduction . . . 560
C.1 Member Forces . . . 561
C.2 Frame and Story Drifts . . . 566
C.3 Gusset Plate Rotations . . . 570
C.4 Column Panel Zone Deformations . . . 570

C.5 Member Rotations 572

Appendix D: SCBF Experimental Plots and Tables 574
D.1 SCBF Displacement and Loading Protocol Information 575
D.2 SCBF Damage Tables 582
D.3 SCBF energy dissipation 593

Appendix E: BRBF Experimental Plots and Tables 595
E.1 BRBF Displacement and Loading Protocol Information 596
E.2 BRBF Damage Tables 604
E.3 BRB axial force-axial deformation envelopes 613
E.4 BRB core elongation stringpot measurements 614
E.5 BRB casing strains 617
E.6 BRBF energy dissipation 620

Appendix F: Material Certificates 622
F.1 Wide flange mill certs 623
F.2 HSS mill certs 630
F.3 BRB core plate mill certs 632

LIST OF FIGURES

Figure Number Page

1.1 Example CBFs: (a) SCBF inverted-V (Chevron) configuration; (b) BRBF in a single-diagonal configuration; (c) SCBF double-story X-configuration. (Source: [Engelhardt, 2008]) . . . 6

1.2 Damage states in UC Berkely tests [Uriz, 2005]: (a) column fracture at "simple" connection; (b) BRB rotation and hinging; (c) beam flange fracture . . . 7

1.3 NEES CBF research program "International Hybrid Simulation of Tomorrows Braced Frame Systems" . . . 8

2.1 Gusset plate design parameters. . . . 40

2.2 Uniform force method free-body diagram and geometry [Thornton, 1991] . . . 40

2.3 SCBF test frame [Uriz, 2005] . . . 41

2.4 UW tests: (a) prototype building; (b) test specimen and typical member sizes (Source: [Johnson, 2005]) . . . 41

2.5 UW experiments: (a) test setup schematic; (b) test setup photo (Source: [Powell, 2010]) . . . 42

2.6 TCBF1 two-story test specimen [Clark, 2009]. Dimensions in mm, 1 in. = 25.4 mm. H506x201x11x19 equivalent to W21x68; H318x307x17x24 equivalent to W12x106; HSS125x125x9 equivalent to HSS5x5x3/8; HSS175x175x7.5x11 equivalent to W6x25. . . . 42

2.7 Three-story test specimen [Lumpkin, 2009] . . . 43

2.8 UW typical loading protocol [Johnson, 2005] . . . 44

2.9 Force-displacement curves [Johnson, 2005] . . . 44

2.10 Single story X-configuration SCBF specimen details tested by Powell at UW: (a) frame elevation; (b) corner gusset plate connection; (c) sandwich plate HSS30 splice connection; (d) HSS31 slotted tube through-plate splice connection. . . . 45

2.11 Single story X-configuration SCBF specimens . . . 46

2.12 Specimen behavior: (a) HSS31 unsymmetric buckling behavior with spliced braces in compression; (b) HSS30 symmetric buckling behavior; (c) HSS30 twisting deformation due to brace splice providing continuity. . . . 47

2.13 Specimen behavior: (a) Gusset deformation due to brace torsion in HSS30; (b) Gusset plate interface tearing at corner connection in HSS30 following brace fracture. . . . 48
2.14 System story shear versus story drift ratio for: (a) HSS30 and (b) HSS31. . . . 48
2.15 BRBF test frame [Uriz, 2005] . . . 49
2.16 BRBF frame damage [Uriz, 2005] . . . 49
2.17 BRBF test parameters [Christopolus, 2005] . . . 50
2.18 BRBF frame damage [Christopolus, 2005] . . . 50
2.19 BRBF test specimen [Fahnestock et al., 2006]: (a) elevation; (b) fixed connection; (c) pinned connection. . . . 51
2.20 Comparison between experimental and FEA: (a) experimental behavior; (b) FE predicted behavior; (c) out-of-plane brace displacement comparison [Yoo, 2006] . . . 52
2.21 Comparison of FE simulations and experiments: (a) HSS01; (b) HSS05 [Yoo, 2006] . . . 53
2.22 Calibration of brace fracture using Equivalent plastic strain [Yoo, 2006] . . . 54
2.23 BRBF numerical model: (a) test frame; (b) continuum FE model of third story [Wigle and Fahnestock, 2010] . . . 54
2.24 Example BRBF connection details: (a) continuous beam, bolted brace; (b) spliced beam, pinned brace; (c) continuous beam, welded brace [Wigle and Fahnestock, 2010] . . . 55
2.25 Equivalent plastic strain at gusset plates: (a) vertical gusset interface (column connection); (b) horizontal gusset interface (beam connection). [Wigle and Fahnestock, 2010] . . . 55
2.26 Finite element model and mesh [Ozcelik and Okazaki, 2010] . . . 56
2.27 Brace and casing finite element model [Ozcelik and Okazaki, 2010] . . . 57
2.28 Hysteretic behavior comparison: (a) Experiment [Christopolus, 2005]; (b) FE simulation [Ozcelik and Okazaki, 2010] . . . 57
2.29 Damage comparison between experiment and simulation: (a) column web yielding and flange buckling; (b) beam yielding and flange buckling [Ozcelik and Okazaki, 2010] . . . 58
3.1 MAST facility with SCBF specimen in place . . . 95
3.2 Specimen photographs: (a) SCBF specimen; (b) BRBF specimen . . . 96
3.3 Specimen floor plans: (a) second floor; (b) third floor . . . 97
3.4 Slab blockout at second floor . . . 98
3.5 SCBF braced frame elevations: (a) Frame 1; (b) Frame B . . . 99
3.6 BRBF braced frame elevations: (a) Frame 1; (b) Frame B . . . 100

3.7 BRBs prior to installation . . . 101
3.8 BRB-1 fabrication drawing . . . 101
3.9 Brace and gusset plate nomenclature: (a) HSS brace net section; (b) gusset plate buckling lengths and Whitmore width . . . 102
3.10 Gusset plate schematics . . . 102
3.11 Balanced Design Procedure yielding hierarchy for SCBF systems . . . 103
3.12 Elliptical clearance geometry (Source: Kotulka 2007) . . . 103
3.13 SCBF gusset plate nomenclature: (a) Frame 1; (b) Frame B . . . 104
3.14 Typical SCBF gusset plate connection to column flange at base, GP-1 . . . 105
3.15 SCBF gusset plate connection to shared column web at base, GP-3 . . . 105
3.16 Typical SCBF gusset plate connection at second and third floor to column flange, GP-2 . . . 106
3.17 SCBF gusset plate connection at second and third floor to shared column web, GP-4 . . . 107
3.18 SCBF slotted-tube, through-plate connection at intersection of single-story X-configuration, GP-5 . . . 108
3.19 BRBF gusset plate nomenclature: (a) Frame 1; (b) Frame B. (see Figure 3.20 for details) . . . 109
3.20 BRBF gusset details: (a) connection to column flange at beam-column joint (BGP-2); (b) connection to column web at beam-column joint (BGP-3); (c) connection at base (BGP-1). (See Table 3.14 for weld sizes) . . . 110
3.21 Column base details: (a) shared column (B-1); (b) braced frame columns A-1 and B-2; (c) gravity column (A-2). . . . 111
3.22 Base of column A-1 during specimen construction . . . 112
3.23 Connection between crosshead and test specimens: (a) plan layout of B7 connecting rods; (b) elevation . . . 113
3.24 Connection detail between top floor slab and crosshead bottom plate . . . 113
3.25 Top floor slab reinforcement plan . . . 114
3.26 Third floor slab: (a) slab reinforcement and crosshead connector sleeves during construction; (b) underside of third floor slab showing crosshead connectors 115
3.27 Brace strain gauge layout, Braced Bays 1 and B (SCBF Test) . . . 116
3.28 Brace OOP string pot layout, second story, Frame B (SCBF Test), as viewed from outside the frame . . . 117
3.29 Brace OOP stringpot support frame (SCBF test) . . . 118
3.30 Gusset plate OOP stringpot nomenclature and locations: (a) Frame 1; (b) Frame B . . . 118
3.31 Gusset plate OOP stringpots: (a) Base gusset plate ; (b) Gusset plate at beam 119

3.32 BRB axial deformation string pot attachment . . . 119
3.33 BRB axial deformation string pot plan detail . . . 120
3.34 BRB axial deformation string pot layout . . . 120
3.35 BRB casing strain gauge layout . . . 121
3.36 Braced frame column strain gauge layout: (a) Frame 1; (b) Frame B . . . 122
3.37 Gravity frame column strain gauge layout: (a) Gravity Bay 2; (b) Gravity Bay A . . . 123
3.38 Second floor column rotation and panel zone deformation LVDT layout, column B1 and shared column (see Figure 3.41 for rotation LVDT attachment point locations) . . . 124
3.39 Joint instrumentation: (a) Column B2 second floor column rotation and panel zone deformation LVDT layout; (b) column rotation LVDT cross-section location (see Figure 3.41 for rotation LVDT attachment point locations) . . . 125
3.40 Column second floor joint instrumentation photographs . . . 126
3.41 Rotation LVDT mounting detail at beams and columns . . . 126
3.42 Frame 1 second floor beam strain gauges: (a) at column B1 side (both test specimens); (b) location along beam depth; (c) at shared column side (SCBF test specimen); (d) at shared column side (BRBF test specimen) . . . 127
3.43 Frame B second floor beam strain gauges: (a) at shared column side; (b) at column B2 side; (c) location along beam depth . . . 128
3.44 Beam rotation LVDTs: (a) at second floor, Frame B at shared column side; (b) photo at second floor, Frame 1, shared column side . . . 129
3.45 Story drift stringpot layout: (a) second floor plan layout; (b) third floor plan layout . . . 129
3.46 Story drift string pots: (a) attachment to strong wall; (b) setup in elevation . 130
3.47 Slip instrumentation: (a) base; (b) third floor / crosshead . . . 131
3.48 Base instrumentation at column B1 . . . 132
3.49 Schematic of cyclic loading protocol in principal direction . . . 132
3.50 Three-story prototype BRBF building: (a) plan; (b) South elevation; (c) East elevation. [Sherman, 2009] . . . 133
3.51 Schematic of bi-directional "cloverleaf" loading protocol: (a) full cloverleaf; (b) cycle 'i' of cloverleaf; (c) cycle 'i+1' of cloverleaf . . . 134

4.1 Yielding levels for frame performance states . . . 173
4.2 Conventional brace Buckling Levels (Source: [Lumpkin, 2009]) . . . 174
4.3 Brace performance states: (a) Cupping and bulging at plastic hinge; (b) Tearing of part of the brace at the plastic hinge (BF); (c) Complete fracture of the brace at the plastic hinge (BF). (Source: [Powell, 2010]) . . . 174

4.4 Local buckling levels (a) B2; (b) B3. 175
4.5 Weld damage performance states: (a) Weld material damage; (b) Base metal damage. (Source: [Lumpkin, 2009]) 175
4.6 Test frame nomenclature: (a) Frames and columns; (b) Story and floor designations; (c) Frame 1 brace designations; (d) Frame B designations; (e) Frame 1 gusset plate designations; (f) Frame B gusset plate designations. 176
4.7 Frame shear-drift hysteresis (SCBF test) 177
4.8 Frame elevations showing SDRs at initial brace buckling 178
4.9 Frame 1 first story braces buckling level B2 179
4.10 Second floor gusset plates at column A-1, yielding level Y1, 0.18% RDRY . . 180
4.11 Braced frame performance states during and at end of initial drift range . . . 181
4.12 Frame 1 braces buckling level B3 182
4.13 Second floor gusset plates at column A-1, yielding level Y2, 1.1% 1SDRY, 1.4% 2SDRY 183
4.14 Second floor gusset plates at column B-1 in Frame 1, yielding level Y3, 1.27% RDRY 184
4.15 Gusset plate at 1st story center splice 185
4.16 Gusset plate at base of column A1 186
4.17 Gusset plate at second floor at column B2, yielding level Y3, 1.28% RDRX . 187
4.18 Gusset plate edge deformation at second floor of column A1 due to frame action, -1.1% 1SDRY, -1.4% 2SDRY 188
4.19 Column A1 base yielding 189
4.20 Column B2 base yielding 189
4.21 Frame B shared column base yielding level Y2, gusset plate yielding level Y1, 0.85% 1SDRY (0.94% RDRY, 0.63% RDRX) 190
4.22 Column A1 3rd floor panel zone, yielding level Y1 191
4.23 Shared column third floor, flange yielding 192
4.24 Second floor beam at shared column in Frame 1, yielding level Y1, 0.94% RDRY 192
4.25 Frame 1 second floor beam at shared column, flange yielding level Y2, 1.3% RDRY 193
4.26 Underside of second floor beam in Frame 1 194
4.27 Second floor beam at shared column in Frame B, yielding level Y1, 1.06% RDRX 194
4.28 Braced frame performance states during and at end of moderate drift range . 195
4.29 Frame B first story braces buckling level B3 196
4.30 Frame 1 second story discontinuous brace plastic hinge damage progression . 197

4.31 Second floor gusset plates at column A-1, yielding level Y3, 2.3% 2SDRY . . 198
4.32 Gusset edge deformation at second floor column A1 199
4.33 Second floor joint at shared column in Frame 1, gusset plate yielding level Y3, column panel zone yielding level Y1, and yielding level Y3 in beam web, 1.9% RDRY 200
4.34 Gusset plate yielding level Y3 and edge deformation, 1.7% RDRX 201
4.35 Third floor joint at shared column in Frame B, gusset plate yielding level Y2, column yielding level Y3, 1.9% RDRY, 1.7% RDRX 202
4.36 Gusset plate at base of column A-1, yielding level Y3, 1.9% RDRY 203
4.37 Gusset plate at base of column B-1, yielding level Y3, 1.6% RDRY 203
4.38 Gusset plate at base of shared column framing into column web in Frame B . 204
4.39 Gusset plate at base of column B-2, yielding level Y3, 1.7% RDRX 204
4.40 Frame B gusset plate at 1st story center splice, yielding level Y3, 1.7% RDRX 205
4.41 Yielding level Y3 at base of columns A1 and B2: (a) 1.4% 1SDRY (1.59% RDRY); (b) 1.4% 1SDRX (1.5% RDRX); (c) 1.57% 1SDRX (1.71% RDRX) ; (d) 1.57% 1SDRX (1.71% RDRX). 206
4.42 Column yielding 207
4.43 Shared column at second floor, yielding level Y1, 1.59% RDRY 208
4.44 Column A1 and Shared column 3rd floor panel zone, 2.1% 2SDRY 209
4.45 Third floor beam bottom flange yielding at Column A1 and Shared column in Frame 1, 1.59% RDRY 210
4.46 Second floor beam yielding at splice at shared column in Frame B, % RDRX 211
4.47 Second floor beam at shared column in Frame 1, yielding level Y3 and deformed web, 1.9% RDRY 212
4.48 Braced frame performance states at end of severe drift range 213
4.49 Pictorial of damage states at end of SCBF test per ATC-58 DS definitions [Roeder et al., 2009] 214
4.50 Frame shear-drift hysteresis (BRBF test) 215
4.51 Second floor, Frame 1 beam web repair at shared column side prior to BRBF test 216
4.52 Gusset plate weld tear above second floor beam at column A-1 in Frame 1 (BRBF test) 216
4.53 Gusset plate weld tear above second floor beam at column B-2 in Frame B (BRBF test) 217
4.54 Progression of flange yielding at base of Column A-1 (BRBF test) 218
4.55 Progession of damage at base of Column A-1 during severe drift ranges (BRBF test) 219

4.56 Progression of flange yielding at base of Column B-2 (BRBF test) 220
4.57 Progession of damage at base of Column B-2 during severe drift ranges (BRBF test) 221
4.58 Progession of damage at base of shared column (BRBF test) 222
4.59 Progression of yielding at base of the gravity column during the severe drift range (BRBF test) 223
4.60 Progression of yielding at the second floor joint of column A-1 during the severe drift range (BRBF test) 224
4.61 Tear in braced frame column A-1 web at gravity beam bolted connection at end of BRBF test 225
4.62 Progression of yielding at the second floor joint of column B-2 during the severe drift range (BRBF test) 226
4.63 Column B-2 flange damage: (a) Divot forming; (b) Tear forming; (c) Tear propagating; (d) Flange connecting to web tear (BRBF test) 227
4.64 Braced frame column B-2 web and flange tearing, 2.4% 1SDSRX and 4.7% 2SDRX (BRBF test) 228
4.65 Column flange tear at beam bottom flange at second floor of column B-2, 2.7% 1SDSRX and 3.7% 2SDRX (BRBF test) 229
4.66 Third floor column panel zone yielding (BRBF test) 230
4.67 Column flange yielding at beam bottom flange at second floor of column A-1, end of test (BRBF test) 231
4.68 Shared column third floor flange yielding (BRBF test) 232
4.69 Beam damage in Frame 1 at second floor, column A-1 (BRBF test) 233
4.70 Beam damage in Frame B at second floor, column B-2 (BRBF test) 234
4.71 Beam damage in Frame 1 at second floor, column B-1 side (BRBF test) . . . 235
4.72 Beam damage in Frame B at second floor, column B-1 (BRBF test) 236
4.73 Beam damage in Frame B at second floor, column B-1 (BRBF test) 237
4.74 Column flange yielding at beam bottom flange at face of third floor column A-1, end of test (BRBF test) 238
4.75 Beam damage in Frame 1 at third floor, shared column side (BRBF test) . . 239
4.76 Beam damage in Frame 1 at third floor, shared column side (BRBF test) . . 240
4.77 Pictorial of damage states per ATC-58 [2009], BRBF test 241

5.1 Story shear resisted by braces in each story (SCBF test) 277
5.2 Envelopes of story shear resisted by both braces in each story, calculated by subtracting column shears from the actuator forces (SCBF test) 278

5.3 Brace axial force calculated from brace strain gauges, not valid after yielding at 0.5% SDR. (CT - strain gauges attached to the top of the continuous brace. DT - strain gauges attached to the top of discontinuous brace. CB - strain gauges attached to the bottom of continuous brace. DB - strain gauges attached to the bottom of discontinuous brace.) 279

5.4 Comparison of story shears resisted by brace as calculated from top (SGt) and bottom (SGb) brace strain gauges and the crosshead actuator forces minus the column shears (CH), not valid after yielding (SCBF test) 280

5.5 Out-of-plane brace deformation at select story drift ratios in continuous and discontinuous braces in the second story of Frame B 281

5.6 Comparison of OOP deformation of second story braces in Frame B at the quarter point of the continuous brace and the quarter point of the top part of the spliced brace (the bottom part did not buckle) 282

5.7 Second-story Frame B brace OOP deformation at 1.9% 2SDRX 283

5.8 BB1 1S Buckled Brace Shapes 284

5.9 BB1 1S Buckled Brace at Zero Drift Cycle 33 285

5.10 Gusset plate rotations in first story of Frame 1 286

5.11 Gusset plate rotations in first story of Frame B 287

5.12 SCBF column moment envelopes at gusset plate reentrant corners. (Legend indicates the column as defined by the grid intersections along with the location in the story. A-1t indicates the moment at the gusset reentrant corner at the top of the story of column A-1) 288

5.13 SCBF column story shear envelopes (Legend indicates column as defined by the grid intersections along with the story. "A-1 2S" indicates the second story shear of column A-1) 289

5.14 SCBF column story shears in each story and global direction. (Legend indicates column as defined by the grid intersections along with the story. "A-1 2S" indicates the second story shear of column A-1) 290

5.15 Column panel zone deformations at second floor joint: (a) shear strain; (b) shear strain normalized by the yeild strain. 291

5.16 Second floor braced frame beam behavior in Frame 1: (a) moment at gusset plate reentrant corner vs. 2SDRY at column A-1 side; (b) moment at gusset plate reentrant corner vs. 2SDRY at column B-1 side; (c) moment at gusset plate reentrant corner vs. average beam rotation at column A-1 side; (b) moment at gusset plate reentrant corner vs. average beam rotation at column B-1 side. 292

5.17 Second floor braced frame beam behavior in Frame B: (a) moment at gusset plate reentrant corner vs. 2SDRX at column B-1 side; (b) moment at gusset plate reentrant corner vs. 2SDRY at column B-2 side; (c) moment at gusset plate reentrant corner vs. average beam rotation at column B-1 side; (b) moment at gusset plate reentrant corner vs. average beam rotation at column B-2 side. 293

5.18 Frame analysis to show effect of composite slab on flexural behavior of frame: (a) SAP model with left-side slab in compression; (b) SAP model with right-side slab in compression; (c) normalized moment diagram from push to the right; (d) normalized moment diagram from push to the left; (e) normalized moment-displacement curve for left-side of beam at column joint; (f) normalized moment-displacement curve for right-side of beam at column joint. 294

5.19 Distribution of story shear to braces, braced frame beams and columns, and gravity bay beams and columns. 295

5.20 Story drift distribution in X and Y directions (SCBF test) 296

5.21 Brace axial load vs. brace axial deformation (BRBF test). Note: dashed line indicates column strain gauges above yield and force estimate no longer accurate. 297

5.22 Story shear resisted by braces in each story as a function of SDR (BRBF test). Note: dashed line indicates column strain gauges above yield and force estimate no longer accurate. 298

5.23 Fractured BRB core. Note part of the core on the left side has curled due to compressive bearing following fracture. 299

5.24 Envelope of brace axial load vs. brace axial deforamtion (BRBF test) 299

5.25 Definition of BRB axial stiffness (see Table 5.4) 300

5.26 Tension strain hardening adjustment factor, ω vs. normalized brace axial deformation 301

5.27 Compression strength adjustment factor, β vs. normalized brace axial deformation 302

5.28 Cumulative inelastic axial deformation for each BRB as a function of the experimentally measured story drift ratio 303

5.29 Estimated BRB casing force 304

5.30 Comparison of top and bottom components of BRB axial elongation 305

5.31 BRBF column moment envelopes at gusset plate reentrant corners. (Legend indicates the column as defined by the grid intersections along with the location in the story. A-1t indicates the moment at the gusset reentrant corner at the top of the story of column A-1) 306

5.32 BRBF column story shear envelopes (Legend indicates column as defined by the grid intersections along with the story. "A-1 2S" indicates the second story shear of column A-1) . . . 307
5.33 BRBF column story shears in each story and global direction. (Legend indicates column as defined by the grid intersections along with the story. "A-1 2S" indicates the second story shear of column A-1) . . . 308
5.34 Envelope of BRBF column panel zone deformations at second floor joint: (a) shear strain; (b) shear strain normalized by the yield strain; (c) shear strain measurements of LVDTs 3 and 4 on column A-1. . . . 309
5.35 BRBF second floor braced frame beam behavior in Frame 1: (a) moment at gusset plate reentrant corner vs. 2SDRY at column A-1 side; (b) moment at gusset plate reentrant corner vs. 2SDRY at column B-1 side; (c) moment at gusset plate reentrant corner vs. average beam rotation at column A-1 side; (b) moment at gusset plate reentrant corner vs. average beam rotation at column B-1 side. . . . 310
5.36 BRBF second floor braced frame beam behavior in Frame B: (a) moment at gusset plate reentrant corner vs. 2SDRX at column B-1 side; (b) moment at gusset plate reentrant corner vs. 2SDRY at column B-2 side; (c) moment at gusset plate reentrant corner vs. average beam rotation at column B-1 side; (b) moment at gusset plate reentrant corner vs. average beam rotation at column B-2 side. . . . 311
5.37 Story shear distribution (BRBF test) . . . 312
5.38 Story drift distribution in X and Y directions (BRBF test) . . . 313
5.39 X-configured frame experimental envelopes: (a) brace axial versus SDR; (b) energy dissipated by the braces. . . . 314
5.40 Brace length, L_{br}, used in buckling strength calculations . . . 314
5.41 Total drift range at last complete cycle prior to failure (SCBF experiments) . 315
5.42 BRBF test specimen story drift ratio range (last complete cycle prior to test stoppage, failure due to beam or column fracture or instability, or BRB fracture. Note that none of Fahnestock's BRBs fractured during the Hybrid PSDT, shown shaded; quasi-static, cyclic protocol in white). See Table 5.10 for definition of "A," "B" and "F." . . . 316
5.43 BRBF test specimen Max BRB ductilities achieved during tests. See Table 5.10 for definition of "A," "B" and "F." . . . 317
5.44 BRBF test specimen cumulative ductility demands. See Table 5.10 for definition of "A," "B" and "F." . . . 317
6.1 SCBF Frame 1 modeled in OpenSees simulations . . . 330
6.2 Element fiber model discreitzation (Note: slab is included only in the beams in Model IV) . . . 330

6.3 Brace force deformation curve for Model II . . . 331
6.4 Kent-Scott-Park concrete material model (http://opensees.berkeley.edu/) . . 331
6.5 Schematic of frame Models III and IV (Note: floor slab used in Model IV not shown in figure) . . . 332
6.6 Brace initial imperfection model, 16 elements . . . 333
6.7 Gusset plate out-of-plane rotation model [Hsiao et al., 2012a] . . . 333
6.8 Beam-column-gusset joint model (Note: NLFBE - Nonlinear forced-based element) . . . 334
6.9 Model frame loading for pushover and cyclic analyses . . . 335
6.10 Pushover results for Models I (Basic Elastic) and II (Basic Nonlinear) . . . 335
6.11 Brace discretization study, brace axial load versus third floor drift . . . 336
6.12 Global hysteretic response, Models III and IV . . . 337
6.13 Second story shear resisted by braces versus average story drift ratio, Models III and IV . . . 338
6.14 First story shared column shear versus average story drift ratio, Models III and IV . . . 339
6.15 Moment at shared column base versus average story drift ratio, Models III and IV . . . 340
6.16 Moment at top of 1st story shared column versus average story drift ratio, Models III and IV . . . 341
6.17 Second floor beam moment at shared column versus average story drift ratio, Models III and IV . . . 342

7.1 BRBF Frame 1 modeled in FE simulation . . . 364
7.2 Base FE model with element types depicted . . . 365
7.3 FE model nodal boundary conditions . . . 366
7.4 FE model third floor slab constraint to rigid “control” node . . . 367
7.5 BRB sections along length . . . 368
7.6 FE model detail of gusset plate, reinforcing pad and pin connecting BRB to gusset plate . . . 368
7.7 Stress and strain sampling locations (thick, dark lines) in beams, columns and gusset plates for parametric study. . . . 369
7.8 Highlighted elements used for sampling maximum stress and strain indices at gusset plate interfaces with beams and columns . . . 370
7.9 Description of plotting method of stress and strain indices along gusset interfaces with beams and columns . . . 370
7.10 BRB uni-axial material curves: (a) Stress v. strain; (b) Kinematic plastic stress v. plastic strain . . . 371

7.11 BRB force-deformation comparison for BRB material model calibration . . . 372
7.12 BRB dissipated energy comparison between simulation and experiment for BRB material model calibration . . . 373
7.13 Wide flange and gusset plate material model calibration comparison plots. (Legend - 0.2E indicates 2% strain hardening modulus; EPP - indicates elastic perfectly plastic) . . . 374
7.14 Global force-displacement envelopes for slab sensitivity study . . . 375
7.15 Comparison of PEEQ values at -3.2% RDR with slab moduli of 2,500 and 5,000 psi with one in. and 3/4 in. gusset plates, column B-1 third floor joint 376
7.16 Mesh densities for mesh refinement study . . . 377
7.17 Mesh densities at joint region for mesh refinement study . . . 378
7.18 von Mises stress distribution at 3% RDR for mesh refinement study . . . 379
7.19 PEEQ stress distribution at 3% RDR for mesh refinement study . . . 380
7.20 Mesh refinement study analysis results comparison . . . 381
7.21 Experimental displacement of crosshead and applied displacement in simulations . . . 382
7.22 Comparison of test results to simulated results . . . 383
7.23 Comparison of test results to simulated results . . . 384
7.24 Comparison of experimental and simulated beam deformation at 3F column B-1 . . . 385
7.25 Comparison of experimental and simulated panel zone yielding . . . 386
7.26 Comparison of experimental and simulated column A-1 base deformation . . . 387
7.27 PEEQ indices for simulations with gusset plate weld material modeled. (REFweld - indicates the welds sized per UFM, SOPweld - indicates welds designed for the strength of the plate) . . . 388
8.1 Global and local force-deformation responses used for comparisons in parametric study . . . 426
8.2 Gusset plate long-edge tie constraint . . . 426
8.3 Global behavior comparison (Parameter - gusset plate thickness) . . . 427
8.4 Stress contours and beam deformation at third floor joint at column B-1 at 3.5% RDR (Parameter - gusset plate thickness) . . . 428
8.5 Stress contours and beam deformation at third floor joint at column B-1 at 2.0% RDR (Parameter - gusset plate thickness) . . . 429
8.6 Stress contours and beam deformation at second floor joint at column B-1 at 2.0% RDR (Parameter - gusset plate thickness) . . . 430
8.7 Stress contours and beam deformation at second floor joint at column B-1 at 3.5% RDR (Parameter - gusset plate thickness) . . . 431

8.8 PEEQ comparison at column B-1 third floor joint at -2% RDR (Parameter - gusset plate thickness) . . . 432
8.9 Von Mises stress comparison at column B-1 third floor joint at -2% RDR (Parameter - gusset plate thickness) . . . 433
8.10 PEEQ and Von Mises stress comparison at column B-1 third floor joint at -2% RDR (Parameter - gusset plate thickness) . . . 434
8.11 Gusset plate long-edge stiffener detail . . . 435
8.12 Global behavior comparison (Parameter - gusset plate edge stiffeners) . . . 436
8.13 Stress contours and beam deformation at second floor joint at column B-1 at 2.0% RDR (Parameter - gusset plate edge stiffeners) . . . 437
8.14 Stress contours and beam deformation at second floor joint at column B-1 at 3.5% RDR (Parameter - gusset plate edge stiffeners) . . . 438
8.15 PEEQ comparison at column B-1 third floor joint at -2% RDR (Parameter - gusset plate edge stiffeners) . . . 439
8.16 Gusset plate geometry: (a) with taper at column; (b) without taper at column (models with "NT" in their designation) . . . 440
8.17 Global behavior comparison (Parameter - gusset plate taper) . . . 441
8.18 Stress contours and beam deformation at third floor joint at column B-1 at 2.0% RDR (Parameter - gusset plate taper) . . . 442
8.19 Stress contours and beam deformation at third floor joint at column B-1 at 3.5% RDR (Parameter - gusset plate taper) . . . 443
8.20 PEEQ comparison at column B-1 third floor joint at -2% RDR (Parameter - gusset plate taper) . . . 444
8.21 Von Mises stress comparison at column B-1 third floor joint at -2% RDR (Parameter - gusset plate taper) . . . 445
8.22 Location of beam web doubler and flange stiffeners at beam-column-gusset joint . . . 446
8.23 Global behavior comparison (Parameter - beam reinforcement) . . . 447
8.24 Stress contours and beam deformation at third floor joint at column B-1 at 3.5% RDR (Parameter - beam reinforcement) . . . 448
8.25 Stress contours and beam deformation at second floor joint at column B-1 at 3.5% RDR (Parameter - beam reinforcement) . . . 449
8.26 PEEQ comparison at column B-1 third floor joint at -2% RDR (Parameter - beam reinforcement) . . . 450
8.27 Von Mises stress comparison at column B-1 third floor joint at -2% RDR (Parameter - beam reinforcement) . . . 451
8.28 PEEQ comparison at column B-1 third floor joint at -2% RDR (Parameter - beam reinforcement) . . . 452

8.29 Von Mises stress comparison at column B-1 third floor joint at -2% RDR (Parameter - beam reinforcement) . . . 453
8.30 Stress contours and beam deformation at third floor joint at column B-1 at 3.5% RDR (Parameter - beam reinforcement) . . . 454
8.31 Stress contours and beam deformation at second floor joint at column B-1 at 3.5% RDR (Parameter - beam reinforcement) . . . 455
8.32 Global behavior comparison (Parameter - Column size and reinforcement) . . . 456
8.33 Stress contours and beam deformation at third floor joint at column B-1 at 3.5% RDR (Parameter - Column size and reinforcement) . . . 457
8.34 PEEQ comparison at column B-1 joints at -2% RDR (Parameter - Column size and reinforcement) . . . 458
8.35 Von Mises stress comparison at column B-1 joint at -2% RDR (Parameter - Column size and reinforcement) . . . 459
8.36 PEEQ comparison at columns A-1 and B-1 second floor joint at -2% RDR (Parameter - beam and column reinforcement) . . . 460
8.37 Beam fixity release detail at second floor beam outside of gusset plate . . . 461
8.38 Global behavior comparison (Parameter - Beam fixity) . . . 462
8.39 Stress contours and beam deformation at second floor joint at column B-1 at 3.5% RDR (Parameter - Beam fixity) . . . 463
8.40 PEEQ comparison at column B-1 second floor joint at -2% RDR (Parameter - Beam fixity) . . . 464
8.41 Von Mises stress comparison at column B-1 second floor joint at -2% RDR (Parameter - Beam fixity) . . . 465
8.42 Global behavior comparison (Parameter - BRB strength) . . . 466
8.43 Stress contours and beam deformation at second floor joint at column B-1 at 3.5% RDR (Parameter - BRB strength) . . . 467
8.44 PEEQ comparison at column B-1 third floor joint at -2% RDR (Parameter - BRB strength) . . . 468
8.45 PEEQ comparison at column B-1 second floor joint at -2% RDR (Parameter - BRB strength) . . . 469
8.46 Stress contours and beam deformation at third floor joint at column B-1 at 3.5% RDR (Parameter - BRB strength) . . . 470
8.47 Stress contours and beam deformation at third floor joint at column B-1 at 3.5% RDR (Parameter - BRB strength) . . . 471
8.48 Gusset plate interface force resultant nomenclature . . . 472
8.49 Normalized, maximum PEEQ demands in the beam at the edge of the gusset plate at -2% RDR from FE simulations as a function of the ratio of the beam web thickness to gusset plate thickness. . . . 473

8.50 Normalized, maximum PEEQ demands in the column at the edge of the gusset plate at -2% RDR from FE simulations as a function of the ratio of the beam web thickness to gusset plate thickness. 474

9.1 Recommended brace length for buckling strength calculations 487

9.2 Brace splice detail at center of single-story, X-configuration: (a) sandwich plate detail; (b) through-plate detail; (c) buckling length for sandwich plate; (d) buckling lengths for through-plate. 488

9.3 Comparison of buckled brace shapes with sandwich plate splice detail 489

9.4 Comparison of buckled brace shapes with through-plate splice detail 489

9.5 Gusset plate schematics 490

9.6 Recommended detailing at corner beam-column-gusset connection region. . . 490

9.7 Beam fixity release detail at BRB gusset plate 491

A.1 Gusset plate buckling lengths per the Thornton method: (a) gussets framing into the shared column web (GP-4); (b) gussets framing into the flanges of all braced frame columns at floor levels (GP-2); (c) gusset framing into web at base of shared column (GP-3); (d) gussets framing into column flange at base of shared column and columns A-1 and B-2 (GP-1). (See Figure 3.13 for gusset plate mark locations) 519

A.2 Gusset plate buckling length at brace splice per the Thornton method) 520

A.3 Column panel zone force diagram 522

B.1 Specimen floor plans 525

B.2 Specimen floor plan 526

B.3 BRBF Frame 1 elevation 527

B.4 BRBF Frame B elevation 528

B.5 Gravity frame elevations 529

B.6 SCBF frame elevations 530

B.7 SCBF gusset plate connection detail 531

B.8 SCBF gusset plate connection detail 532

B.9 SCBF gusset plate connection detail 533

B.10 SCBF gusset plate connection detail 534

B.11 SCBF gusset plate connection detail 535

B.12 WFWW beam-to-column connection detail 536

B.13 Shear connection details 537

B.14 Base plate details 538

B.15 Base plate detail 539

B.16 Shear connection details 540

B.17 Column reinforcement details . . . 541
B.18 CJP weld details . . . 542
B.19 Beam splice detail . . . 543
B.20 Floor slab details . . . 544
B.21 BRBF gusset plate detail . . . 546
B.22 BRBF gusset plate detail . . . 547
B.23 BRBF gusset plate detail . . . 548
B.24 BRBF gusset plate detail . . . 549
B.25 BRBF gusset plate detail . . . 550
B.26 BRBF gusset plate detail . . . 551
B.27 BRBF gusset plate detail . . . 552
B.28 BRBF shop drawings . . . 554
B.29 BRBF shop drawings . . . 555
B.30 BRBF shop drawings . . . 556
B.31 BRBF shop drawings . . . 557
B.32 BRBF shop drawings . . . 558
B.33 BRBF shop drawings . . . 559

C.1 Column strain gauge and moment nomenclature for curvature, moment and shear calculations . . . 563
C.2 Triangulation of point D on test frame . . . 568
C.3 Story displacement and drift quantities: (a) plan view; (b) elevation . . . 569
C.4 Parameters used to calculate deformations: (a) OOP gusset rotation and beam rotation; (b) panel zone shear deformation . . . 571
C.5 Column rotation calculation parameters: (a) side view; (b) rear view; (c) cross-sectional view . . . 573

D.1 Imposed Crosshead Displacements (SCBF test) . . . 575
D.2 Measured second-story drift ratios, percent (SCBF test) . . . 576
D.3 Measured first-story drift ratios, percent (SCBF test) . . . 580
D.4 SDR cloverleaf traces, percent (SCBF test) . . . 580
D.5 Actuator forces in X and Y directions, kips (SCBF test) . . . 581
D.6 Energy dissipation comparison: (a) total energy dissipated in each principal direction; (b) energy dissipated by braces in each frame and story; (c) energy dissipated in the Y-directions frames; (d) energy dissipated in the X-direction frames. . . . 593

D.7 Energy dissipation comparison: (a) second story frames in Y-direction; (b) second story frames in X-direction; (c) first story frames in Y-direction; (d) first story frames in X-direction. . . . 594
E.1 Imposed Crosshead Displacements (BRBF test) . . . 596
E.2 Measured second-story drift ratios, percent (BRBF test) . . . 597
E.3 Measured first-story drift ratios, percent (BRBF test) . . . 598
E.4 SDR cloverleaf traces, percent (BRBF test) . . . 598
E.5 Actuator forces in X and Y directions, kips (BRBF test) . . . 601
E.6 Normalized brace axial load vs. normalized brace axial deformation (BRBF test). Note that the yield load in tension is not equal to the yield load in compression. . . . 613
E.7 BRB elongation stringpot measurements at each BRB end (two pots at each end in each plot), Frame 1 . . . 614
E.8 BRB elongation stringpot measurements at each BRB end (two pots at each end in each plot), Frame B . . . 615
E.9 BRB axial deformations at ends of braces ('Bot' indicates the average of the two stringpot measurements at the bottom of the BRB, 'Top' indicates the average of the two stringpot measurements at the top of the BRB), Frames 1 and B . . . 616
E.10 BRB casing strains (BRBF) . . . 617
E.11 Average BRB casing strains (BRBF) . . . 618
E.12 Estimated BRB casing forces from casing strain gauges (BRBF) . . . 619
E.13 BRBF energy dissipation comparison: (a) total energy dissipated in each principal direction; (b) energy dissipated by braces in each frame and story; (c) energy dissipated in the Y-directions frames; (d) energy disspiated in the X-direction frames. . . . 620
E.14 BRBF energy dissipation comparison: (a) second story frames in Y-direction; (b) second story frames in X-direction; (c) first story frames in Y-direction; (d) first story frames in X-direction. . . . 621
F.1 Mill certification . . . 624
F.2 Mill certification . . . 625
F.3 Mill certification . . . 626
F.4 Mill certification . . . 627
F.5 Mill certification . . . 628
F.6 Mill certification . . . 629
F.7 Mill certification . . . 631
F.8 Mill certification . . . 633

F.9 Mill certification 634
F.10 Mill certification 635
F.11 Mill certification 636
F.12 Mill certification 637

LIST OF TABLES

Table Number Page

2.1 UW SCBF experimental parameters [Johnson, 2005] . . . 34
2.2 UW SCBF experimental parameters [Herman, 2007] . . . 34
2.3 UW SCBF experimental parameters [Kotulka, 2007] . . . 35
2.4 UW SCBF experimental parameters [Powell, 2010] . . . 36
2.5 Wide flange and HSS material properties for HSS30 and 31 . . . 37
2.6 TCBF1 test frame parameters [Clark, 2009] . . . 37
2.7 Test frame parameters [Lumpkin, 2009] . . . 38
2.8 UW SCBF experimental failure modes . . . 38
2.9 Ductility capacities of BRBF *system* tests . . . 39
2.10 Ductility capacities of BRB component tests . . . 39

3.1 Wide flange and HSS material properties . . . 88
3.2 Concrete floor slab compression test results . . . 89
3.3 Concrete floor slab MEAN compression test results . . . 89
3.4 Concrete floor slab splitting-tensile test results . . . 90
3.5 Concrete floor slab MEAN splitting-tensile test results . . . 90
3.6 Comparison of AISC and BDP limit states . . . 91
3.7 SCBF brace properties and design forces . . . 92
3.8 BRB properties and design parameters . . . 92
3.9 Braced frame column design demand to capacity ratios for SCBF test . . . 92
3.10 Braced frame column design demand to capacity ratios for BRBF test . . . 92
3.11 Column panel zone information . . . 93
3.12 SCBF gusset plate demand capacity ratios (see Figure 3.13 for gusset marks) 93
3.13 BRBF gusset plate demand capacity ratios (see Figure 3.19 for gusset marks) 93
3.14 BRBF gusset plate interface weld schedule (units are inches, see Figure 3.20) 94
3.15 Cyclic loading protocol in principal directions for SCBF and BRBF tests . . . 94

4.1 Performance State Nomenclature . . . 171
4.2 Acronyms used for story drift ratios . . . 172
4.3 Maximum story drift ranges prior to brace fracture (SCBF test) . . . 172

4.4 Maximum story drift ranges in the last complete cycle prior to brace fracture (BRBF test) . . . 172

5.1 SCBF peak story shear resisted by both braces in a story . . . 272
5.2 SCBF experimentally measured buckling loads . . . 272
5.3 BRB yield values . . . 273
5.4 BRB axial pre- and post-yield stiffness, k/in. (see Figure 5.25) . . . 273
5.5 BRB overstrength curve-fitting parameters . . . 274
5.6 BRB overstrength factors at 1, 2 and 3% story drift ratios . . . 274
5.7 BRB experimental ductility demands (at the end of the last complete cycle prior to core fracture) . . . 275
5.8 Maximum SDRs in last complete cycle prior to brace fracture (percent) for single-story X-configured frames . . . 275
5.9 Brace buckling strengths and estimated effective length factors for single-story X-confgiured frames . . . 276
5.10 Wide flange and HSS material properties for HSS30 and 31 . . . 316

6.1 Model II Steel Model Parameters . . . 329
6.2 Model IV Concrete Model Parameters . . . 329

7.1 Equivalent cross-sectional area parameters for simulated BRBs . . . 363
7.2 Material Parameters for FE Simulations . . . 363
7.3 FE models for slab sensitivity study . . . 363
7.4 Weld tearing analysis results . . . 364

8.1 FE Models for Parametric Study . . . 392
8.1 FE Models for Parametric Study . . . 393
8.2 Gusset plate demand-capacity ratios for parametric study . . . 425
8.3 Gusset plate interface force ratios from brace force only in FE simulations at third floor, column B-1 (see Fig. 8.48 for nomenclature) . . . 425

A.1 SCBF Gusset plate buckling limit state parameters . . . 518

D.1 Maximum frame resistances and average roof drifts in each cycle (SCBF test) 576
D.1 Maximum frame resistances and average roof drifts in each cycle (SCBF test) 577
D.1 Maximum frame resistances and average roof drifts in each cycle (SCBF test) 578
D.2 Maximum frame story drift ratios in each cycle (SCBF test) . . . 578
D.2 Maximum frame story drift ratios in each cycle (SCBF test) . . . 579
D.3 Brace Performance State Progression Table (SCBF test) . . . 582
D.4 Frame 1 Gusset Plate Performance State Progression Table (SCBF test) . . . 584

D.5 Frame B Gusset Plate Performance State Progression Table (SCBF test) . . . 586
D.6 Column A-1 Performance State Progression Table (SCBF test) 588
D.7 Column B-1 Performance State Progression Table (SCBF test) 589
D.8 Column B-2 Performance State Progression Table (SCBF test) 590
D.9 Frame 1 Beams Performance State Progression Table (SCBF test) 591
D.10 Frame B Beams Performance State Progression Table (SCBF test) 592

E.1 BRBF experimental damage description (Fig. E.1) 597
E.2 Maximum frame resistances and average roof drifts in each cycle (BRBF test) 599
E.2 Maximum frame resistances and average roof drifts in each cycle (BRBF test) 599
E.2 Maximum frame resistances and average roof drifts in each cycle (BRBF test) 600
E.3 Maximum frame story drift ratios in each cycle (BRBF test) 601
E.3 Maximum frame story drift ratios in each cycle (BRBF test) 602
E.3 Maximum frame story drift ratios in each cycle (BRBF test) 603
E.4 Gusset Plate Performance State Progression Table (BRBF test) 605
E.5 Column A-1 Performance State Progression Table (BRBF test) 607
E.6 Column B-1 Performance State Progression Table (BRBF test) 608
E.7 Column B-2 Performance State Progression Table (BRBF test) 609
E.8 Frame 1 Beams Performance State Progression Table (BRBF test) 611
E.9 Frame B Beams Performance State Progression Table (BRBF test) 612

ACKNOWLEDGMENTS

The financial support for this research was provided by the National Science Foundation's Network for Earthquake Engineering Simulation (Grant No. CMS-619161) and the American Institute of Steel Construction. Their support is greatly appreciated.

I would like to express my gratitude to my advisers Professors Charles Roeder and Dawn Lehman for their guidance and advice over the course of this research and for their invitation that brought me to the University of Washington. Thanks to Professors Jeffrey Berman and Laura Lowes for serving on my committee and their many suggestions that helped improve this dissertation. I would also like to thank my Graduate Student Representative, Professor Giovanni Migliaccio. Special thanks to Professors Taichiro Okazaki and Carol Shield whose guidance and friendship throughout the project were invaluable.

The success of the experimental portion of this work is due in large part to my friends and colleagues at the MAST facility: Paul Bergson, Drew Daugherty, Rachel Gaulke, Angela Kingsley and Mitch Reierson, who helped make my time in the lab nearly non-stop fun.

I would not have been able to stay at least partly sane without the good friends that I've met and shared offices with over the years: Ozer Dereli, Roberto Piccinin, Jim Hambleton and Andrey Pyatigorets who made my time at Minnesota unforgettable; my UW office mates Dave Lattanzi, Joshua Pugh and Dave Webster, who helped make my transition to UW easier with their friendship, humor and help.

I could not have done this without the love and support of my family and I cannot express in words the level of my gratitude, appreciation and love for my parents and siblings who have always supported and encouraged me in all of my endeavors. You mean the world to me.

DEDICATION

To my parents.

Chapter 1

INTRODUCTION

1.1 General

Concentrically braced frames (CBF) are lateral force resisting systems (LFRS) commonly used to resist wind and seismic loading. CBFs are essentially vertical trusses composed of beams, columns and braces that resist lateral load primarily through axial loads in these members. The longitudinal axis of the brace in a CBF is typically aligned with the intersection of the centerlines of the beams and/or columns into which the brace frames. Figure 1.1 shows three examples of modern buildings utilizing CBFs in three common configurations. Figure 1.1a shows a CBF with "conventional" buckling braces in a Inverted-V (Chevron) configuration, Fig. 1.1b shows a Buckling Restrained Braced Frame (BRBF) in a single-diagonal configuration and Fig. 1.1c shows a CBF with "conventional" buckling braces in a double-story X-configuration. CBFs are attractive systems due to their large strength and stiffness relative to other systems such as moment-resisting frames (MRFs) which typically require relatively large members and numerous, field-welded moment connections.

The braces in CBFs are intended to be the primary fuses that dissipate the seismic energy and ideally, are the elements in which the damage would be concentrated. Conventional braces accomplish this through buckling in compression and yielding in tension. Novel braces such as buckling-restrained braces (BRB) have been developed relatively recently to mitigate the effects associated with brace buckling. As the name implies, this bracing system prevents buckling of the brace and dissipates seismic energy through brace yielding in both tension and compression. Current design standards require details that are intended to ensure that the maximum amount of brace ductility is developed prior to other system failures or instabilities. For example, gusset plate interface weld failure or brace net section fracture of conventional braces should not occur prior to brace buckling in compression or extensive yielding in tension because that can limit the strength and ductility of the system.

Similarly for BRBFs, gusset plate buckling or interface weld failure should not occur prior to extensive yielding of the BRB in tension or compression.

1.2 Research Motivation

Braced frame research in the last three decades of the 20th century has focused mainly on the individual components that make up braced frame systems (i.e. the braces and gusset plates), with little focus on the ***system*** behavior. Much has been gained from this research including an understanding of important component failure modes and the development of design methods for these limit states along with limits on brace slenderness (local and global). However, experiments performed at the University of California, Berkeley [Uriz, 2005] on three one-story, one-bay buckling-restrained braced frames (BRBFs) and one two-story, one-bay SCBF with buckling HSS braces showed that current design provisions fall short of the design intent for CBF systems subject to cyclic loading of the type seen during earthquakes.

Figure 1.2a shows column fracture near the bottom flange of the CBF beam. The column was designed according to the 1997 AISC Seismic Design Provisions [AISC, 1997] and the beams were assumed to be "pin-connected" to the column. This is clearly a bad assumption and shows the large amount of restraint induced in the connection by the gusset plate, which is not shown in the figure but is present at the top flange of the beam. Figure 1.2b shows the out-of-plane rotation of the BRB just outside the casing which resulted in a dramatic loss of system stiffness and resistance. This rotation was a result of the brittle beam fracture shown in Fig. 1.2c. These failures, which occurred at story drifts expected to be seen during a design event and less than those expected during a severe seismic event, demonstrate the importance of considering ***system*** behavior and show the shortcomings of understanding and predicting behavior based on ***component*** tests and simulations.

1.3 NEES CBF Research Program

In response to the need for a better understanding of CBF system behavior, a relatively large research program funded by the National Science Foundation (NSF) under the banner of the George E. Brown Network for Earthquake Engineering Simulation (NEES) was un-

dertaken. This program is entitled "International Hybrid Simulation of Tomorrows Braced Frame Systems" and the main objective of the program is to assess seismic performance of CBFs in terms of true system response and develop the tools necessary to design these systems to attain their full potential. A multi-institutional approach was taken utilizing the strengths of the University of Washington (UW), University of California at Berkeley (UCB), University of Minnesota (UMN), National Taiwan University (NTU), and the National Center for Research in Earthquake Engineering in Taiwan (NCREE). Each institution has unique experimental facilities allowing the study of different aspects of the problem.

Figure 1.3 describes the work performed by each university and the interdependence between studies. The research began with tests of single-story, one-bay CBF systems at UW to study the effect of various connection design parameters on the behavior and performance of the system [Christopolus, 2005; Herman, 2007; Johnson, 2005; Kotulka, 2007; Powell, 2010]. Additionally, a large suite of validated finite element simulations were performed on CBF frames to study a broader range of parameters than could not be economically tested in the lab [Yoo, 2006]. This initial research resulted in improvements to the design philosophy and brace connection detailing which were then tested on six, planar, multi-story CBF systems at NCREE [Clark, 2009; Lumpkin, 2009]. These tests were unique as they included gusset plates attached to the mid-span of the beam and a more realistic concrete floor system. Again, prior to and concurrent with these tests, finite element simulations were performed to assess the performance of specific design parameters and inform the specimen design [Yoo, 2006]. Four tests were also performed at UCB on two-story, one-bay planar frames with various bracing configurations and loading histories, including hybrid, pseudo-dynamic testing methods.

1.3.1 Scope and Objectives of Author's Research

Building upon the research described above, the author performed experiments on two, large-scale 3D CBF systems. These tests, the first of which is shown at the bottom of Fig. 1.3, are the first true 3D tests of CBF systems, incorporating realistic boundary conditions and simultaneous loading in two horizontal directions. Additionally, a finite element

model was validated from the results of the second test and parametric studies were performed. As graphically described in Fig. 1.3, these tests and simulations were the culmination of the previous research.

The primary objectives of the author's research were as follows:

1. To investigate and evaluate ***system*** behavior and performance of 3D SCBFs with realistic boundary conditions. These systems included:
   - Single-story X-configured SCBF designed according to the Balanced Design Procedure (BDP).
   - Pin-ended, collar-type BRBFs designed according to state-of-the-practice procedures.
2. To assess the effect of bi-directional loading on the ductility of the frame.
3. To evaluate and calibrate continuum finite element models of the BRBF system tested.
4. To investigate the effects of gusset plate thickness and geometry, brace strength, and beam and column size and reinforcement on the performance and behavior of the beam-column-gusset joint in a BRBF.
5. To provide design recommendations, to the extent possible, for SCBF and BRBF systems.

1.4 Organization of Dissertation

This dissertation describes the 3D CBF experiments and numerical simulations performed by the author to address the objectives discussed in the previous section. The organization of this dissertation is as follows:

- Chapter 1 provides a brief background on CBFs, the need for system research and the scope of the author's work.
- Chapter 2 presents a review of past research on CBFs and their components including "conventional" brace and BRB research, gusset plate research and CBF system research.

- Chapter 3 describes the large-scale experimental program undertaken by the author and performed at the NEES-MAST laboratory at the University of Minnesota. MAST is an acronym for Multi-Axial Subassemblage Testing. This chapter includes a description of the MAST facility along with the frame design, instrumentation and loading protocol development.
- Chapter 4 discusses the results of the experiments including the behavior, performance and damage states that occurred in the frames during the experiments. Heavy reliance on photographic evidence is used and supplemented by the instrumentation data recorded during the experiments.
- Chapter 5 provides a more detailed analysis of the data recorded during the experiments. This analysis includes brace force-displacement behavior, analysis of BRB overstrength, and behavior of the beams, columns and gusset plates.
- Chapter 6 discusses the numerical simulations of the SCBF test frame performed using OpenSees.
- Chapter 7 discusses the numerical simulations of the BRBF test frame performed using ABAQUS and the suite of parametric studies.
- Chapter 8 provides connection design recommendations based on the work described in the previous chapters.
- Chapter 9 summarizes the research program and main findings and provides recommendations for future study.
- Six appendices are included that provide extra information pertaining to the design of the test frame, test frame drawings, data reduction methods and formulas, experimental data and material certificates.



(a) (b)



(c)

Figure 1.1: Example CBFs: (a) SCBF inverted-V (Chevron) configuration; (b) BRBF in a single-diagonal configuration; (c) SCBF double-story X-configuration. (Source: [Engelhardt, 2008])

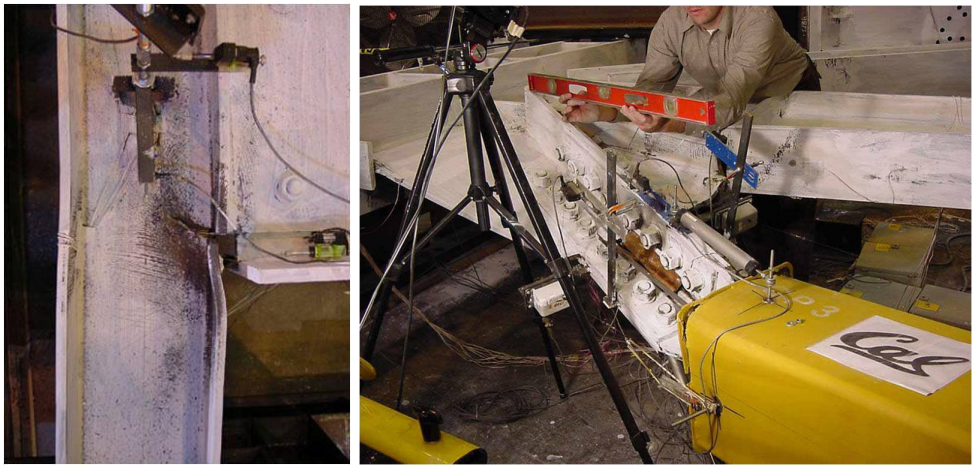

(a) (b)



(c)

Figure 1.2: Damage states in UC Berkely tests [Uriz, 2005]: (a) column fracture at "simple" connection; (b) BRB rotation and hinging; (c) beam flange fracture

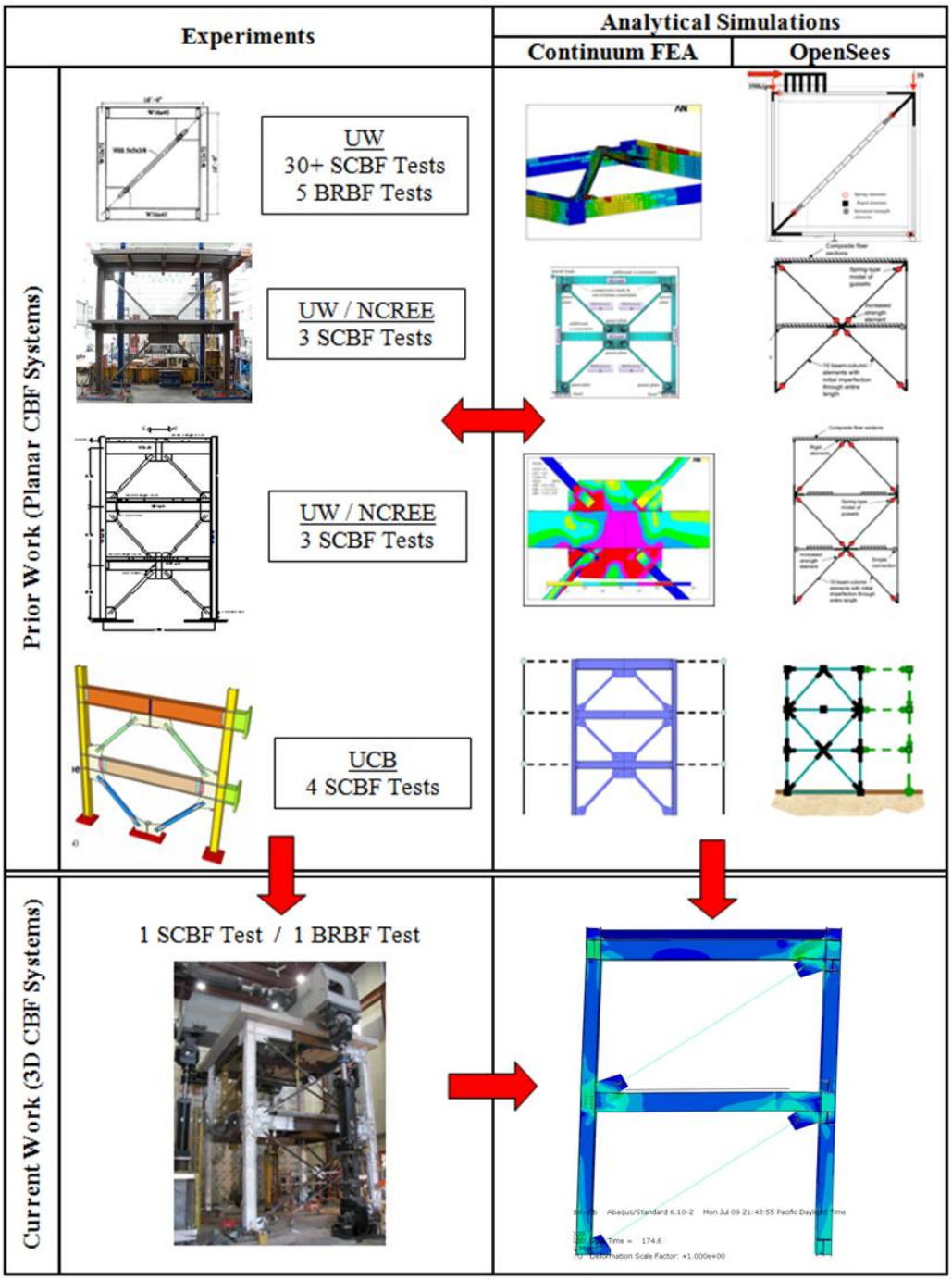

Figure 1.3: NEES CBF research program "International Hybrid Simulation of Tomorrows Braced Frame Systems"

Chapter 2

LITERATURE REVIEW

2.1 Introduction

There is a large body of work on the behavior of the individual components of braced frame systems; namely, the braces and gusset plates. The majority of the early work focused on the behavior of these elements under monotonic and cyclic loading with boundary conditions that did not realistically simulate the braced frame system behavior under seismic loading. In fact, current design standards for the seismic design of braced frames are in large part based on the above research. While this research has resulted in a good understanding of element behavior (e.g. hysteretic pinching due to brace buckling) and particular failure modes (e.g. block shear rupture), many questions remain about the performance of these systems under strong seismic motion. This has been demonstrated by recent system research that will be described in this section.

The following review will cover four components of braced frame research: (1) brace research; (2) gusset plate research; (3) CBF system research and (4) analytical and numerical simulations of CBFs. Due to the large amount of research, some of it is omitted in this section but the literature cited was chosen to highlight the key issues pertaining to this topic. The review will cover both buckling-type braces and BRBs.

2.2 Conventional Brace Component Research

2.2.1 Black, Wenger, and Popov (1980)

Black et al. [1980] performed cyclic axial load tests on 24 steel bracing members. Six of these were pinned at one end and fixed at the other and had slenderness ratios of 40 and 80. The remainder of the specimens were pinned at both ends and had slenderness ratios of 40, 80 and 120. The sections tested were wide flanges (9), square (3) and round (5) hollow sections, double-angles (4), structural tees (2) and double-channels (1).

The primary goals of their program were to investigate the effects of end conditions, cross-section, loading history and slenderness ratios on the cyclic behavior of bracing members. The first conclusion reached in this study was that the slenderness ratio of a member appeared to be the most significant parameter affecting the hysteretic behavior with the stockier members exhibiting fuller hysteretic loops than the slender ones. Based on the energy calculated from the hysteretic loops, they concluded that the best performing cross-section was a pipe, followed by square HSS, wide flange, structural tee, and finally double angle. Additionally, significant reduction in compressive load was observed during subsequent inelastic cyclic loadings.

2.2.2 Tremblay (2002)

Tremblay [2002] provides an extensive survey of brace experiments performed over the last 3 decades. He reviewed 76 brace tests from nine different testing programs. The braces were subjected to quasi-static cyclic loading and covered a wide range of section type, slenderness ratios, material properties and boundary conditions. Various loading histories were applied to the braces with the majority of them being symmetric about zero with a few centered about a compression or tension displacement to simulate near-field seismicity.

A number of conclusions were arrived at in this study with the first being that the measured yield stress of the steel exceeded the nominal properties in all specimens but one with an average actual to nominal ratio of 1.24 and a COV of 0.16. However, the tests were performed over a large time period and are not necessarily indicative of steel shapes currently produced. The buckling strength of the braces typically exceeded the strength estimated using the 1994 AISC and Canadian Standards Association column equations with higher values predicted for the more slender braces. Stockier braces exhibited the ability to maintain a compressive force equal to the initial buckling strength at the tensile yield deformation level while more slender braces degraded in strength to approximately 80% of the initial buckling strengths at the tensile yield deformation.

The maximum tensile force developed in the braces was dependent on the loading history and strain hardening occurred in approximately 65% of the tests. The largest tensile forces

were observed for the loading histories with large excursions applied early in the histories. On average, the maximum tensile forces in the HSS braces were 10% larger than the yield load, and 5% larger for hot rolled shapes. In all tests, the compressive resistance of the brace degraded upon application of larger compressive deformations or at the subsequent compressive cycles at the same deformation. This is due to the formation of a plastic hinge and out-of-plane brace deformation. An equation based on regression analysis of the test data was developed to determine the value of the compressive strength of braces at ductility levels of 2, 3 and 5 that can be used in design although the influence of b/t on this was not explicitly considered.

Local buckling developed in the plastic hinges of all HSS members, followed by fracture except in the thick walled pipes. Tremblay reports that fracture was found to be strongly dependent on the slenderness ratio of the bracing members, and on the b/t ratios and loading history to a lesser extent. More slender braces achieved higher levels of ductility prior to fracture. This is most likely due to smaller curvatures at the plastic hinge in more slender members. An equation was also proposed to predict the lateral deformation that results from buckling.

2.2.3 Tremblay, Archambault and Filiatrault (2003)

Tremblay et al. [2003] studied the experimental response of single-story, single-diagonal braces and braces in a single-story X-configuration. 24 tests were performed on a full-scale braced frame with two different loading histories. The first loading history was symmetrical, and increased in amplitude at every step while the second history consisted of five cycles at three different mean values of displacement. Ten tests were performed on the X-configuration and 14 were performed on the single-diagonal configuration. The braces in all tests were HSS ranging in size from 64 mm x 64 mm (2.5" x 2.5") to 127 mm x 76 mm (5" x 3") with nominal yield strength of 450 MPa (65 ksi). The b/t ratios ranged from 8.0 to 22.7. The gusset plates were attached only to the beam and the braces are offset $2t$ from the beam according to current practice. As such, only the behavior of the brace with limited effect from the gusset was studied.

The response of two single-diagonal tests was combined for comparison with the tests on the X-configuration. The hysteretic behavior of the combined single-diagonal and the X-configuration were very similar, displaying similar initial stiffnesses and loads at a given displacement amplitude and similar shapes of the force-displacement curves. Additionally, the behavior of the specimens was similar regardless of the loading history except at the first cycle of large displacement of the unsymmetric history, where the force was much larger but after repeated cycles, the resistance degraded to a magnitude similar to that of the symmetric history. As expected, fracture occurred in the braces after the occurrence of local buckling at the plastic hinge.

The tests verified the applicability of using the tension brace in the X-configuration as a lateral support when calculating the capacity of the compression brace. Additionally, the estimated initial buckling loads per the American Institute of Steel Construction (AISC) and the Canadian Standards Association were very close to those observed in the test when an effective length using the estimated effective length factor, K, and the actual length of the brace.

The stockier braces exhibited fatter hysteresis loops than the slender braces. It was shown that the energy dissipation decreases nearly linearly with the brace slenderness regardless of the type of configuration. The tests also demonstrated that the fracture life of HSS sections increases with slenderness ratio. An expression for fracture life (ductility at fracture) as a function of the slenderness ratio was developed based on the experimental data. However this expression was unconservative for the X-configuration due to the fact that for a given ductility level, the out-of-plane deformations of the braces in the X-configuration are greater than the single-diagonal out-of-plane deformations resulting in larger plastic curvatures at the hinge.

2.2.4 Fell, Kanvinde, Deierlein and Myers (2009)

Fell et al. [2009] performed 18 large-scale tests on three different types of cross-sections typically used as bracing members in CBFs. The main parameters in the study were the slenderness ratio, width-thickness ratio, cross-section type, loading history and loading rate,

grout-fill, and net-section reinforcement. The braces were loaded axially and were attached at the ends with a gusset plate with an offset of $3t$ to allow for rotation. Two different square HSS sections, two different pipe sections and a W-section were tested.

Three different loading histories were used, the standard loading protocol (far-field) modified for CBFs and loading protocol to simulate near-field seismic demand with the principal demand in compression and tension, respectively. All specimens were tested until brace fracture occurred. For the far-field loading histories, the HSS braces reached story drift ratios between 2.7 and 5.0% prior to significant strength loss; the pipes reached story drift ratios between 4.0 and 5.0% and the wide-flange reached 5.0% prior to significant strength loss. Global buckling occurred at SDRs between 0.2 to 0.4% for all specimens subjected to far-field histories. Only two pipes out of all specimens subjected to the near-fault loading fractured while the rest fractured after the appended symmetric cycles. In all cases, tearing initiated very soon after the occurrence of local buckling and significant strength loss occurred very soon after tearing began.

As expected, the tendency for fracture increased with increasing width-thickness ratio and decreasing slenderness ratios with the square HSS showing greater tendency to fracture at drifts smaller than those for pipes and wide-flange sections. It was concluded that width-thickness ratios have the largest impact on fracture with slenderness ratios and loading history showing lesser impact. Additionally, the near-field loading histories were more damaging than the far-field loading histories.

The authors suggest that the current AISC limits on width-thickness ratios are not stringent enough to provide ductility capacities that are typically seen during the MCE but were generally adequate for design level earthquakes. Additionally, the loading rates appeared to have little effect on the ductility capacities of the braces. The ratio of the measured strengths to the AISC recommended strengths using R_y had a mean value of 1.23 with a standard deviation of 0.25. These values indicate conservatism for the brace design but have negative implications for the capacity design of the brace connections and beam and column design.

2.3 Buckling-Restrained Brace Component Research

2.3.1 Black, Makris and Aiken (2002)

Black et al. [2002] performed stability analyses and tests on five BRBs with various configurations. The BRBs were Unbonded Braces manufactured by Nippon Steel Corporation with two of the brace cores having rectangular cross-section and the remaining have cruciform cross-sections. The stability analyses showed that the brace is stable globally when the Euler buckling load of the restrainer is greater than the yield load of the core. It was also concluded that the core should have a width-thickness ratio below five to prevent plastic torsional buckling of the core. The BRBs were loaded cyclically with a number of loading histories including the SAC basic loading history [SAC, 1997] and a low-cycle fatigue history. The loading was purely axial and no attempt was made to simulate connection rotational demands. All specimens exhibited stable behavior with the cumulative ductility exceeding that required by AISC [2010].

2.3.2 Merrit, Uang and Benzoni (2003)

Merrit et al. [2003] conducted eight full-scale experiments at the University of California, San Diego on PowerCat BRBs manufactured by Star Seismic. The braces were subjected to cyclic axial and transverse loading protocol in accordance with SEAOC-AISC [2001] qualification testing. Additionally, after the standard test, dynamic axial loading simulating the Sylmar ground motion recorded during the 1994 Northridge earthquake was applied to one of the specimens without the transverse loading applied to the other specimens. The core cross-sections were all rectangular but the number of plates varied between the specimens from one to four. No specimen fractured during the standard loading protocol and no significant distress was observed in the casing or the collars. Two specimens fractured during the low-cycle fatigue tests while the cumulative plastic deformation ranged from 600 to 1,650 which is well in excess of the recommended value of 200 [AISC, 2010].

2.3.3 Romero, Reaveley, Miller and Okahashi (2007)

Romero et al. [2007] performed seven tests at the University of Utah on Wildcat BRBs manufactured by Star Seismic. The braces were subjected to cyclic axial and transverse loading protocol in accordance with AISC [2005a] qualification testing. Four of the specimens fractured, two of the specimens failed due to bending of the collar and wall of the restraining tube, and one test was ended due to failure of the gusset weld. The maximum ratio of compressive force to tensile force was 1.29 and the range was between 0.98 and 1.29. The maximum cumulative inelastic deformation ranged from 246 to 810 with the specimen with the failed gusset exhibiting the lower value. All specimens conformed to the requirements of AISC [AISC, 2005a].

2.4 Gusset Plate Research

2.4.1 General

Gusset plates in CBFs are used to transfer the loads between the braces and beams and columns. In addition to satisfying typical limit states of yielding and buckling, gusset plates for buckling braces are required to accommodate inelastic rotation demands imposed as a result of brace buckling [AISC, 2010]. The accommodation of rotation is typically accomplished by offsetting the brace a distance of $2t$ from the line of restraint as shown in Fig. 2.1. This is based on experiments performed by Astaneh-Asl [Astaneh-Asl et al., 1985] on double-angle bracing members attached to tapered gussets at each end. Gusset plates for BRBs should satisfy the typical limit states and provide stability to ensure global stability of the BRB.

Some of the earliest work relating to gusset plates was performed by Whitmore [1952] at the University of Tennessee on gusset connections in trusses. This work resulted in a method that is still used today for estimating the tensile and compressive capacity of gusset plates. He defined a width that effectively resists the tension and compressive brace loads that is used to size the thickness of gusset plates. This width is shown in Figure 2.1 and is found by extending lines at 30 degrees from the beginning to the end of the connection. This width, combined with the gusset thickness is assumed to resist the axial brace loads.

Chambers and Ernst [2005] present a review of relevant research relating to gusset plates prior to 2004. A review of portions of this and other gusset plate research is presented below.

2.4.2 Gross and Cheok (1988)

Gross and Cheok [1988] were the first to conduct braced frame subassemblages that considered the impact of framing action in the test setup (however, brace buckling was prevented). Additionally, their tests investigated the effect of framing the brace and gusset plate into the column web, and also the effect of work point location that is not at the intersection of the beam-column centerlines. The columns were W10x49, the beams were W16x40 and the braces were W8x21 in all cases. Each specimen was loaded monotonically with the top brace in tension up to failure and then unloaded. Loading then proceeded in the other direction monotonically until failure. Gusset plate buckling was considered to be the mode of failure for the concentric and eccentric strong axis connections. The weak axis connection specimen failed in block shear at the brace splice connection to the gusset plate. The weak axis eccentric connection had a higher buckling capacity due to the more compact gusset plate resulting from the eccentricity. Additionally, the weak axis connection did not appear to negatively impact the capacity of the system

The connections were evaluated according to the UFM and Richard's equations [Thornton, 1991] for distributing the bracing loads to the members. The experimental capacities exceeded these values by a factor greater than two. The experimental gusset plate buckling capacity was 50 to 70% times greater than that predicted by Thornton's method (see below) using an effective length factor of 0.5. No comment is made on the impact of frame action on the system other than stating that frame action tended to oppose the diagonal bracing forces and may have contributed to the excess capacity of the gusset interface connections.

2.4.3 Thornton (1991)

Current design of the welds connecting the gusset plates to the framing members typically follows the Uniform Force Method (UFM) as recommended by Thornton [1991]. This recommendation was based on a survey of five different models which concluded that the UFM

provides a safe design and the best prediction of the design strengths and critical limit states. This was based on a comparison of the tests by Bjorhovde and Chakrabarti [1985], and Gross and Cheok [1988]. This method only considers the brace force and ignores the effects of frame action on the interface forces. Figure 2.2 depicts the free body diagram associated with this model and assumes that the line of action of the brace force, gusset-beam interface force and gusset-column interface force intersect at a point. The resulting geometric and force equations shown in the figure are a result of this. The maximum stress in the weld is then determined by elastically combining the stresses due to the vertical and horizontal forces, and moments at the interface. The weld is then designed for the larger of these or 1.25 times the average stress [AISC, 2005b]. The factor of 1.25 is a so-called "ductility factor" to account for the uneven distribution of stresses in the weld [Hewitt and Thornton, 2004] which was based on Williams' work [Williams, 1986] as described below.

2.4.4 Rabern (1983), Williams (1986)

Rabern [1983] utilized an in-house program, INELAS, to analyze the brace connections tested by Bjorhovde and Chakrabarti [1985]. The results of these analyses showed significant redistribution of stresses as the material yields. Williams [1986] also used INELAS to analyze three types of braced frame subassemblages under monotonically increasing loads. Williams' models include the action of the beams and columns and it is reported that the gusset plate loads resulting from frame action are of the same order as those from the braces and may cause gusset buckling when the brace is in tension. It was also shown that the direction of the forces at the edge of the gussets tended to align with the angle of the brace as the brace force increases. The "ductility factor" mentioned previously was justified based on the results of the gusset-beam interface forces found in these analyses, where the maximum interface force divided by average was found to be approximately 1.4.

2.4.5 Yam and Cheng (2002)

Yam and Cheng [2002] report on the experimental and numerical investigations of the compressive behavior of gusset plates. In addition to the experiments described in the

previous paragraph, similar tests were performed with the addition of beam and column moments being applied in a fixed, constant ratio for the majority of these tests. These do not realistically simulate the moments that a braced frame system will be subjected to as they did not typically increase with increasing brace force. The results of the experiments showed that the Thornton method for calculating the buckling load of gusset plates using an effective length factor of 0.65, dispersion angle of 30 degrees and the maximum length of l_1, l_2 and l_3 shown in Figure 2.1 is very conservative with the average ratio of actual buckling strength to predicted of 1.67 and a range of 1.51 to 1.87. The authors proposed modifying the dispersion angle to 45 degrees and the resulting ratios ranged from 0.92 to 1.19 with an average of 1.06.

2.4.6 Yoo (2006)

Yoo [2006] evaluated the accuracy of the Thornton buckling model and the modified Thornton buckling model based on the results of many of the tests previously described and found that the Thornton model was conservative for all test specimens with the mean ratio of experimental to predicted being 1.54 with a COV of 12.6% for the Thornton model and a mean ratio of 1.11 and COV of 13% for the modified Thornton model. The modified Thornton model was conservative for most cases except when the gusset slenderness ratio was greater than 75.

2.4.7 Walbridge, Grondin and Cheng (2005)

Walbridge et al. [2005] present the results of a suite of finite element analyses performed on brace-gusset plate assemblies that partially included the effect of the beams and columns but did not realistically include opening and closing of the joint due to frame action. Geometric nonlinearity was considered. A parametric study was performed with the calibrated model and showed that more energy dissipation results when the gusset plate is designed to buckle prior to brace buckling (weak gusset - strong brace). It was also shown that the performance was similar regardless of the whether the gusset plate or brace yielded first in tension. It was also shown that the post-buckling strength of the gusset plates stabilized after the initial

drop in load immediately after plate buckling and that the degradation in compressive capacity was much greater when brace buckling occurred.

2.5 Braced Frame System Research

2.5.1 SCBF experiments

Uriz (2005) SCBF experiment

Uriz [2005] tested the two-story, one-bay SCBF with HSS6x6x3/8 braces in a chevron configuration shown in Fig. 2.3 at the University of California, Berkeley (test denoted as SCBF1). The braces were the same in both stories and the likelihood of soft story formation was studied. Tapered gusset plates were used at the corner joints with a $2t$ linear offset. The frame was designed by a practicing professional engineer and was code compliant according to the 1993 AISC LRFD and the 1997 AISC Seismic Design Provisions. The flanges were not connected to the columns with welds and it was assumed in the design of the column that the beam was "pinned" to the column in order to assess the effect of frame action not accounted for in the design. To allow for direct comparison between this test specimen and BRBF tests Uriz performed, the same loading protocol was used for all tests. The loading protocol outlined in the AISC/SEAOC Recommended BRBF Provisions [SEAOC-AISC, 2001] was used and consisted of monotonically increasing displacement levels with six, four or two cycles at each displacement level.

This test highlighted the problems that may arise when the system is designed as a truss, ignoring rigidity supplied by the gusset connection. This test also highlighted the potential of these systems to soft-story formation, as a soft-story developed in the lower story after brace buckling. Brace fracture began in this story at a story drift ratio of approximately 1.2% and the entire cross-section fractured at approximately 2.1%. Following this, considerable damage occurred in the beams and columns at the second story joints which included column web yielding, cracking of the beam web shear tab connected to the column and finally, fracture of the column flanges of both columns.

University of Washington and NCREE SCBF experiments (2005-2010)

Approximately 40 concentrically braced frame experiments were performed at the University of Washington (UW) between 2005 and 2010. Approximately 34 of these simulated a planar, one-bay, one-story subassemblage of a braced frame with conventional buckling braces [Johnson, 2005; Herman, 2007; Kotulka, 2007; Powell, 2010]. These tests allowed for the assessment of system performance and a parametric study of the important parameters affecting system behavior. These planar test specimens were a representative frame subassemblage from the prototype building shown in Figure 2.4a. Figure 2.4b shows the typical test specimen with members sizes used for the majority of the tests. Figure 2.5a shows a schematic of the test specimen in the testing rig with strongwalls at top and left of the figure and the actuator at the bottom right. The specimens were constructed and tested in the horizontal position. A photograph of the setup is shown in Figure 2.5b. Tables 2.1 through 2.4 give a description of each single-story test specimen including the connection details and design parameters.

Six planar, multi-story, one-bay by one-bay frames were also tested at NCREE. These included three, two-story frames [Clark, 2009] and three, three-story frames [Lumpkin, 2009]. An example of Clark's tests specimens is shown in Fig. 2.6 while an example of Lumpkin's test specimens is shown in Fig. 2.7. Tables 2.6 and 2.7 describe the test parameters in greater detail.

The loading protocol used for the majority of the above tests was based on ATC-24 [1992] and the SAC loading protocol [SAC, 1997]. This protocol is shown in Figure 2.8 and is symmetric and centered at zero displacement with increasing displacement every two cycles except for the first six cycles and cycles 9 through 14. The increment in displacement is a function of the drift at which first yield or buckling occurs.

The experiments were used to study a number of parameters and are listed below:

- Brace offset method (linear or elliptical) and clearance dimension
- Gusset shape (rectangular or tapered)
- Gusset weld type (fillet or CJP) and weld reinforcement at reentrant corner
- Gusset plate thickness
- Brace type (HSS5x5x3/8 or W6x25)

- Brace configuration (single-diagonal, single story X)
- Beam size
- Net section reinforcement
- Brace connection type and length
- Beam and gusset connection type to column
- Loading protocol (far-field vs. near-field earthquake)

The general behavior of the SCBF test specimens during the early drift ranges was similar. The majority of the frames failed initially by brace fracture but other less than desirable failure modes were observed. These included failure of the gusset welds and net section fracture of the braces. Additionally, secondary failure mechanisms occurred soon after brace fracture in a number of the specimens. Table 2.8 lists the primary mode of failure for the tests specimens along with any other detrimental failures that occurred soon after the initial failures.

The two most important outcomes of these tests were the development of the Balanced Design Procedure (BDP) for SCBFs and the validation of the use of an $8t$ elliptical brace offset. Both of these will be described in more detail in Chapter 3.

The drift capacities of the UW test frames ranged from 1.32 to 5.89%. The drift capacity is defined as the sum of the largest absolute value of the negative and positive drifts achieved prior to or during the last complete cycle before brace fracture. The brace offset that is currently used by designers ($2t_p$ linear offset, UFM) performed relatively poorly with a drift capacity of 2.75% (HSS01) and 3.5% (HSS12). Figure 2.9 compares the response of an SCBF designed according the current state-of-the-practice (HSS01) with an otherwise similar SCBF designed with an elliptical brace offset and the BDP (HSS05). The increased energy dissipation of HSS05 relative to HSS01 is clear from the figure and this dramatic difference was attributed to the improved design philosophy.

Larger gusset plates were observed to provide more fixity at the joint and caused more yielding and damage to the beams and columns. Tapered gussets were observed to be more flexible but resulted in more damage to the interface welds. Ductile weld tearing at the gusset interface occurred in a large number of the tests. HSS01 and WF23 failed by interface weld tearing and brace fracture never occurred. HSS01 had large gusset plates

designed by the current provisions while WF23 had large demands along the gusset plate interface due to the use of the wide-flange brace which fractures at larger story drift ratios due to smaller plastic strain concentration relative to that which occurs at the corners of HSS sections.

Powell X-configured SCBF experiments

Powell performed two tests on a single-story X-configuration with HSS3x3x1/4 braces using the same beams and columns and test setup as the typical UW experiments shown in Figures 2.4 and 2.5. The primary objectives of the experiments were: (1) to investigate the effect of the brace splice detail at the X-intersection on the behavior and performance of this type of configuration; (2) to inform the design of this connection for the author's 3D SCBF experiment and (3) to provide a comparison between planar loading and the out-of-plane loading done by the author and discussed in the following chapter. The frames are denoted as HSS30 and HSS31 and the frame geometry and members sizes are shown in Fig. 2.10 and photos of each specimen test setup are shown in Figs. 2.11a and 2.11b for HSS30 and HSS31, respectively. The frames are exactly the same except for the brace splice detail at the X-intersection and the braces in HSS30 were not supplied with net section reinforcement at the end slots. The splice detail for HSS30 (Fig. 2.10c) utilizes a sandwich plate which provided continuity across the joint. A gap of 2" between the end of the spliced brace and the continuous brace was provided for erection tolerances only as an offset providing rotation ability is not desirable for a connection designed to provide continuity across the joint. The splice detail for HSS31 (Fig. 2.10d) utilizes a single-plate connection passing through a slot in the continuous brace and slotted tube connections for the continuous brace. This connection provides very little flexural continuity as the flexural stiffness of the brace is approximately 70 times larger than the flexural stiffness of the splice plate. The ends of the spliced braces were offset from the continuous brace by a distance of 1.5" ($4t_p$) to accomodate the brace end rotation. The design limit states for the center splice connection are the same as those used for the corner gusset plates. The weld connecting the center splice plate to the continuous brace in HSS31 is required only for erection purposes.

The beam flanges and webs were attached to the column flanges with complete joint penetration welds providing fully restrained beam-column connections at all four locations. The beams and columns were designed according to capacity principles based on the chosen brace size with additional demands determined from structural analysis. The resulting beam demand-capacity ratio (DCR) was 0.7 while the column DCR was 1.0.

The $8t_p$ elliptical offset and the BDP were used for the design of the corner gusset plates at the beam-column joints. The BDP was also used for the splice connections in both the HSS30 and HSS31 frames. The weld sizes connecting the gussets to the framing elements were sized for the strength of the gusset plate; this follows the BDP and requires welds that are larger than those estimated by the Uniform Force Method [AISC, 2005b]. Fig. 2.10b shows the corner gusset plate with the $8t_p$ elliptical brace offset. See Section 3.4 for a complete discussion of the BDP and the state-of-the-practice design methodology.

The wide-flange columns and beams in the frame were specified as ASTM 992 steel with a nominal yield strength of 50 ksi. The HSS3x3x1/4 were specified as ASTM A500B with a nominal yield strength of 46 ksi. The gusset plates were specified as ASTM A572 with a nominal yield strength of 50 ksi. Table 2.5 indicates the measured material properties of the members.

Each frame was monitored with nearly 100 instruments each including strain gauges, linear variable displacement transducers (LVDT), and string potentiometers. The strain gauges were placed on the beams and columns and used to estimate the moments and corresponding story shears resisted by these elements. Additional strain gauges were placed on the braces to estimate the brace axial forces and monitor the strain ranges experienced by the braces. String pots were used to monitor the brace buckling behavior and magnitudes of out-of-plane displacement. LVDTs and string pots were used to measure support slippage, estimate story drifts along with beam and column average rotations at the joints (Powell 2008). Both specimens were loaded using the displacement history shown in Figure 2.8.

Brace buckling was detected in both tests at story drift ratios between 0.2% and 0.34%. The braces in tension provided lateral support at the center of the braces in compression. As a result, the continuous braces formed a mode-2-type buckled shape (S-shape) for both specimens. This mode-2-type buckled shape (S-shape) was also observed for the spliced

braces in HSS30 (sandwich plate connection) as shown in Fig. 2.12b while a different compressive response was noted for Specimen HSS31. The connection at the brace intersection for HSS31 did not provide continuity and only one-half of the spliced brace buckled in compression while the other half remained straight as shown in Fig. 2.12a. Therefore, inelastic damage was concentrated in one-half of the system similar to the author's frame behavior.

The brace response changed at story drifts larger than 1.2%. At zero percent story drift, when the buckled brace was returning from a relatively large story drift excursion, the braces that had buckled did not fully straighten. This resulted in a different progression of buckling for the opposite brace. That brace deformed out-of-plane at the brace intersection as it began to sustain compressive demand, resulting in an initial mode-1-type shape. This shape then transitioned into the S-shape when the opposite, previously buckled brace became straight and stiff enough to resist the tensile force.

One effect of providing full continuity across the center splice is that torsional forces and deformations resulting from the opposing brace (as shown in Fig. 2.12c) resulted in gusset plate distortions such as those shown in Fig. 2.13a. This places increased demand on the gusset plate and the interface welds between the gusset and framing members. This increased demand appeared to exacerbate the interface tearing shown in Fig. 2.13b. While some torsion demands were transferred into the spliced brace in HSS31, it was more limited than HSS30. As a result, tearing at the interface between the gusset plate and the framing elements were observed earlier in HSS30 than HSS31, 1% vs. 1.5% SDR. The lengths of the torn region were comparable at and after brace fracture in both specimens. These tears occurred in three to four locations in each test and were on the order of 25-50mm at brace fracture at approximately 2% SDR (see Fig. 2.13b) and grew to 100mm in two locations at approximately 4% SDR.

The behavior of the beams and columns in both test frames was similar. Flaking of the column whitewash was concentrated near the joints, in the flanges on the opposite side of the gusset plates with minor yielding at the beam flanges at the CJP welds. Column panel-zone yielding was also observed in both frames along with local flange buckling (LFB) at the base. This LFB was observed at approximately 2.3% SDR in each test and occurred after brace fracture. It should be noted that the W12x72 columns did not satisfy the limiting

flange width-thickness ratios for columns in seismic applications [AISC, 2010] but resistance was not noticeably affected after LFB occurred.

Figure 2.14 shows the global force-displacement responses for HSS30 and HSS31. The hysteretic loops are relatively full and display the pinching typical of buckling brace systems. The total story drift range in the last complete cycle prior to brace fracture, defined as the drift capacity in this work, was 3.83% for both specimens. Previous studies by Tremblay et al. [2003] have shown that single-story X-braced configurations exhibited less ductility capacity than single-story diagonal or double-story X-configurations. The drift capacities of Powell's X-frames were less than 70% of the planar frame drift capacities tested at UW and NCREE discussed in the previous section. The planar frames that exhibited less ductility than the single-story X-frames were those detailed with the $2t$ linear brace offset or failed through some mechanism other than brace fracture.

Following brace fracture, both tests were continued to assess their post-fracture behavior. In Figs. 2.14a and 2.14b, the force-deformation response following brace fracture is shown with dashed lines. It can be seen that in the positive drift range, the strength of HSS30 has been reduced by approximately 60% from its peak strength, while in the other direction the strength either remains similar or exceeds the pre-fracture strength. This is logical as the unfractured brace is in compression in the positive region and in tension in the negative drift region. The strength of the frame in the positive direction is primarily due to the strength of the moment frame. In the negative direction, the strength results from a combination of moment frame action and the response of the unfractured brace in tension. The frame was able to reach 4.2% SDR in the negative region without brace fracture occurring before the test was stopped due to actuator stroke limitations. Similar behavior was observed in HSS31 following brace fracture except that this frame was not pushed as far following fracture.

The ability of the frames to maintain the level of strength they did following brace fracture is encouraging and lends support to the argument of providing a moment connection between the beams and columns in the braced frame or elsewhere in the building. Additionally, a new plastic hinge forms in the unfractured brace at a different location than the first plastic hinge and may prolong the life of the remaining brace as shown by the large

drifts attained in HSS30 following fracture of the first brace.

2.5.2 BRBF experiments

Uriz BRBF experiments (2005)

In addition to experiment SCBF1 described earlier, Uriz [2005] performed experiments at the University of California, Berkeley on three one-story, one-bay BRBFs. Figure 2.15 shows the test frame setup for the BRB tests. Test 1 consisted of two BRBs in a chevron configuration and Tests 2 and 3 consisted of a single BRB in a diagonal configuration. The same test frame was used for all three tests and the upper story was designed to remain elastic and transfer the shear from the actuator into the BRB story. The BRBs were the Unbonded Brace^{TM} manufactured by Nippon brace. The cores of Tests 1 and 2 had a rectangular cross section with an area of 6.33 in^2 and yield strength of 40.9 ksi. The core of Test 3 had a cruciform cross section with an area of 11.69 in^2 and yield strength of 40.9 ksi. The same loading protocol used in the SCBF test was used for these BRBF tests.

The first two BRBFs tested sustained maximum story drifts of approximately 2 and 2.3% before the tests were stopped. Neither BRB fractured but there was significant column yielding during both tests and gusset plate weld tearing occurred during the second test. During the third test, beam flange tearing occured at the CJP connection to the column where the BRB was not connected and this occurred at a story drift of -1.7%. During the next excursion out to 2.6% story drift, the bottom beam flange fractured at the gusset edge at 1.7% story drift and caused the BRB to rotate out of plane and preventing the BRB from reaching its full capacity (Fig. 2.16). This happened at story drifts less than those expected during the Design Basis Earthquake suggesting that the collapse prevention limit state may not be satisfied during an extreme event. This is despite the fact that the maximum ductility achieved by the BRB during this test was 14 and comparable to those achieved during component tests by Merritt et al. [2003] and Black et al. [2002] as a comparison between the values for Uriz in Table 2.9 and those for the component tests in Table 2.10 shows. Additionally, the cumulative ductility achieved by the BRB during this test was 219 which is larger than the requirement of 200 per the Seismic Provisions [AISC,

2010] but much less than those achieved in the component tests (Tables 2.9 and 2.10). One very imporant point regarding these detrimental behaviors during the third test is that this was the third test on the same frame and the previous tests had subjected the frame to a relatively large number of inelastic cycles. Additionally, gusset plate removal and rewelding occurred at the location of the beam fracture and the backing bar was not removed on the gusset plate to beam CJP weld. All of these conditions may have contributed to the beam fracture.

Christopolus (2005)

Christopolus [2005] tested five BRBFs with the same configuration and beam and column sizes as that shown in Fig. 2.4 for the SCBF tests. The braces were Unbonded Braces manufactured by Nippon Steel, had a rectangular core cross section with an area of 4.77 in^2 and nominal yield strength of 46 ksi (44.7 actual) for a yield capacity of 219 kips. The parameters studied included tapering of the gusset plate, splice design of bearing bolts versus slip critical, orientation of core relative to plane of frame and displacement history. The parameters for each test are shown in Figure 2.17.

None of the BRBs fractured during these experiments due to excessive beam yielding, instabilities or flange fracture which caused out-of-plane rotation of the BRB and plastic hinge formation in the BRB core just outside of the casing (Fig. 2.18). In four of the five tests, the maximum story drifts attained prior to this detrimental behavior ranged between 2.2 and 2.4% which are only slightly above that expected during a design event suggesting that these frames may not satisfy the collapse prevention limit state during a maximum considered earthquake event. This detrimental behavior occurred in the other specimen following attainment of a maximum story drift of 3.3% which is approaching that expected during an MCE event. It should be noted that this final specimen's drift protocol was not symmetric like the previous four tests were but only reached -0.9%.

As shown in Table 2.9, the maximum cumulative ductilities achieved during the tests ranged between 19 and 22 which are larger than those achieved in the component tests listed in Table 2.10. Additionally, the cumulative ductilities achieved during the experiments

ranged between 333 and 377 which are larger than the minimum value of 200 required by the Seismic Provisions [AISC, 2010]. It is obvious that system performance may be poor even if the ductilities reached are relatively large.

Fahnestock, Sause, Ricles (2006)

Fahnestock et al. [2006] performed experiments on a 0.6 scaled, four-story BRBF in a chevron configuration. Figure 2.19a shows the elevation of the test frame along with member sizes and brace yield forces. The braces were PowerCat BRBs manufactured by Star Seismic. These braces are manufactured with end collars to prevent instability of the core when it extends outside of the concrete restraining material. Additionally, the braces are attached to the gusset plates with pins allowing rotation and minimal moment transfer to the gusset plates. Given the behavior of BRBs due to frame action seen in previous research, the beam connection to the frame allowed for axial load transfer with minimum moment transfer. This detail is shown in Figure 2.19c.

The test frame was loaded at each floor level by hydraulic actuators and was subjected to four levels of the Saticoy 180 record from the 1994 Northridge Earthquake followed by a quasi-static cyclic loading protocol. The first four tests were performed using the hybrid pseudo-dynamic method with the explicit Newmark algorithm to solve the equations of motion. The three levels of intensity were intended to represent the demand imposed by an earthquake with a 50% probability of exceedence in 50 years (50/50, FOE), a 10/50 (DBE), and a 2/50 (MCE). The final pseudo-dynamic loading was meant to represent an aftershock event (AE) and was 4/5 of the DBE level. Finally, a quasi-static cyclic loading protocol was applied to the test frame.

There was no brace fracture or any local or global instabilities observed during the earthquake simulations, and the maximum story drift ratio observed during the 2/50 event was 4.8%. The maximum story drift range during the PSDT was approximately 5.5%. All BRBS except those at the 4th story and one in the 1st story fractured during the quasi-static test and the story drift ranges prior to or in the last complete cycle before BRB fracture were relatively large, between 6.5% and 7.1%.

This frame outperformed all of the other BRBF systems tests reviewed here and no instabilities occurred prior to brace fracture. This can potentially be attributed to a number of factors including: (1) the end detail of the BRB which includes a collar that helps stabilize the core region outside of the casing, (2) the pin connection of the BRB to the gusset plate and (3) the beam splice at the edge of the gusset plate which limits the amount of frame action that occur. Interestingly, the beam splice was changed to a rigid splice at the 1st floor prior to the quasi-static cyclic test and no negative impact due to this was observed. Very little damage to the beams, columns and gusset plates were observed during any of the PSDT; only some slight yielding at the column bases and yielding of the WT beam splice. During the quasi-static cyclic tests, there was considerable yielding at the beam splice that was changed to a rigid connection. This is expected as there is considerable more frame action with the rigid beam to column connection.

As shown in Table 2.9, the maximum ductility demands of the BRBs ranged between 18 and 26 and the cumulative ductility demands ranged between 388 and 453. The ductility demands were comparable to those seen in Christopolus' tests and greater than the component tests listed in Table 2.10. Additionally, the cumulative ductilities are greater than the minimum of 200 prescribed by the Seismic Provisions [AISC, 2010].

2.6 Continuum Finite Element Simulations

The following three subsections on SCBF and BRBF simulations are discussed in some detail as they relate to the BRBF simulations discussed in Chapters 7 and 8.

2.6.1 Yoo (2006)

Concurrent with the single-story frame tests at UW by Johnson [2005] and Herman [2007], Yoo [2006] performed a number of finite element simulations on single and multi-story braced frames. The simulations were performed in ANSYS and were validated by the UW experiments. The simulations were performed with a number of goals including:

- The development of accurate models to predict braced frame behavior at the system level

- Aid in the design of the ongoing experiments at UW
- Perform parametric studies to study the impact of various design parameters on the ductility of braced frame systems
- Extend the analysis to systems that could not be economically tested
- Verification of brace fracture and gusset tearing models to assess the strength and ductility of these structures under seismic loading

The ANSYS models used 4-node quadrilateral shell elements with six degrees of freedom at each node in addition to including transverse shearing deformations. Reduced integration was used along with large-displacement geometric nonlinearity to capture local and global buckling. Material yielding was modeled with kinematic and isotropic hardening laws (multi-linear was used for the first three tests and bilinear for the subsequent tests). The typical mesh size at areas of expected inelasticity was 1" by 1" These areas included the brace plastic hinge location, gusset plates, and beam and column joints. Figure 2.20 shows the mesh along with a comparison of the behavior between the FEA and experiments. Figure 2.20c compares the out-of-plane brace displacement while Figure 2.21 shows the comparison of the force-displacement response of two of the experiments and the FE simulation. The figures show that the simulation accurately modeled the global behaviors of those two tests with differences less than 8%.

Prediction of brace fracture at the plastic hinge and weld tearing at the gusset plates were of prime importance in this study. This topic has been studied by researchers in recent years and a typical method of predicting this phenomenon is through evaluation of the stress and strain environment at potential fracture locations. In this case, the equivalent plastic strain (PE) was used to predict when tearing or fracture would occur by correlating the strain at the critical locations with the occurrence of tearing and fracture in the experiments. An example of this correlation is shown in Figure 2.22 for a number of experiments and show that the PE is bracketed by a relatively narrow range and can be used to make brace fracture predictions in extended simulations with similar mesh sizes as that used to calibrate the model.

The results of the parametric studies using the above fracture models resulted in a number of methods to increase system ductility. The gusset plate size must strike a balance between brace fracture and gusset interface weld tearing. A relatively large, stiff and strong gusset plate reduces the demand on the interface welds but increases the plastic strain at the brace plastic hinge causing brace fracture at lower drift levels. In contrast, a relatively small, flexible gusset plate reduces the strain in the brace while increasing the demand at the gusset interface. It was shown that a gusset plate designed using an $8t_p$ elliptical clearance strikes this balance. Tapered gusset plates resulted in decreased local yielding in the beam and column elements adjacent to the gusset and resulted in similar drifts at brace fracture to well-designed rectangular gussets but the demand at the interface was increased relative to rectangular gussets. Additionally, steeper braces had a greater potential for brace fracture at lower drift levels.

2.6.2 Wigle and Fahnestock (2010)

Wigle and Fahnestock [2010] performed nonlinear finite element analysis of the 0.6-scale BRBF tested at Lehigh [Fahnestock et al., 2006]. The intent of the analyses was to study the effect of various connection parameters on the local stress and strain environment at the connection region to improve the global behavior of BRBF systems. The third story of the test frame was studied in detail as the FEM model in Figure 2.23 shows. The continuum elements were modeled using three-node and four-node shell elements that consider transverse shear deformation, finite member strain and large rotations. Material yielding was modeled with the von Mises model with isotropic and kinematic hardening. The BRB restrainer was modeled as an element with negligible axial stiffness and a flexural stiffness equal to the HSS restrainer and tied to the nodes of BRB core. Outside of this detailed area, the BRBs were modeled with nonlinear spring elements while the beams and columns were modeled with frame elements with lumped plastic hinges. Welded interfaces were modeled with ties or shared nodes and bolt slip was not modeled. No description was given as to how the BRB connection pin at the gusset plate was modeled.

The model was verified by comparing the global force-displacement and BRB force-

displacement behavior with the experimentally observed behavior. Following calibration, 12 different analyses were performed. Three different types of BRB-gusset connections were analyzed as shown in Figure 2.24 along with two different beam connections. The beam connections consisted of rigid connections (a and c) and pinned spliced connections (b). Additionally, gusset thicknesses of 1.0" and 0.5" were analyzed.

The von Mises stress and the equivalent plastic strains were studied at regions 1, 2, 3 and 4 shown in Figure 2.24c for each analysis case. Figure 2.25 shows these for each continuous beam case at the gusset plate edges. The effect of frame action can clearly be seen in these figures as the stress and stress increase significantly at the edge of the gusset plates. The type of beam connection has a considerable effect on the stress and strain environment at the gusset plate connections to the framing elements. The spliced connection results in stresses due only to brace action as expected.

2.6.3 Ozcelik and Okazaki (2010)

Ozcelik and Okazaki [2010] performed finite element simulations of the BRBF tested by Christopolus [2005]. The beams, columns and braces were modeled with shell elements and material kinematic and isotropic hardening using ABAQUS. Geometric nonlinearity was used to capture P-Delta effects. Figure 2.26 shows the test frame and members along with the mesh. As shown in the figure, a relatively dense mesh was used in the beams and columns at locations of expected nonlinearities. As the total length of the brace is expected to yield and instabilities to occur in the end regions, a dense mesh was used for the whole brace.

The material and geometric nonlinearities of the BRB dominates the behavior of the frame, especially the instabilities of the core just outside the casing at larger deformations. Due to the latter behavior, it was imperative that the restraint provided by the casing and the buckling of the core end be modeled accurately. Therefore, a single truss element could not be used to model the BRB. The method for accomplishing this is shown in Figure 2.27. Two restrainers are tied to the brace with Restrainer I bracing the yielding core and having near zero axial stiffness and a flexural stiffness equal to the restraining concrete and tube.

Restrainer II braces the end region of the core and has near zero axial stiffness and a flexural stiffness on the order of 1/400 to 1/20 to that of Restrainer I.

The analyses were fairly successful relative to previous attempts. Figure 2.28 shows the global hysteretic curves for the experiment and for the simulation. The peaks loads in tension and compression are overestimated and by as much as 40% in compression. The drift at which BRB plastic hinging occurs is accurately estimated however the load is not. Local behaviors such as beam and column web yielding and flange buckling were adequately captured as shown in Figure 2.29. The inaccuracies in the simulations can be attributed to a number of factors including but not limited to:

- Inaccurate BRB core cyclic material model.
- Difficulty in accurately modeling the experimental boundary conditions at the loading beam, column bases, and lower beam shear transfer area.
- The Restrainer II model which attempts to account for the changing unbraced length of the core outside of the casing.

Table 2.1: UW SCBF experimental parameters [Johnson, 2005]

Specimen Mark	Brace	Gusset plate parameters				Brace offset	Comments
		Shape	Thick. (in.)	Interface connection	Size b x d (in.)		
HSS01	HSS5x5x3/8	R	0.5	1/4 fillets	34 x 30	2t L	State-of-the-practice connection design
HSS02	HSS5x5x3/8	R	0.5	1/2 fillets	25 x 21	6t E	Sim to HSS01 but with elliptical clearance
HSS03	HSS5x5x3/8	R	0.375	7/16 fillets	25 x 21	6t E	Sim to HSS02 but with thinner gusset plate
HSS04	HSS5x5x3/8	R	0.375	7/16 fillets	25.5 x 21.4	10t E	Shorter brace to gusset connection than HSS03 to reduce Whitmore yield capacity. Increase of brace offset to reduce gusset compression capacity.
HSS05	HSS5x5x3/8	R	0.375	5/16 fillets	25 x 21	8t E	Similar to HSS but with smaller gusset interface welds and brace offset

Table 2.2: UW SCBF experimental parameters [Herman, 2007]

Specimen Mark	Brace	Gusset plate parameters				Brace offset	Comments
		Shape	Thick. (in.)	Interface connection	Size b x d (in.)		
HSS06	HSS5x5x3/8	R	0.375	1/4 fillets	25 x 21	8t E	Gusset reentrant corner weld reinforcement of 3/8 in. for 4 in.
HSS07	HSS5x5x3/8	R	0.875	3/4 fillets	28.5 x 24.5	6t E	Thick gusset plate
HSS08	HSS5x5x3/8	R	0.375	7/16 fillets	23.5 x 19.5	3t E	Small elliptical clearance
HSS09	HSS5x5x3/8	R	0.5	CJP	25 x 21	6t E	Thicker plate with CJP interface welds
HSS10	HSS5x5x3/8	T	0.5	1/2 fillets	18.7 x 16.25	6t E	Tapered gusset plate
HSS11	HSS5x5x3/8	R	0.875	CJP	28.5 x 24.5	6t E	Thick gusset plate, large W16x89 beam and CJP interface welds

Table 2.3: UW SCBF experimental parameters [Kotulka, 2007]

Specimen Mark	Brace	Shape	Gusset plate parameters				Comments
			Thick. (in.)	Interface connection	Size b x d (in.)	Brace offset	
HSS12	HSS5x5x3/8	R	0.5	CJP	34 x 30	2t L	HSS01 with CJP interface welds
HSS13	HSS5x5x3/8	T	0.5	CJP	18.7 x 16.25	6t E	Similar to HSS10 but with CJP interface welds
HSS14	HSS5x5x3/8	R	0.375	7/16 fillets	25 x 21	7.7t E	No net section reinforcement on brace
HSS15	HSS5x5x3/8	R	0.375	7/16 fillets	21 x 17	6t E	Reduced length (11.25 compared to typical 14.75 in.) brace-gusset weld but larger throat (7/16 in. relative to 5/16). No net section reinforcement.
HSS16	HSS5x5x3/8	R	0.375	7/16 fillets	25 x 21	see comments	Bolted splice brace to gusset connection, 2t offset in splice plate between gusset plate and brace.
HSS17	HSS5x5x3/8	T	0.375	3/8 fillets	18.7 x 16.25	8t E	Thinner, tapered gusset plate

Table 2.4: UW SCBF experimental parameters [Powell, 2010]

Specimen Mark	Brace	Gusset plate parameters				Brace offset	Comments
		Shape	Thick. (in.)	Interface connection	Size b x d (in.)		
HSS18	HSS5x5x3/8	R	0.375	3/8 fillets	25 x 21	8t E	Bolted beam web (shear only) connection to column at gusset plate connection.
HSS19	HSS5x5x3/8	R	0.5	1/2 fillets	23 x 21.6	6.8t E	Bolted splice brace to gusset connection with two WTs and splice plate. Failed by splice plate fracture.
HSS20	HSS5x5x3/8	R	0.375	3/8 fillets	24 x 21	6.8t E	Bolted (18-3/4 A490) end plate beam and gusset connection to column, beam flanges not welded to end plate, only the web (flanges beared against the column)
HSS21	HSS5x5x3/8	R	0.375	3/8 fillets	24 x 21	6.8t E	Bolted (14-3/4 A490) end plate beam and gusset connection to column, beam flanges not welded to end plate, only the web (flanges beared against the column)
HSS22	HSS5x5x3/8	T	0.375	3/8 fillets	18.7 x 16.25	9t E	Bolted beam web (shear only) connection to column at gusset plate connection.
WF23	W6x25	R	0.375	3/8 fillets	21.9 x 20	8t E	Wide flange brace. Failed simultaneously by fracture of the NW gusset interface welds and shear tab connection.
HSS24	HSS5x5x3/8	R	0.375	3/8 fillets	25 x 21	8t E	Welded flange, bolted web beam to column connection at gusset plate.
HSS25	HSS5x5x3/8	R	0.875	CJP	28.5 x 24.5	4t E	Thick gusset plate and large W16x89 beam WFWW, no net section reinforcement.
HSS26	HSS5x5x3/8	R	0.875	CJP	28.5 x 24.5	4t E	HSS25 with near-fault loading history
HSS30	HSS3x3x1/4	T	0.25	1/4 fillets	11.7 x 9.25	8t E	Single-story, X-configuration. Sandwich plates at brace splice provides full continuity.
HSS31	HSS3x3x1/4	T	0.25	1/4 fillets	11.7 x 9.25	8t E	Single-story, X-configuration. Single through-plate at brace splice provides little continuity.

Table 2.5: Wide flange and HSS material properties for HSS30 and 31

Shape	Measured Properties	
	F_y (ksi)	F_u (ksi)
W12x72	56	70
W16x45	61	76
HSS3x3x1/4	65	82

Table 2.6: TCBF1 test frame parameters [Clark, 2009]

Specimen Mark	Brace	Gusset plate parameters					
		Shape	Thick. (in.)	Interface fillet weld	Size (in.)	Edge stiffeners	Brace offset
TCBF1-HSS-R	HSS5X5X3/8	R	0.39	1/2”	19.4 x 24.4 (base corner)	None	8t E
		R			23.8 x 19.6 (beam middle)	1/2” all around	
		R			23.6 x 19.7 (upper corner)	None	
TCBF1-WF-R	W6X25	R	0.39	1/2”	18.9 x 23.6 (base corner)	None	8t E
		R			23 x 19 (beam middle)	1/2” all around	
		R			22.9 x 19 (upper corner)	None	
TCBF1-HSS-T	HSS5X5X3/8	T	0.79	0.6”	9.1 x 17 (base corner)	None	2t L
		T			15.9 x 5 (beam middle)	None	
		T			15.6 x 9.1 (upper corner)	None	

Table 2.7: Test frame parameters [Lumpkin, 2009]

Specimen Mark	Brace	Gusset plate parameters					
		Shape	Thick. (in.)	Interface fillet weld	Size (in.)	Edge stiffeners	Brace offset
TCBF2-HSS	HSS5X5X3/8	R	0.375	0.39”	21.9 x 19.6 (2nd (floor corners)	None	8t E
		R			19 x 16.5 (beam middle)	None	
		R			19.6 x 23.9 (base corner)	None	
TCBF2-WF	W6X25	R	0.39	0.39”	21.5 x 19.1 (2nd (floor corners)	None	8t E
		R			21 x 16.3 (beam middle)	None	
		R			19.1 x 23.5 (base corner)	None	
TCBF2-IP	HSS5X5X3/8	R	0.7	0.6”	12.7 x 9.7 (2nd (floor corners)	None	2t L
		T			13.9 x 9.4 (beam middle)	None	
		T			9.5 x 14.2 (base corner)	None	

Table 2.8: UW SCBF experimental failure modes

Failure Type	No. of failures
Brace fracture (followed soon after by column fracture)	2
Brace fracture	29
Gusset weld interface failure	2
Brace net section fracture	1
Net section fracture of brace extension plate connecting to gusset	1

Table 2.9: Ductility capacities of BRBF *system* tests

Researcher	Specimen	P_y (kips)	BRB Ductility Demand	
			Max	Cumulative
Uriz (2005)	BRBF-1	259	16	326
	BRBF-2	259	14	299
	BRBF-3	478	14	219
Christopolus (2005)	REF BRBF	220	20	333
	BRB01	220	22	377
	BRB02	220	20	374
	BRB03	220	19	352
	BRB04	220	19	363
Fahnestock (2006)	4th story	30	23	438
	3rd story	60	23	453
	2nd story	80	26	444
	1st story	100	18	388

Table 2.10: Ductility capacities of BRB component tests

Researcher	Specimen	P_y (kips)	BRB Ductility Demand	
			Max	Cumulative
Merritt et al. (2003)	1	160	15	900
	2	250	15	600
	3	350	10	1600
	4	500	15	1100
	5	750	15	1300
	6	750	15	800
	7	1198	10	1000
	8	1202	10	1000
Black et al. (2002)	99-2	364	10	879
	99-3	486	10	279
	00-11	454	15	1045
	00-12	454	15	538

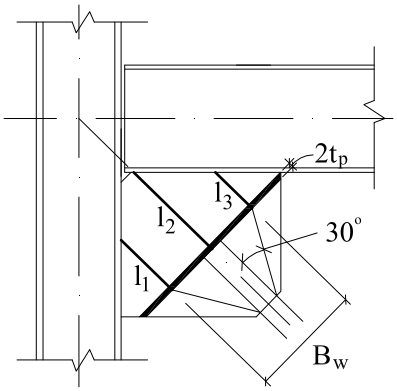

Figure 2.1: Gusset plate design parameters.

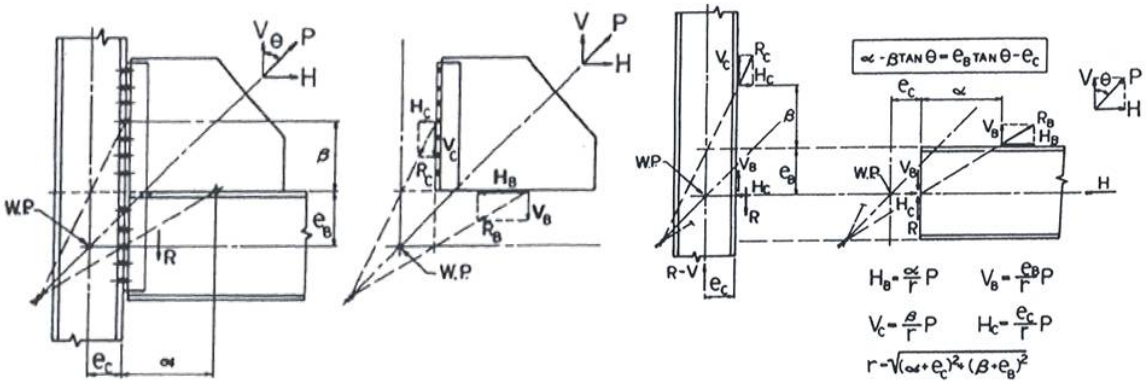

Figure 2.2: Uniform force method free-body diagram and geometry [Thornton, 1991]

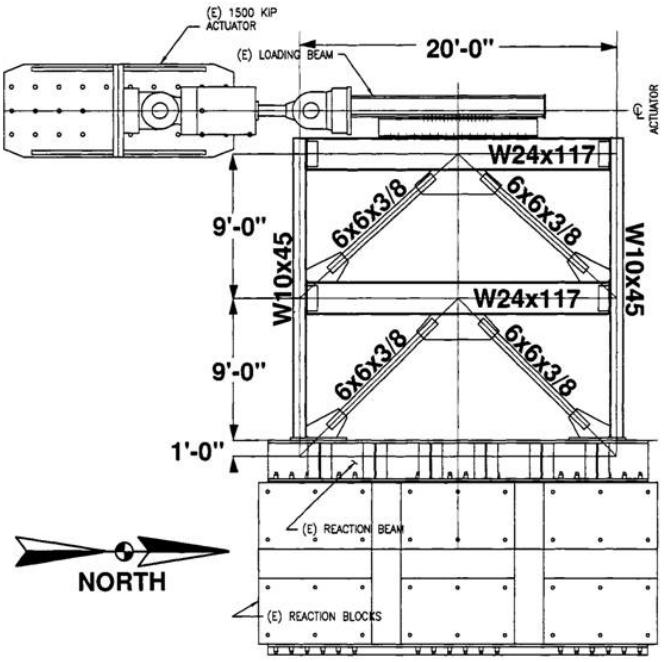

Figure 2.3: SCBF test frame [Uriz, 2005]

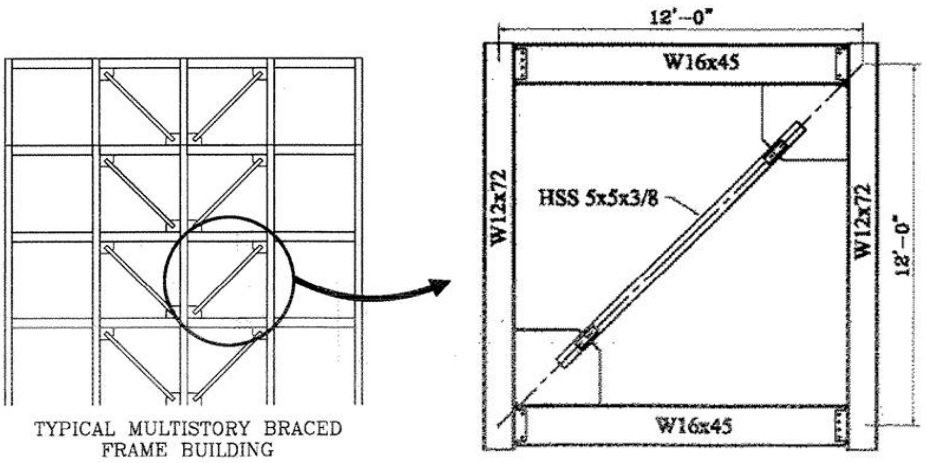

(a) (b)

Figure 2.4: UW tests: (a) prototype building; (b) test specimen and typical member sizes (Source: [Johnson, 2005])

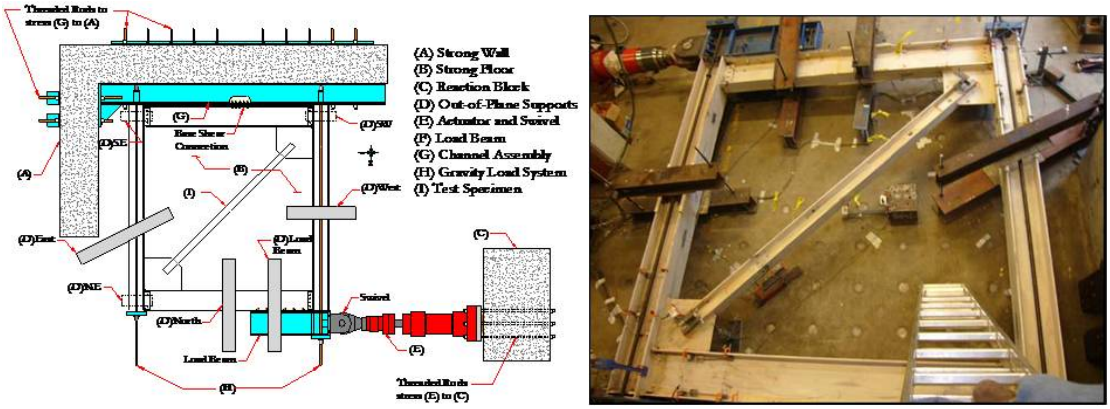

(a) (b)

Figure 2.5: UW experiments: (a) test setup schematic; (b) test setup photo (Source: [Powell, 2010])

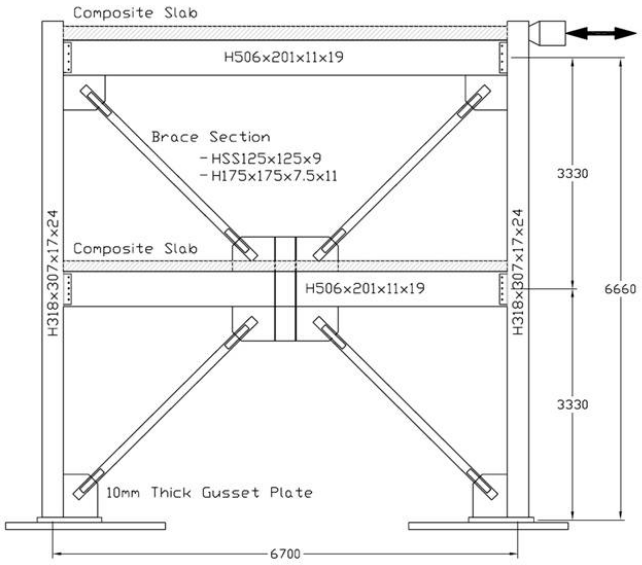

Figure 2.6: TCBF1 two-story test specimen [Clark, 2009]. Dimensions in mm, 1 in. = 25.4 mm. H506x201x11x19 equivalent to W21x68; H318x307x17x24 equivalent to W12x106; HSS125x125x9 equivalent to HSS5x5x3/8; HSS175x175x7.5x11 equivalent to W6x25.

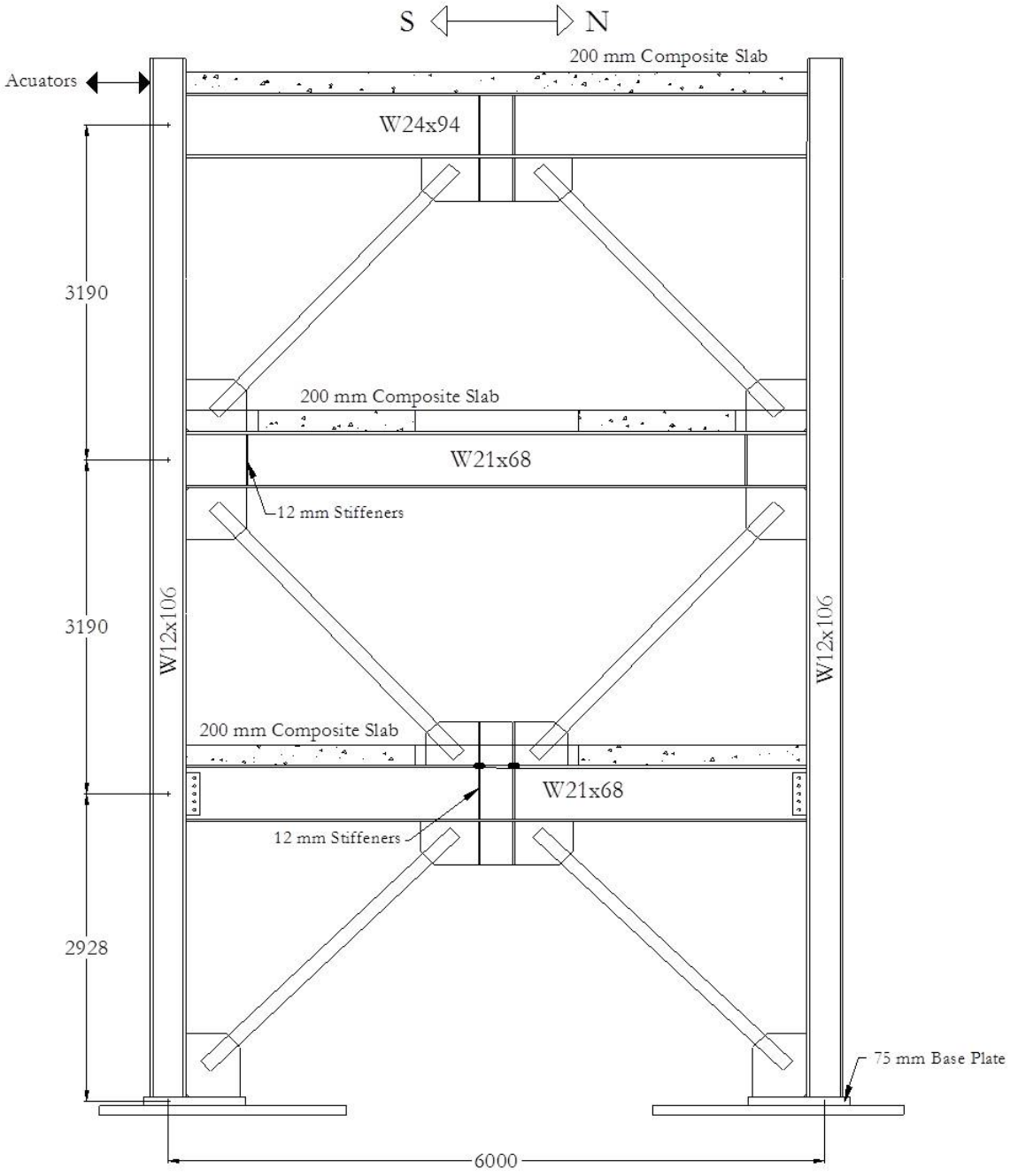

Figure 2.7: Three-story test specimen [Lumpkin, 2009]

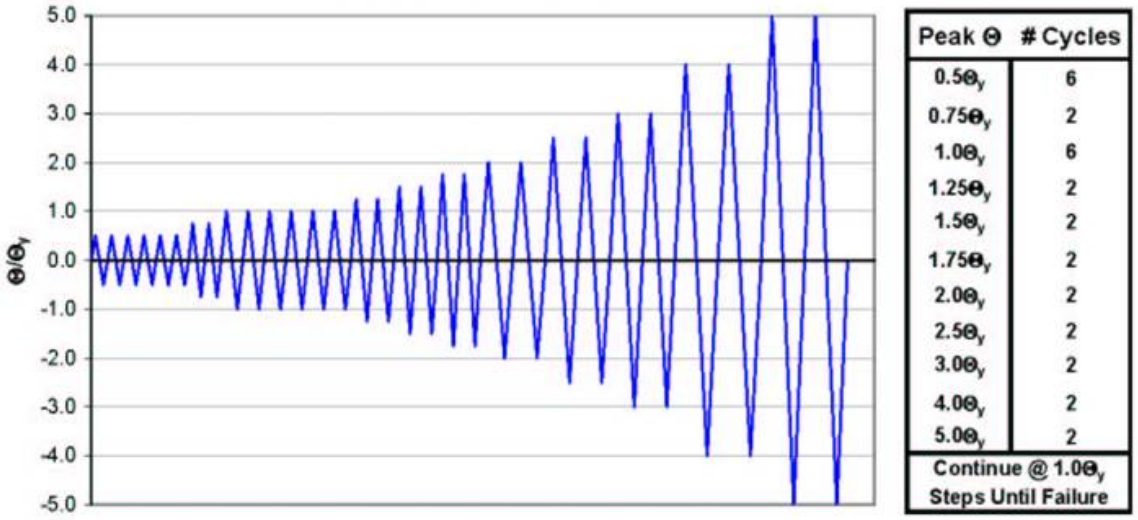

Figure 2.8: UW typical loading protocol [Johnson, 2005]

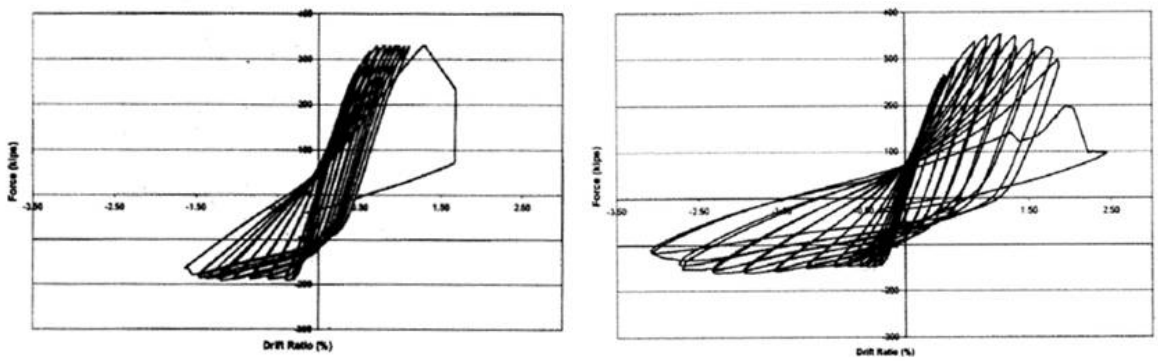

(a) UW HSS01 (b) UW HSS05

Figure 2.9: Force-displacement curves [Johnson, 2005]

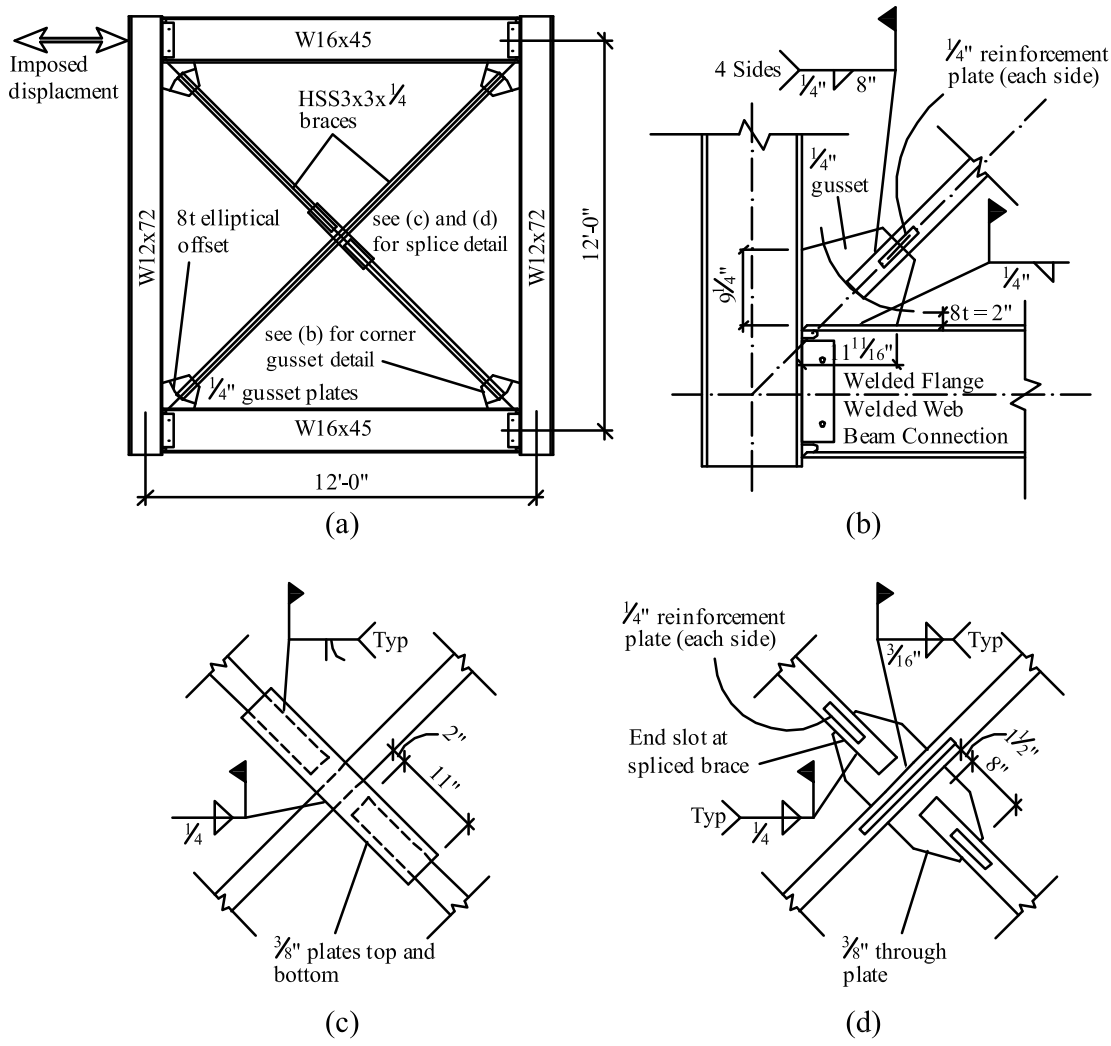

Figure 2.10: Single story X-configuration SCBF specimen details tested by Powell at UW: (a) frame elevation; (b) corner gusset plate connection; (c) sandwich plate HSS30 splice connection; (d) HSS31 slotted tube through-plate splice connection.



(a) HSS30 (b) HSS31

Figure 2.11: Single story X-configuration SCBF specimens



(a) (b)



(c)

Figure 2.12: Specimen behavior: (a) HSS31 unsymmetric buckling behavior with spliced braces in compression; (b) HSS30 symmetric buckling behavior; (c) HSS30 twisting deformation due to brace splice providing continuity.



(a) (b)

Figure 2.13: Specimen behavior: (a) Gusset deformation due to brace torsion in HSS30; (b) Gusset plate interface tearing at corner connection in HSS30 following brace fracture.

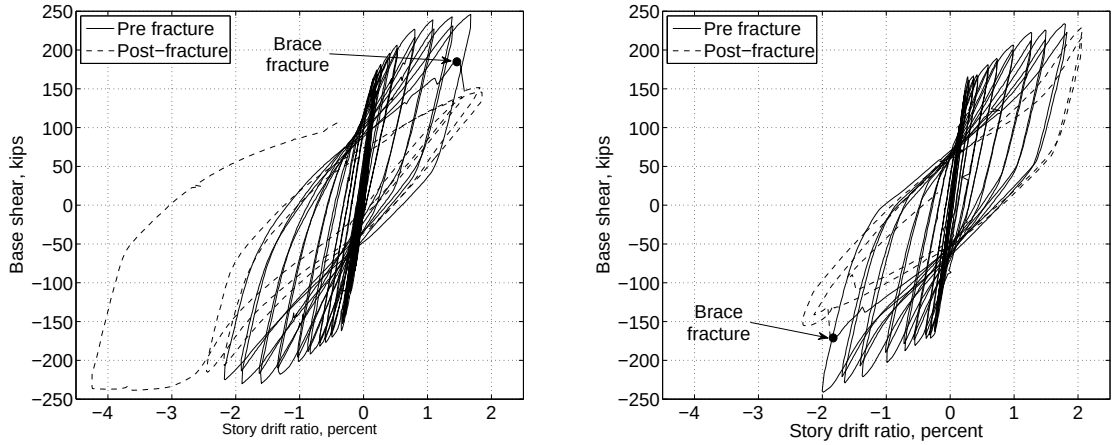

(a) (b)

Figure 2.14: System story shear versus story drift ratio for: (a) HSS30 and (b) HSS31.

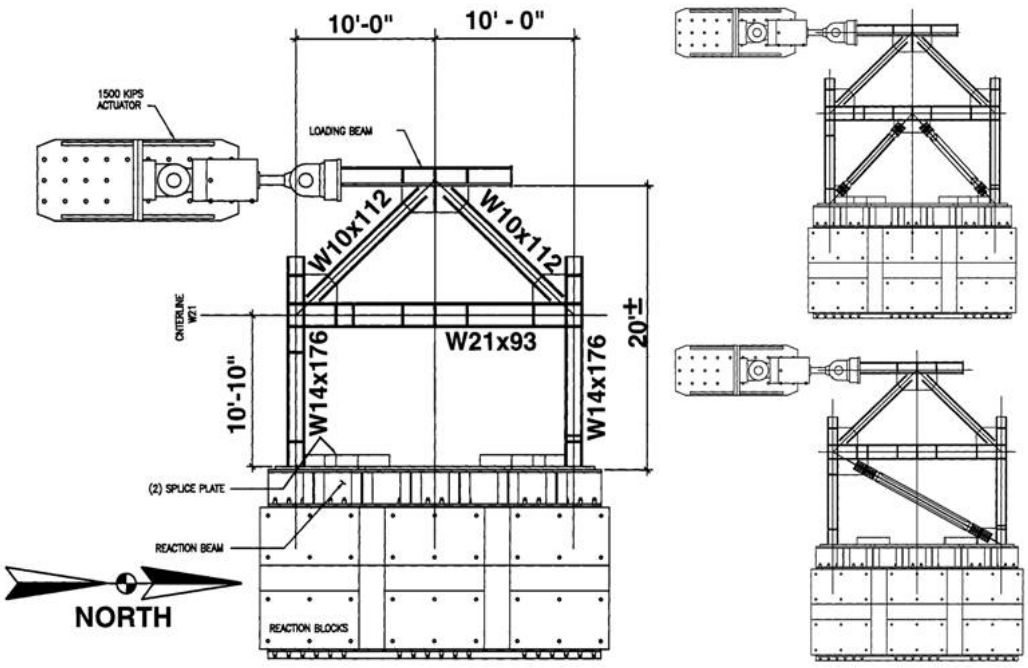

Figure 2.15: BRBF test frame [Uriz, 2005]

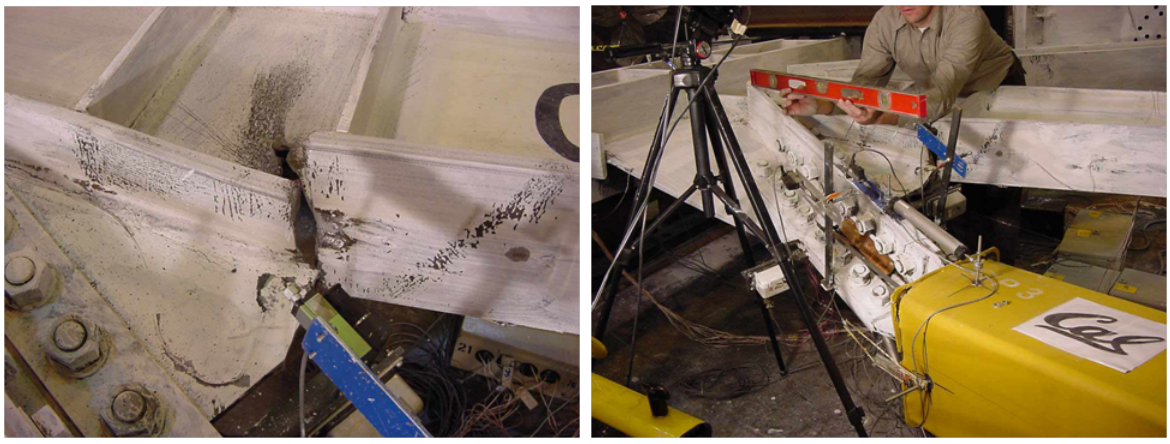

(a) (b)

Figure 2.16: BRBF frame damage [Uriz, 2005]

	GUSSET PLATE	BOLTED CONNECTION	BRB ORIENTATION	PURPOSE OF TEST
REF BRB	SQUARE	(10) SLIP CRITICAL	STRONG FLOOR	BASELINE FOR COMPARISON
BRB02	15° TAPER	(10) SLIP CRITICAL	STRONG FLOOR	EVALUATE EFFECT OF TAPERED GUSSET PLATE
BRB03	15° TAPER	(8) BEARING/ SHEAR	STRONG FLOOR	EVALUATE EFFECT OF BEARING CONNECTION
BRB04	15° TAPER	(8) BEARING/ SHEAR	STRONG FLOOR	EVALUATE EFFECT OF ROTATED CORE PLATE
BRB01	SQUARE	(10) SLIP CRITICAL	STRONG FLOOR	EFFECT OF DIFFERENT DEFORMATION HISTORY

Figure 2.17: BRBF test parameters [Christopolus, 2005]

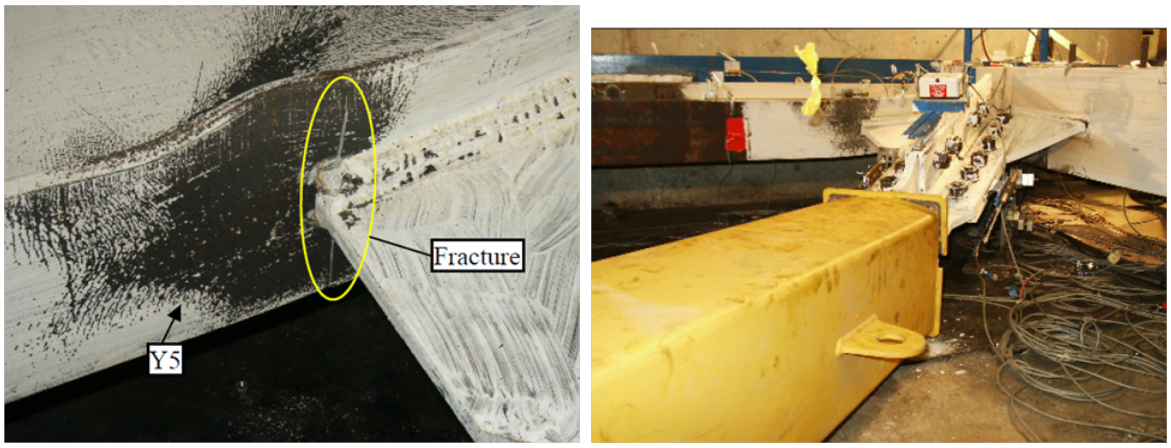

(a) (b)

Figure 2.18: BRBF frame damage [Christopolus, 2005]

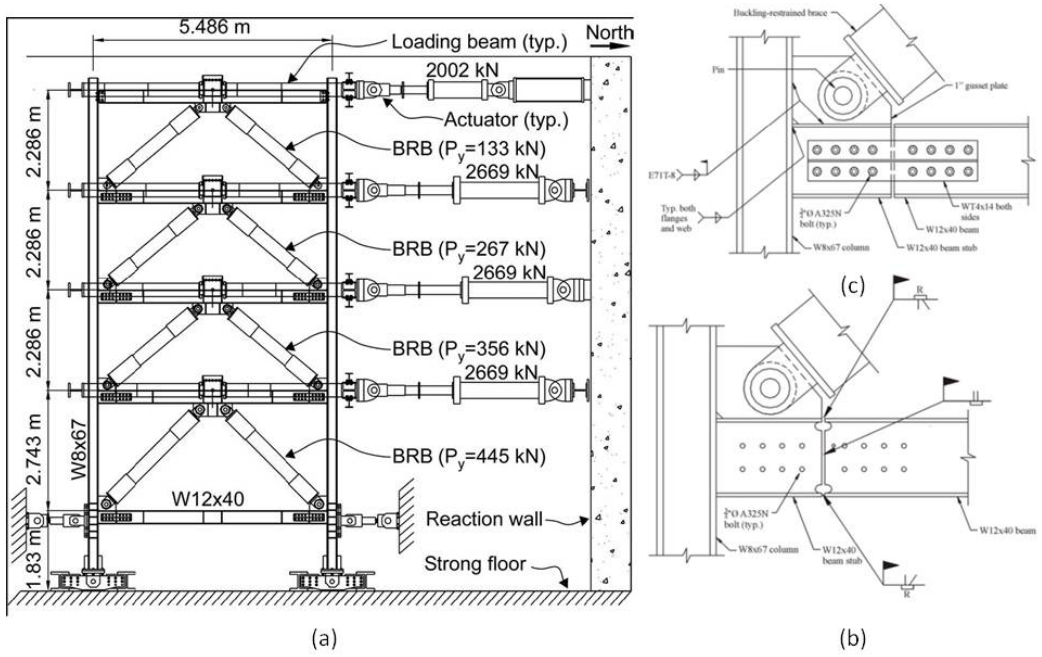

Figure 2.19: BRBF test specimen [Fahnestock et al., 2006]: (a) elevation; (b) fixed connection; (c) pinned connection.

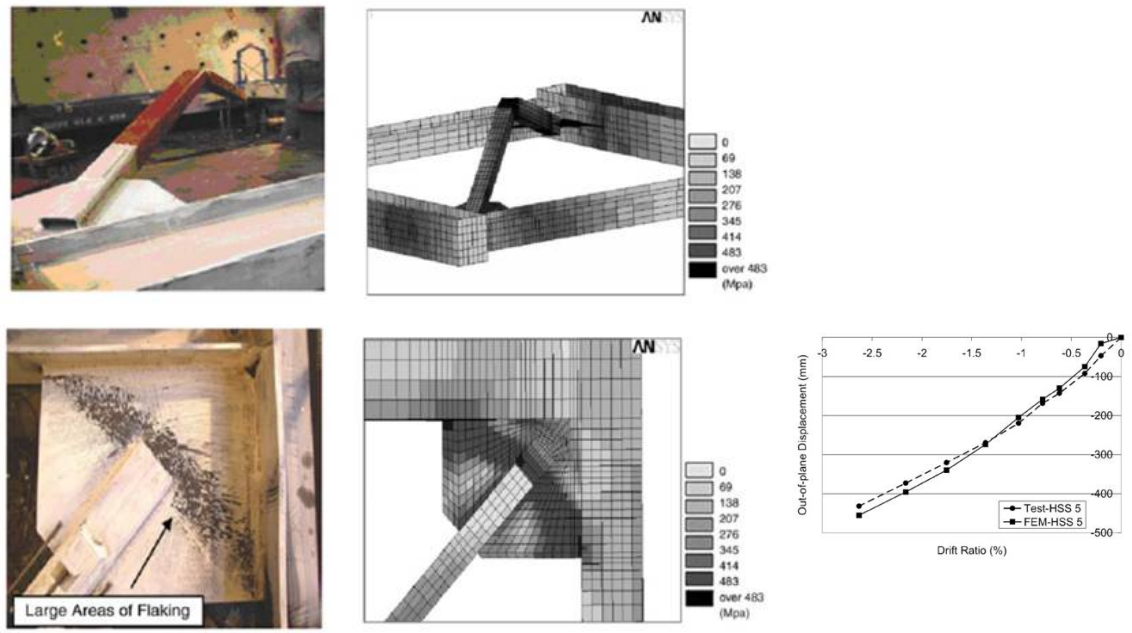

(a) (b) (c)

Figure 2.20: Comparison between experimental and FEA: (a) experimental behavior; (b) FE predicted behavior; (c) out-of-plane brace displacement comparison [Yoo, 2006]

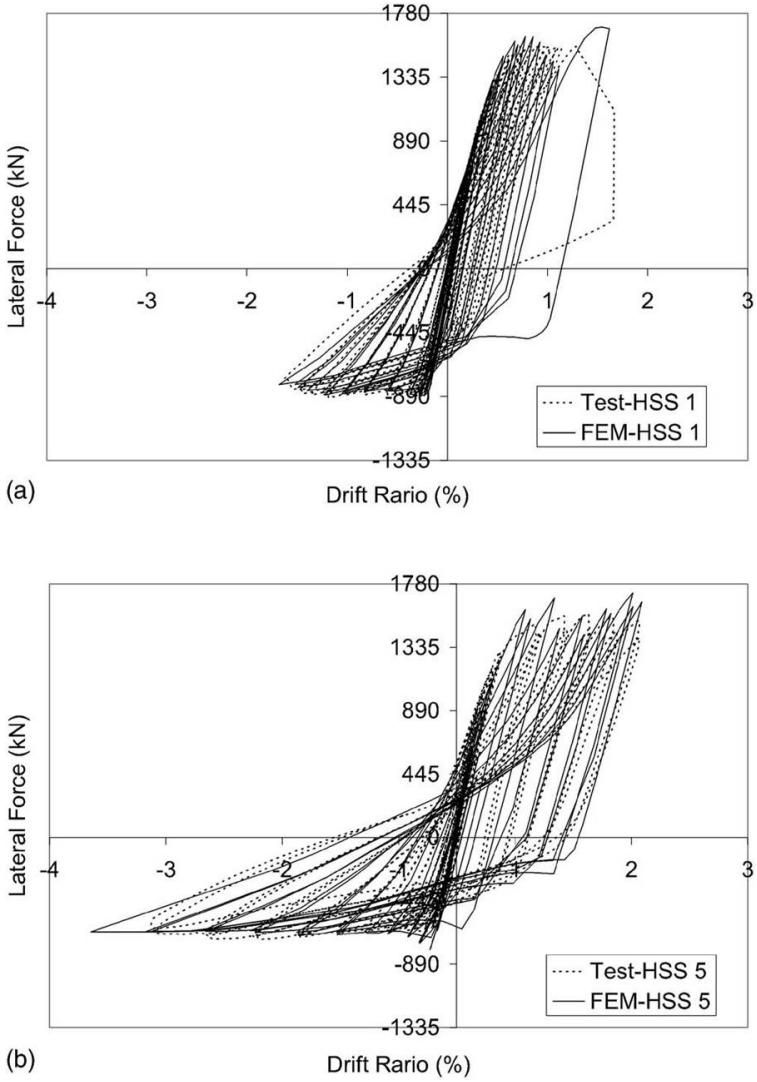

Figure 2.21: Comparison of FE simulations and experiments: (a) HSS01; (b) HSS05 [Yoo, 2006]

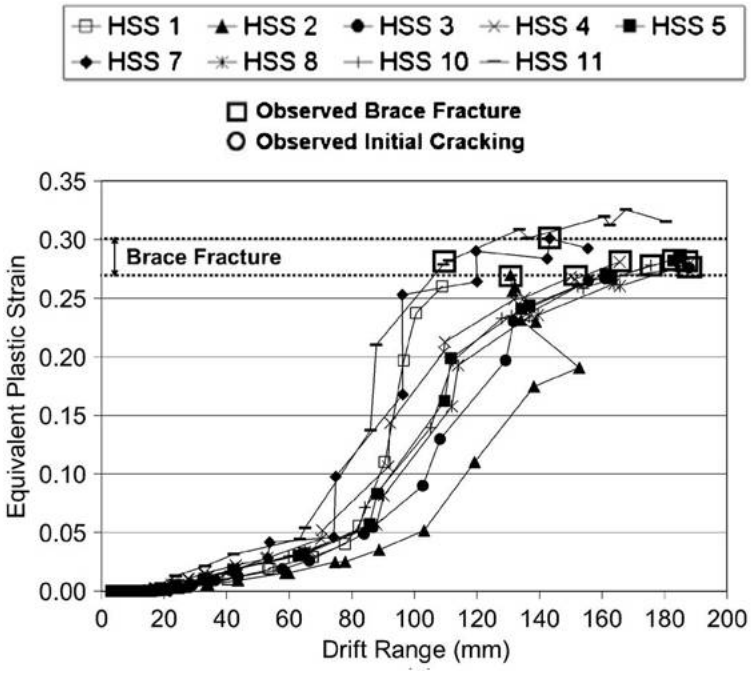

Figure 2.22: Calibration of brace fracture using Equivalent plastic strain [Yoo, 2006]

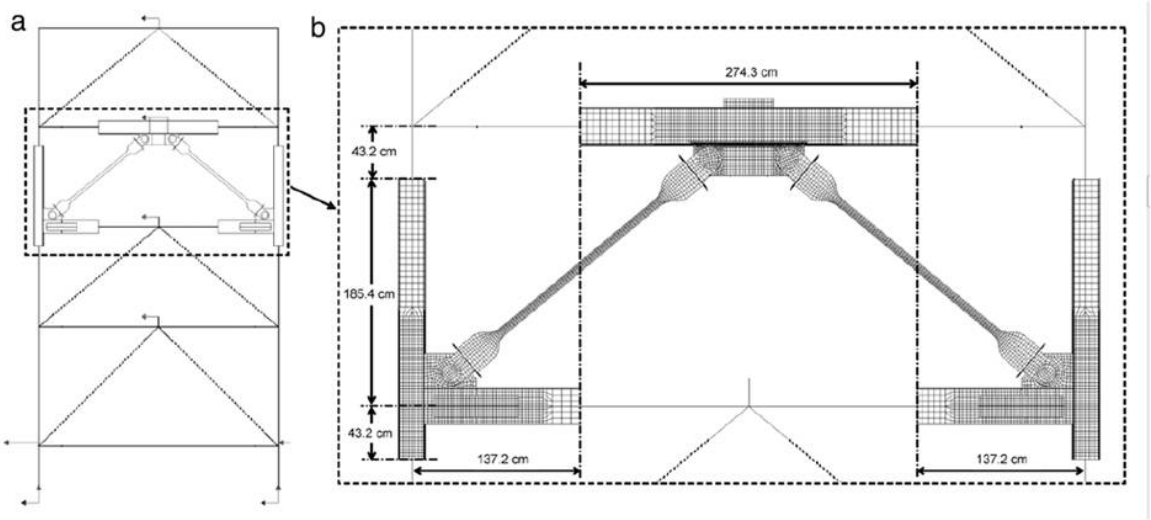

Figure 2.23: BRBF numerical model: (a) test frame; (b) continuum FE model of third story [Wigle and Fahnestock, 2010]

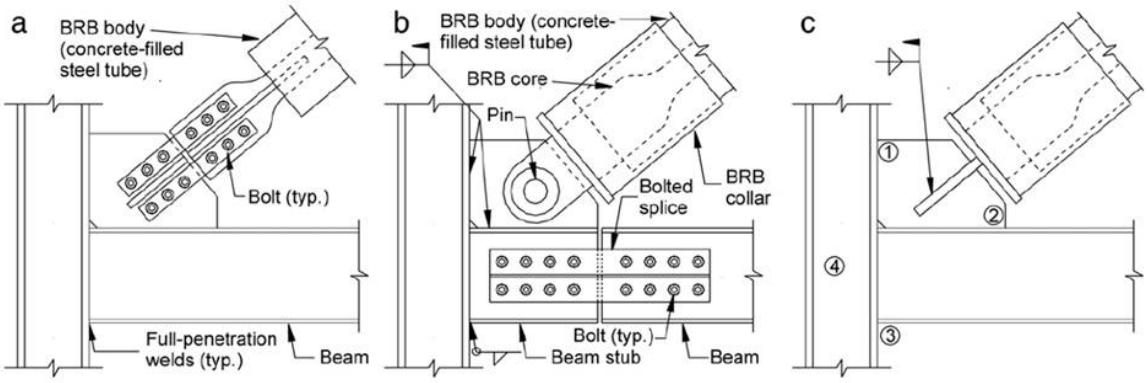

Figure 2.24: Example BRBF connection details: (a) continuous beam, bolted brace; (b) spliced beam, pinned brace; (c) continuous beam, welded brace [Wigle and Fahnestock, 2010]

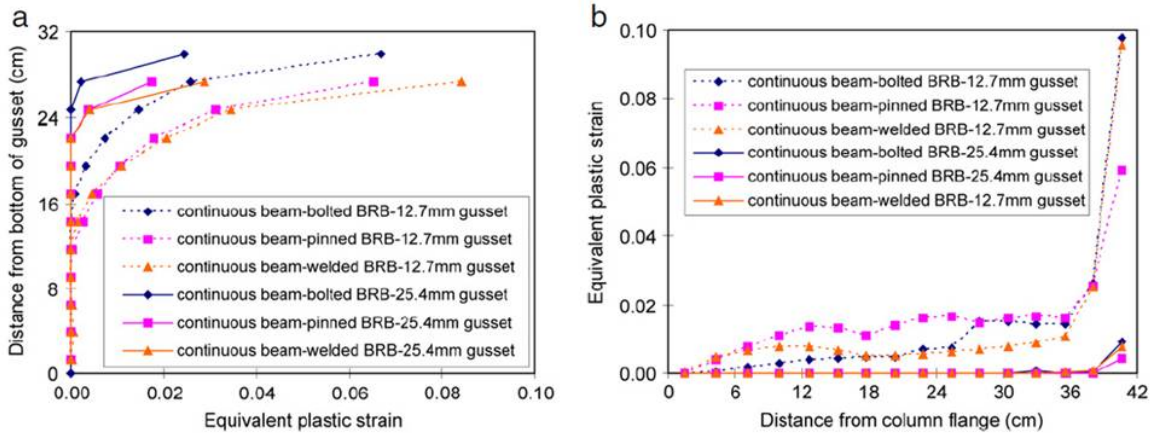

Figure 2.25: Equivalent plastic strain at gusset plates: (a) vertical gusset interface (column connection); (b) horizontal gusset interface (beam connection). [Wigle and Fahnestock, 2010]

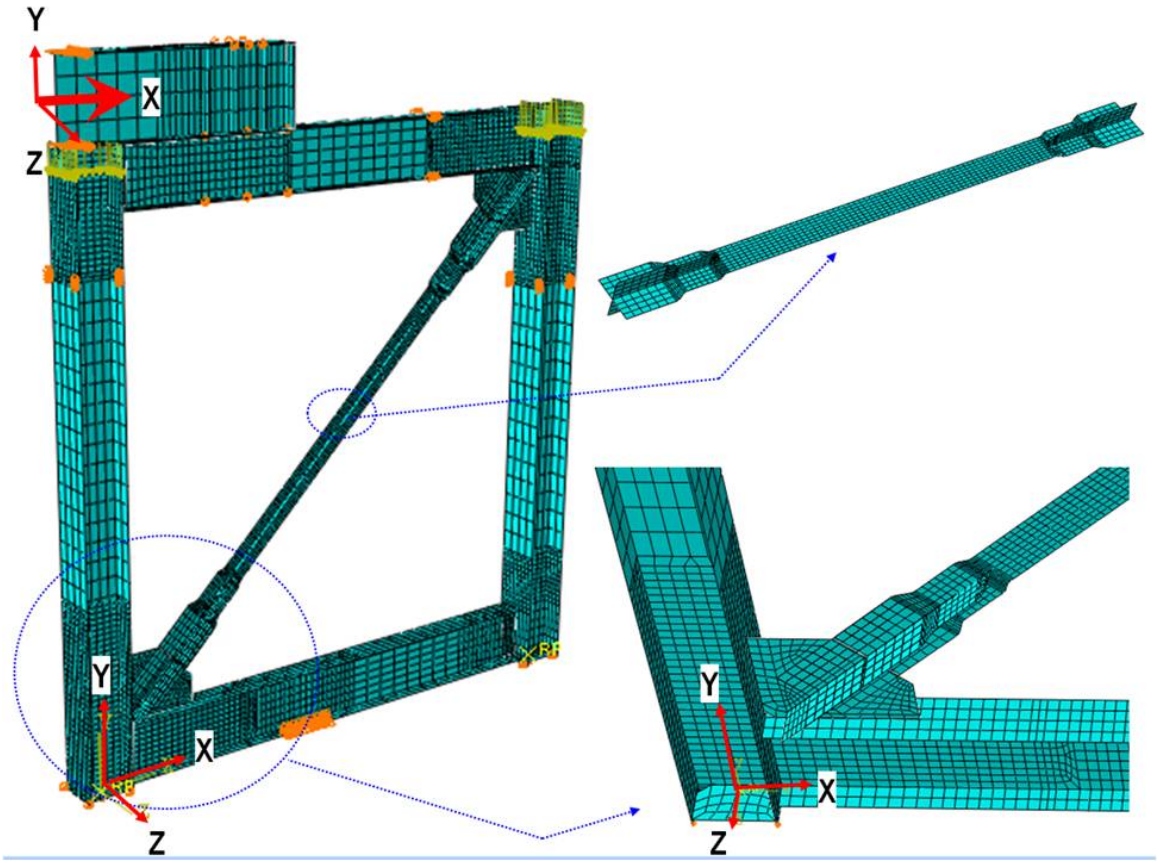

Figure 2.26: Finite element model and mesh [Ozcelik and Okazaki, 2010]

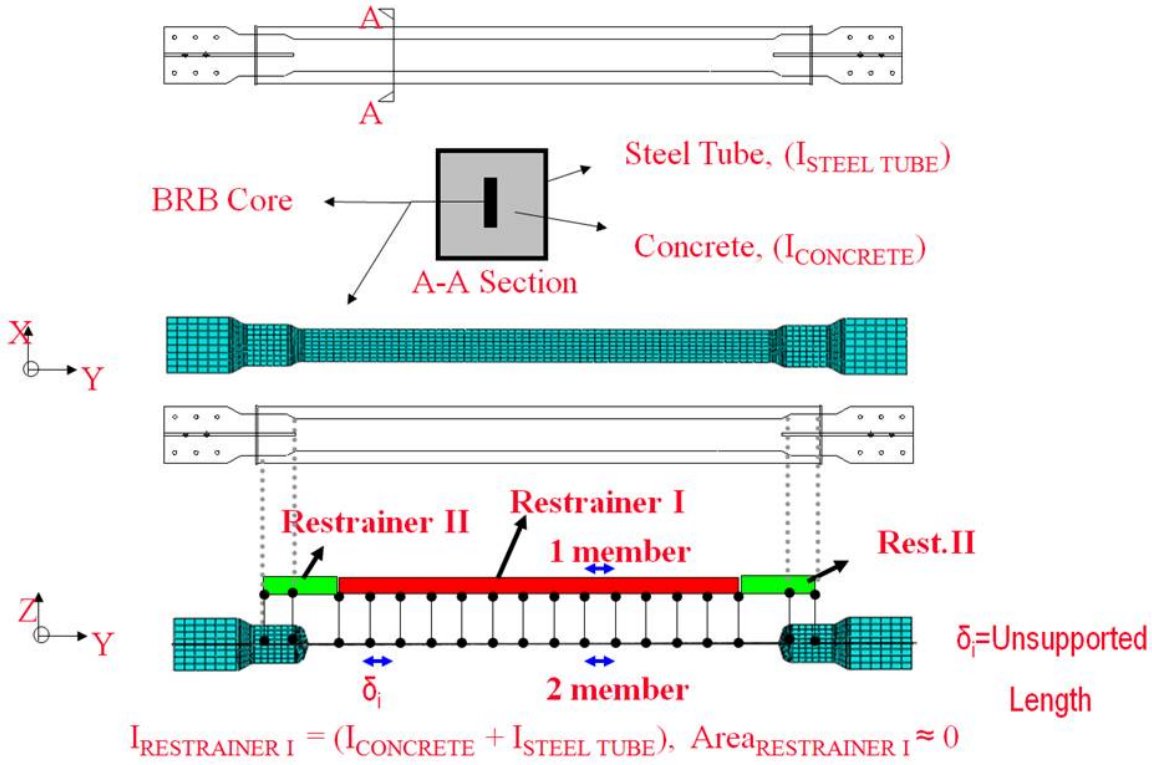

Figure 2.27: Brace and casing finite element model [Ozcelik and Okazaki, 2010]

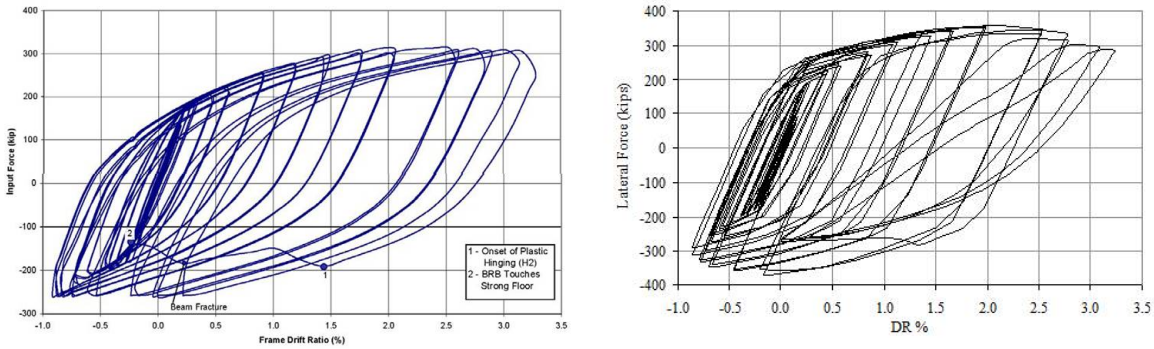

(a) (b)

Figure 2.28: Hysteretic behavior comparison: (a) Experiment [Christopolus, 2005]; (b) FE simulation [Ozcelik and Okazaki, 2010]

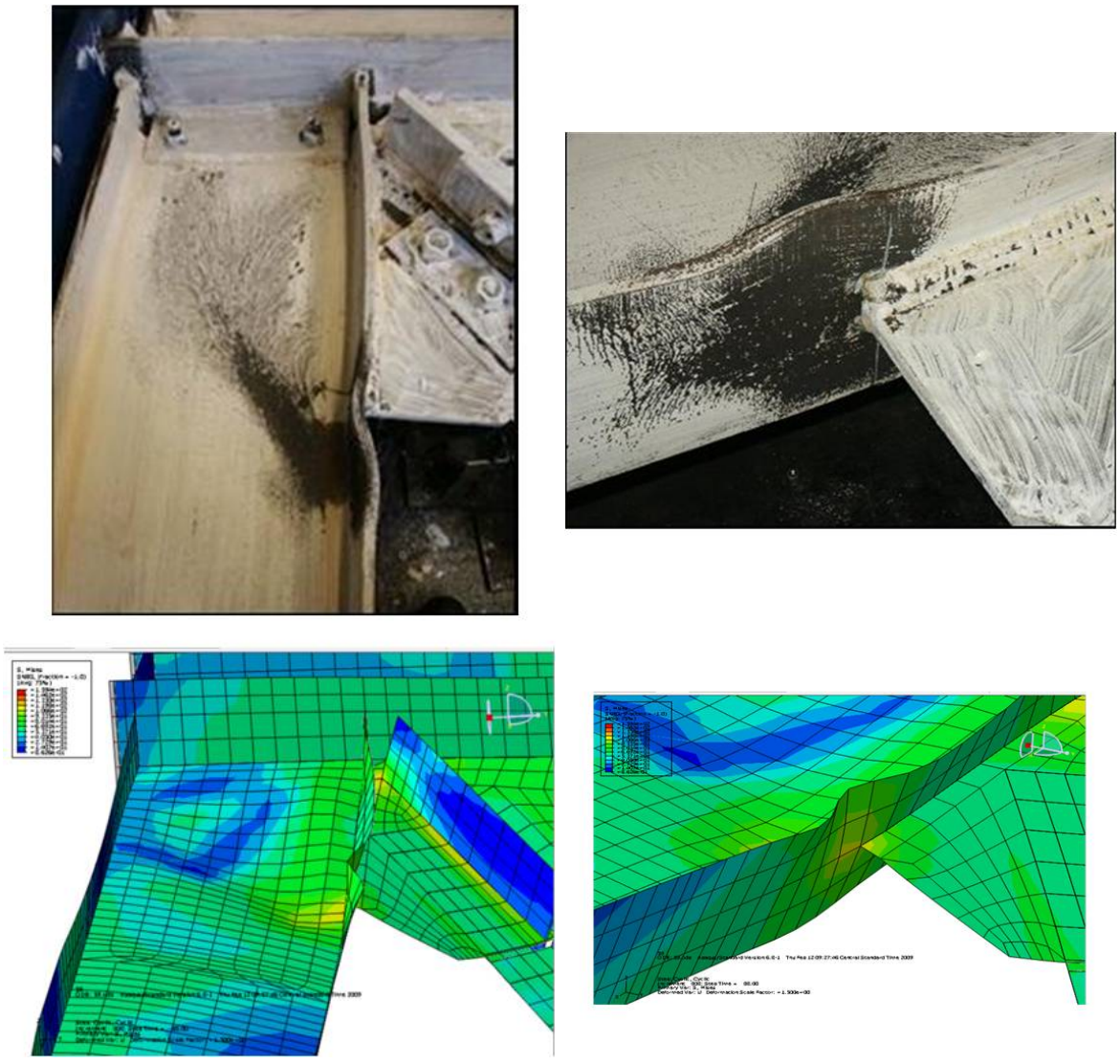

(a) (b)

Figure 2.29: Damage comparison between experiment and simulation: (a) column web yielding and flange buckling; (b) beam yielding and flange buckling [Ozcelik and Okazaki, 2010]

Chapter 3

EXPERIMENTAL PROGRAM

3.1 Introduction

Chapters 1 and 2 discussed the previous work performed on SCBFs and BRBFs and highlighted key issues that required further study. Specifically, further understanding of the splice connection at the center of single-story X-configured SCBFs is needed along with a better understanding of the corner connection region in a BRBF designed according to current design provisions. Additionally, an understanding is needed of the effect of out-of-plane deformation and loading perpendicular to the braced frames on the system ductility when the frames are subjected to bi-directional deformation with realistic boundary conditions. These boundary conditions include a gravity framing system which included a floor system of beams and concrete on metal deck typical of modern buildings.

To accomplish this, two large-scale experiments were performed on a two-story, one-bay by one-bay SCBF and BRBF at the Multi-Axial Subassemblage Testing (MAST) facility at the University of Minnesota. This facility is a member of the George E. Brown, Jr. Network for Earthquake Engineering Simulation (NEES), an NSF-sponsored consortium.

3.2 MAST Facility Description

The MAST lab has the capability of testing structures up to 28.75 ft. in height and 20 ft. x 20 ft. in plan and applying large loads and deformations in all six degrees of freedom (DOF). The test structure is attached to the strong floor and a rigid, steel crosshead through which vertical and lateral loads and displacements may be applied. A picture of the lab with the first specimen in place is shown in Figure 3.1 with the important components labeled. The actuators can deliver a maximum vertical force of 1,320 kips, maximum lateral force in each horizontal direction of 880 kips, vertical displacements of ± 20 inches, and horizontal displacements of ± 16 inches. Each DOF can be controlled in force or displace-

ment control independent of all other DOFs. More information on the lab may be found at http://nees.umn.edu/facilities/mast.php.

3.3 Specimen Description

The two specimens were nearly full-scale, one-bay by one-bay, two-story frames with braces in two orthogonal bays which framed into a "shared" column (column B-1) as shown in Figures 3.2 and 3.3. The first specimen, denoted as SCBF, had HSS braces in a single-story X-configuration, while the second specimen, denoted as BRBF, used BRBs in a single-diagonal configuration. The member sizes and dimensions of the test specimens were chosen to approximate large scale framing for a three or four story building constructed in a high-seismic zone, match as closely as possible the members sizes used in the UW planar frame experiments (see Section 2.5.1) and to meet the constraints of the MAST lab. The MAST constraints included the capacities of the actuators and strong floor, and the height and plan dimensions of the crosshead and strong floor. The brace sizes chosen represent the lower bound of brace sizes used in practice. The design of the frame members are discussed in Section 3.4.

Figures 3.3a and 3.3b show the second and third floor plans, respectively, of both test specimens. The braced frames occur along grid lines 1 (Frame 1) and B (Frame B) as indicated by the dashed lines near the girders. The frames along grids 2 and A are gravity frames with typical "simple" beam-column connections. The bay widths between column centerlines were 16'-6" in each direction. A W12x106 section was used for the "shared" column, W12x72s were used for the other two braced frame columns (A-1 and B-2), and a W12x45 was used for the "gravity" column (A-2). The W12x72 matches the column sizes used in the planar experiments performed at UW.

Figures 3.5 and 3.6 show the braced frame elevations of the SCBF and BRBF, respectively. The first story height was 10'-5" from the top of the column base plate to the centerline of the second floor beam while the second story height was 10'-5" from centerline to centerline of the second and third floor beams. The SCBF braces were HSS3x3x1/4, while the BRBs were PowerCat braces manufactured by Star Seismic with a single plate core. The single-story X-configuration of the SCBF requires that one of the braces be continuous while

the other brace is split into two discrete braces that are spliced at the intersection of the X. The BRBs are arranged such that the top of the braces in each story frame into the shared column while the bottom of the braces frame into columns A-1 and B-2.

The floor system was designed and constructed to closely approximate realistic conditions. The intermediate floor beams were W14x22 sections while W16x31 sections are used in the gravity frames 2 and A. The braced frame beams at the second and third floor are W16x50 in Frames 1 and B. The intermediate sizes were chosen to match those typically seen in practice when framing into the sizes used for the braced frame beams. The second floor deck consists of 2" 20 gage, ribbed metal deck topped by 3.25" of normal weight concrete for a total depth of 5.25" as in typical steel buildings. Nominal reinforcement consisting of #4 bars at 16" o.c. in each direction was placed in the slab. This system is attached to the floor beams with 3/4" diameter shear studs welded to the beams at the spacing shown in Figure 3.3. Slab blockouts were required at the second floor at the location of the gusset plates in order to remove them from the first experiment and replace them for the second experiment. This occurred at columns A-1, B-1 and B-2. The blockout extended from the face of the column for 25.75" as shown in Fig. 3.4.

The third floor slab was used to transfer the load from the MAST crosshead/actuator system into the test specimen and required a 10" thick concrete slab with a reinforcement ratio of 1.5%. This slab was attached to the wide flange beams with two rows of 7/8" diameter shear studs at a much closer spacing than at the second floor (see Fig. 3.3).

Photographs of the BRBs prior to installation are shown in Figure 3.7 and Figure 3.8 shows the fabrication drawings for the second story BRBs in each frame. As seen in the figures, the BRB core (yielding element) is of rectangular cross section with a curved transition at the end to the elastic section. The end of the core plate is connected to an end plate with CJP welds. The restrainer is composed of an outer HSS12x8x5/16 with a cementicious grout infill while the end collar is composed of two bent plates welded together to encapsulate the HSS12x8 restrainer. The complete fabrication and erection drawings for the BRBs can be found in Appendix B.

The wide flange beams and columns were specified as ASTM A992 material which has a minimum yield stress of 50 ksi. The gusset plates for both specimens were specified as

ASTM A572 Gr. 50 with a minimum yield stress of 50 ksi. The HSS braces were specified as ASTM A500B with a minimum yield stress of 46 ksi while the BRBs were specified as ASTM A36 with a minimum yield strength of 36 ksi. Table 3.1 lists the measured material properties of the wide flanges, HSS braces and BRB steel core as measured from coupons. Due to laboratory error, the coupon steel for these specimens was accidentally discarded and the material properties given are based on the mill certifications performed during the rolling process as supplied by the testing agency performing the material tests on the pieces. The BRB steel core material tests were performed by an independent laboratory during fabrication of the BRBs. Unfortunately, the material properties of the gusset plates were not able to be measured due to the laboratory errors noted above. Appendix F provides the material certification for the material listed in Table 3.1.

The specified concrete strength for the third floor slab was 6 ksi and the specified strength for the second floor slab was 4 ksi. Slump tests were performed during the pours and 21, four-by-eight cylinders were cast for material testing which included 15 cylinders tested in compression and six, splitting-tensile tests. The concrete was delivered to the lab in three trucks with the first truck for the second floor slab and the last two trucks for the third floor slab. Table 3.2 lists the results of the compression tests for each cylinder while Table 3.4 lists the results of the splitting-tensile tests for each cylinder. The mean results for the compressive tests and split cylinder tension tests are shown in Tables 3.3 and 3.5, respectively. The mean 28-day compressive strength of the second floor slab concrete was 6028 psi while the mean 28-day strength of the third floor slab concrete was 7951 psi.

3.4 Specimen Member and Connection Design

3.4.1 State-of-the-practice CBF design

SCBFs and BRBFs designed in the U.S. typically follow the guidelines outlined in ASCE 7 [2010] and the AISC Seismic Provisions [2010]. The basic design procedure can be summarized in the following steps:

1. Analyze the building under the code prescribed design lateral and gravity loads. For typical buildings, the Equivalent Lateral Force procedure or response spectrum anal-

ysis is used to determine the seismic lateral loads. Response-history analysis, and static pushover analysis may also be used but these methods are typically reserved for complicated and/or atypical buildings.

2. Determine the brace sizes required to resist this loading along with satisfying lateral drift limits.

3. Design and detail the brace connection region to resist the maximum expected forces delivered by the brace.

4. Design the braced frame beams and columns to resist the maximum expected brace forces (capacity design) or design loading combinations from the applicable building code, including member overstrength. The forces from the latter method need not exceed that determined from the capacity design approach.

If a member is used to resist lateral load in two orthogonal directions in Seismic Design Category C through E, ASCE 7 requires that the loading combination include 100 percent of the forces from one direction plus 30% of the forces from the perpendicular direction. If response-history analysis is performed, simultaneous application of orthogonal ground motions need to be applied in the model.

Items 3 and 4 above require the estimation of the maximum expected brace force. For conventional buckling braces, this is defined as the required tensile and compressive force in the 2005 AISC Seismic Provisions Sections 13.3 and 13.4; and for BRBs this is defined as the required tensile and compressive force in Section 16.2. This force depends on the type of brace being used, the yield strength, cross-sectional area, manufacturing method, and in the case of the BRB, the expected deformation demands. Rectangular hollow structural sections (HSS) are the most common type of buckling brace but wide-flange, pipe, channels and angles are also used. The maximum expected brace force in tension for conventional buckling braces is given by Equation 3.1

$$P_t = R_y F_y A_g \tag{3.1}$$

where R_y is the ratio of the expected material yield strength of the brace to its nominal yield strength, F_y is the nominal material yield strength, and A_g is the gross cross-sectional area of the brace. The maximum expected compressive force delivered by the brace is given by Eqn. 3.2.

$$P_c = R_y P_n \tag{3.2}$$

where P_n is the nominal compressive strength of the brace. For the design of the gusset plate, the required demand is given by 1.1 times Eqn. 3.2.

The determination of the maximum expected brace forces for BRBs relies on qualification testing of the type of BRB to be used in the building. This qualification testing can be performed specifically for the project or results from similar BRBs may be used. The maximum adjusted brace force in tension is given by Equation 3.3, where ω is the strain hardening adjustment factor and is calculated as the ratio of the maximum tensile force measured in the qualification tests at a deformation corresponding to $2.0\Delta_{bm}$ to the measured core yield strength, where Δ_{bm} is the core elongation at the design story drift or the expected deformation [AISC, 2010]. The expected deformation is defined as two times the design story drift or 2%, whichever is larger. F_{ysc} is the yield strength of the steel core and A_{gsc} is the gross cross-sectional area of the steel core. The maximum adjusted brace force in compression is given by Equation 3.4 where β is the ratio of the maximum compressive force to the maximum tensile force at the expected deformation, from the qualification tests and shall not be taken less than unity. The factor R_y is not applied in Equations 3.3 and 3.4 when F_{ysc} is determined from coupon tests.

$$P_t = \omega R_y F_{ysc} A_{gsc} \tag{3.3}$$

$$P_c = \beta \omega R_y F_{ysc} A_{gsc} \tag{3.4}$$

SCBFs and BRBFs are also required to satisfy stability limits to ensure satisfactory energy dissipation. For SCBFs, the brace global slenderness ratio, KL/r must satisfy Equation 3.5 below.

$$\frac{KL}{r} \leq 200 \tag{3.5}$$

The braces and beams and columns in the lateral system must also satisfy element slenderness limits (width-thickness ratios) to ensure adequate cyclic behavior. The braces and columns must satisfy the requirements for *highly ductile members* while the beams must satisfy the requirements for *moderately ductile members*. These are prescribed in the Seismic Provisions [2010] and these limits for HSS and WF braces are shown below in Equations 3.6 and 3.7, respectively.

$$\lambda_{hd}(HSS) = 0.55\sqrt{\frac{E}{F_y}} \tag{3.6}$$

$$\lambda_{hd}(WF) = 0.3\sqrt{\frac{E}{F_y}} \tag{3.7}$$

The restraining system in BRBs must limit the local and overall buckling of the brace and is prohibited from global buckling at deformations less than or equal to the expected deformations. This latter requirement is typically satisfied by ensuring that the buckling load of the restraining system is greater than the yield strength of the core.

To ensure adequate performance, a number of limit states in the connection region must be checked. The design described here is for Load and Resistance Factor Design (LRFD) according to the AISC Steel Construction Manual [2005b]. The general equation that describes this philosophy is given by Equation 3.8.

$$\phi R_n \geq R_u \tag{3.8}$$

where ϕ is a resistance factor, typically less than unity, accounting for statistical variations in strength and R_u is the required strength from the load effect.

The brace connection region must satisfy a number of limit states including:

1. Brace to gusset plate connection (typically welded or bolted)
2. Brace net section fracture
3. Gusset plate yielding on the Whitmore width
4. Gusset plate fracture on the Whitmore width
5. Gusset plate block shear rupture
6. Gusset plate buckling

7. Gusset plates connection to beams and columns (interface welds or bolts)

Gusset plate design is a trial and error process that generally requires a number of iterations to satisfy the above limit states and the rotation flexibility requirements for buckling braces. These limit states and requirements are described below for the current state-of-the-practice LRFD methodology and followed up by a description of the Balanced Design Procedure (BDP) recently developed for buckling brace frames [Roeder et al., 2011].

Brace to gusset plate connection (LRFD)

The brace is joined to the gusset plate through welds or bolts depending on the brace type and demands. HSS braces are typically fillet welded to gusset plates. For welded connections, two criteria must be checked which include the strength of the weld and the strength of the base material being welded. The strength of the fillet weld per LRFD is given by Equation 3.9 below.

$$\phi R_n = \phi(0.6) F_{EXX} N_w L_w t_{eff} \tag{3.9}$$

where ϕ=0.75, F_{EXX} is nominal electrode strength, N_w is the number of welds used, L_w is the length of the welds and t_{eff} is the effective throat of the fillet weld. The strength of the base metal per LRFD is given by Equation 3.10 below.

$$\phi R_n = \phi(0.6) F_u N_w L_w t_{bm} \tag{3.10}$$

where ϕ=0.75, F_u is the tensile strength of the base metal and t_{bm} is the thickness of the base metal.

Brace net section fracture (LRFD)

Brace material is typically removed in order to join the brace to the gusset plate which weakens the brace at this net section location and often times requires reinforcement. This area is shown in Figure 3.9a. The design expression for net section fracture per LRFD is given by Equation 3.11 below and must be greater than the expected yield capacity of the brace.

$$\phi R_n = \phi F_u A_n U \tag{3.11}$$

where ϕ=0.75, A_n is the net area of the section where material was removed plus any reinforcement, and U is the factor accounting for shear lag of the force transfer from the weld to the brace and is given by Equation 3.12.

$$U = 1 - \frac{x}{L_w} \tag{3.12}$$

where x is given by Equation 3.13 for a HSS brace attached to a single concentric gusset plate.

$$x = \frac{B^2}{4(B+H)} \tag{3.13}$$

where B and H are the dimensions of the HSS shown in Figure 3.9a. If net section reinforcement is used, Equation 3.11 becomes Equation 9.5

$$\phi R_n = \phi U \left(R_{tb} F_{ub} A_{nb} + F_{urp} A_{rp}\right) \tag{3.14}$$

where $R_{tb}F_{ub}$ is the expected tensile strength of the brace, A_{nb} is the net area of the brace where the material has been removed, F_{urp} is the tensile strength of the net section reinforcement and A_{rp} is the area of the net section reinforcement.

Gusset plate yielding on the Whitmore width (LRFD)

Whitmore [1952] developed a method to estimate the yield force resistance of a gusset plate and found that a safe estimate can be made by assuming the brace force is resisted by the gusset plate width, B_w, shown in Figure 3.9b. This width, the so-called Whitmore Width, is found by extending two lines at 30 degrees from the beginning to the end of the connection as shown in Fig. 3.9b. The area of the gusset plate resisting the load is then found by multiplying the gusset thickness times the Whitmore width. The LRFD capacity is given by Equation 3.15 below.

$$\phi R_n = \phi F_y B_w t_g \tag{3.15}$$

where ϕ=0.9 and t_g is the thickness of the gusset plate.

Gusset plate fracture on the Whitmore width (LRFD)

Fracture in tension across the Whitmore width is also a possibility and the expression governing this limit state per LRFD is given by Equation 3.16 below.

$$\phi R_n = \phi F_u B_w t_g \tag{3.16}$$

where ϕ=0.75

Gusset plate block shear rupture (LRFD)

Block shear rupture is a tearing limit state as shown in Figure 3.10a where the material tears in shear and tension. The LRFD capacity expression for block shear rupture is given by Equation 3.17.

$$\phi R_n = \phi 0.6 F_u A_{nv} + U_{bs} F_u A_{nt} \leq \phi 0.6 F_y A_{gv} + U_{bs} F_u A_{nt} \tag{3.17}$$

where ϕ=0.75, A_{nv} is the net area subject to shear, U_{bs} is a factor that accounts for the uniformity of the tensile stress in the plate at the end of the bracing member,A_{nt} is the net area subject to tension, A_{gv} is the gross area subject to shear. U_{bs} is generally unity for brace connections used in typical construction.

Gusset plate buckling (LRFD)

Gusset plate buckling due to the brace compressive force must also be prevented, and the method to determine the buckling capacity of the gusset plates is typically the so-called Thornton method. This method assumes that the area of the gusset plate that resists the load is defined by the product of the Whitmore width and the gusset plate thickness. The effective buckling length of the plate is typically defined as the average of the three lengths (l_1, l_2, l_3) originating at the ends and the middle of the Whitmore width and is shown in Figure 3.9b. The buckling capacity is given by Equation 3.18.

$$\phi R_n = \phi F_{cr} B_w t_g \tag{3.18}$$

where ϕ=0.9 and F_{cr} is the critical load defined by Equations 3.19 or 9.12.

When $KL/r \leq 4.71\sqrt{E/F_y}$ (or $F_e \geq 0.44F_y$)

$$F_{cr} = \left[0.658^{\frac{F_y}{F_e}}\right] F_y \tag{3.19}$$

When $KL/r > 4.71\sqrt{E/F_y}$ (or $F_e < 0.44F_y$)

$$F_{cr} = 0.877F_e \tag{3.20}$$

where F_e is the Euler buckling load defined by Equation 3.21.

$$F_e = \frac{\pi^2 E}{\left(\frac{KL}{r}\right)^2} \tag{3.21}$$

There is no clear consensus on the "correct" value of the effective length factor to be used. Roeder et al. [2011] recommend using 0.65 for gusset plates with two edges restrained (corner gussets) and 1.5 for gussets occurring at the beam mid-span of chevron-configured braces.

Gusset plate interface welds (LRFD)

The welds connecting the gusset plate to the beams and columns are typically designed using the forces that result from application of the Uniform Force Method (UFM). This method is thoroughly described in AISC [2005b] and Chambers and Ernst [2005]. Application of this method helps the designer choose the dimensions of the gusset plates, the brace work point, and resolve the brace forces at each gusset edge. Typically, designers choose the geometry such that the brace workpoint intersects the beam and column centerline intersection. The use of Eq. 3.22 below theoretically results in a connection with no moments at the gusset interfaces. This is a result of the assumptions used in the development of the UFM and does not necessarily reflect reality.

$$\alpha - \beta \tan\theta = e_b \tan\theta - e_c \tag{3.22}$$

where α, β, θ, e_c and e_b are defined in Figure 3.10b. The designer chooses α and β to satisfy the above expression. The interface forces are then found from the following expressions:

$$V_c = \frac{\beta}{r} P \tag{3.23}$$

$$H_c = \frac{e_c}{r}P \tag{3.24}$$

$$V_b = \frac{e_b}{r}P \tag{3.25}$$

$$H_b = \frac{\alpha}{r}P \tag{3.26}$$

$$r = \sqrt{(\alpha + e_c)^2 + (\beta + e_b)^2} \tag{3.27}$$

Once the above forces have been calculated, the interface welds can be sized by resolving the horizontal and vertical forces at each interface and using Equation 3.28 below.

$$\phi R_n = \phi(0.6)F_{EXX}N_w L_w t_{eff}\left[1 + 0.5(\sin\gamma)^2\right] \tag{3.28}$$

where γ is the angle between the longitudinal axis of the fillet weld and the resultant interface force.

Tensile rupture on net effective area of pin-connected members

The design of the BRB gusset plate must include the limit states relating to the pin which include tensile rupture on the net effective area, shear rupture on the effective area, bearing on the projected area, and yielding on the gross section. The last one, yielding on the gross section is yielding on the Whitmore width and is governed by Equation 3.15. There are no clear guidelines on the definition of the Whitmore width for a pin-connected member. Tensile rupture on the net effective area is governed by Equation 3.29 below.

$$\phi R_n = \phi 2 t_g b_{eff} F_u \tag{3.29}$$

where ϕ=0.75 and b_{eff}=$2t_g$+0.63 but not more than the actual distance from the edge of the hole to the edge of the part measured in the direction normal to the applied force.

Shear rupture on the effective area of pin-connected members

Shear rupture on the effective area of pin-connected members is governed by Equation 3.30 below.

$$\phi R_n = \phi(0.6) F_u A_{sf} \tag{3.30}$$

where ϕ=0.75 and A_{sf}=$2t_g(a + d/2)$, where d is the pin diameter and a is the shortest distance from edge of the pin hole to the edge of the member measured parallel to the direction of the force.

Bearing on the projected area of pin

The limit state of pin bearing on the projected area is given by Equation 3.31 below.

$$\phi R_n = \phi(1.8) F_y A_{pb} \tag{3.31}$$

where ϕ=0.75 and A_{pb} is the projected bearing area.

Brace rotation clearance

For brace buckling in the plane of the gusset plate, the Provisions [AISC, 2010] recommend the connection to be designed for the expected brace axial strength along with the brace flexural strength. For brace buckling out of the plane of the gusset plate, the post-buckling brace deformations result in weak-axis rotation of the gusset plate and the gusset plate must be detailed to accommodate those rotations. Current practice is to provide a $2t_g$ linear clearance as shown in Figure 3.10b.

3.4.2 Balanced Design Approach (BDP)

Dissipation of seismic energy requires that the main fuse(s) possess a large amount of ductility in addition to adequate strength. Current seismic design guidelines attempt to ensure this but research carried out in the past decade has resulted in a new design and detailing approach [Roeder et al., 2011]. This method, called the balanced design procedure (BDP), differs than the state-of-the-practice method described in the previous section. This proce-

dure not only focuses on the strength of bracing connections and framing members, but also attempts to maximize yielding and drift capacity resulting in improved seismic performance.

The method ensures that failure limit states are suppressed using capacity design principles. These objectives are accomplished through a balanced hierarchy of yielding mechanisms and failure modes. Multiple yielding mechanisms are encouraged to maximize system ductility. In the case of SCBFs this yielding hierarchy is shown in Figure 3.11.

This is in contrast to the current, traditional design method that allows only the first two mechanisms, brace buckling and yielding, to occur. Mathematically, the BDP can be described by Equation 3.32 below.

$$R_{yield,mean} = R_y R_{yield} \leq \beta_{y,1} R_y R_{yield,1} \leq \beta_{y,2} R_y R_{yield,2} ... \leq \beta_{y,i} R_y R_{yield,i} \tag{3.32}$$

This inequality shows that the secondary yielding mechanisms have strengths greater than the primary mechanism, $R_{yield,mean}$, and are separated by balance factors, β. The β factors appear to be similar to the resistance factors, ϕ, from AISC [2005b] but are fundamentally different. Resistance factors account for uncertainties in the capacity, whereas the balance factors are used to ensure a sequence of yielding. As a result, energy dissipation is shared between a number of elements and the ductility and deformation capacity of the system increases.

In addition to balancing yielding mechanisms, it is imperative that failure modes occur in an order that maximizes system performance. In the case of SCBFs, the primary failure mode is brace fracture and all others follow after that. This is accomplished in a similar manner as that described by Equation 3.32 and is described by Equation 3.33 below.

$$R_{yield,mean} = R_y R_{yield} \leq \beta_{fail,1} R_{fail,1} \leq \beta_{fail,2} R_{fail,2} ... \leq \beta_{fail,i} R_{fail,i} \tag{3.33}$$

where $R_{fail,1}$ is brace fracture. Again, the failure modes are separated from the primary yield strength by balance factors that are calibrated to ensure ductile behavior without failure.

In the following, the BDP will be discussed as it pertains to each limit state. A complete description of the development of the β factors may be found in Lumpkin [2009] and Roeder [2011]. This methodology has been developed for SCBF systems and has not yet been

extended to BRBF systems including the pin-type connection used in the author's second experiment.

BDP Brace to gusset plate connection

The design expressions for the welded connection between the brace and the gusset remain unchanged and the β factors equal the current ϕ factors.

BDP Brace net section fracture

The BDP expression for brace net section fracture remains the same but the β factor is equal to 0.9 as opposed to the ϕ factor of 0.75.

BDP Gusset plate yielding on the Whitmore width

The BDP expression for gusset plate yielding is similar to the current LRFD expression except for the use of the expected yield stress as opposed to the nominal yield stress currently in use in the LRFD method. The BDP expression for Whitmore yielding is given by Equation 3.34 below.

$$\beta R_n = \beta R_y F_y B_w t_g \tag{3.34}$$

where $\beta = 1.0$.

BDP Gusset plate fracture on the Whitmore width

The BDP expression for Whitmore width fracture is essentially the same as the current LRFD expression but β=0.85 instead of the 0.75 ϕ factor.

BDP Gusset plate block shear rupture

The BDP block shear expression has been changed to reflect experimental results [Lumpkin, 2009], reduce conservatism and to encourage yielding by removing the yielding part of the expression. This results in Equation 3.35 below.

$$\beta(0.6F_u A_{nv} + U_{bs} F_u A_{nt}) \tag{3.35}$$

where β=0.85

BDP Gusset plate buckling

The BDP expression for gusset plate buckling is essentially the same but β=0.9 instead of ϕ=0.85.

BDP Gusset plate interface welds

The most significant and arguably the most important aspect of the BDP is the design of the gusset interface welds. Currently, the UFM is typically used to calculate the weld design forces but this ignores the demands due to frame action which tends to open and close the joint, and the demands due to post-buckling gusset rotation. It was shown in previous research [Lumpkin, 2009] that designing these welds for the strength of the gusset plate not only simplifies design but also provides adequate resistance prior to brace fracture. The BDP expression for these interface welds is shown in Equation 3.36 below.

$$2(1.5)\beta(0.6)F_{EXX}t_{eff} \geq R_y F_y t_g \tag{3.36}$$

where β=0.75, t_{eff} is the effective throat size defined in Equation 3.37 and the factor of two accounts for the weld occurring on both sides of the plate. This equation is a modification of Equation 3.28 with the 1.5 factor used to account for the strength increase of a fillet weld loaded at an angle to its longitudinal axis.

$$t_{eff} = \frac{\sqrt{2}}{2}\frac{D}{16} \tag{3.37}$$

where D is the weld leg size in sixteenths.

BDP comparison with LRFD

Table 3.6 compares the SCBF connection limit state design equations and ϕ factors per the current AISC method [2005b] and those proposed per the BDP.

Elliptical brace clearance

Lehman et al. [2008] demonstrated that the linear $2t_g$ brace offset commonly used by designers negatively affects the ductility capacities of SCBFs. An elliptical clearance model

was proposed based on numerous experiments and numerical simulations [Lehman et al., 2008; Yoo et al., 2008] and was shown to result in comparable or significantly better system behavior. Figure 3.12 shows a schematic drawing highlighting the important geometric parameters of the elliptical clearance method. N_t defines the distance that the ellipse is offset from the beam and consequently defines where the brace terminates. A method for calculating all of the parameters may be found in Kotulka [2007]. A value of N=8 has been shown to provide the best system behavior by balancing the limit states of weld interface failure and brace fracture [Yoo, 2006].

3.4.3 Column and Beam Design

The beams and columns were designed according to capacity principles based on the chosen brace sizes with additional demands determined from structural analysis. The demands from gravity load are relatively small due to the inability to apply gravity load to the floor system in the laboratory. Therefore, the gravity demands on the system are only from the self weight of the beams and the concrete floor.

The structural analysis for design was performed with SAP 2000 [CSI, 2010] by pushing the test specimen model out to 0.4% story drift ratio (SDR) in a purely elastic analysis. The limit of 0.4% SDR was chosen as it corresponds to the maximum allowable SDR per ASCE 7 [2010] that is commonly used (2%) divided by the deflection amplification factor, C_d, which equals 5 for SCBFs (2/5 = 0.4). The beam and column end moments were found from the above structural analysis while the beam axial loads were found from the horizontal component of the expected brace forces. The column axial loads were found from the vertical component of the expected brace forces. These brace forces are described by Eqns. 3.1 and 3.2 for the first test specinem with conventional buckling braces and Eqns. 3.3 and 3.4 for the BRBF test specimen. Tables 3.7 and 3.8 list the design parameters and forces used for the conventional buckling braces and the BRBs, respectively.

Since the shared column is part of the braced frames in each direction, the design of this member must consider simultaneous seismic loading in orthogonal directions [ASCE, 2010]. In other words, 100% of the brace and beam loads in one direction were added

to 30% of the brace and beam loading in the orthogonal direction. Two cases required consideration for each brace type: (1) frame deformed in the positive X and Y directions simultaneously (see Fig. 3.2 for directions) and (2) frame deformed in the negative X and Y directions simultaneously. The first case results in the maximum compressive load in the shared column while case 2 results in the maximum tensile load in the shared column.

The demand-capacity ratios (DCR) of the beams and columns were determined according to AISC Eqns. H1-1a and H1-1b shown below as Eqns. 3.38 and 3.39.

For $P_u/\phi P_n > 0.2$

$$\frac{P_u}{\phi P_n} + \frac{8}{9}\left(\frac{M_{ux}}{\phi M_{nx}} + \frac{M_{uy}}{\phi M_{ny}}\right) \leq 1.0 \tag{3.38}$$

For $P_u/\phi P_n < 0.2$

$$\frac{P_u}{2\phi P_n} + \left(\frac{M_{ux}}{\phi M_{nx}} + \frac{M_{uy}}{\phi M_{ny}}\right) \leq 1.0 \tag{3.39}$$

These DCRs for the frame beams and columns are shown in Tables 3.9 and 3.10 for the SCBF and BRBF, respectively. Also shown in the tables are the DCRs due to axial load only. The DCRs for the columns ranged from 0.64 to 0.82 while the braced frame beam DCRs ranged from 0.86 to 0.95. The columns were designed with some conservatism to ensure that they were not damaged considerably during the first test which was expected to sustain smaller drifts at failure than the second test (BRBF).

The panel zones of the braced frame columns were analyzed to determine if the webs were adequately sized to prevent yielding according to the current philosophy used for moment frames [AISC, 2010]. This check is typically not performed by practicing engineers during the design of braced frame columns and is not required by AISC [2010]. The check was performed as a basis for assessing the behavior of panel zones in braced frame systems where gussets plate occur above, below or at both locations on a beam at the joint. The forces on the panel zones were determined assuming that the beams formed plastic hinges at a distance of $d/2$ from the gusset plate reentrant corners. The column shears were determined from equilibrium assuming plastic hinges formed at all joints away from the joint in question at a distance of $d/2$ from the gusset edge and the column moments at the joint in question were found by moment equilibrium at that joint. The plastic moment at the beam face was determined ignoring axial load in the beam. No other forces were considered.

The calculations are shown in Appendix A and the results are shown in Table 3.11.

The analysis demonstrated that panel zone yielding is expected in the webs of all three braced frame columns with a demand-capacity ratios of 1.01 in the shared column and 1.7 for columns A-1 and B-2. These capacities are based on Eqn. J10-11 of AISC [2005b] and the measured material strengths (which were very close to R_yF_y of the wide flanges). However, web doubler plates were not provided in order to assess the effect of flexible panel zones on braced frame behavior.

3.4.4 SCBF Gusset plate design

The design of the gusset plates for the SCBF specimen followed the BDP and the elliptical clearance method described above. Example calculations for the a typical gusset plate at the beam-column connection are shown in Appendix A. Figure 3.13 shows the braced frame elevations for the SCBF test with the gusset plate nomenclature (GP-1, etc.). Table 3.12 lists the demand capacity ratios for each limit state described earlier. The BDP and the current state-of-the-practice methodologies are both listed. The specified nominal yield strength for the gusset plates was 50 ksi.

The DCRs based on current practice are in the column labeled "SOP" (state-of-the-practice). It can be seen that based on the current strength design method that many of the limit states are not satisfied. This is expected as the BDP encourages yielding and the β factors for fracture were updated based on the UW research. Yielding on the Whitmore area governs the design of GP-1, GP-2 and GP-5 when the BDP is used while buckling governed the design of GP-3 and GP-4. However, it can be argued that the buckling lengths used for GP-3 and GP-4 are conservative since they ignore the fact that there is a column web stiffener that will prevent buckling over the length used in the calculations. The stiffeners were used for GP-3 and GP-4 because these framed into the web of column B-1 and were required to prevent excessive demands on the web of this column. The final gusset plate designs for each gusset are shown in Figures 3.14 through 3.17. Note that the gusset interface fillet welds are double-sided and the same size as the gusset plates. This is typical in the BDP since the welds are designed for the strength of the gusset plate. The $8t_g$ elliptical

offset is also shown in the figures (except at the brace splice connection where it is a $4t_g$ linear offset).

The brace splice connection at the intersection of the single story X is shown in Figure 3.18. This same connection and braces were tested by Powell (2010) and the design followed the BDP. The same geometry was used in the author's SCBF test that was used by Powell. Effort was made to supply as compact a gusset plate as possible while keeping the thickness within a reasonable limit. To this end, the plate was made 9 13/16" wide which is less wide than the Whitmore width of 12.24 in and a thickness of 3/8."

3.4.5 BRBF Gusset plate design

BRBs are not expected to deform out-of-plane (nor is it desirable) and therefore, the clearance model for CBFs does not apply to BRBFs. Given that much less research has been performed on gusset plates for this system, it was decided that the gusset plates in the BRBF specimen would be designed according to the current standards using the uniform force method and the limit states outlined in AISC [2010] instead of the balanced design approach. The gusset plates were designed by the BRB manufacturer, Star Seismic. The BRB load was transferred to the gusset plates via a pin resulting in a large concentrated load. As a result, the governing limit state for the gusset plate was bearing at the pin hole requiring a relatively thick gusset plate (1") with 1/2" reinforcing plates on each side of the hole. Table 3.13 shows the DCRs for each limit state and gusset plate type according to Figure 3.19. It can be seen that the capacities for all limit states except bearing are much larger than the demands. The gusset details are shown in Figure 3.20 with the gusset interface weld schedule shown in Table 3.14.

3.5 Base and Crosshead Connections

3.5.1 Base Connection

The column connections to the laboratory strong floor were designed to provide a rigid connection that would prevent uplift and slip. The bottom of all columns were attached to 3" thick A572 plates with CJP welds at the flanges and double-sided fillet welds at the

webs. The column base plates were bolted to 4" thick A572 plates, denoted hereafter as strong floor plates, with 1"ϕ A490 bolts. The 4" strong floor plates had 1"ϕ holes that were tapped at 3" on center (o.c.). These braced frame strong floor plates were anchored to the strong floor with 3"ϕ B7 threaded rods that were pretensioned to 440 kips. The gravity column strong floor plates were anchored to the strong floor with a combination of 1 1/2" and 3"ϕ B7 rods pretensioned to 125 and 440 kips, respectively. Figure 3.21 shows the detail of these base connections for each column along with the bolt layouts and plate sizes. The 4" plates were required because the anchoring holes in the strong floor are located at a relatively large 18" o.c. and therefore, require a large plate to attach enough anchors to resist the column and brace forces. These 4" strong floor plates are owned by the MAST laboratory and were provided to ease connection of the test specimen to the strong floor. Additionally, the strong floor plates allow typical base details to be used in the test specimen. The structural drawings for the column base plates that were supplied to the steel fabricator are shown in Figures B.14 through B.15 in Appendix B. A photo taken of the base of column A-1 during installation is shown in Figure 3.22.

3.5.2 Crosshead Connection

The loads were transferred from the crosshead actuators into the test specimens through a pretensioned, bolted connection between the bottom plate of the crosshead and the third floor slab of the specimen. Sixty-four 1-1/2"ϕ B7 rods, each pretensioned to 125 kips, were used at the locations shown in Figure 3.23a. The large pretension force ensured that the lateral forces could be transferred from the crosshead to the slab via friction. A schematic of the crosshead above Frame 1 with relevant dimensions are shown in Figure 3.23b while the detail at each B7 rod is shown in Figure 3.24. PVC sleeves were cast in the slab to allow for rod installation after the concrete floor slab has attained the required strength. A one to two inch gap was maintained between the top floor slab and the bottom of the crosshead that was filled in with high-strength grout prior to bolt tensioning. Due to the large in-plane forces in the slab, a 10" slab with a reinforcement ratio of approximately 1.5% in each direction was utilized. The slab reinforcement layout is shown in Figure 3.25

and a photo of the in-place reinforcement and connector sleeves is shown in Figure 3.26a. The connection of the through rods to the underside of the slab is shown in Figure 3.26b.

3.6 Instrumentation

The test specimen's behaviors were determined with a number of instruments which included strain gauges, string potentiometers (string pots), linear variable differential transformers (LVDTs), dial gauges, and the optical Krypton system. Over 450 channels of instruments were used in each test. Whitewash, a mixture of lime and water, was applied to the steel in locations where yielding was expected to illustrate the sequence and distribution of yielding. Additionally, a large number of photographs and video were taken using the four MAST laboratory telepresence towers which were equipped with two still and two video cameras. Data was measured and recorded at 1 Hz. Each test spanned four to five days and data was recorded at 0.01 Hz during the overnight breaks while the specimen was at rest.

Many of the measurements were used to calculate quantities such as story drifts, panel zone shear strain, and internal forces. These calculations are explained in Appendix C.

The strain gauges were placed on the braces, columns and beams. These strain gauges were used to estimate the internal forces and moments in the system and estimate when member yielding occurred. Two different types of strain gauges were used. Tokyo Sokki Kenkyuho Co. Ltd. FLA-6-11-5LT were used at the locations where no yielding was expected. These are uni-axial, temperature-integrated gauges with 6 mm gauge length and a gauge factor of 2.12. YEFLA5-5LT were used in the areas where yielding was expected. These gauges are uni-axial, temperature-integrated, high elongation gauges.

LVDTs were used to measure column and beam rotations, column panel zone rotations, base slip and uplift and slip between the crosshead and the third floor slab. The LVDTs were Macro Sensors models PRH and SQ with ranges of $\pm$0.1, 0.5, 1.0 and 2.0 inches. String pots were used to measure story displacements, OOP brace and gusset displacements, brace axial deformation, and base slip. The string pots used were UniMeasure models P1010 with total movement ranges between 2 and 40 inches.

3.6.1 MAST Crosshead Instrumentation

The loads transfered to the specimen were measured with load cells within the actuators. The displacement of the actuators were calculated with LVDTs within the actuators.

3.6.2 Brace and Gusset Plate Instrumentation

A combination of strain gauges and string potentiometers were attached to the braces and gusset plates to measure strains, axial deformations, and out-of-plane (OOP) brace and gusset plate deformation. The following two sections describe these instruments for the SCBF and the BRBF, respectively.

SCBF Specimen

Four strain gauges were placed at each end of the conventional braces on each face in order to estimate the axial load in the brace and to determine when buckling and yielding occurred. Figures 3.27a and 3.27b show the brace strain gauge layout for Frames 1 and B, respectively. The numbering scheme is shown in the figure, with gauge number 1 occurring on the brace side on the exterior of the frame while gauge number 3 occurs on the interior side of the brace. Strain gauge number 2 occurs on the top face, and gauge number 3 occurs on the bottom face. All brace strain gauges were YEFLA5-5LT.

The second story braces and gusset plates in Frame B were heavily instrumented with string pots to determine the OOP deformation magnitudes and profiles. Figure 3.28 shows the location of these 13 string pots on the braces along with the range of each stringpot used. The stringpot housings were mounted on a support frame constructed of a light gage angle system with regular holes spaced at three inch (manufactured by EFCO©) and hung from the third floor slab just inboard of Gravity Bay A as shown in plan in Figure 3.29a and the photo in Figure 3.29b. Additionally, two rotation meters were installed on the EFCO frame at the bottom to measure the rotations of this frame to correct the stringpot measurements affected by this movement. The rotation meter installed on the bottom of the south side of the support frame is shown in Fig. 3.29b.

Twelve out of 16 corner gusset plates were instrumented with string pots to measure

the gusset rotation angle after brace buckling and to capture any change in the direction of brace OOP deformation. Figures 3.30a and 3.30b show the location of these string pots in Frame 1 and Frame B, respectively. At the base, the pots were mounted to EFCO stands anchored to the strongfloor and an example is shown in Figure 3.31a. At the second floor, the pots were mounted to an aluminum rig that was attached to the floor beams and an example is shown in Figure 3.31b. The method of calculating the gusset rotation angle is described in Appendix C.

BRBF Specimen

Two string pots were installed at each end of each BRB to measure the core axial deformation. As shown in Figure 3.32, the string pot housing was attached to the casing while the opposite end of the string was attached to the collar. Two string pots were used at each end on opposite sides of the broad face of the BRB as shown in Figure 3.33. The stringpot layout with corresponding labels are shown in elevation in Figure 3.34. To estimate the axial force resisted by the casing, a longitudinal strain gauge was installed on each broad face at the center of the brace at each story. Figure 3.35 shows the layout and naming convention for these gauges.

3.6.3 Column Instrumentation

At least four strain gauges were placed on a column cross-section at two locations in each story to estimate the column moments and story shears (see Appendix C) from the cross-section curvatures. Figures 3.36a and 3.37 show the column strain gauge layout for Braced Bays 1 and B, and Gravity Bays 2 and A. The frames are viewed from the outside of the test specimen in these elevations. The strain gauge numbering scheme is made clear from the sections below each column in the elevations. As shown in Figure 3.36, six strain gauges were placed at each location on the shared column. This was done to understand the strain distribution and variation across the column flanges. All column strain gauges were FLA-6-11-5LT.

Average column joint rotations above and below the second floor at the shared column

and columns B1 and B2 were estimated with LVDTs. Panel zone deformations were also estimated at the second floor joints of these same columns. Figures 3.38 and 3.39 show the detail and LVDT labels at each joint. The rotations about the strong and weak column axes were estimated with four LVDTs placed near the tips on the outside of each flange as shown in Figure 3.39b. The LVDTs were mounted on aluminum plates and fixed at a distance of $d_c/3$ from the gusset corner while the measurement endpoint of the LVDT occurred at d_c away from the gusset corner and joint center as shown in Figure 3.41. Figure 3.40a shows a photograph of two column rotation LVDTs installed at the bottom of the second floor joint on column B2. The aluminum support plates were attached to the column at each end with studs welded to the column flange and bolted to the plates. The hole furthest away from the joint was slotted to allow the LVDT housing to move when the column rotated with enough play to prevent binding while providing support for a clean measurement.

Panel zone deformations within the beam depth were measured at each braced frame column at the second floor. Additionally, shear deformations withing the gusset plate regions were measured above and below the second floor joint at columns B1 and B2. Figures 3.38 and 3.39 depict the layout and labels of this instrumentation at each joint. A photo of the panel zone instrumentation at column B1 is shown in Figure 3.40b.

3.6.4 Beam Instrumentation

Braced frame beams at the second floor were heavily strain gauged near the beam ends outside the gusset plate to capture curvatures and the location of the neutral axis. Figure 3.42 shows the strain gauge layout on the second floor beams in Frame 1 at the column B1 side and the shared column side. The first line of gauges occurs at approximately $d_b/2$ away from the gusset reentrant corner while the second line of gauges occurs at a distance of d_b away from the gusset reentrant, where d_b is the beam depth. Three gauges are spaced evenly in the web with one at the centroid and a gauge is placed on each flange. Due to the floor slab, the top flange gauge was placed on the bottom of the flange. Figure 3.43 shows the strain gauge layout on the second floor beams in Frame B at the shared column side and the column B2 side. All beam strain gauges were YEFLA5-5LT.

Average beam rotations were calculated at the second floor braced frame beams at the gusset area at each column with LVDT mounted on the inside of the top and bottom flanges. Figure 3.38 shows the beam rotation LVDTs in Frame 1 at column B1 and shared column side while Figure 3.39 shows the same at column B2. Figure 3.44a shows the same at the shared column side in Frame B and Fig. 3.44b shows a photograph of this.

3.6.5 Story Drift Instrumentation

Story drifts at each level were estimated with string pots located at three corners of the floor plan as shown in Fig. 3.45. Assuming a rigid diaphragm and using triangulation, the drifts in each principal direction were calculated along with any twist of the story (see Appendix C).

The string pot housings were attached to strongwall (Figure 3.46a) while the other ends were attached to the columns at the beam centerlines as shown in the schematic in Figure 3.46b.

3.6.6 Base and Crosshead Slip Instrumentation

A combination of string pots and LVDTs were used to measure the slip and uplift at the base and the slip between the crosshead and the top floor slab. The base instrumentation is shown in Figure 3.47a while the crosshead / slab instrumentation is shown in Figure 3.47b. Figure 3.48 shows a photograph of slip and uplift instrumentation at the base of column B1.

3.7 Loading Protocol

The loads were transferred to the specimen from the crosshead to the top floor slab, through the frame and finally to the strongfloor. Limitations of the lab prevented the second story from being loaded laterally and therefore, the horizontal shear is constant throughout the height of the specimen. A vertical force could not be directly applied to the columns since it would have been transferred through the top floor beam connections. A vertical force large enough to make a difference in the response would have required connections much larger

than typical connections or a direct connection from the crosshead to the columns. These details were cost prohibitive and it was more important to provide accurate connection details than large gravity loads since the response of braced frames is dominated by lateral loads and displacements. A downward axial load of 5 kips was applied to the top slab to ensure contact between the crosshead and the slab.

The lateral displacements at the top of the specimen were the primary control parameters. Cyclic displacements were applied bi-directionally in plan in the X and Y directions (see Fig. 3.2 for coordinate system). Due to the large difference in stiffness between the braced frames and the gravity frames in each direction, the center of rigidity of the system is near the corner where the braced frames connect to the "shared" column. The torsional rotation (Z-axis rotation) of the crosshead was maintained at zero to prevent substantial torsional deformation from occurring at the top. Torsional deformation was not restricted below this but instrumentation showed that very little twisting occurred below. No overturning moments about the X and Y-axes were applied to the specimen by the crosshead.

To maintain consistency with the previous planar experiments performed as part of this overall research program, the basic loading protocol in each principal direction was the same as that used in the UW tests and is based on the SAC and ATC-24 loading protocols [SAC, 1997; ATC, 1992]. The drift level at each cycle is a multiple of the yield drift, which is defined as the drift at which the first buckling of the brace occurs (SCBF) or first yielding occurs in the BRB. Fig. 3.49 shows the cyclic deformation history up to the 26th cycle in one direction while Table 3.15 lists the basic deformation values at each step. There are eight cycles prior to six cycles at the yield drift, Δ_y, followed by groups of two cycles at the subsequent deformation levels until failure occurs. Figure 3.49 shows only the first 26 cycles while Table 3.15 lists the first 29. However, more cycles were performed in each test as described completely in Chapter 4. Beginning at cycle 25 and beyond, the drift levels were incremented by $1.0\Delta_y$ every two cycles until the test was stopped. Predicting the yield drift requires an accurate numerical model and was closely estimated but differed slightly from that determined during the experiment. As a result, the cyclic displacement history in the actual test deviated slightly from this target history as will be discussed in Chapter 4.

The development of the bi-directional characteristics of the loading protocol was fa-

cilitated through nonlinear response-history analyses of prototype braced frame buildings [Sherman, 2009]. Three and six-story single diagonal BRBF buildings were designed and subjected to the X and Y-component of 10 ground motions from the SAC program. The X and Y-components were applied simultaneously to the buildings and the ground motions were scaled to represent a hazard of 10% in 50 years. The floor plan and south and west elevations of the three-story prototype are shown in Figure 3.50. One, single-bay braced frame was located at each building corner in each direction and shared the corner building column, similar to the test specimen.

The nonlinear response-history analyses were conducted in PERFORM-3D [CSI, 2007]. Rigid diaphragms were used and a 5% mass eccentricity was applied. The displacement time histories in each principal direction for each story were extracted and used to develop the loading protocol. Rainflow cycle counting [ASTM, 1985] was performed on each displacement history to convert the random history to an ordered sequence of cycles with the deformation ranges determined from the rainflow counting. Consistent with the hypothesis used by other researchers [ATC, 1992], it was assumed that damage to the frames is proportional to the plastic deformation range. The cumulative inelastic deformation in each orthogonal direction was then determined from the displacement histories. Braces typically buckle and/or yield between 0.25 to 0.4% story drift and therefore, 0.25% was chosen as the yield drift beyond which damage accumulates.

For each corner frame system in the prototype, the ratio of the damage (cumulative plastic deformation) in the X-direction and the Y-direction was found. If the number was less than unity, the inverse was used. The majority of the damage ratios fall between one and two with the mean ratio for all of the records for the three-story prototype being 1.38 while that for the six-story prototype being 1.4. Based on these results, a ratio of damage in the Y-direction to damage in the X-direction was chosen as 1.5. For the step-wise increasing loading protocol with equal number of cycles in each orthogonal direction, this amounts to a deformation in the principal direction equal to 1.5 times the deformation in the orthogonal direction. The principal direction for the SCBF was the Y-direction while the principal direction for the BRBF was the X-direction (see Fig. 3.2 for the directions relative to the specimen orientation). The final displacement-controlled, bi-directional protocol is shown

in Fig. 3.51a.

In Fig. 3.51a, the 1-direction is the principal loading direction and therefore the displacement in the 2-direction is 2/3 the displacement in the 1-direction (i.e. $2/3 = 1/1.5$). This defined points a, c, e and g. Points b, d, f and h were defined by minimizing the difference in area between the ellipse (shown dashed) defined by points a, c, e and g, and the area defined by the cloverleaf. A complete cloverleaf consists of two complete cycles in each direction with the first cycle consisting of deformation in quadrants I and III (Fig. 3.51b) and the second cycle in quadrants II and IV (Fig. 3.51c). The first four cycles of ramp 1 were performed uni-directionally in each direction with the cloverleaf beginning at cycle 5 of ramp 1. The cloverleaf protocol was performed until failure occurred in the principal direction frame. Loading was then done uni-directionally in the unfailed direction until failure occurred in that direction. Failure was defined as brace fracture for both test specimens.

Table 3.1: Wide flange and HSS material properties

Shape	Measured Properties	
	F_y (ksi)	F_u (ksi)
W12x106	56	74
W12x72	57	73
W12x45	57	72
W16x50	53	69
W16x31	55	69
W14x22	55	68
HSS3x3x1/4	65	79
BRB-1	43	66
BRB-2	42	65

Table 3.2: Concrete floor slab compression test results

Cylinder	Floor	Truck	f'_c (psi)	Cylinder age (days)
1	3rd	2	4828	3
2	3rd	2	4743	3
3	3rd	2	4760	3
4	3rd	3	5069	3
5	3rd	3	4974	3
6	3rd	3	5093	3
7	2nd	1	6544	28
8	2nd	1	5110	28
9	2nd	1	6430	28
10	3rd	2	7439	28
11	3rd	2	8512	28
12	3rd	2	8118	28
13	3rd	3	8220	28
14	3rd	3	8046	28
15	3rd	3	7368	28

Table 3.3: Concrete floor slab MEAN compression test results

Floor	Truck	f'_c, ave (psi)	Cylinder age (days)
3rd	2	4777	3
3rd	3	5045	3
2nd	1	6028	28
3rd	2	8023	28
3rd	3	7878	28

Table 3.4: Concrete floor slab splitting-tensile test results

Cylinder	Floor	Truck	f'_{ct} (psi)	Cylinder age (days)
16	3rd	2	534	28
17	3rd	2	565	28
18	3rd	2	691	28
19	3rd	3	608	28
20	3rd	3	501	28
21	3rd	3	438	28

Table 3.5: Concrete floor slab MEAN splitting-tensile test results

Floor	Truck	f'_{ct} (psi)	Cylinder age (days)
3rd	2	596	28
3rd	3	516	28

Table 3.6: Comparison of AISC and BDP limit states

Limit State	**AISC Design** ($\phi\ R_n$)	ϕ	**Balanced Design** ($\beta\ R_n$)	β
Brace to Gusset Plate Weld	$\phi(0.6)F_{EXX}N_wL_wt_{eff}$	0.75	$\beta(0.6)F_{EXX}N_wL_wt_{eff}$	0.75
Brace to Gusset Plate Base Metal	$\phi(0.6)F_uN_wL_wt_f$	0.75	$\beta(0.6)F_uN_wL_wt_{bm}$	0.75
Net Section Fracture	$\phi U(R_{tb}F_{ub}A_{nb} + F_{urp}A_{rp})$	0.75	$\beta U(R_{tb}F_{ub}A_{nb} + F_{urp}A_{rp})$	0.9
Whitmore Yielding	$\phi F_yB_wt_g$	0.9	$\beta R_yF_yB_wt_g$	1.0
Whitmore Fracture	$\phi F_uB_wt_g$	0.75	$\beta F_uB_wt_g$	0.85
Block Shear	$\phi 0.6F_uA_{nv} + U_{bs}F_uA_{nt} \leq \phi 0.6F_yA_{gv} + U_{bs}F_uA_{nt}$	0.75	$\beta(0.6F_uA_{nv} + U_{bs}F_uA_{nt})$	0.85
Gusset Plate Buckling	$\phi F_{cr}B_wt_g$	0.9	$\beta F_{cr}B_wt_g$	0.9
Interface Welds	$\phi(0.6)F_{EXX}N_wL_wt_{eff}[1 + 0.5(\sin\gamma)^2]$	0.75	$2(1.5)\beta(0.6)F_{EXX}t_{eff} \geq R_yF_yt_g$	0.75

Table 3.7: SCBF brace properties and design forces

R_y	F_y (ksi)	A_g	P_t (kips)	P_n (kips)	P_c (kips)	$0.3P_n$
1.4	46	2.44	157	90	99	27

Table 3.8: BRB properties and design parameters

BRB	A_{gsc} (in.^{2})	P_y (kips)	ω	β	$\omega\beta$	ωP_y (kips)	$\omega\beta\ P_y$ (kips)
BRB-1	2.84	123	1.36	1.4	1.9	167	235
BRB-2	2.92	123	1.36	1.4	1.9	167	235

Table 3.9: Braced frame column design demand to capacity ratios for SCBF test

Member	Shape	+X, +Y drift		-X, -Y drift	
		Axial only	Equation 3.38	Axial only	Equation 3.38
Column B-1 (shared)	W12x106	0.29	0.78 (0.82)	0.22	0.71 (0.75)
Columns A-1, B-2	W12x72	0.29	0.72	0.29	0.72
Beam	W16x50	0.22	0.86	0.22	0.86

Table 3.10: Braced frame column design demand to capacity ratios for BRBF test

Member	Shape	+X, +Y drift		-X, -Y drift	
		Axial only	Equation 3.38	Axial only	Equation 3.38
Column B-1 (shared)	W12x106	0.25	0.74 (0.78)	0.29	0.78 (0.82)
Columns A-1, B-2	W12x72	0.16	0.64	0.22	0.65
Beam	W16x50	0.28	0.93	0.3	0.95

Table 3.11: Column panel zone information

Mark	Shape	d_c, in.	t_w, in.	V_{pz}, kips	R_v, kips	$\frac{V_{pz}}{R_v}$
A-1, B-2	W12x72	12.3	0.43	364	214	1.7
B-1	W12x106	12.9	0.61	340	338	1.01

Table 3.12: SCBF gusset plate demand capacity ratios (see Figure 3.13 for gusset marks)

Element	**Limit State**	GP-1		GP-2		GP-3		GP-4		GP-5	
		BDP	SOP	BDP	SOP	BDP	SOP	BDP	SOP	BDP	SOP
Brace	Brace-gusset welds	0.88	0.88	0.88	0.88	0.88	0.88	0.88	0.88	0.88	0.88
	Net section fracture	0.95	1.2	0.95	1.2	0.95	1.2	0.95	1.2	0.98	1.25
Gusset plate	Whitmore yielding	0.94	1.14	0.94	1.14	0.94	1.14	0.94	1.14	0.78	0.95
	Whitmore fracture	0.93	1.05	0.93	1.05	0.93	1.05	0.93	1.05	0.78	0.95
	Block shear	0.9	1.24	0.9	1.24	0.9	1.24	0.9	1.24	0.6	0.83
	Buckling	0.75	0.75	0.88	0.88	1.02	1.02	1.04	1.04	0.63	0.63
	Interface welds	0.83	1.02	0.83	0.61	0.83	0.95	0.83	0.53	NA	NA

Table 3.13: BRBF gusset plate demand capacity ratios (see Figure 3.19 for gusset marks)

Limit State	BGP-1	BGP-2	BGP-3
Pin Bearing	0.97	0.97	0.97
Whitmore Yielding	0.61	0.61	0.61
Tensile Rupture	0.5	0.5	0.5
Shear Rupture	0.55	0.55	0.55
Buckling	0.61	0.63	0.63

Table 3.14: BRBF gusset plate interface weld schedule
(units are inches, see Figure 3.20)

Mark	W1	L1	W2	L2
BGP-1	7/16	10.75	5/16	13.5
BGP-2a	7/16	5	3/8	14
BGP-2b	3/8	5.5	5/16	15.5
BGP-2c	7/16	5	5/16	15.5
BGP-3	3/8	5	5/16	22

Table 3.15: Cyclic loading protocol in principal directions for SCBF and BRBF tests

Cycle number at start of new drift level	1	7	9	15	17	19	21	23	25	27	29
Number of cycles at drift level	6	2	6	2	2	2	2	2	2	2	2
$\frac{\Delta}{\Delta_y}$	0.5	0.75	1.0	1.25	1.5	1.75	2.0	2.5	3	4	5
Estimated SCBF RDR (percent)	0.15	0.23	0.3	0.38	0.45	0.53	0.6	0.75	0.9	1.2	1.5
Estimated BRBF RDR (percent)	0.17	0.26	0.34	0.43	0.51	0.60	0.68	0.85	1.0	1.36	1.7

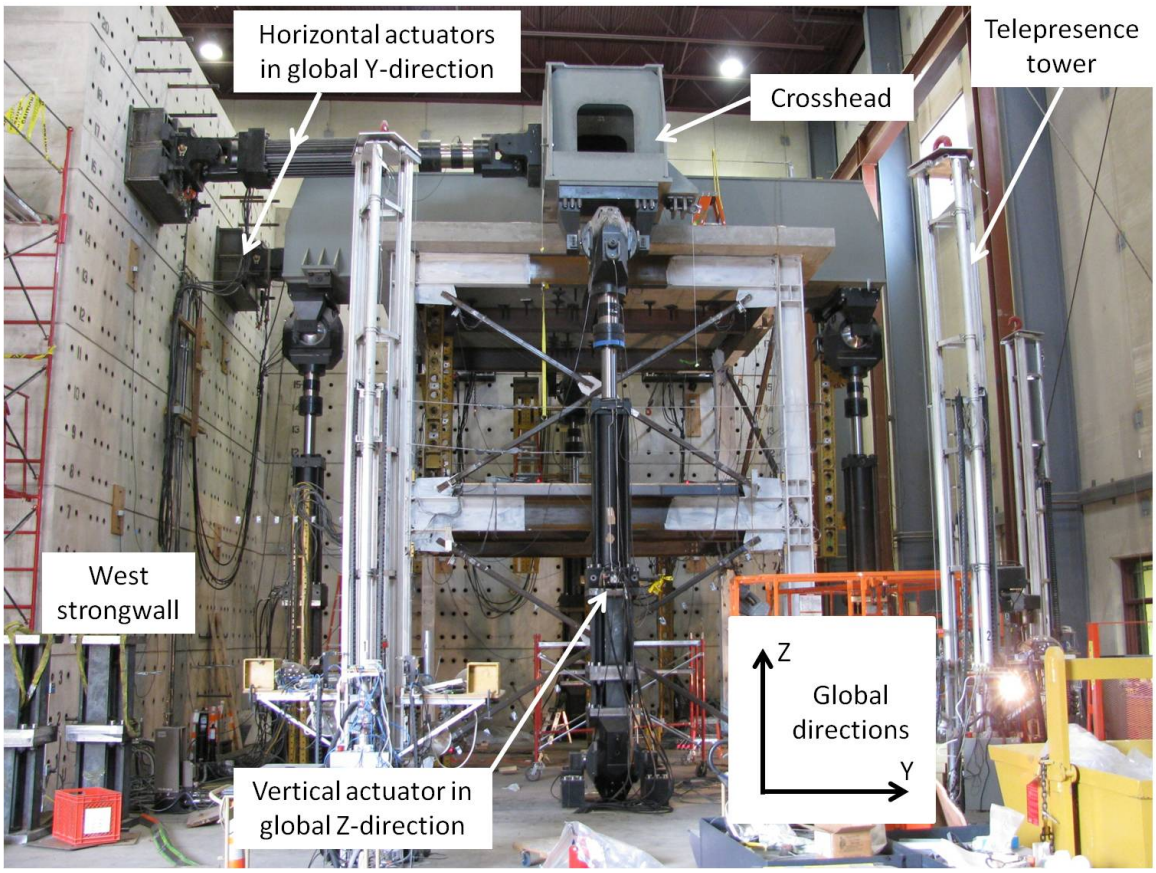

Figure 3.1: MAST facility with SCBF specimen in place

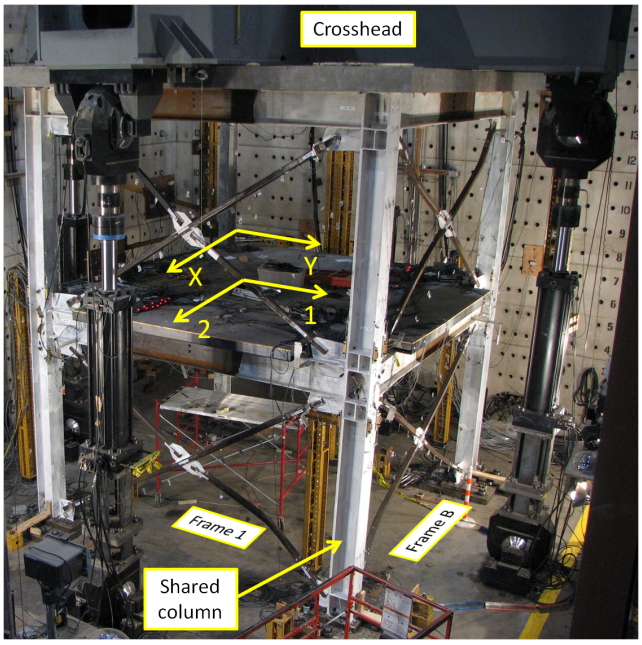

(a)

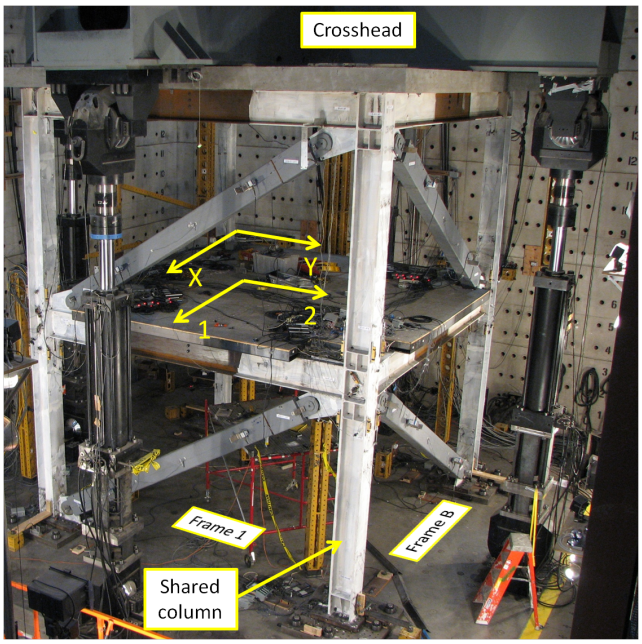

(b)

Figure 3.2: Specimen photographs: (a) SCBF specimen; (b) BRBF specimen

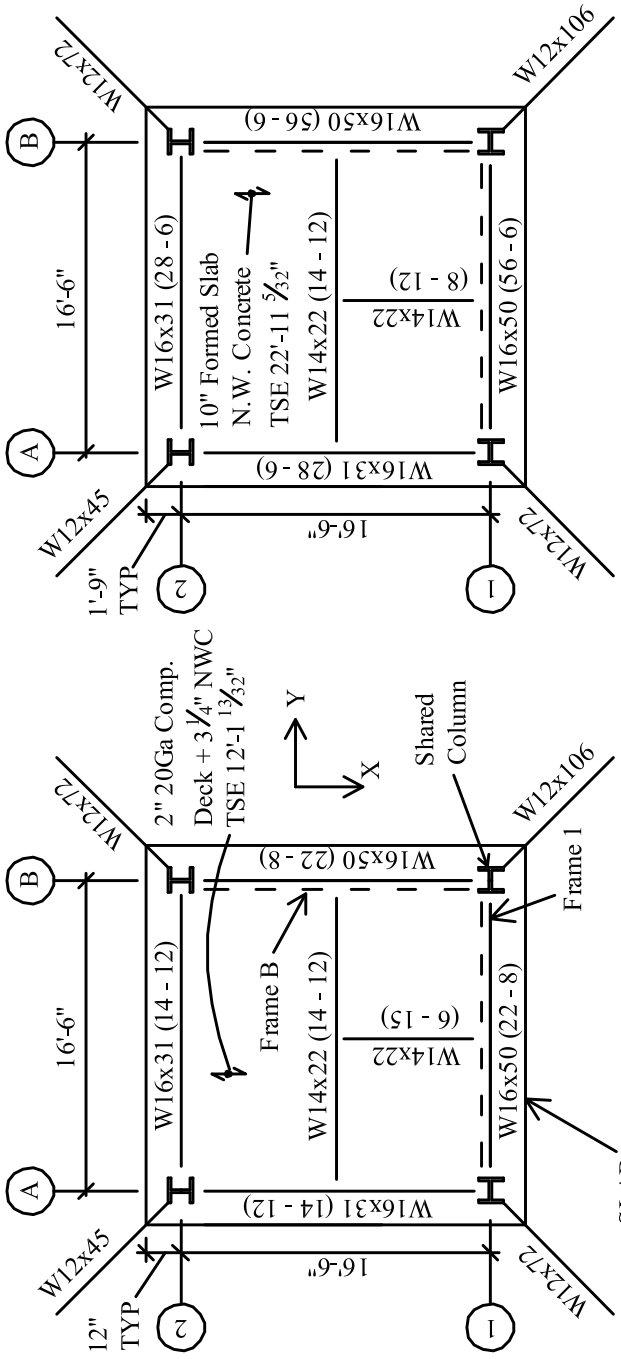

Figure 3.3: Specimen floor plans: (a) second floor; (b) third floor

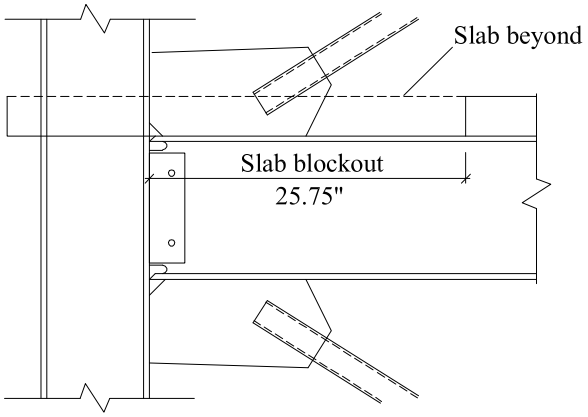

Figure 3.4: Slab blockout at second floor

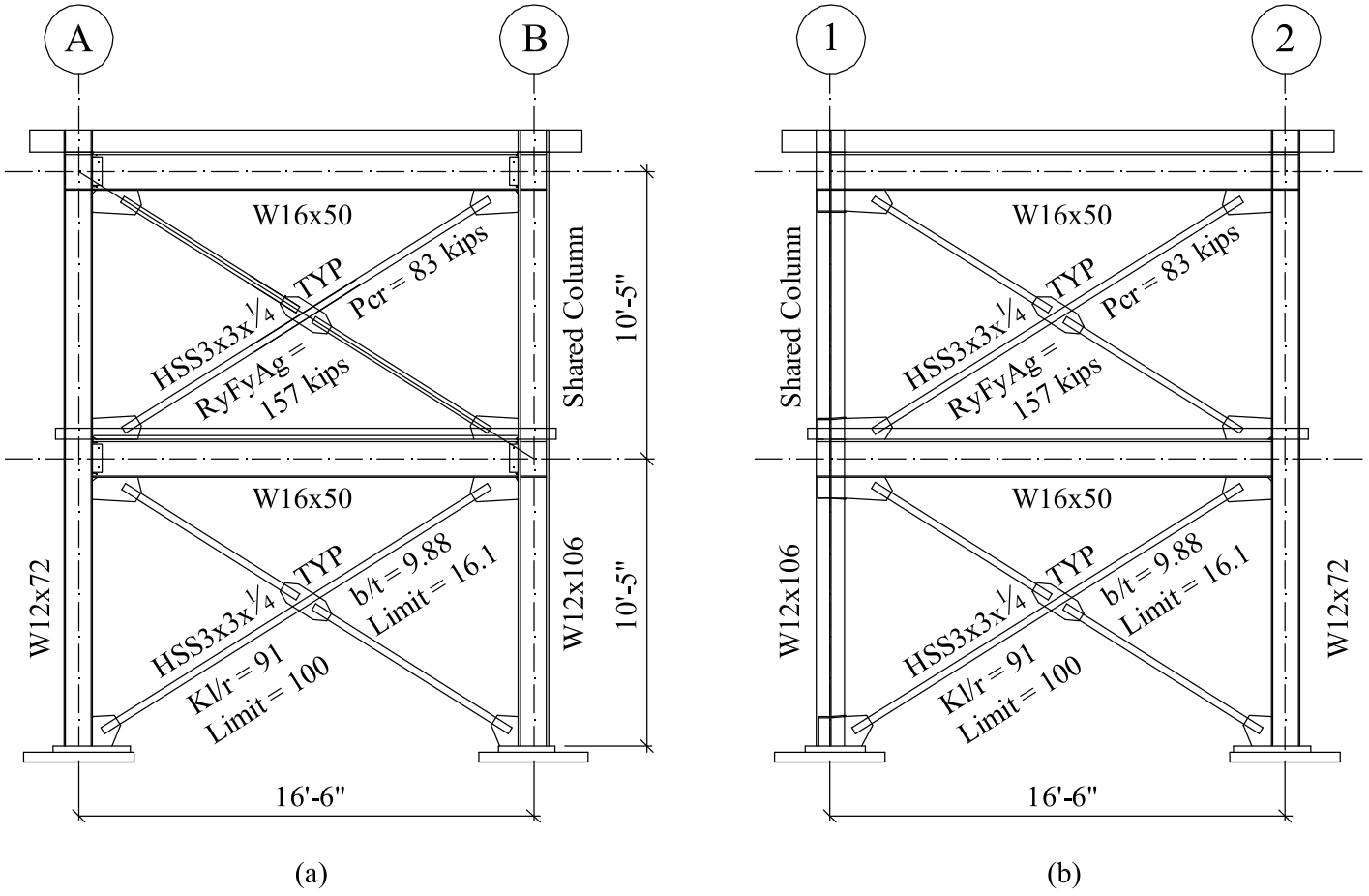

Figure 3.5: SCBF braced frame elevations: (a) Frame 1; (b) Frame B

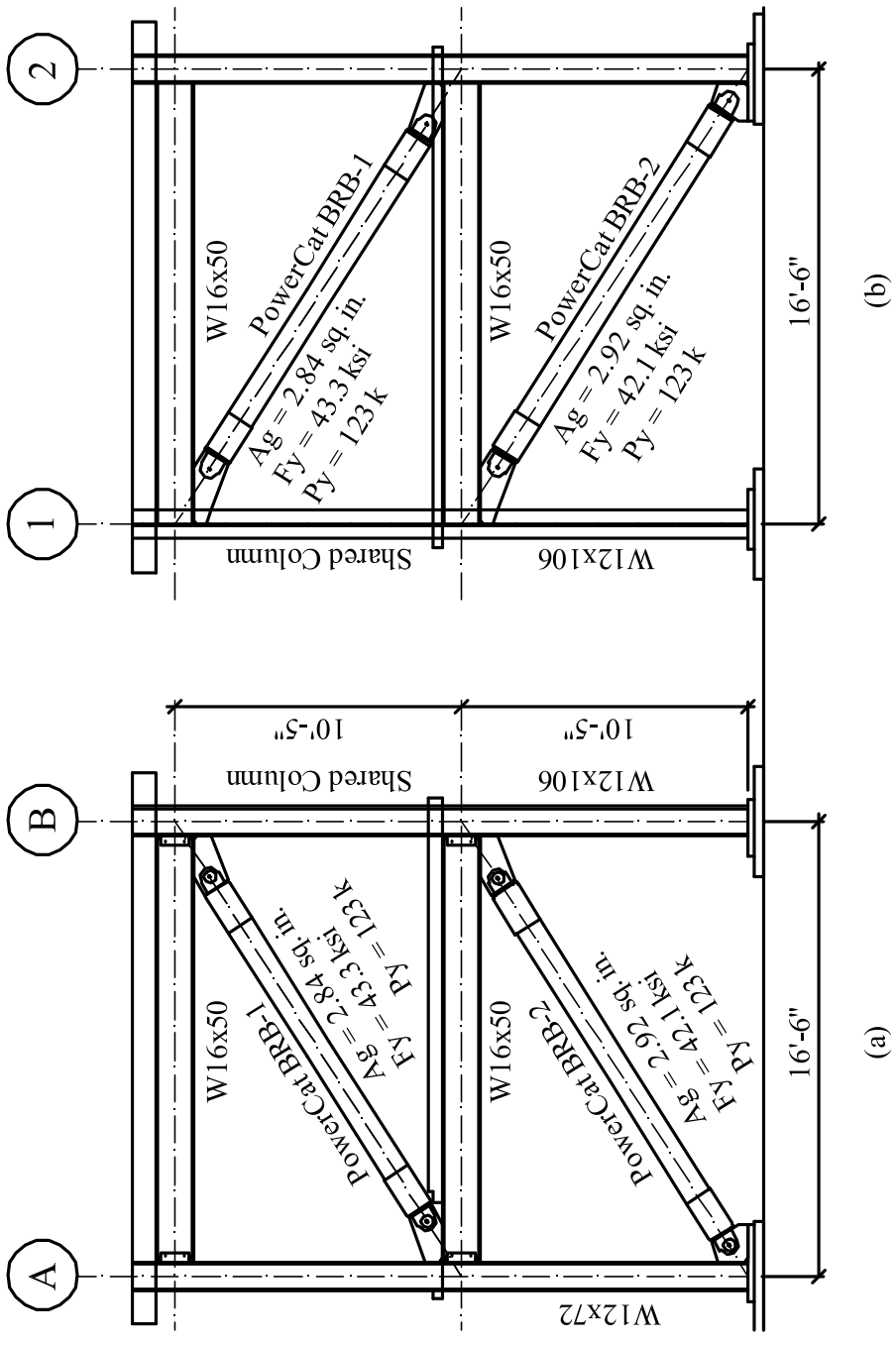

Figure 3.6: BRBF braced frame elevations: (a) Frame 1; (b) Frame B

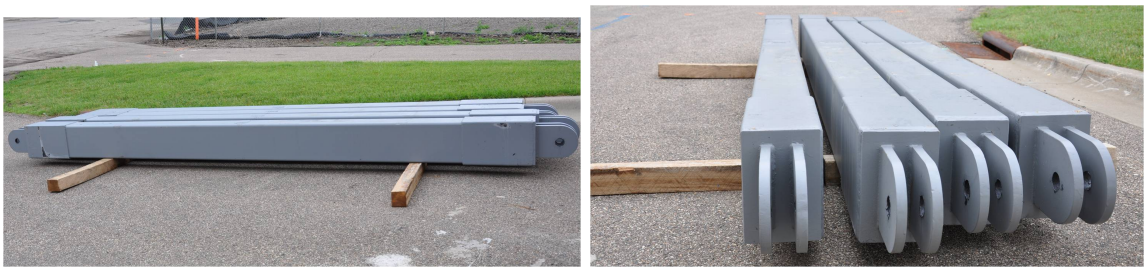

(a) (b)

Figure 3.7: BRBs prior to installation

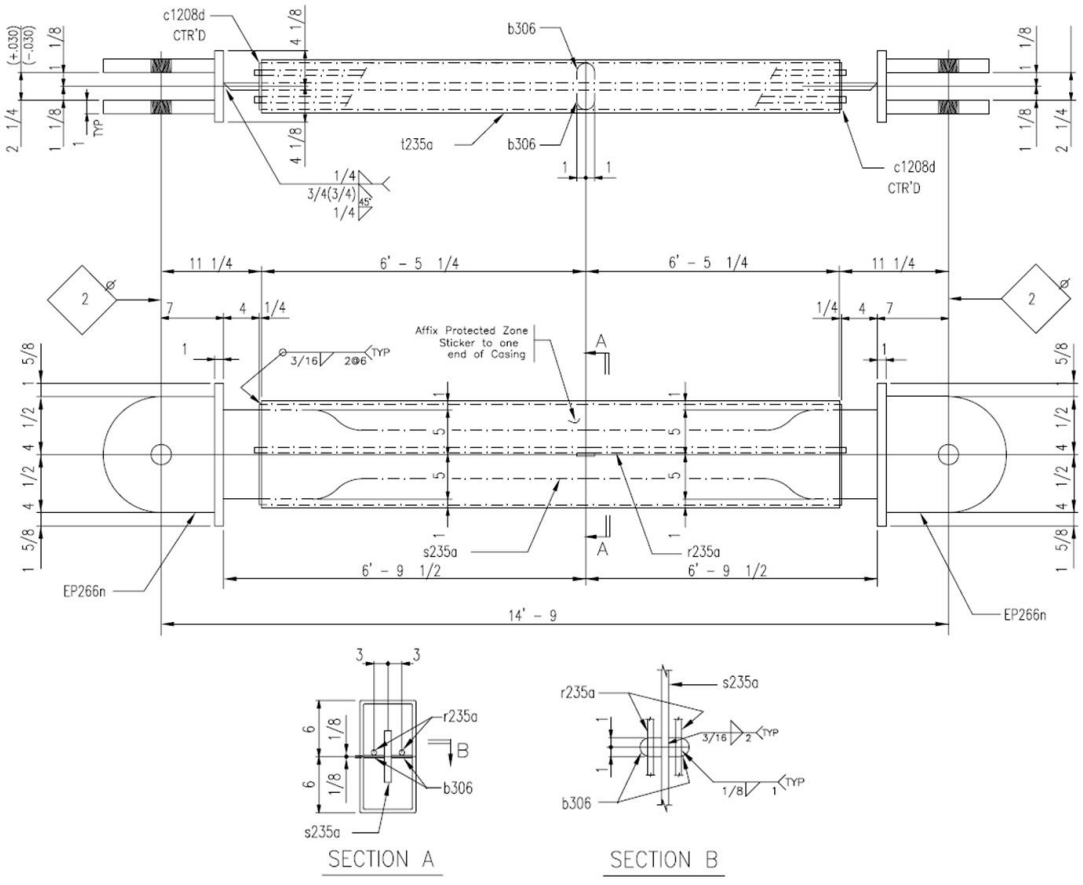

Figure 3.8: BRB-1 fabrication drawing

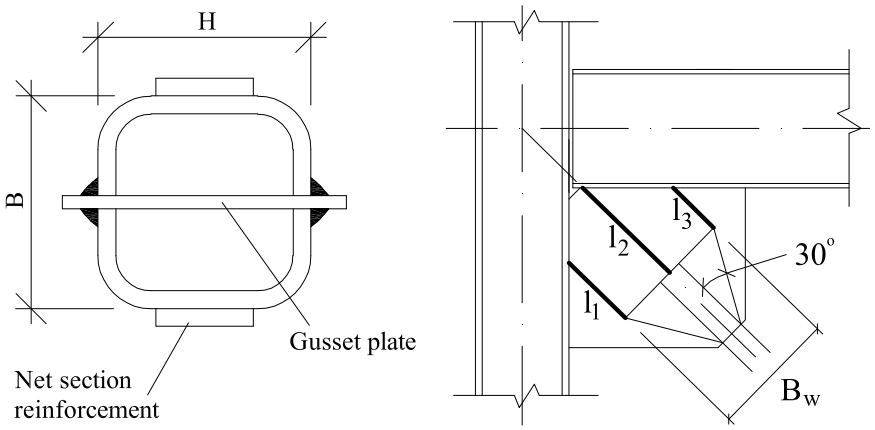

(a) (b)

Figure 3.9: Brace and gusset plate nomenclature: (a) HSS brace net section; (b) gusset plate buckling lengths and Whitmore width

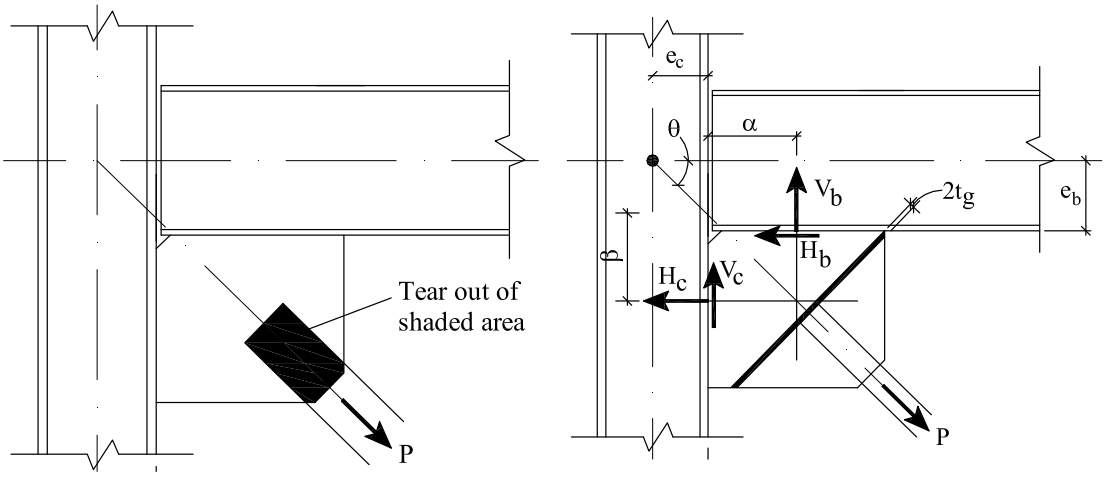

(a) Block shear rupture (b) Uniform force method and $2t_g$ linear offset

Figure 3.10: Gusset plate schematics

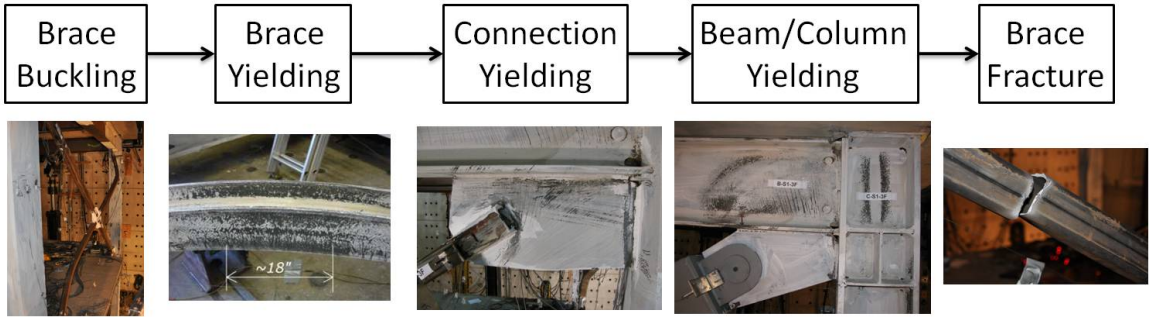

Figure 3.11: Balanced Design Procedure yielding hierarchy for SCBF systems

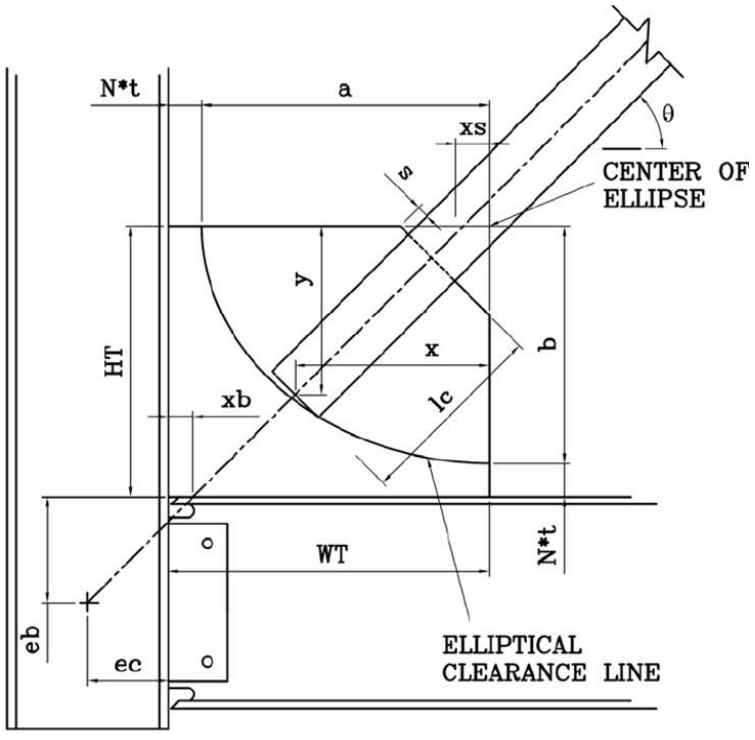

Figure 3.12: Elliptical clearance geometry (Source: Kotulka 2007)

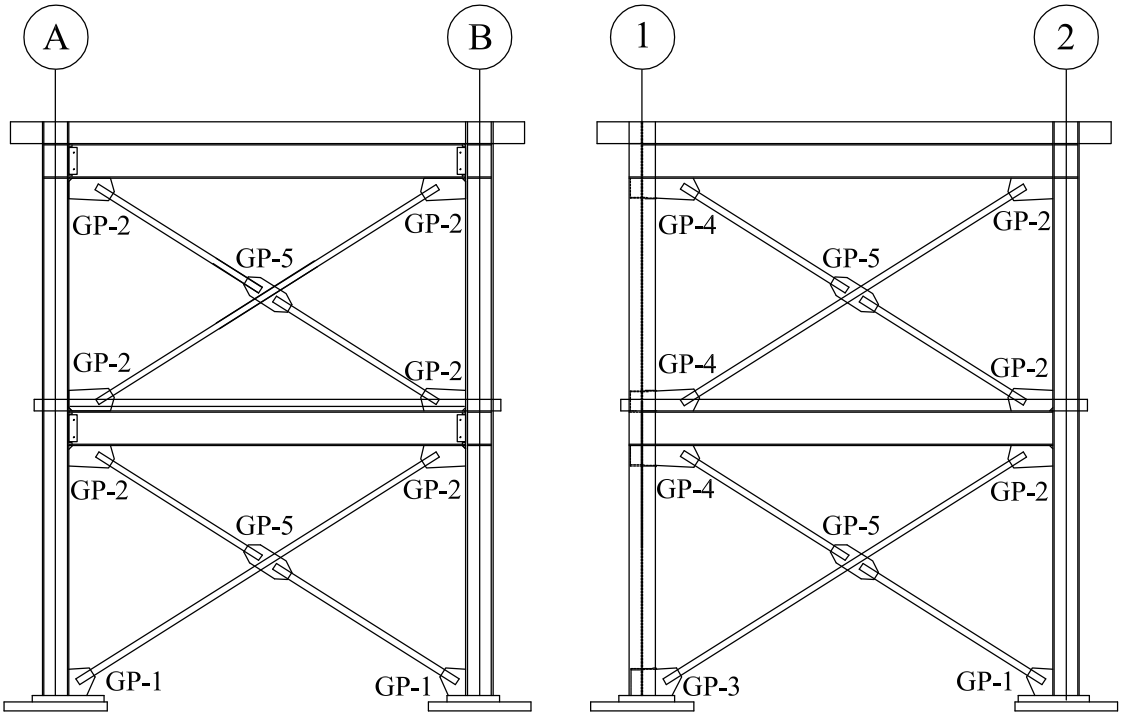

(a) (b)

Figure 3.13: SCBF gusset plate nomenclature: (a) Frame 1; (b) Frame B

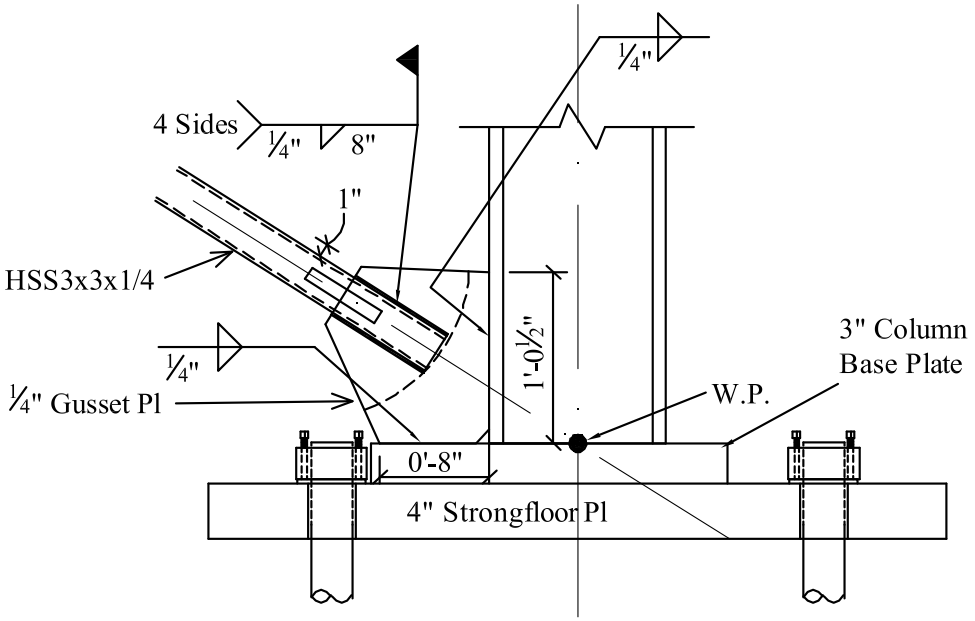

Figure 3.14: Typical SCBF gusset plate connection to column flange at base, GP-1

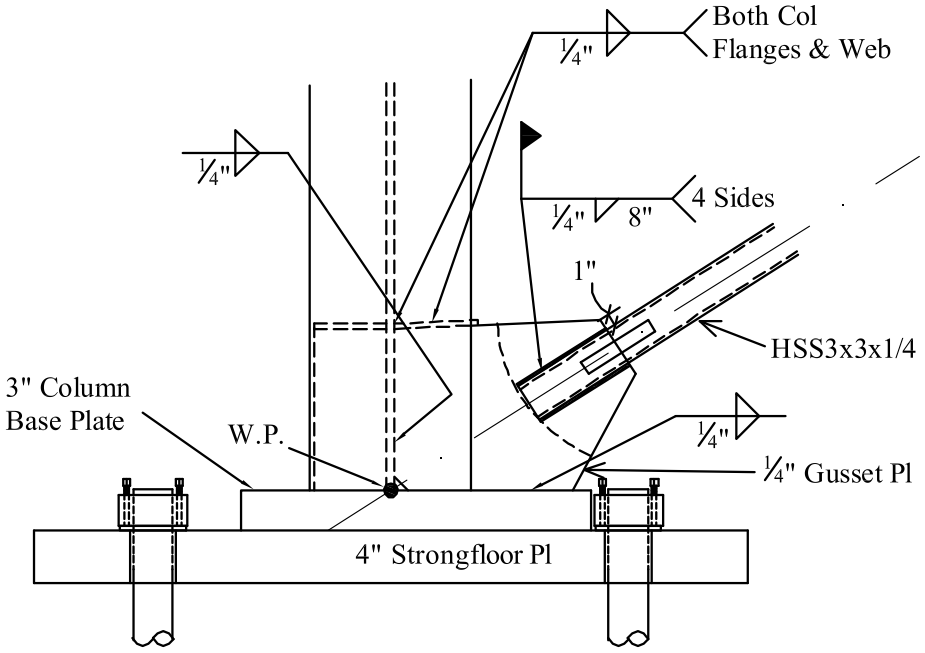

Figure 3.15: SCBF gusset plate connection to shared column web at base, GP-3

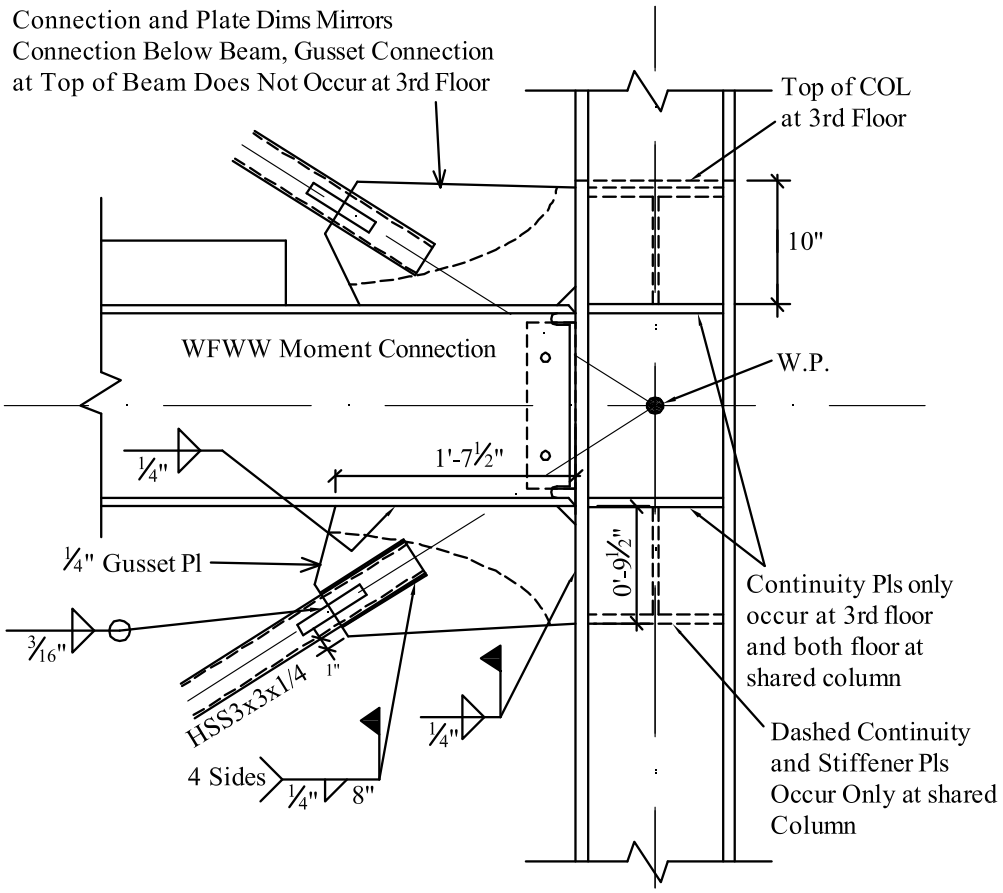

Figure 3.16: Typical SCBF gusset plate connection at second and third floor to column flange, GP-2

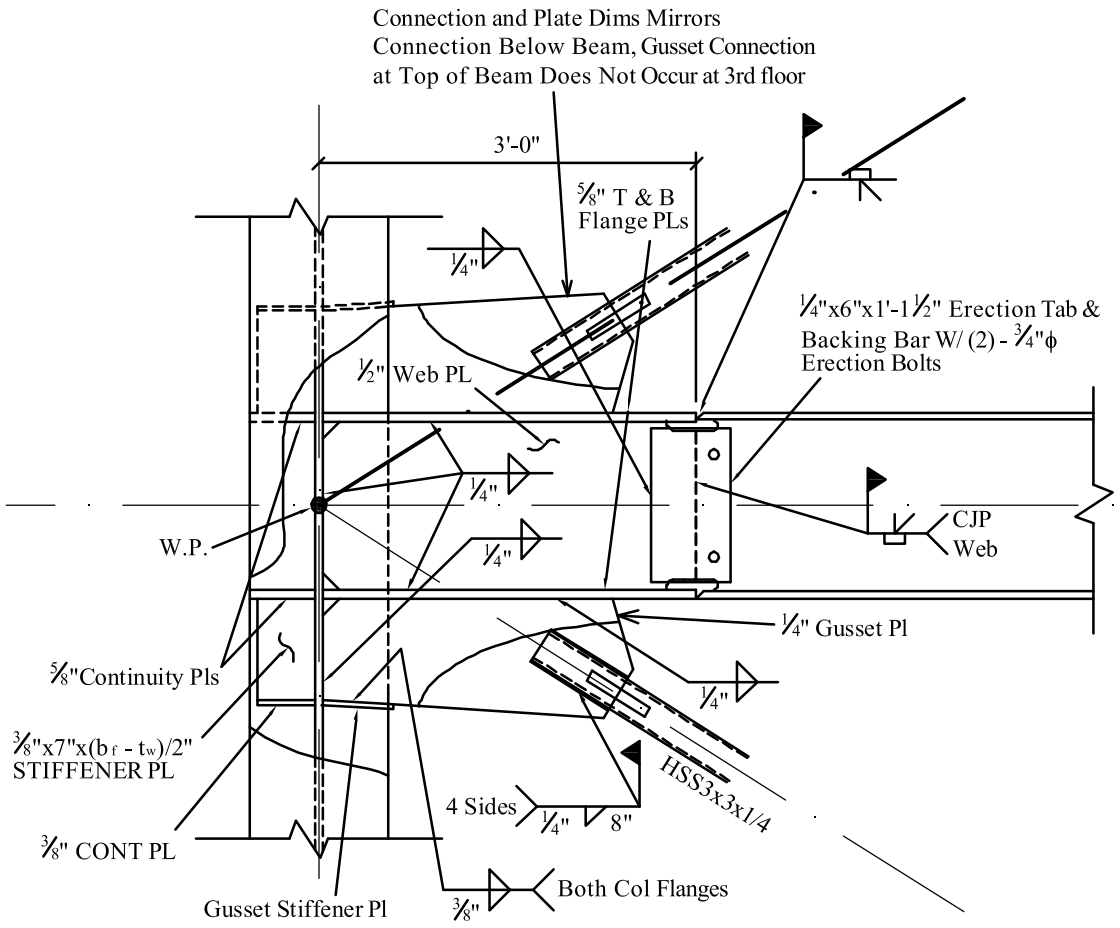

Figure 3.17: SCBF gusset plate connection at second and third floor to shared column web, GP-4

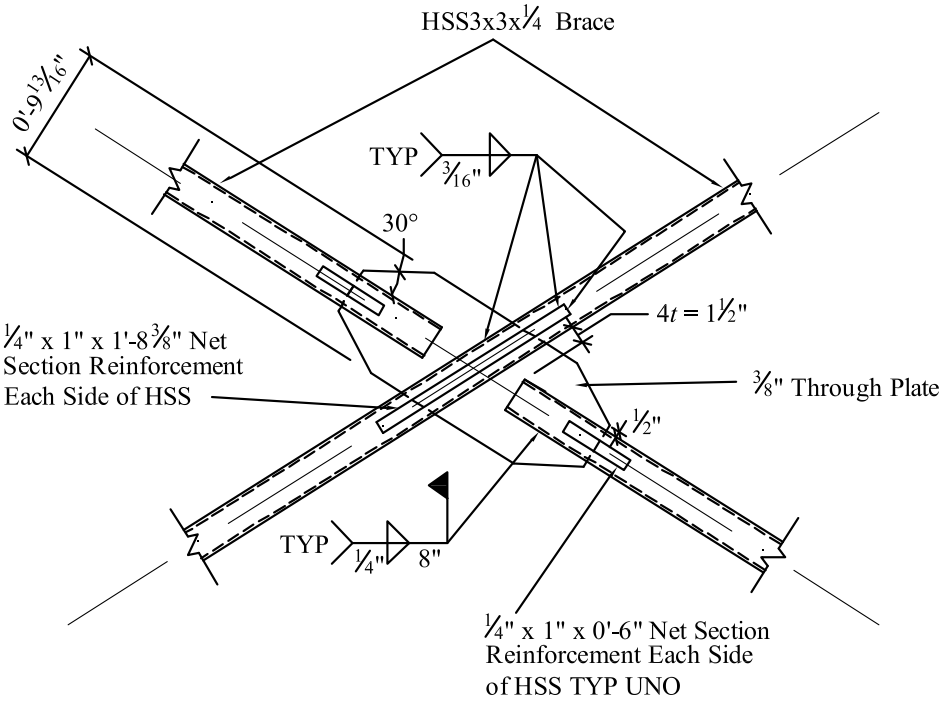

Figure 3.18: SCBF slotted-tube, through-plate connection at intersection of single-story X-configuration, GP-5

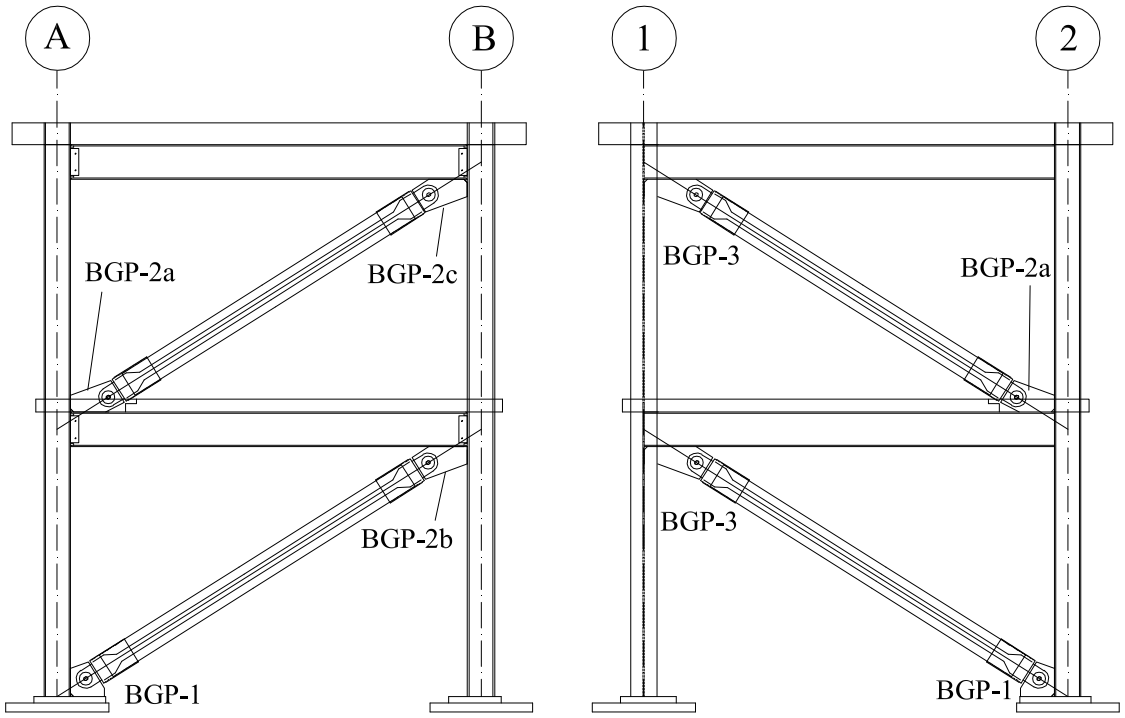

(a) (b)

Figure 3.19: BRBF gusset plate nomenclature: (a) Frame 1; (b) Frame B. (see Figure 3.20 for details)

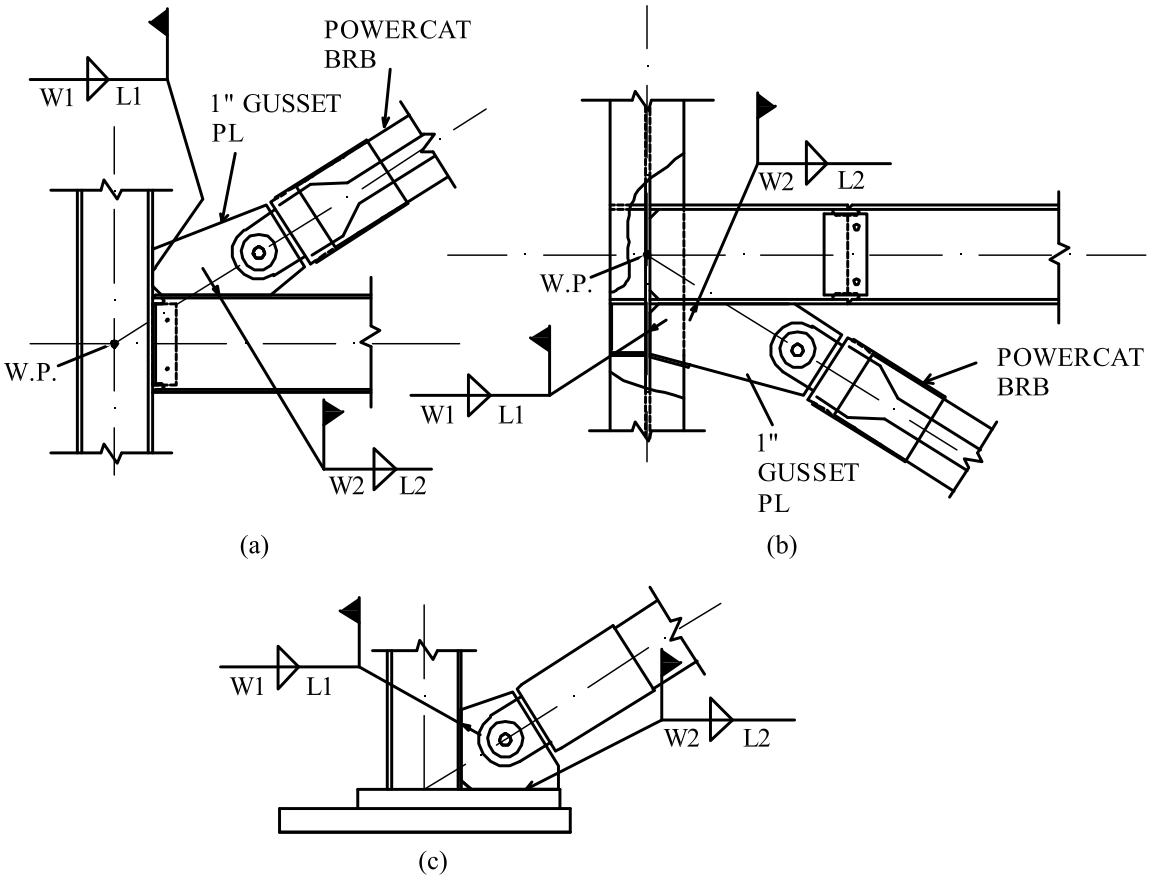

Figure 3.20: BRBF gusset details: (a) connection to column flange at beam-column joint (BGP-2); (b) connection to column web at beam-column joint (BGP-3); (c) connection at base (BGP-1). (See Table 3.14 for weld sizes)

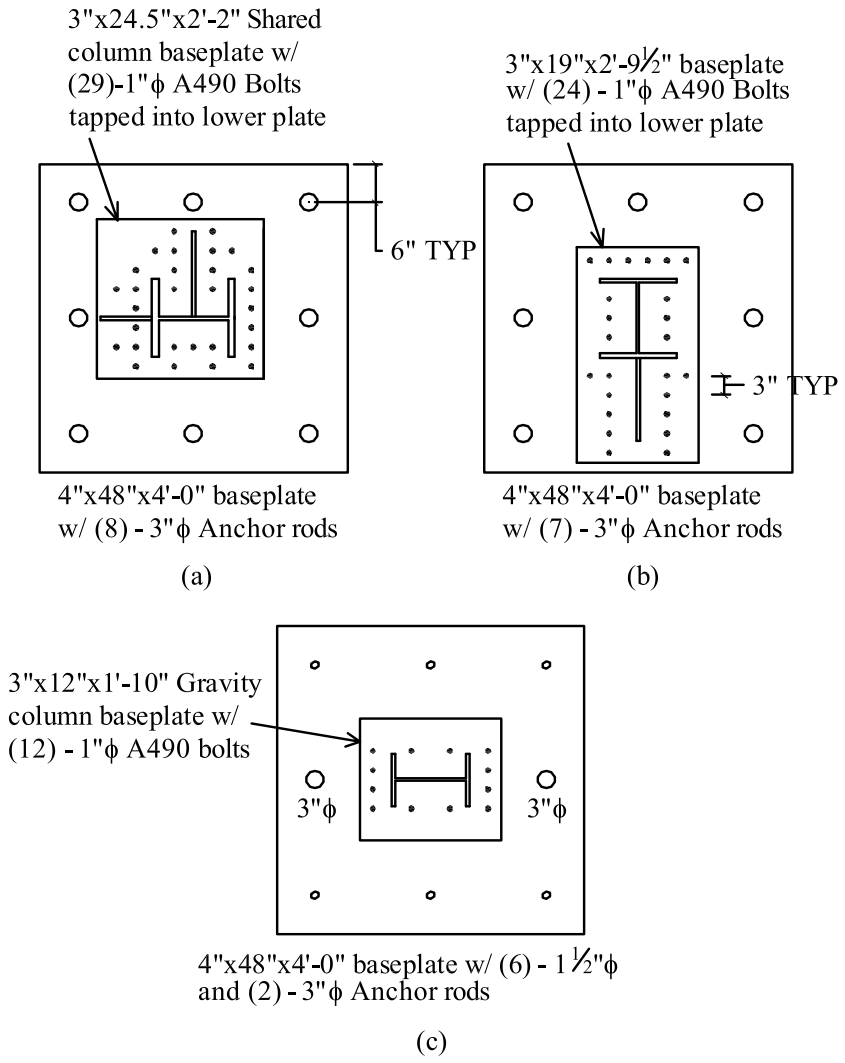

Figure 3.21: Column base details: (a) shared column (B-1); (b) braced frame columns A-1 and B-2; (c) gravity column (A-2).

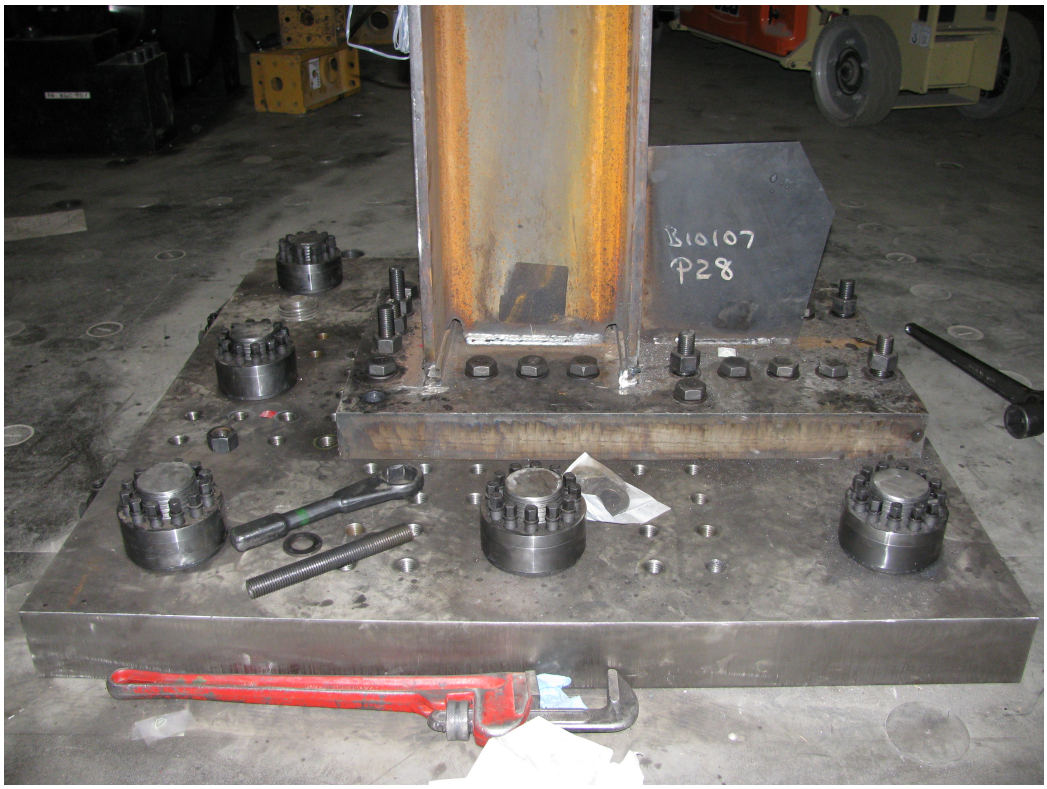

Figure 3.22: Base of column A-1 during specimen construction

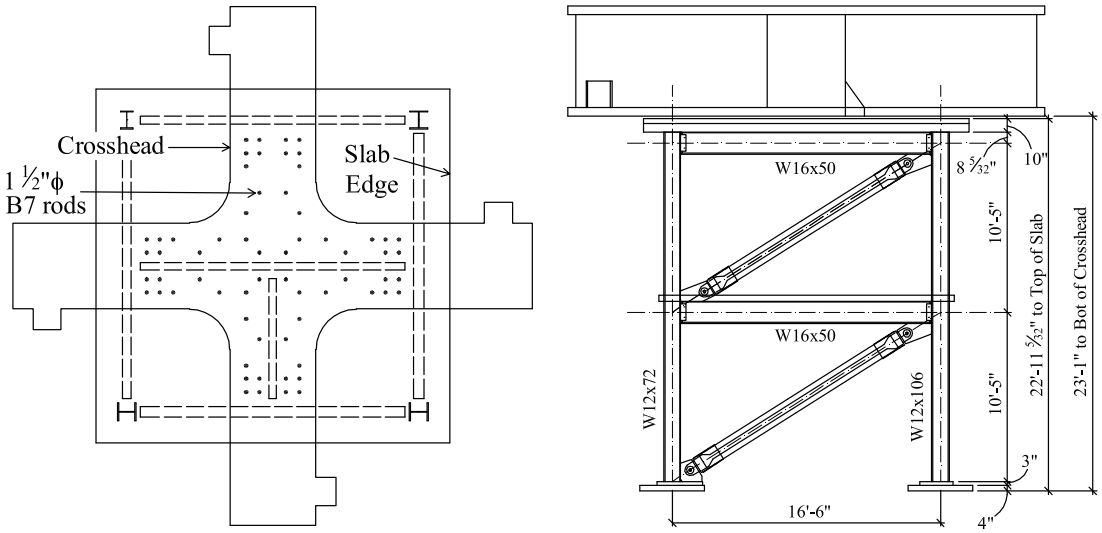

(a) (b)

Figure 3.23: Connection between crosshead and test specimens: (a) plan layout of B7 connecting rods; (b) elevation

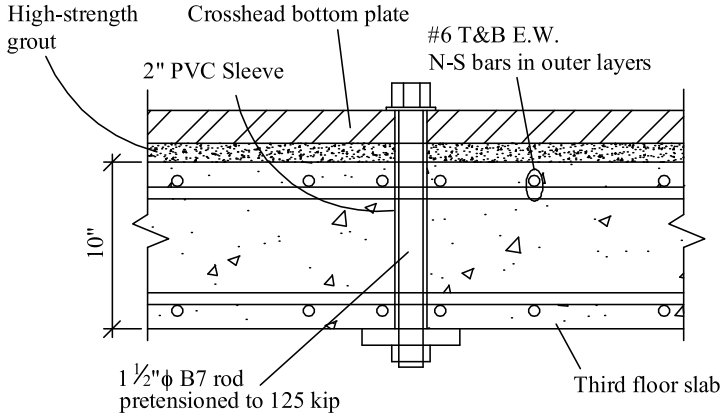

Figure 3.24: Connection detail between top floor slab and crosshead bottom plate

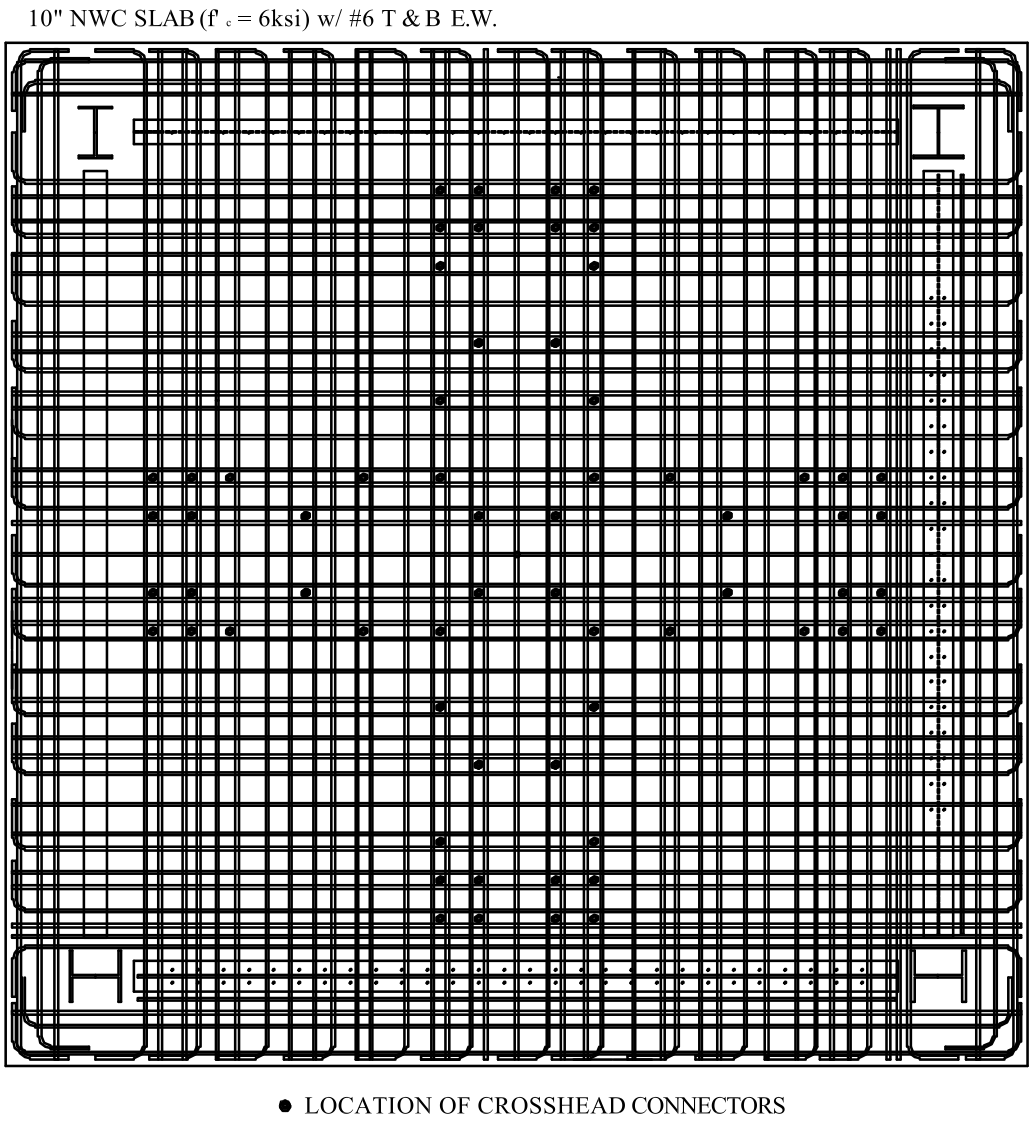

Figure 3.25: Top floor slab reinforcement plan



(a) (b)

Figure 3.26: Third floor slab: (a) slab reinforcement and crosshead connector sleeves during construction; (b) underside of third floor slab showing crosshead connectors

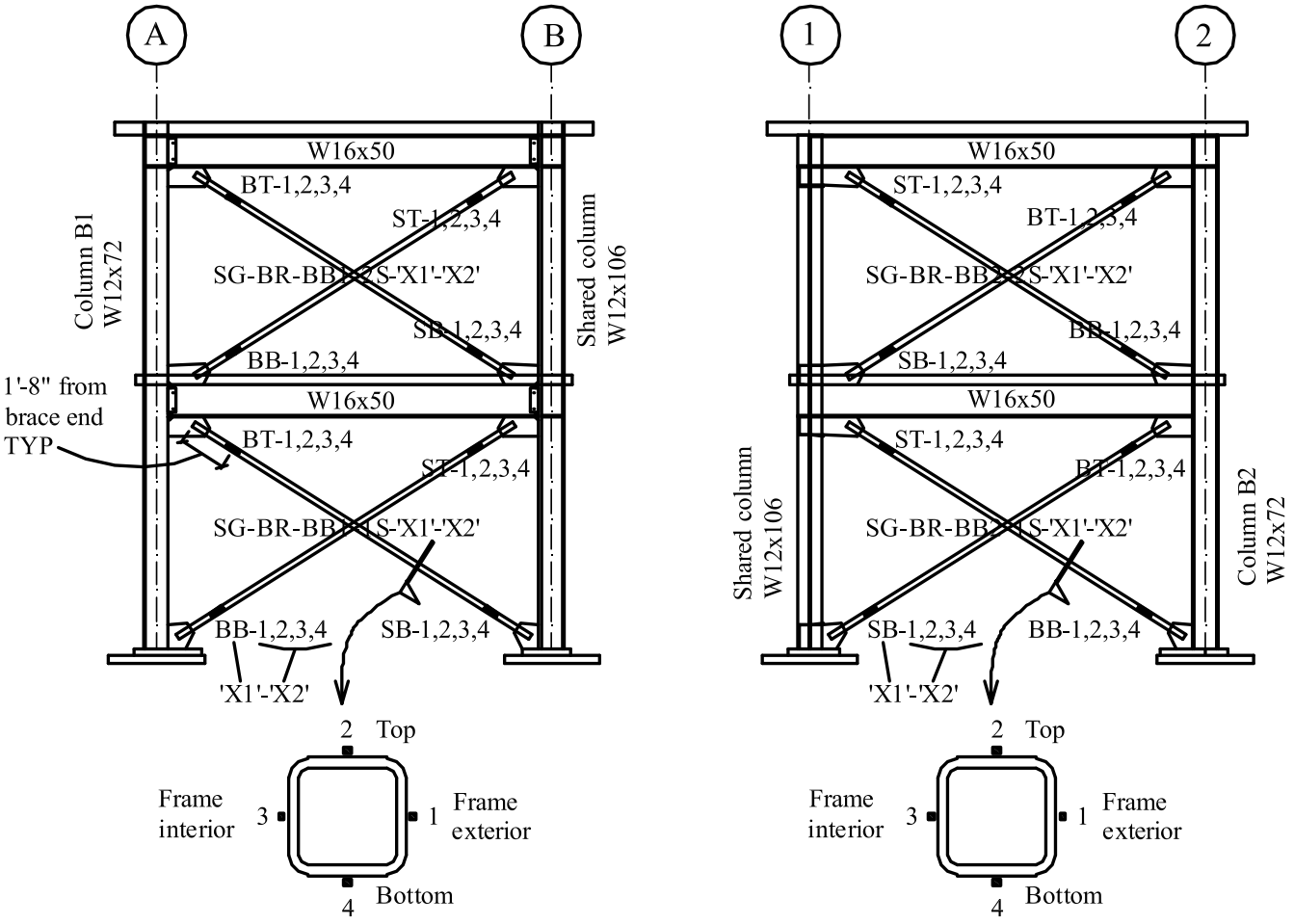

Figure 3.27: Brace strain gauge layout, Braced Bays 1 and B (SCBF Test)

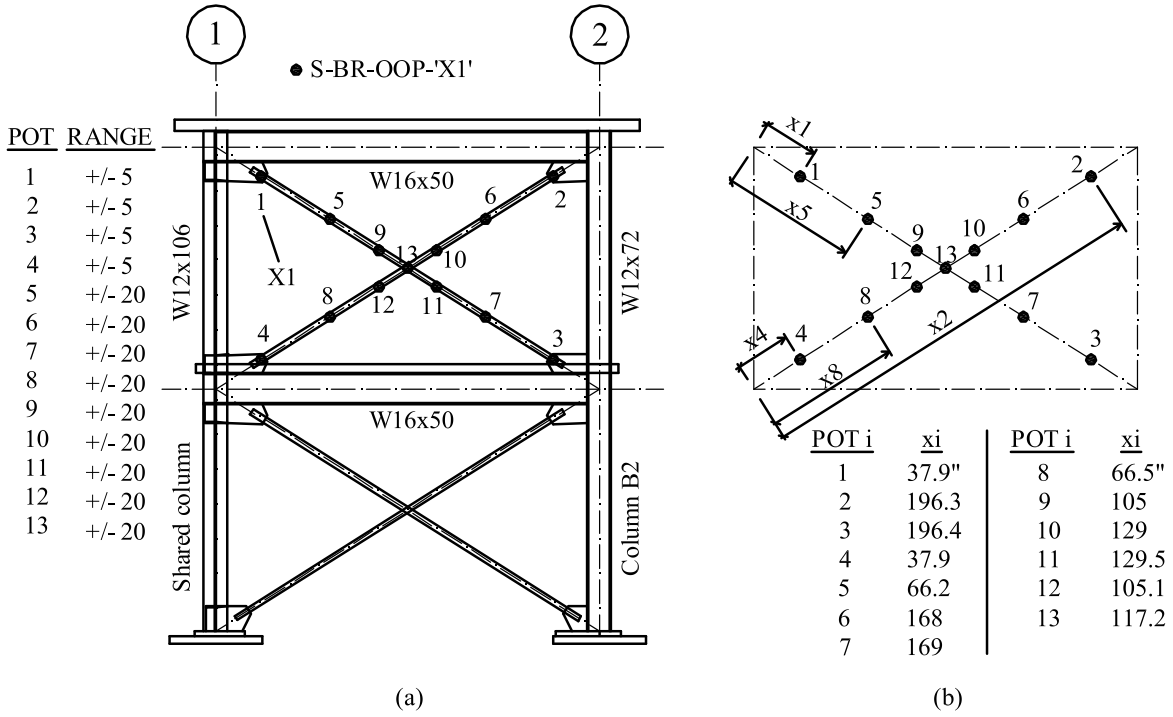

Figure 3.28: Brace OOP string pot layout, second story, Frame B (SCBF Test), as viewed from outside the frame

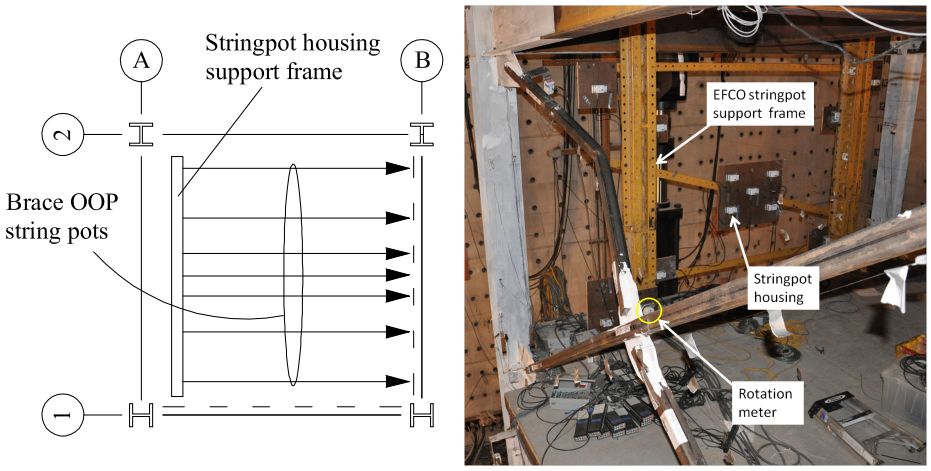

(a) Plan view (b) Photograph

Figure 3.29: Brace OOP stringpot support frame (SCBF test)

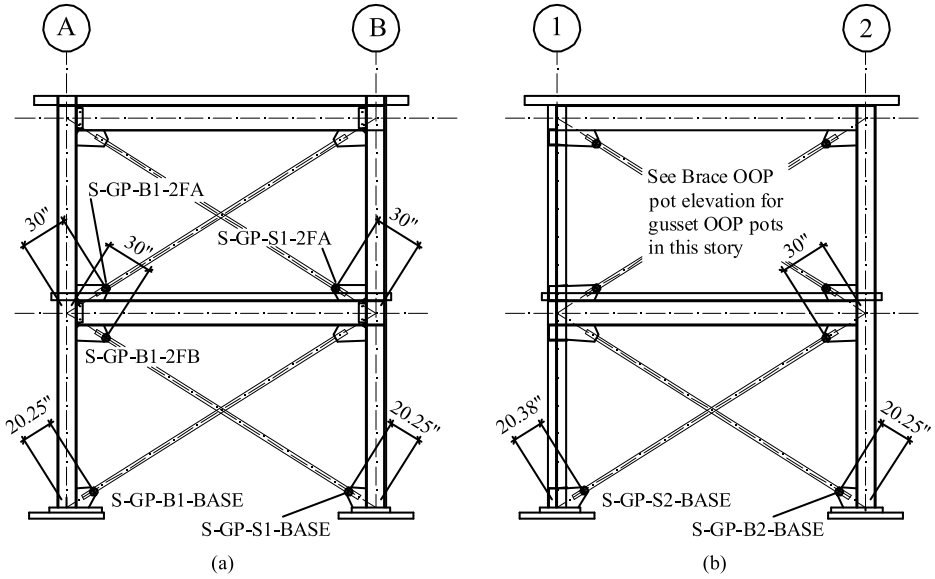

Figure 3.30: Gusset plate OOP stringpot nomenclature and locations: (a) Frame 1; (b) Frame B



(a) (b)

Figure 3.31: Gusset plate OOP stringpots: (a) Base gusset plate ; (b) Gusset plate at beam

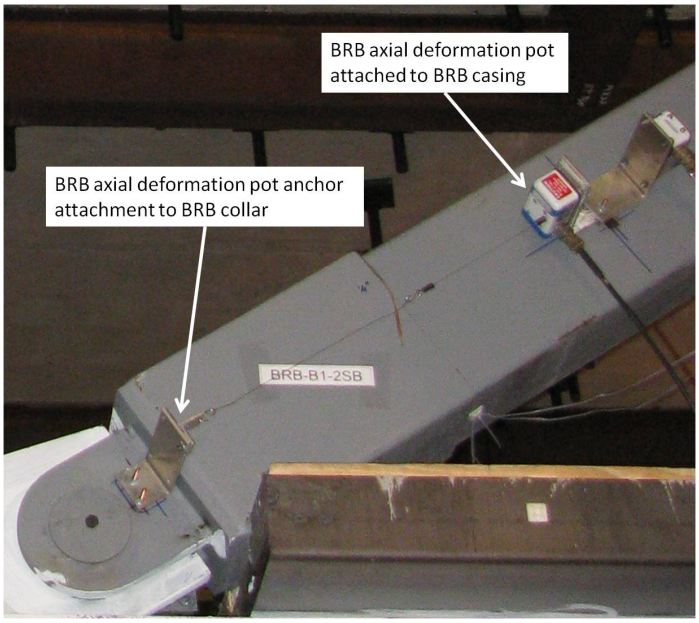

Figure 3.32: BRB axial deformation string pot attachment

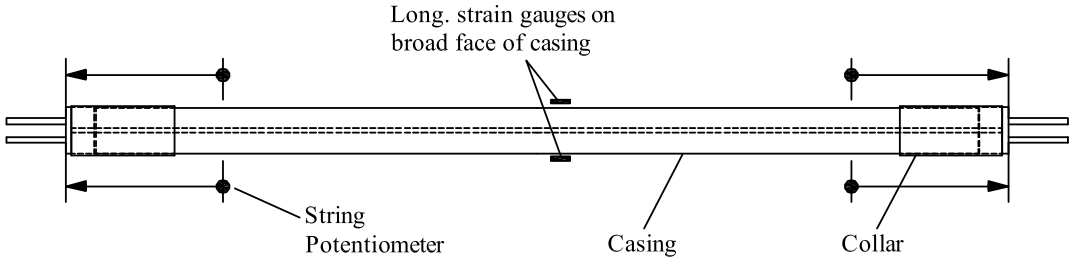

Figure 3.33: BRB axial deformation string pot plan detail

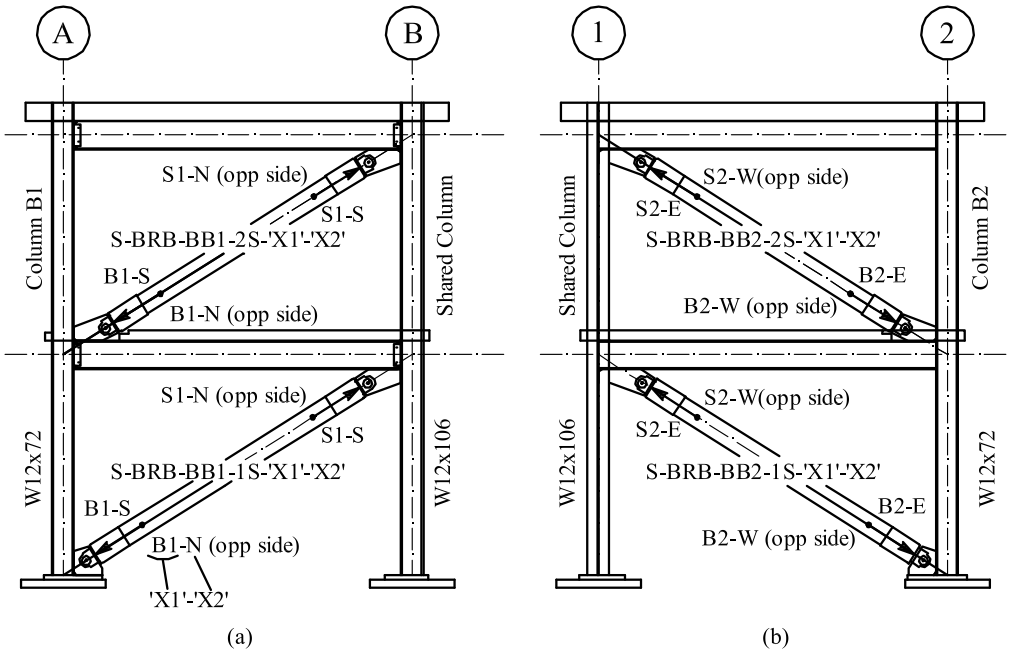

Figure 3.34: BRB axial deformation string pot layout

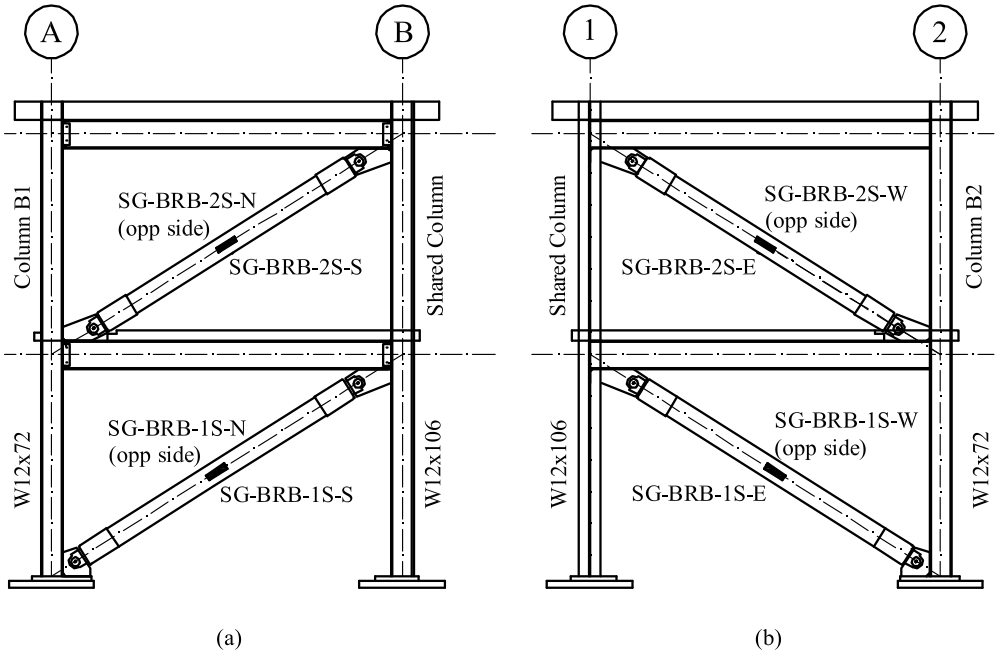

Figure 3.35: BRB casing strain gauge layout

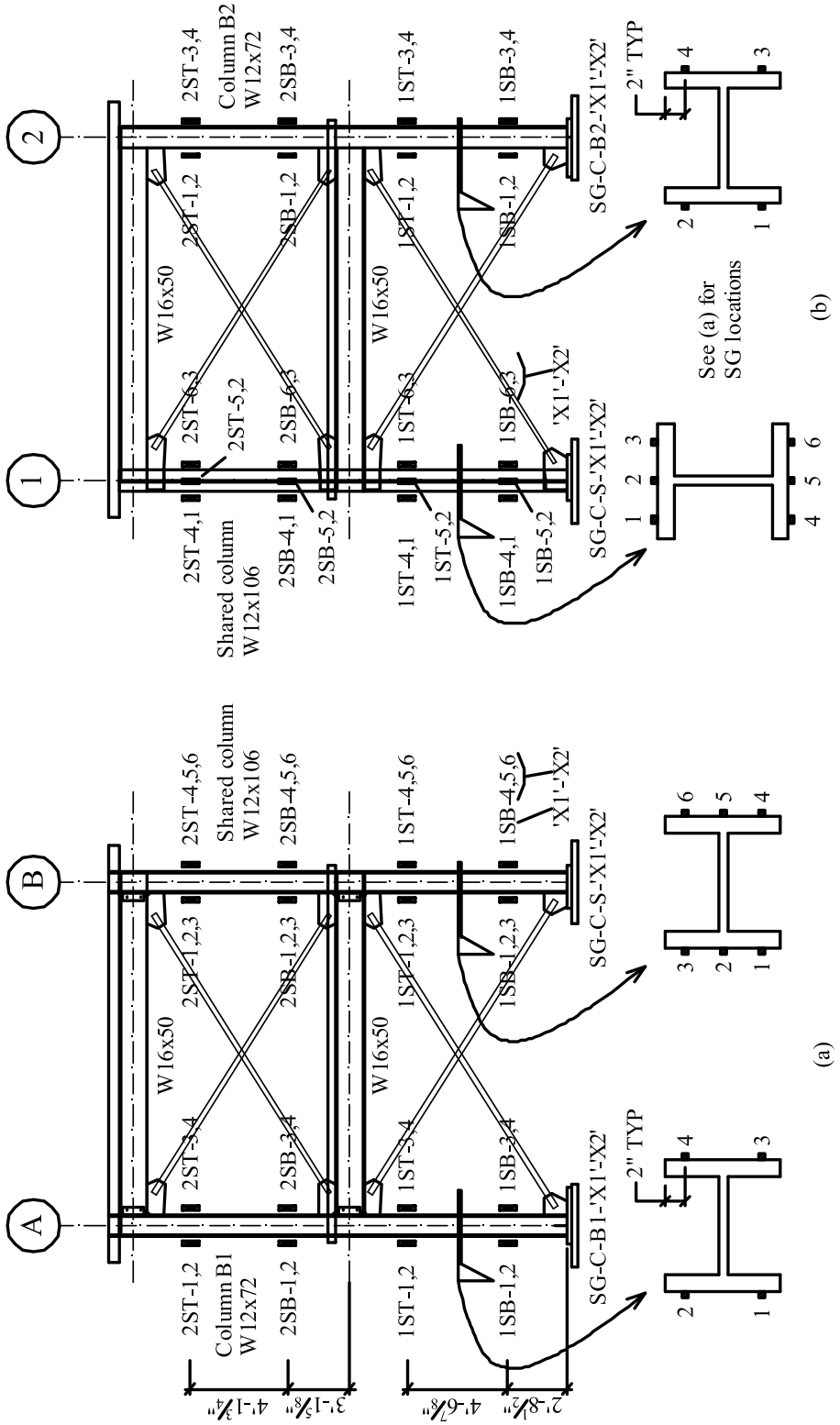

Figure 3.36: Braced frame column strain gauge layout: (a) Frame 1; (b) Frame B

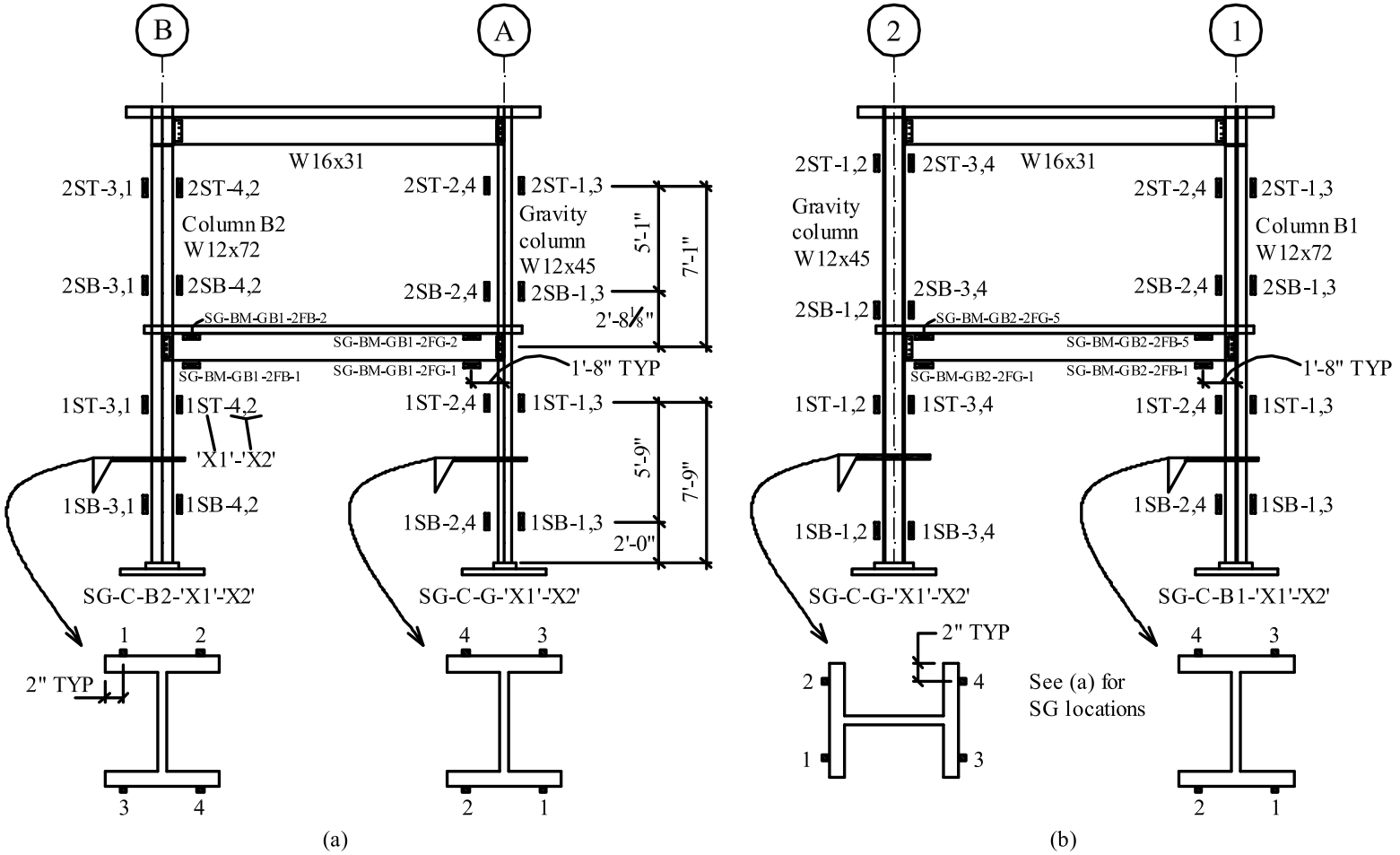

Figure 3.37: Gravity frame column strain gauge layout: (a) Gravity Bay 2; (b) Gravity Bay A

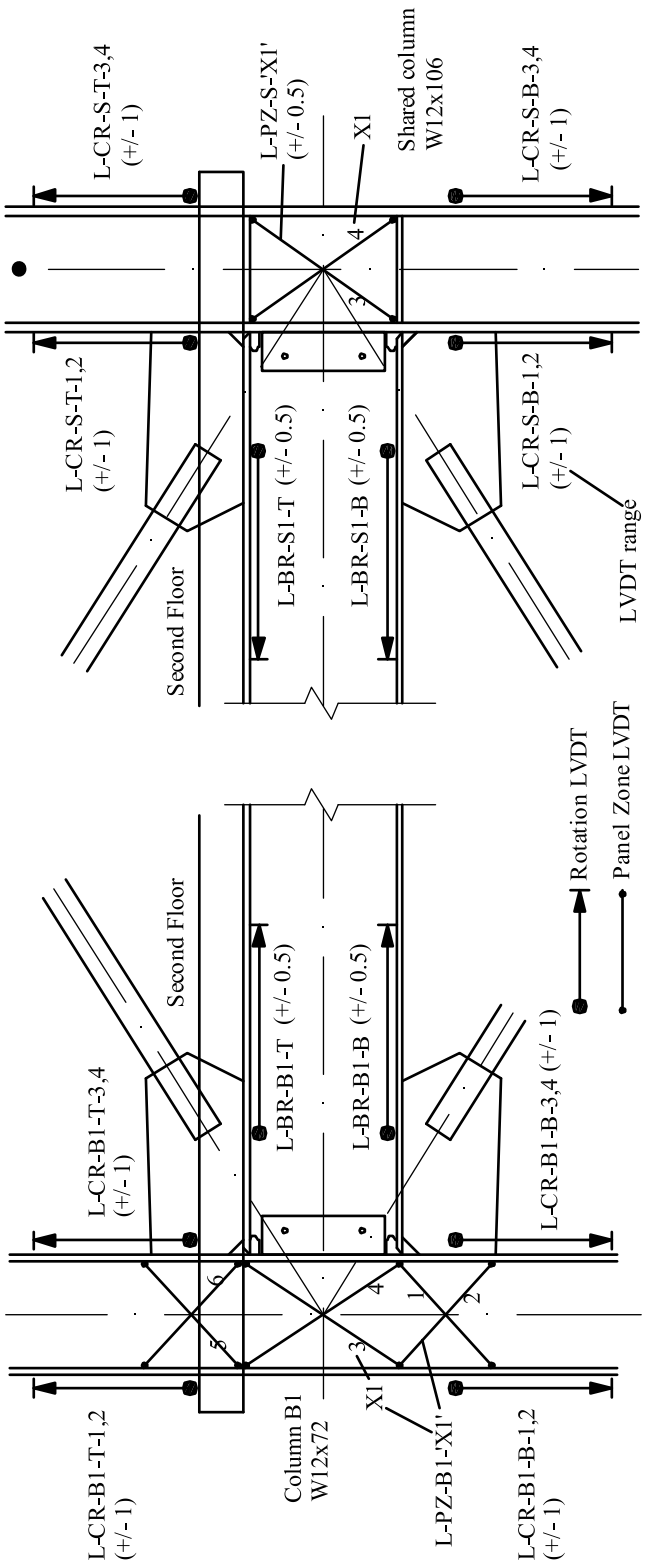

Figure 3.38: Second floor column rotation and panel zone deformation LVDT layout, column B1 and shared column (see Figure 3.41 for rotation LVDT attachment point locations)

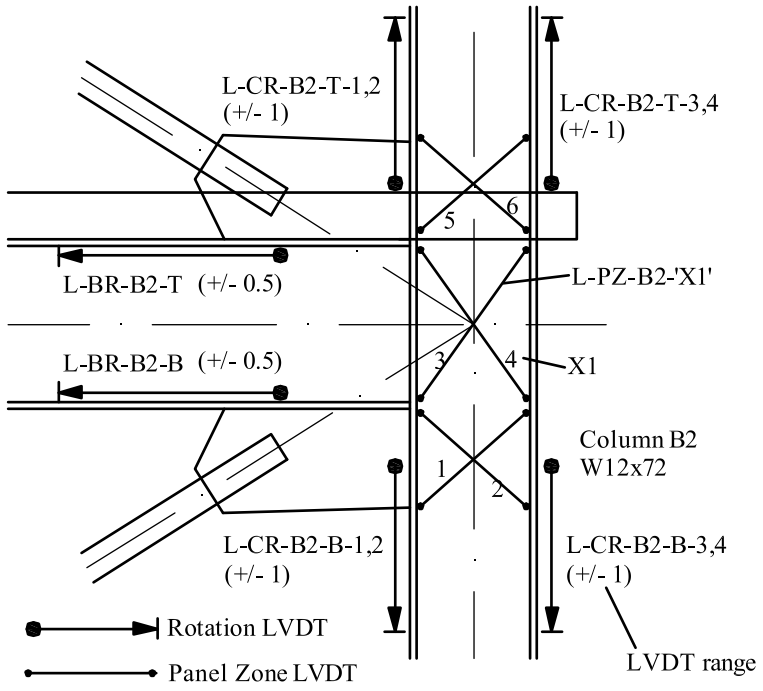

(a)

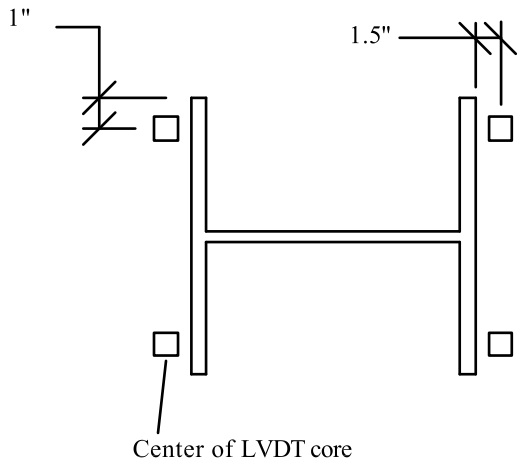

(b)

Figure 3.39: Joint instrumentation: (a) Column B2 second floor column rotation and panel zone deformation LVDT layout; (b) column rotation LVDT cross-section location (see Figure 3.41 for rotation LVDT attachment point locations)

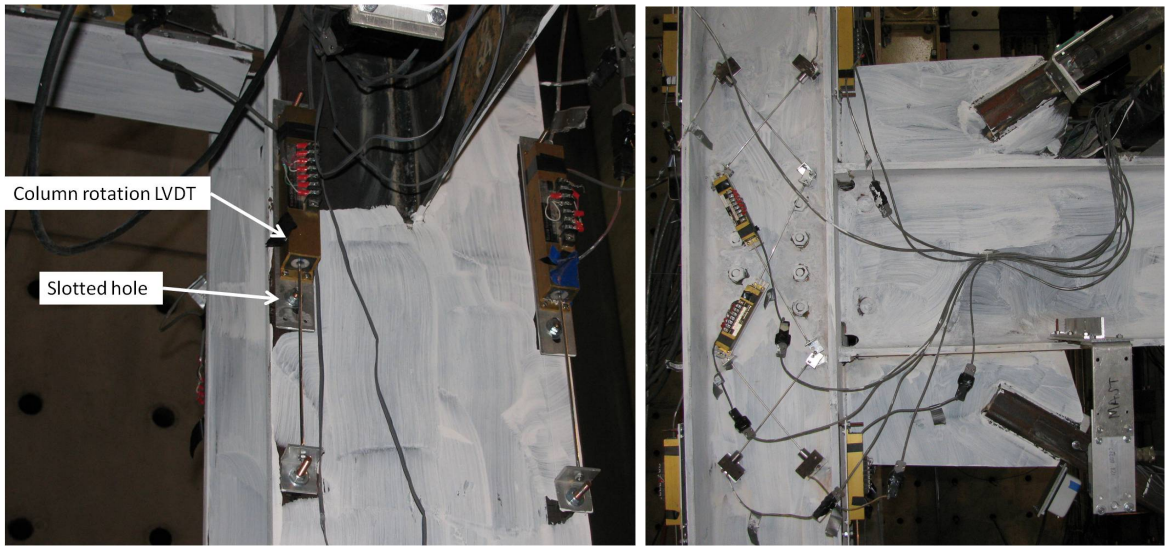

(a) Column rotation LVDT at bottom of second floor joint, column B2

(b) Column panel zone instrumentation, column B1

Figure 3.40: Column second floor joint instrumentation photographs

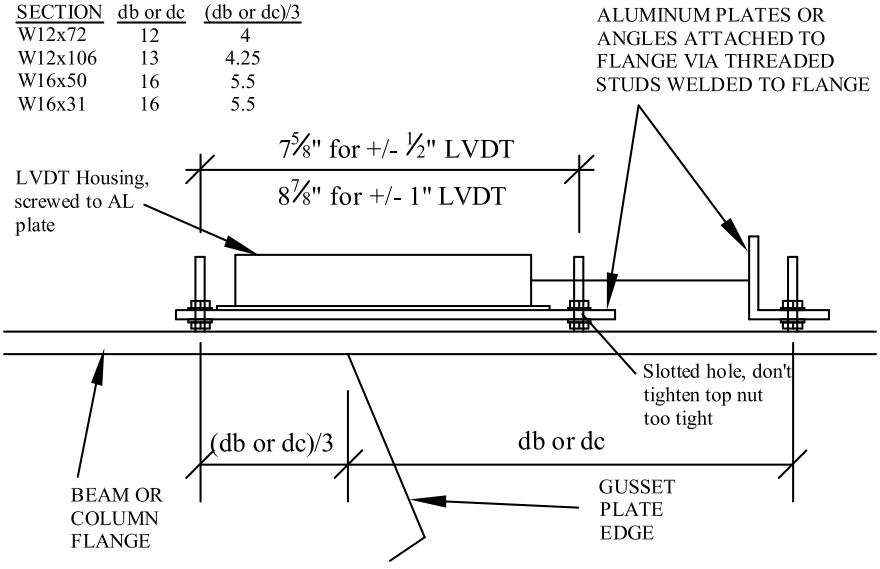

Figure 3.41: Rotation LVDT mounting detail at beams and columns

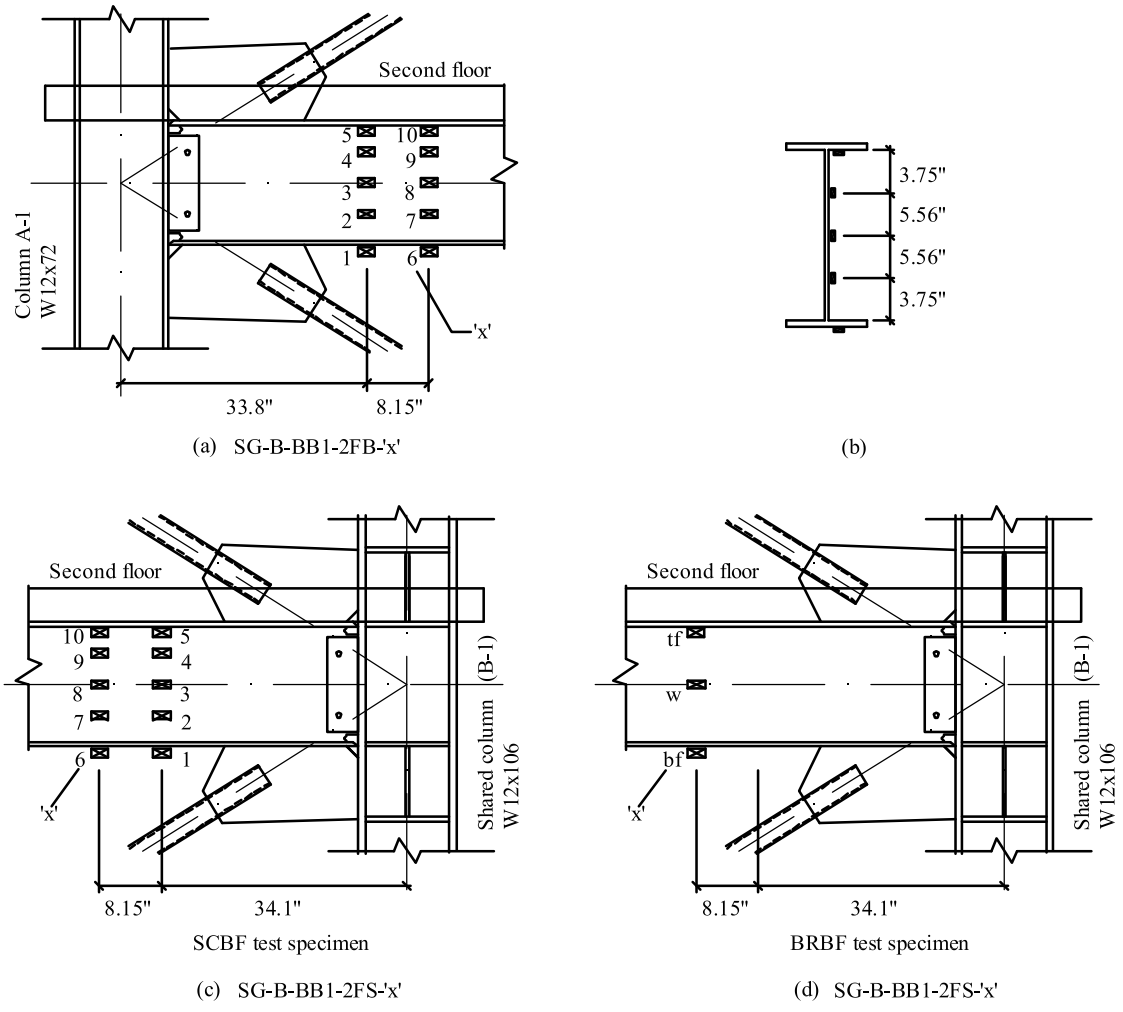

Figure 3.42: Frame 1 second floor beam strain gauges: (a) at column B1 side (both test specimens); (b) location along beam depth; (c) at shared column side (SCBF test specimen); (d) at shared column side (BRBF test specimen)

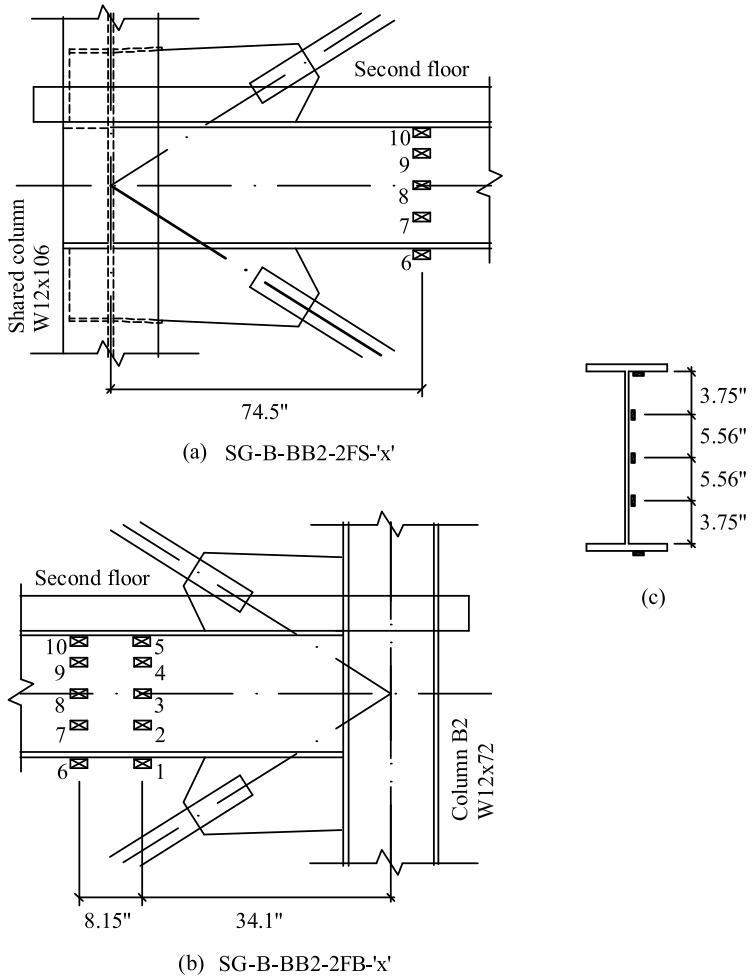

Figure 3.43: Frame B second floor beam strain gauges: (a) at shared column side; (b) at column B2 side; (c) location along beam depth

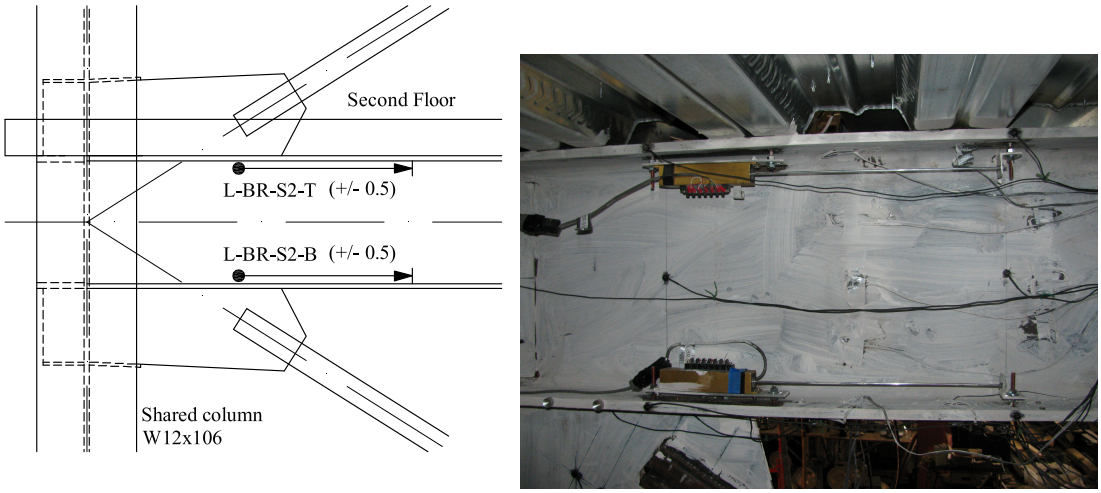

(a) (b)

Figure 3.44: Beam rotation LVDTs: (a) at second floor, Frame B at shared column side; (b) photo at second floor, Frame 1, shared column side

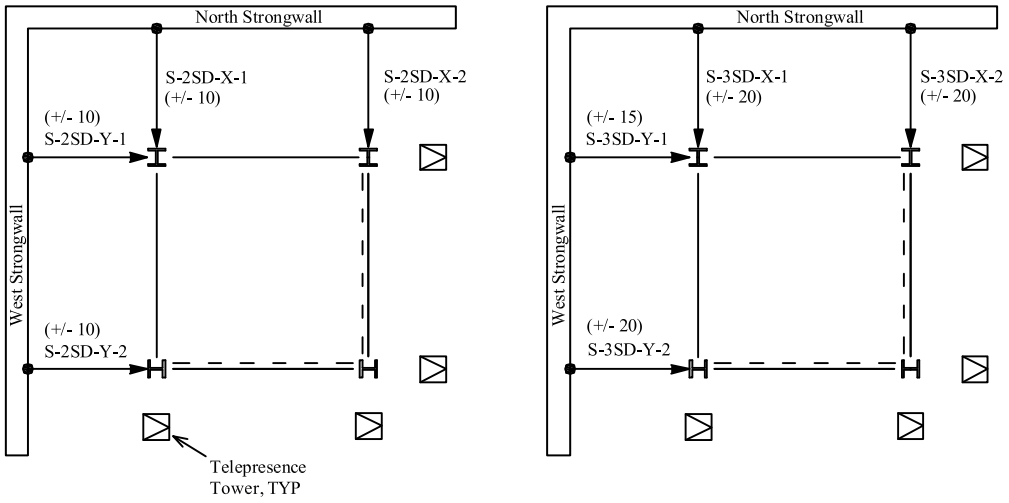

Figure 3.45: Story drift stringpot layout: (a) second floor plan layout; (b) third floor plan layout

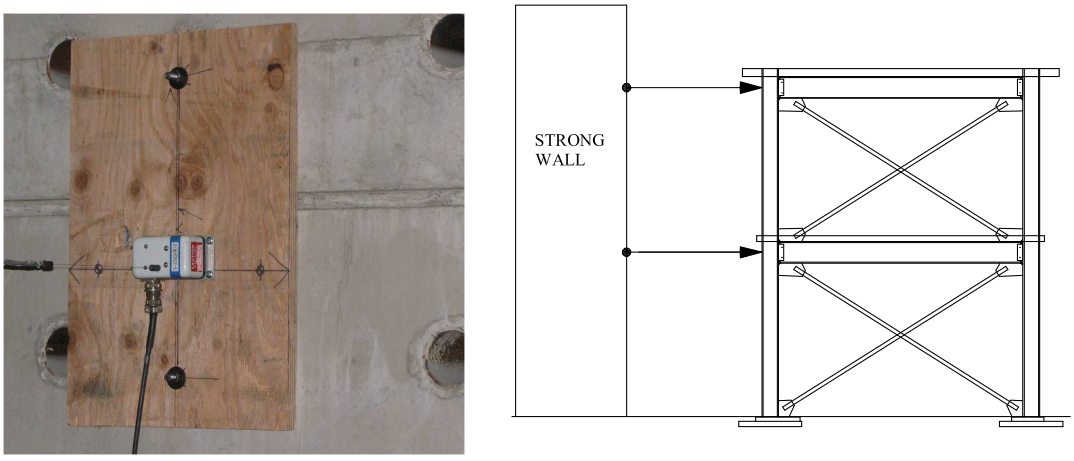

(a) (b)

Figure 3.46: Story drift string pots: (a) attachment to strong wall; (b) setup in elevation

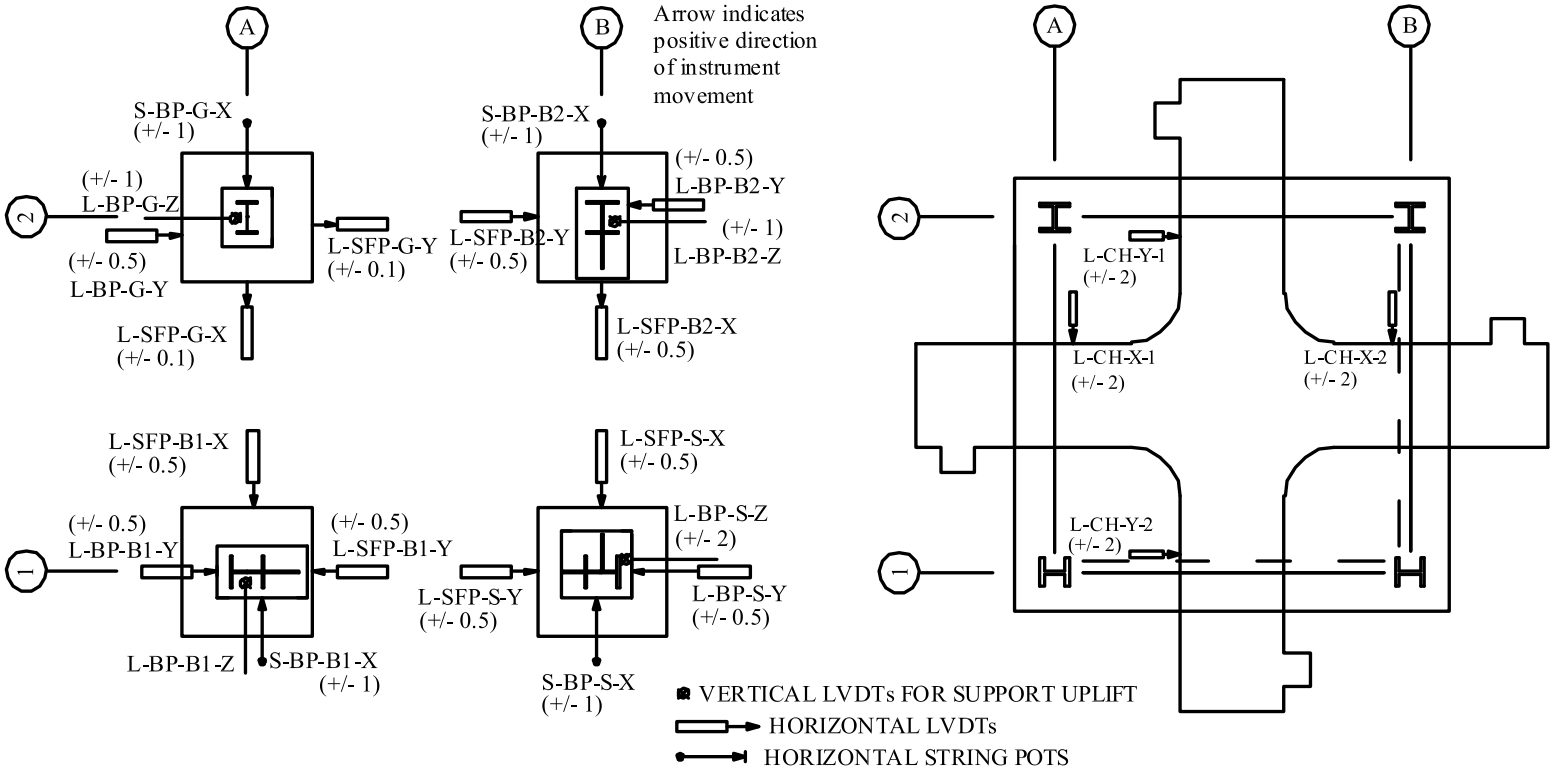

Figure 3.47: Slip instrumentation: (a) base; (b) third floor / crosshead

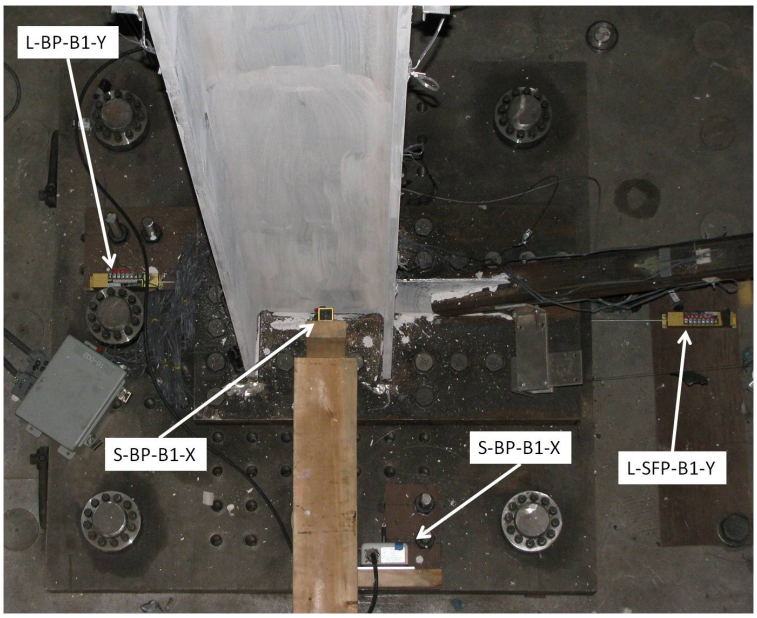

Figure 3.48: Base instrumentation at column B1

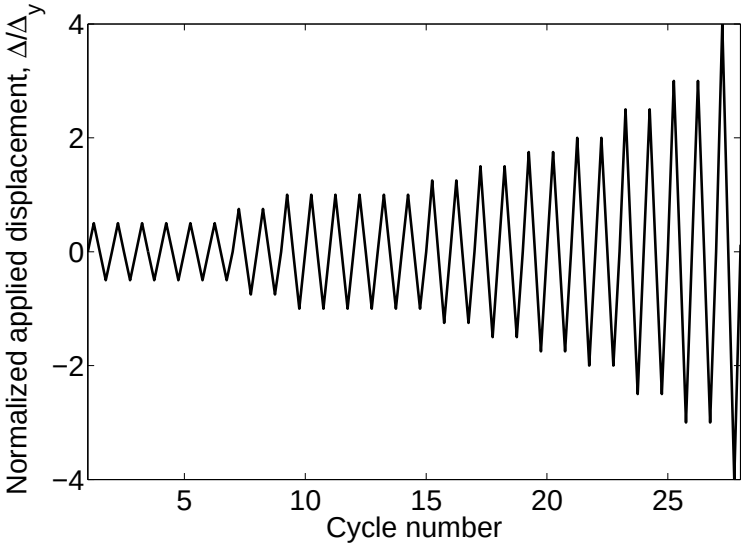

Figure 3.49: Schematic of cyclic loading protocol in principal direction

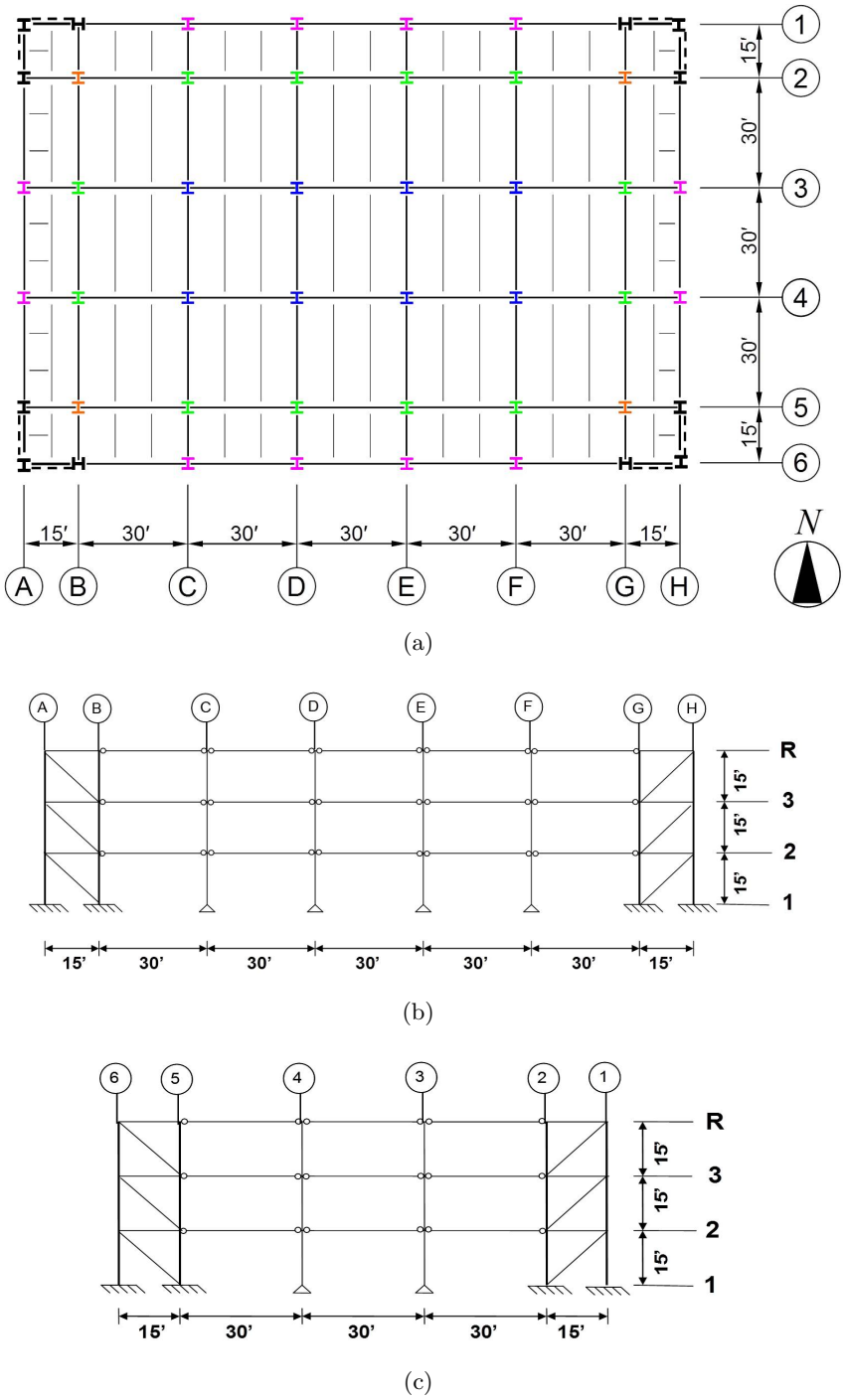

Figure 3.50: Three-story prototype BRBF building: (a) plan; (b) South elevation; (c) East elevation. [Sherman, 2009]

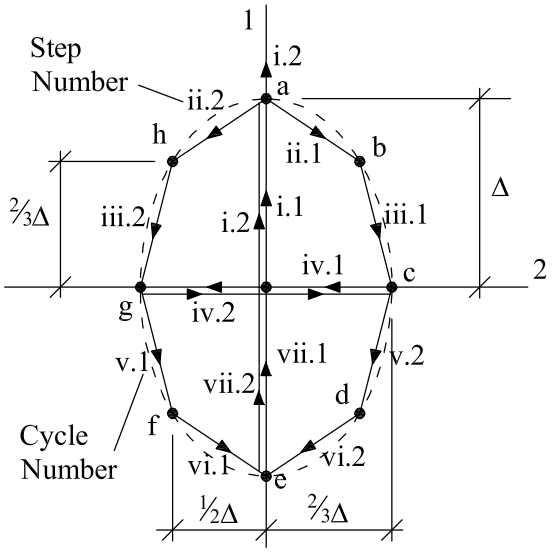

(a)

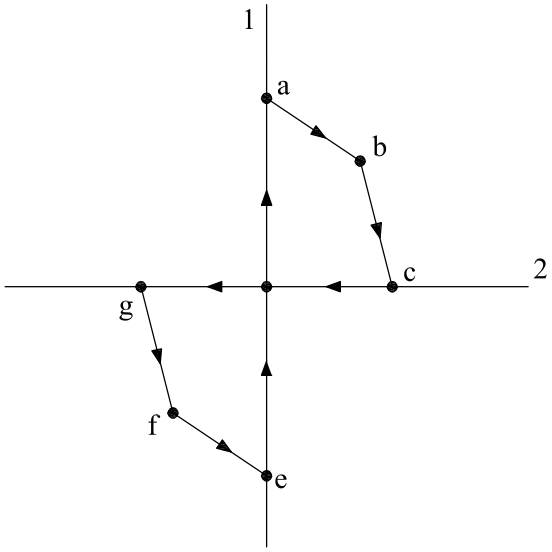

(b)

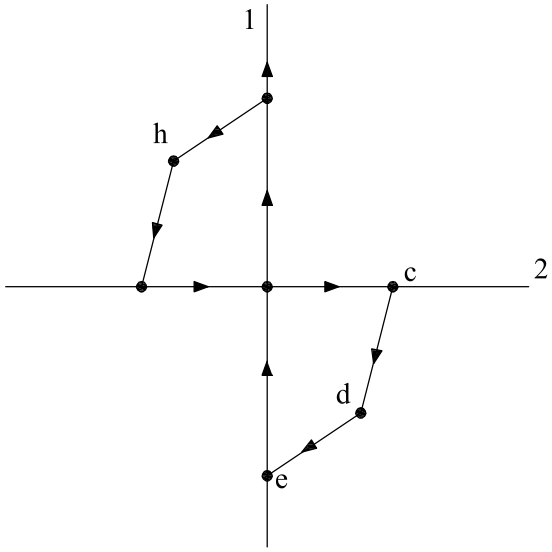

(c)

Figure 3.51: Schematic of bi-directional "cloverleaf" loading protocol: (a) full cloverleaf; (b) cycle 'i' of cloverleaf; (c) cycle 'i+1' of cloverleaf

Chapter 4

EXPERIMENTAL RESULTS

4.1 Introduction

This chapter will present the principal results from the two, three-dimensional CBF experiments performed at the University of Minnesota MAST Laboratory. These results will include global force and deformation histories along with a description of the specimen performance and damage that occurred to the components at various drift levels. These components include the braces, gusset plates, beams and columns. Typically, the tests were paused at the peak and valley of each cycle in each principal direction to allow for inspection of the frame. As such, the point in time at which damage such as yielding or gusset plate tearing occurred is not exactly known. The point of occurrence of other performance states and damage such as brace buckling and yielding, and sudden fracture of brace and beam elements were estimated from the numerical data collected. These damage and performance states will be described at three different drift ranges: initial, moderate and severe. These drift ranges along with the definition of damage follow that used by the previous researchers who reported on the planar CBF experiments (for example, [Lumpkin, 2009] 2009). Chapter 5 will provide a more extensive analysis of the data, including local element force and deformation behavior, collected from the strain gauges, string potentiometers and LVDTs.

The next two sections will provide the background information required to understand the results and behavior of the test specimens. This information includes a description of the damage states and the specimen component nomenclature used to assess the performance of the system.

4.2 Description of Performance States

The primary performance or damage states are yielding, buckling, weld damage, and tearing or fracture of the components. Three different levels of yielding are defined: Y1, Y2 and

Y3 where Y3 indicates more damage than Y1. Three buckling levels are also defined in a similar way (i.e. B1, B2 and B3). Table 4.1 provides a list of all performance states used including a detailed description of each. The following four sections will discuss these in greater detail along with providing photographic descriptions of each.

4.2.1 Yielding (Y)

The wide flange beams and columns and the gusset plates were painted with whitewash to provide visual evidence that yielding was occurring. Yielding of the HSS buckling braces was determined from strain gauge data while BRB yielding was determined from the axial string pot data converted to an average strain. Figure 4.1 depicts gusset plate yielding at the three yielding levels defined in Table 4.1. Level Y1 (see Fig. 4.1a) is the lowest level of yielding and typically occurs initially in the gusset plates at or near the ends of the braces. Y2 is a moderate level of yielding (see Fig. 4.1b) and typically occurs in the gusset plate as a result of tensile yielding and bending of the gusset plate following brace buckling. Y3 is severe yielding with large concentrated areas of flaked whitewash on the member (see Fig. 4.1c) that typically occurs following large OOP movement of the brace. The yielding levels occurring in the beams and columns is defined the same.

4.2.2 Brace Buckling and Damage (B)

Conventional HSS braces buckle out-of-plane (OOP) when the critical load is reached. As the frame deformation is increased, the OOP deformation of the brace also increases and may cause damage in an actual building to walls, windows and other building systems. Therefore, this deformation is an important performance state for the SCBF system. Figure 4.2 depicts the brace buckling performance levels B1, B2 and B3. Buckling level B1 is defined as an OOP deformation not exceeding the depth of the brace, B2 occurs when the brace OOP deformation exceeds the depth but is less than twice the depth, and B3 is defined as an OOP deformation greater than twice the member depth. Performance states are also defined for the near complete loss of compressive resistance (BC) which generally accompanies large amounts of cupping and bulging at the plastic hinge as shown in Fig. 4.3a and when the

brace looses tensile resistance when a tear(s) form and the brace ultimately fractures (BF) as shown in Fig. 4.3b and c.

4.2.3 Local Buckling (B)

Buckling performance states are also defined for elements where deformation is local such as the flange or web at a particular location on the frame. Similar to brace buckling, the levels B1, B2 and B3 are used to describe the performance but instead of the the deformation level depending on the length of the element, the definition is based on the thickness of the element (see Table 4.1). Figure 4.4 shows the local buckling of the outer flange of the column at the base during the BRBF experiment at levels B2 and B3.

4.2.4 Weld and Base Metal Damage (W)

Damage to the welds occurred during the experiments at the welds connecting the gusset plates to the framing elements and also at the welds connecting the braced frame beam in Frame B at the second floor to column B-1. This weld damage is noted as "Wc" if it occurred at a column interface or "Wb" if it occurred at a beam interface. Additionally, damage also occurred at the interfaces in the base metal just outside the weld also known as the heat affected zone (HAZ). If damage occurred in the base metal, the notation "WBc" and "WBb" were used for the column and beam locations, respectively. Figure 4.5a shows an example of damage to the weld metal at the gusset interface with the beam (Wb) while Fig. 4.5b shows an example of damage to the gusset plate HAZ at the beam-gusset interface (WBb).

4.3 Nomenclature

To facilitate the description of damage that occurred in the frame components, descriptors are explained in this section that define the location of the elements in the frames and are mainly used in the tables that describe the progression of damage in each element in Appendices D and E. Figure 3.2 shows a picture of each test frame in the lab with the global coordinate system defined (X and Y). Figure 4.6a shows a plan view of the test

frame with the braced frame and column names; the column names correspond to the grid intersections. Figure 4.6b shows an elevation with the definitions of the stories and floors. The brace configuration for the first test is shown in this figure but the definitions apply to the BRBF test also. Figures 4.6c and 4.6d provides the nomenclature used to describe the braces and points of interest on the braces for the first test in Frames 1 and B. The braces are defined as "continuous" and "discontinuous" along with the location in the story. For example, "Dt" stands for the discontinuous brace at the top of the story (above the splice connection). The nomenclature used for the gusset plates is shown in Figs. 4.6e and 4.6f.

Drift ratio is used frequently to describe the ratio of the difference between the displacements of the top and bottom of a story or between the roof and the base of the structure, divided by the story or building height, with the former being defined as the *story drift ratio* (SDR) and the latter defined as the *roof drift ratio* (RDR). Additional acronyms will be used to describe the story drift for each story and in each direction as shown in Table 4.2 below.

4.4 Test 1: Buckling Brace SCBF

The first specimen was tested at the University of Minnesota MAST Laboratory over the course of four days beginning on Friday, June 11, 2010 when the first six cycles were performed. The test was resumed the following Monday and was completed on the afternoon of Wednesday, June 16, 2010. The frame remained in an unloaded state at the end of each test day and data collection continued overnight to assess any changes in the specimen during these extended pauses. No changes in the data were observed other than minor drifts in the strain gauges and the data was corrected to capture these changes which turned out to be insignificant.

This section will present an overview of the SCBF specimen performance. This will include story drift and story force histories, a summary of performance states, and detailed observations during the initial, moderate and severe drift ranges. These observations will rely mainly on photographic data taken throughout the test.

4.4.1 Overview

The loading protocol for the specimen was a modified version of the SAC protocol in two dimensions and was described in Chapter 3 in Figs 3.49, 3.51 and Table 3.15. The first four cycles consisted of uni-directional loading at approximately $0.5\Delta_y$ where Δ_y is the drift at which brace buckling first occurs. Bi-directional loading commenced at cycle five. Detailed plots of the imposed story displacements and story drift ratio histories in each direction and plots of the cloverleaf histories for each story are shown in Figs. D.1 through D.4 in Appendix D. Also included in this appendix are tables listing the peak negative and positive roof and story drift ratios for each cycle along with the maximum force in the actuators (Tables D.1 and D.2).

The maximum second-story drift ratio in the Y-direction was -2.35% occuring at the negative excursion of Cycle 33. Brace fracture occured in the upper discontinuous brace at the second story in the Y-direction frame (Frame 1) at -2% 2SDR. Prior to fracture during the negative excursion, the specimen reached a peak positive second story drift ratio of 2.13% for a total range of 4.48%. The maximum second story drifts determined from the last complete cycle prior to brace fracture were -1.83% and 1.78% for a total drift range of 3.61%. The latter story drift range is typically used to assess the seismic performance of systems.

Immediately following brace fracture, the test was paused while the frame was inspected. The force in the Y-direction was then removed resulting in residual story drifts of approximately -1% and -0.6% for the second and first story, respectively, in the Y-direction. Loading continued uni-directionally in the X-direction to a maximum positive second-story drift ratio of 1.92% and maximum negative second-story drift ratio of -1.85% in Cycle 38 for a total drift range of 3.77%. The test was stopped after Cycle 38 prior to brace fracture in the X-direction frame (Frame B). The maximum story drift ratios in each global frame direction and story reached during the last complete cycle prior to brace fracture are listed in Table 4.3.

The story shear-drift response in each story and direction are shown in Figure 4.7 with Figures 4.7a, 4.7c and 4.7e showing the Y-direction response for the average roof drift,

second-story drift, and first-story drift ratio, respectively. Figures 4.7b, 4.7d and 4.7f show the X-direction response for the average roof drift, second-story drift, and first-story drift ratio, respectively. The instance of brace fracture can clearly be seen in Figure 4.7c from the dramatic loss in load from -300 kips to approximately -200 kips at -2% SDR.

4.4.2 Performance State Summary

The performance of the system and individual components during the test is important; particularly within a performance-based earthquake engineering context where the expected losses due to damage are estimated from engineering demand parameters (EDP) such as story drift, determined from an appropriate numerical structural model. This and the following sections in this chapter will describe the progression of damage to the four main components which are the braces, gusset plates, beams and columns. The descriptions will be done in three sections based on the drift range of the frame. The drift range is defined as the sum of the positive and negative value of the drift ratio in one cycle. The ranges used are as follows:

- Initial Drift Range ($0\% \leq$ Frame Drift Range $\leq 1.1\%$)
- Moderate Drift Range ($1.1\% <$ Frame Drift Range $\leq 2.6\%$)
- Severe Drift Range (Frame Drift Range $> 2.6\%$)

The point at which brace buckling occurred was determined through brace strain gauge data, brace string pot data and the recorded global and local force-displacement behavior (see Section 5.2.1 for a complete discussion of buckling loads). Local member yielding was determined through a combination of instrumentation and observations of whitewash flaking and are documented below with photographs. A summary of the performance states for each component may be seen in the tables located in Appendix D:

- Braces - Table D.3
- Gusset plates - Tables D.4 and D.5
- Columns - Tables D.6, D.7 and D.8
- Beams - Tables D.9 and D.10

These tables follow the damage state definitions discussed in Section 4.2 and will be used in tandem with the photo documentation in the following sections.

4.4.3 Pretest Observations

As this was the first test performed on the frame, there was no damage prior to the start of the test. The initial lateral displacement of the columns was measured before and after welding of the braces and beams and columns. The movement during the welding was insignificant and barely measurable. All columns had an initial out-of-plumbness no greater than $h/1000$, where h is the story height. This is one-half of the maximum recommended in the AISC Code of Standard Practice [2005c]. Prior to the start of the official test, a number of cycles in each direction were performed at approximately 0.1% RDR to check the instrumentation and ensure that everything was working as expected. There was no observable damage in any component during these small cycles and no observable nonlinearities in the force-displacement behavior of the frame and components.

4.4.4 Initial Drift Range (0% ≤ Frame Drift Range ≤ 1.1%)

Brace behavior in the initial drift range

No nonlinear brace behavior was observed during the first 10 cycles up to a maximum 0.25% SDRY in the first and second stories and a maximum of 0.16% SDRX in both stories. Brace buckling occurred in the braces in Frame 1 (Y-direction frames) during the 11th and 12th cycles. This was not visible to the naked eye but was determined through the brace strain gauges and the force-deformation behavior. The braces in Frame B (X-direction frames) buckled during cycles 17 through 20. Buckling occurred in the X-direction frames during later cycles because the X-direction RDR was two-thirds of that in the Y-direction. Figure 4.8 shows the braced frame elevations and the corresponding drift level at which brace buckling occured. Note that only one of the discontinuous braces in each story buckled. This was expected as the effective lengths of the discontinuous braces in each story are not exactly equal due to construction tolerances and minor differences in the rigidity of the gusset plates at each end of the brace. Therefore, following initial buckling of one discontinuous brace, the

force in the other discontinuous brace is limited to the initial buckling load of the buckled brace and can not reach its own buckling load.

During the 21st and 22nd cycles, the buckled braces in Frame 1 experienced out-of-plane deformation greater than the brace depth (B2), which was three inches in this case. This occurred at first and second SDRs of ±0.5% and ±0.59%, respectively. Photos of the first story braces at this buckling level can be seen in Figures 4.9a and 4.9b for the continuous brace and discontinuous brace, respectively. Figure 4.9a shows that the continuous brace buckled in a Mode-2 type shape in reverse curvature with the discontinuous braces in tension providing out-of-plane restraint at the center splice. Figure 4.9b shows that only the lower discontinuous brace buckled and the top one remaining straight. The buckled braces in Frame B experienced buckling level B2 during the 25th and 26th cycles and the behavior was the same as that described above for the braces in Frame 1. Similar to the braces in Frame 1, the SDRs at this level of brace buckling were 0.5% and 0.53% in the first and second story, respectively.

Gusset plate behavior in the initial drift range

Very minor yielding (level Y1) took place in all of the gusset plates during the initial drift ranges. The gussets above and below the second floor beam at column A1 were the first with observable whitewash flaking at 0.17 and 0.19% SDRY in the first and second story, respectively. This is shown in Figure 4.10 and this pattern of striations which began near the end of the brace and propogated at angles relative to the brace axis was typical of early yield lines in the gusset plates attached to the beams. The other gusset plates exhibited similar patterns of whitewash flaking during the initial drift ranges. It should be noted that this initial yielding occurred at low drift levels and prior to brace buckling even though the gussets were designed to yield after brace buckling and yielding. However, this design yield force is the force at which yield occurs across the entire Whitmore width. In reality, gusset plate yielding typically initiates in a small area and eventually spreads throughout the gusset. This early yielding is not a cause for concern and does not negatively impact the behavior of the brace or gussets.

Column behavior in the initial drift range

During the initial drift range there was minor flaking of whitewash (Y1) observable in the shared column only. This occurred at the base of the column at the location of the horizontal stiffener used to transfer the load of the gusset framing into the web of the shared column but only covered an area of approximately one in^2. This flaking occurred in the final drift cycle of the initial range at 0.42% 1SDRY . Yielding level Y1 also occurred in the shared column flange just above the second floor beam at the location of the stiffener.

Beam behavior in the initial drift range

There was no noticeable yielding or signs of nonlinear behavior in the beams during the initial drift range.

Initial drift range summary

A summary of the performance states of the specimen at the conclusion of the initial drift range are shown in Figure 4.11. Additionally, the performance states during each cycle are summarized in Tables D.3 through D.10. All braces except the discontinuous braces that never buckled, experienced buckling level B2 while the majority of the gusset plates exhibited very minor yielding in small localized areas. The shared column also exhibited minor yielding at two locations while the beams had no observable yielding.

4.4.5 Moderate Drift Range (1.1% < Frame Drift Range ≤ 2.6%)

The moderate drift range began in cycle 23 and ended in cycle 30 for the Y-direction, and for the X-direction, this range began in cycle 27 and ended in cycle 33.

Brace behavior in the moderate drift range

All of the braces that buckled reached the B3 performance state in this drift range (out-of-plane brace deformation greater than twice the brace depth). The braces in Frame 1 (Y-direction frames) reached this level during cycle 27 with maximum SDRs of 0.85% and 1.05% in the first and second story, respectively. The braces in Frame B (X-direction

frames) reached this performance state during cycle 31 with maximum SDRs of 0.99% and 1.13% in the first and second story, respectively. Figure 4.12a shows the first story continuous brace in this buckled state at a 1SDRY of -0.84%. The single curvature of the discontinuous brace, and the double curvature of the continuous brace can be clearly seen in these figures. Figure 4.12b demonstrates the unsymmetric buckling behavior of the second story discontinuous brace in Frame 1 at buckling level B3.

Gusset plate behavior in the moderate drift range

All of the gusset plates entered the Y2 yielding level during this drift range with the majority of them reaching Y3 also. All of the gusset plates in Frame 1 except those at the center brace splice reached level Y2 during cycles 25 through 27 at RDRYs between 0.78 and 0.94%. Not all gussets reached Y2 at exactly the same drift level and the occurrence of this is shown in Tables D.4 and D.5. Figure 4.13 shows the gusset plates at the second floor at column A1 at 1.1 and 1.4% SDRY in the first and second story, respectively. Figure 4.14 shows the gusset plates at the second floor framing into the flange of the shared column at 1.1 and 1.4% SDRY in the first and second story, respectively. It can be seen that the yielding is much more substantial in the gusset plate at the shared column than for the gusset plate at column A1. This is due to the fact that the brace framing into the bottom of the second floor beam at column A1 does not buckle and therefore places smaller demands on the gusset plate. This type of behavior was typical. The third floor gusset plates in Frames 1 displayed nearly identical yielding patterns to those on the underside of the second floor beams. The gusset plates at the center splice reached Y2 at approximately 0.6% SDR in each frame at each story. Figures 4.15a and Figures 4.15b show these gussets at the first story in Frame 1 and Frame B, respectively at the drift levels shown. Yielding was generally concentrated on the half of the gusset attached to the discontinuous brace that buckled, on the compression side of the gusset plate (due to flexure from brace buckling) and on the part of the gusset that had a shorter effective length between the corner of the end of the brace and the opposing continuous brace (this is due to the angle of the brace).

The gusset plates at the column bases reached Y2 at an RDR of approximately 0.94%

in each direction and Y3 at 1.27% RDR. Figure 4.16 shows these yield levels at the base of column A1. The progression of yielding can clearly be seen in these figures and there is a relativley large amount of whitewash flaking between the two drift levels. The gusset plate framing into the flange of the shared column at the base exhibited very similar yielding patterns to those at column A-1 shown in Figs. 4.16a and 4.16c. The gusset plates in Frame B showed similar yielding patterns and occurrences of Y2 and Y3 as those in Frame 1. Figure 4.17 shows the gusset plates at the second floor framing into column B-2 at 1.2 and 1.4% SDR in the first and second story,respectively.

During cycle 29, the long edge of two gusset plates deformed out-of-plane due to the beam and column moments at those joints causing the joint to close, thus inducing a compressive force in the gusset plate. This occurred while the brace framing into these gusset plates was in tension. Figure 4.18a shows this deformation at -1.1 and -1.4% 2SDRY and 1SDRY, respectively. Figure 4.18b shows the diagonal yielding that occurred as a result of this behavior.

Column behavior in the moderate drift range

The base of all three braced frame columns entered yielding level Y2 during the moderate drift range at 1SDRs between 0.57 (shared) and 1.1%. The bases of the shared column and column B2 entered yielding level Y3 at approximately 1.1% 1SDRY. Figure 4.19 shows the base of column A1 at yielding levels Y1 and Y2 which occurred at 0.71% 1SDRY and 1.13% 1SDRY, respectively. Figure 4.20 shows the base of column B2 at yielding levels Y1 and Y3 which occurred at 0.99% and 1.18% 1SDRX, respectively. It can be seen that a large amount of base yielding took place in this column as the drift level progressed from 0.99% to 1.18%. Figure 4.21 shows the extend of yielding at the base of the shared column at 0.85% 1SDRY and it can be seen that it was concentrated near the base plate and the stiffener transferring the gusset plate force to the column flanges. There was limited yielding in column A1 at the third floor in the outer flange at the stiffener location along with some initial flaking of small areas of the panel zone. The progression of panel zone yielding at the intermediate drift level in column A1 at the third floor is shown in Figure 4.22. The outer

flange of the shared column at the third floor had a limited amount of whitewash flaking at 0.86% 2SDRY and entered level Y2 yielding at 1.42% Y2SDR as seen in Figure 4.23.

Beam behavior in the moderate drift range

All of the braced frame beams displayed some level of whitewash flaking during the intermediate drift range. Initial yielding took place in three main areas of the beams: 1) in the web near the erection bolts; 2) in the bottom flange at the gusset reentrant corner and 3) in the the bottom flange outside the backing bar at the column face. Tables D.9 and D.10 list the exact location in each beam where the yielding took place and at what story drift level. Figure 4.24 shows the initial yielding of bottom flange of the second floor beam at the shared column at the gusset reentrant (Figure 4.24a) and at the column face (Figure 4.24b). This pattern is typical of all other braced frame beams. Flaking of the whitewash in the beam web near the erection bolts occurred relatively early and typically did not propagate in the web except in the second and third floor beams framing in the shared column flange (Frame 1 beams).

During cycles 29 and 30 (1.13% 1SDRY and 1.44% 2SDRY), the yielding intensified in the second floor beam framing into the shared column flange as shown in Figure 4.25. The yielding in the web and in the bottom flange along the length of the gusset plate can be clearly seen in the photo. Figure 4.26 shows a comparison of the bottom flange yielding in the second floor beam at column A1 (Figure 4.26a) and at the shared column (Figure 4.26b) at 1.13% 1SDRY. It can be seen that there is no yielding in the beam on the column A1 side while there is a relatively large amount of flange yielding on the shared column side. There was little to no panel zone yielding in the shared column at the second floor while there was a relatively large amount in column A1. As such, at column A1, a larger percentage of the joint deformation occurred in the panel zone and relived the stress at the end of the beam while the opposite occurred at the shared column side.

The second floor beam framing into the shared column web yielded at the field splice location as shown in Figure 4.27. The top and bottom flange along with the web yielded at this location as opposed to near the gusset reentrant corner or the column face because

the beam stub that was shop-attached to the column was tapered for fabrication ease and therefore had a larger section at the column face and the gusset reentrant corner.

Moderate drift range summary

A summary of the performance states of the specimen at the conclusion of the moderate drift range and for the drift range immediately preceding the final cycle of this range are shown in Figure 4.28. Additionally, the performance states at each cycle end are shown in Tables D.3 through D.10. All of the braces except those that did not buckle, reached out-of-plane deformations greater than two times the brace depth which is six inches for this test frame. The discontinuous braces that did not buckle when the continuous braces and the other half of the discontinuous buckled remained straight. All gusset plates except for three in Frame B reached yielding levels of Y3 during this range and the two gusset plates attached to the second floor beam and column A1 experienced out-of-plane edge deformation due to frame action when the brace connected to the respective gusset plate was in tension. Low levels of yielding initiated in the columns and beams at the majority of the joints, and the base of the shared column and column A1 reaching level Y3 towards the end of this range. Additionally, column panel zone yielding was observed in columns A1 and the shared column at both floors with yielding reaching level Y2 at third floor panel zones.

4.4.6 Severe Drift Range (Frame Drift Range > 2.6%)

The final drift range, the severe drift range, began in cycle 31 and ended in cycle 33 for the Y-direction; and for the X-direction, this range began in cycle 35 and ended in cycle 38. The story drift distribution remained similar to that in the moderate drift range with the second story drift ratios on the order of 20% greater than the those in the first story.

Brace behavior in the severe drift range

The out-of-plane deformation of the braces began to increase dramatically in this drift range reaching 10" (10% of the discontinuous brace lengthbetween the corner gusset plate and cen-

ter splice plate) at the largest story drifts. Plastic hinges began to form in the discontinuous braces that had previously buckled. They began to form in these braces prior to forming in the continuous braces because all of the deformation in the discontinuous braces was concentrated in only one-half of the brace while the deformation in the continuous braces was more evenly distributed between each half of the X-configured brace. This can be seen in Figure 4.29. The buckled shape of the braces began to lose the sinusoidal shape and took on the shape of two straight lines rotating about the plastic hinge. Figure 4.29b demonstrates that the continuous braces maintained the sinusoidal shape while the discontinuous brace in that same bay and story did not (Figure 4.29a). The discontinuous brace in the second story of Frame 1 was the first brace to form a plastic hinge with the walls bulging and cupping as shown in Figure 4.30a. This cupping and bulging began in cycle 31 at approximately 1.8% 2SDRY. When a cupped brace is straightened out in tension, small tears generally begin to form as shown in Figure 4.30b which typically signify complete fracture will occur within the next cycle or two if the drift level is kept constant or increased. Figure 4.30c shows the increased bulging and cupping at the next cycle which had a second story drift ratio of 2.13%. Follwing this compression excursion, the brace fractured at a 2SDRY of 2% as shown in Figure 4.30d.

Following fracture of this brace, the load in Y-direction was removed and the test continued with uni-directional loading in the X-direction. The discontinuous brace in the second story of Frame B began to cup and bulge at the plastic hinge during cycles 37 and 38 at a second-story drift ratio of 1.92%. The test was stopped after these cycles due to concern about excessive damage to the frame following brace fracture. Therefore, the discontinuous brace in the second-story of Frame 1 was the only brace that ultimately fractured.

Gusset plate behavior in the severe drift range

Gusset plate yielding continued in the severe drift range in all of the gusset plates with extensive yielding occurring at the gusset interfaces between the beams and the columns at the gusset plates attached to the beams. Additional yielding took place due to the gusset edge deformation of the long side of the gusset plates attached to the beams as a result

of frame action. This edge deformation occurred in all of the gusset plates except those attached to the base and those attached to the web of the shared column. This deformation occurred in many of the plates at approximately 1.5% RDR and also at larger drifts near 2%. The occurrence of this for each gusset can be seen in Tables D.4 and D.5. Figure 4.31 shows the yielding in the gusset due to the brace force and brace buckling along with that due to edge deformation for the gussets at the second floor beam at column A1 at 2.3% 2SDRY. The edge deformation can be clearly seen in Figure 4.32 for these two gusset plates along with the extensive yeilding at the beam and column interfaces. Figure 4.33 shows the gussets plates at the second floor at the shared column in Frame 1. The large amount of yielding in the lower gusset plate can be seen along with the much smaller amount of yielding in the gusset plate on top of the beam. The gusset plate on top demonstrated much less yielding due to the fact that the discontinuous brace attached to this top gusset never buckled and therefore did not place any rotational demands on this gusset plate.

Unlike the gusset plates in the previous planar tests performed at UW (for e.g. Powell 2010), the gusset plates attached to the beams and columns (as opposed to the base) did not exhibit elliptical yielding patterns. This is obvious from the second floor gusset plates in the figures just previously referenced and the and second and third floor gusset plates shown in Figure 4.34. This lack of elliptical yielding pattern is most likely due to the shallow brace angle which brings the brace closer to the beam when using the 8t elliptical offset thus changing the rotational behavior of the gusset plate and preventing the elliptical yielding pattern from forming. The elliptical yielding patterns in the base gusset plates at column A1 and the shared column in Frame 1 can be seen in Figures 4.36 and 4.37 and those at the base in Frame B can be seen in Figures 4.38 and 4.39. Figure 4.39 demonstrates that the majority of yielding was limited to the side of the gusset plate that was in compression due to the post-buckling bending demands of the brace. However, the buckled shape of the continuous braces in the first story of Frame 1 changed direction during cycle 31 while those in the first story of Frame B changed direction during cycle 32. As a result, yielding was extensive on both sides of these gusset plates as seen in Figures 4.36. Section 5.2.1 discusses the behavior of the brace as it changes buckling direction in more detail.

Slight tears also began to form at the gusset reentrant corners at the beam and column

interfaces at four gusset plates, three in Frame 1 and one in Frame B. These occurred at story drifts between 1.6 and 1.7%. The tears occured at the column in two instances and at the beam in the other two and were stable and never reached tear lengths greater than two inches. In three cases, it was the base metal that tore while the weld metal tore in the fourth instance.

The yielding of the gusset plates at the brace splice connection can be seen in Figure 4.40. The yielding in the lower half is due to a combination of yielding in tension and that due to brace post-buckling deformations while the yielding in the top half is due purely to yielding in tension as the top discontinuous brace did not buckle. This type of yielding was similar for all of the gusset plates at the center splice.

Column behavior in the severe drift range

The base of columns A1 and B2 both reached yielding level Y3 in the severe drift range at 1.4% 1SDRY and 1.0% 1SDRX, respectively. Figure 4.41a shows the base of column A1 at 1.4% 1SDRY while Figure 4.41b shows the base of column B2 at 1.4% 1SDRX. It can be seen that the yielding is relatively extensive and the patterns are simialr for both columns. It can be seen by comparing Figures 4.41b and 4.41c that a relatively large amount of yielding took place at the base of column B2 between first-story drift ratios of 1.4% and 1.6% as the yielding continued to spread above the base of the column. Addtionally, the yielding at the base of the columns was typically concentrated in the flange on the opposite side of the gusset plate as seen in Figure 4.41d. This is expected as the gusset plate and column form a built-up section which reduces the flexural stress in the column on the side of the gusset plate. The base of the shared column reached Y3 in the previous drift range and whitewash continued to flake off in large quantities during the severe drift range. The flange at the base of the shared column on the opposite side of the gusset plate at 1.71% 1SDRY is shown in Figure 4.42a.

Whitewash flaking continued to occur in the columns at the second and third floor joints but was not as extensive as the base yielding. Figure 4.43 shows the yielding on the outside flange of the shared column at the second floor at 1.6% RDRY. Note that all of this yielding

occurred at either the location of the stiffeners or the beam flanges and never progressed much further than that shown in the figure even at larger story drifts. Yielding did progress to level Y3 at the third floor of the shared column during the larger drift excursions as shown in Figure 4.35. Again, the yielding occurrs on the flange opposite of the gusset plates at the location of the stiffener and the bottom beam flange. Yielding level Y2 also occured in the column flanges at the CJP welds connecting the beam flanges at SDRs between 1.7 and 1.9%. This yielding may be seen in Fig. 4.42b for columns B2 at the second floor.

Panel zone yielding continued to occur in column A1 at both floors, and in column B2 and the shared column at the third floor as shown in Fig. 4.44. It can be seen in Figure 4.44a that the panel zone yielding in column A1 at the second floor was mainly concentrated along the bolt holes connecting the in-framing gravity beam to the column web while the panel zone yielding at the third floor was distributed more evenly as seen in Figs. 4.44b and 4.44c.

Beam behavior in the severe drift range

Yielding in the majority of the braced frame beams progressed to level Y3 in the flanges just outside of the CJP connection to the columns. At the third floor this occurred only in the bottom flanges as shown in Figure 4.45 for the beam in Frame 1. The top flange never yielded at this location mainly due to the thicker slab at this floor which shifted the beam neutral axis up. Yielding in the beam top flanges at the second floor at the column face did occur in the beams framing into the shared column in both Frame 1 and Frame B. There was not a floor slab near the column in this location due to the blockout required to facilitate replacement of the gusset plates for the second experiment. Figure 4.46 shows the extent of yielding in the second floor beam in Frame B framing into the web of the shared column. As noted in the previous section, the yielding occurred at the location of the CJP field splice.

There was a large amount of yielding in the second floor beam in Frame 1 framing into the flange of the shared column. Additionally, at the instance of brace fracture, the web of this beam just outside of the gusset plate deformed out-of-plane. The yielding in the web in this region prior to this deformation is shown in Figure 4.47a and it can be seen

that there is extensive web yielding in addition to extensive yielding in the top and bottom flanges (Figure 4.47d). The location of the web deformation occurred where the arc of flaked whitewash is shown in Figure 4.47b which shows the north side of the beam (looking at the beam from inside the frame). The actual deformation can be seen in Figure 4.47c.

Severe drift range summary

A summary of the performance states of the specimen at the conclusion of the severe drift range is shown in Figure 4.48 and the performance states at each cycle end are shown in Tables D.3 through D.10. The majority of the gusset plates had extensive yielding and the yielding was typically worse for the gusset plates connecting the braces that buckled and produced larger rotational demands on the gussets. Tears developed at the gusset reentrant corners in four of the gusset plates but were ductile and did not propagate to lengths larger than two inches. Three of these tears were in the gusset plate while the remaining one was through the fillet weld connecting the gusset to the beam. Additionally, the long edge of the gusset plates attached to columns A1 and B2 deformed out-of-plane due to the joint-closing action of the beams and columns when the brace is in tension. This deformation occurred between story drifts of 1.5% and 2%.

The base of the braced frame columns continued to yield considerably, especially in the flanges on the opposite side of the gusset plates and all bases were yield level Y3 in this drift range if they had not reached it in the previous range. Column yielding above the base was relatively limited except in the shared column at the first and second floors which reached level Y3 at approximately 2% 2SDRY. Additionally, column panel zone yielding reached level Y3 at the second and third floors of column A1, and at third floor in column B2 and the shared column. This panel zone yielding level was reached at approximately 1.5% story drift.

The second-story, top, discontinuous brace in Frame 1 fractured during the negative excursion of cycle 33 at a 2SDRY of -1.9% following the first positive excursion of 2% 2SDRY which placed this brace initially in compression. Upon brace fracture, the web of the second floor beam in Frame 1 framing into the shared column deformed out-of-plane

after it had undergone extensive yielding in the previous cycles. Yielding or deformation of this magnitude was not observed in any other beams in the frame and is most likely a result of the relative rigidity at the second floor joint provided by the shared column, the thicker column web and possibly by the large amount of stiffening due to the stiffeners required for the braces framing into the shared column web in the orthogonal direction. This limited the amount of column deformation and panel zone yielding and increased the moment in the beam relative to the beam moment in the other joints. As a result, there was much more yielding and deformation in this beam, setting it up for the instability that occurred when the brace fractured.

After brace fracture, the test was continued uni-directionally in the X-direction. At brace fracture, the force being resisted by this brace was transferred to the rest of the frame due to the lag in the time required by the actuator feedback sensor to arrest this force. Due to this, it was decided to stop the uni-directional test in the X-direction to prevent any more damage to the frame prior to the second test and the test was therefore stopped prior to fracture of the brace(s) in Frame B.

4.4.7 SCBF Test Summary

The SCBF, the first test performed on this frame, was subjected to the maximum story drift ratio ranges in the cycle prior to brace fracture shown in Table 4.3. The upper discontinuous brace in the second story of Frame 1 was the first to buckle and this occurred at a story-drift ratio of 0.25%. Only one-half of each discontinuous brace buckled in compression in each story, with the continuous brace in tension acting as an out-of-plane support. The upper disonctinuous braces buckled in both Frame 1 and Frame B in the second stories while the lower discontinuous braces buckled in both Frame 1 and Frame B in the first stories. The gusset connections at the base were more flexible than those at the beams and the lower, first-story discontinuous brace being 10 inches longer than the upper brace. Thus, it is logical that the lower discontinuous braces buckled in the first story. It is not obvious as to why the upper discontinuous braces buckled in the second story since the connections and brace lengths were theoretically the same for the discontinuous braces in the second story.

It is most likely due to the fact that the upper braces were slightly longer or had a slightly larger initial camber than the lower discontinuous braces in the second story.

The braces in tension provided lateral support at the center of the braces in compression. As a result, the continuous braces formed a mode-2-type buckled shape (S-shape) while the discontinuous brace that buckled took the form of a mode-1-type shape. However, at zero story drift after undergoing a relatively large story drift excursion, the buckled braces had not fully straightened out and as a result, the braces now in compression deformed out-of-plane at the brace intersection in a mode-1 type shape until the previously buckled brace became straight and stiff enough to resist the tensile force. This type of behavior caused the first-story continuous braces to reverse buckling direction at approximately 1.4% 1SDRY and 1.2% 1SDRX for Frame 1 and Frame B, respectively. Plastic hinges eventually formed in the upper, second-story discontinuous braces in both Frame 1 and Frame B but not in any other braces. However, the out-of-plane displacements of all of the buckled braces were relatively large with the discontinuous braces reaching OOP deformations of 11% of the brace length and the continuous braces reaching OOP deformations of approximately 8% of the brace length (eight to ten inches of OOP displacements). The second-story, upper, discontinuous brace in Frame 1 fractured in tension at -1.9% 2SDRY after reaching 2% 2SDRY in compression. There was considerable bulging and cupping in the plastic hinge prior to fracture. The second-story, upper, discontinuous brace in Frame B also had considerable bulging and cupping but did not fracture since the test was stopped to prevent this.

All of the gusset plates exhibited yielding with all of them being at yield level Y3 at the end of the test. In general, the gusset plates connecting the discontinuous braces that never buckled had less whitewash flaking than those connecting the braces that did buckle. The gusset plates at the base had elliptical yielding patterns similar to those observed in the previous tests at UW and NCREE (e.g. [Lumpkin, 2009]) while those attached to the beams did not exhibit this pattern. Instead, these elevated gusset plates demonstrated considerable yielding at the end of the brace and at the beam and column interfaces. This is due to the relatively shallow brace angle and the location of the workpoint at the column and beam intersection which places the brace end closer to the beam than if the brace were oriented

at 45 degrees. At the base, the workpoint was at the top of the baseplate which resulted in an equal distance between the end of the brace and the column and the baseplate.

All of the long edges of the gusset plates attached to the beams except those framing into the web of the shared column, deformed out-of-plane. This occurred when the brace was in tension and therefore not due to the brace force, but to the beam and column moments closing the joint (i.e. frame action). There was no obvious drop in frame resistance when this deformation occurred. Small tears also occurred at the gusset interfaces with the beams and/or columns in four locations. These tears did not exceed two inches at the end of the test. Similar to the gusset edge deformation, there was no noticeable drop in frame resistance when these tears occurred.

Significant yielding occurred at the base of the three braced frame columns. This occurred on the flange opposite the gusset plate, and by the end of the test, extended from the baseplate to approximately 24 inches above the baseplate. Extensive yielding at these bases initiated at approximately 1.0% to 1.2% first-story drift ratio. Column yielding at the floors was generally limited to the flanges at the location of the beam flange CJP connecting it to the column. However, in the shared column, yielding progress up to level Y3 on the outerflanges at the third floor at the locations of the beam flange connected to the inside of the column flange and also at the stiffeners used to transfer the gusset plate connection to the web of the column. Panel zone yielding also occurred at both floors in column A1, and in the shared column and column B2 at the third floor. There was very little panel zone yielding in the shared column at the second floor.

Yielding in the majority of the braced frame beams was limited, and occurred in the flanges just outside the CJP connection to the column flanges. However, the second floor beam in Frame 1 at the shared column yielded significantly during the larger drift ranges and eventually the web deformed out-of-plane when the brace fractured. This deformation occurred at the location of significant prior yielding and occurred near the end of the gusset plate. This yielding is attributed to the relative rigidity at the second floor joint provided by the shared column, the thicker column web and possibly by the large amount of stiffening due to the stiffeners required for the braces framing into the shared column web in the orthogonal direction. At the other joints, the deformations were shared more equally

between beam and column yielding and panel zone yielding while at the shared column at the second floor, panel zone and column yielding did not occur and forced the majority of the deformation into the beam. The second floor beam framing into the web of the shared column also demonstrated a relatively significant amount of yielding but not nearly as much as the previously mentioned beam. The yielding was concentrated at the location of the splice and was more advanced in the bottom flange than the top flange due to the presence of the floor slab at this location.

Finally, while the descriptors used to describe yielding and buckling (Y1, Y2, Y2, B1, B2, B3) in this section are helpful for the reader to get a feel for these levels at the various drift ranges, they say nothing in regards to the repair that may be required after an earthquake. Roeder et al. [2009] developed fragility curves for CBFs and defined four different damage states that correspond to repairs required and the level of repairs if required. These levels are defined as DS1, DS2, DS3 and DS4. The DS1 level corresponds to minor yielding or buckling that will not require any action; levels DS2 and DS3 are moderate levels of damage that may or may not require repair or replacement and will depend on the extent of damage and engineering judgment; and level DS4 is a severe damage state that will require replacement of the braces due to fracture, gusset plates due to tearing or large, permanent residual deformations and repair or replacement of framing members if instabilities such as local buckling or tearing occur. In most cases, when braces are rectangular HSS, a level of DS3 indicates replacement will be required. See Roeder et al. [2009] for more information. Figure 4.49 shows the pictoral of these damage states overlain on Frames 1 and B at the end of the SCBF test. It can be seen that all of the braces and the gusset plates would require replacement.

4.5 Test 2: Buckling-Restrained Braced Frame (BRBF)

The second specimen, the BRBF, was tested at the University of Minnesota MAST Laboratory over the course of five days beginning on Friday, July 16, 2010 when the first 18 cycles were performed. The test was resumed the following Monday and was completed on the afternoon of Thursday, July 22, 2010. Similar to the first test, the frame remained in an unloaded state at the end of each test day and data collection continued overnight to

assess any changes in the specimen during these extended pauses. No changes in the data were observed other than minor drifts in some of the strain gauges and these were corrected with insignificant effects.

This section will present an overview of the BRBF specimen performance. This will include story drift and story force histories, a summary of performance states, and detailed observations during the initial, moderate and severe drift ranges. These observations will rely mainly on photographic data taken throughout the test.

4.5.1 Overview

The loading protocol for the BRBF specimen was similar to that for the SCBF specimen except that the principal direction (1-direction in Figure 3.51a) for the BRBF specimen was the global X-direction as opposed to the global Y-direction for the SCBF specimen (see Figure 3.2). The first four cycles were uni-directional loading at approximately $0.5\Delta_y$ where Δ_y is the drift at which BRB core yielding first occurs. This was estimated as 0.34% roof drift ratio prior to the test from numerical simulations using SAP2000. Bi-directional loading began at cycle five and was discontinued following cycle 41. During the positive excursion of cycle 41, a divot began to form in the flange of braced frame column B-2 indicating that a tear was about to form. It was decided to stop loading in the X-direction and continue only in the Y-direction and return to X-direction loading following brace fracture in the Y-direction.

The BRB core in the second story of Frame 1 (Y-direction frame) fractured at a second story drift ratio of 4.2% during cycle 47. Following this BRB fracture, the frame was pushed through the complete cycle at this drift level and brought back to zero displacement. Loading was then performed uni-directionally in the X-direction for two and one half cycles until BRB core fracture occurred in the second story brace in Frame B at a second story drift ratio of 3.6%.

The maximum story drift ratios in each global frame direction and story reached during the last complete cycle prior to brace fracture are listed in Table 4.4. The largest SDR ranges occurred in the second story in Frames 1 and B and were 7.5 and 7.1%, respectively.

Detailed plots of the imposed story displacements and story drift ratio histories in each direction and plots of the cloverleaf histories for each story are shown in Appendix E in Figs. E.1 through E.4. Also included in this appendix are tables listing the peak negative and positive roof and story drift ratios for each cycle along with the maximum force in the actuators (Tables E.2 and E.3).

The story shear-drift response in each story and direction are shown in Figure 4.50 with Figures 4.50a, 4.50c and 4.50e showing the Y-direction response for the average roof drift, second-story drift, and first-story drift ratio, respectively. Figures 4.50b, 4.50d and 4.50f show the X-direction response for the average roof drift, second-story drift, and first-story drift ratio, respectively. The instance of brace fracture can clearly be seen in the figures as sharp drop in the load from approximately 320 kips to 200 kips in the positive drift range.

4.5.2 Performance State Summary

The performance states of the frame during the BRBF test will be described in the following sections in the same manner as that done previously for the SCBF test. The same damage state definitions apply for the BRBF test specimen as for the SCBF with the exception of brace buckling which did not occur in the BRBs.

A summary of the performance states for each component may be seen in the following tables located in Appendix E:

- Gusset plates - Table E.4
- Columns - Tables E.5, E.6 and E.7
- Beams - Tables E.8 and E.9

These tables will be used in tandem with the photo documentation in the following sections. It is important to note that the frame excluding the braces and gusset plates was reused for the second test. Therefore, there was initial damage in these members as described in Figure 4.48. Further yielding at the locations where whitewash had flaked off in the first test was not observable during the second test and could only be noted at the locations where yielding did not occur in the first test.

4.5.3 Pretest Observations

Following the end of the SCBF test, the horizontal actuator forces were released resulting in residual story drifts. The residual RDR was 0.5% in the X and Y-directions. The braces and gusset plates were then removed followed by installation of the new gusset plates and BRBs. The installation of these did not result in an appreciable change in the residual frame drifts.

To relieve concerns that prior damage may adversely affect the BRBF test results, a 3/8" thick web doubler plate was welded to the web of the braced frame W16x50 beam in Frame 1 that deformed out-of-plane at the end of the first test and shown in Figure 4.47. The web doubler plate extended approximately 16" on either side of the gusset-beam reentrant and was welded to the web with 5/16" fillet welds all around (Figure 4.51).

4.5.4 Initial Drift Range

Brace behavior in the initial drift range

No nonlinear BRB behavior was observed during the first 12 cycles. BRB yielding in tension occurred in Frame B in both stories at 0.3% SDR during cycle 13. In Frame 1, yielding in tension of the BRB occurred in the second story at 0.33% SDR during cycle 19 while the BRB in the first story yielded in tension at 0.3% during cycle 21. The BRB in the first story of Frame B yielded in compression at -0.45% SDR while the second story BRB yielded in compression at 0.42% SDR. This occurred during cycles 19 and 21 for the second and first stories, respectively. The BRBs in both stories of Frame 1 yielded at 0.4% SDR during cycles 21 and 25 for the second and first stories, respectively. This yielding was determined from the backbone force-displacement curves of each BRB as discussed in greater deatil in Section 5.3.

Gusset plate behavior in the initial drift range

No observable damage occurred to the gusset plates during the initial drift range. This was expected as the gusset plates were 1.6 times thicker than that required for yielding or buckling.

Column behavior in the initial drift range

No observable damage occurred in the columns during the initial drift range.

Beam behavior in the initial drift range

No observable damage occurred in the beams during the initial drift range.

4.5.5 Moderate Drift Range

Brace behavior in the moderate drift range

Yielding continued in the BRBs during the moderate drift range with no visible distress in the casing or at the ends.

Gusset plate behavior in the moderate drift range

Very slight yielding was observed in the gusset plate below the second floor beam at the shared column in Frame B at 1.22% 1SDRX. This occurred at the beam-gusset reentrant corner with approximately 0.5 in^2 of whitewash flaking off. Whitewash did not flake off in any other gusset plates during this drift range.

Column behavior in the moderate drift range

Visible yielding at the base of column A-1 began in this drift range at 1.3% 1SDRY which corresponded to 1.9% 1SDRX. Visible yielding at the base of column B-2 was observed at 1.0% 1SDRY which corresponded to 1.5% 1SDRX. Note that both of these drifts in the X-direction are in the severe drift range. The yielding in both column bases occurred in the column flange opposite the gusset plate and is shown in Figs. 4.54b and 4.56b for columns A-1 and B-2, respectively.

Beam behavior in the moderate drift range

There was no observable damage in the beams during the moderate drift range. However, as noted previously, the ends of the braced frame beams had yielded during the first test.

Therefore, it is likely that these areas had again reached yield by this point but yielding was not visible since the whitewash had already flaked off by this point. As will be discussed in the next chapter on data analysis, the beam strain gauges indicated yielding had in fact taken place near the gusset plate region.

4.5.6 Severe Drift Range

Brace behavior in the severe drift range

The core of the second-story BRB in Frame 1 fractured at a second-story drift ratio of 4.2% and the core of the second-story BRB in Frame B fractured at a second-story drfit ratio of 3.6%. A much more extensive discussion of the BRB behavior is given in Section 5.3 using the instrumentation data recorded during the experiment.

Gusset plate behavior in the severe drift range

Minimal yielding took place in the gusset plates and occurred only at the column and beam reentrant corners in a very localized area not exceeding two square inches. This yielding took place at SDRs ranging between 1.5 to 2.5%. This lack of extensive yielding was expected as pin bearing governed the design of the gusset plate with the yielding and buckling capacities being 1.6 times the demand. The most significant damage occurred in the welds connecting the vertical gusset plate edge to the columns. Weld tearing occurred in four of the eight gusset connections with two of these tears propagating the total length of the weld. The tears were first observed at SDRs ranging between 1.9 to 2.5%. Figure 4.52 shows the gusset plate yielding and weld tearing at the gusset plate above the second floor beam attached to column A-1 in Frame 1. The weld tear has propagated the length of the connection due to the column and beam moments opening the joint. Figure 4.53 shows the gusset plate and weld damage at the second floor gusset attached to column B-2. Initial yielding is shown in Figure 4.53b while the weld tears are shown in Figures 4.53c and 4.53d. The joint opening due to the beam and column moments can clearly be seen in these photos.

Column behavior in the severe drift range

At the base of column A-1, the column flange opposite the gusset plate underwent a considerable amount of yielding during this drift range and this progression is shown in Figures 4.54a through 4.54d with Figure 4.54a showing this flange at the beginning of the test. The first visible signs of yielding in this flange during the BRBF test occurred at approximately 1.3% 1SDRY and 1.9% 1SDRX as shown in Figure 4.54b. The yielding progressed with increasing story drift and eventually extended from the baseplate to approximately three feet above the baseplate as shown in Figure 4.54d.

The web at the base of column A-1 began to yield in a triangular pattern with the vertex near the k-region at the gusset reentrant corner and was first visible at a 1SDRY of -1.5%. The yielding gradually increased with increasing story drift until the majority of whitewash had flaked off in this triangular region by the end of the test at -2.7% 1SDRY. The flange opposite the gusset plate also reached local flange buckling level B2 at -2.7% and progressed to level B3 by the end of the test. Figures 4.55a through 4.55d show the progression of damage at this location and the local flange buckling and the final yielding damage can be seen in Figure 4.55d.

As expected, the base of column B-2 displayed very similar behavior to column A-1. Figures 4.56a through 4.56d show the progression of yielding on the flange opposite of the gusset plate. Figure 4.56a shows the yielding that occurred during the previous test. By the end of the BRBF test, extensive yielding had progressed approximately 30" up the column from the base as shown in Figure 4.56d.

Figures 4.57a through 4.57d show the progression of yielding in the web at the base of column B-2 along with the local flange buckling in the flange opposite the gusset plate. The web yielding was not as extensive as it was at the base of column A-1 but the triangular pattern was similar as a comparison of Figures 4.57d and 4.55d show.

The base of the shared column did not experience any local flange buckling or extensive web yielding like columns A-1 and B-2 did. Flange yielding did progress upward from the baseplate throughout the test but the whitewash flaking was not as extensive as that shown in Figures 4.54 and 4.56 for columns A-1 and B-2. Figure 4.58 shows the progression of

yielding on the outer flange of the shared column from the start of the test (Figure 4.58a) to the end of the test Figure 4.58b). Minor flaking at the edges of each flange extended approximately 40" above the baseplate with the large areas of flakes whitewash concentrated within the first 24" above the baseplate.

The gravity column flanges yielded extensively at the base from the baseplate to approximately 24" above the baseplate. Figures 4.59a through 4.59d show the progression of yielding throughout the test at various drift levels beginning at 1.3% 1SDRY and 1.8% 1SDRX.

The majority of yielding and damage in column A-1 at the second floor occurred in the panel zone and the web within the gusset plate region above the beam. The flange yielding reached level Y3 at the location of the beam flanges but did not extend further than the area approximately 1/2" on either side of the beam flanges.

The gravity beam along gridline A was connected to the web of this column with double angles with four rows of bolts in each leg as shown in Fig. B.13c. This connection affected the behavior of this joint at larger story drifts. Panel zone yielding, which typically originates in the center of the panel spreads radially outward did not occur in this fashion. Instead, yield lines developed along the lines of bolts and then propagated horizontally between bolt lines. Figures 4.60a through 7.25c shows the progression of yielding in this location from the start of the test through the severe drift range until the end of the test. Additionally, tears developed in the bottom two column web bolt holes on the interior side of the connection during the first cycle at 2.7% 1SDRY (cycle 47). These tears propagated vertically through the total length of the bolted connection during the second cycle at 2.7% 1SDRY (cycle 48). Figure 4.61 shows the tear between the top two bolts at the end of the test at zero drift.

Considerable amount of column web yielding also took place in the area within the gusset plate region. At this location, the gusset plate was connected to the top of the beam while no gusset plate was connected to the beam bottom flange. The progression of yielding at this location may also be seen in Figs. 4.60a through 7.25c with the majority of the yielding occurring near the k-region on the side of the gusset plate. This did not occur below the beam which suggests that this was caused by the force transfer from the gusset plate which was 2.3 times thicker than the column web.

The damage at the second floor joint of column B-2 was very similar in nature to that at the second floor joint of column A-1 with the addition of extensive column flange tearing occurring at the bottom beam flange CJP weld. Figures 4.62a through 4.62d show the progression of damage at this start from the beginning of the test through the severe drift range until the end of the test. The linear yield pattern along the bolt lines in the column web can be seen along with the web yielding in the gusset plate region above the top beam flange similar to that which occurred at column A-1. Like column A-1, there was no visible column web yielding below the beam where no gusset plate was attached.

The first tear in this column web was observed in the inboard line of bolts at the bottom two bolt holes at 2.4% 1SDRX. This tear propagated through the whole bolt line at 2.8% 1SDRX. Concurrent with this web tearing, tearing occurred in the column flange at the CJP weld connection to the beam bottom flange. A divot began to form on the inside of the column flange near the k-region on the outboard side of the column web at the bottom beam flange giving the first indication that a tear was about to form. At this point, loading in the X-direction (Frame B direction) was stopped and the frame was loaded in the Y-direction only until BRB fracture in Frame 1. Following this, loading continued uni-directionally in Frame B. The column flange divot along with the ensuing tear at various drift levels are shown in Figure 4.63. Eventually, the vertical tear through the bolt line propagated horizontally and connected with the flange tear as shown in Figures 4.63d and 4.64.

It is noted that the beam bottom flange backing bar at the CJP weld to the column flange was not removed as is typically done in earthquake prone regions and is certainly required for ductile moment frames in the U.S. This may have contributed to the column flange tearing as these CJP welds are prone to defects which is the reason for the requirement of backup bar removal for moment frames. Figure 4.65 shows the beam bottom flange pulling away from the column flange and the gap is clearly visible.

Limited damage occurred in the shared column at the second floor during the BRBF test. The observable yielding that did occur was concentrated in the flanges at the location of the beam flange plates that were shop-attached to the column flanges. Whitewash flaking was minimal and nearly covered the width of the flanges and approximately three inches above and below the continuity plates. Insignificant amounts of whitewash flaked off in the

panel zone at this floor.

The third floor panel zones in columns A-1 and B-2 had yielded during the first test and continued to yield more during the BRBF test with whitewash flaking first noticeable at approximately 1% SDR. Figures 4.66a and 4.66b compares the panel zone yielding at the third floor of column A-1 at the beginning of the test to that at the end. Figures 4.66c and 4.66d shows the same comparison for the third floor panel zone of column B-2. The figures show that the entirety of the panel zones had yielded by the end of the test. The shear tab welded to the opposite side of the column webs can be clearly seen in the figures as the vertical area where none of the whitewash flaked off in the middle of the panel zones. Limited flange yielding occurred in these columns at the third floor and mainly occurred near the CJP connecting the bottom beam flanges to the column flanges as shown in Figure 4.67.

Minimal additional yielding was observed in the shared column panel zone at the third floor even during the severe drift range. The additional whitewash that flaked off of the panel zone in this area was difficult to notice. The flange yielding at this location was observable though not nearly the amount that occurred at the base. Figure 4.68 shows the progression of flange yielding at this location from the start of the test through the severe drift range. The pattern of yielding on the flange indicates that this this yielding was due more to weak axis column bending as the larger areas of flaked whitewash occurred at the edges of the flanges.

Beam behavior in the severe drift range

Extensive damage occurred at the ends of the braced frame beams in the four locations where gusset plates were attached. Little to minimal damage occurred at the other braced frame beam ends where no gusset plate was attached. The major damage included yielding, local flange buckling, OOP web deformation and flange and web tearing.

Yielding occurred at the ends of the second floor braced frame beams attached to columns A-1 and B-2 as shown in Figures 4.69 and 4.70. This yielding was mainly confined to the top flange and top half of the web at the location of the slab blockout as seen in the figures. Local flange buckling occurred at the end attached to column A-1 as seen in Figures 4.69d

and 4.69e but did not exceed buckling level B1. This local flange buckling did not occur at the beam end at column B-2 which is likely due to the damage that occurred in the column flange and web at this location which relieved the demands on the beam. This damage included column flange and web tearing as discussed previously and shown in Figures 4.62 through 4.65.

Extensive yielding and local flange buckling also occurred at the second floor beam on the shared column side in Frame 1 at the location between the slab blockout and gusset plate. This is the same location that extensive yielding and OOP web deformation occurred at during the first test (SCBF) and where the web doubler was installed prior to the BRBF test. The progression of this yielding and local flange buckling is shown in Figure 4.71. It can be seen in Figure 4.71d that the local flange buckling had reached level B3 by 2.7% 1SDRY and occurred in the flange that the gusset plate was connected to, similar to the other end of the beam connected to column A-1.

Nearly-complete fracture of the beam occurred at the second floor framing into the web of the shared column in Frame B. The progression of this failure from the beginning of the test through the severe drift range to the end of the test is shown in Figure 4.72. The occurrence of web yielding near the bottom erection bolt at the beam splice at -2.2% 1SDRX can be seen in Figure 4.72c This yielding increased dramatically in the following cycles as shown in Figure 4.72d at -3.0% 1SDRX. Extensive yielding of the bottom flange can also be seen in this figure. Small tears were observed in the beam web at the bottom of the web CJP splice and at the bottom erection bolt hole. These are shown in Figure 4.73a and were first observed at -2.6% 1SDRX. The tears propagated upward in the web to approximately one-quarter of the beam depth during the first cycle to -3.1% 1SDRX (Figure 4.72d). During the second cycle out to -3.1% 1SDRX, the bottom flange fractured suddenly and without warning and the web tear propagated up to half the beam depth. As seen in Figure 4.73b, this flange fracture occurred in the HAZ of the field-erected portion of the beam just outside of the CJP weld to the shop-attached beam stub. Testing continued for one more cycle and the tear propagated through the whole depth of the beam including the top erection bolt hole but not the top flange which remained intact. Figures 4.73c and 4.73e show the large gap opening in the beam at the fracture at -3.1% 1SDRX.

Limited yielding occurred in third floor braced frame beams near the connection to columns A-1 and B-2. No gusset plates occurred in this location. The bottom flange at the CJP weld to column and the lower portion of the web had minor yielding during the first test (see Fig. 4.44b) and very little additional yielding occurred in the beams at this location during the BRBF test as Fig. 4.74 shows.

Extensive damage occurred in the third floor braced frame beam on the shared column side in Frame 1. This progression of damage from the beginning of the test through the severe drift range is shown in Figure 4.75. Figure 4.75b shows the web yielding that occurred during the first test. The first signs of visible yielding during the BRBF test occurred at 1.5% 2SDRY in the web near the bottom flange k-region at the gusset reentrant corner. Yielding of the web and the bottom flange continued during the remainder of the test with significant yielding occurring between 3 and 3.8% 2SDRY. Local flange buckling of the bottom flange at the gusset reentrant corner was first observed at 2.3% 2SDRY and reached level B1 at this point. This occurred at the same time that slight OOP web deformation was observed. This web deformation was difficult to capture on film but is shown, along with the flange deformation, in Figures 4.76a and 7.24c. The axis of web deformation is a line at approximately 45 degrees angled toward the column and originating near the bottom flange with the web deforming OOP to the right in the figures. A tear developed in the bottom flange at the gusset reentrant corner and propagated through the entire flange width and approximately two inches into the web. This occurred during cycle 46 in the ramp to -3.7% 2SDRY and is shown in Figures 4.76c and 4.76d. The tear propagated up to half the beam depth during the last cycle to -4.5% 2SDRY.

Virtually no yielding was observed in the third floor braced frame beam framing into the shared column web in Frame B.

4.5.7 BRBF Test Summary

The BRBF, the second test performed on this frame, was subjected to the maximum story drift ratio ranges in the cycle prior to brace fracture shown in Table 4.4. All of the BRBs yielded in tension at 0.3% SDR while they yielded in compression at SDRs between 0.4 and

0.45%. This difference is expected due to the compression overstrength inherent in BRB construction. The second-story BRB in Frame 1 fractured at a SDR of 4.2%, while the second-story BRB in Frame B fractured at a SDR of 3.6% SDR. Upon force reversal, the fractured BRB went into bearing at the fracture point and was able to provide resistance until the concrete at this area crushed and each half of the fractured steel core slid past each other.

Unlike the gusset plates for the SCBF specimen, the gusset plates for the BRBF specimen were 1.6 times as thick as required for the limit states of yielding and buckling. These gusset plates sustained very little damage throughout the test with only moderate yielding occurring at the gusset-column reentrant corners beginning at approximately 2% SDR. However, weld fracture was observed in the vertical welds connecting the gusset plates to the columns. This was observed in three of the four joints in Frame 1 and one joint in Frame B. At two locations, the vertical weld completely fractured. At the other two locations, the tears were stable after propagating to 50mm in length. This was likely due to the damage sustained by the beams and columns at these locations that relieved the demands at these gusset welds. Considering that weld tearing occurred when the BRB was in compression, it is suspected that these tears were a result of frame action and not the brace demand.

The frame sustained extensive damage. Considerable yielding and local flange buckling occurred near the base of braced frame columns A-1 and B-2. This flange buckling initiated at -2.6% SDR. The panel zones at the second floor of columns A-1 and B-2 yielded and eventually fractured around the bolt holes supporting a double angle shear connection for the gravity beams perpendicular to the braced frames. At column B-2, the column flange tore completely through and connected with the web tears just described. The gravity beam being supported by this web was not subjected to applied gravity loading during the test other than its self weight. Obviously, this kind of damage has a negative impact on the integrity of the gravity system at this location. At the third floor of these columns, the gravity beams perpendicular to the braced frames framing into these webs were connected with welded, extended shear tabs. These panel zones did not sustain any damage other than yielding.

Significant beam damage occurred at the edge of the gusset plates. At the third floor

beam framing into the shared column in Frame A, the beam bottom flange buckled at the gusset reentrant corner while the web deformed out-of-plane. As loading was continued beyond this stage (2.3% SDR), the bottom flange fractured at the gusset reentrant across the entire flange width and six inches into the web. At the second floor beam framing into the web of the shared column, fracture initiated in the web at the bottom weld access hole at 3.1% SDR and propagated upward through the bottom erection bolt. Ultimately, the bottom flange fractured suddenly followed by web fracture, leaving only the top flange intact.

The second floor beams in Frame 1 underwent extensive flange and web yielding in the region between the gusset reentrant corner and the end of the slab blockout, beginning at approximately -3% second story SDR. The region between the blockout and gusset plate was susceptible to damage since it is weak relative to the remaining portion of the beam that is either composite with the slab or stiffened by the gusset plate. Local flange buckling also occurred in these locations but neither beam developed tears this location.

Finally, as the frame had undergone yielding in the first test, the damage pictorials were not able to be drawn for the BRBF test as they were for the SCBF since yielding could no longer be observed due to whitewash having already flaked off. However, the damage states per ATC-58 [2009] may be noted for the later drift ranges since considerable more damage occurred after 2% SDR and was observable and clear as to whether or not repair was necessary. Figures 4.77a and 4.77c shows the damage states of Frame 1 at 2.2% and 3.6% RDR, respectively. Figures 4.77b and 4.77d shows the damage states of Frame B at 2.5% and 3.6% RDR, respectively. For the most part, the damage to the framing members in Frame 1 at 2.2% RDR and Frame B at 2.5% RDR has not progressed beyond that which occurred at the end of the first test at 2% RDR except at the beam and column areas near the gusset plates. In particular, the column webs of columns A-1 and B-2 just above the second floor at the gusset plate have yielded considerably more, and so have the beams at this location. Additionally, the third floor beam framing into the shared column in Frame 1 has also yielded considerably more. There are tears in the vertical gusset welds at the four locations shown with tear lengths ranging from 1/2 to 2 inches. Repair of these welds would be warranted in this case.

At 3.6% RDR, there is considerable damage that would require repair or replacement as seen in Figures 4.77b and 4.77d. The second story BRBs in both frames have fractured and would require replacement. The gusset plate weld tears above the second floor beam at columns A-1 and B-2 have propagated the length of the weld while the other two tears were arrested at approximately 2 inches. Beam repair or complete repalcement would be required in the locations shown at damage state DS4. Columns A-1 and B-2 would require repair at the base including heat straightening of the buckled flanges and possible installation of web doublers and continuity plates. Additionaly, column B-2 would require serious repair (or complete replacement) at the second floor where the flange and web fractured.

Table 4.1: Performance State Nomenclature

Symbol	Description	Detailed Description
Y1	Initial Yielding	Yield lines first visible to yield lines cover less than one half of the gusset plate or member width
Y2	Moderate Yielding	Yield lines cover more than the majority of the gusset plate or member width
Y3	Severe Yielding	The entire width of the member or gusset is yielded and large, concentrated areas of yielding are visible through large areas of whitewash flaking
B1	Initial Buckling	Brace - buckling does not exceed the member depth; Element - local buckling first visible
B2	Moderate Buckling	Buckling greater than the member depth or element thickness
B3	Severe Buckling	Buckling exceeds twice the member depth or element thickness
BC	Loss of Brace Compressive Resistance	The brace resists very little compressive load because local damage has occurred at the plastic hinge location
BF	Brace Fracture	Visible tearing of brace or complete fracture of brace or element
Wc	Weld Damage at Column	The interface weld connecting the gusset plate to the column is damaged
Wb	Weld Damage at Beam	The interface weld connecting the gusset plate to the beam is damaged
WBc	Base Metal Damage on Column	The base metal at the gusset -column interface is damaged
WBb	Base Metal Damage on Beam	The base metal at the gusset -beam interface is damaged

Table 4.2: Acronyms used for story drift ratios

Acronym	Definition
RDRY	roof drift ratio in the global Y-direction
2SDRY	second-story drift ratio in the global Y-direction
1SDRY	first-story drift ratio in the global Y-direction
SDRY	story drift ratio in the global Y-direction
RDRX	roof drift ratio in the global X-direction
2SDRX	second-story drift ratio in the global X-direction
1SDRX	first-story drift ratio in the global X-direction
SDRX	story drift ratio in the global X-direction

Table 4.3: Maximum story drift ranges prior to brace fracture (SCBF test)

Global	Roof drift ratio			Second story drift ratio			First story drift ratio		
direction	Range	Neg	Pos	Range	Neg	Pos	Range	Neg	Pos
X	3.4	-1.7	1.7	3.8	-1.9	1.9	3.1	-1.6	1.5
Y	3.2	-1.6	1.6	3.6	-1.8	1.8	2.8	-1.4	1.4

Table 4.4: Maximum story drift ranges in the last complete cycle prior to brace fracture (BRBF test)

Global direction	Roof drift ratio			Second story drift ratio			First story drift ratio		
	Range	Neg	Pos	Range	Neg	Pos	Range	Neg	Pos
X	6.5	-3.2	3.2	7.1	-3.4	3.7	5.7	-3.0	2.7
Y	6.4	-3.2	3.2	7.5	-3.7	3.8	5.4	-2.8	2.6

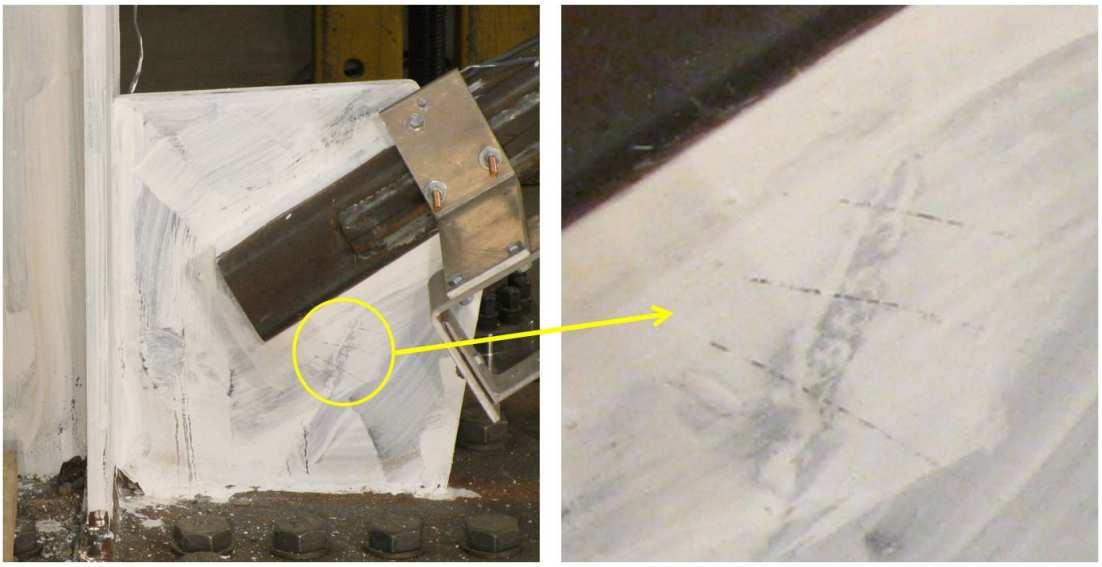

(a) Yielding level Y1



(b) Yielding level Y2



(c) Yielding level Y3

Figure 4.1: Yielding levels for frame performance states



Figure 4.2: Conventional brace Buckling Levels (Source: [Lumpkin, 2009])

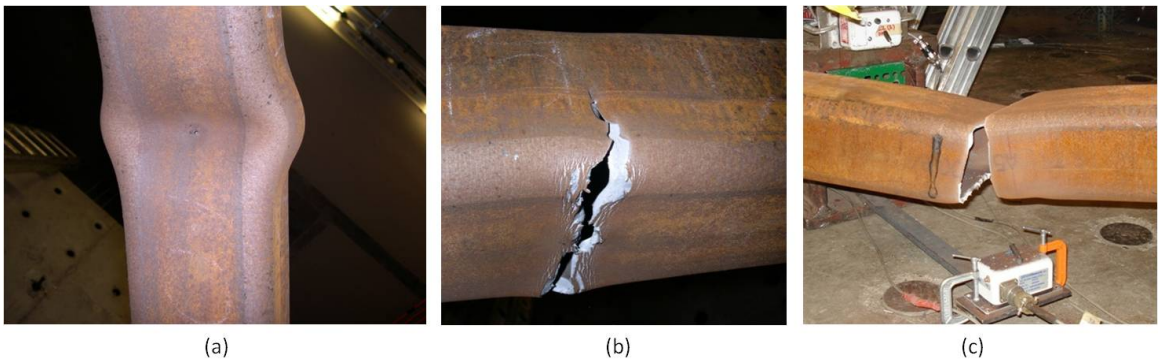

Figure 4.3: Brace performance states: (a) Cupping and bulging at plastic hinge; (b) Tearing of part of the brace at the plastic hinge (BF); (c) Complete fracture of the brace at the plastic hinge (BF). (Source: [Powell, 2010])



(a) (b)

Figure 4.4: Local buckling levels (a) B2; (b) B3.



(a) (b)

Figure 4.5: Weld damage performance states: (a) Weld material damage; (b) Base metal damage. (Source: [Lumpkin, 2009])

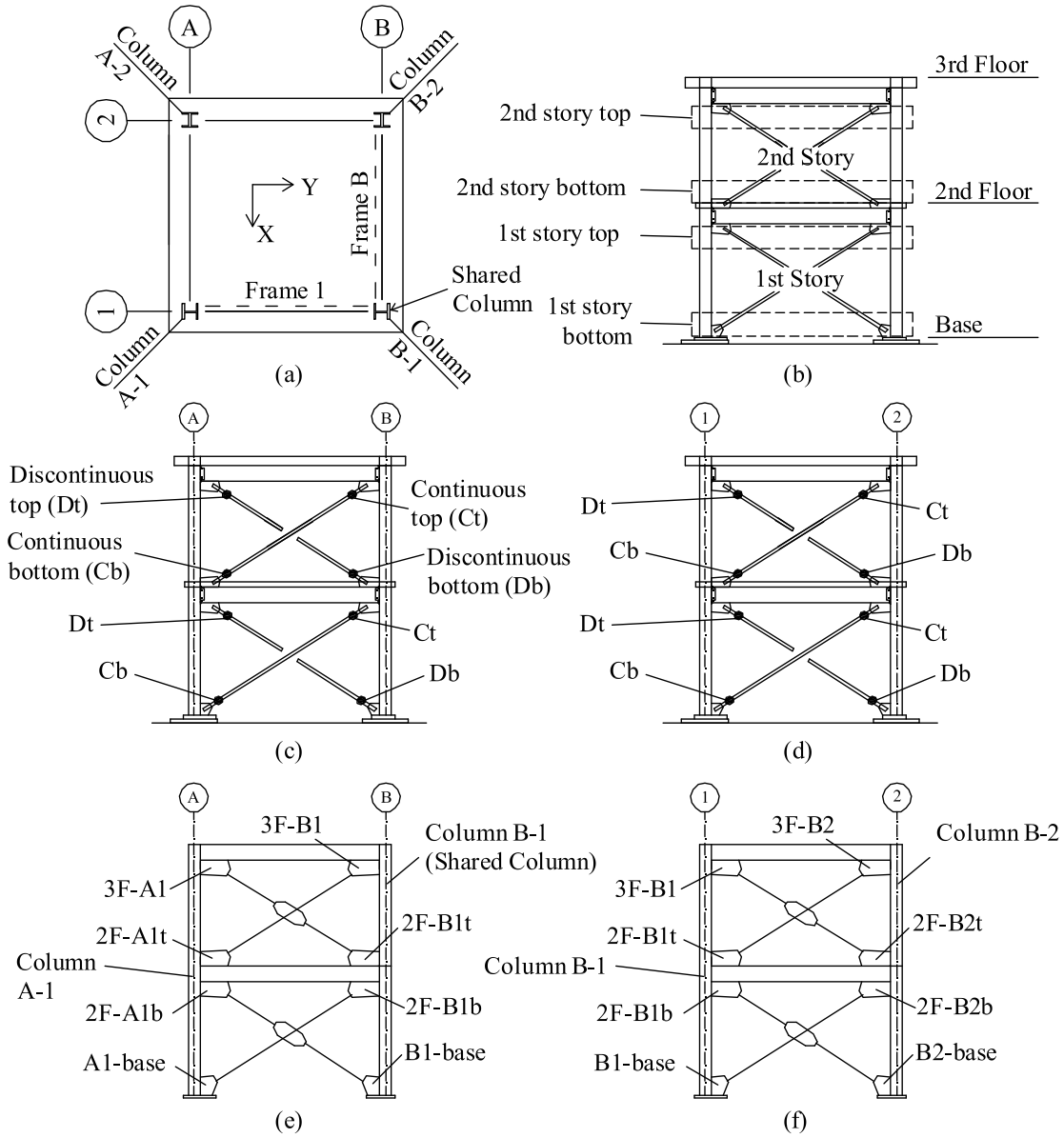

Figure 4.6: Test frame nomenclature: (a) Frames and columns; (b) Story and floor designations; (c) Frame 1 brace designations; (d) Frame B designations; (e) Frame 1 gusset plate designations; (f) Frame B gusset plate designations.

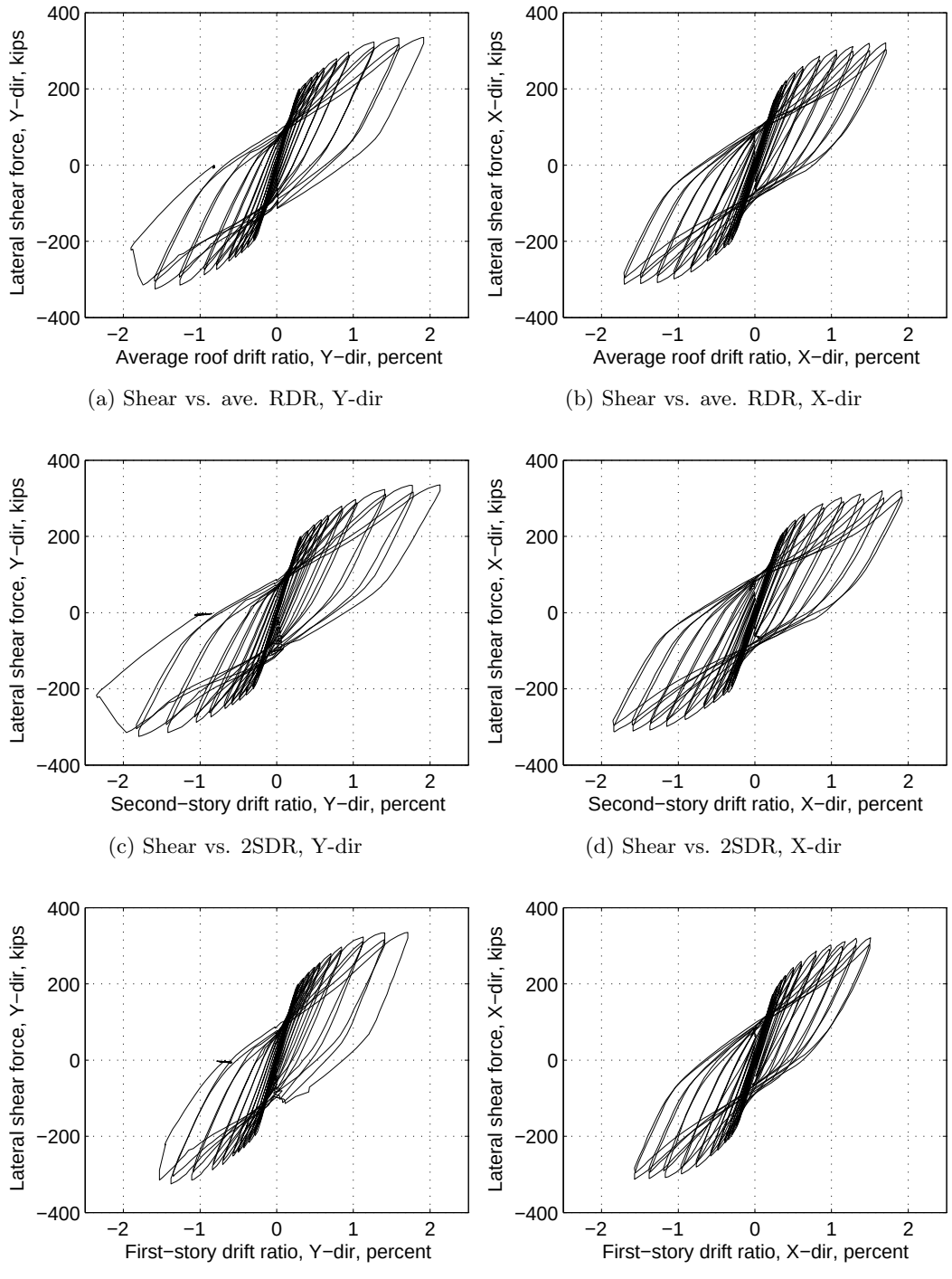

(a) Shear vs. ave. RDR, Y-dir

(b) Shear vs. ave. RDR, X-dir

(c) Shear vs. 2SDR, Y-dir

(d) Shear vs. 2SDR, X-dir

(e) Shear vs. 1SDR, Y-dir

(f) Shear vs. 1SDR, X-dir

Figure 4.7: Frame shear-drift hysteresis (SCBF test)

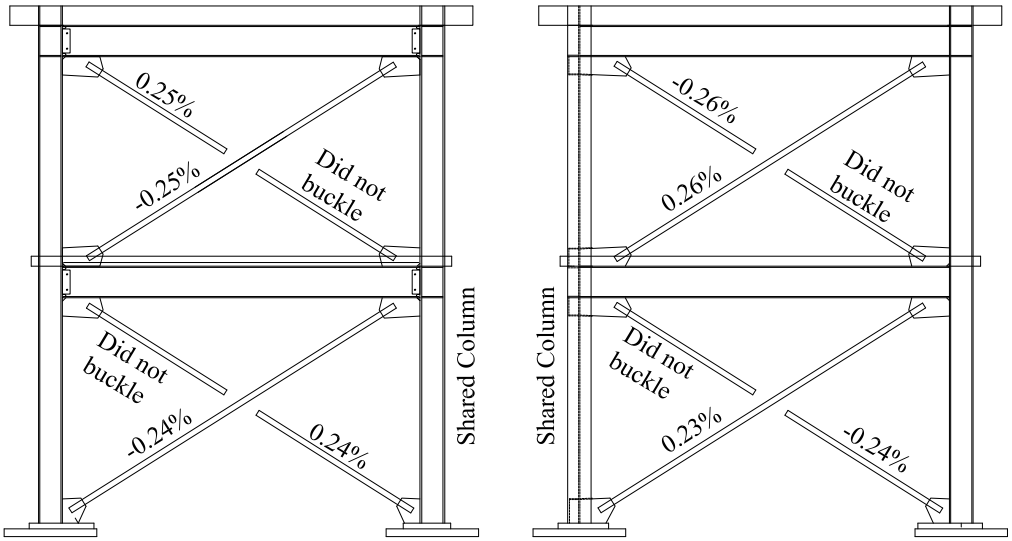

(a) Frame 1

(b) Frame B

Figure 4.8: Frame elevations showing SDRs at initial brace buckling



(a) Continuous brace, -0.5% SDR (b) Discontinuous brace, 0.5% SDR

Figure 4.9: Frame 1 first story braces buckling level B2

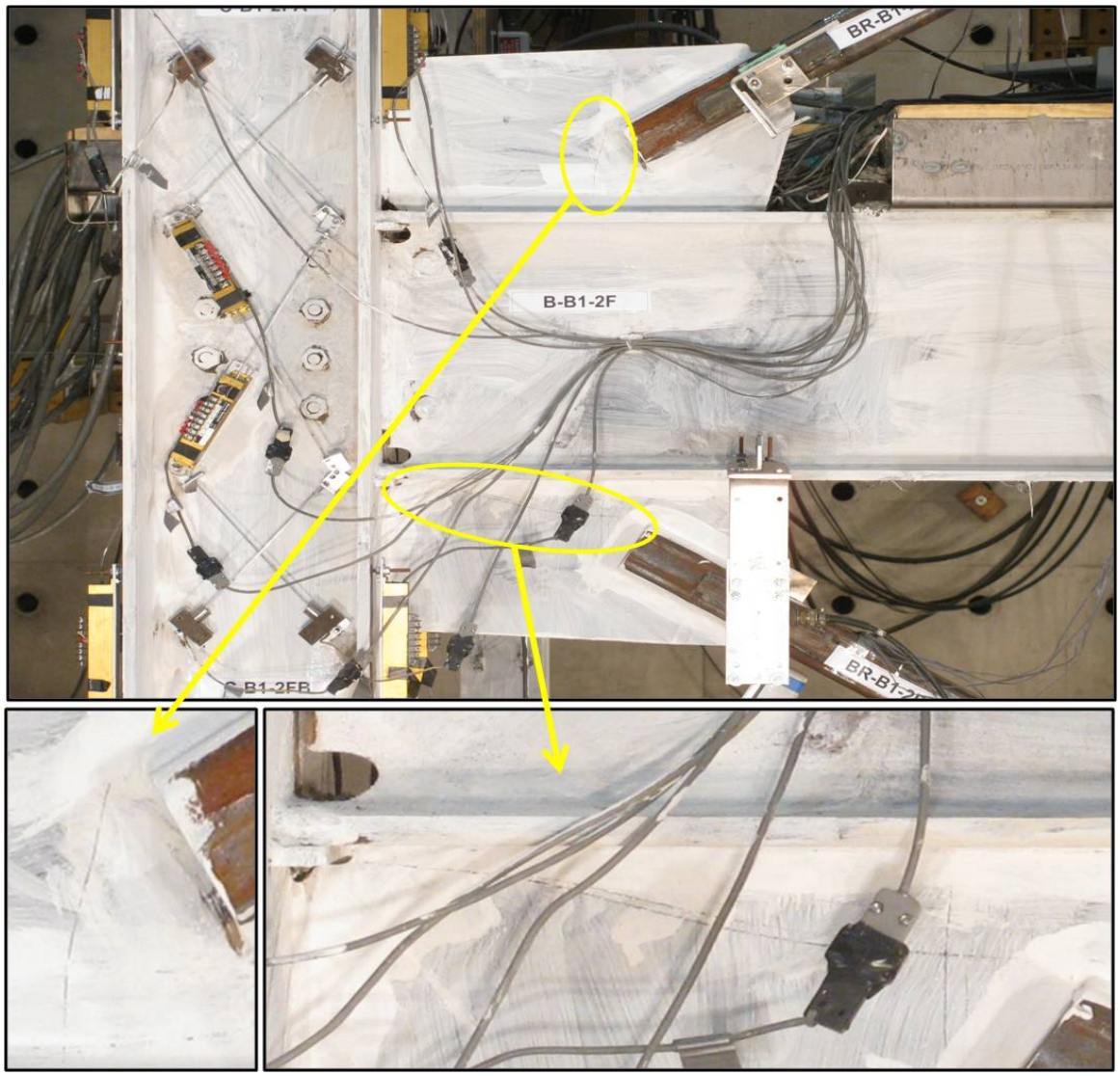

Figure 4.10: Second floor gusset plates at column A-1, yielding level Y1, 0.18% RDRY

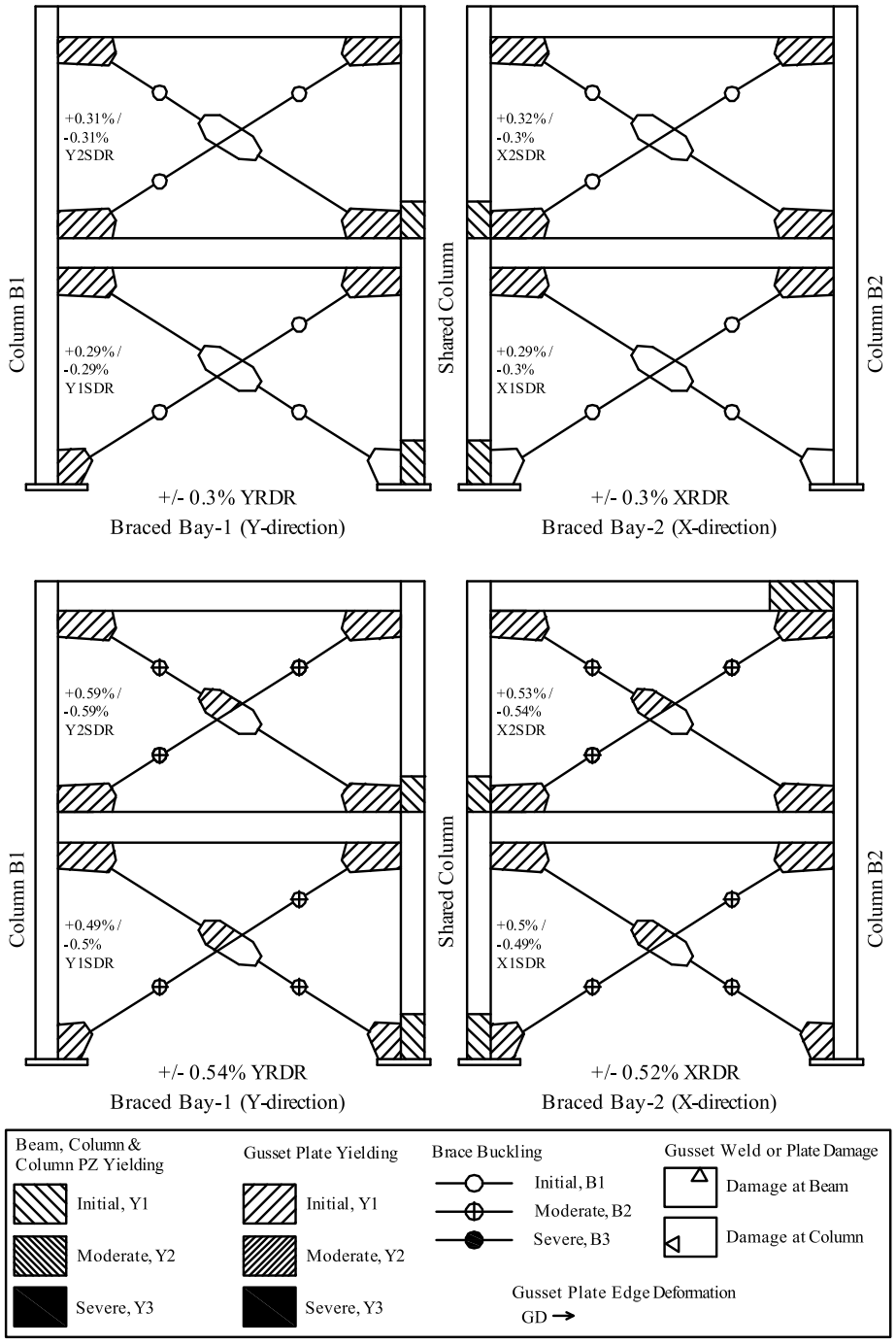

Figure 4.11: Braced frame performance states during and at end of initial drift range

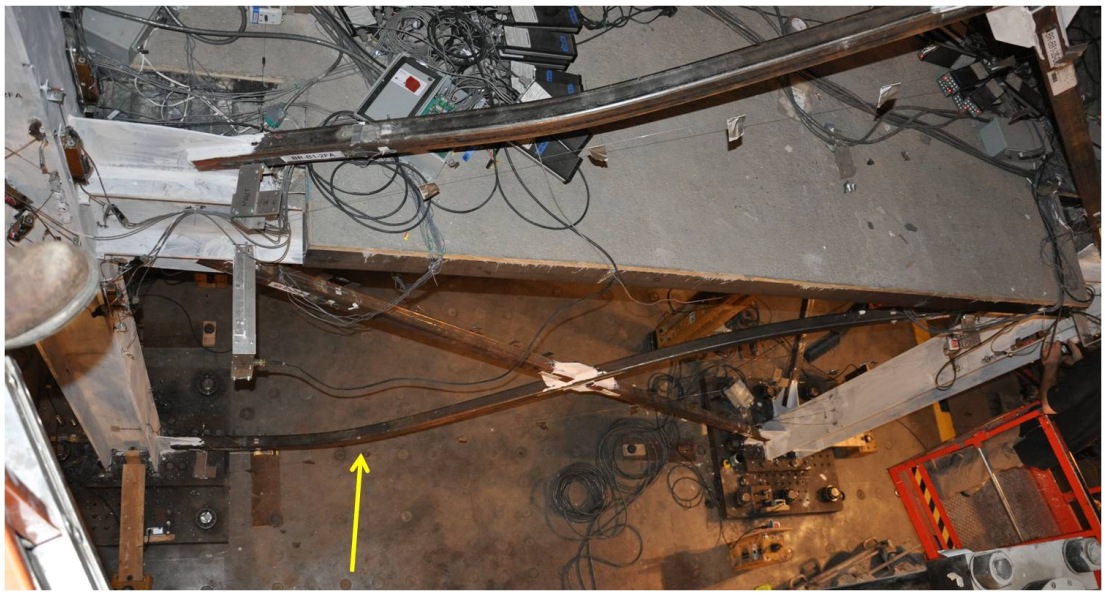

(a) First story continuous brace, -0.84% 1SDRY

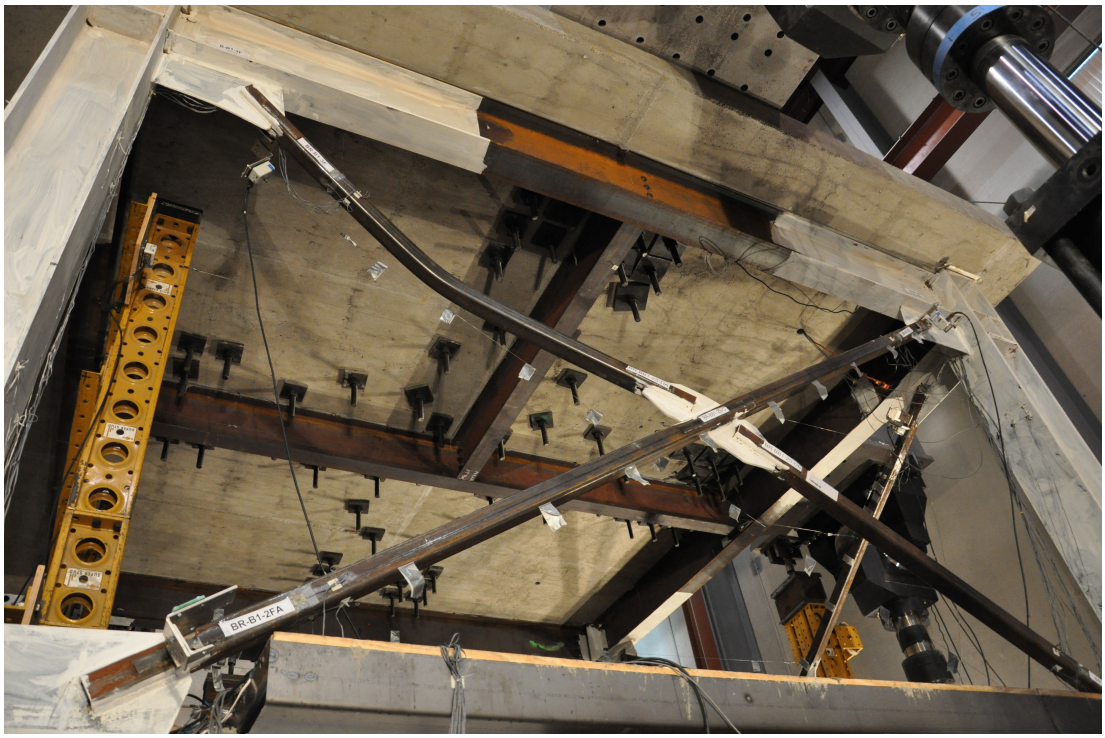

(b) Second story discontinuous brace, 1.42% 2SDRY

Figure 4.12: Frame 1 braces buckling level B3

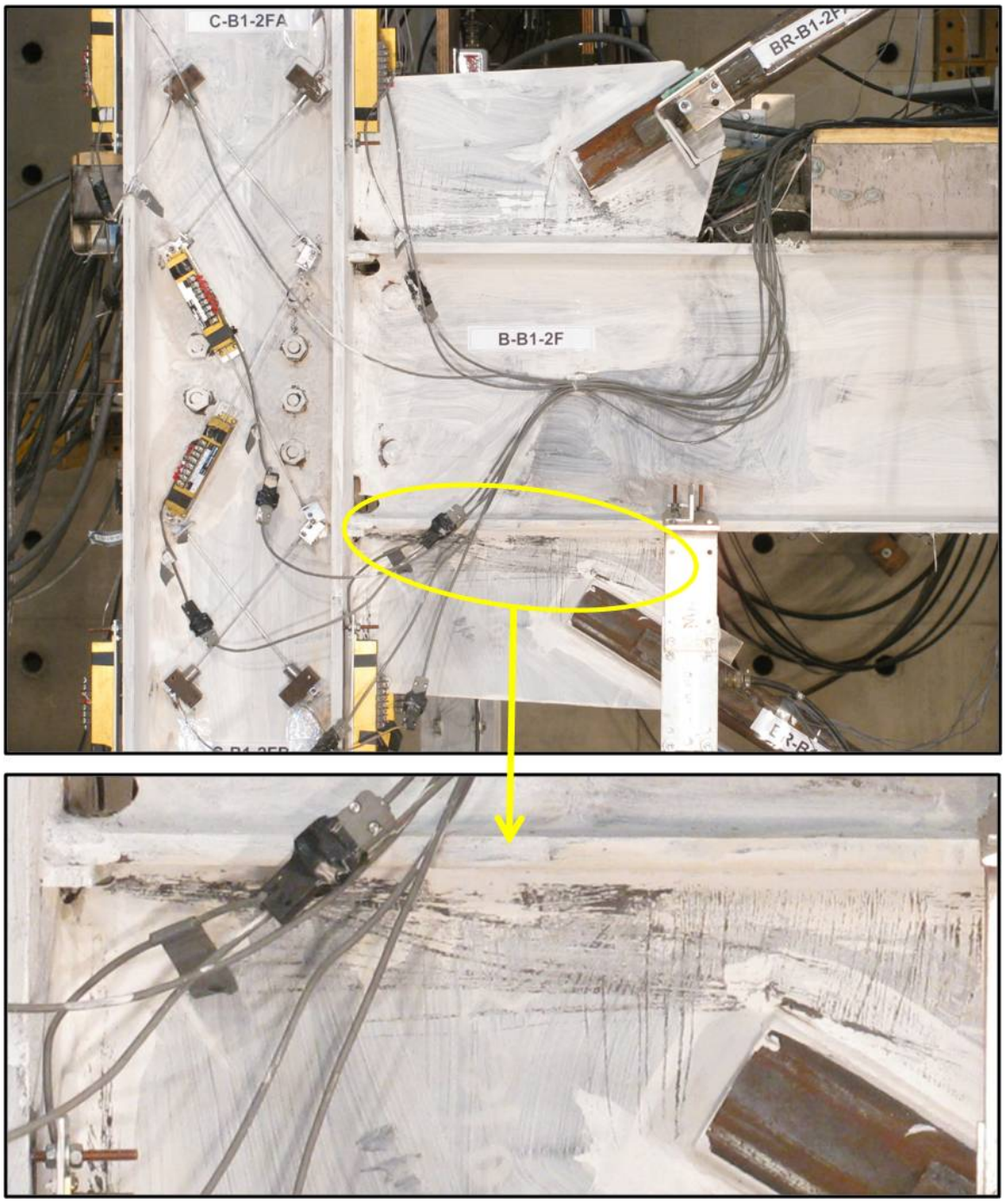

Figure 4.13: Second floor gusset plates at column A-1, yielding level Y2, 1.1% 1SDRY, 1.4% 2SDRY

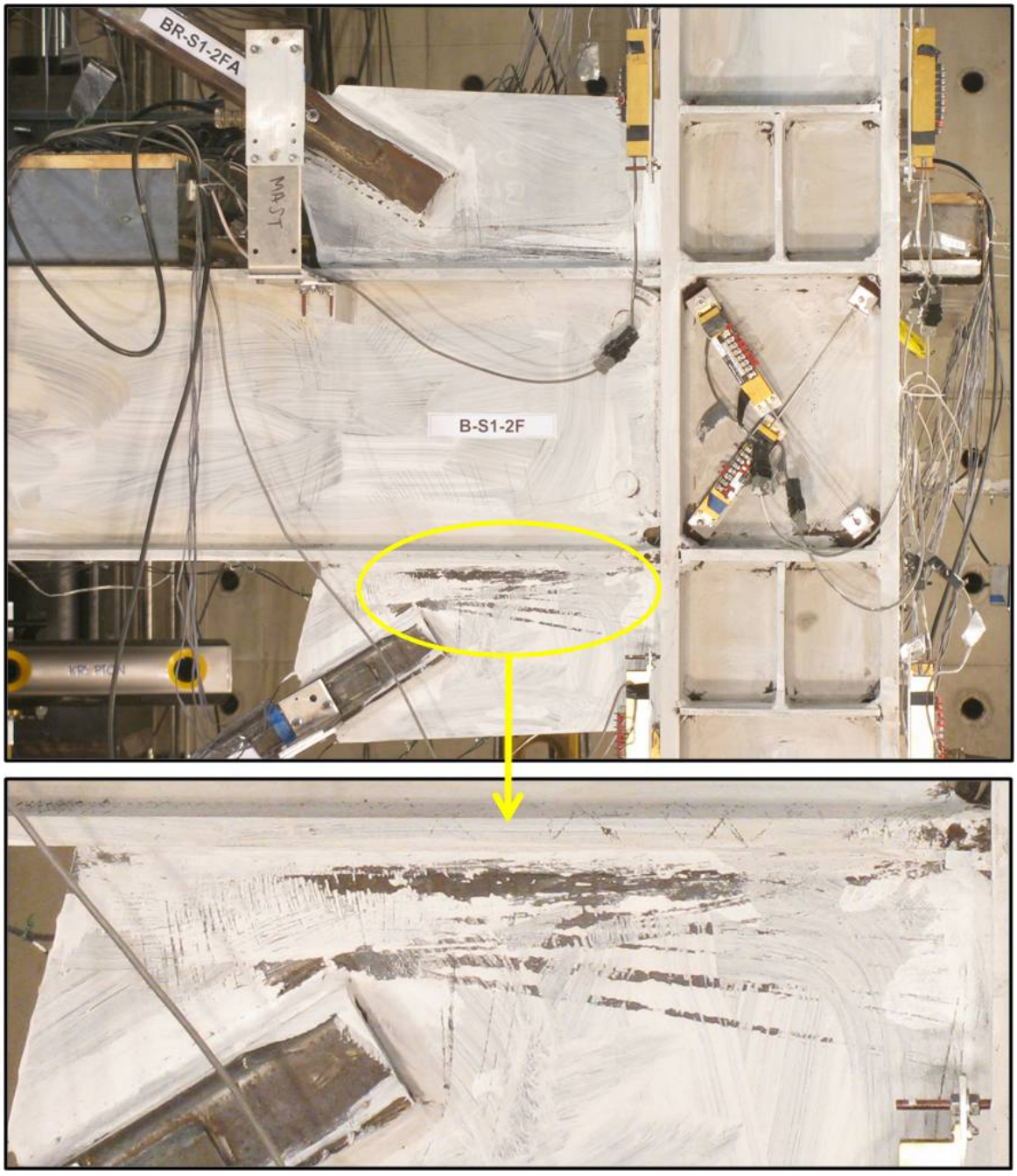

Figure 4.14: Second floor gusset plates at column B-1 in Frame 1, yielding level Y3, 1.27% RDRY

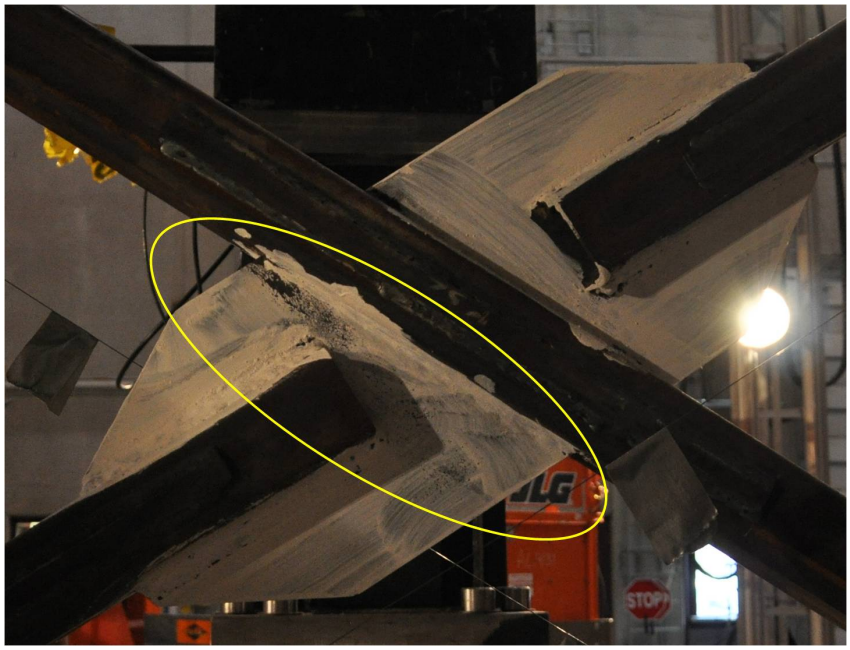

(a) Frame 1, yielding level Y3, 0.94% RDRY

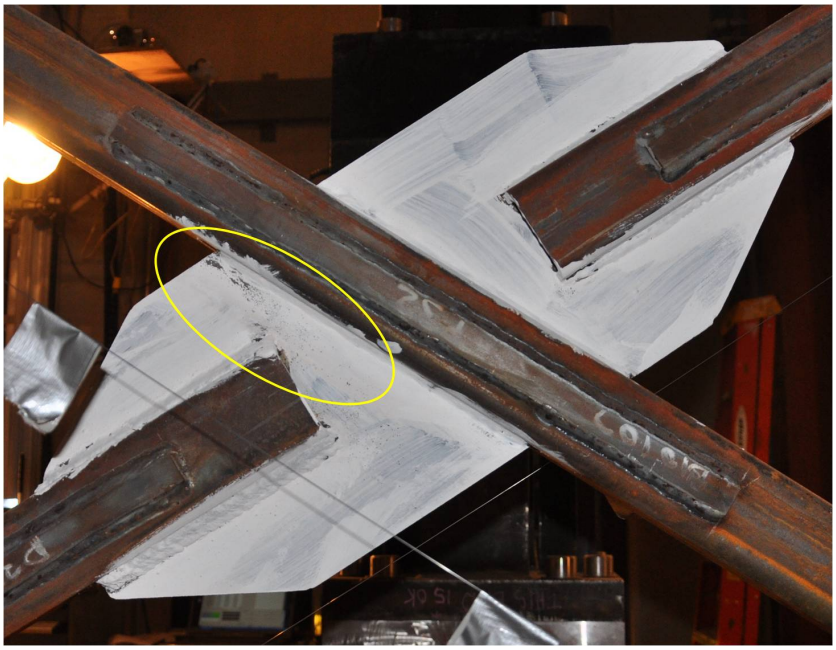

(b) Frame B, yielding level Y1, 0.62% RDRX

Figure 4.15: Gusset plate at 1st story center splice

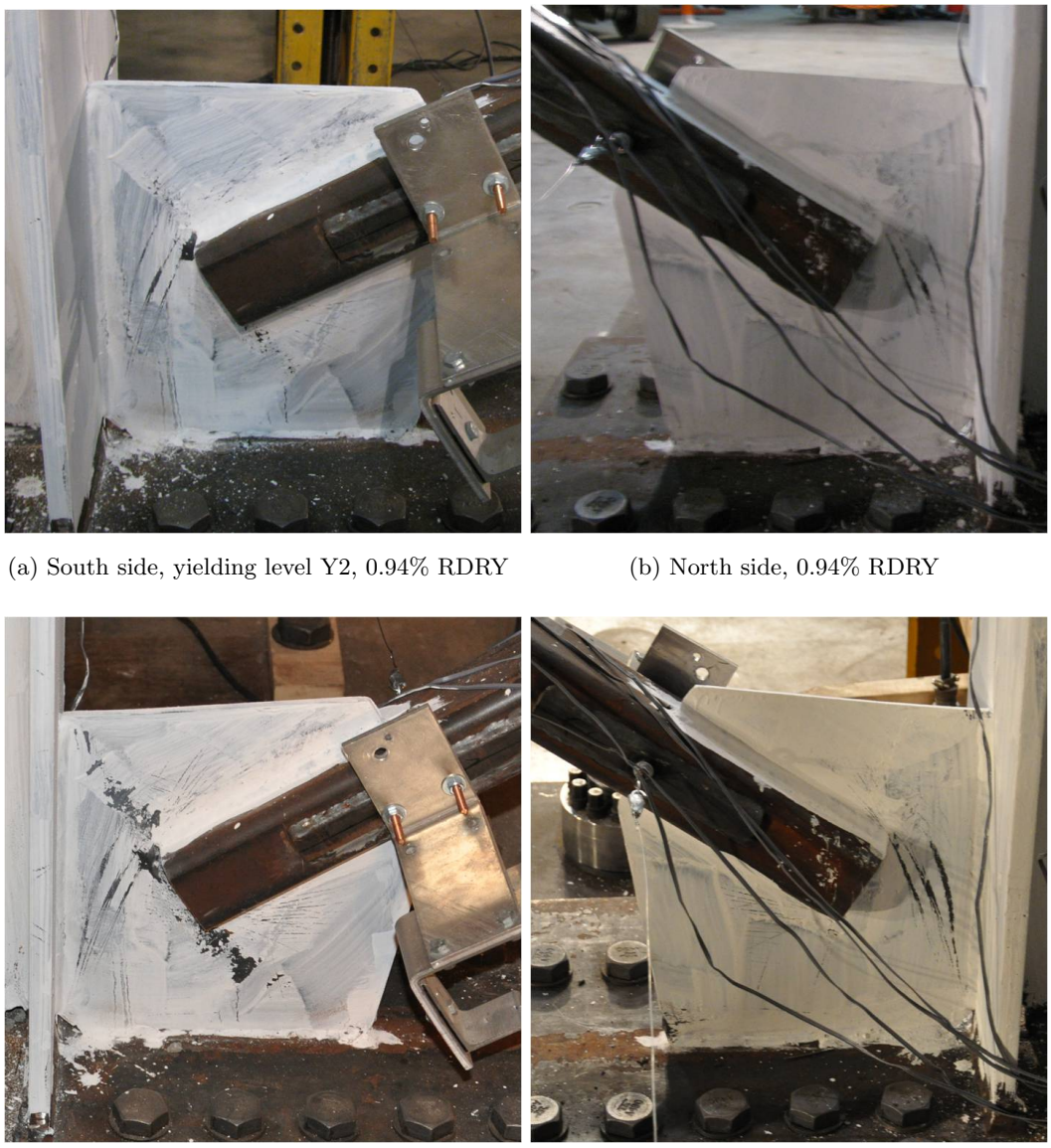

(a) South side, yielding level Y2, 0.94% RDRY

(b) North side, 0.94% RDRY

(c) South side, yielding level Y3, 1.27% RDRY

(d) North side, 1.27% RDRY

Figure 4.16: Gusset plate at base of column A1

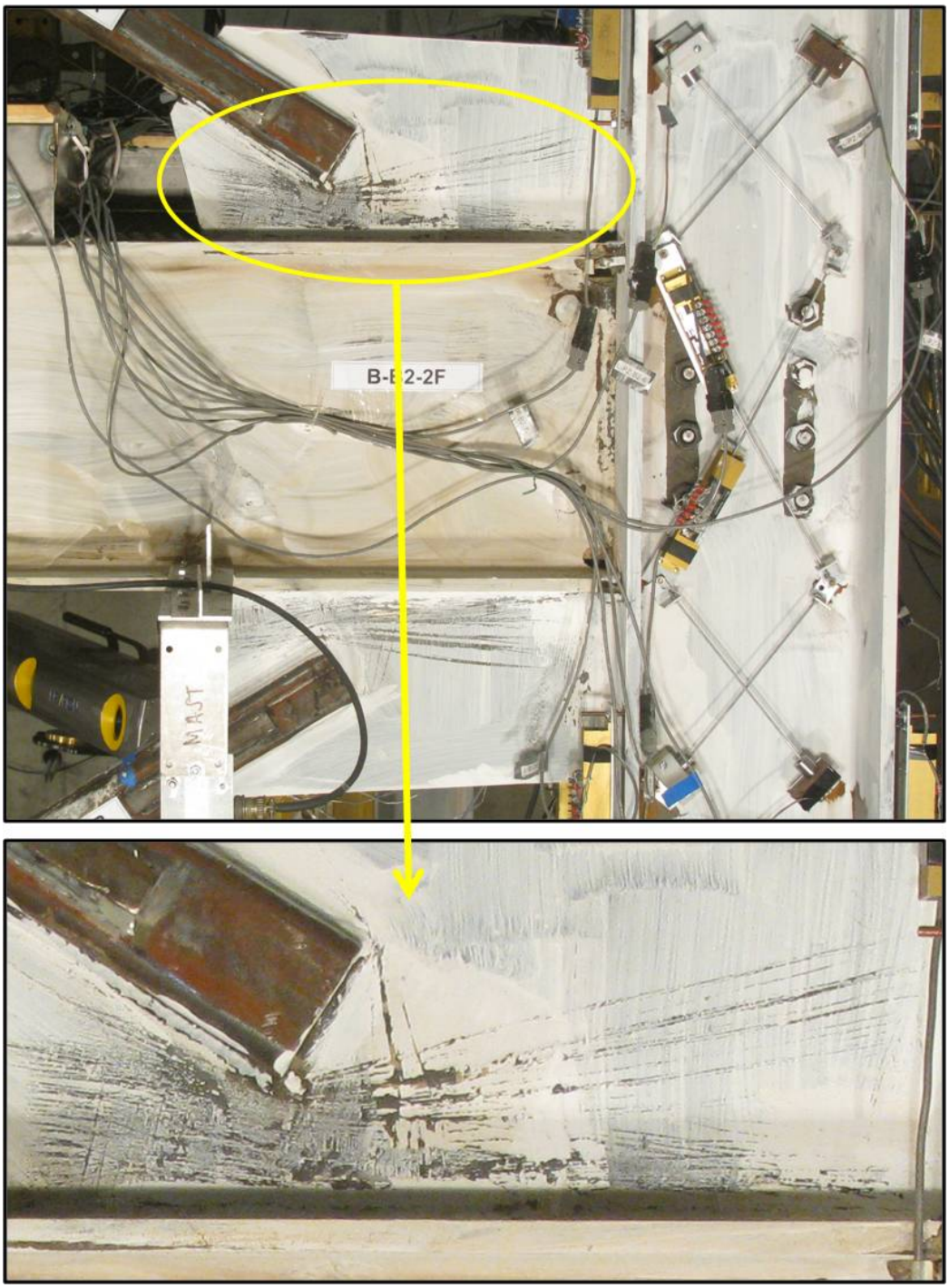

Figure 4.17: Gusset plate at second floor at column B2, yielding level Y3, 1.28% RDRX



(a) Gusset plate below second floor

(b) Gusset plate yielding due to frame action

Figure 4.18: Gusset plate edge deformation at second floor of column A1 due to frame action, -1.1% 1SDRY, -1.4% 2SDRY



(a) Yielding level Y1, 0.78% RDRY, 0.5% RDRX (b) Yielding level Y2, 1.27% RDRY, 0.85% RDRX

Figure 4.19: Column A1 base yielding



(a) Yielding level Y1, 0.99% 1SDRX (1.06% RDRX)(b) Yielding level Y3, 1.18% 1SDRX (1.28% RDRX)

Figure 4.20: Column B2 base yielding



Figure 4.21: Frame B shared column base yielding level Y2, gusset plate yielding level Y1, 0.85% 1SDRY (0.94% RDRY, 0.63% RDRX)



(a) 0.94% RDRY (b) 1.27% RDRY

Figure 4.22: Column A1 3rd floor panel zone, yielding level Y1



(a) Yielding level Y1, 0.86% 2SDRY (0.78% RDRY)

(b) Yielding level Y2, 1.42% 2SDRY (1.27% RDRY)

Figure 4.23: Shared column third floor, flange yielding



(a) Bottom flange at gusset reentrant

(b) Bottom flange at column face

Figure 4.24: Second floor beam at shared column in Frame 1, yielding level Y1, 0.94% RDRY



Figure 4.25: Frame 1 second floor beam at shared column, flange yielding level Y2, 1.3% RDRY



(a) At column A1, 1.13% 1SDRY (1.27% RDRY)

(b) At shared column, 1.13% 1SDRY (1.27% RDRY)

Figure 4.26: Underside of second floor beam in Frame 1

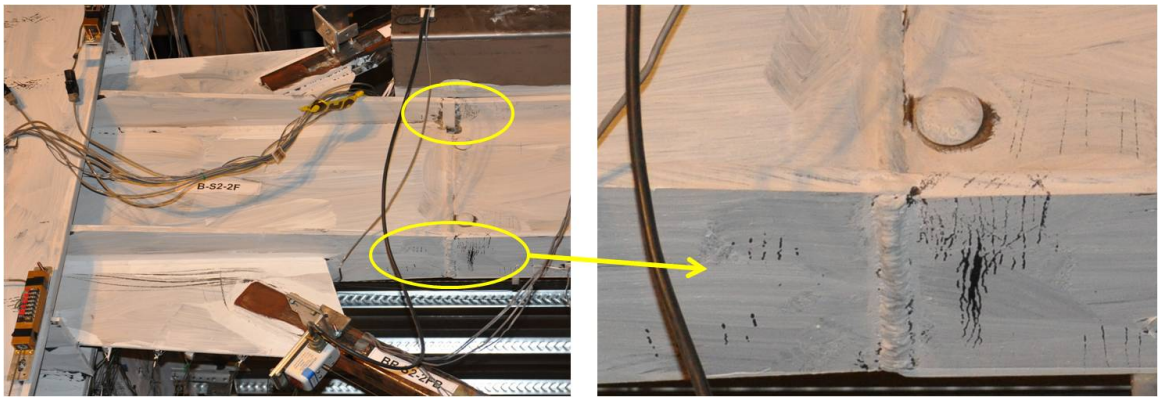

Figure 4.27: Second floor beam at shared column in Frame B, yielding level Y1, 1.06% RDRX

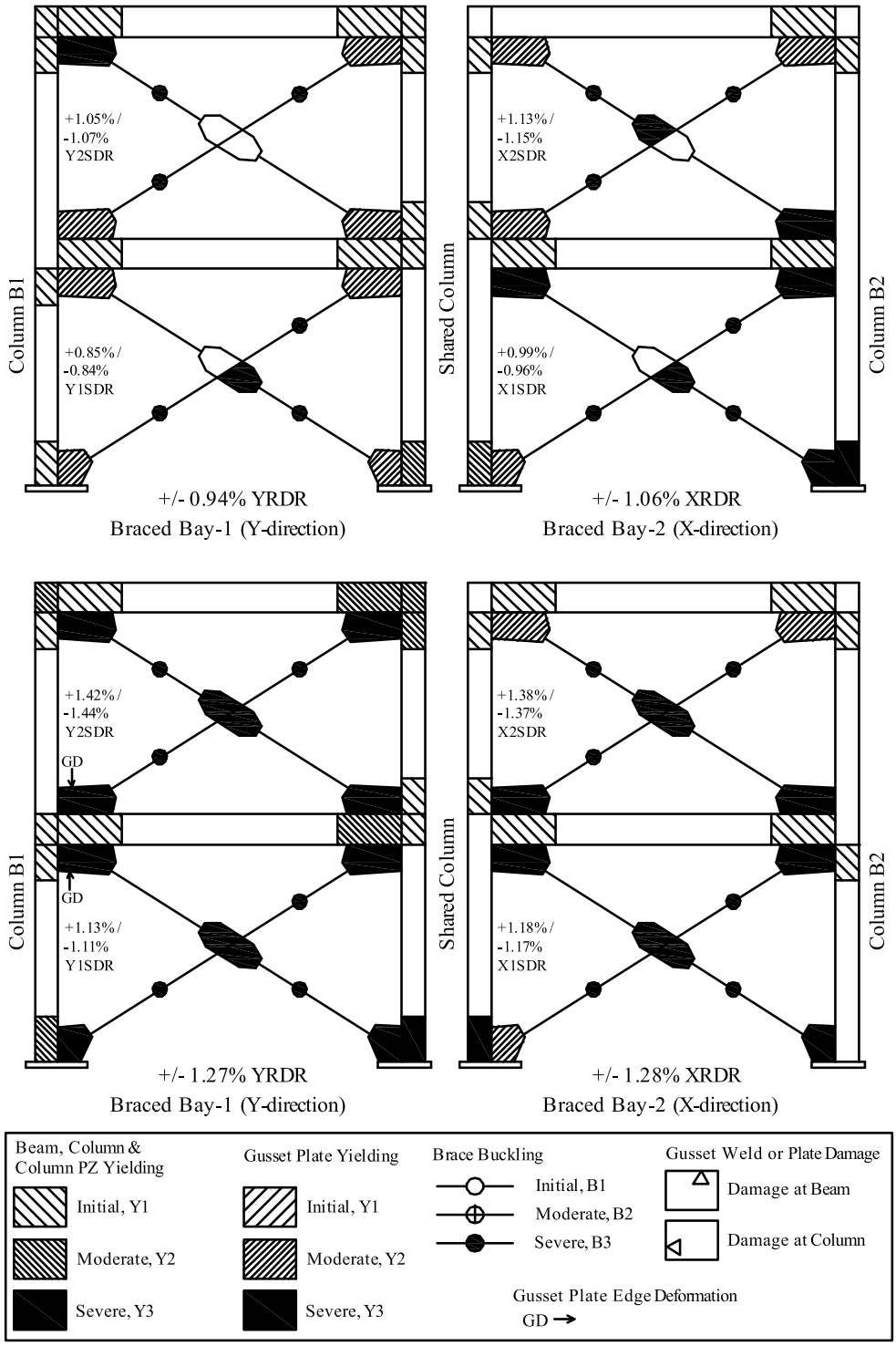

Figure 4.28: Braced frame performance states during and at end of moderate drift range



(a) Discontinuous brace, -1.5% 1SDRX (b) Continuous brace, 1.5% 1SDRX

Figure 4.29: Frame B first story braces buckling level B3



(a) Initial cupping and bulging, 1.59% 2SDRY

(b) Small tears beginning to form, 1.92% 2SDRY



(c) Large cupping and bulging, 1.78% 2SDRY

(d) Brace fracture, 2% 2SDRY

Figure 4.30: Frame 1 second story discontinuous brace plastic hinge damage progression

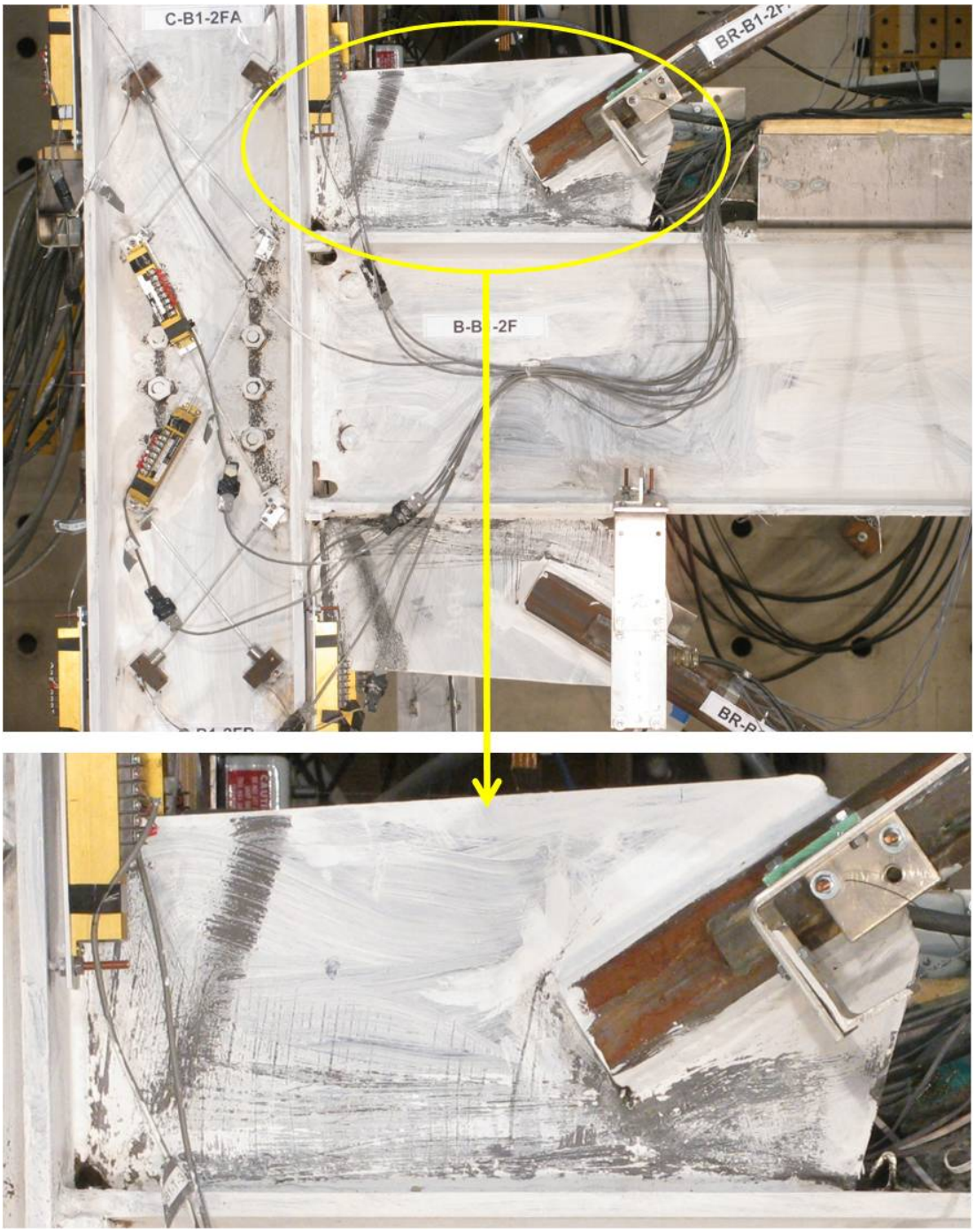

Figure 4.31: Second floor gusset plates at column A-1, yielding level Y3, 2.3% 2SDRY

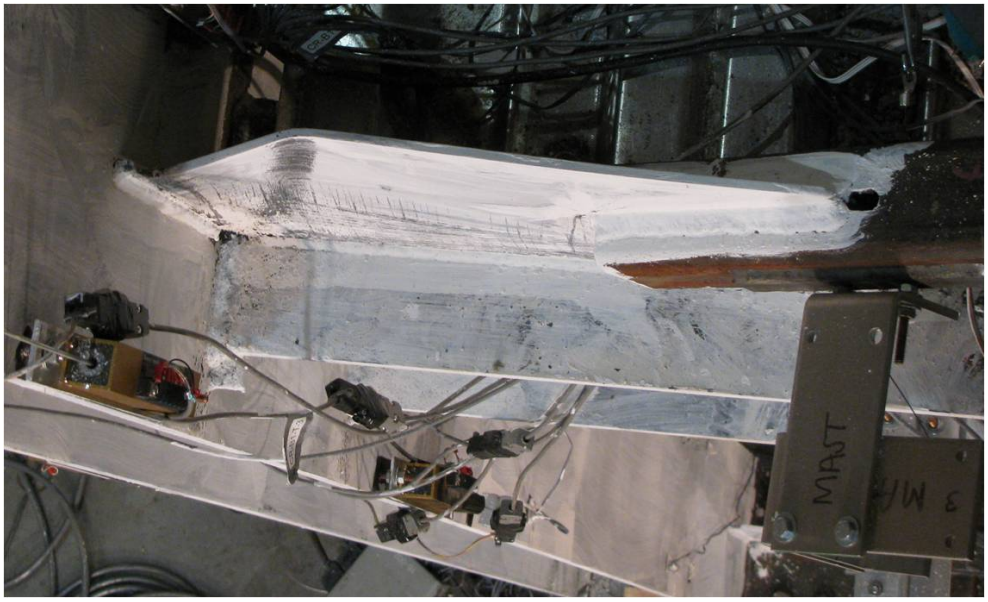

(a) Gusset plate above the beam, 1.6% RDRY

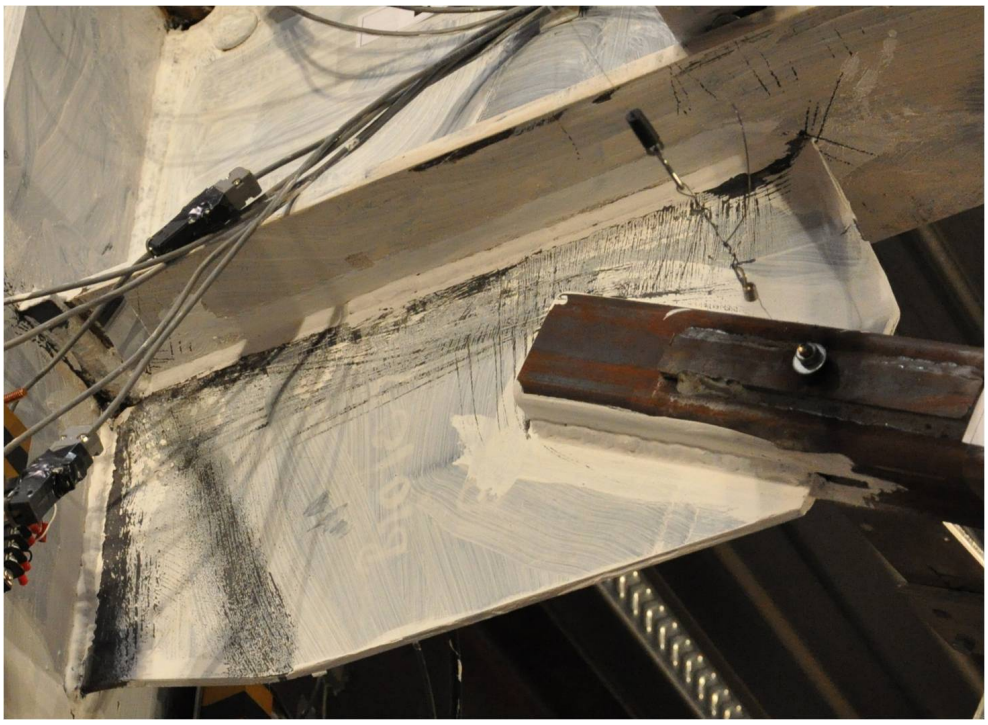

(b) Gusset plate below the beam, -1.9% RDRY

Figure 4.32: Gusset edge deformation at second floor column A1

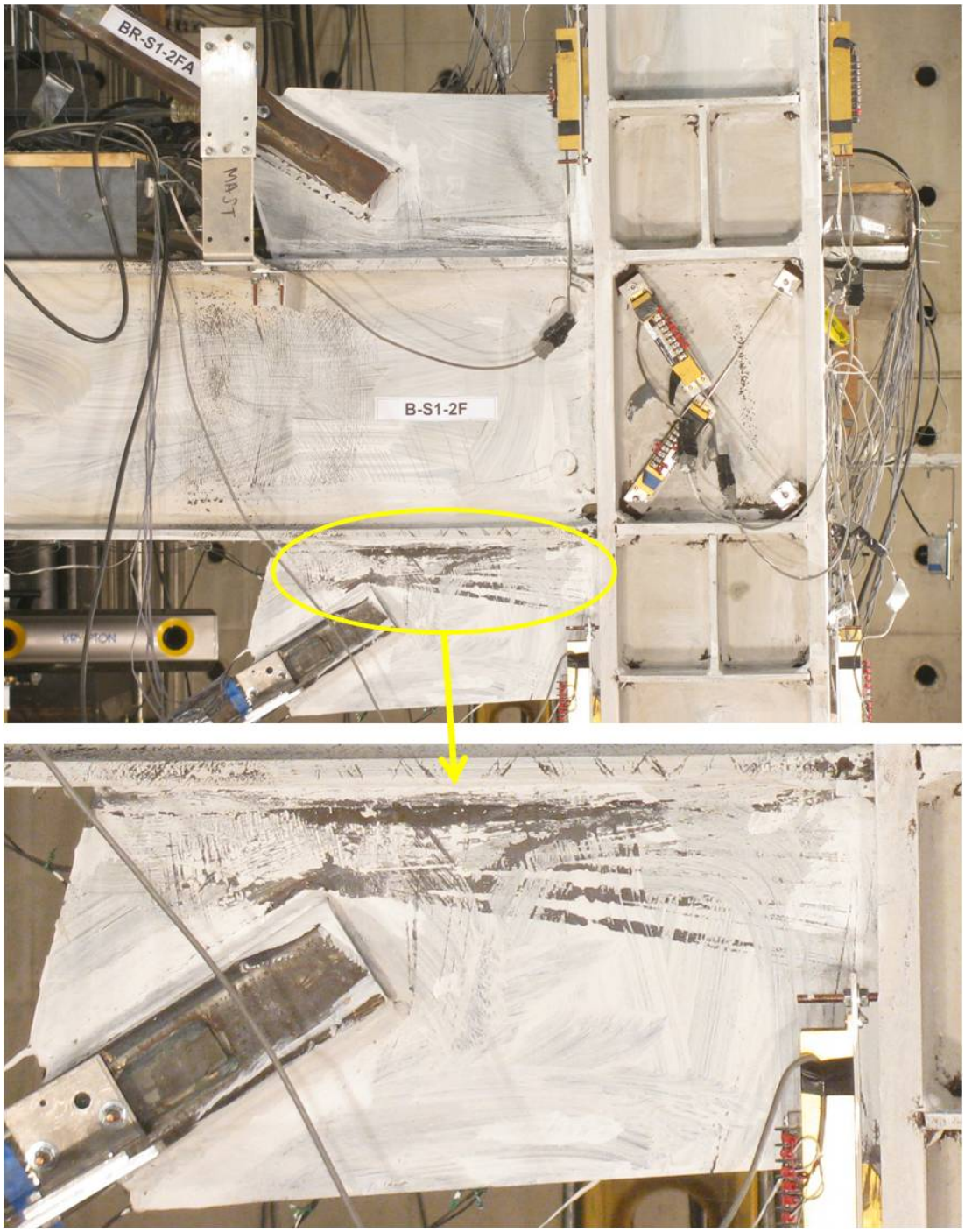

Figure 4.33: Second floor joint at shared column in Frame 1, gusset plate yielding level Y3, column panel zone yielding level Y1, and yielding level Y3 in beam web, 1.9% RDRY

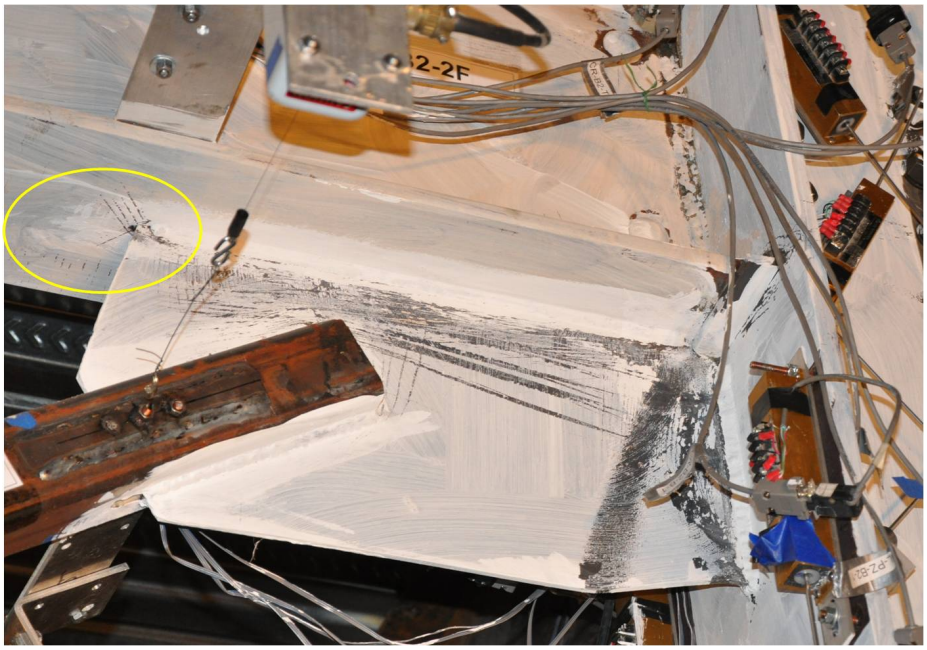

(a) Second floor gusset plate at column B2



(b) Third floor gusset plate at column B2

Figure 4.34: Gusset plate yielding level Y3 and edge deformation, 1.7% RDRX

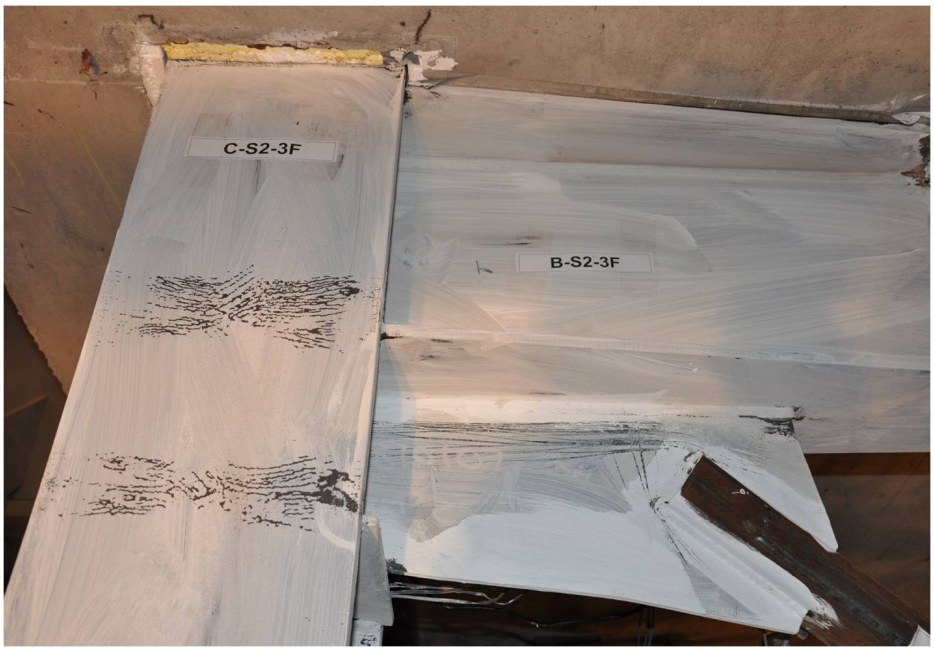

Figure 4.35: Third floor joint at shared column in Frame B, gusset plate yielding level Y2, column yielding level Y3, 1.9% RDRY, 1.7% RDRX



(a) South side (b) North side

Figure 4.36: Gusset plate at base of column A-1, yielding level Y3, 1.9% RDRY



Figure 4.37: Gusset plate at base of column B-1, yielding level Y3, 1.6% RDRY



(a) Yielding level Y3, 1.3% RDRX (b) Yielding level Y3, 1.7% RDRX

Figure 4.38: Gusset plate at base of shared column framing into column web in Frame B



(a) East side (b) West side

Figure 4.39: Gusset plate at base of column B-2, yielding level Y3, 1.7% RDRX

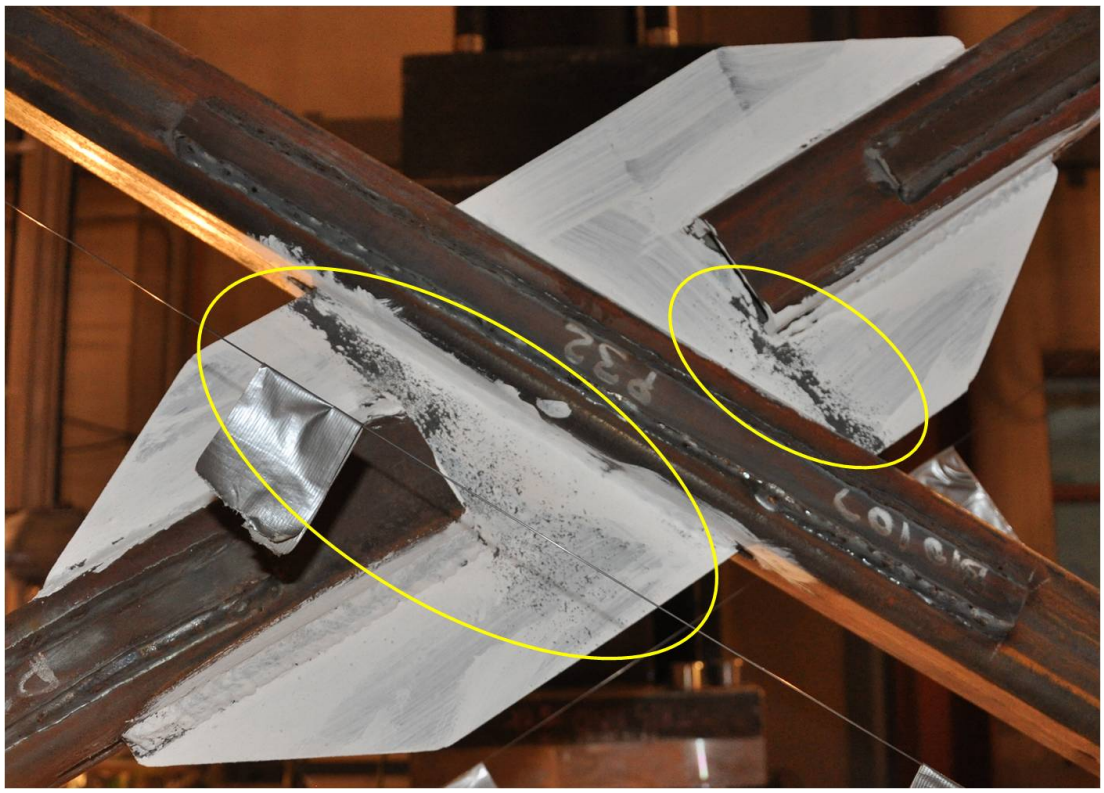

Figure 4.40: Frame B gusset plate at 1st story center splice, yielding level Y3, 1.7% RDRX

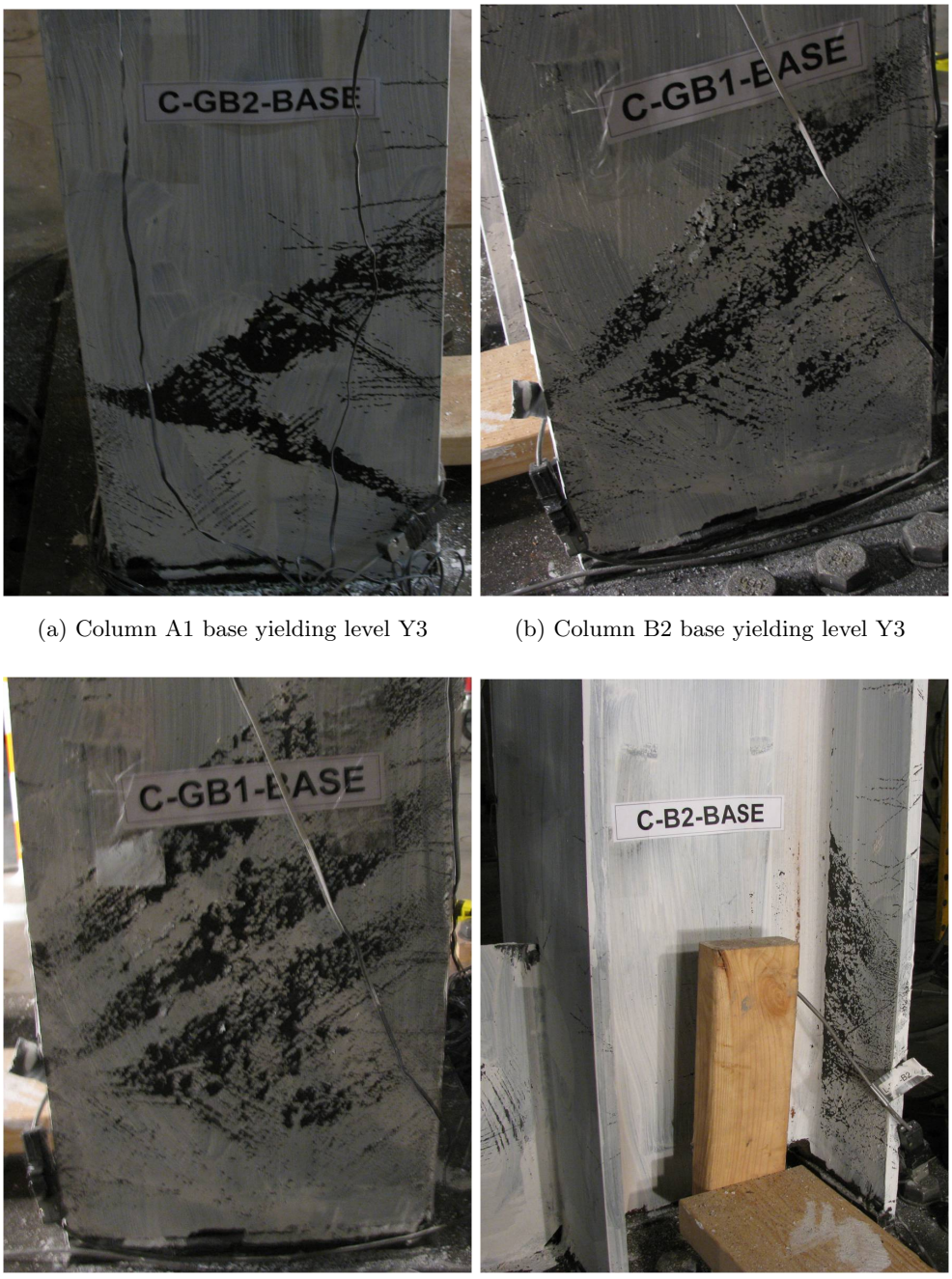

(a) Column A1 base yielding level Y3

(b) Column B2 base yielding level Y3

(c) Column B2 base yielding level Y3

(d) Column B2 base yielding level Y3

Figure 4.41: Yielding level Y3 at base of columns A1 and B2: (a) 1.4% 1SDRY (1.59% RDRY); (b) 1.4% 1SDRX (1.5% RDRX); (c) 1.57% 1SDRX (1.71% RDRX) ; (d) 1.57% 1SDRX (1.71% RDRX).



(a) Shared column base, flange yielding level Y3, 1.7% 1SDRY

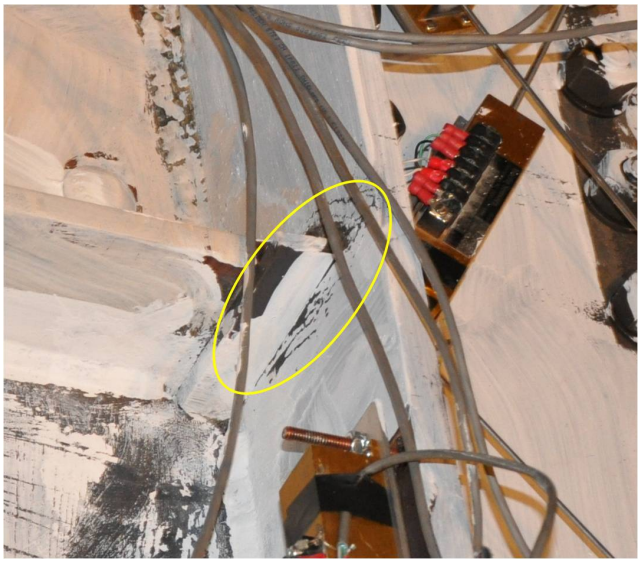

(b) Column B2 second floor, flange yielding level Y2, % RDRX

Figure 4.42: Column yielding

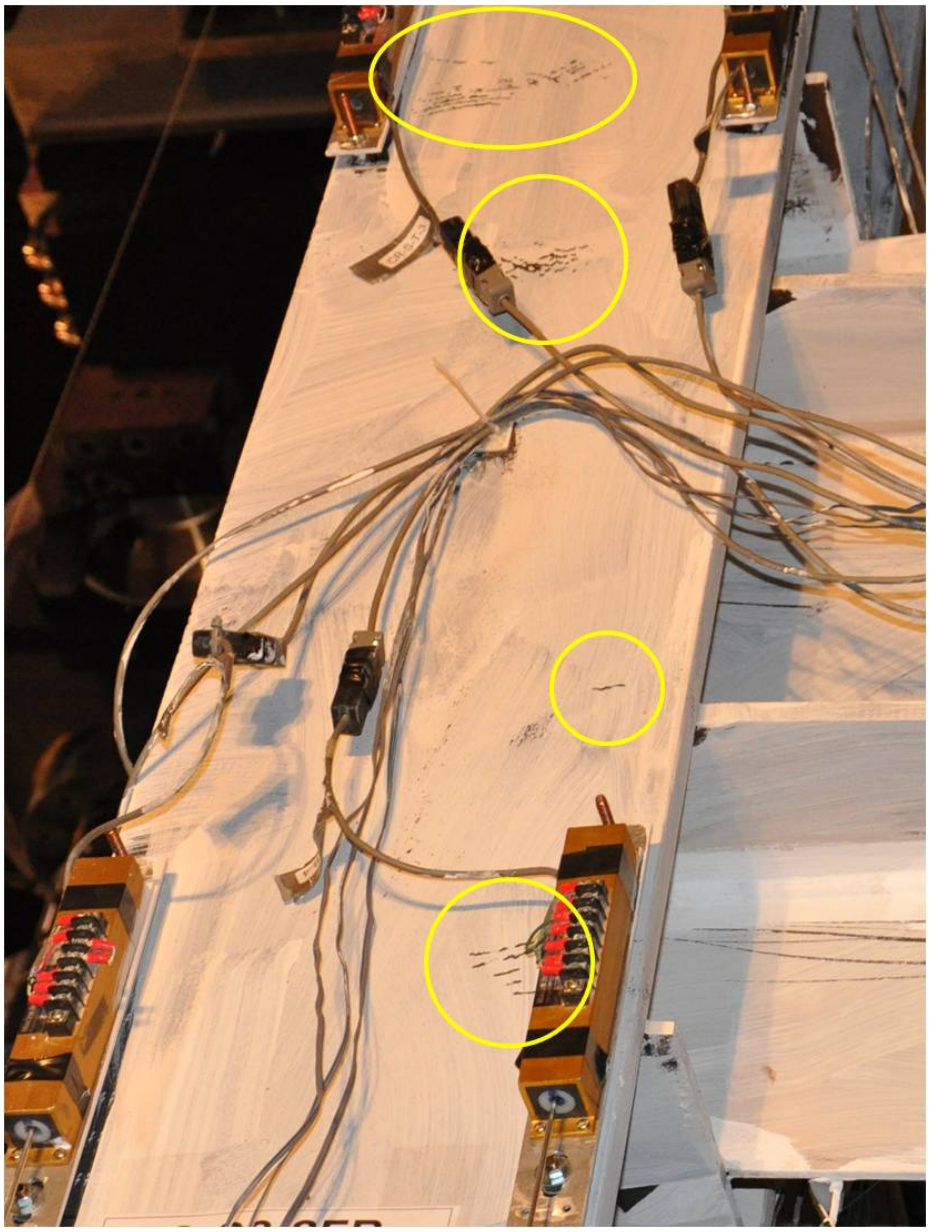

Figure 4.43: Shared column at second floor, yielding level Y1, 1.59% RDRY

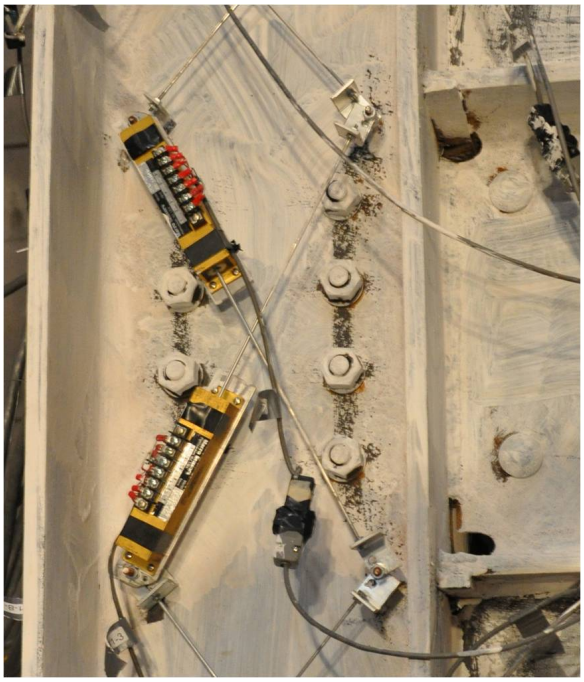

(a) Column A1 2nd floor panel zone yielding at bolt holes, 1.9% RDRY



(b) Column A1 panel zone yielding, level Y3



(c) Shared column panel zone yielding, level Y3

Figure 4.44: Column A1 and Shared column 3rd floor panel zone, 2.1% 2SDRY

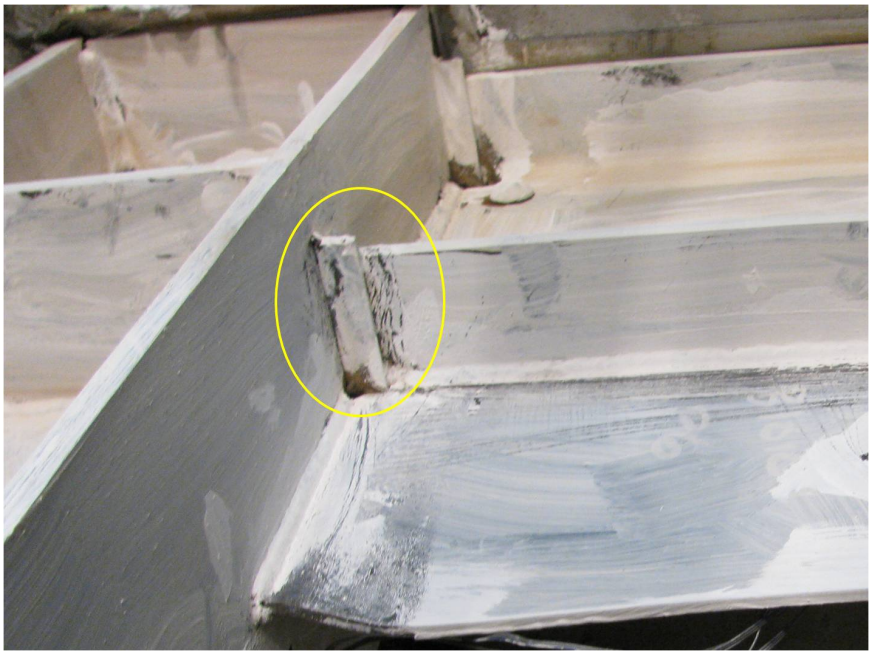

(a) Beam at column A1

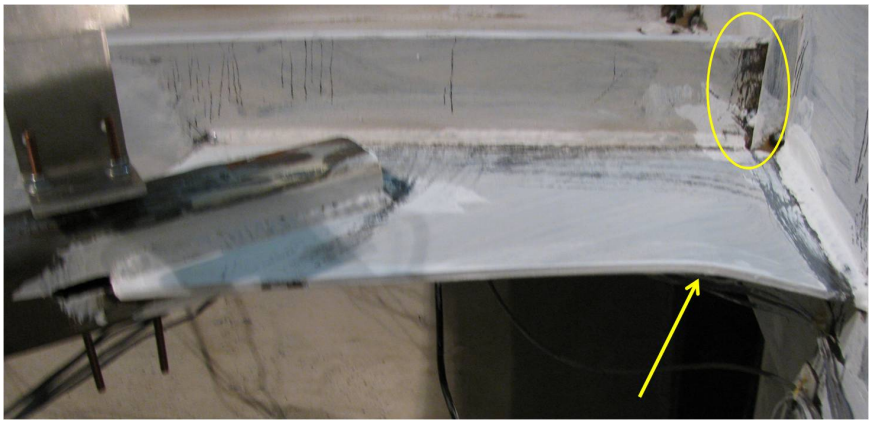

(b) Beam at shared column

Figure 4.45: Third floor beam bottom flange yielding at Column A1 and Shared column in Frame 1, 1.59% RDRY

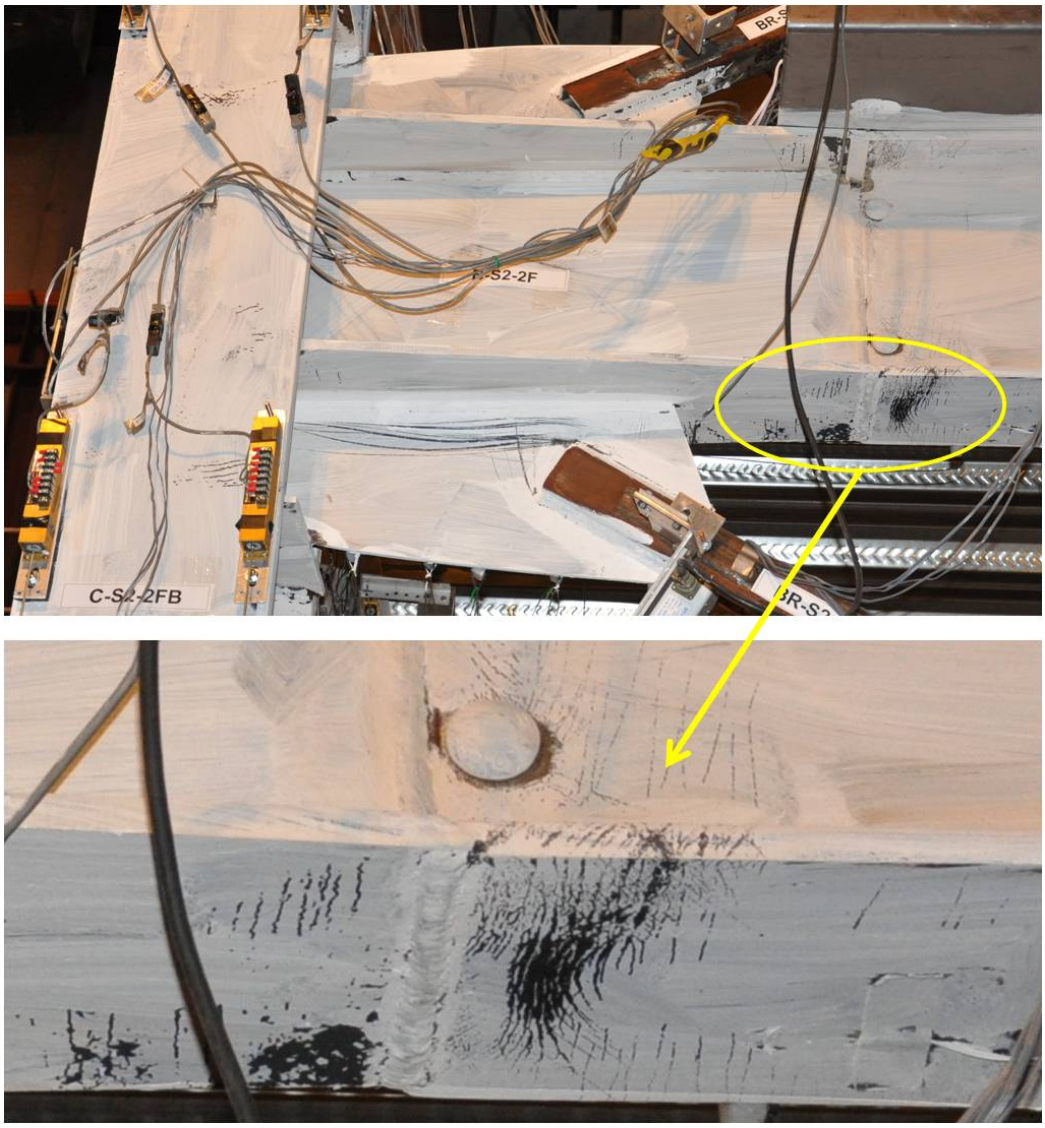

Figure 4.46: Second floor beam yielding at splice at shared column in Frame B, % RDRX

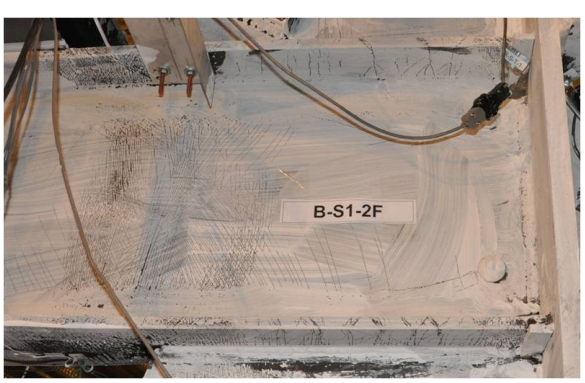

(a) South side

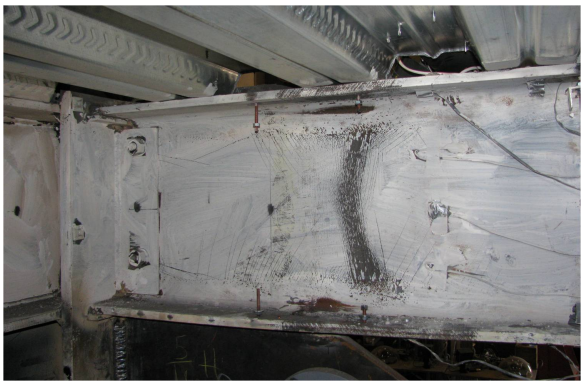

(b) North side

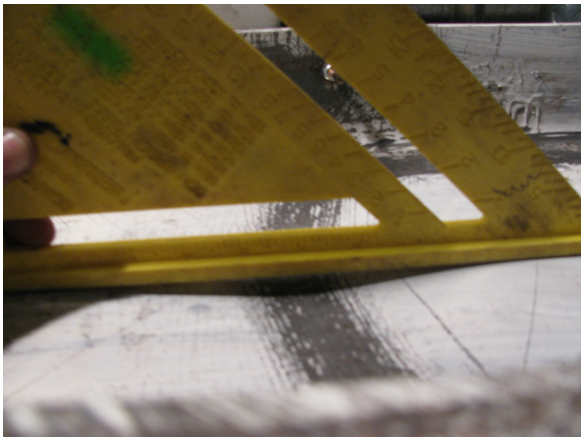

(c) Deformed web

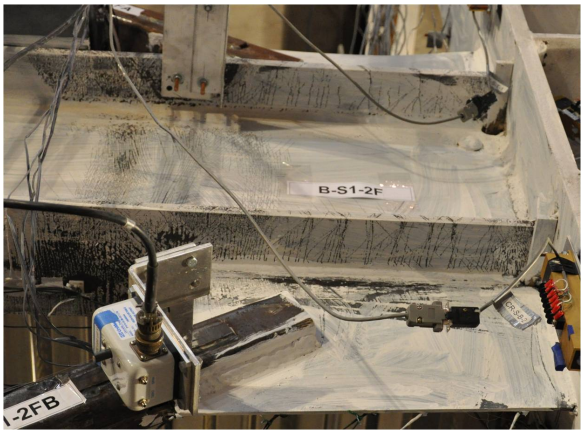

(d) Bottom flange

Figure 4.47: Second floor beam at shared column in Frame 1, yielding level Y3 and deformed web, 1.9% RDRY

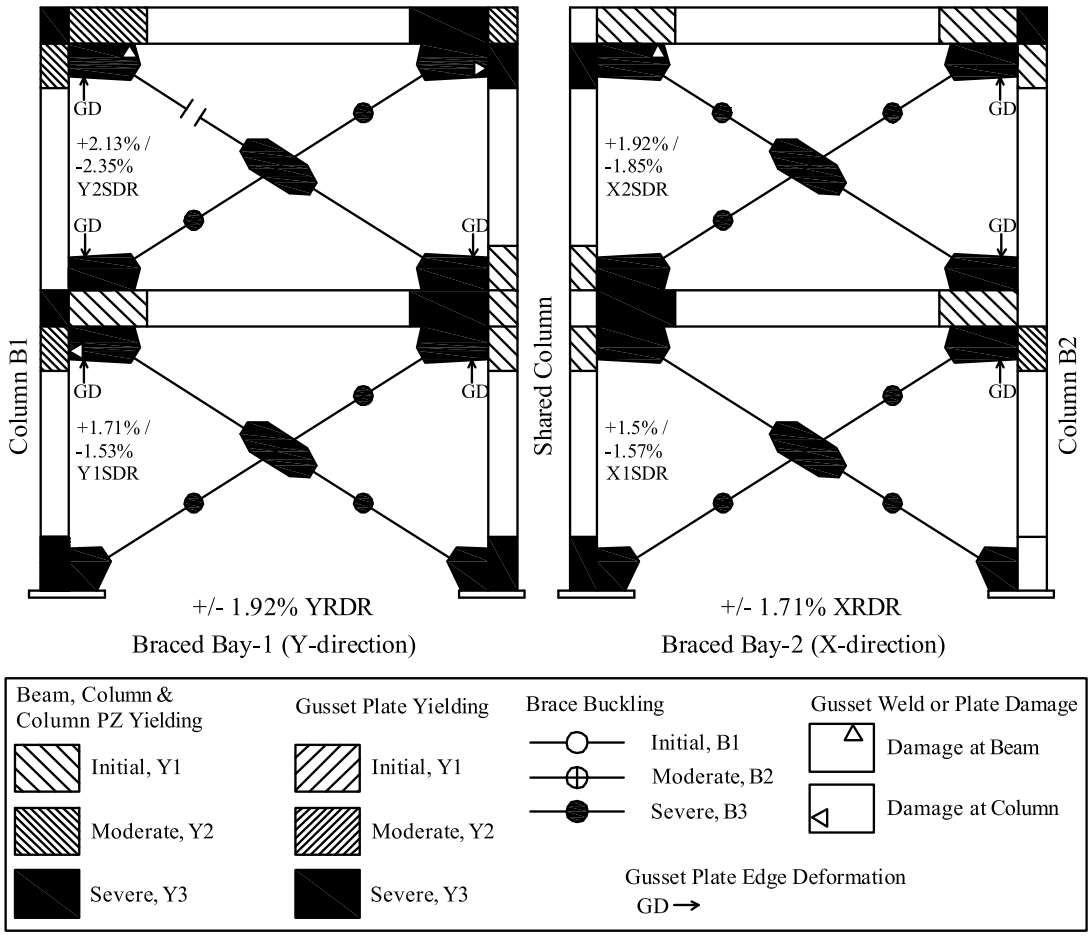

Figure 4.48: Braced frame performance states at end of severe drift range

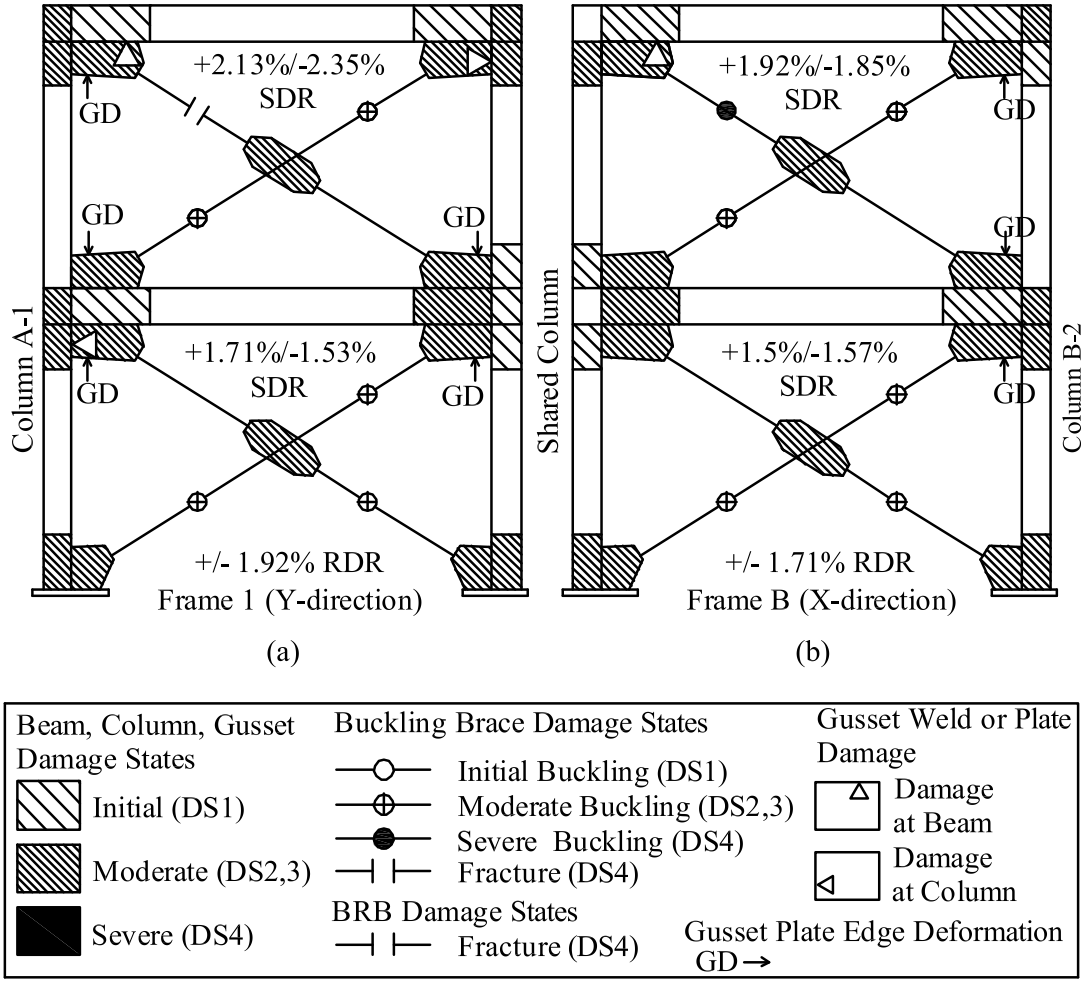

Figure 4.49: Pictorial of damage states at end of SCBF test per ATC-58 DS definitions [Roeder et al., 2009]

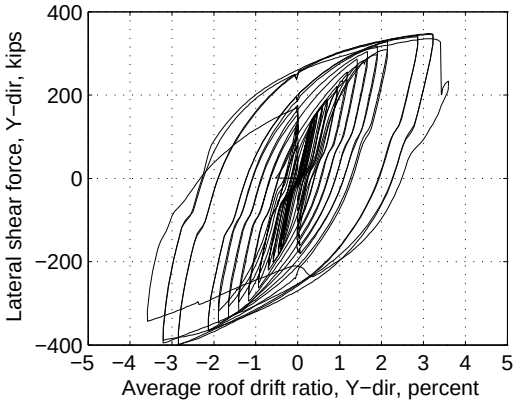

(a) Shear vs. ave. RDR, Y-dir

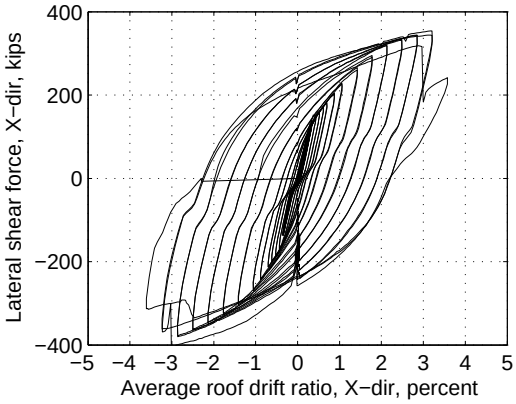

(b) Shear vs. ave. RDR, X-dir

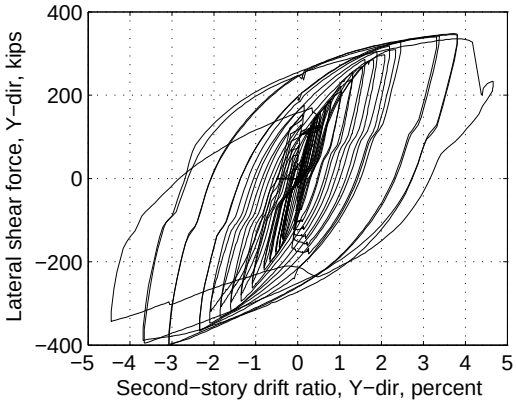

(c) Shear vs. 2SDR, Y-dir

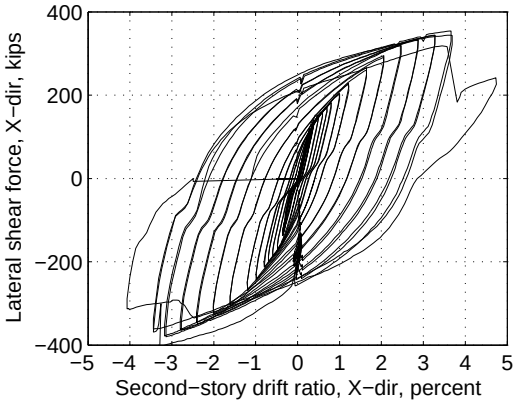

(d) Shear vs. 2SDR, X-dir

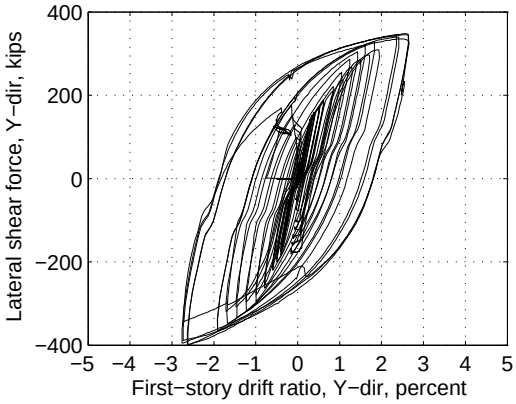

(e) Shear vs. 1SDR, Y-dir

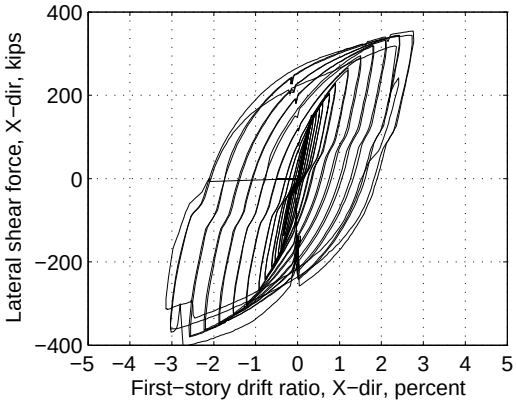

(f) Shear vs. 1SDR, X-dir

Figure 4.50: Frame shear-drift hysteresis (BRBF test)

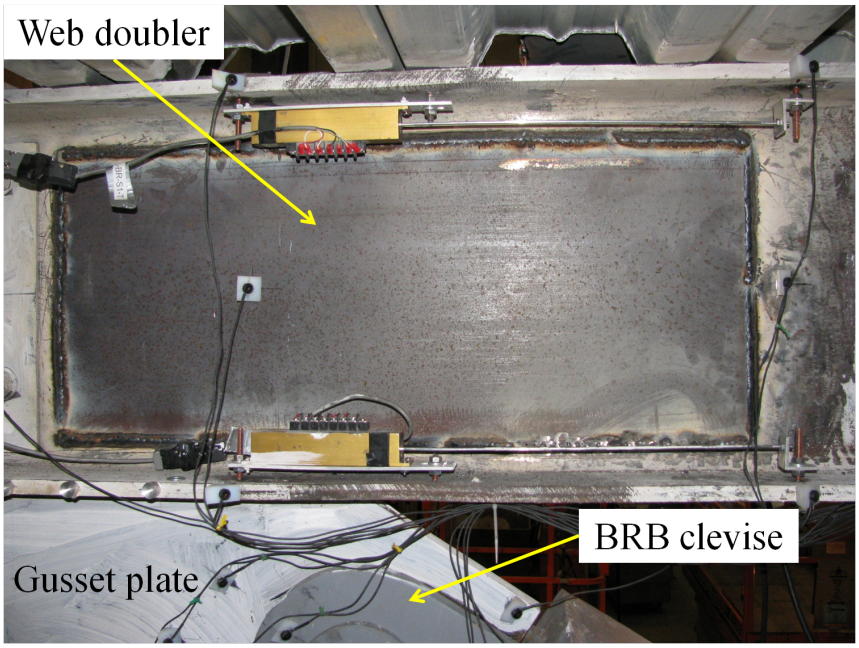

Figure 4.51: Second floor, Frame 1 beam web repair at shared column side prior to BRBF test



(a) (b) -2.7% 1SDRY, -4.5% 1SDRX

Figure 4.52: Gusset plate weld tear above second floor beam at column A-1 in Frame 1 (BRBF test)



(a)

(b) 1.5% 1SDRX, 2.1% 2SDRX

(c) 2.4% 1SDRX, 3.3% 2SDRX

(d) 2.4% 1SDRX, 3.3% 2SDRX

Figure 4.53: Gusset plate weld tear above second floor beam at column B-2 in Frame B (BRBF test)

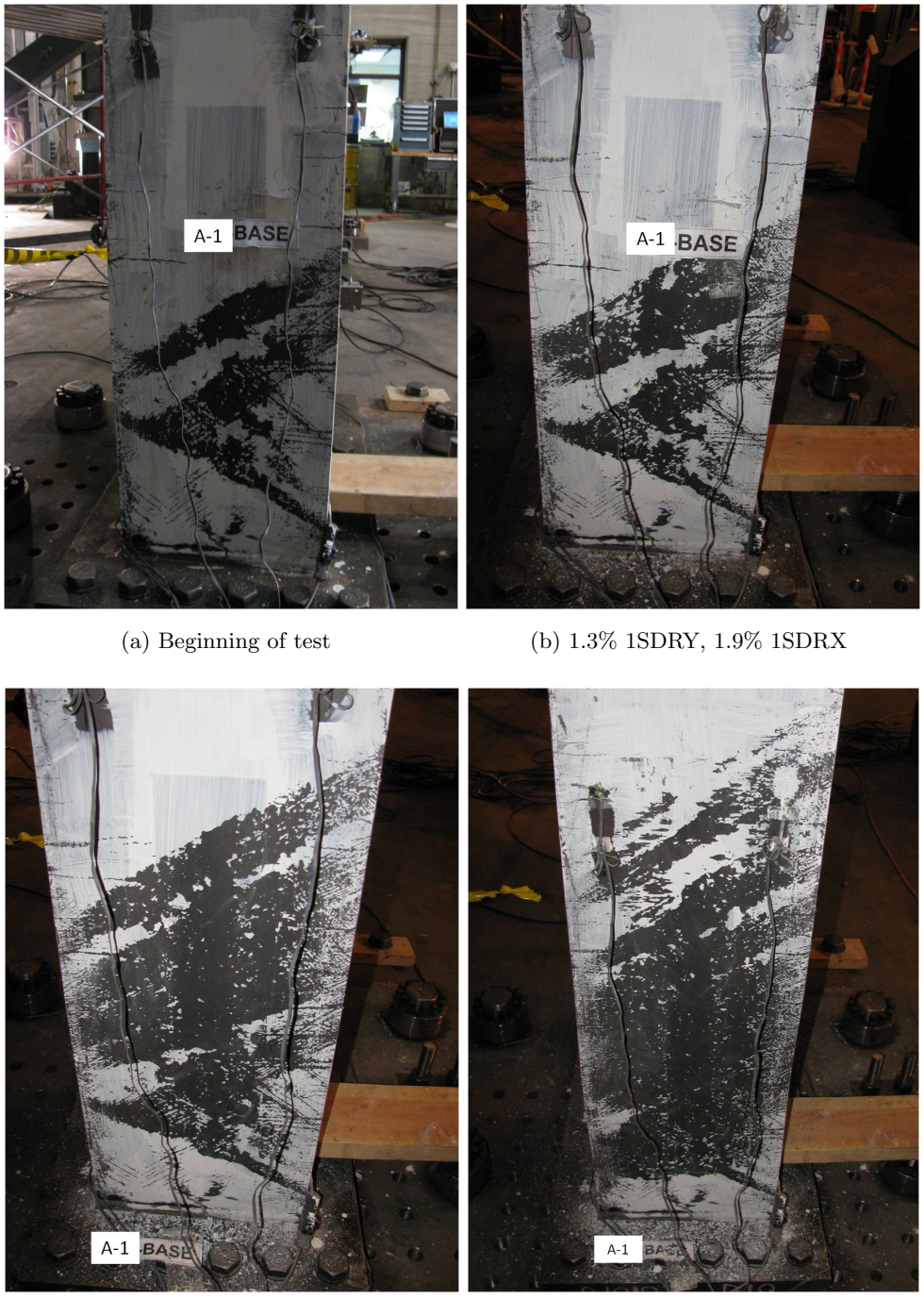

(a) Beginning of test

(b) 1.3% 1SDRY, 1.9% 1SDRX

(c) 1.7% 1SDRY, 2.5% 1SDRX

(d) 2.7% 1SDRY, 2.8% 1SDRX

Figure 4.54: Progression of flange yielding at base of Column A-1 (BRBF test)

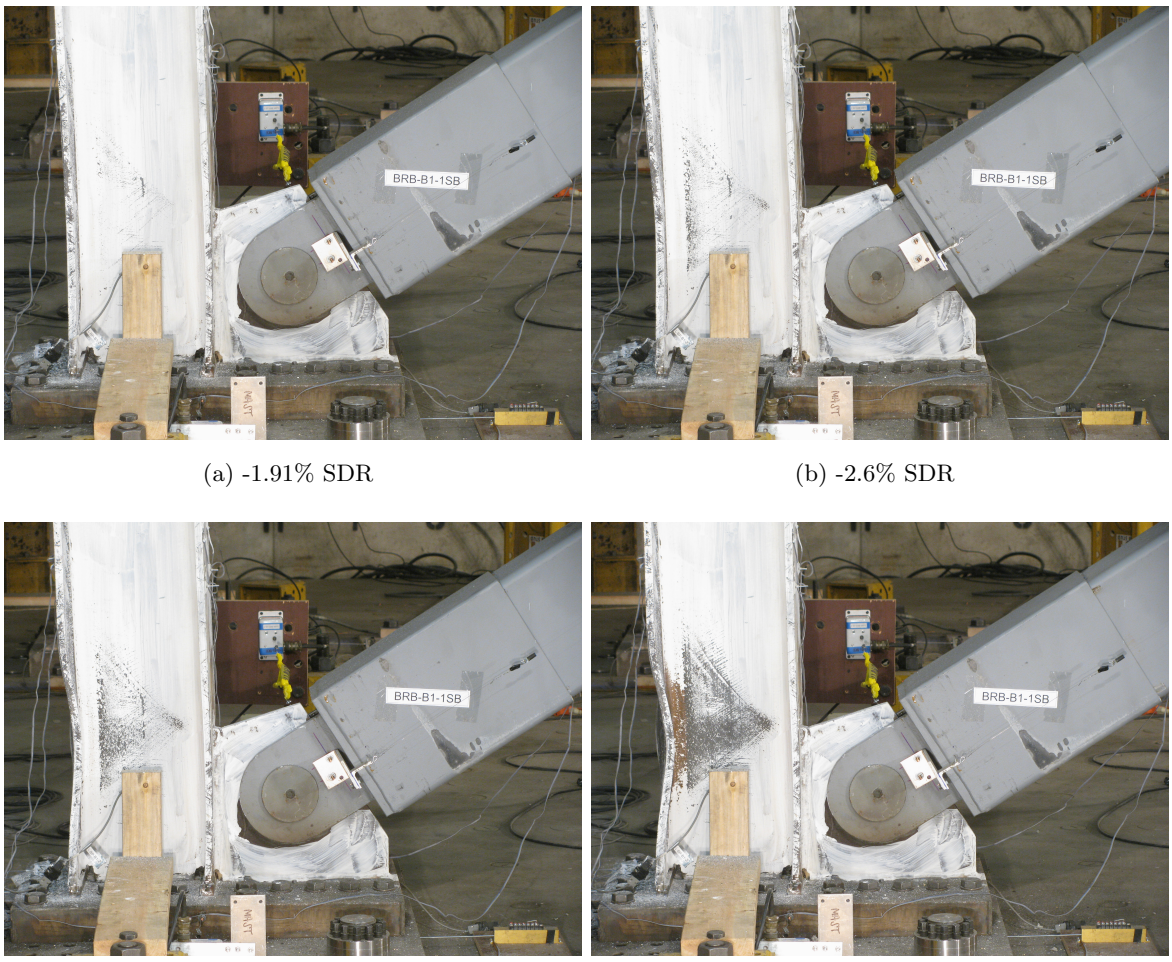

(a) -1.91% SDR

(b) -2.6% SDR

(c) 2nd cycle at -2.6% SDR

(d) -2.7% SDR

Figure 4.55: Progession of damage at base of Column A-1 during severe drift ranges (BRBF test)

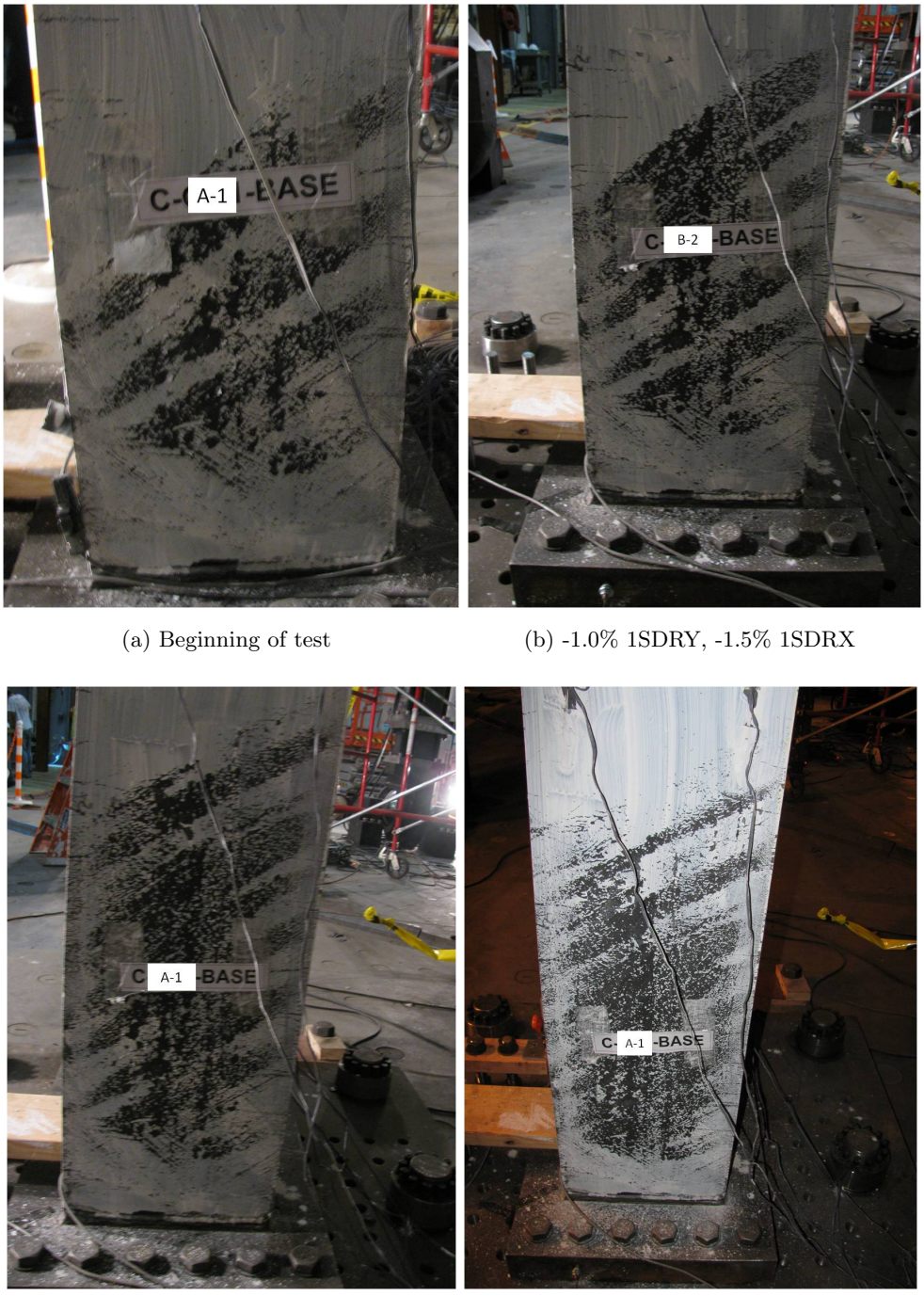

(a) Beginning of test

(b) -1.0% 1SDRY, -1.5% 1SDRX

(c) -1.2% 1SDRY, -1.9% 1SDRX

(d) -1.7% 1SDRY, -2.6% 1SDRX

Figure 4.56: Progression of flange yielding at base of Column B-2 (BRBF test)

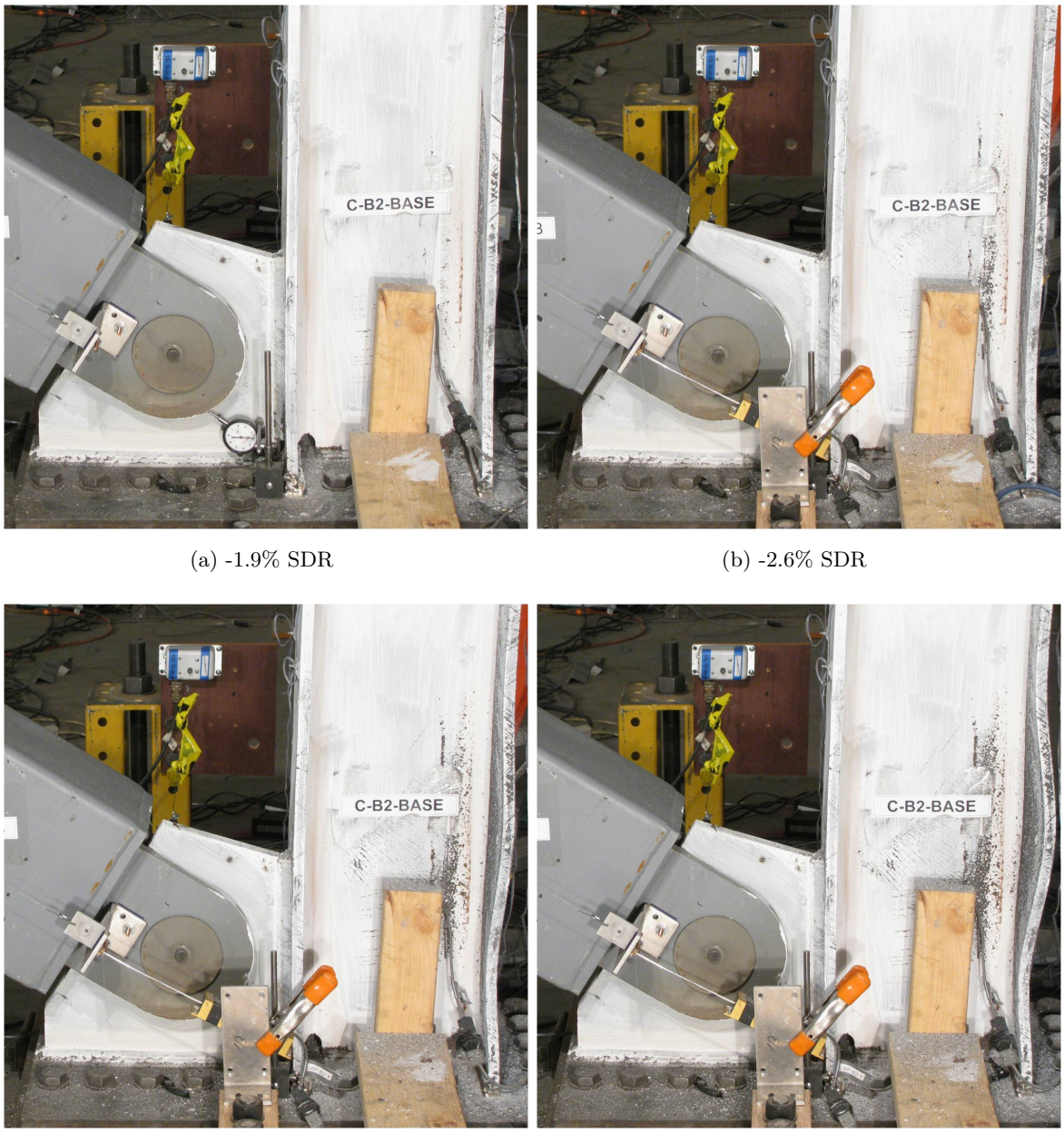

(a) -1.9% SDR

(b) -2.6% SDR

(c) -3.1% SDR

(d) 2nd cycle at -3.1% SDR

Figure 4.57: Progession of damage at base of Column B-2 during severe drift ranges (BRBF test)



(a) Beginning of test (b) 2.7% 1SDRY, 2.8% 1SDRX

Figure 4.58: Progession of damage at base of shared column (BRBF test)

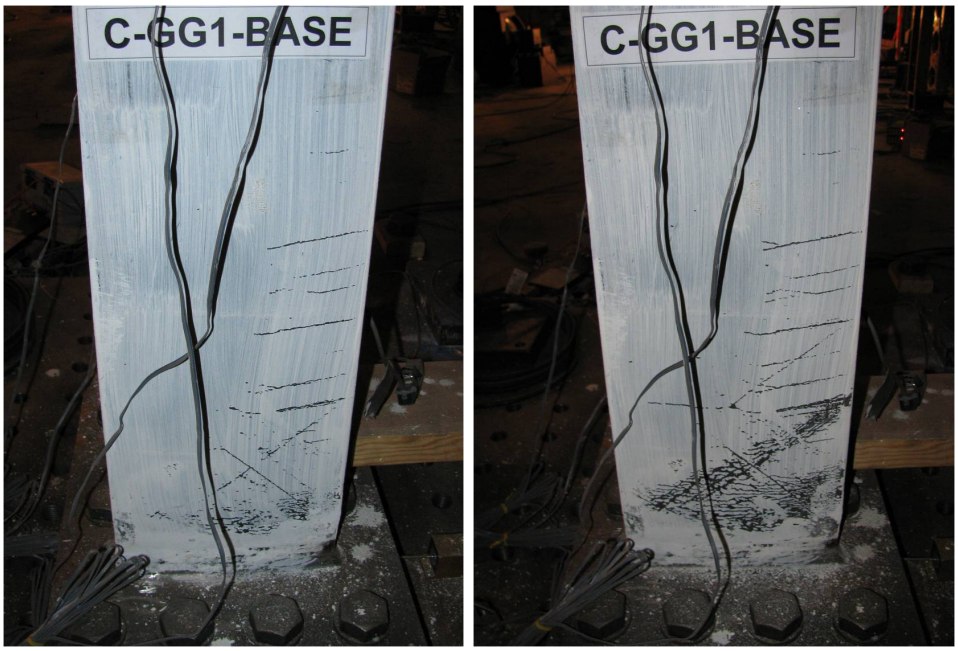

(a) 1.3% 1SDRY, 1.8% 1SDRX (b) 1.5% 1SDRY, 2.1% 1SDRX

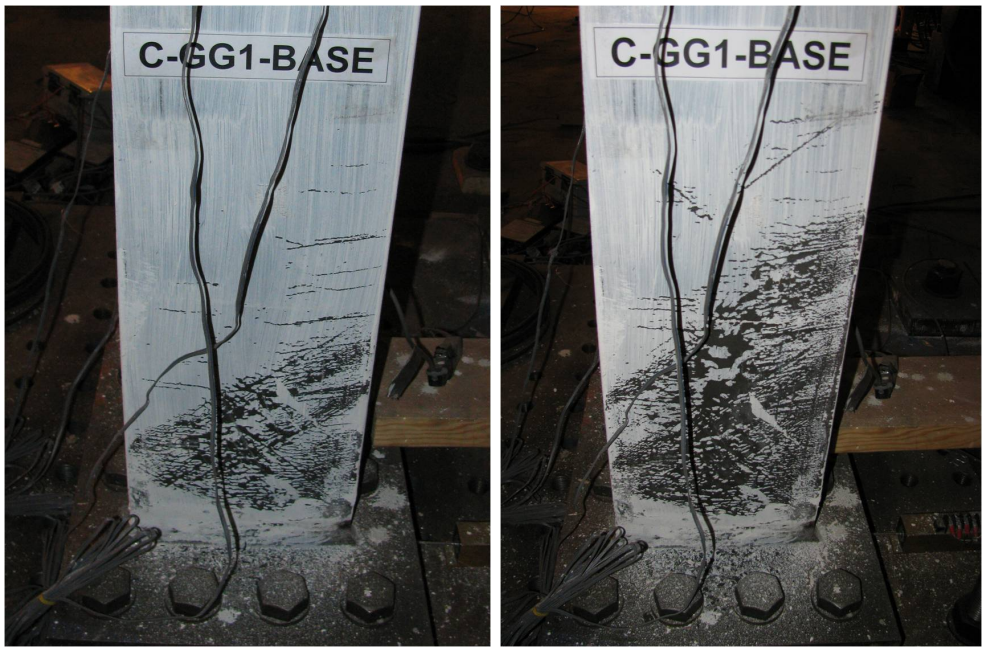

(c) 1.7% 1SDRY, 2.4% 1SDRX (d) 2.6% 1SDRY, 2.9% 1SDRX

Figure 4.59: Progression of yielding at base of the gravity column during the severe drift range (BRBF test)

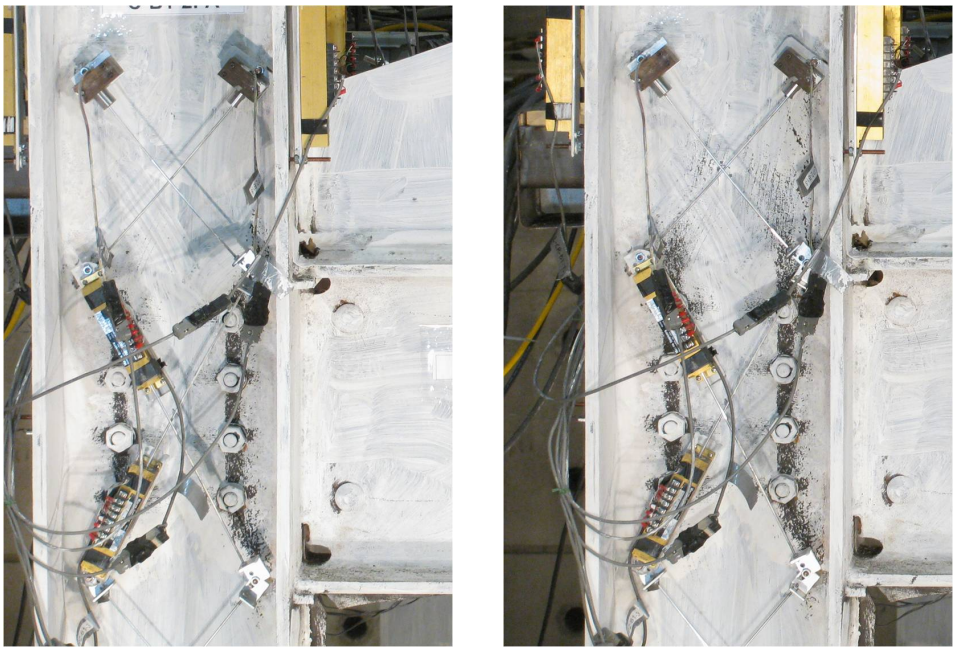

(a) Beginning of test

(b) 2% 1SDRY, 2.3% 2SDRY

(c) 2.4% 1SDRY, 3.3% 2SDRY

(d) -2.7% 1SDRY, -4.7% 2SDRY

Figure 4.60: Progression of yielding at the second floor joint of column A-1 during the severe drift range (BRBF test)

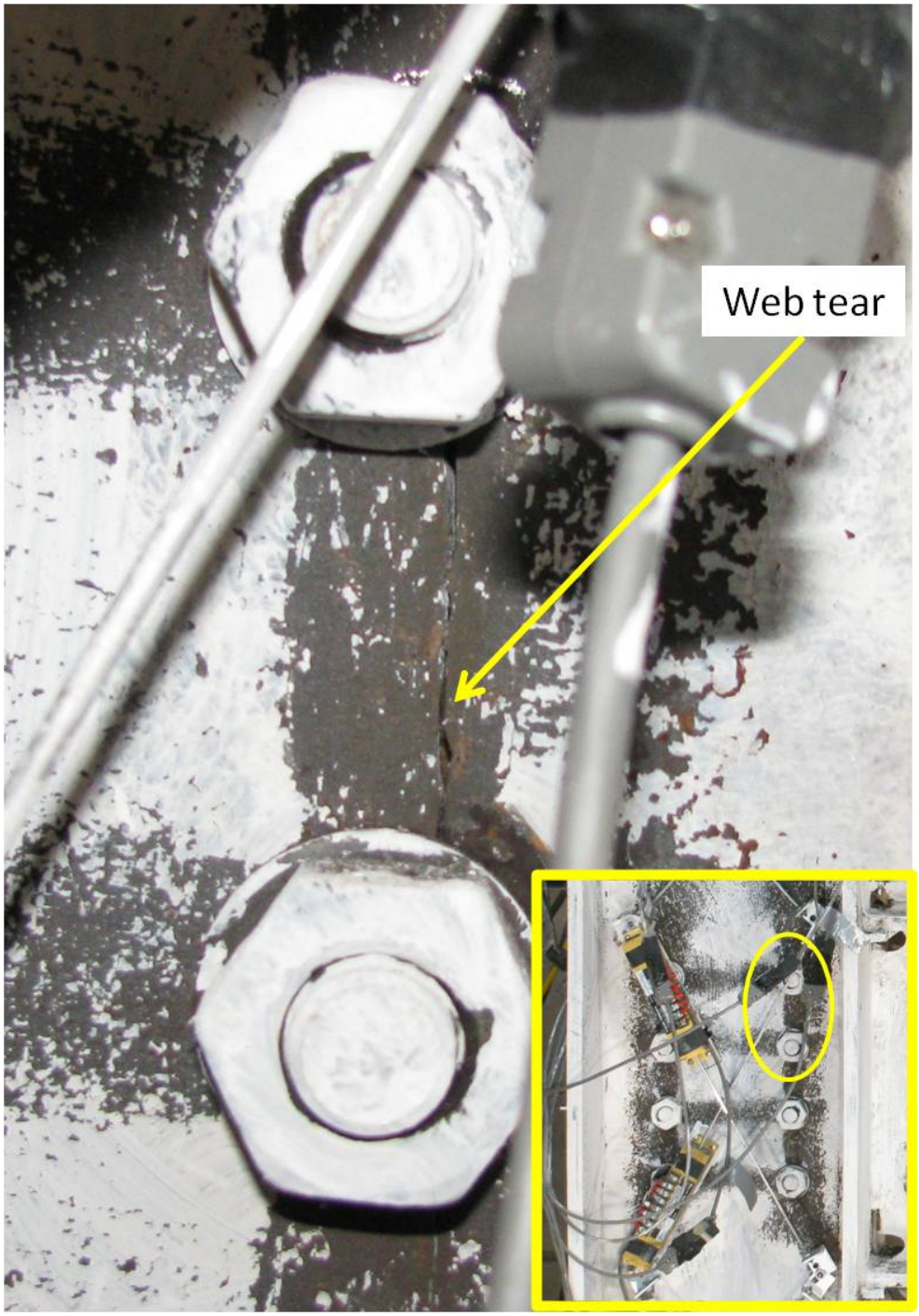

Figure 4.61: Tear in braced frame column A-1 web at gravity beam bolted connection at end of BRBF test

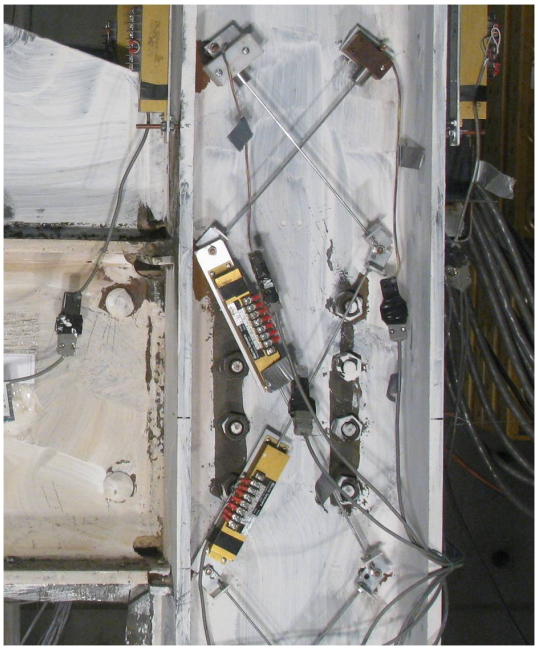

(a) Beginning of test

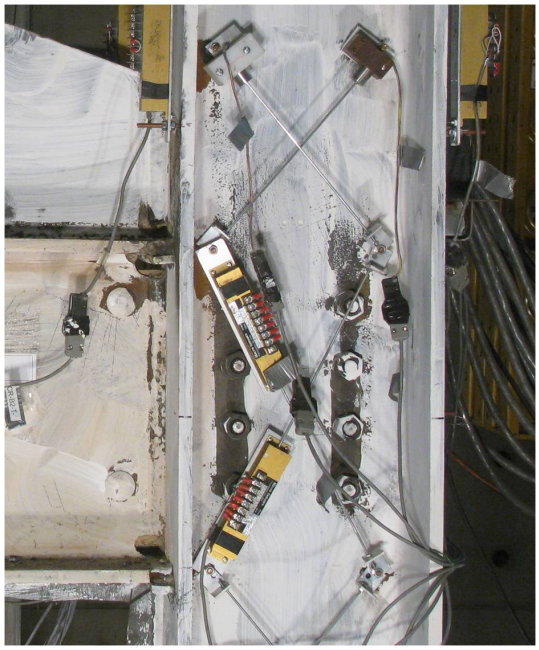

(b) -1.9% 1SDRX, -2.4% 2SDRX



(c) -2.6% 1SDRX, -3.1% 2SDRX

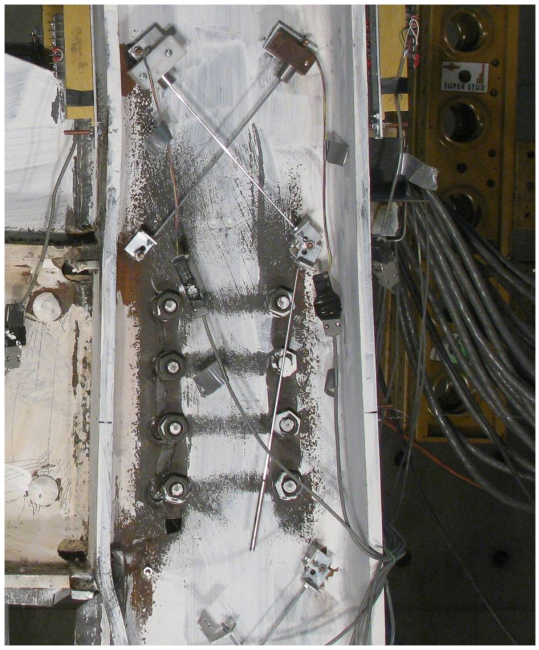

(d) 2.4% 1SDRX, 4.7% 2SDRX

Figure 4.62: Progression of yielding at the second floor joint of column B-2 during the severe drift range (BRBF test)

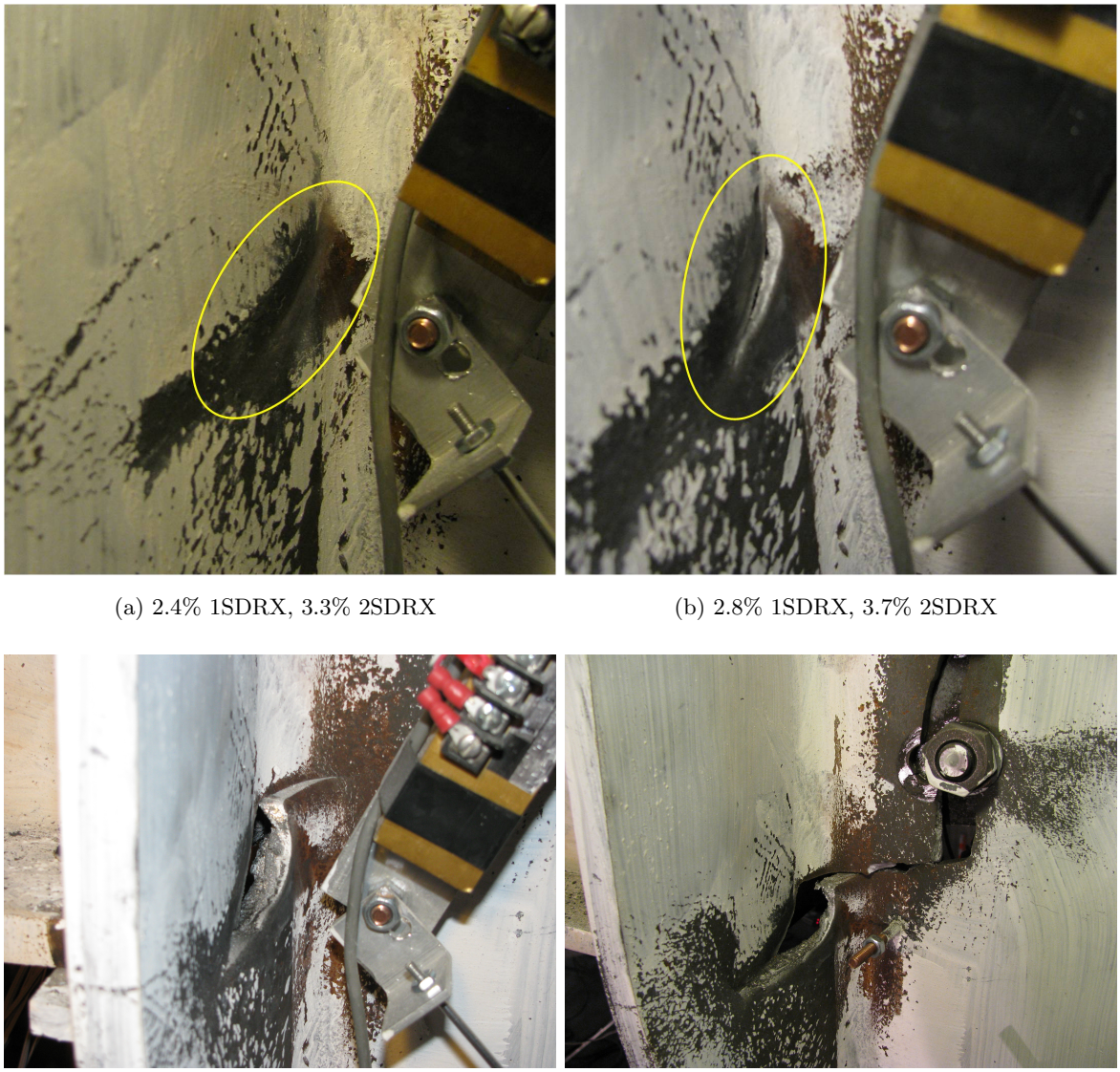

(a) 2.4% 1SDRX, 3.3% 2SDRX

(b) 2.8% 1SDRX, 3.7% 2SDRX

(c) 2nd cycle at 2.8% 1SDRX, 3.7% 2SDRX

(d) 2.4% 1SDRX, 4.7% 2SDRX

Figure 4.63: Column B-2 flange damage: (a) Divot forming; (b) Tear forming; (c) Tear propagating; (d) Flange connecting to web tear (BRBF test)



Figure 4.64: Braced frame column B-2 web and flange tearing, 2.4% 1SDSRX and 4.7% 2SDRX (BRBF test)



Figure 4.65: Column flange tear at beam bottom flange at second floor of column B-2, 2.7% 1SDSRX and 3.7% 2SDRX (BRBF test)



(a) Column A-1, beginning of BRBF test



(b) Column A-1, end of BRBF test



(c) Column B-2, beginning of BRBF test

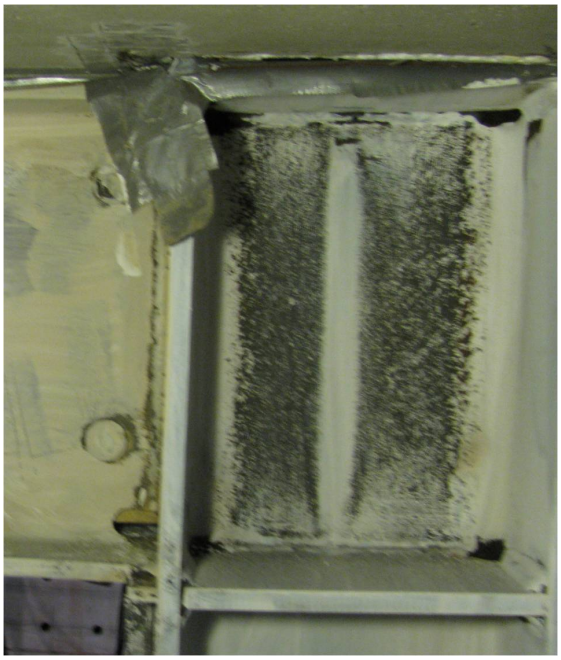

(d) Column B-2, end of BRBF test

Figure 4.66: Third floor column panel zone yielding (BRBF test)



Figure 4.67: Column flange yielding at beam bottom flange at second floor of column A-1, end of test (BRBF test)

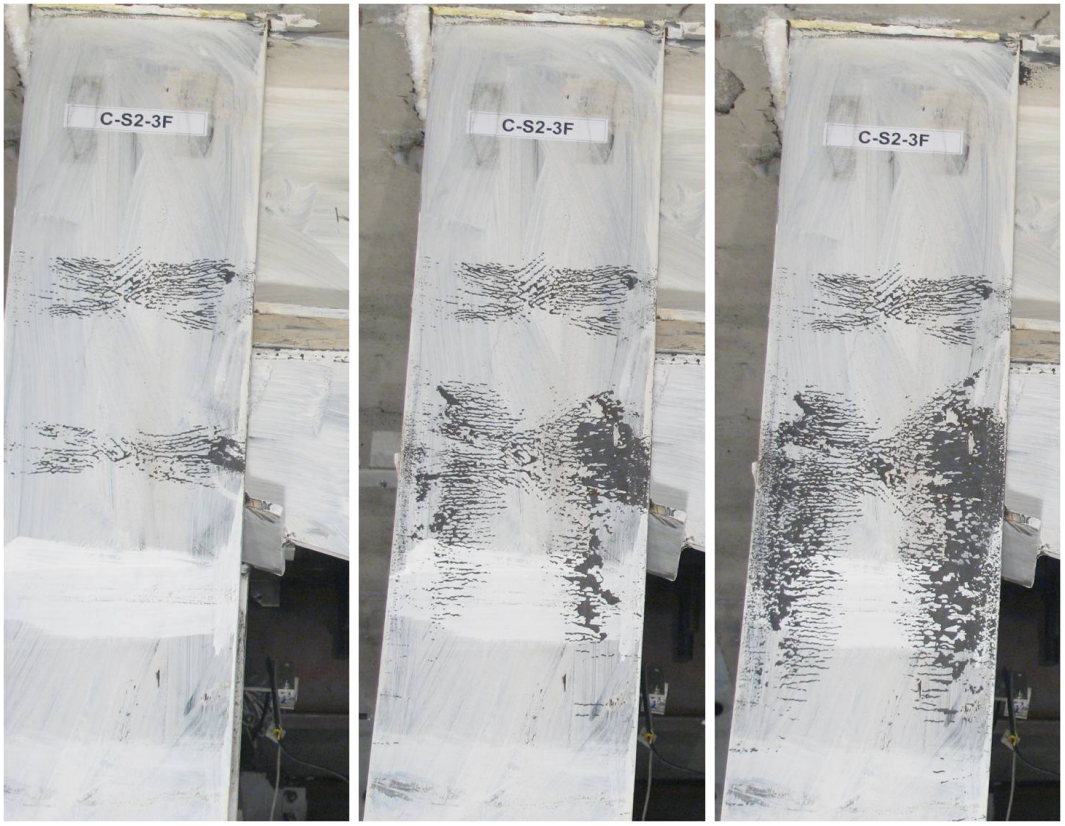

(a) Beginning of BRBF test (b) 3.2% 2SDRX, 2.1% 2SDRY (c) End of BRBF test

Figure 4.68: Shared column third floor flange yielding (BRBF test)

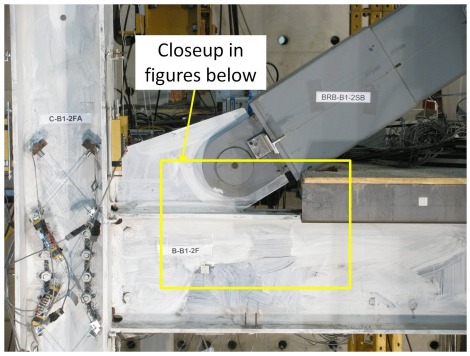

(a)

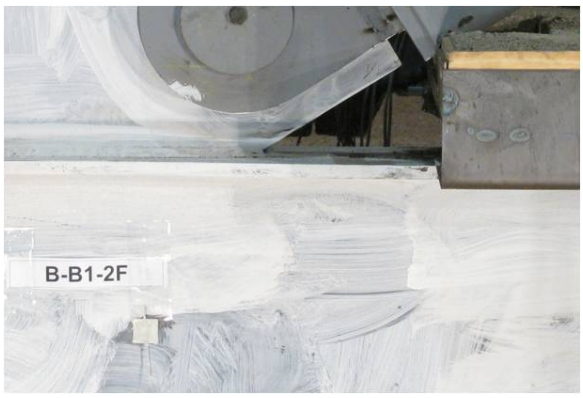

(b) Beginning of test



(c) 2.4% 1SDRY, 3.3% 2SDRY



(d) 2.7% 1SDRY, 3.8% 2SDRY



(e) 2.7% 1SDRY, 4.7% 2SDRY

Figure 4.69: Beam damage in Frame 1 at second floor, column A-1 (BRBF test)

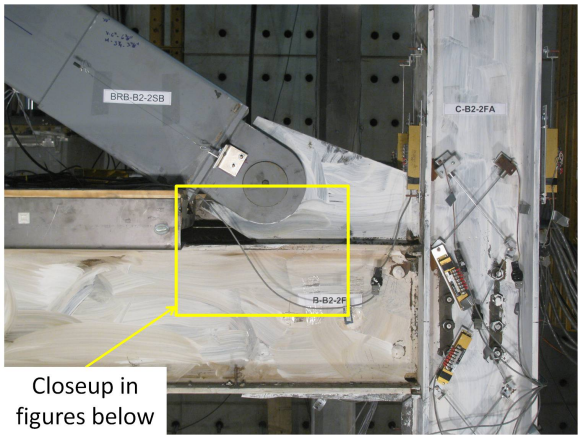

(a)



(b) Beginning of test



(c) End of test

Figure 4.70: Beam damage in Frame B at second floor, column B-2 (BRBF test)

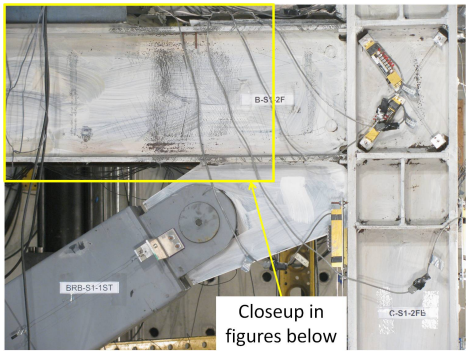

(a)

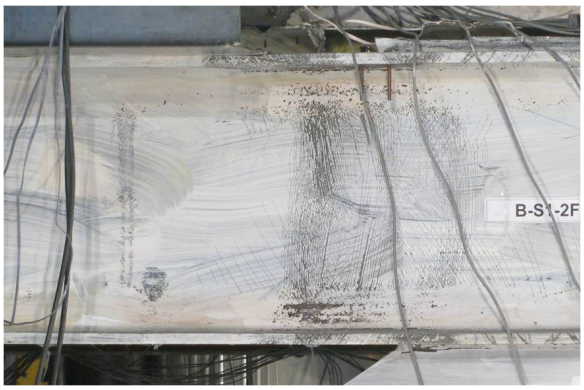

(b) Beginning of test



(c) 2.4% 1SDRY, 3.3% 2SDRY

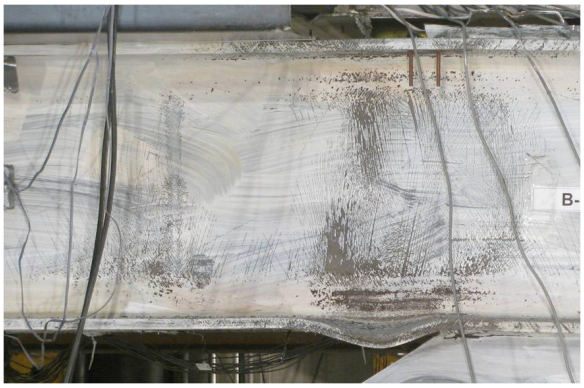

(d) 2.7% 1SDRY, 3.8% 2SDRY



(e) End of test near zero SDR

Figure 4.71: Beam damage in Frame 1 at second floor, column B-1 side (BRBF test)

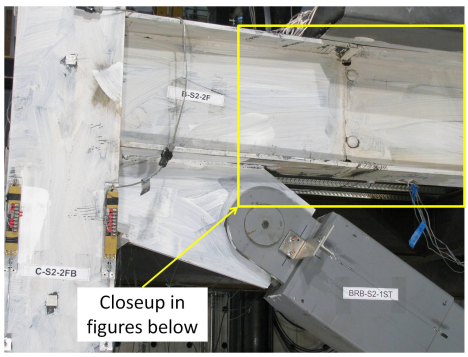

(a)

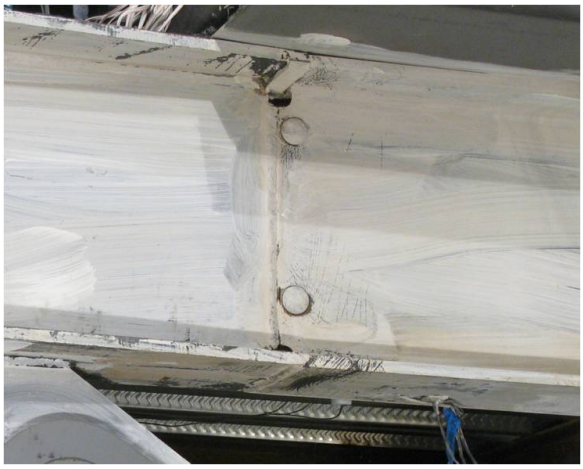

(b) Beginning of test



(c) -2.2% 1SDRX, -2.8% 2SDRX

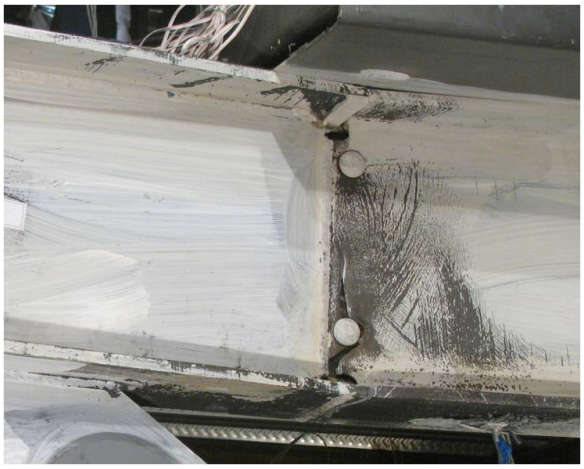

(d) -3.1% 1SDRX, -3.4% 2SDRX



(e) -3.1% 1SDRX, -4.1% 2SDRX

Figure 4.72: Beam damage in Frame B at second floor, column B-1 (BRBF test)

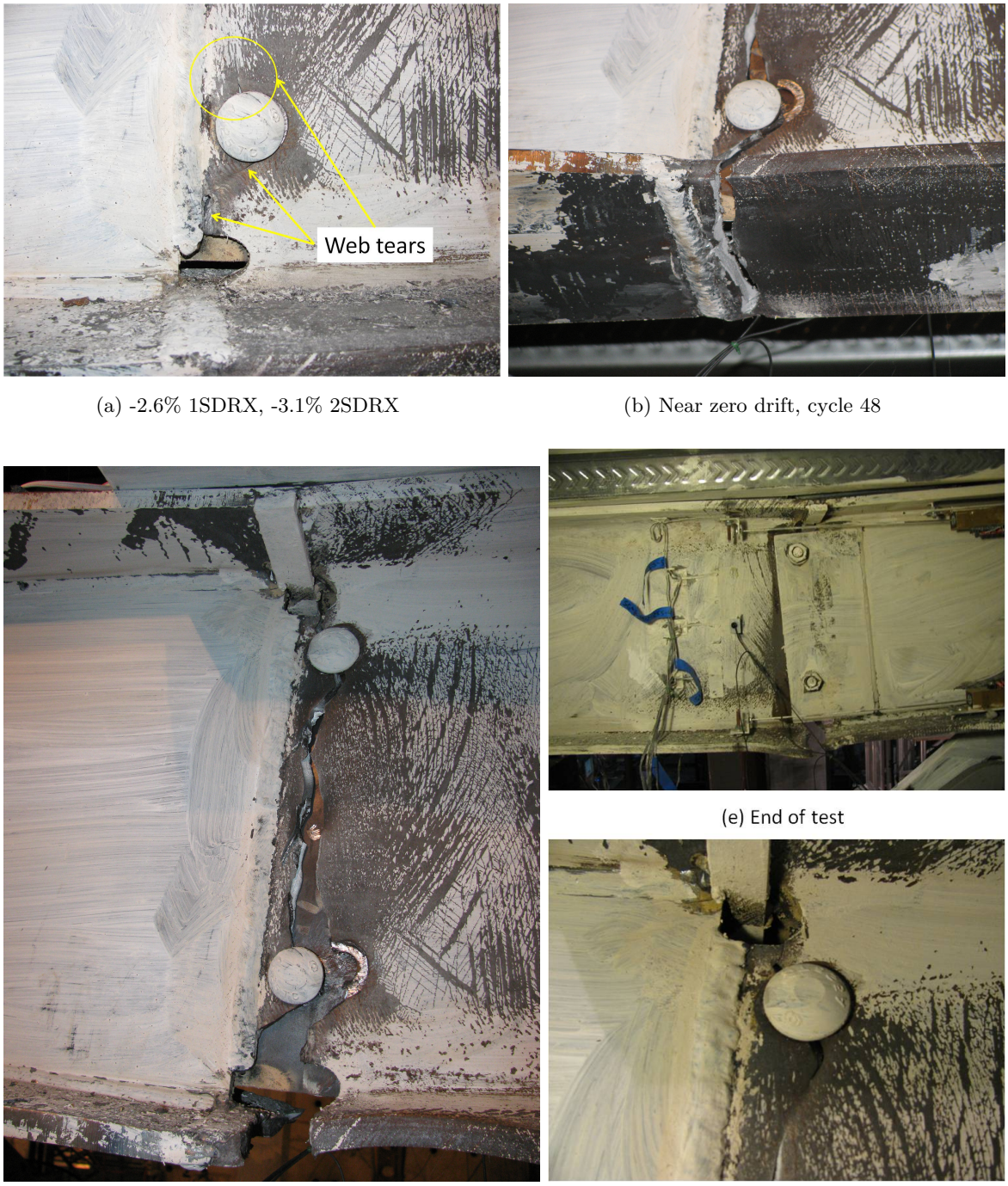

(a) -2.6% 1SDRX, -3.1% 2SDRX

(b) Near zero drift, cycle 48

(c) -3.1% 1SDRX, -4.1% 2SDRX

(d) Upper erection bolt area

Figure 4.73: Beam damage in Frame B at second floor, column B-1 (BRBF test)



Figure 4.74: Column flange yielding at beam bottom flange at face of third floor column A-1, end of test (BRBF test)

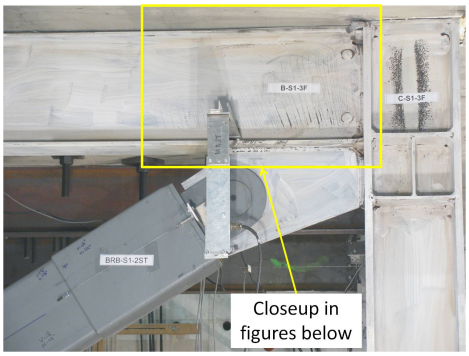

(a)



(b) Beginning of test



(c) 3.3% 2SDRY



(d) 3.8% 2SDRY



(e) 2nd cycle at 3.8% 2SDRY

Figure 4.75: Beam damage in Frame 1 at third floor, shared column side (BRBF test)



(a) OOP web deformation 3.3% 2SDRY



(b) OOP web deformation 3.8% 2SDRY



(c) -3.7% 2SDRY



(d) -4%% 2SDRY

Figure 4.76: Beam damage in Frame 1 at third floor, shared column side (BRBF test)

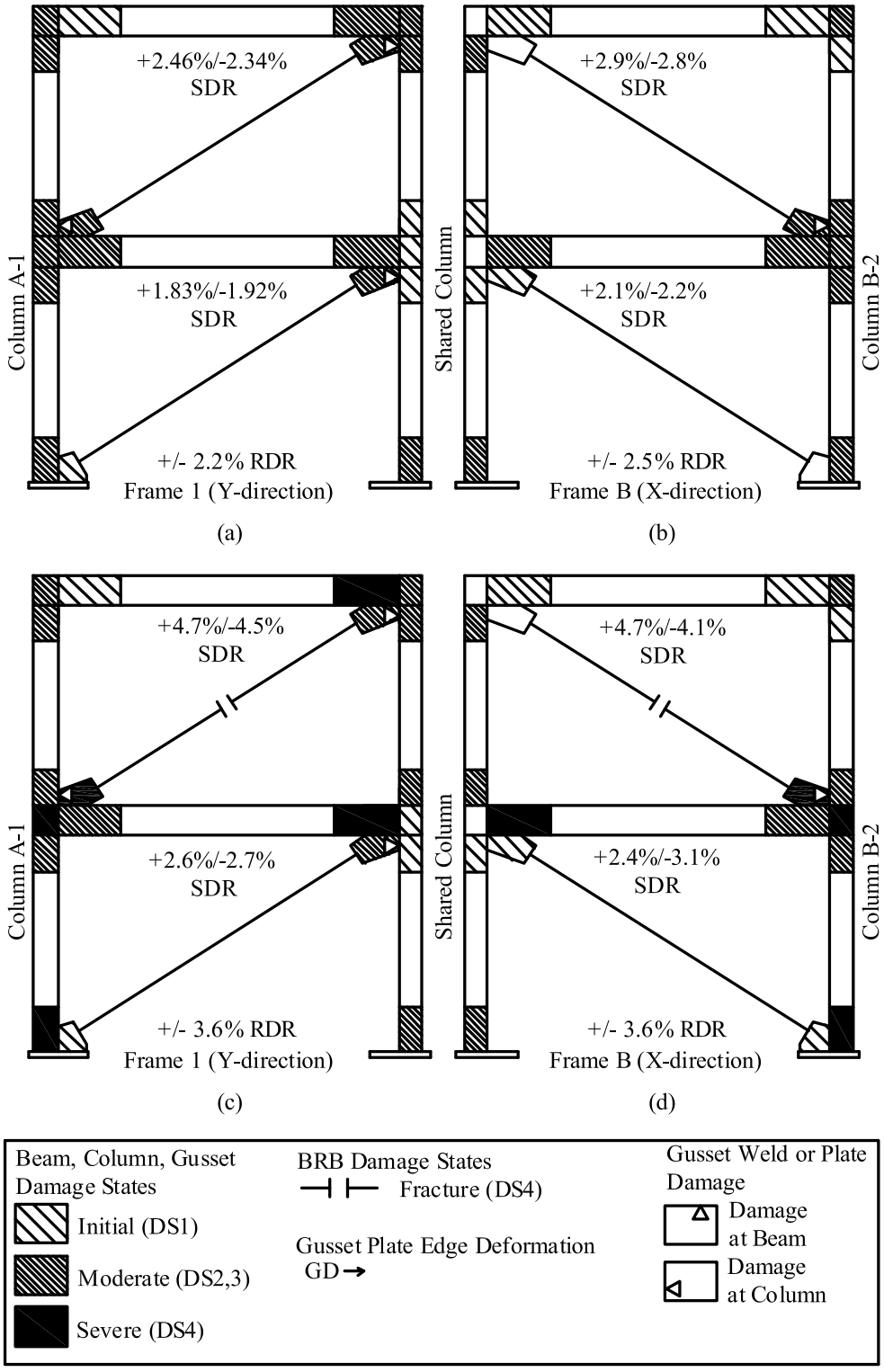

Figure 4.77: Pictorial of damage states per ATC-58 [2009], BRBF test

Chapter 5

DATA ANALYSIS

5.1 Introduction

This chapter expands upon the test results discussed in the previous chapter and presents analysis of the local behavior of the components during the experiments. This analysis is performed using the sensor data recorded during the experiments. The SCBF test is presented first followed by the BRBF test. Following these discussions, a comparison is made between the SCBF test and the two single-story, planar X-braced frame experiments performed by Powell and described in Section 2.5.1.

5.2 SCBF Experimental Data Analysis

This section presents the data analysis of the first tests specimen. This analysis includes a discussion on the brace and gusset plate behavior, and braced frame beam and column behavior along with a discussion of the column panel zone behavior.

5.2.1 Brace and Gusset Plate Behavior

Figure 5.1 shows the cyclic behavior of the brace pairs in each story in each frame during the experiment. The vertical axes of the plots are the horizontal story shear resisted by both braces while the horizontal axes are the SDRs of the particular story. These brace story shears were calculated by subtracting the story shears resisted by all of the columns in that story from the force measured by the actuators. The column story shears were found using the column strain gauge data and Euler-Bernoulli beam theory as described in Appendix C. The column strain gauges were placed in locations that remained elastic and therefore this estimate is reliable as will be shown in the following section describing the calculation of the brace buckling loads.

It can be seen from the figures that these braces display relatively full hysteresis with

the pinching that is expected to occur in systems with brace buckling. It can be seen that the peak strengths at successive cycles and at SDRs larger than 1% to 1.5% are smaller than the peak strengths in the preceding cycle(s). This is due to the tension brace yielding along the flat portion of the stress-strain curve with the compressive brace softening due to prior yield deformation and accumulated damage. It can also be seen that upon reversal of load, the unloading stiffness is elastic but is smaller than the original stiffness due to the fact that the buckled braces never fully straighten out following plastic rotations at the plastic hinge locations. The initial hardening and subsequent softening of the braces can also be see in Fig. 5.2 which shows the envelope of the hysteretic plots shown in Fig. 5.1. It can be seen that all of the braces exhibited the same initial stiffness prior to yield and very similar measured yield loads in the positive drift range with the maximum difference on the order of 10%. The yield loads in the negative drift range varied more than those in the positive range with the maximum difference on the order of 20%. The measured peak strengths of the braces in the second story of Frame B were approximately the same in each direction. This was also true for the first story braces in Frame B but was not true for the braces in both stories of Frame 1 but the largest difference was only 10% which was for the first story braces. The peak story shears resisted by each brace pair are listed in Table 5.1. Differences would be expected and occur for a number of reasons which include the nature of the approximations used to calculate the internal forces using strain gauges which also have inherent inaccuracies in measurements, and also the locked in brace forces that occur due to the welding sequence. For example, the continuous braces were welded first to a relatively flexible frame that would "give" and in the process, relieve the internal braces forces induced by weld cooling. The frame is now much more rigid and would not "give" as much when the spliced braces are welded and therefore these braces will develop residual tensile stresses which will increase the measured buckling load in these members. This may be the reason that the buckling loads in the spliced braces are larger than those in the continuous braces. The largest difference between the peaks in the negative and positive direction occur in the second story of Frame 1 and is on the order of the difference in buckling loads between the braces in this frame in the two opposing directions. This trend occurs in all frames. The buckling loads are discussed in more detail in the next

section.

Brace buckling loads

Brace buckling loads are an important design parameter and are necessary for capacity design of beams and columns. The buckling loads for the eight braces in the test frame were estimated from the the strain gauges at each end of the braces shown in Fig. 3.27 using elastic theory (Eqn. C.12). Fig. 5.3 plots the brace axial loads in each frame and story based on the measured brace strains and Eqn. C.12 as a function of the story drift ratio. Four curves are shown in each plot: two for each brace in the story based on the top and the bottom strain gauges as noted in the legend and the note in the figure caption. The calculated buckling loads along with the SDR at which buckling occurred are shown in the plots and Table 5.2. Both of these quantities were determined by averaging the results from the strain gauges at the top and the bottom of the brace. The buckling load can clearly be seen in each plot as the peak negative load followed by softening. The calculated forces did vary depending on where the strain gauges were located but this variation was not significant for the majority of cases with the most significant difference being 26% for the continuous braces in the first story of Frame 1 (see Fig. 5.3c).

To ensure that the brace forces calculated using the strain gauges were correct, a comparison was made between the horizontal story shears resisted by the braces as estimated from the brace strain gauges and those estimated from subtracting the column story shears from the force measured in the actuators. The column shears were estimated from the column strain gauges as described in Appendix C. This comparison is shown in Fig. 5.4 which shows for each frame and story, the story shear resisted by the braces versus the story drift ratio. The point at which brace tensile yield occurs is also shown and beyond this point, the forces estimated from the brace strain gauges are no longer accurate. Each plot shows three curves: one for the force estimated from the crosshead and column strain gauges (labeled as "CH"), and two for the force estimated from the brace strain gauges installed at the top of the brace (labeled as "SGt") and from those installed at the bottom of the brace (labeled as "SGb"). Inspection of the plots show that prior to yield, the forces estimated from all of

the methods match each other quite well with differences in initial stiffness no greater than 10% for the worst case. Therefore, there is confidence in both the brace force estimates using the brace strain gauges prior to brace yielding and the column shear force estimating method.

Brace out-of-plane (OOP) behavior

OOP deformation of braces due to buckling may cause damage to nonstructural components during an earthquake and therefore it is desirable to understand the OOP behavior and expected magnitudes of OOP deformation. As discussed in Chapter 3, the second-story braces in Frame B were instrumented with string potentiometers in 13 locations to measure the OOP deformation of the braces as shown in Fig. 3.28. Figure 5.5 shows the OOP deformed shape of the continuous and discontinuous braces along their lengths at four story drift levels: 0.5, 0.9, 1.4 and 1.9%. The continuous brace is displayed as a solid line while the discontinuous brace is displayed as a dashed line. As expected, the OOP deformation increases with story drift and the one-sided behavior of the discontinuous brace can clearly be seen. The half of the discontinous brace from 0 to 0.5L (physically, the upper half of the brace) shows OOP deformation while the half from 0.5L to 1.0L (physically, the lower half of the brace) displays no OOP deformation.

Figure 5.6 shows the measured OOP brace deformations at the brace quarter points as a function of the absolute second story drift ratio. At a given SDR, the discontinuous brace OOP deformations are approximately 15% greater than the OOP deformations of the top half of the continuous brace. This makes sense intuitively as both halves of the continuous brace are deforming OOP while only the top half of the discontinuous brace is deforming OOP. The maximum OOP deformation of the discontinuous brace is 10" at an SDR of 1.84% while the maximum OOP deformation of the continuous brace is 8.9" at an SDR of 1.9%. SDRs of this magnitude are expected to occurr during the Design Basis Earthquake and therefore damage to nonstructural components would be expected if partition walls or elements are in the vicinity of the brace.

Interestingly, the measurements for the continuous brace suggest that the OOP defor-

mations are different for each half of the brace with the portion spanning from 0 to 0.5L (physically, the lower half of the brace) deforming approximately one-half of the deformations of the portion spanning from 0.5L to 1.0L (physically, the upper half of the brace). This was also observed in the experiments performed by Powell described in Chapter 2 and is also corroborated by photographic evidence as seen in Fig. 5.7. This figure shows the deformed shape of the continuous brace at 1.9% SDR. The larger curvature of the top portion of the brace is visible indicating larger OOP and plastic deformation at this location. The reason for this difference in OOP deformation between the two halves of the same brace is the same reason that the lower story continuous braces reversed buckling direction and is discussed below.

Figure 5.7 provides evidence that the tension brace acts as an OOP support for the compression brace in a single-story X-configured system. Immediately upon load reversal at SDRs of approximately 1% and greater, this is not the case until the brace that was previously in compression straightens out and begins to resist load and provide non-negligible tensile stiffness. Until this occurrs, the brace that was previously in tension and is now in compression begins to buckle as if the tension brace were not there. This phenomenon caused a reversal of OOP deformation due to buckling at larger SDRs in the first-story continuous braces in both Frame 1 and Frame B. A comparison of the deformed continuous braces in the first-story of Frame 1 at an SDR of -0.83% and -1.4% is shown in Figs. 5.8a and 5.8b, respectively. It can be seen that the OOP deformations of the braces at -0.83% are in different directions than the OOP deformation at -1.4%. Figure 5.9 shows the frame at zero SDR and provides insight into why the brace OOP deformation reversed direction and also why the OOP deformation is greater in one-half of the brace than the other (in this case, it is greater in the bottom half than the upper half). In the photograph, the test frame has just returned to zero drift from a positive SDR of 1.4% (out of the page) and is heading to a negative story drift (into the page). It can be seen that the lower, discontinuous brace that was in compression has not fully straightened out and that the curvature of the continuous brace suggests that it has begun to buckle in a mode similar to end conditions consisting of a flexible lower boundary condition and more rigid upper boundary condition. This is in fact the case, with the lower gusset plate at the base plate being more flexible

than the upper gusset plate at the beam. The preferred direction of the continuous brace buckling as if no tension brace was there was to the north (to the right in the figure). The brace that was previously in compression had a relatively large OOP deformation which allowed a relatively large OOP deformation of the single-curvature continuous brace to then occurr which caused a reversal of the double-curvature pattern once the tension brace fully straightened out.

The reversal of the brace OOP deformation direction was also captured in the response of the gusset plates. Figures 5.10 and 5.11 show plots of the gusset rotations as a function of SDR for the first story of Frame 1 and B, respectively. The rotation of the base gusset plate in Frame 1 attached to column A-1 is shown in Fig. 5.10a. In the negative drift range, the brace OOP deformation causes a positive rotation of the gusset plate for the majority of the test. However at approximately 1% SDR, it can be seen that the rotation changes sign due to the change of direction of the brace OOP deformation. Similar behavior may be seen in Figs. 5.11b and 5.11c for the base and upper gusset plates for the continuous brace in Frame B.

5.2.2 Column Behavior

Column moments were calculated at the gusset reentrant corners based on a linear distribution of the moments calculated at the strain gauge locations as described in Appendix C. Figure 5.12 shows these bending moment envelopes as a function of the roof drift ratio for each braced frame column in each story in each direction. Each plot contains four curves, one for the moment at the top and bottom of each column in the frame of interest. The trend of the curves and the relative magnitude between the moments in the different columns and locations was as expected. For example, the base of the columns were provided with full fixity as described in Section 3.5.1 and therefore attracted the largest bending moments. The shared column was the largest and stiffest (labeled "B-1b" and "B-1t" in the figures) and therefore attracted the largest moment at the base as shown in Fig. 5.12c ("B-1b") while the base of column A-1 resisted the second largest moment ("A-1b"). The ratio of these moments closely matched the ratio of the moments of inertia of the columns.

All of the curves show varying levels of stiffness reduction as the drift increases, indicating yielding of the columns or some other mechanism such as beam yielding at the floor levels, which reduces the stiffness of the joint and results in a perceived softening of the column. For example, the moment at the top of the shared column (B1-t in Fig. 5.12c) reaches a maximum of 96 kip-ft at 1.3% RDR and begins to decrease at larger drift ratios. In this case, the beam is yielding and its rotation is increasing considerably (see Section 5.2.3) causing reduced stiffness at this joint which reduces the column moment and shifts the column inflection point upward. Strain gauges, whitewash and the moment magnitude indicate that the column is not yielding in this location. The moment at the top of the first story of column A-1 does not display this softening response because the beam framing into it at the second floor did not yield as dramatically as it did at the shared column joint. Also note that in the positive drift range, the moment at the top of the first story of column A-1 is larger than B-1 even though B-1 is 50% stiffer. This is attributed to the increase in beam stiffness when the floor slab is in compression which occurs at column A-1 in the positive drift range and column B-1 in the negative drift range. This explains why the moment at A-1t is greater than B-1t in the positive drift range while the moment at A-1t is smaller than B-1t in the negative drift range.

The story shears resisted by the columns were estimated from the column end moments as described in Appendix C. The envelopes of the story shear resisted by the braced frame columns in each story in Frame 1 and Frame B are shown in Figs. 5.13a and 5.13b, respectively. These are shown as a function of the story drift ratio for the story of interest. As expected, the story shears resisted by the first story columns are larger than those resisted by the second story columns due to the base fixity of the first-story columns. This can be seen in Fig. 5.13a by a comparison of "A-1 1S" with "A-1 2S" or by comparing "B-1 1S" with "B-1 2S," where "A-1 1S" indicated the first story of column A-1. Similar behavior is seen in Fig. 5.13b for the columns in Frame B. Additionally, the stiffer columns resist more shear in each story as can be seen by comparison of "A-1 1S" with "B-1 1S" in Fig. 5.13a, where B-1 is stiffer than A-1 and resists more shear. Similar behavior occurred in Frame B (5.13b) with column B-2 resisting more shear than B-1 due to the fact that column B-1 is bigger but is bent about its weak axis.

The envelopes of the story shears resisted by all of the columns including the gravity column are shown in Fig. 5.14. Four curves are shown with each plot corresponding to a story and a specific direction of frame deformation (X or Y, see Fig. 3.2 for coordinate system). The solid lines in each figure correspond to the two columns in the braced frame in the stated direction while the dashed lines correspond to the two columns in the gravity frame. As expected, the braced frame columns carry a much larger portion of the story shear since the gravity frame beams are connected to the columns with flexible "shear-only" connections.

Column panel zone behavior

The braced frame column panel zone shear strains at the second floor were estimated at the second floor using the measurements of the panel zone diagonal deformation recorded during the experiment with LVDTs as shown in Figs. 3.38 through 3.40 and calculated according to the method described in Appendix C. The panel zone shear strain envelopes for the three braced frame columns are shown in Fig. 5.15 where Fig. 5.15a shows the magnitudes in radians and Fig. 5.15b shows the magnitudes normalized by the shear yield strain of the panel zone. It can be seen in Fig. 5.15b that the shared column panel zone (column B-1) did not yield at any point during the experiment while the panel zones of both columns A-1 and B-1 did yield. The panel zone of column A-1 reached over four times the yield strain and column B-2 reached over three times the yield strain. This yielding is not surprising since calculations showed that the panel zone demands based on the beam reaching its plastic moment capacity were well in excess of its strength for columns A-1 and B-2 but not for column B-1 (see Section 3.4.3 and Appendix A). The panel zone demand-capacity ratio (DCR) for columns A-1 and B-2 were 1.7 while the DCR for column B-1 was 1.0. This yielding or lack thereof is believed to have had a significant impact on the behavior of the braced frame beams at the second floor, particularly in Frame 1. This will be discussed in greater detail in the following section.

5.2.3 Beam Behavior

Beam moments in the braced frames at the second floor were calculated at the gusset plate reentrant corners based on the strain gauges placed on the beams and the methodology discussed in Appendix C assuming a linear distribution of moment along the length of the beams. This ignores the contribution from gravity loads which was significantly less than the moments produced by lateral deformation of the frame. Beam moments were calculated first using the strain gauges on the top and bottom flanges in the column of strain gauges furthest away from the gusset plate edges (strain gauges 6 and 10 shown in Figs. 3.42a, b and c, and 3.43a, b and c. There was no concrete floor slab at this location due to the slab blockouts required for the gusset plates and therefore, composite action due to the contribution from the slab was not considered in the moment calculation. Additionally, the gauges were far enough away from the location of beam yielding such that linear elastic theory assuming plane sections remaining plane could be used. The self weight of the beam and floor slab was also neglected in these calculations. Ignoring this is insignificant as will be discussed in what follows.

Figures 5.16a and 5.16c show the beam moment in Frame 1 at the second floor on the column A-1 side while Fig. 5.16b and 5.16d show the beam moment in Frame 1 at the second floor on the shared column side (column B-1). Figures 5.16a and 5.16b plot the moment as a function of the SDR while Figs. 5.16c and 5.16d plot the moment as a function of the measured average beam rotation. The beam rotation was estimated from LVDTs placed on the top and bottom flanges as discussed in Section 3.6.4 and Appendix C and was based on average deformation over a 16" gauge length.

It can be seen that a larger moment was resisted at the shared column (B-1) side which is not surprising since the shared column is stiffer than column A-1. The beam moment at the shared column side reached the plastic moment, M_p, in the negative drift region at approximately -1.5% SDR and was slightly below M_p in the positive region. The larger moment in the negative region can be attributed to the increase beam stiffness at this location when the slab was in compression. This phenomenon is also seen for the moment at column A-1 but in the opposite sense with the larger moment in the positive region when

the slab on the beam at column A-1 was in compression. The beam moment at the column A-1 side never reaches the plastic moment but does exceed the yield moment in the positive drift range at apprxoimately 0.75% 1SDR and in the negative drift range at approximately -1.3% 1SDR.

To show that the disparity in moments at each beam end between the positive and negative drifts was mainly due to the composite slab contribution when it was in compression, a linear elastic analysis was performed in SAP2000 [CSI, 2010] on the frames shown in Figs. 5.18a and 5.18b (This disparity is also due to the gravity load but to a significantly smaller extent and was not considered in the calculations). The models are one-story, one-bay moment frames with the beam and column sizes matching those used in the test frame and with the slab blockouts considered. The models consider the composite action of the slab when the slab is compression assuming a point of inflection in the beam at mid-span and the approximate lower bound moment of inertia, I_{LB}, of the composite beam as calculated according to the method used in Table 3-20 of the Steel Construction Manual [AISC, 2005b]. For example, the model in Fig. 5.18a with the composite slab modeled on the left half of the beam was pushed towards the right as the arrow indicates in the figure. This direction causes the slab on the left half of the beam to act in compression while the slab on the right half of the beam is in tension and therefore ignored. Similarly, the model in Fig. 5.18b used a composite section for the beam to the right of mid-span and the frame was pushed to the left in the figure as the arrow indicates. Each frame was pushed in the respective direction shown in the figure to the same displacement and the resulting moment diagram for each analysis are shown in Figs. 5.18c and 5.18d. The normalized moment-displacement curves for each beam end are shown in Figs. 5.18e and 5.18f. It can be seen in these figures that beam end moment when the slab is in compression is approximately 20% larger than the moment at the beam end where the slab is in tension and ineffective. This difference is nearly the same as the difference of the peak moments at positve and negative drifts measured in the experiment and shown in Figs. 5.16. The end moment due to gravity loads is approximately 8 kip-ft which would cause an initial shift in the curve at zero displacement but is considerably less than the peak moments at SDRs larger than 0.25%.

Of particular note is the rotational behavior of each end of the beam. A comparison of Fig. 5.16c with Fig. 5.16d shows that the rotation of the beam end at the shared column side (B-1) was nearly two to three times as large as the rotation of the beam end at the column A-1 side, depending on the drift direction. This indicates that significant yielding was occurring in the end of the beam at the shared column side. This caused a reduction in stiffness of the joint at the shared column and a resulting reduction of moment transferred to the shared column as discussed in the previous section. This disparity in behaviors at each beam end can be attributed to the difference in flexural stiffness of the columns at each beam end in addition to the difference in panel zone strength and stiffness of each column. Not only is column A-1 less stiff than column B-1 by 50%, the panel zone shear strains of column A-1 exceeded five times the yield strain whereas the panel zone shear strains of column B-1 did not exceed the yield strain (see previous section and Fig. 5.15).

The second floor braced frame beam moments in Frame B are shown in Fig. 5.17. Figures 5.17a and 5.17c show the beam moment on the column A-1 side while Fig. 5.17b and 5.17d show the beam moment at the second floor on the column B-2 side. Figures 5.17a and 5.17b plot the moment as a function of the SDR while Figs. 5.17c and 5.17d plot the moment as a function of the measured beam rotation. The same trends noted above for the beams in Frame 1 were also observed in the beams of Frame B. For example, larger bending moments occurred in the beam at the shared column (B-1) side during negative drift than during the positive drift due to the impact of the slab stiffness when the slab is in compression. Additionally, the bending moments are greater on the shared column side than on the column B-2 side even though column B-2 is bent about its strong axis and is twice as stiff as the shared column bent about its weak axis. This is due to the flexibility of the panel zone of column B-2 which yielded considerably, similar to the panel zone of column A-1 in Frame 1 and discussed above. Additionally, smaller beam rotations occurred at column B-2 than at column B-1 because more of the frame deformation was due to column panel zone yielding at column B-2 and none occurred at column B-1 since the “panel zone” in this case consisted of both flanges since column B-1 was bent about its weak axis in this frame.

5.2.4 Distribution of Story Shear

The horizontal story shears are resisted by a combination of the horizontal component of brace axial force, and frame action of the beams and columns producing shear forces in the columns. The relative resistance is dependent on the stiffness of each element which is dependent on the axial deformation in the member and in the case of the braces, the post-buckling stiffness. Figure 5.19 shows the fraction of story shear resisted by the braces and frame action for each global deformation direction and story. The braces are shown in a bold, solid line; the braced frame beams and columns are shown in a thin, solid line, and the gravity frame is shown dashed. The resistances in the global Y-direction are shown in Figs. 5.19a and 5.19c while the resistances in the global X-direction are shown in Figs. 5.19b and 5.19d. The story shears were calculated from the crosshead actuators and column strain gauges as discussed previously. It can be seen that for SDRs below 0.3% the braces resisted approximately 80% of the story shear, the braced frame columns resist approximately 18% and the gravity frame columns resist 2%. The braces buckle at 0.3% SDR, lose stiffness and continue to soften at increasing drifts due to compressive P-δ effects and yielding in tension. As the braces soften, frame action resists a larger percentage of the story shear at larger drifts. At SDRs of 1%, the story shear resisted by the braces has dropped to values ranging between 50 and 65% of the total shear (a 38% drop in resistance relative to the initial resistance). At this SDR, the percentage of shear resisted by the gravity frames has increased to approximately 5% for Frame 2 and 10% for Frame A. The difference in resistance between these gravity frames is due to the fact that one column of Frame A is bent about its strong axis while both columns of Frame 2 are bent about their weak axis. This relative resistance is not indicative of every braced frame as it depends on the relative size of the braces and framing members. For example, column shear forces resisted between 15 and 30% of the total story shear at 1% SDR in the three-story frame tests by [2009] and [2009].

5.2.5 Distribution of Story Drift

Story drift distribution analysis shows which stories are contributing more to the overall frame deformation and suggests the story most likely to form a soft-story mechanism. Figure 5.20a and 5.20b show a plot of the first and second SDRs and the RDRs plotted as a function of the RDR for the frames being deformed in the Y-direction and X-direction, respectively. Only the negative drift range is shown for clarity, the behavior in the positive drift range is similar. The RDR line is a 45 degree line and a line below this line (larger negative drift) represents a story whose SDR is greater than the RDR and a line above (smaller negative drift) represents a story whose SDR is less than the RDR. It can be seen that in both the X and Y directions, the second story drift is greater than the roof and first story drifts. This is due mainly to fixity at the base of the columns providing greater rigidity to the first story columns. This distribution of story drift remains relatively constant throughout the experiment except at brace fracture when a large jump in the second story drift occurs. This can be seen in Fig. 5.20a at -1.6% RDR as a change in slope of the 2SDRY and 1SDRY lines.

5.3 BRBF Experimental Data Analysis

This section presents the data analysis of the second test specimen, the Buckling-Restrained Braced Frame. This analysis includes a discussion on the brace and gusset plate behavior, including estimated BRB design parameters such as ω and β. Additionally, braced frame beam and column behavior is discussed along with the column panel zone behavior.

5.3.1 Brace Behavior

Figure 5.21 shows the cyclic behavior of the BRBs in each story in each frame during the experiment. The vertical axes of the plots represent the estimated BRB axial load while the horizontal axes represent the brace elongation. Figure 5.22 shows the estimated horizontal story shear resisted by the BRBs as a function of the story drift ratio of the story of interest. The brace story shears were calculated by subtracting the story shears resisted by all of the columns in that story from the force measured by the laboratory actuators. The column story shears were found using the column strain gauge data and Euler-Bernoulli beam theory as described in Appendix C. This method was used to calculate the story shears resisted by the braces because elastic theory can not be used to calculate forces once the member has reached yield which the braces do at relatively small SDRs, on the order of 0.3%. No cyclic material tests were performed on the BRB steel and therefore, a reliable plastic material model was not available to determine the brace stresses following yield. The column strain gauges were placed in locations that remained elastic and therefore this estimate is more reliable.

The behavior of the BRBs in Frame 1 are shown in Figs. 5.21a and 5.21c while those in Frame B are shown in Figs. 5.21b and 5.21d. Note that the plots for the BRBs in the first story in both frames (Figs. 5.21c and 5.21d) show a solid line and a dashed line. The dashed line indicates that the force estimates are not accurate because the steel at the height of the strain gauges at the base of the columns had reached yield and therefore, the elastic theory used to estimate the column shear forces is no longer valid.

It can be seen in the figures that the BRBs display full hysteretic behavior with no negative stiffness or loss of resistance until brace fracture occurs. This fracture occurs at

point 'A' in Figs. 5.21a and 5.22a for Frame 1 and at point 'C' in Figs. 5.21b and 5.22b for Frame B and is followed by a complete loss of tensile resistance. Following this loss of tensile resistance, the frame was pushed further in the positive direction and it can be seen in the figures that there was still some reserve tensile strength. This reserve strength is thought to be due to the friction between the fractured core and the grout fill in the BRB casing along with mechanical force transfer due to the high-mode buckled deformation of the core. This reserve strength is much less than the yield force of the core.

Upon drift reversal following BRB core fracture, one to two inches of BRB axial deformation occurs with no increase in resistance. This is logical as the core has been fractured and a gap forms between the two fractured halves of the core. However, following the initial increase in compressive axial deformation (decrease in tensile elongation), the compressive resistance of the BRB does increase with a stiffness similar to its pre-fracture stiffness until point 'B' in Fig. 5.21a for Frame 1 and point 'D' in Fig. 5.21b for Frame B. At these points, the BRB compressive resistance begins to reduce dramatically. The compressive stiffness and resistance that follows core fracture appears to be due to each side of the fractured core bearing against each other as the brace is compressed. At points 'B' and 'D' where resistance is lost, it is thought that one side of the fractured core begins to deform and "curl" around itself. Indeed, postmortem investigation reveals that the core did indeed "curl" around itself as shown in Fig. 5.23. Additionally, there was no other visible damage to the BRB, restraining system, or connection region at points 'B' and 'D' in the figures that would explain this loss of compressive resistance.

Figure 5.21 also demonstrates the difference between the compressive and tensile resistances of the BRBs. All four BRBs displayed an overstrength in compression which is typical of BRBs and is due to the BRB casing and grout resisting part of the compressive load. At a BRB axial elongation of -3" (approximately 1.5% strain), the compressive resistance is 50% greater than the tensile resistance at 3" This will be discussed in greater detail in a subsequent discussion.

Comparison of Fig. 5.21 with Fig. 5.22 also shows the effect of the slip of the pin connecting the BRB clevis to the gusset plate. For ease of construction, the hole in the gusset plates and clevises must be slightly larger than the diameter of the pin. As a result, some

of the story drift is due to the pin slipping in the hole. This pin slip can be clearly seen in Fig. 5.22 as an increase in the story drift ratio with no accompanying increase in BRB resistance as the load in the brace reverses between tension and compression. Additionally, the gusset plate and pin may yield in the vicinity of the hole causing additional story drift and this is also seen in the plots as an increase in length of these horizontal portions of the curves at increasing SDRs. The amount of story drift attributable to this slip varies between 10 to 20% of the total story drift and the percentage is larger at smaller story drifts.

The BRB axial force-deformation envelopes are shown in Fig. 5.24. This plot was constructed by plotting the peak axial force that occurred at each peak axial deformation. It can be seen that the curves are essentially on top of each other in the positive region (tension) prior to and after yield and also display similar yield loads. In the compression region, the initial and post-yield stiffness of the BRBs are similar but the yield loads vary more. The calculated yield loads for each BRB and for each direction are listed in Table 5.3. Also listed in the table is the estimated BRB strain at yield and the SDR at yield. The estimated yield load of the BRBs based on the nominal area and measured yield stress of the cores is 123 kips. The measured tensile yield loads of the BRBs, P_{yt}, varied between 108 and 117 kips, or a five to 14% difference from the yield load ($A_g F_y$). Tensile yield occurred at SDRs that ranged between 0.29 and 0.33% which is similar to the SDRs at which conventional brace buckling occurs. As expected, the estimated yield loads in compression were larger than the tensile yield loads. The compressive yield loads ranged from 124 to 152 kips and occurred at SDRs ranging between 0.4 and 0.45% SDR. The yield loads are defined as the point at which the slope changes in Fig. 5.24.

The magnitudes of the axial stiffness, k_i, in each region are listed in Table 5.4 and are defined in Fig. 5.25. Also listed in the table is the analytical estimate of the axial stiffness of the core considering the varying sizes of the core and end regions. A comparison between the analytical estimate of the axial stiffness and k_3 shows that the analytical estimate provides an excellent prediction of the initial stiffness in tension, with the largest error being only 6%. The estimate is not as good when the BRB is in compression since it is extremely difficult to evaluate the interaction between the core and the grout and tubular casing.

BRB overstrength factors

Design of the BRBF beam and column elements is typically performed using the capacity design philosophy which applies the maximum expected force of the yielding elements to the beams and columns regardless of the design earthquake force. In order to do this, an accurate estimate of the post-yield BRB force must be made at the level of BRB deformation expected during a design event. This force is greater than the yield load due to strain hardening in the tensile and compression regions and overstrength in the compression region due to the casing and grout resisting part of the load.

Figure 5.26 plots the normalized, measured BRB axial tensile load as a function of the normalized BRB axial elongation for each BRB. The points shown are the loads that correspond to the peak deformation in each cycle and the line shown has been fit to the data points using a linear, least-squares regression. Also shown on the plots are the BRB deformations at which SDRs of 1, 2 and 3% occur. The strain hardening adjustement factor, ω, is the value of this normalized axial tensile load at the design story drift (AISC 2010).

Figure 5.27 plots the ratio of the measured BRB axial compressive load and the axial tensile load as a function of the normalized BRB axial elongation for each BRB. The first step in developing these curves was to fit a least-squares line through the compressive axial load data points at the axial deformation peaks in the same manner as was done for the lines shown in Fig. 5.26 except normalization was not done. This line was then divided by the least-squares line developed for the tensile half of the history. The quotient of these two lines results in the dashed curve shown in Fig. 5.27 and is defined as β, the compression strength adjustment factor. The solid linear curve shown is a result of fitting a least-squares line through the curve in the range shown and it can be seen that the two curves are essentaily on top of each other in this range. The slopes and y-intercepts of the lines shown in Figs. 5.26 and 5.27 are listed in Table 5.5.

Numerical values of these factors and their products are listed in Table 5.6 at SDRs of 1, 2 and 3%. The deformation expected during a design event is defined by the 2010 Seismic Provisions [AISC, 2010] as 2% or two times the *design story drift*, whichever is larger. The story drift limit commonly used for typical commercial buildings is 2% [ASCE, 2010]. It can

be seen that at this SDR, the average values of ω, β, and their product are 1.36, 1.43 and 1.94, respectively; indicating that for these BRBs, the design force on the connections and beams and columns in the braced frame is nearly twice the yield load of the braces. The value of $\omega\beta$ is consistent with that typically assumed at the beginning of design [Bruneau et al., 2011] while the value of ω is slightly more and β slightly less than that typically assumed.

BRB ductility demands

A common measure used to assess the performance of a BRB is the cumulative plastic ductility (CPD) and the maximum ductility demand. The CPD is the normalized summation of the inelastic axial deformation of the BRB and is described by Equation 5.1 below. The maximum ductility demand is simply the maximum axial deformation that occurs in the BRB divided by the yield deformation.

$$CPD = \sum \frac{U_{p_i}^{max} - U_{p_i}^{min}}{u_y} \tag{5.1}$$

where $U_{p_i}^{max}$ and $U_{p_i}^{min}$ are the maximum and minimum plastic axial deformations during each excursion i into the inelastic regime and u_y is the yield deformation.

The history of CPD as function of SDR for each BRB is shown in Fig. 5.28. Note that the dashed lines, which indicate the first-story BRBs, stop at approximately 2.7% SDR while the second-story BRBs continue due to the concentration of drift that occurred at the second stories. The values of the CPD at the end of the last complete cycle prior to core fracture are listed in Table 5.7 along with the maximum ductilities at the peak of the last complete cycle prior to brace fracture. The second-story BRBs, which ultimately fractured, reached CPD levels of 597 and 611 and maximum ductility demands of 20 and 17, respectively. The measured CPD for each brace are approximately three times the value of 200 required by the Seismic Provsisions [AISC, 2010].

BRB casing and grout forces

The overstrength in compression was discussed earlier and is clear from the measured force-deformation curves shown in Figs. 5.21. This overstrength is due to the casing and grout resisting part of the compressive load. Strain gauges were placed on two sides of the casing at the center of each BRB to estimate the amount of force resisted by the steel HSS tube casing (see Figs. 3.33). Unfortunately, it was not possible to place instrumentation within the grout and therefore, no independent estimate of the load resisted by the grout was made. The force was estimated as was done for SCBF braces by averaging the strains and multiplying them by the modulus of elasticity and the area of the HSS tube. The envelopes of these estimated casing forces for each BRB are shown in Fig. 5.29. It can be seen that very little force is resisted by the casing when the brace is in tension (positive drift) and remains relatively constant as the frame drift increases in the positive direction except for the sharp increase that is registered at brace fracture. In contrast, a relatively large force is resisted by the casing when the brace is in compression and increases with increasing frame drift. However, this estimated force does not make up for the difference between the measured BRB tensile and compressive loads at the same corresponding positive and negative drift levels. For example, at -3.7% SDR, the axial load in the BRB in the second story of Frame 1 is -300 kips while it is 200 kips at +3.7% SDR resulting in a compression overstrength magnitude of 100 kips. The estimated force in the casing is 40 to 48 kips at -3.7% SDR. This suggests that the grout is also resisting load approximately equal to the load in the steel casing. If the assumption is made that the strains in the grout are the same as the strains in the casing and that the grout has a modulus of elasticity of 3600 ksi ($57\sqrt{f'_c}$), the transformed area of the grout is 10 in^2, which is slightly less than the area of the casing (11.1 in^2). The estimated grout force based on this is then slightly less than the estimated casing force, the sum of which is slightly less than the measured compression overstrength. The remainder is minimal and can be accounted for by the load resisted by the casing in tension shown in Fig. 5.29.

BRB casing shift

The BRB axial elongation was measured with four string potentiometers as discussed in Section 3.6.2 and shown in Figs. 3.32 and 3.33. Previous experiments (for e.g. [Christopolus, 2005]) have demonstrated the tendency of the BRB casing to shift away from its origin as it undergoes cyclic deformation. This also occurred in the author's tests as demonstrated by the envelope plots in Fig. 5.30. The figures plot the average of the measured deformation of the string pot pairs at each brace end at each peak deformation level. The pots are labeled as "Top" for the average of the two pots at the top of the brace and "Bottom" for the average of the two pot measurements at the bottom of the BRBs. It can be seen that during the majority of the test, very little shift took place in the BRB in the second story of Frame 1 and the first story of Frame B (see Figs. 5.30a and 5.30d). Some shift did take place under compression beginning at -3% SDR for the BRB in the second story of Frame 1 and at ±2.5% SDR for the BRB in the first story of Frame B. Considerably more casing shift took place in the BRBs in the first story of Frame 1 and the second story of Frame B as seen in Figs. 5.30b and 5.30c. The complete cyclic history of each string pot may be found in Section E.4 in Appendix E.

5.3.2 Column Behavior

Column moments were calculated at the gusset reentrant corners based on a linear distribution of the moments calculated at the strain gauge locations as described in Appendix C. Figure 5.31 shows these bending moment envelopes as a function of the roof drift ratio for each braced frame column in each story in each direction. Each plot contains four curves, one for the moment at the gusset edge at the top and bottom of each column in the frame of interest. The trend of the curves was, for the most part, similar to the trends discussed in Section 5.2.2 for the SCBF experiment, and the relative magnitude between the moments in the different columns and locations was as expected. For example, the base of the columns were provided with full fixity as described in Section 3.5.1 and therefore attracted the largest bending moments. The shared column was the largest and stiffest and therefore attracted the largest moment as shown in Fig. 5.31c ("B-1b" in the figure) while the base of column

A-1 resisted the second largest moment ("A-1b").

All of the curves show varying levels of reduced stiffness as the drift increases indicating yielding of the columns or some other mechanism such as beam yielding or local buckling, which reduces the stiffness of the joint and results in a perceived softening of the column. For example, Fig. 5.31a shows the moment at the top column of the second story of column B-1 (labeled 'B-1t' in the figure) reaches its peak at approximately 2.0% RDR and softens at larger drifts. This is due to the extensive yielding and local flange and web buckling that initiated in the beam at this drift level and caused a reduction in stiffness of the beam with a corresponding reduction in column moment. The beam yielding and local buckling increased with increasing drift with a corresponding reduction in stiffness at this location and hence, the softening behavior shown in the figure.

The story shears resisted by the columns were estimated from the column end moments as described in Appendix C. The envelopes of the story shear resisted by the braced frame columns in each story in Frame 1 and Frame B are shown in Figs. 5.32a and 5.32b, respectively. These are shown as a function of the story drift ratio for the story of interest. The story shears resisted by the first story columns are typically but not always larger than those resisted by the second story columns with the differences on the order of 0 to 20% for a given SDR. This can be seen in Fig. 5.32a by a comparison of "A-1 1S" with "A-1 2S" (differences of up to 20%) or by comparing "B-1 1S" with "B-1 2S" (small to no difference), where "A-1 1S" indicates the first story of column A-1. Similar behavior is seen in Fig. 5.13b for the columns in Frame B. Additionally, the stiffer columns resist more shear in each story as can be seen by comparison of "A-1 1S" with "B-1 1S" in Fig. 5.32a, where B-1 is stiffer than A-1 and resists more shear. Similar behavior occurred in Frame B (5.32b) with column B-2 resisting more shear than B-1 due to the fact that column B-1 is bigger but is bent about its weak axis.

The envelopes of the story shears resisted by all of the columns including the gravity column are shown in Fig. 5.33. Four curves are shown with each plot corresponding to a story and a specific direction of frame deformation (X or Y, see Fig. 3.2 for coordinate system). The solid lines in each figure correspond to the two columns in the braced frame in the stated direction while the dashed lines correspond to the two columns in the gravity

frame. As expected, the braced frame columns carry a much larger portion of the story shear since the gravity frame beams are connected to the columns with flexible "shear-only" connections.

Column panel zone behavior

The braced frame column panel zone shear strains were estimated at the second floor using the measurements of the panel zone diagonal deformation recorded during the experiment with LVDTs as shown in Figs. 3.38 through 3.40 and calculated according to the method described in Appendix C. The second floor panel zone shear strain envelopes for the three braced frame columns are shown in Fig. 5.34 where Fig. 5.34a shows the magnitudes in radians and Fig. 5.34b shows the magnitudes normalized by the shear yield strain of the panel zone. It can be seen in Fig. 5.34b that the shared column panel zone (column B-1) normalized shear strain peaked at 1.3 at approximately 2.9% RDR, indicating yielding of the panel zone. The panel zone of column A-1 peaked at nearly ten times the yield strain at approximately 2.9% RDR while Column B-2 peaked at eight times the yield strain at approximately 2.9% RDR. As discussed in Section 5.2.2, this yielding in columns A-1 and B-2 is not surprising since calculations showed that the panel zone demands based on the beam reaching its plastic moment capacity were well in excess of its strength for columns A-1 and B-2 but not for column B-1.

The estimated panel zone shear strain in columns B-1 and B-2 was reasonably symmetric about the origin but was not for column A-1. This is unlike the panel zone shear strains estimated for column A-1 in the SCBF test which displayed more symmetry (see Fig. 5.15). It is not entirely clear what the reason for this is but the shear strain estimate was based on the average of two diagonal LVDTs as shown in the instrumentation layout Fig. 3.38. The envelopes of the normalized shear strain for both LVDTs on column A-1 used for the average are shown in Fig. 5.34c and it can be seen that in the negative direction there is a relatively large disparity between the two LVDT measurements after 1% SDR with very little change occuring in LVDT 4. It is highly unlikely that there was no diagonal deformation occurring and is more likely that the LVDT was sticking in this direction as LVDT 3 shows a clear

trend of increasing movement in the negative drift range and a symmetry about the origin. Therefore, LVDT 3 is most likely a better represenation of the shear strain at this location than the average of the two LVDTs.

5.3.3 Beam Behavior

Beam moments in the braced frames at the second floor were calculated at the gusset plate reentrant corners based on the strain gauges placed on the beams and the methodology discussed in Appendix C assuming a linear distribution of moment in the beams as was discussed thoroughly in Section 5.2.3. Figures 5.35a and 5.35c show the beam moment in Frame 1 at the second floor on the column A-1 side while Fig. 5.35b and 5.35d show the beam moment in Frame 1 at the second floor on the shared column side (column B-1). Figures 5.35a and 5.35b plot the moment as a function of the SDR while Figs. 5.35c and 5.35d plot the moment as a function of the measured beam rotation. The beam rotation was estimated from LVDTs placed on the top and bottom flanges as discussed in Section 3.6.4 and Appendix C and was based on average deformation over a 16" gauge length.

From Fig. 5.35 it can be seen that the behavior of each end of the second floor braced frame beams in Frame 1 is similar. The estimated moments are larger in the drift direction that places the composite slab in compression (positive drift for the column A-1 side and negative drift for the column B-1 side). The maximum moments and rotations reached at each end are approximately the same except that the maximum negative rotation of the column B-1 side is 20% greater than that on the column A-1 side. Additionally, there is more strength degradation on the column B-1 side (45% reduction from peak) than on the column A-1 side (16% reduction from peak). The larger amount of strength degradation on the column B-1 side is due to the larger amount of beam yielding and local flange buckling at the gusset reentrant corner (compare Fig. 4.71d with Fig. 4.69e). The large differences in behavior at each end that occurred during the first test (compare Fig. 5.16d with 5.16c) did not occur in the second test due to the web doubler that was installed on the beam at the column B-1 side due to the large amount of yielding and web deformation that occurred during the latter stages of the first test. This web doubler appears to have mitigated the

potential for larger amounts of damage from occurring at this location during the BRBF test.

The second floor braced frame beam moments in Frame B are shown in Fig. 5.36. Figures 5.36a and 5.36c show the beam moment on the column B-1 side while Fig. 5.36b and 5.36d show the beam moment at the second floor on the column B-2 side. Figures 5.36a and 5.36b plot the moment as a function of the SDR while Figs. 5.36c and 5.36d plot the moment as a function of the measured beam rotation. It can be seen from Fig. 5.36a and 5.36c that the moment in the beam at the column B-1 side reached and exceeded the plastic moment by approximately 20 and 40% in the positive and negative drift regions, respectively. The moment at the column B-2 side exceeded the yield moment but never reached the plastic moment (see Figs. 5.36b and 5.36d). Addtionally, the beam rotation at the column B-1 side is considerably larger than the rotation at the column B-2 side. It is believed that this occurred for two reasons. The first being that the panel zone shear strain of column B-2 exceeded the yield shear strain by nearly eight times and therefore a relatively larger part of the story deformation was due to panel zone deformation instead of beam deformation. This panel zone yielding reduced the stiffness of the joint and therefore the beam never reached its plastic moment. Additionally, this panel zone yielding was accompanied by large tears along the bolt lines and column flange tearing (see Figs. 4.63 through 4.65) which also reduced the stiffness of the joint and helped prevent the beam from resisting a large moment and undergoing plastic rotation.

Distribution of Story Shear

The horizontal story shears are resisted by a combination of the horizontal component of brace axial force, and frame action of the beams and columns producing shear forces in the columns. The relative resistance is dependent on the stiffness of each element which is dependent on whether or not the material has yielded. For example, as the BRB strain goes beyond the yield, the stiffness is drastically reduced because the modulus is drastically reduced. Figure 5.37 shows the envelopes of the fraction of story shear resisted by the braces and frame action for each global deformation direction and story. The braces are shown in

a bold, solid line; the braced frame beams and columns are shown in a thin, solid line, and the gravity frame is shown dashed. The resistances in the global Y-direction are shown in Figs. 5.37a and 5.37c while the resistances in the global X-direction are shown in Figs. 5.37b and 5.37d.

It can be seen that for negative drifts at approximately -0.13%, the BRBs resist approximately 42% of the story shear, frame action in the braced frames resists 53% and the gravity frame action resists 5% of the story shear. This is not the case at positive 0.13% SDR where the BRBs resist approximately 70% of the story shear, frame action in the braced frames resists20 to 30% and the gravity frame action resists between 3 and 7% of the story shear. The reason for this disparate relative resistances in the small drift range is due to the slip of the pin which results in very little brace resistance until the pin begins to bear on the BRB clevis and gusset plate. This engagement of bearing is seen as a steady increase in story shear resisted by the BRB as the negative drift increases from -0.13 to approximately -0.4% and in the positive range from zero to +0.3% where it reaches a peak and the BRB begins to yield and lose its initial stiffness.

Following the peak BRB story shear resistances at positive 0.3% SDR, the BRBs begin to resist relatively less story shear at increasing drifts. At 0.3% SDR, the BRBs resist between 70 and 75% of the total story shear, frame action of the braced frame resists 20 to 28% and the gravity frames resist less than 5% of the total shear. Between 0.8 to 1.6% SDR (depending on the frame), the BRBs and framing members in the braced frames resist equal amounts of the story shear as can be seen in Fig. 5.37. Beyond this point, frame action begins to resist a larger amount of the story shear.

In compression, the BRBs yield at approximately -0.4% SDR and resist approximately 70 to 75% of the story shear at this point. Frame action of the braced frame elements resist between 19 to 29% and the gravity frames resist less than 6%. Beyond compression yield, the BRBs begin to resist less of the story shear but unlike in tension, the BRBs resist a greater amount of the story shear at all SDRs. This is due to the compression overstrength in the BRBs discussed in Section 5.3.1. This overstrength increases with increasing negative SDR and at approximately -1.5% SDR, the relative resistance of the BRB begins to increase.

Distribution of Story Drift

Figure 5.38a and 5.38b show a plot of the first and second SDRs and the RDRs plotted as a function of the RDR for the frames being deformed in the Y-direction and X-direction, respectively. The RDR line is a 45 degree line and the locations of the SDR lines indicate how the drift is distributed between stories. It can be seen that in both the X and Y directions, the second story drift is greater than the roof and first story drifts. This is due mainly to fixity at the base of the columns providing greater rigidity to the first story columns. This distribution of story drift remains relatively constant throughout the experiment except at brace fracture and when the fractured brace curls over itself (see Section 5.3.1 for this discussion) and then a large jump in the second story drift occurs. This can be seen in Fig. 5.38a at -1.6% and 3.2% RDR and in Fig. 5.38b at -3.2% and 3.2% RDR as a change in slope of the 2SDRY and 1SDRY lines.

5.4 Analysis and Comparison of Powell's Tests

This section compares the author's first 3D experiment with Powell's planar experiments (see Sections 2.5.1 and 2.5.1) to evaluate the relative performance and the impact of bi-directional loading. In particular, the brace buckling loads, force-deformation behavior, energy dissipation and ultimate drift capacities will be discussed. Additionally, analysis will be presented for the determination of the effective length factors for the compression brace in a single-story X-configuration.

5.4.1 X-configured frame comparisons

This section compares the results of Powell's experiments discussed in the previous section with the author's 3D X-configured frame. In particular, the brace buckling loads, force-deformation behavior, energy dissipation and ultimate drift capacities will be discussed.

Figure 5.39a shows the envelopes of the sum of the absolute value of the brace axial loads in each story as a function of the story drift ratio. The brace axial loads were calculated by dividing the story shear resisted by the braces by the cosine of the brace angle from the horizontal. There is variation in the maximum loads resisted by the braces in each frame with the maximum difference on the order of 10 and 20% in the positive and negative drift ranges, respectively. Most display some hardening behavior in the post-yield range followed by slight softening. The center splice detail of HSS31 and the first test performed by the auther does not appear to have a significant effect on the peak strength of the bracing system. As seen in Fig. 5.39a, the peak strengths of the the author's experiments are similar to or larger than the peak strengths of HSS30 which the detail that provides full continuity at the splice. HSS30 and HSS31 have essentially the same peak strength in the positive drift range while the braces in HSS31 are 15% stronger than the braces in HSS30 in the negative drift range.

The center splice detail does not significantly impact the system drift capacity. Table 5.8 lists the maximum story drift ratios reached in the last complete cycle prior to brace fracture, if it occurred. The last column lists the total SDR range, which is the sum of the peak positive and negative values from the second and third columns. HSS30 and HSS31 had the

same SDR range prior to fracture of 3.83% with slightly different peaks in each direction. Frames 1 2S and B 2S of the 3D experiment had ranges prior to fracture of 3.61 and 3.77%. These were six percent less for Frame 1 2S and two percent less for Frame B 2S than the ranges HSS30 and HSS31. It is noted that Frame B 2S did not have a brace that fractured prior to stopping the test and therfore the potential was there for the drift capacity of this frame to exceed the others.

Figure 5.39b shows the cumulative energy dissipated by the braces as a function of the total story drift range. It can be seen that the braces in each frame dissipated energy at slightly different rates but the energy for all braces was bounded within a relatively small zone. As seen in the figure, HSS30 and HSS31 had similar dissipation to Frame 1 2S and 1S while Frame B 2S and 1S typically had smaller energies except at an SDR range of 3.83% where they were equal. Most importantly, the dissipated energy in the braces that fractured was essentially the same for each frame in the complete cycle immediately prior to brace fracture (differences of less than 10%). This indicates that the frames and the loading protocols were similar enough to provide a good comparison of behaviors and allow for confident use of the SDR ranges prior to fracture as a comparative parameter between the frames. In addition and most importantly, the results suggest minimal impact of the bi-directional loading demands on the frame performance.

The story drift ratios at the occurrence of buckling for the braces ranged between 0.23 to 0.4% (see Table 5.9). Buckling was determined from brace strain gauge data along with the global force-displacement behavior. Prior research (e.g., Tremblay 2002) and these experiments suggest that the buckling strength of this type of X-bracing system can be estimated assuming out-of-plane support at the brace intersection. Table 5.9 lists the experimentally measured buckling strengths for the two planar frames and the 3D frame. Also listed in the table are the story drift ratios at which buckling occurred and the actual brace length L_{br} defined in Fig. 5.40.

Interestingly, the measured buckling loads, $P_{cr,meas}$, for the spliced braces were greater than the buckling loads for the continuous braces in all cases except in HSS30 and the first story of Frame B in the 3D test. It is not entirely clear as to why this is the case and it is not consistent between frames with similar splice details.HSS30 was detailed with the splice

detail that provided full flexural continuity.

Using the estimated critical stress, F_{cr}, and measured material yield strengths given in Tables 2.5 and 3.1, the slenderness ratio required to reach F_{cr} for each brace was calculated. This slenderness ratio is denoted as $(KL/r)_{test}$ in Table 5.9. The values were used to calculate effective length factor, K, which correspond to the actual brace lengths L_{br}. The last column of Table 5.9 lists the experimentally determined effective length factors. They range between 0.46 to 0.56 with a mean value of 0.5 and a coefficient of variation of 6.3%, which is relatively small. For these systems, an effective length factor of 0.5 is recommended in conjunction with the actual brace length, L_{br}, defined in Fig. 5.40.

5.5 Drift and Ductility Capacity Comparison

The drift capacities of the planar BRBF system experiments described in Section 2.5 are shown in Fig. 5.42. The drift capacity is defined as the sum of the largest absolute value of the negative and positive drifts achieved prior to or during the last complete cycle before brace fracture. Also shown in the figure is the range of drift capacities of the SCBF system experiments shown in Fig. 5.41. It can be seen that all of the frames tested by Uriz [2005] and Christopolus [2005] fall below the maximum drift capacity of the SCBF experiments. This is important as it is a commonly-held belief that BRBFs are superior to SCBFs but as this shows, that is not always the case. The drift capacities of all of the BRBs that fractured during the system tests performed by Fahnestock [2006] (all but the fourth story) and those that fractured during the author's experiments are higher than the maximum SCBF drift capacity.

The maximum ductilities achieved by the BRBs during the system tests are shown in Fig. 5.43. The ductility is defined as the maximum brace deformation divided by the yield deformation. These generally follow the trend for the drift capacities shown in Fig. 5.42 but not exactly as the two are related, but the drift capacities are the sum of the maximum positive and negative drift while the maximum ductility is only the maximum value observed in one direction. All maximum ductilities are greater than 10 then with only two less than 15. These values are comparable to the maximum ductilities measured during BRB component tests [Merritt et al., 2003; Black et al., 2002] which ranged from 10 to 15.

A comparison of the cumulative ductility demands for the BRBF system tests are shown in Fig. 5.44. The cumulative ductility is the sum of the total cyclic plastic deformation divided by the yield deformation. These ranged from 219 to 611 and all were above the prequalification limit of 200 prescribed by the Seismic Provisions [AISC, 2010]. The cumulative ductilities of the author's BRBs were the highest and could be the reason that these same BRBs had lower maximum ductilities than those tested by Fahnestock.

Table 5.1: SCBF peak story shear resisted by both braces in a story

Braces	Peak brace story shears (kips)	
	+ Drift	- Drift
Frame 1 2S	182	-170
Frame 1 1S	180	-163
Frame B 2S	195	-195
Frame B 1S	173	-170

Table 5.2: SCBF experimentally measured buckling loads

Brace			$P_{cr,meas}$ (kips)	SDR at $P_{cr,meas}$ (%)
Frame 1	2S	Discontinuous	88	0.31
		Continuous	72	0.31
	1S	Discontinuous	79	0.28
		Continuous	68	0.26
Frame B	2S	Discontinuous	81	0.3
		Continuous	78	0.34
	1S	Discontinuous	62	0.24
		Continuous	70	0.23

Table 5.3: BRB yield values

BRB	Compression			Tension		
	P_{yc} (kip)	ϵ_{yc} ($\mu\epsilon$)	SDR (%)	P_{yt} (kip)	ϵ_{yt} ($\mu\epsilon$)	SDR (%)
Frame 1 2S	-124	-1156	-0.4	114	1464	0.33
Frame 1 1S	-143	-1510	-0.4	117	1593	0.3
Frame B 2S	-135	-1140	-0.42	108	1456	0.3
Frame B 1S	-152	-1593	-0.45	114	1442	0.29

Table 5.4: BRB axial pre- and post-yield stiffness, k/in. (see Figure 5.25)

BRB	k_1	k_2	k_3	k_4	Analytical k_3
Frame 1 2S	54	770	576	23	572
Frame 1 1S	42	699	527	21	563
Frame B 2S	43	888	543	28	572
Frame B 1S	44	701	547	22	563

Table 5.5: BRB overstrength curve-fitting parameters

BRB	ω		β	
	m	b	m	b
Frame 1 2S	36.9×10^{-3}	0.96	26.7×10^{-3}	1.12
Frame 1 1S	37.8×10^{-3}	0.96	17.3×10^{-3}	1.23
Frame B 2S	49.9×10^{-3}	0.95	6.4×10^{-3}	1.28
Frame B 1S	36.5×10^{-3}	0.96	15.6×10^{-3}	1.34
Average	40.3×10^{-3}	0.96	16.5×10^{-3}	1.24

Table 5.6: BRB overstrength factors at 1, 2 and 3% story drift ratios

BRB	ω			β			$\omega\beta$		
	1%	2%	3%	1%	2%	3%	1%	2%	3%
Frame 1 2S	1.14	1.34	1.53	1.26	1.42	1.54	1.44	1.9	2.36
Frame 1 1S	1.13	1.31	(1.48)	1.31	1.4	1.47	1.48	1.83	2.18
Frame B 2S	1.19	1.42	1.63	1.31	1.35	1.37	1.56	1.92	2.23
Frame B 1S	1.16	1.37	(1.48)	1.43	1.53	1.57	1.66	2.1	2.32
Average	1.16	1.36	1.53	1.33	1.43	1.49	1.54	1.94	2.27

Table 5.7: BRB experimental ductility demands (at the end of the last complete cycle prior to core fracture)

BRB	Core fracture?	Ductility demand	
		Maximum	Cumulative
Frame 1 2S	Yes	20	611
Frame 1 1S	No	12	377
Frame B 2S	Yes	17	597
Frame B 1S	No	16	391

Table 5.8: Maximum SDRs in last complete cycle prior to brace fracture (percent) for single-story X-configured frames

Frame	Brace fracture?	Positive	Negative	Total range
HSS30	Yes	1.67	-2.16	3.83
HSS31	Yes	1.83	-2.0	3.83
Frame 1 2S	Yes	1.78	-1.83	3.61
Frame 1 1S	No	1.41	-1.35	2.76
Frame B 2S	No	1.92	-1.85	3.77
Frame B 1S	No	1.5	-1.57	3.07

Table 5.9: Brace buckling strengths and estimated effective length factors for single-story X-confgiured frames

Brace	$P_{cr,meas}$ (kips)	$F_{cr,meas}$ (ksi)	$\text{SDR}_{buckling}$ (percent)	L_{br} (in.)	$(KL/r)_{test}$	K
HSS30 cont	98	40.2	0.4	168	71	0.47
HSS30 discont	93	38.1	0.28	168	75	0.50
HSS31 cont	96	39.3	0.28	168	73	0.48
HSS31 discont	100	41.0	0.29	168	69	0.46
Frame 1 2S cont	72	29.5	0.31	188.2	91	0.54
Frame 1 2S discont	88	36.1	0.31	188.2	79	0.47
Frame 1 1S cont	68	27.9	0.26	199	95	0.53
Frame 1 1S discont	79	32.4	0.28	199	86	0.48
Frame B 2S cont	78	32.0	0.34	188.2	86	0.51
Frame B 2S discont	81	33.2	0.3	188.2	84	0.50
Frame B 1S cont	70	28.7	0.23	199	93	0.52
Frame B 1S discont	62	25	0.24	199	100	0.56
					MEAN	0.50
					COV	6.3%

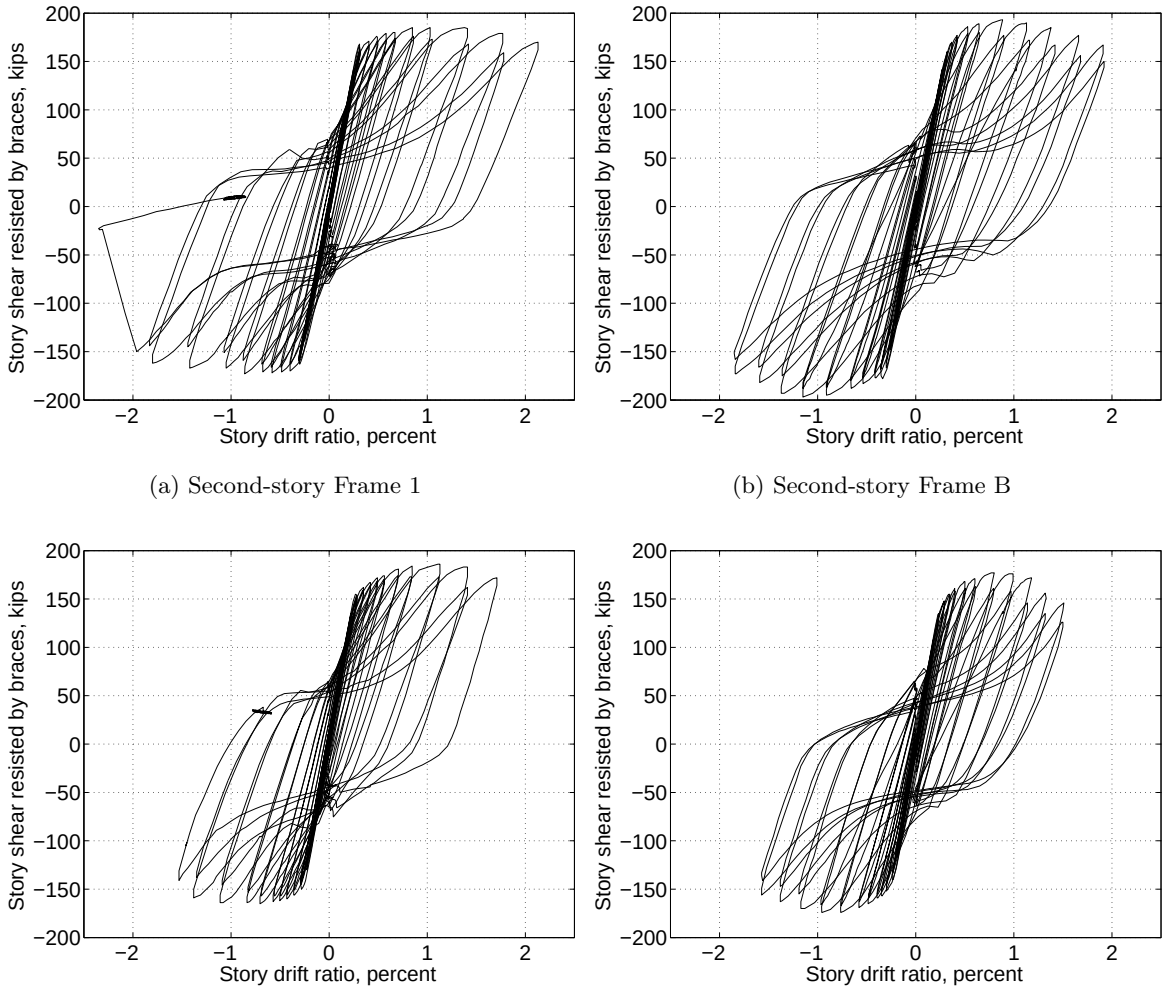

(a) Second-story Frame 1

(b) Second-story Frame B

(c) Fisrt-story Frame 1

(d) First-story Frame B

Figure 5.1: Story shear resisted by braces in each story (SCBF test)

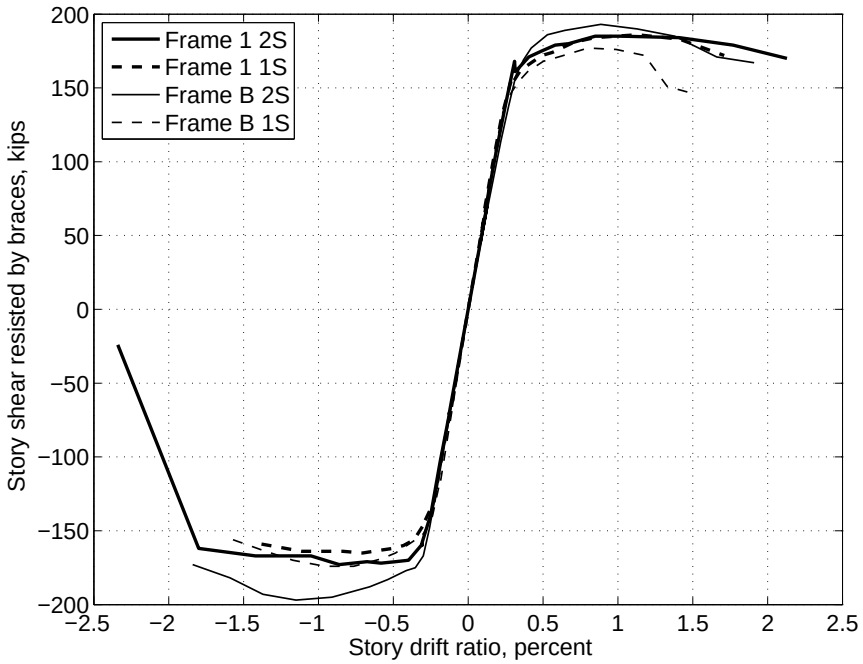

Figure 5.2: Envelopes of story shear resisted by both braces in each story, calculated by subtracting column shears from the actuator forces (SCBF test)

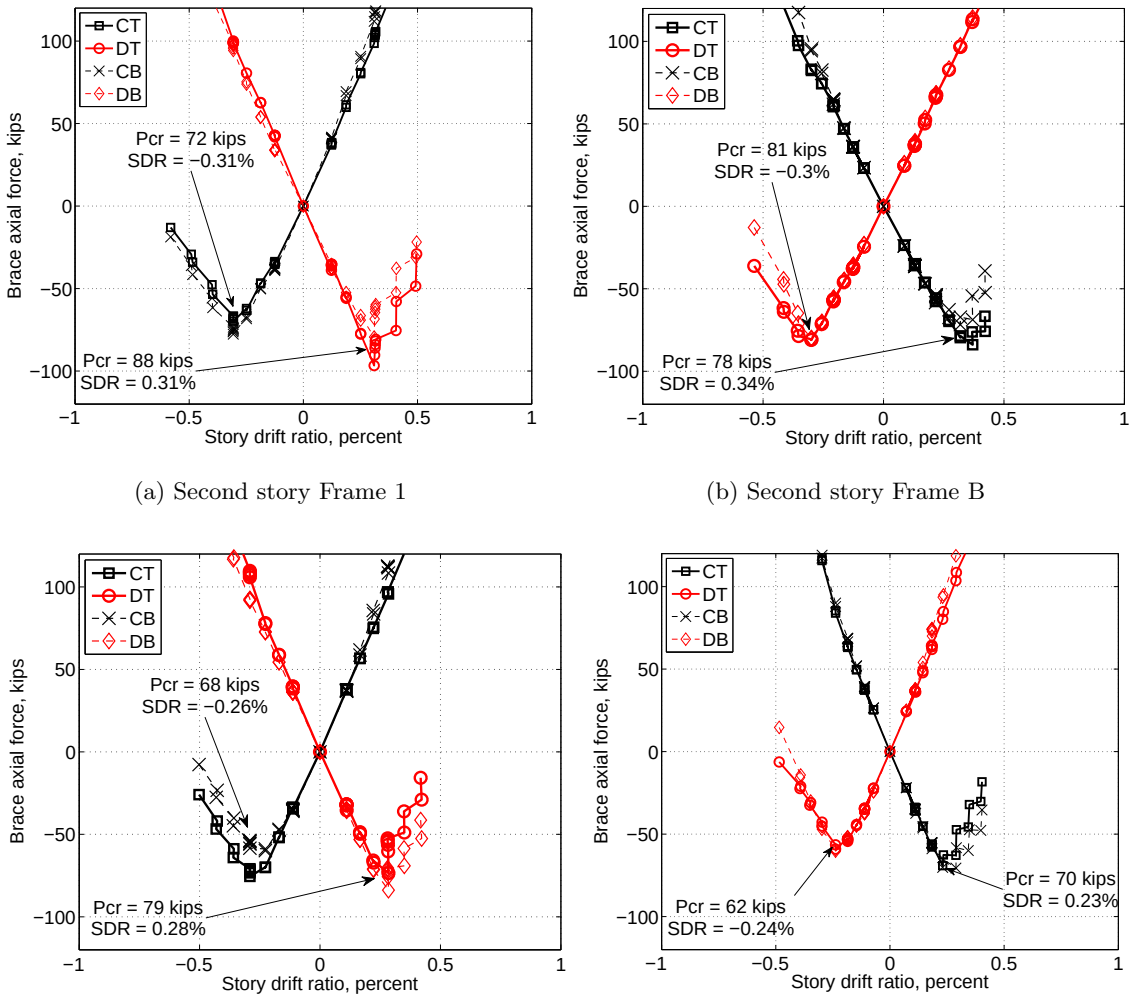

(a) Second story Frame 1

(b) Second story Frame B

(c) First story Frame 1

(d) First story Frame B

Figure 5.3: Brace axial force calculated from brace strain gauges, not valid after yielding at 0.5% SDR. (CT - strain gauges attached to the top of the continuous brace. DT - strain gauges attached to the top of discontinuous brace. CB - strain gauges attached to the bottom of continuous brace. DB - strain gauges attached to the bottom of discontinuous brace.)

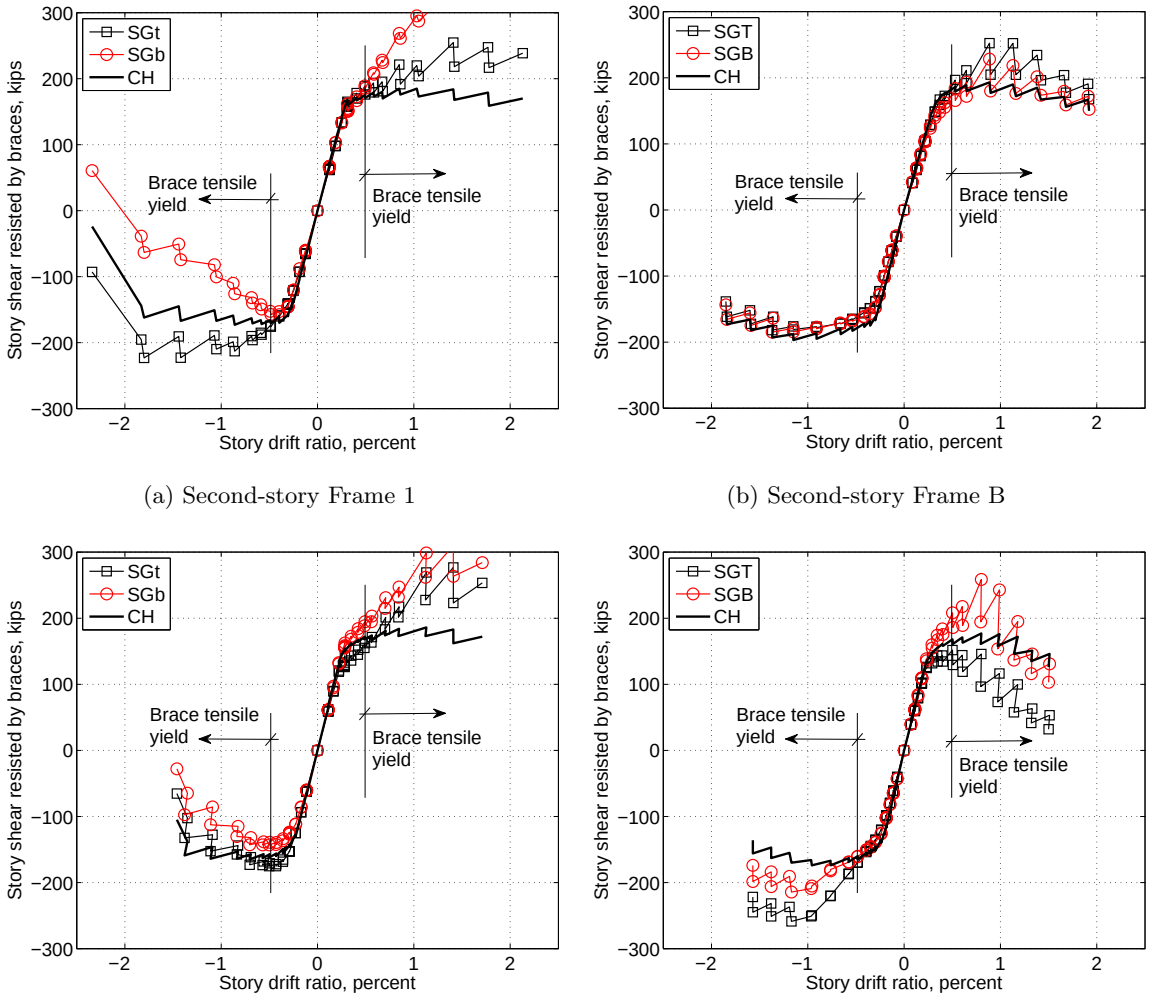

(a) Second-story Frame 1

(b) Second-story Frame B

(c) Fisrt-story Frame 1

(d) First-story Frame B

Figure 5.4: Comparison of story shears resisted by brace as calculated from top (SGt) and bottom (SGb) brace strain gauges and the crosshead actuator forces minus the column shears (CH), not valid after yielding (SCBF test)

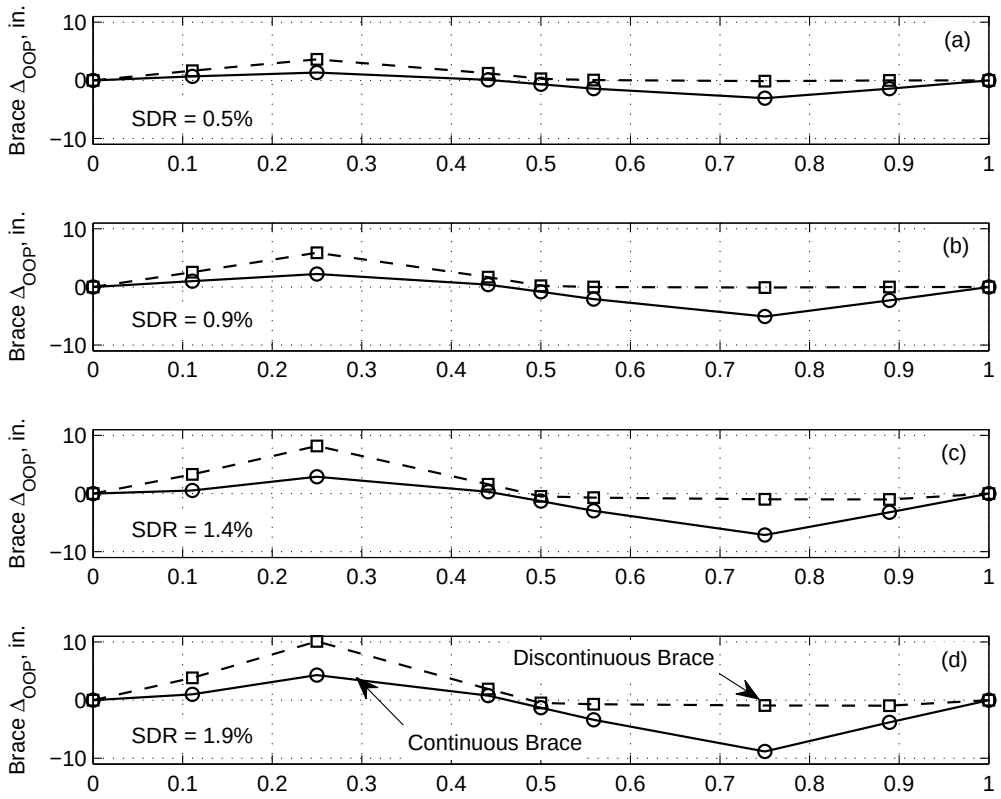

Figure 5.5: Out-of-plane brace deformation at select story drift ratios in continuous and discontinuous braces in the second story of Frame B

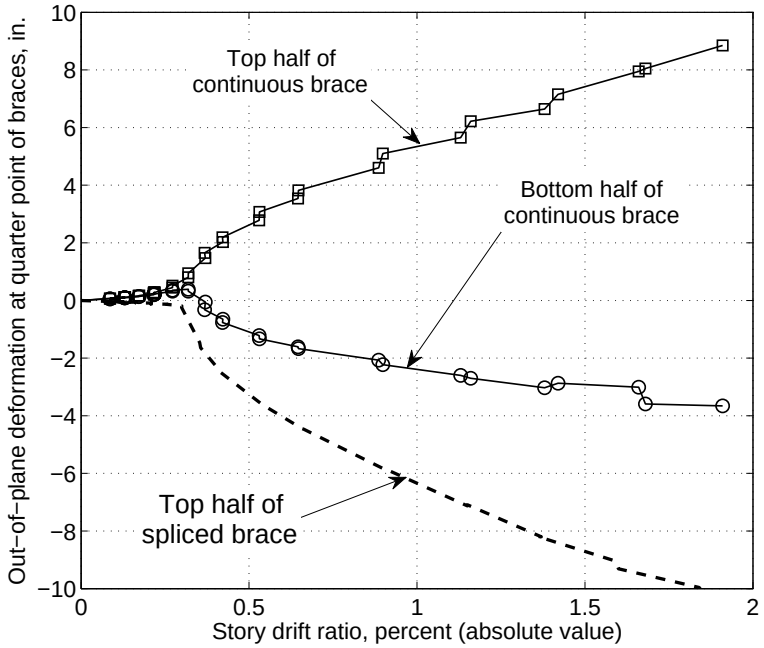

Figure 5.6: Comparison of OOP deformation of second story braces in Frame B at the quarter point of the continuous brace and the quarter point of the top part of the spliced brace (the bottom part did not buckle)

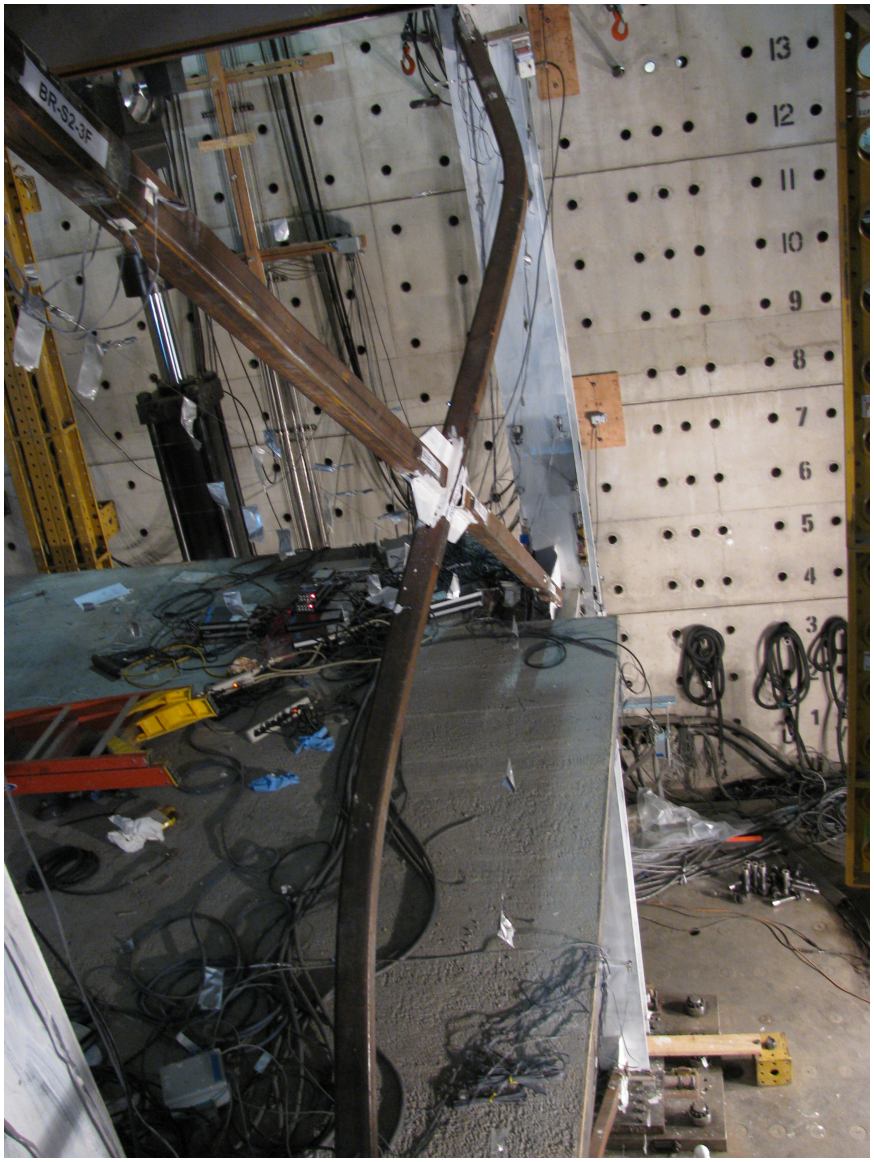

Figure 5.7: Second-story Frame B brace OOP deformation at 1.9% 2SDRX

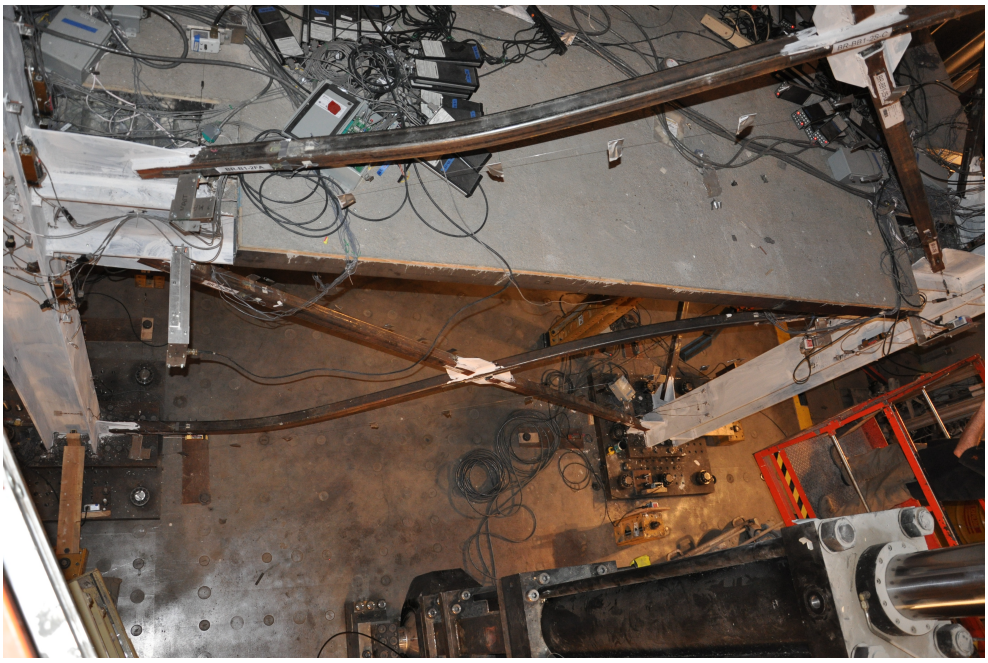

(a) -0.83% SDR

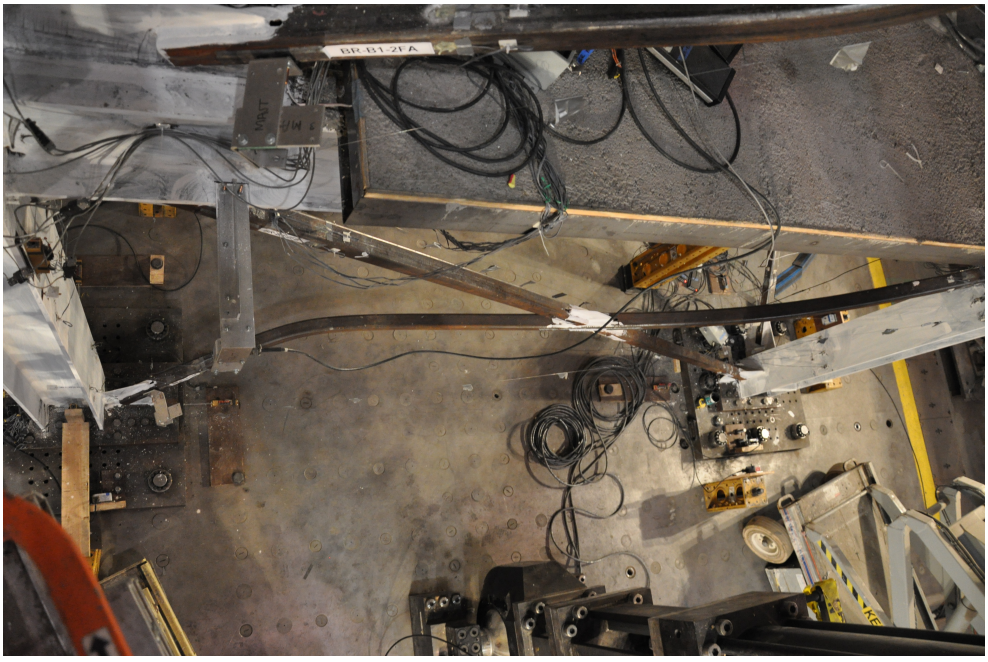

(b) -1.4% SDR

Figure 5.8: BB1 1S Buckled Brace Shapes



Figure 5.9: BB1 1S Buckled Brace at Zero Drift Cycle 33

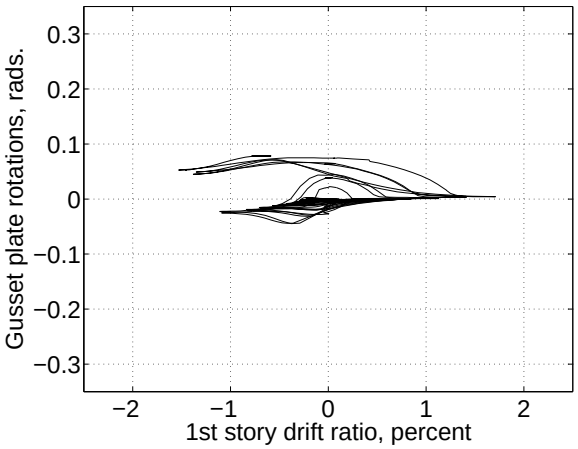

(a) below 2nd floor, column A-1

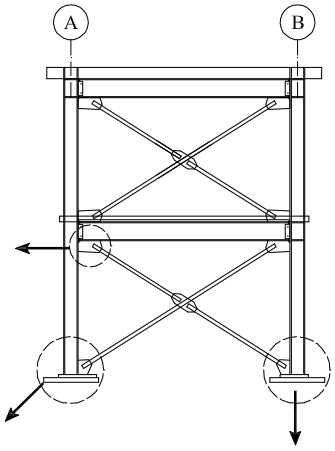

(b)

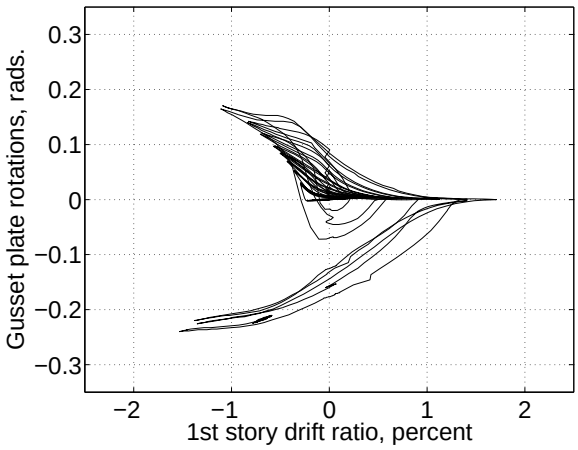

(c) base of column A-1

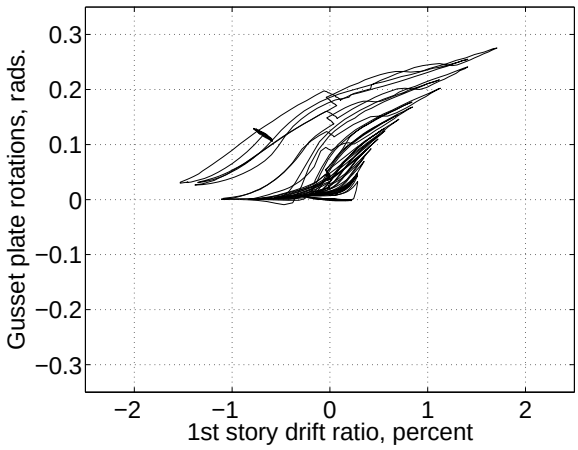

(d) base of column B-1

Figure 5.10: Gusset plate rotations in first story of Frame 1

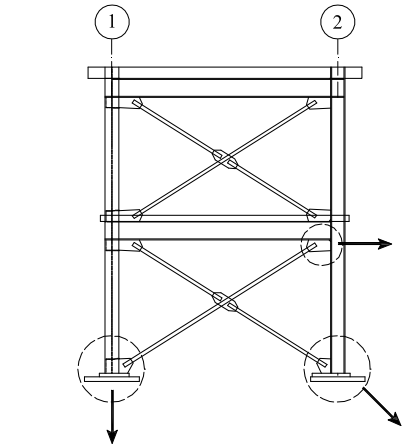

(a)

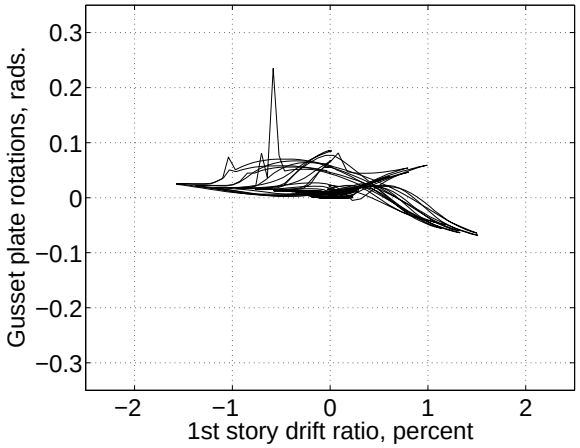

(b) below second floor, column B-2

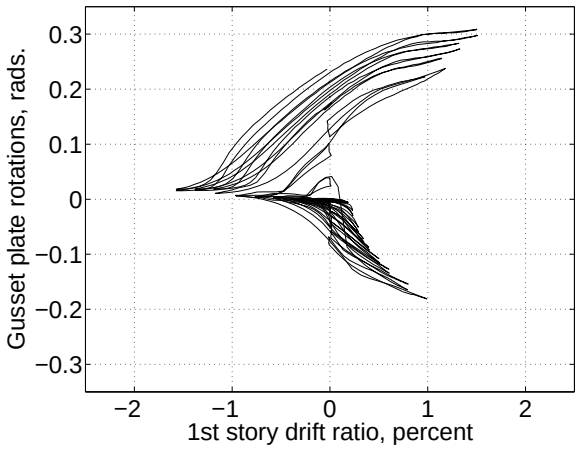

(c) base of column B-1

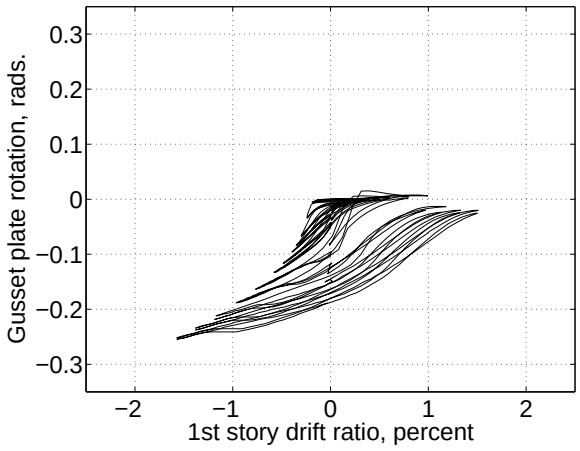

(d) base of column B-2

Figure 5.11: Gusset plate rotations in first story of Frame B

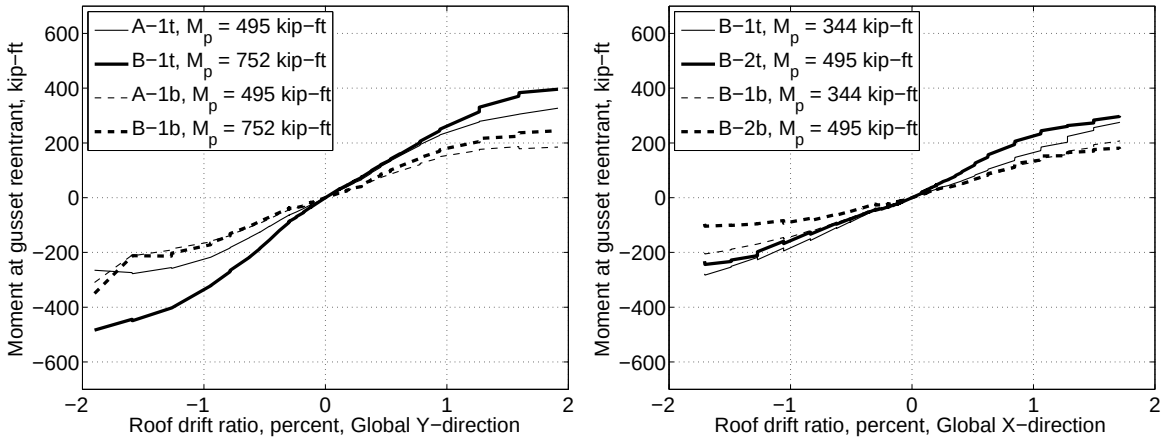

(a) Second story Frame 1

(b) Second story Frame B

(c) First story Frame 1

(d) First story Frame B

Figure 5.12: SCBF column moment envelopes at gusset plate reentrant corners. (Legend indicates the column as defined by the grid intersections along with the location in the story. A-1t indicates the moment at the gusset reentrant corner at the top of the story of column A-1)

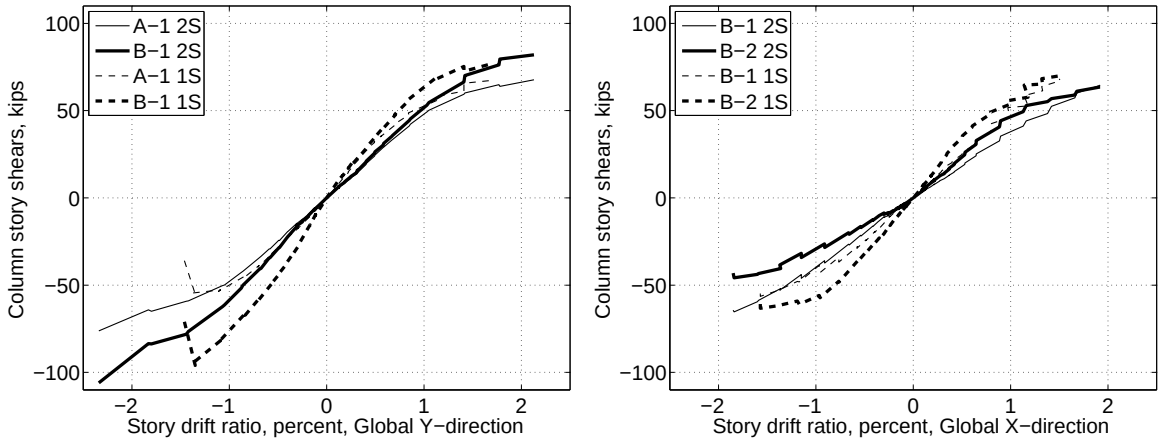

(a) Braced Frame 1, global Y-direction

(b) Braced Frame B, global X-direction

Figure 5.13: SCBF column story shear envelopes (Legend indicates column as defined by the grid intersections along with the story. "A-1 2S" indicates the second story shear of column A-1)

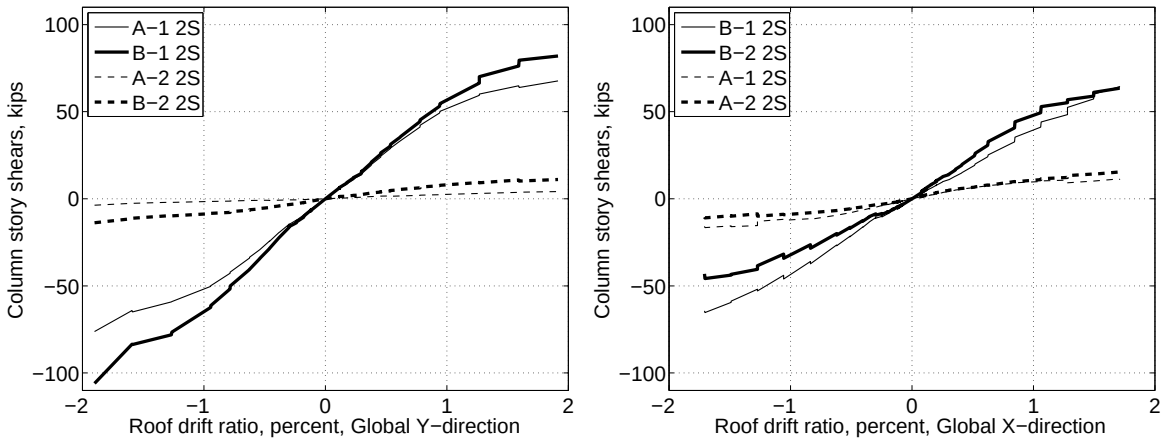

(a) Global Y-direction, second story

(b) Global X-direction, second story

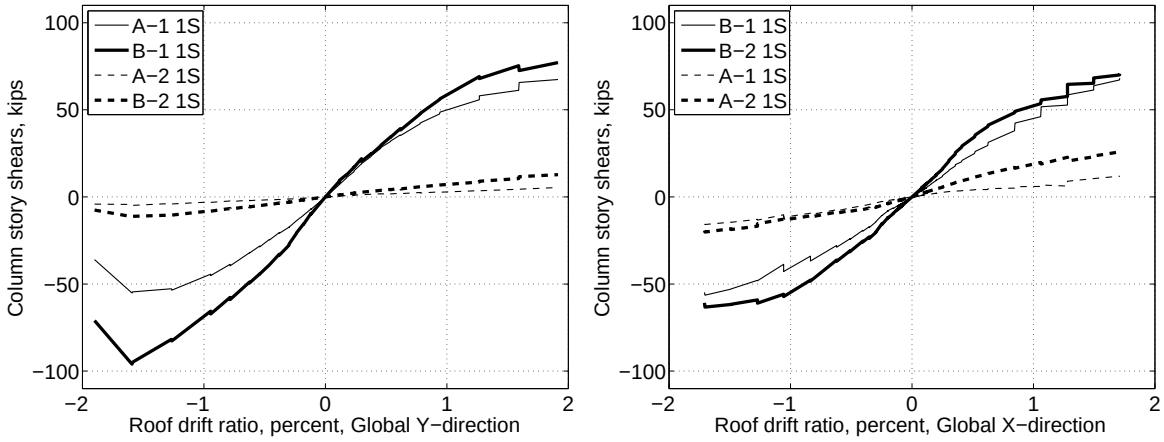

(c) Global Y-direction, first story

(d) Global X-direction, first story

Figure 5.14: SCBF column story shears in each story and global direction. (Legend indicates column as defined by the grid intersections along with the story. "A-1 2S" indicates the second story shear of column A-1)

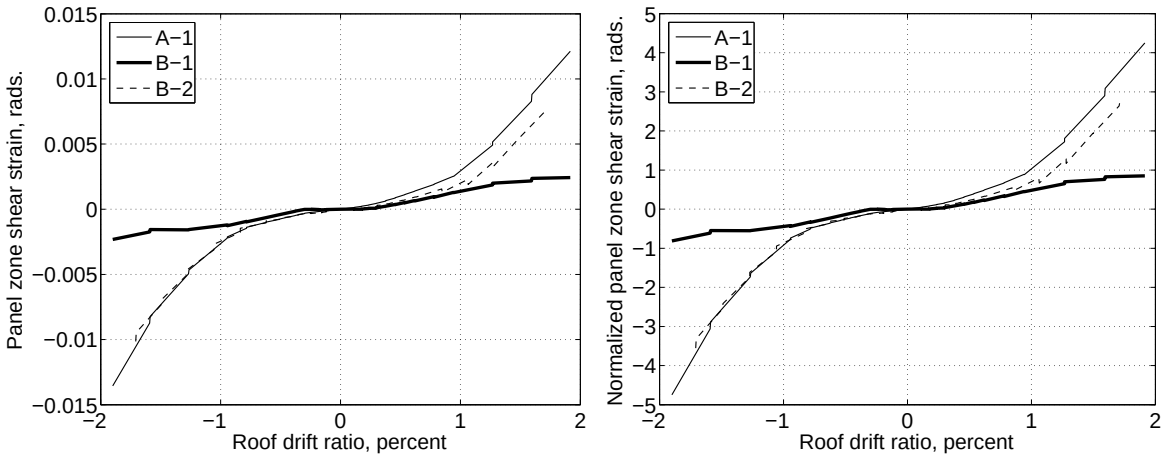

(a) (b)

Figure 5.15: Column panel zone deformations at second floor joint: (a) shear strain; (b) shear strain normalized by the yeild strain.

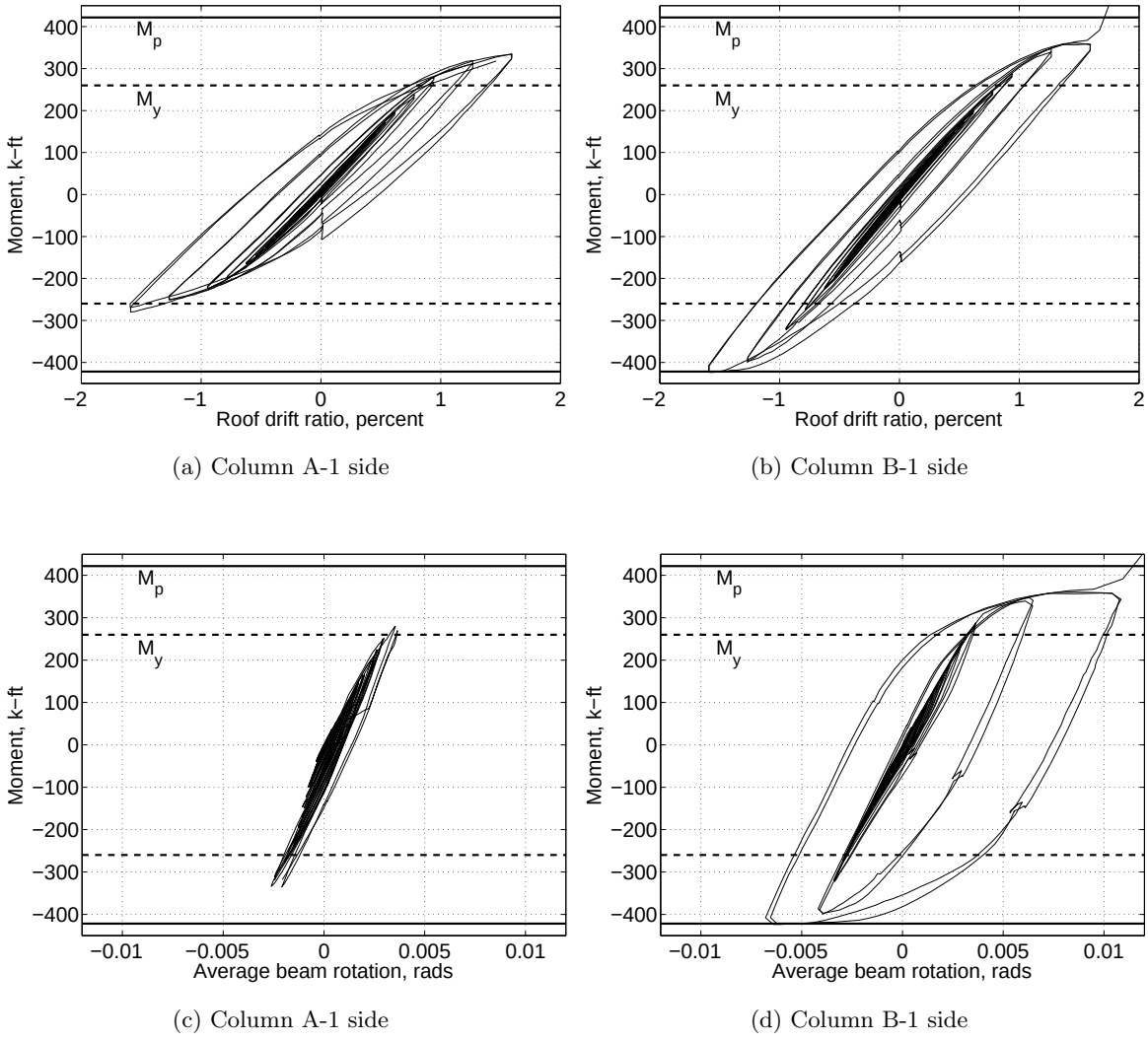

(a) Column A-1 side

(b) Column B-1 side

(c) Column A-1 side

(d) Column B-1 side

Figure 5.16: Second floor braced frame beam behavior in Frame 1: (a) moment at gusset plate reentrant corner vs. 2SDRY at column A-1 side; (b) moment at gusset plate reentrant corner vs. 2SDRY at column B-1 side; (c) moment at gusset plate reentrant corner vs. average beam rotation at column A-1 side; (b) moment at gusset plate reentrant corner vs. average beam rotation at column B-1 side.

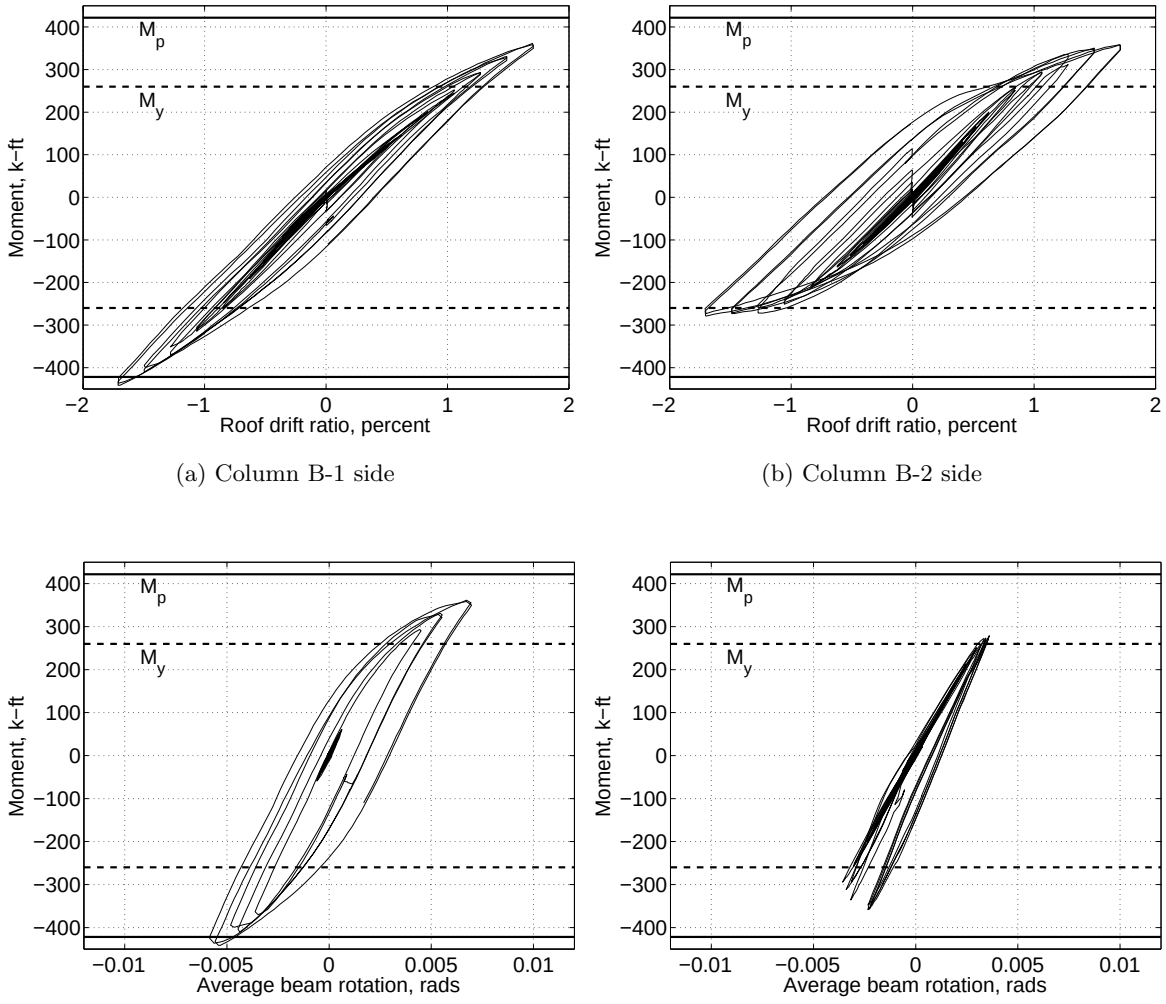

(a) Column B-1 side

(b) Column B-2 side

(c) Column B-1 side

(d) Column B-2 side

Figure 5.17: Second floor braced frame beam behavior in Frame B: (a) moment at gusset plate reentrant corner vs. 2SDRX at column B-1 side; (b) moment at gusset plate reentrant corner vs. 2SDRY at column B-2 side; (c) moment at gusset plate reentrant corner vs. average beam rotation at column B-1 side; (b) moment at gusset plate reentrant corner vs. average beam rotation at column B-2 side.

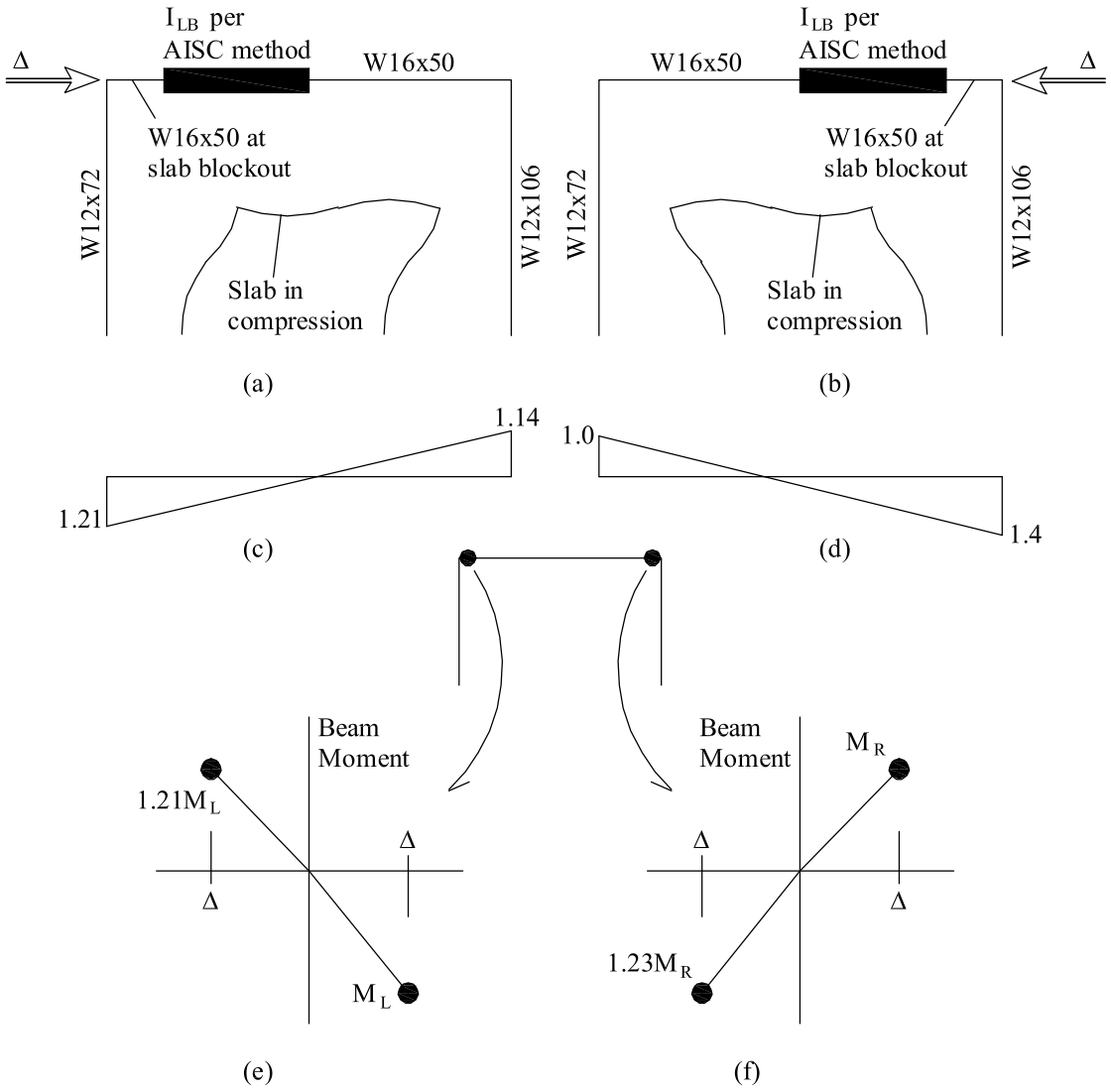

Figure 5.18: Frame analysis to show effect of composite slab on flexural behavior of frame: (a) SAP model with left-side slab in compression; (b) SAP model with right-side slab in compression; (c) normalized moment diagram from push to the right; (d) normalized moment diagram from push to the left; (e) normalized moment-displacement curve for left-side of beam at column joint; (f) normalized moment-displacement curve for right-side of beam at column joint.

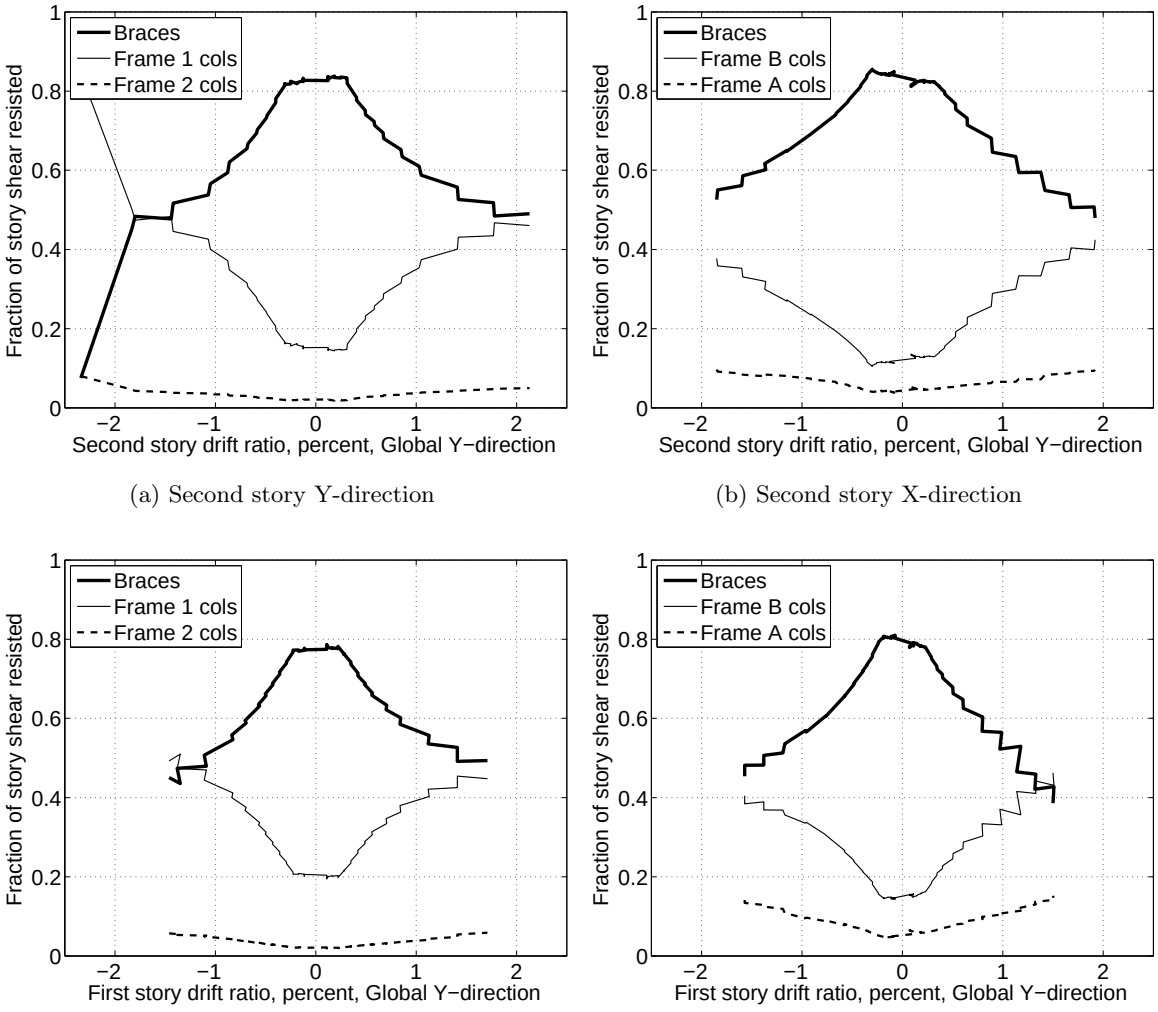

(a) Second story Y-direction

(b) Second story X-direction

(c) First story Y-direction

(d) First story X-direction

Figure 5.19: Distribution of story shear to braces, braced frame beams and columns, and gravity bay beams and columns.

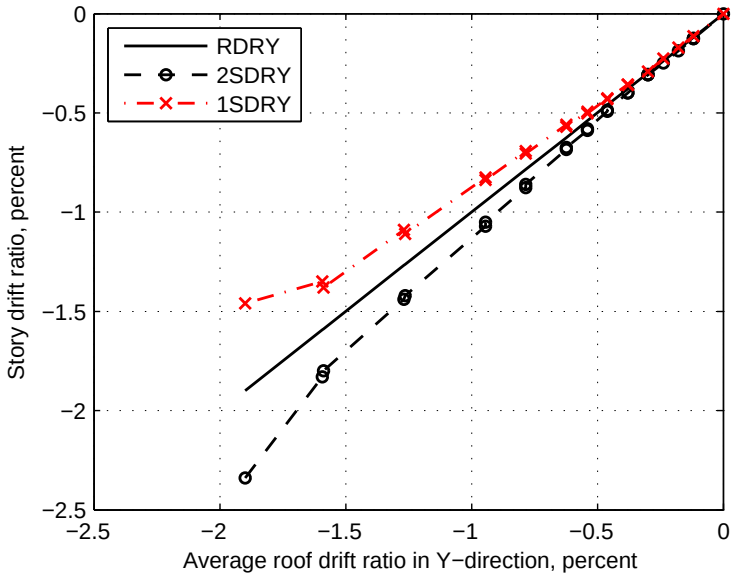

(a) Y-direction

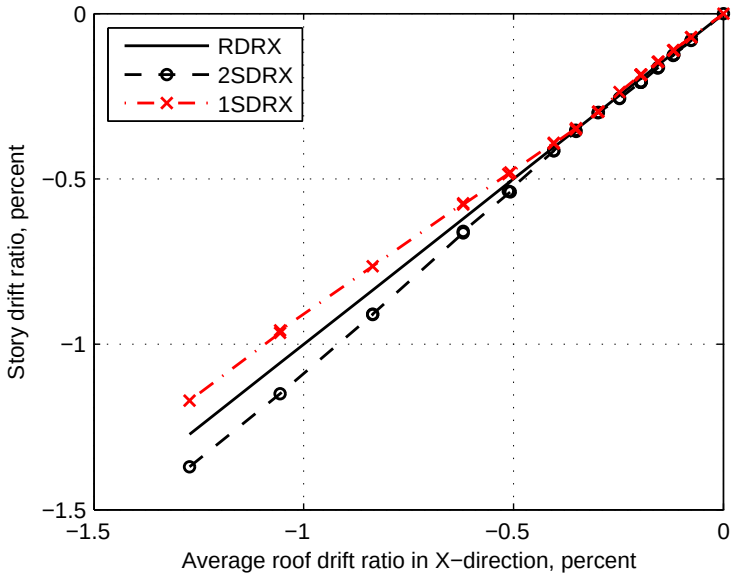

(b) X-direction

Figure 5.20: Story drift distribution in X and Y directions (SCBF test)

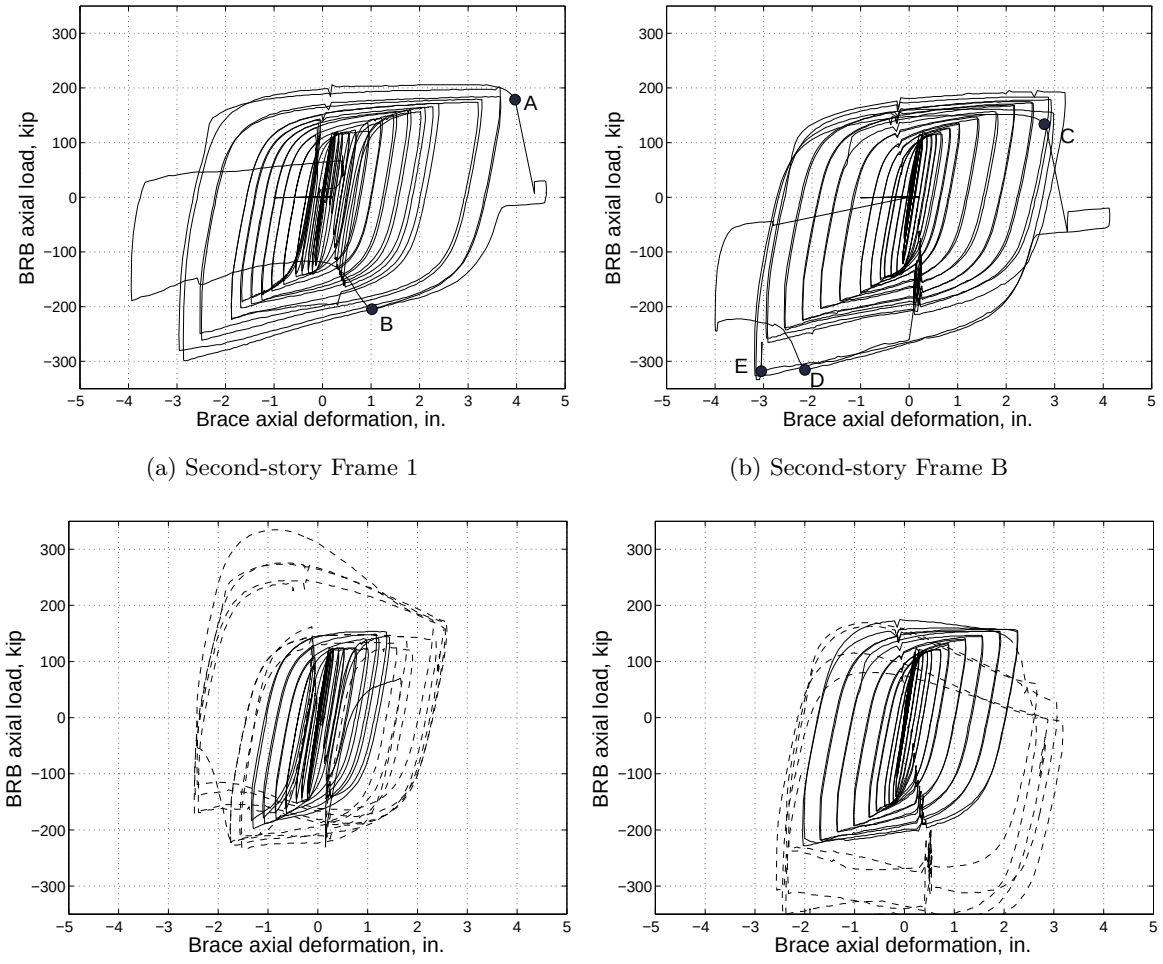

(a) Second-story Frame 1

(b) Second-story Frame B

(c) Fisrt-story Frame 1

(d) First-story Frame B

Figure 5.21: Brace axial load vs. brace axial deformation (BRBF test). Note: dashed line indicates column strain gauges above yield and force estimate no longer accurate.

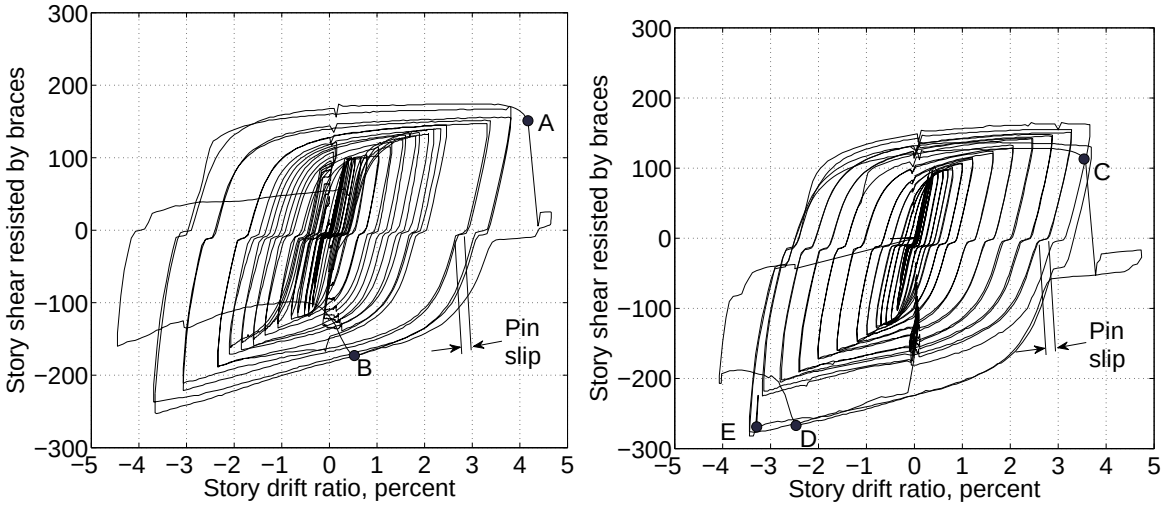

(a) Second-story Frame 1

(b) Second-story Frame B

(c) First-story Frame 1

(d) First-story Frame B

Figure 5.22: Story shear resisted by braces in each story as a function of SDR (BRBF test). Note: dashed line indicates column strain gauges above yield and force estimate no longer accurate.



Figure 5.23: Fractured BRB core. Note part of the core on the left side has curled due to compressive bearing following fracture.

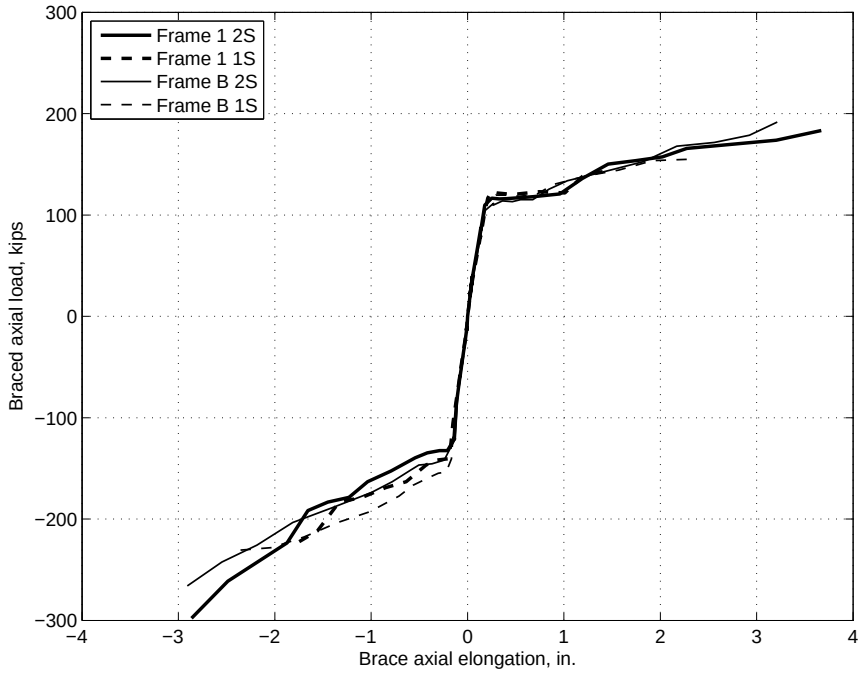

Figure 5.24: Envelope of brace axial load vs. brace axial deforamtion (BRBF test)

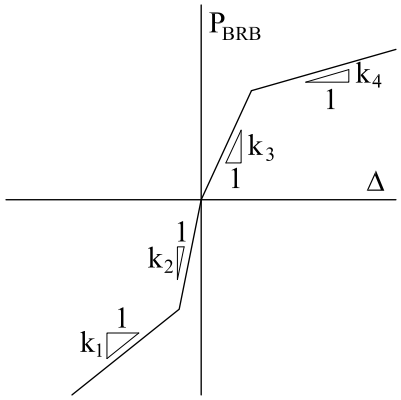

Figure 5.25: Definition of BRB axial stiffness (see Table 5.4)

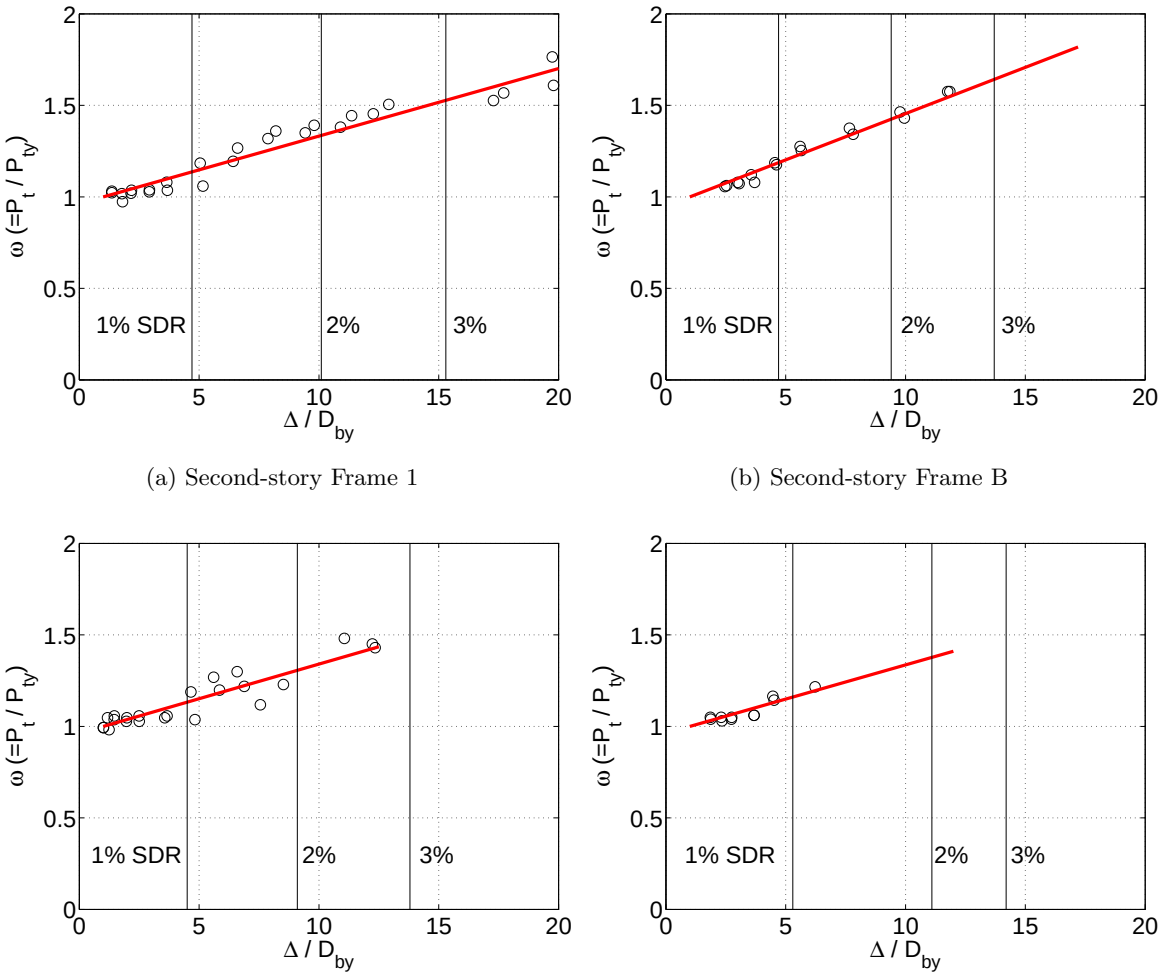

(a) Second-story Frame 1

(b) Second-story Frame B

(c) First-story Frame 1

(d) First-story Frame B

Figure 5.26: Tension strain hardening adjustment factor, ω vs. normalized brace axial deformation

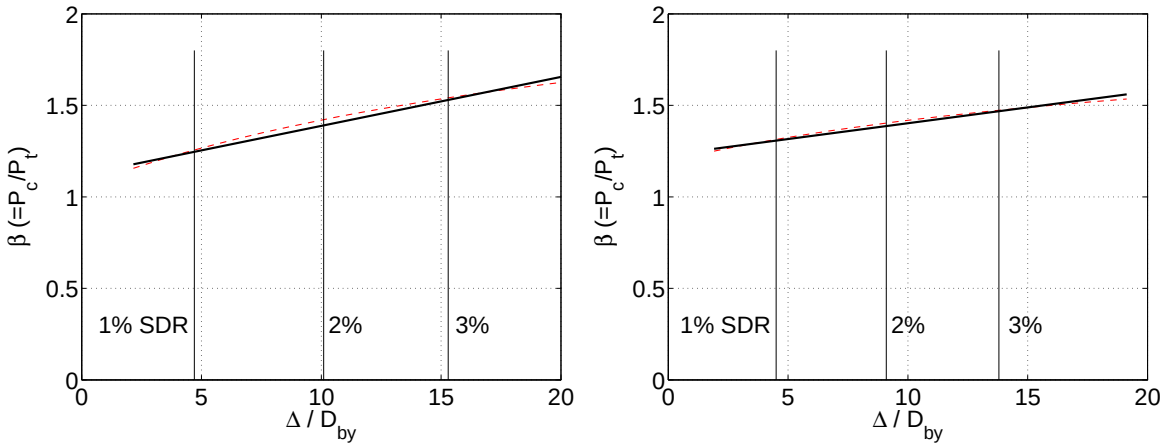

(a) Second-story Frame 1

(b) Second-story Frame B

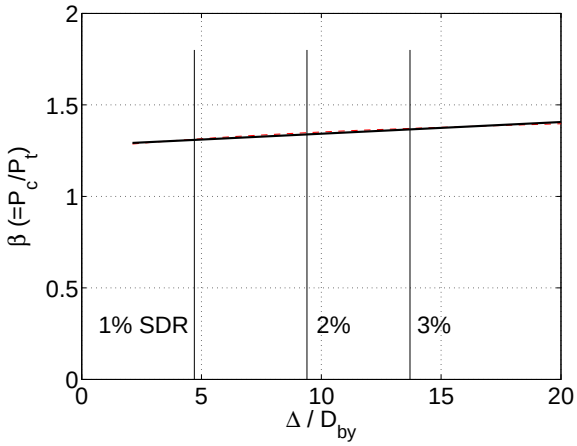

(c) First-story Frame 1

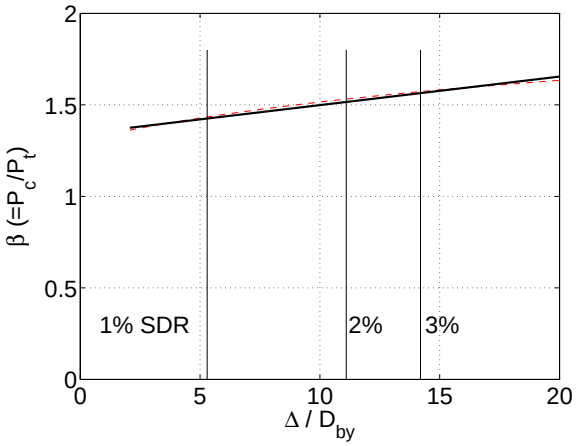

(d) First-story Frame B

Figure 5.27: Compression strength adjustment factor, β vs. normalized brace axial deformation

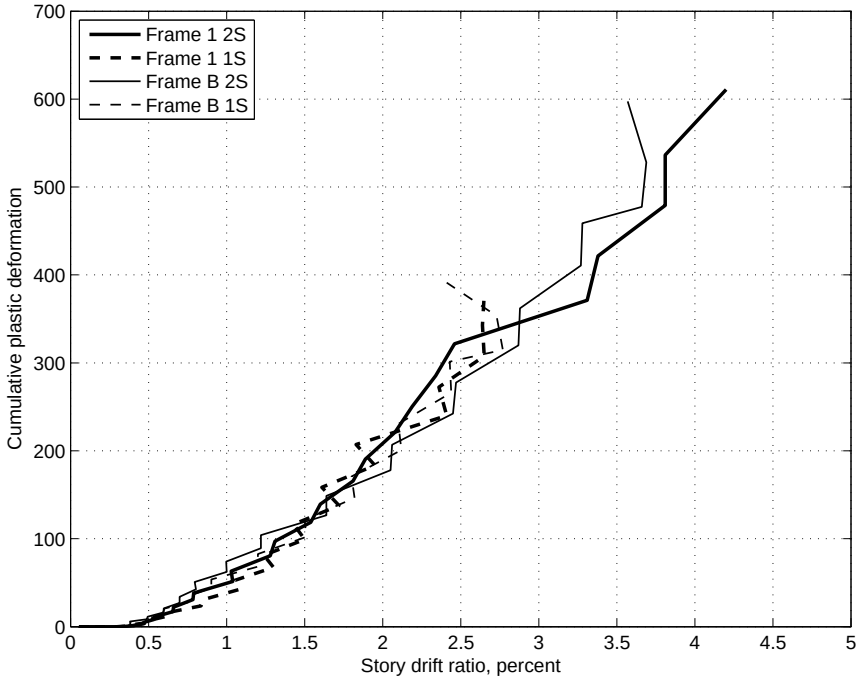

Figure 5.28: Cumulative inelastic axial deformation for each BRB as a function of the experimentally measured story drift ratio

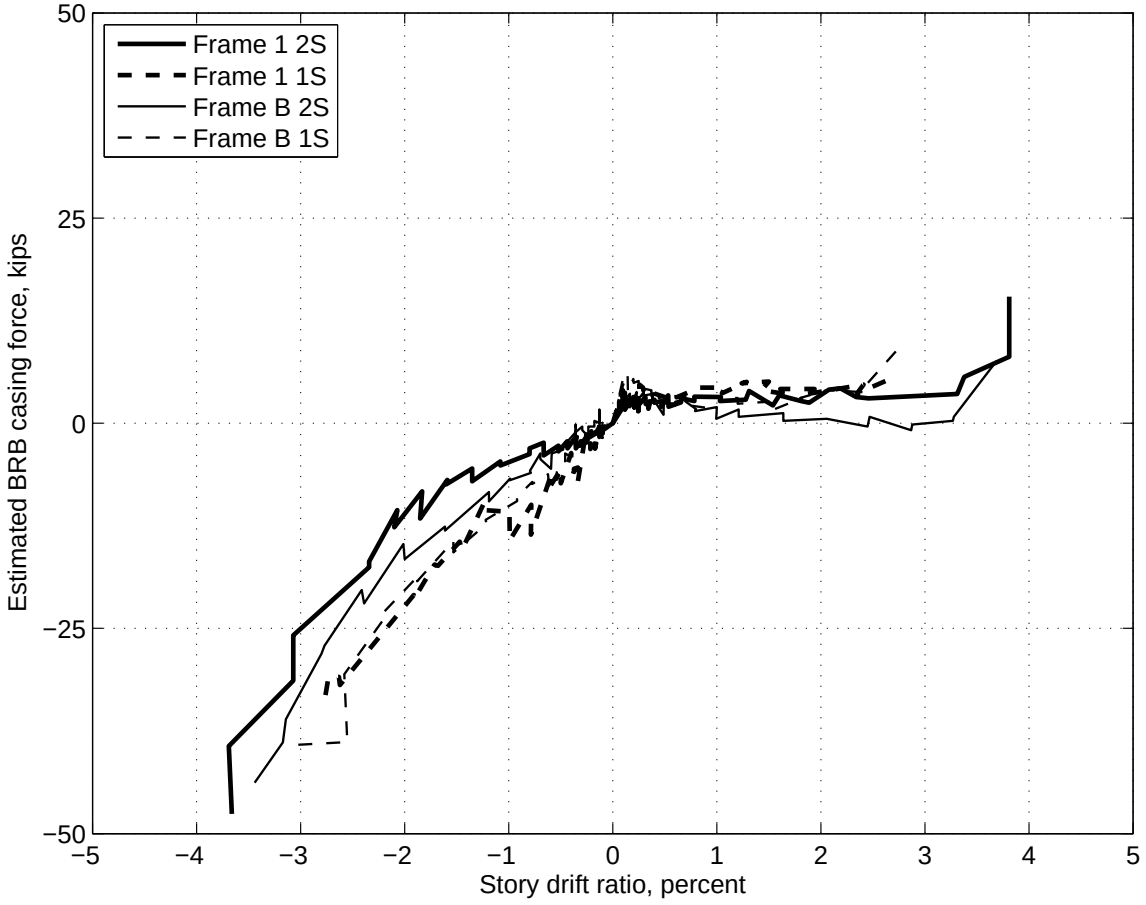

Figure 5.29: Estimated BRB casing force

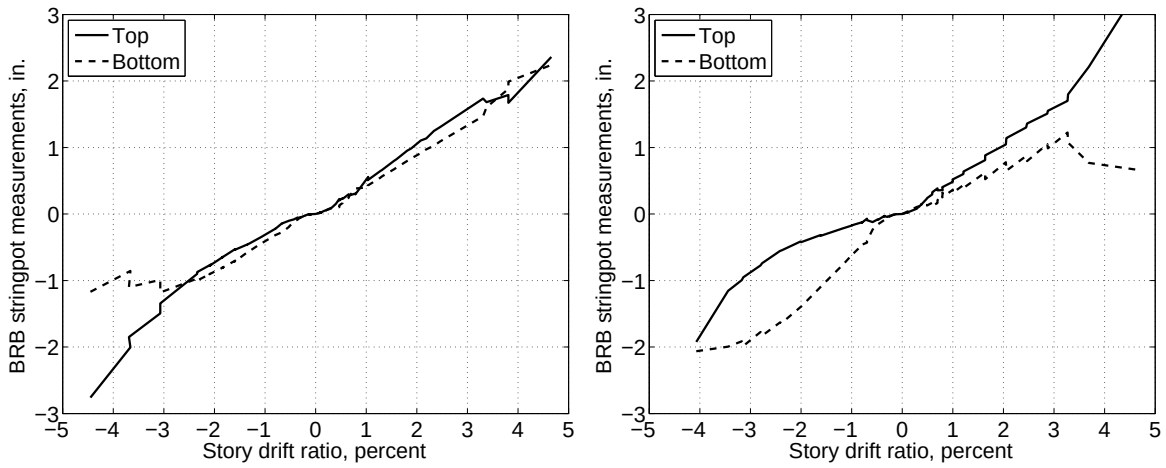

(a) Second-story Frame 1

(b) Second-story Frame B

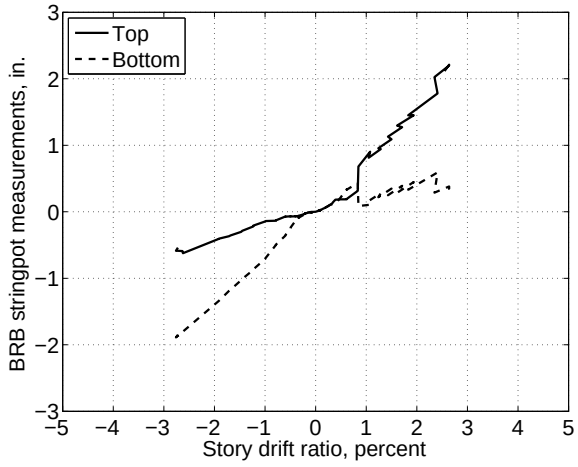

(c) First-story Frame 1

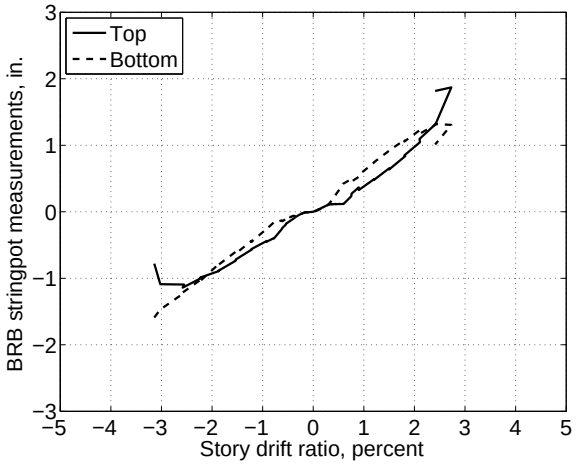

(d) First-story Frame B

Figure 5.30: Comparison of top and bottom components of BRB axial elongation

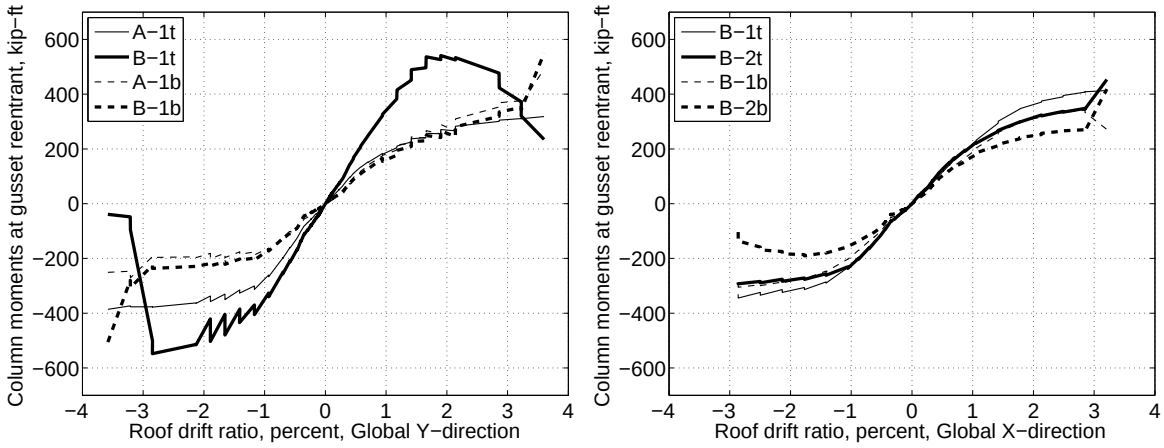

(a) Second story Frame 1

(b) Second story Frame B

(c) First story Frame 1

(d) First story Frame B

Figure 5.31: BRBF column moment envelopes at gusset plate reentrant corners. (Legend indicates the column as defined by the grid intersections along with the location in the story. A-1t indicates the moment at the gusset reentrant corner at the top of the story of column A-1)

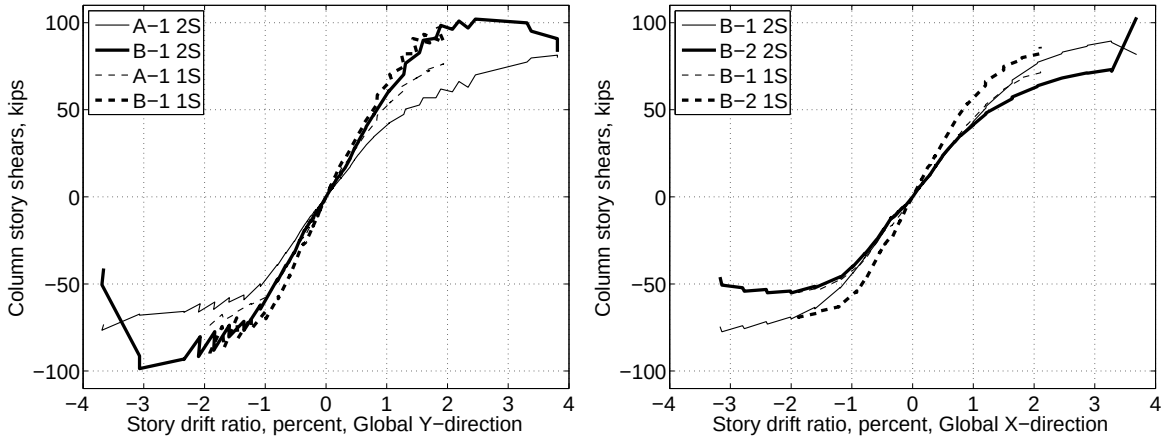

(a) Braced Frame 1, global Y-direction

(b) Braced Frame B, global X-direction

Figure 5.32: BRBF column story shear envelopes (Legend indicates column as defined by the grid intersections along with the story. "A-1 2S" indicates the second story shear of column A-1)

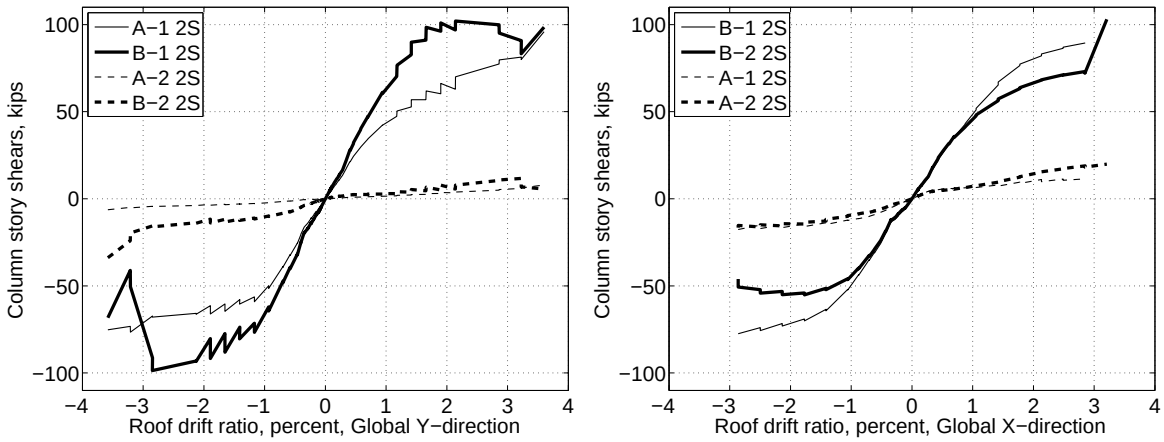

(a) Global Y-direction, second story

(b) Global X-direction, second story

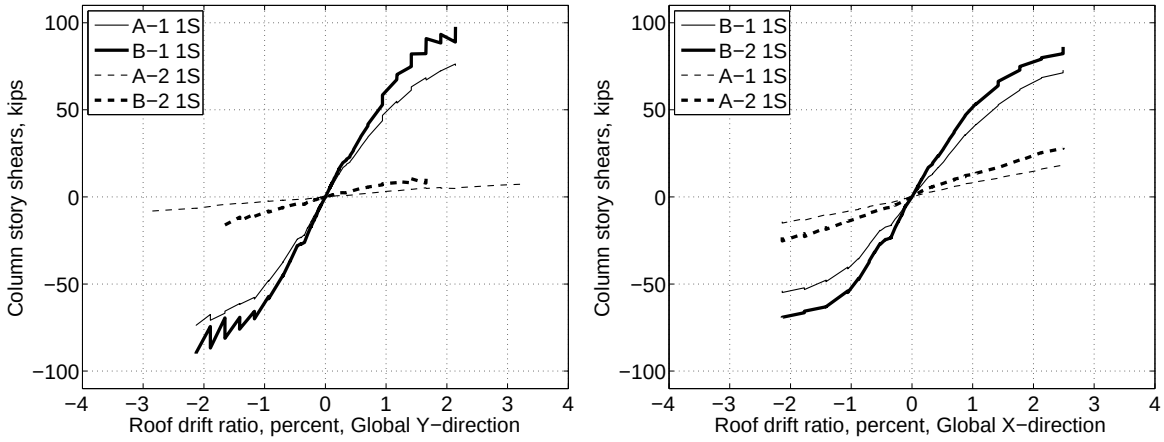

(c) Global Y-direction, first story

(d) Global X-direction, first story

Figure 5.33: BRBF column story shears in each story and global direction. (Legend indicates column as defined by the grid intersections along with the story. "A-1 2S" indicates the second story shear of column A-1)

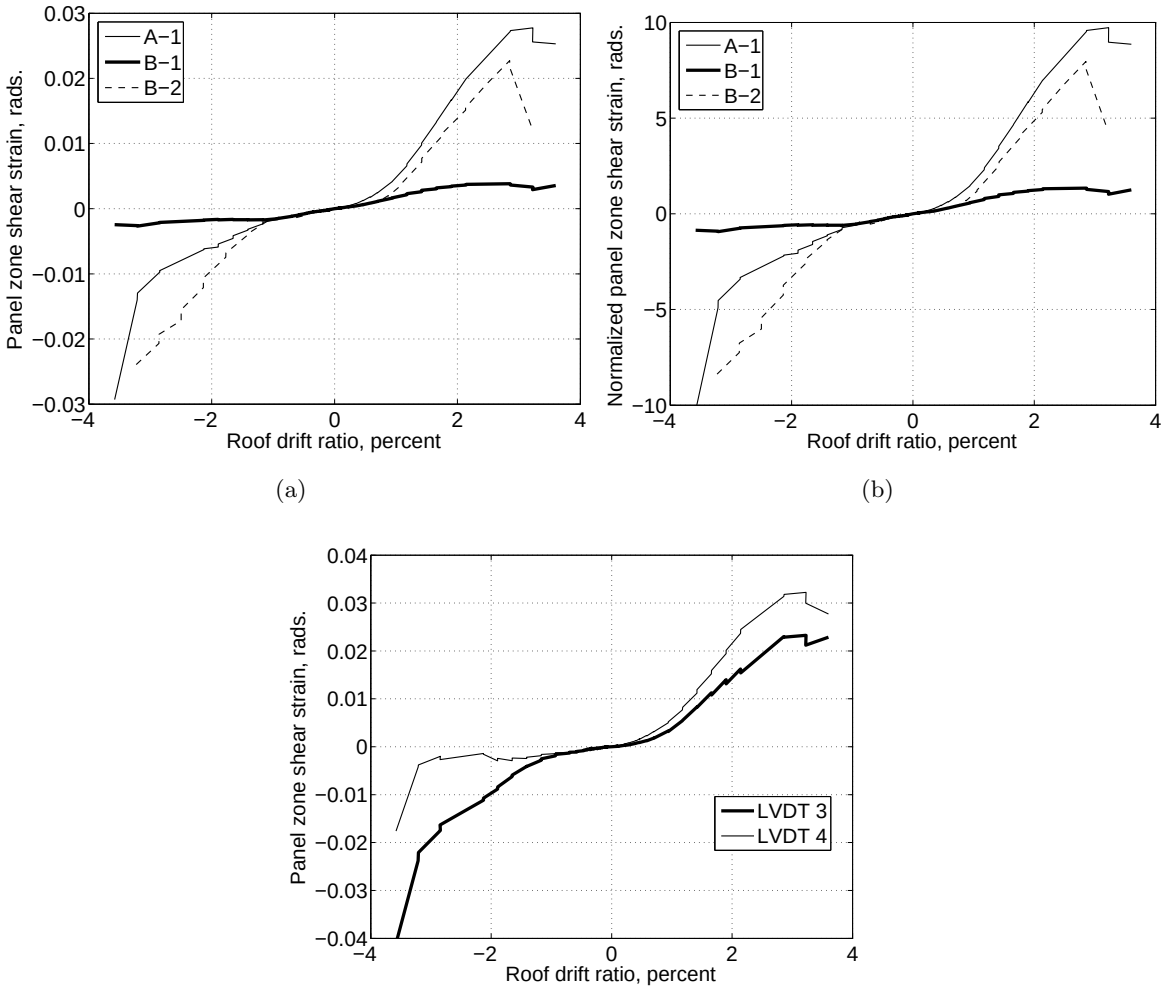

Figure 5.34: Envelope of BRBF column panel zone deformations at second floor joint: (a) shear strain; (b) shear strain normalized by the yield strain; (c) shear strain measurements of LVDTs 3 and 4 on column A-1.

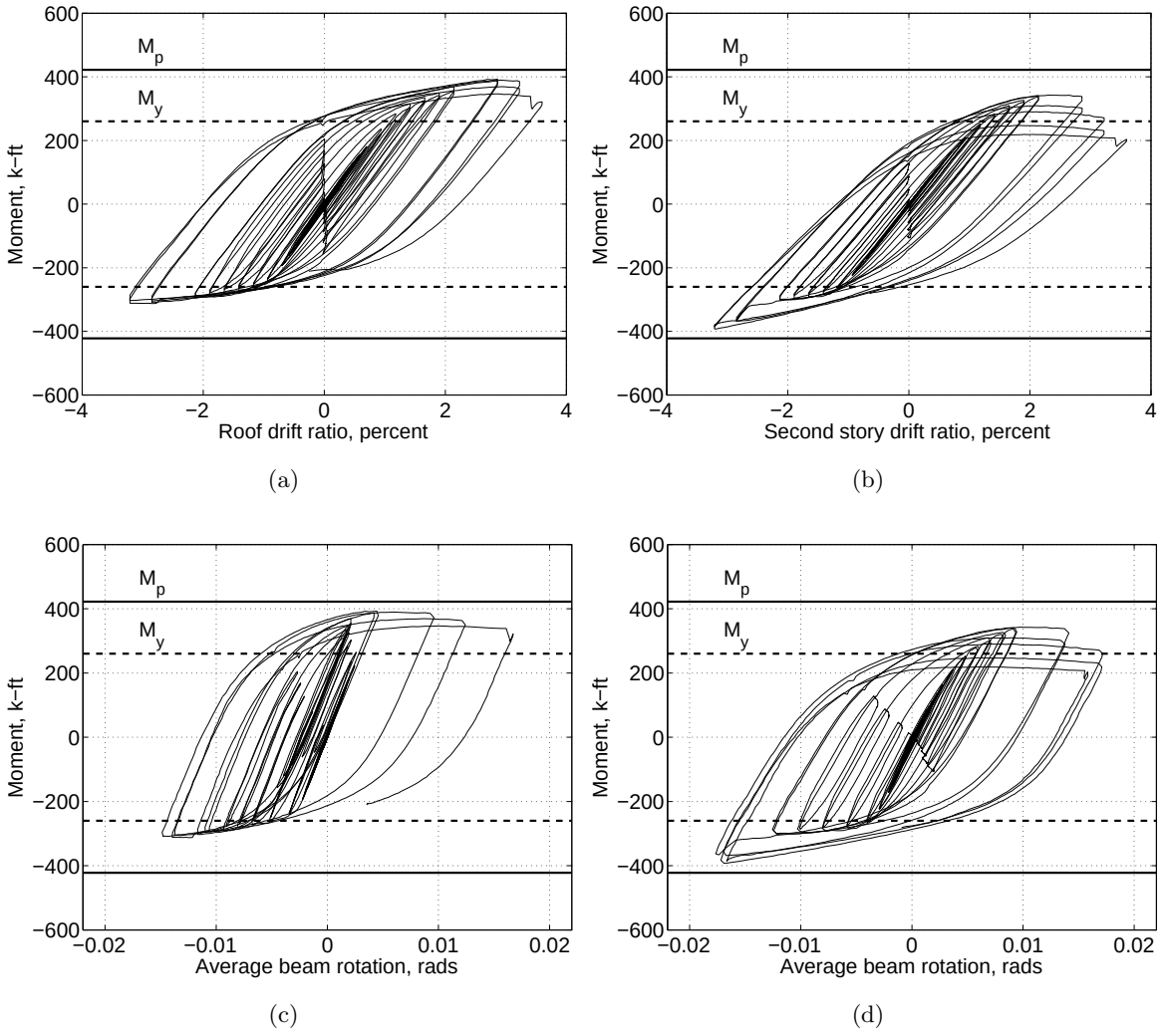

Figure 5.35: BRBF second floor braced frame beam behavior in Frame 1: (a) moment at gusset plate reentrant corner vs. 2SDRY at column A-1 side; (b) moment at gusset plate reentrant corner vs. 2SDRY at column B-1 side; (c) moment at gusset plate reentrant corner vs. average beam rotation at column A-1 side; (b) moment at gusset plate reentrant corner vs. average beam rotation at column B-1 side.

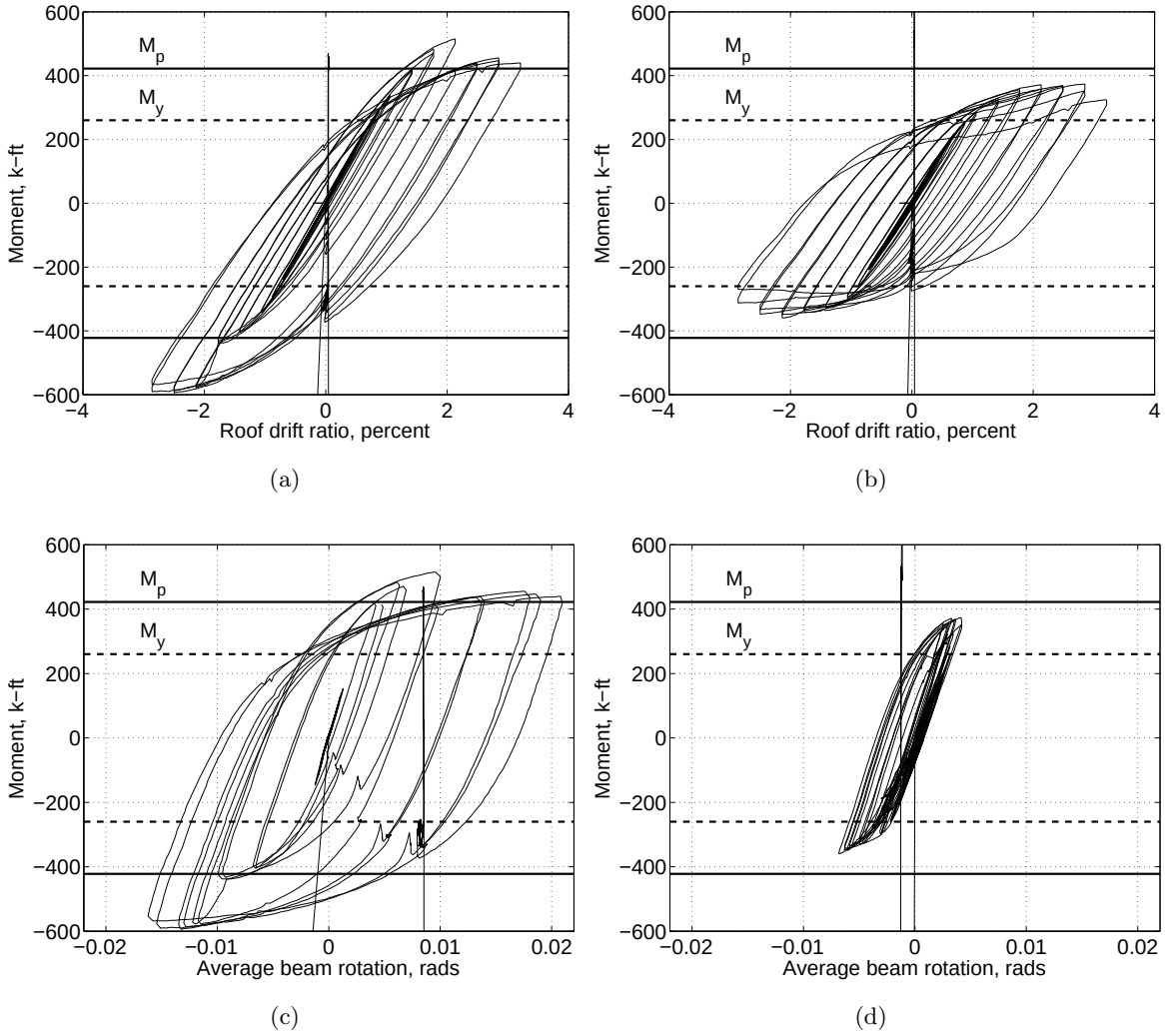

Figure 5.36: BRBF second floor braced frame beam behavior in Frame B: (a) moment at gusset plate reentrant corner vs. 2SDRX at column B-1 side; (b) moment at gusset plate reentrant corner vs. 2SDRY at column B-2 side; (c) moment at gusset plate reentrant corner vs. average beam rotation at column B-1 side; (b) moment at gusset plate reentrant corner vs. average beam rotation at column B-2 side.

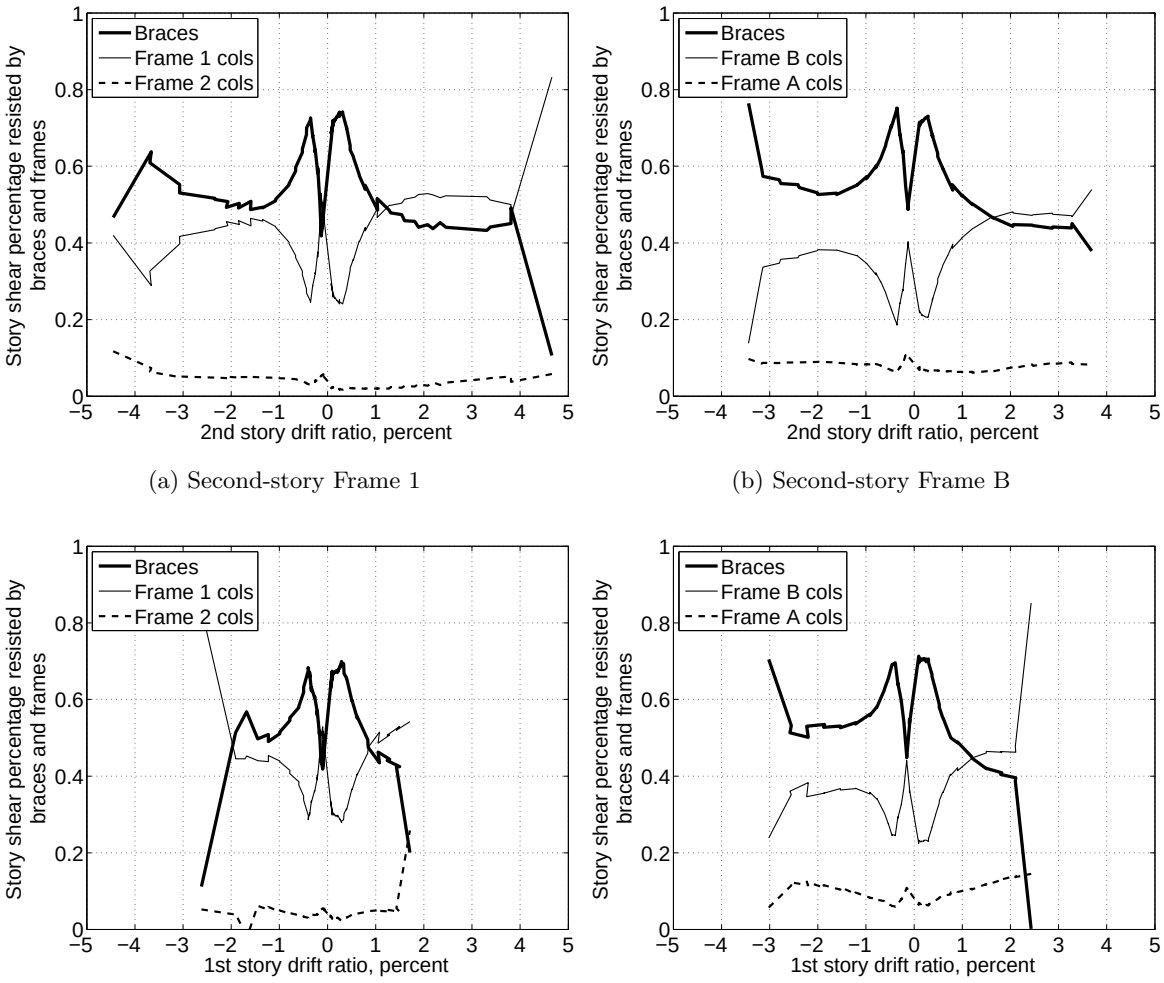

(a) Second-story Frame 1

(b) Second-story Frame B

(c) First-story Frame 1

(d) First-story Frame B

Figure 5.37: Story shear distribution (BRBF test)

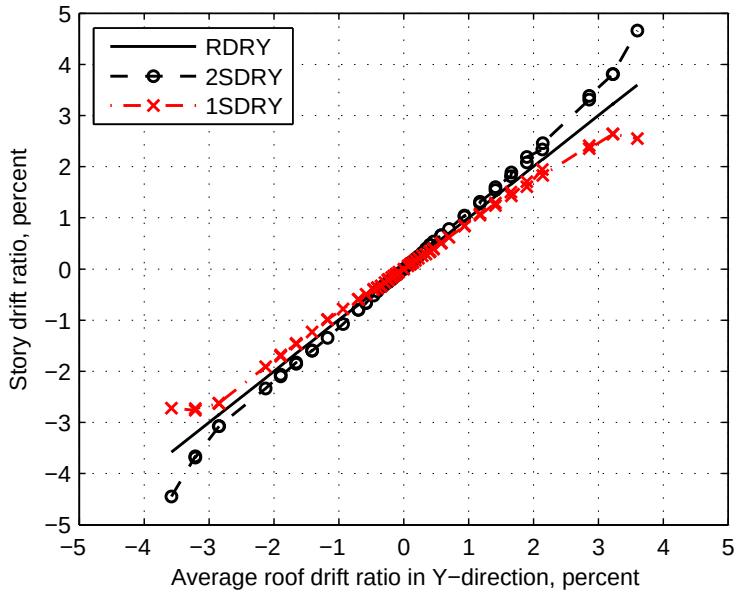

(a) Y-direction

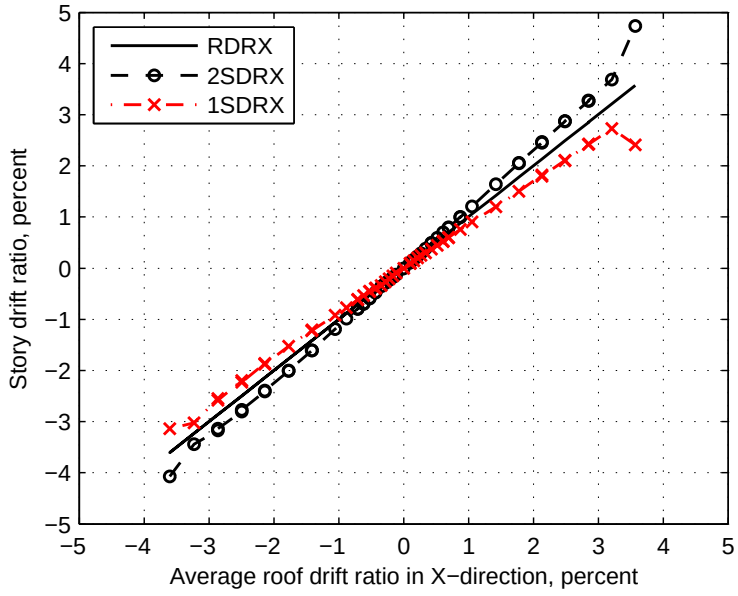

(b) X-direction

Figure 5.38: Story drift distribution in X and Y directions (BRBF test)

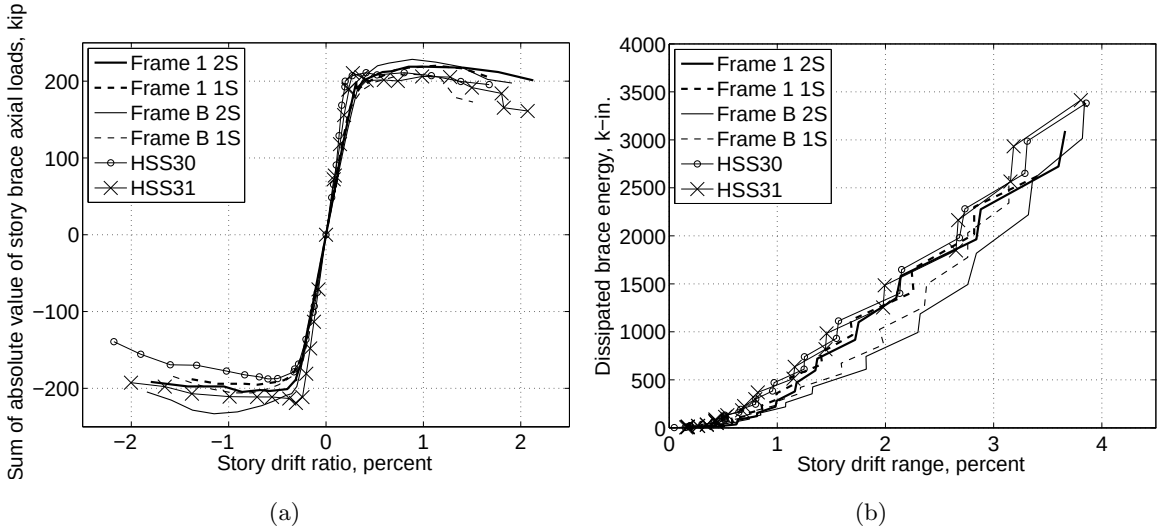

Figure 5.39: X-configured frame experimental envelopes: (a) brace axial versus SDR; (b) energy dissipated by the braces.

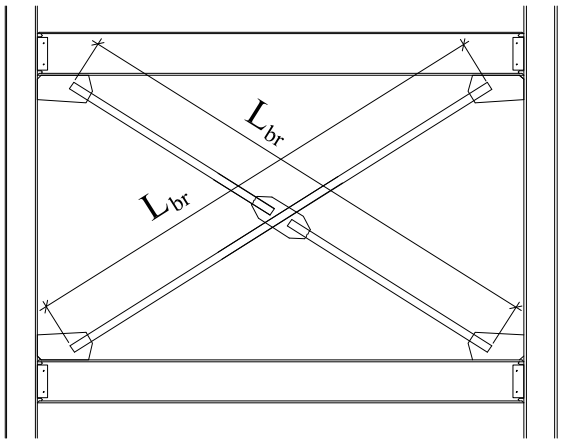

Figure 5.40: Brace length, L_{br}, used in buckling strength calculations

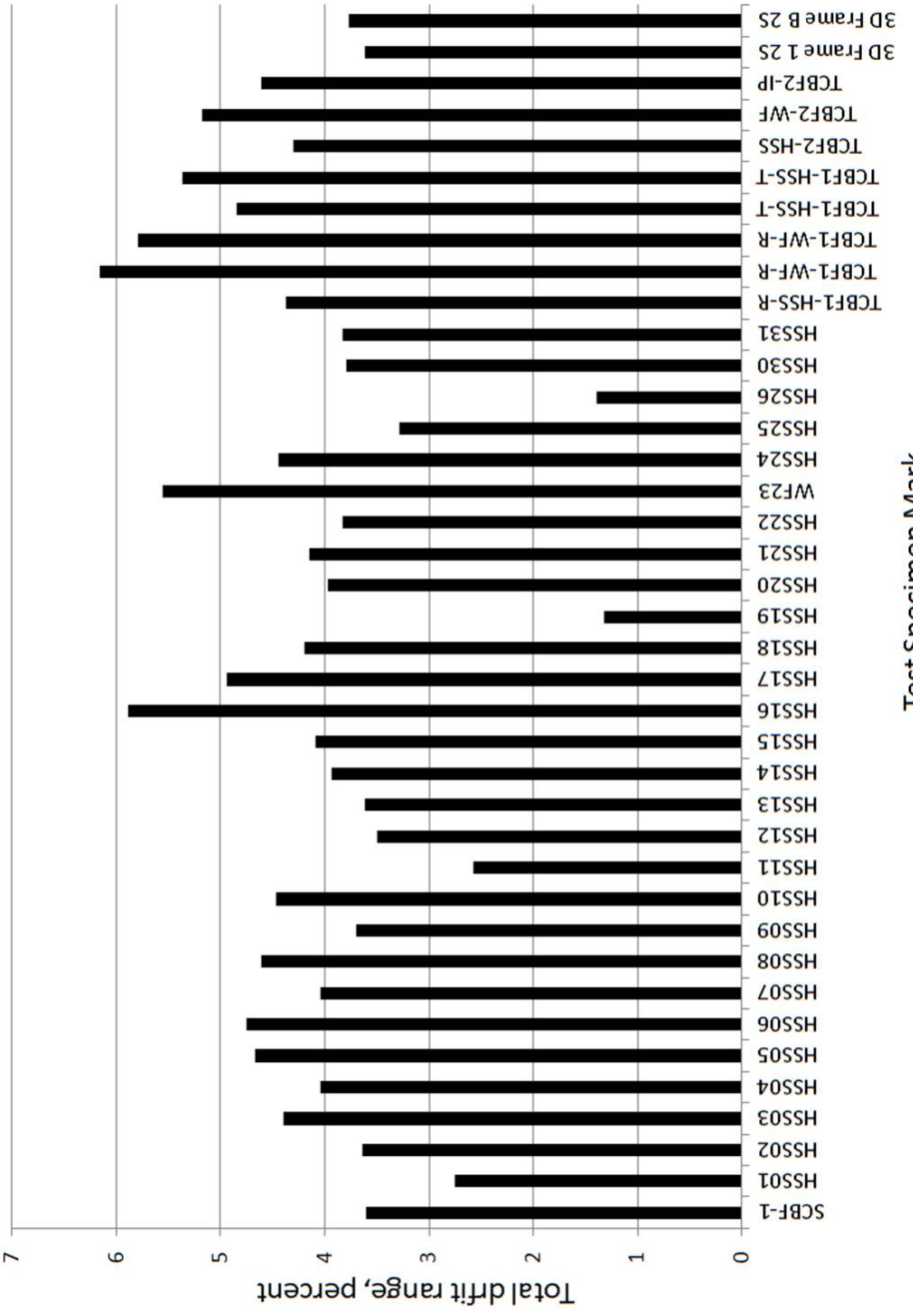

Figure 5.41: Total drift range at last complete cycle prior to failure (SCBF experiments)

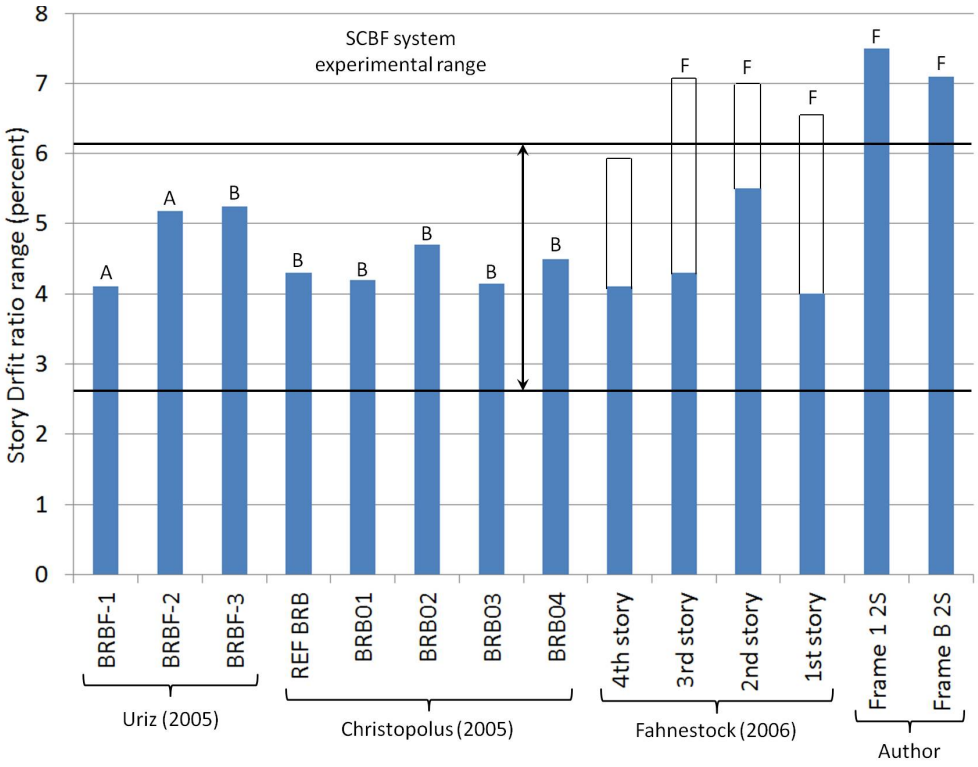

Figure 5.42: BRBF test specimen story drift ratio range (last complete cycle prior to test stoppage, failure due to beam or column fracture or instability, or BRB fracture. Note that none of Fahnestock's BRBs fractured during the Hybrid PSDT, shown shaded; quasi-static, cyclic protocol in white). See Table 5.10 for definition of "A," "B" and "F."

Table 5.10: Wide flange and HSS material properties for HSS30 and 31

Mark	Description
A	Test stopped prior to component failure or BRB fracture
B	Beam flange/web fracture or excessive beam yielding and twisting causing OOP rotation of BRB
F	BRB core fracture

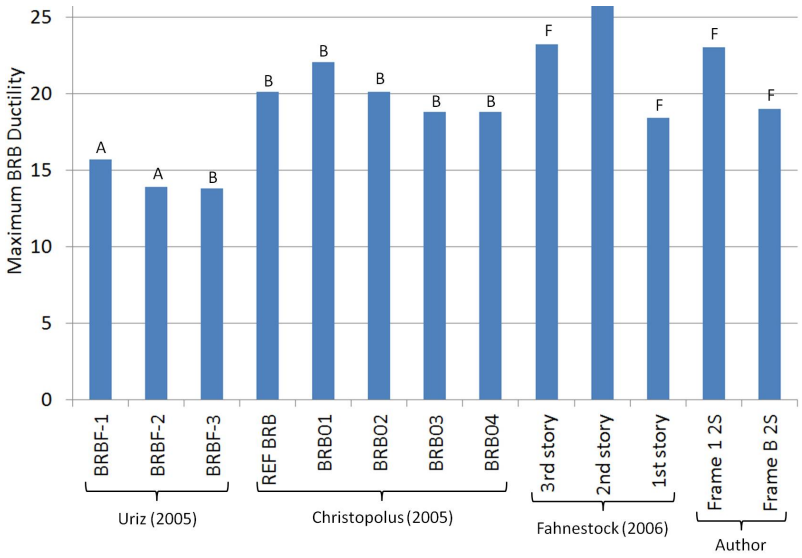

Figure 5.43: BRBF test specimen Max BRB ductilities achieved during tests. See Table 5.10 for definition of "A," "B" and "F."

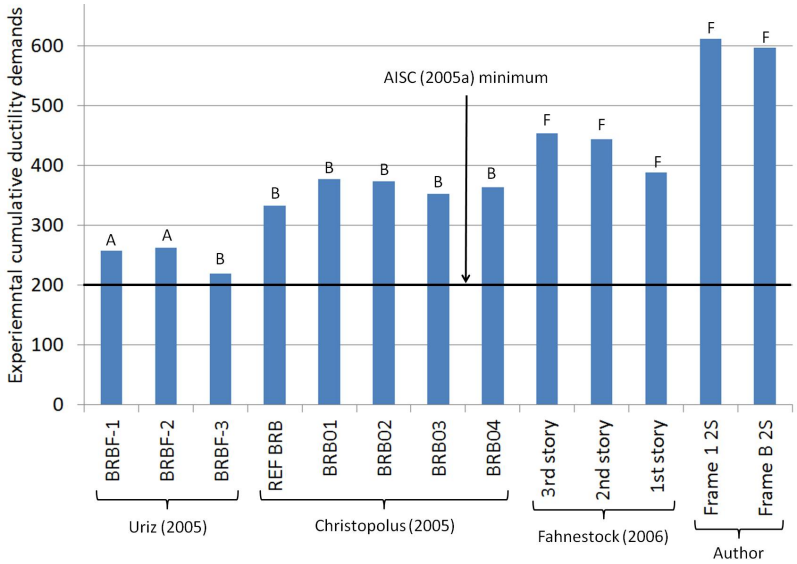

Figure 5.44: BRBF test specimen cumulative ductility demands. See Table 5.10 for definition of "A," "B" and "F."

Chapter 6

SCBF TEST FRAME SIMULATIONS

6.1 Introduction

The open-source finite element software platform OpenSees [McKenna, 1997] was used to analyze Frame 1 of the SCBF test specimen. This Frame is highlighted in Fig. 6.1. Six different models were analyzed beginning with a simple elastic model and progressing up to a much more complicated nonlinear model. The primary objectives of these simulations were to assess the ability of existing "simple" simulation methods to accurately predict the behavior of a highly nonlinear system such as buckling-brace SCBFs. The "simple" models consist of line elements that are less complicated and time-intensive than more detailed continuum finite element models that are generally impractical for design office use. Additionally, validation of these models provide justification for their use in assessing the performance of these systems under suites of ground motions representing various hazard levels and proximity to faults. These studies may make use of the FEMA P695 [2009] methodology to assess the system seismic performance factors, R, Ω, and C_d or assess the performance with the method utilized by Hsiao [2012b].

6.2 Model I Description

Model I was the simplest and was analyzed to ensure the basic geometry and initial stiffness of the frame matched that of the test frame. The floor slabs were not included in this model and all of the steel was modeled as elastic line elements with a modulus of elasticity of 29,000 ksi and neglecting the stiffness added by the concrete floor slab. Since the model was elastic, fiber elements were not used at the element cross-section level. The length of the braces, beams and columns were based on the joint center-to-center dimensions. Therefore, the stiffening effects due to the gusset plates and finite dimensions of the beams and columns at the joint were ignored. The brace end conditions were modeled as a true pin and the

beams were rigidly connected to the columns. Additionally, the opposing braces in each story were not connected at the intersection because brace buckling was not modeled. A pushover analysis was performed with no consideration given to geometric nonlinearities (P-Δ effects).

6.3 Model II Description

The second model added nonlinear behavior by assigning a bilinear material model to the braces, beams and columns. Force-based nonlinear beam-column elements with five Gauss points along the length of the member were used for the beams, columns and braces. Fiber elements were used at each gauss point, and the cross section was subdivided with 12 fibers across the depth and width of the brace, and 20 fibers across the depth and width of the wide flange beams and columns. The cross-section discretization for each element is shown in Figure 6.2 and was based on previous studies by Hsiao [2012a]. Note that for this model, the slab shown in this figure was not modeled (it was only modeled with Model IV).

The yield stress used in the analysis was $R_y F_y$, where R_y is the ratio of the actual to nominal yield strength and F_y is the nominal yield strength. The Giuffre-Menegotto-Pinto steel model was used to model the nonlinear behavior of the steel. This model is bilinear with isotropic hardening and is the Steel02 model defined in OpenSees. The modeling parameters required for Steel02 material are shown in Table 6.1 for each element. As this analysis was a pushover in one direction, two brace material models were used, one for the brace in tension and one for the brace in compression. The yield stress for the brace in compression was set at the stress at which buckling occurred during the experiments. Additionally, to capture the brace strength degradation due to P-Δ effects, a negative post-yield stiffness was used. The resulting brace force deformation curves for the braces due to this material model is shown in Figure 6.3. Similar to Model I, a pushover analysis was performed with no consideration given to P-Δ effects.

6.4 Models III and IV Description

Models III and IV added more complexity to Models I and II by adding a number of nonlinear effects which include:

- Initial brace camber with corotational formulation to capture brace buckling and the corresponding strength and stiffness degradation
- Column corotational formulation to capture the effects of geometric nonlinearities.
- Gusset out-of-plane bilinear moment-rotation model at the end of the brace.
- Three models to bound the behavior of the beam-column-gusset joint which include:
  - Rigid elements
  - Elastic elements
  - Force-based nonlinear beam-column elements with five Gauss points
- Slab fiber element included in the wide flange beam element (Model IV)

The element fiber discretization shown in Fig. 6.2 remained the same. Models IIIa through IIIc did not include the slab while Model IV did. Figure 6.5 depicts the schematic drawing of Models III and IV and the following sections will describe this is more detail.

6.4.1 Material Models

Similar to Model II, the steel material model for Models III and IV was based on the Giuffre-Menegotto-Pinto model which is a bilinear model with isotropic hardening. The yield stress for the brace was set at 64 ksi which corresponds to $R_yF_y = 1.4(46)$, while the yield stress for the wide flange beams and columns was set at 55 ksi which corresponds to $R_yF_y = 1.1(50)$. The post-yield strain hardening slope was set at $0.03E$, where E is the modulus of elasticity.

The concrete model for Model IV was based on the Kent-Scott-Park model which has no tension capacity and corresponds to the OpenSees Concrete01 model. Table 6.2 lists the parameters used in describing the concrete curve shown in Figure 6.4. The effective width of the concrete slab was determined based on the recommendations of ACI 318-08 8.10.3 which states that the effective overhanging flange width shall be the lesser of: (a) one-twelfth the span length of the beam, (b) six times the slab thickness or (c) one-half the clear distance to then next web. This resulted in an total effective slab width (including the overhanging slab width of 12") of 28.5."

6.4.2 Brace model - Models III and IV

The braces for Models III and IV were modeled as built with one continuous brace and two spliced braces connected at the center of the continuous brace. The boundary conditions at the ends and at the splices were modeled using an out-of-plane rotational spring described in the next section. Four different brace discretizations were studied to determine the required number of elements that would adequately capture the brace buckling load and the degradation of strength and stiffness of the compression braces. The number of brace elements studied were four, eight, 16 and 32. Sixteen elements were ultimately chosen as will be described in Section 6.6.2. Additionally, an initial imperfection was applied to the brace to capture buckling and was defined as a first-mode sine wave in the continuous brace and a straight segment in one half of the discontinuous brace and a sine wave in the other half. This brace imperfection is shown in Figure 6.6 for the second story braces with 16 elements along the length of the brace. Only one half of the discontinuous brace buckled during the test and therefore, the straight portion of the discontinuous brace was required to ensure that only one half of the brace buckled during the simulations. The peak amplitude of the initial imperfection was set at $L_{br}/500$ where L_{br} is the length of the brace. This value was based on studies performed by Gunnarsson [2004] and verified by Hsiao [2012a]. The brace elements were composed of the same fiber model that was described for Model II and shown in Figure 6.2.

6.4.3 Gusset Plate Model

The gusset plate model used was based on the model developed by Yoo [2006] and Hsiao [2012a]. The model is based on Euler-Bernoulli beam theory with some parameters based on the Whitemore width and the gusset plate effective length concept [Thornton, 1991]. The elastic out-of-plane rotational stiffness of the gusset plate is described by Equation 6.1 where W_w is the width of the Whitemore section, t is the thickness of the gusset plate, and L_{ave} is the average of L_1, L_2 and L_3 shown in Figure 6.7. Equation 6.1 is essentially $\frac{EI}{L}$, or the rotational stiffness of a cantilever beam subjected to an end moment. The yield moment of the gusset plate is calculated as SF_y, where S is the section modulus of the gusset plate

at the Whitemore section. The post-yield stiffness of the spring model was assumed to be 3% of the initial rotational stiffness. This spring was placed at the physical end of the brace with the remaining gusset plate degree of freedoms assumed to be rigid.

$$K_{gusset}^{rotation} = \frac{E}{L_{ave}} \left(\frac{W_w t^3}{12} \right) \tag{6.1}$$

6.4.4 Beam-Column-Gusset Joint Model

Modeling of the beam-column-gusset joint is complicated by a number of factors that influence the behavior of this zone. These factors include:

- Column panel zone deformation
- Gusset stiffness and degradation due to gusset edge buckling and weld or plate tearing at the interface
- Relative depth of beams and columns

In moment frame analysis, it is typical to assume that the column is rigid within the beam depth while the portion of the beam within half of the column depth is assumed to be rigid. For braced frames, the length of the rigid end zone (REO) is not as clear but has been studied by Hsiao [2012a] and is shown in Figure 6.7. It can be seen that the suggested length of the rigid column end zone be taken as the length from the beam centerline to the end of the gusset plate. The length of the rigid beam end zone is calculated as 75% of the distance from the column centerline to the edge of the gusset plate.

Given that yielding was observed in the beams and the columns within the gusset region during the experiments performed by the author, these REO offsets may not accurately reflect the true stiffness of this region. Therefore, with reference to Figure 6.8, three different cases of end zone flexibility were modeled as:

1. Model IIIa - Nonlinear force-based elements with the same fiber cross-section as the columns and beams comprising all members in the joint except the gusset plate region which was modeled as rigid. Slab was not included.
2. Model IIIb - Rigid elements within the beam column-joint, inelastic beam and column elements within the gusset region. Slab was not included.

3. Model IIIc - Rigid elements within the beam column-joint, inelastic beam elements within the gusset region, elastic column elements within the gusset region. This model was used based on the experimental behavior of the frame. The beams yielded throughout the gusset region up to the face of the column while the columns displayed limited to no yielding within this region. Slab was not included.

4. Model IV - Same as Model IIIc but with the concrete slab included in the beam model.

6.5 Displacement-Based Loading Protocol

The pushover and the cyclic analyses were performed in displacement control. Two point loads were applied at each node at the top floor of the frame as shown in Figure 6.9. The applied cyclic displacement matched that applied to Frame 1 during the actual experiment and shown in Fig. D.1 as the Y-direction curve. The nonlinear analyses made use of the Newton algorithm with the convergence tolerance set at 10^{-4} and the maximum number of iterations set at 50. A step size of 0.01 inches was chosen based on a preliminary study of that required to ensure convergence. In the cases where convergence was a problem, the Newton algorithm with line search was used.

6.6 Analysis Results

6.6.1 Models I and II Results

The results of the pushover analyses performed on the "simple" models, Models I and II are shown in Figure 6.10. It can be seen that the elastic stiffness predicted by Model I is fairly good and slightly less stiff than that measured from the experiment. This is expected as the the length of the brace in the model extends from joint center to joint center and neglects the stiffness provided by the beams, columns and gusset plates within the beam-column-gusset end zones. The pushover curve for Model II follows the test results fairly well but underpredicts the strength at drift levels greater than one inch. The elastic stiffness of Model II is greater than that predicted by Model I due to the fact that the axial stiffness of the brace in the end zone is modeled as rigid.

6.6.2 Models III and IV Results

Models I and II performed relatively well under the nonlinear static analyses and indicated that the basic geometry and material properties had been adequately modeled and could be expanded upon. As described previously, Models III and IV included a number of features that added to the nonlinearity of the models. The initial imperfection and discretization of the braces was the most significant of these as the brace dominates the nonlinear behavior of this type of system. Therefore, a study was performed to determine the optimal number of displacement-based elements to be used in the brace. Four discretizations were investigated: 4, 8, 16 and 32 elements in the total length of the brace. Figure 6.11 shows a comparison of the axial load in the compression brace as a function of the top floor displacement. It can be seen that the critical load of the brace with four elements is approximately 10% greater than the other other three discretizations. The models with 16 and 32 elements display nearly identical response and therefore it was decided to use a brace with 16 displacement-based elements.

Figures 6.12 through 6.17 compare the hysteretic response of the frame as measured in the experiment to that estimated by the OpenSees analyses. Four plots are shown in each figure corresponding to Models IIIa, IIIb, IIIc and IV. Figure 6.12 depicts the global hysteretic curve of the story shear versus top story relative displacement for the four models described above. It can be seen that all four models predict the global response fairly well with varying degrees of accuracy. Figure 6.12a shows the response of the model with nonlinear elements in the joint region and underpredicts the strength, as would be expected, by approximately 9%. Figure 6.12b shows the response of the model with rigid end zones within the beam-column depths. It can be seen that this model provides a better prediction than the first, especially at drifts less than approximately 1.25 inches. At drift levels greater than this, the strength is similar to that predicted by the first model. Figure 6.12c shows the response of the model with inelastic beam elements and elastic column elements within the gusset region. There is improvement over the previous model with slightly greater strength predicted which is still less than the experimentally measured strength but only by less than 5%. Figure 6.12d shows the response of the model with the slab and provides the best

global response prediction. The model repsonse overpredicts the strength by approximately 5% up to 1.5 inches of drift, and underpredicts the strength at larger positive drifts by less than 4%.

Figure 6.13 shows the second story horizontal shear resisted by both braces in that story. Close inspection of the four plots from the simulations shows that there is little if any difference between the models. This is expected as there is no difference in the way the brace was modeled between the four analyses. It was observed in the experiments that the braces buckled at approximately 0.3% story drift ratio (SDR). Figure 6.13 indicates that the simulations predicted a brace story shear strength of approximately 8% less than that measured in the test at positive 0.3% SDR while the simulations predicted a brace story shear strength of 7% greater than that measured in the test at negative 0.3% SDR. The simulated brace story shear force at negative 0.3% SDR was 12% higher than at positive 0.3% SDR. This difference is logical as the continuous brace, which is loaded in compression when the SDR is negative and has a smaller effective length than the discontinuous brace, has a larger simulated buckling load. The difference between the measured, experimental story shears at plus and minus 0.3% SDR during the test is approximately 3%. Given the expected errors associated with measuring forces from load cells, strain gauges and nominal material properties, this difference is negligible.

At negative SDRs larger than 0.3%, the difference between the simulated brace story shear strengths and those measured in the test were less than 3%. However, at postive SDRs larger than 0.3%, the simulated brace story strengths are less than the actual by six to 16%, a much larger disparity. This is due more to the fact that the measured positive shears are greater than the measured negative shears than the difference in simulated positive and negative shears. It can be seen that the simulated brace response is approximately symmetric. As discussed in Section 5.2.1, the difference in measured response between the positive and negative drift ranges was likely due to the locked in brace tensile stresses from weld cooling which was not modeled in the simulations.

Figure 6.14 shows the story shear resisted by the shared column in the first story as a function of the average roof drift ratio for the four analyses. The first two analyses, shown in Figures 6.14a and b, predict the response fairly well but underpredict the positive and

negative strengths with the first model underpredicting the strengths by as much as 14% and the second model by approximatley 9%. The response of the model with inelastic beam elements and elastic column elements within the gusset region, shown in Figure 6.14c, matches the response of the experiments well at drift ratios greater than positive 1% but overpredicts the strength and stiffness at positive drift ratios smaller than 1%. In the negative drift region, the model predicts the response extremely well. The inclusion of the slab increases the stiffness and strength of the positive response as seen in Figure 6.14d while the negative response matches well. The response predicted by these last two models are very similar at drifts greater than 1% with the slab model displaying slightly greater and more accurate hysteresis than that without. The same observations can be made for the moment at the base of the shared column shown in Figure 6.15.

As shown above, the differences in the global responses and some local responses between the four nonlinear analyses models was minimal. The difference between the models is most apparent when comparing the local element behaviors. Figure 6.16 shows the moment in the shared column at the top of the first story. None of the models do an adequate job of predicting the response at this location. The model with the slab, Figure 6.16d, provides the best prediction up to 0.5% drift in each direction. However, the strength and stiffness of the simulation degrade much more rapidly than the observed experiments. This most likely indicates that the column model within the gusset region should be more rigid than that assumed in the elastic model that was used. The other three models shown in Figures 6.16a, b and c display curious behavior which indicate that the column inflection point is well above mid-height and actually propagates above the second floor indicating that the column is bending in single curvature at the first story, which does not match the experimental behavior.

The response of the second floor beam at the shared column is shown in Figure 6.17. Surprisingly, The first model with inelastic members within the whole beam-column-gusset joint provides the best prediction of the initial stiffness while the more physically accurate model with the slab provides an initial stiffness that is approximately 50% greater than that observed in the experiments. The model with the slab does an adequate job of predicting the strength in the positive region at larger drifts while Model IIIa underpredicts the strength

by approximately 15%.

It is worth noting that while the local response at the top of the first story shared column is not simulated accurately, the brace response and the global response is simulated very well. This is due to the fact that the brace response is affected very little by the conditions at the joint other than the boundary conditions of the brace and the rigid end offset of the gusset plate within the joint which remained the same for Models III and IV. These boundary conditions were modeled with the rotational spring that was found to be superior to other conditions such as a true pin or full fixity [Hsiao et al., 2012a]. Additionally, while the global behavior is affected by the post-buckling and tensile yielding of the brace and the resistance of the moment frame (see Section 5.2.4), the resistance of the moment frame is dominated by the base fixity of the columns. This can be seen by comparing the shared column moment magnitudes at the base shown in Figure 6.15 with the moments at the top of the first story shown in Figure 6.16. At 1% average roof drift, the experimentally measured moment at the base is four times larger than that at the top of the column and this ratio increases to 12 at the maximum story drift ratio of 2%. Since the story shear is a function of these moments, the moment at the top of the first story plays a smaller role in the magnitude of the shear at this story and therefore, has minimal effect on the overall story shear response.

6.7 OpenSees Analysis Summary and Conclusions

The open source finite element software OpenSees was used to model one planar frame of the SCBF test. Six different models were analyzed which included a simple elastic pushover model (Model I), a simple nonlinear pushover model (Model II), a more complicated cyclic model (Model III) and finally a more complicated cyclic model that included the floor slab (Model IV). For Model III, three different gusset-beam-column joint models were investigated. Models III and IV accounted for brace buckling and beam and column geometric nonlinearities through a corotational formulation.

The simple elastic pushover analysis (Model I) estimated the initial stiffness fairly accurately but was slightly less stiff because the length of the brace was modeled to be the length from column-beam intersections which disregard the additional stiffness provided by

the gusset, beams and columns within the joint. The simple nonlinear analysis (Model II) also predicted the response envelope quite well with a slightly larger initial stiffness due to the rigid end zone offset of the brace.

The more complicated analyses that included an initial imperfection in the brace with a corotational formulation captured the brace behavior very well in the negative drift region and underpredicted the strength in the positive drift range by at most 8%. Some local behaviors were not captured as well but were shown to have a relatively small influence on the global response of the simulations. The inclusion of the floor slab improved the predictions of most global and local behaviors except at the beams where the slab provided a stregnth and stiffness prediction greater than that observed by approximately 15%.

The results of these models are promising and indicate that these may be extrapolated to analyze multi-story model building designs in the single-story X-configuration to assess their performance under a suite of ground motions representing various hazard levels. By including the brace fracture model developed by Hsiao [2012b] in these studies, an assessment of the fracture potential of the braces may be made. Additionally, assessment of Incremental Dynamic Analysis (IDA) may be performed to study the effectiveness of IDA in predicting collapse potential similar to the method used by Hsiao [2012]. If the collapse predictions are shown to be acceptable, studies may be performed to assess the system seismic performance factors, R, Ω and C_d according to FEMA P695 [2009].

Table 6.1: Model II Steel Model Parameters

Element	F_y, ksi	$\frac{E_{sh}}{E}$	R_o	cR1	cR2
WF beams and columns	55	0.05	5	0.925	0.15
Tension brace	46	0.05	5	0.925	0.15
Compression brace	35	-0.05	5	0.925	0.15

Table 6.2: Model IV Concrete Model Parameters

fpcu, ksi	epsc0	fpcu	epsU
-5	0.002	-4.5	-0.004

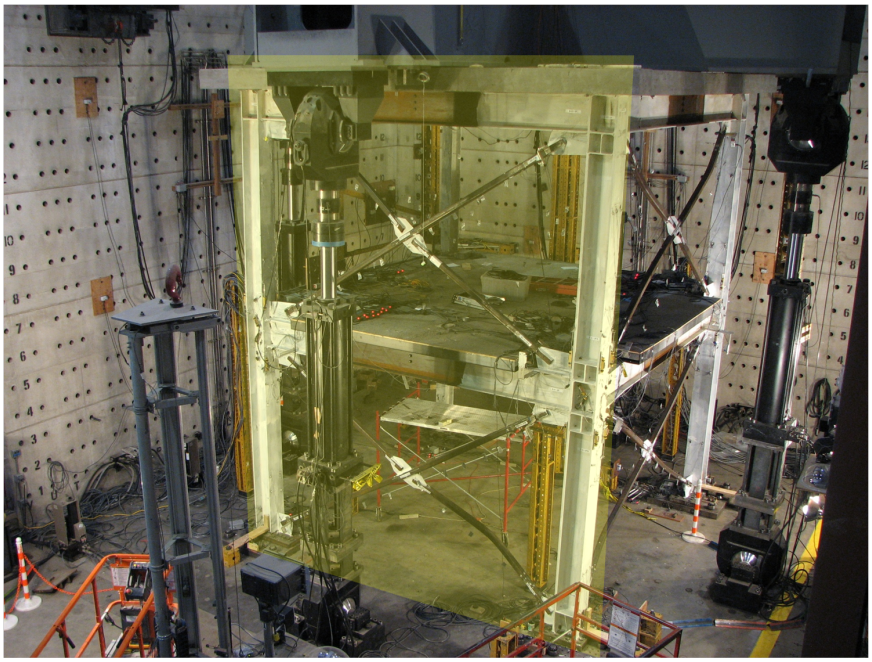

Figure 6.1: SCBF Frame 1 modeled in OpenSees simulations

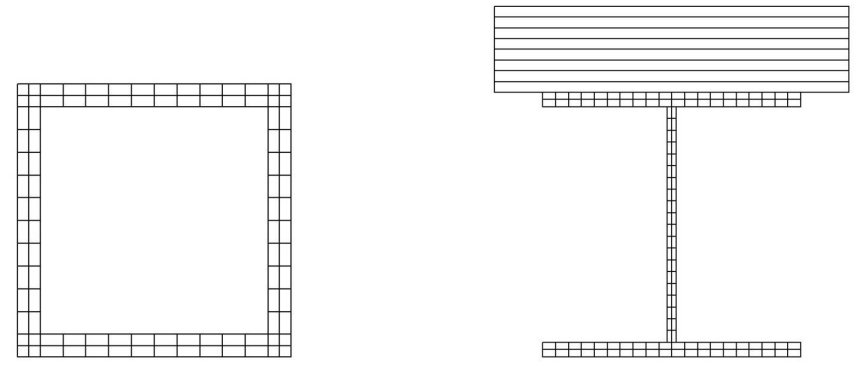

(a) HSS brace fiber discretization

(b) Wide flange fiber discretization

Figure 6.2: Element fiber model discreitzation (Note: slab is included only in the beams in Model IV)

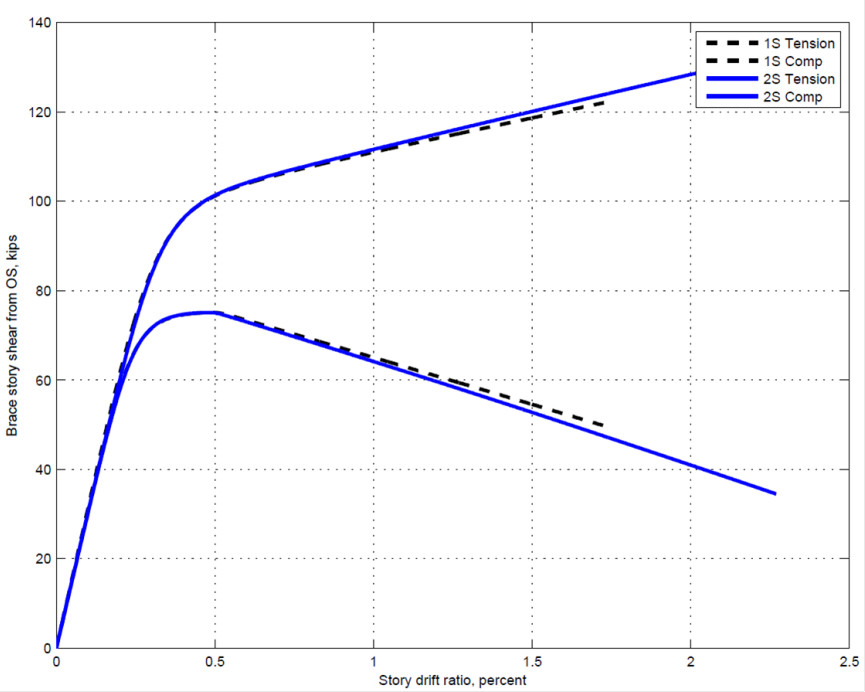

Figure 6.3: Brace force deformation curve for Model II

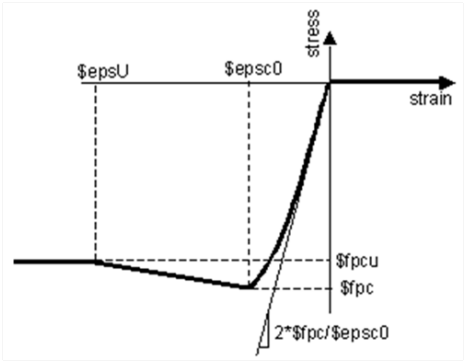

Figure 6.4: Kent-Scott-Park concrete material model (http://opensees.berkeley.edu/)

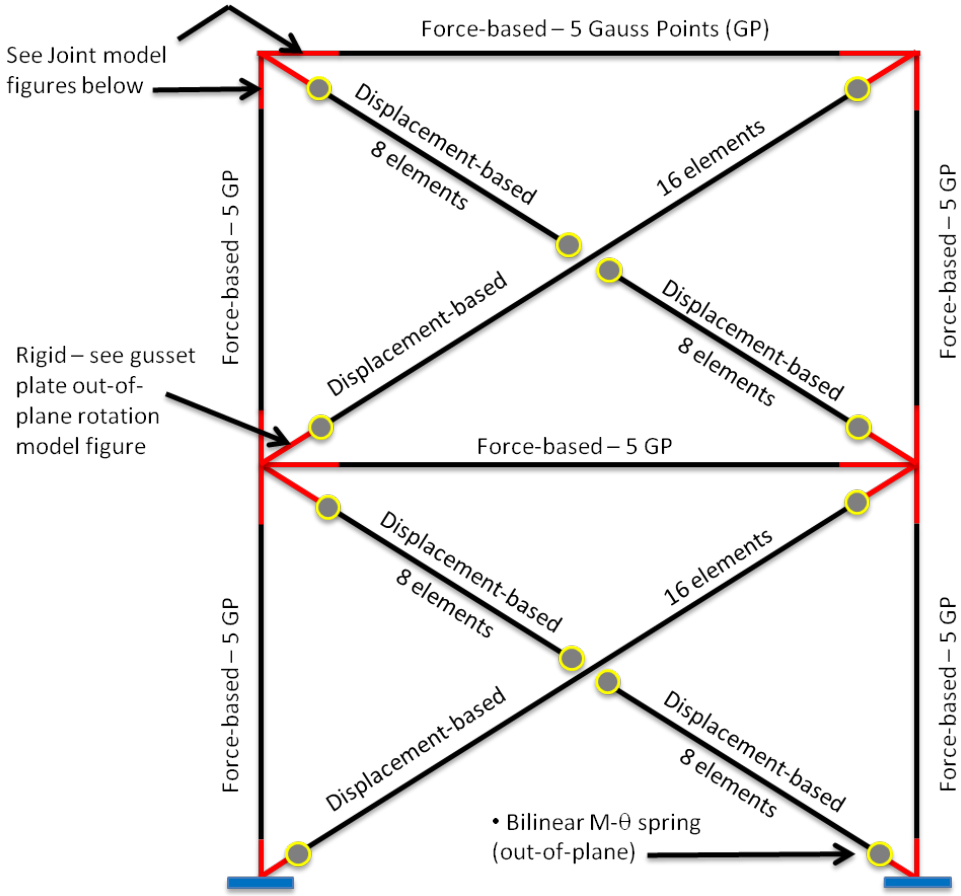

Figure 6.5: Schematic of frame Models III and IV (Note: floor slab used in Model IV not shown in figure)

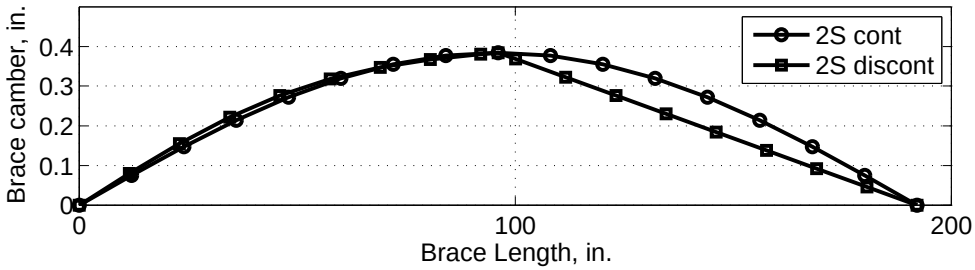

Figure 6.6: Brace initial imperfection model, 16 elements

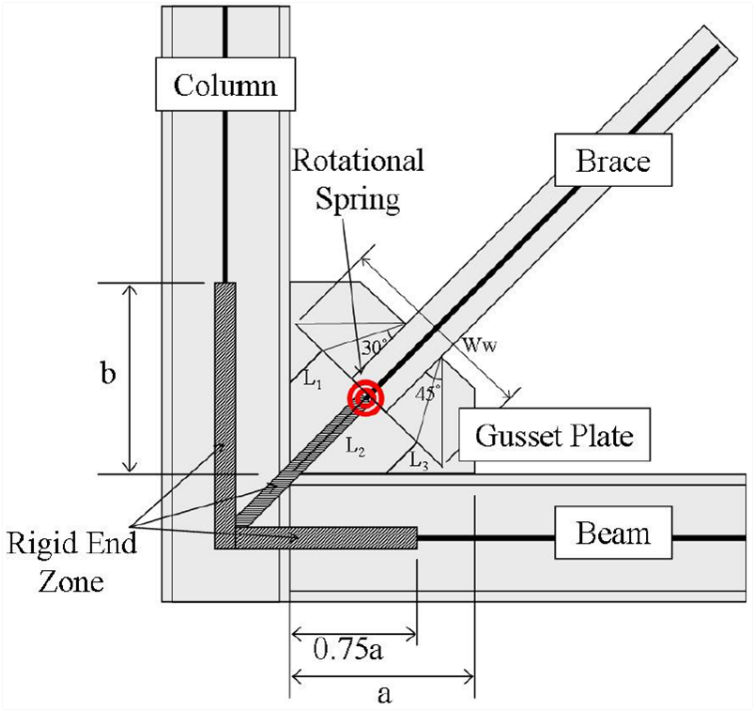

Figure 6.7: Gusset plate out-of-plane rotation model [Hsiao et al., 2012a]

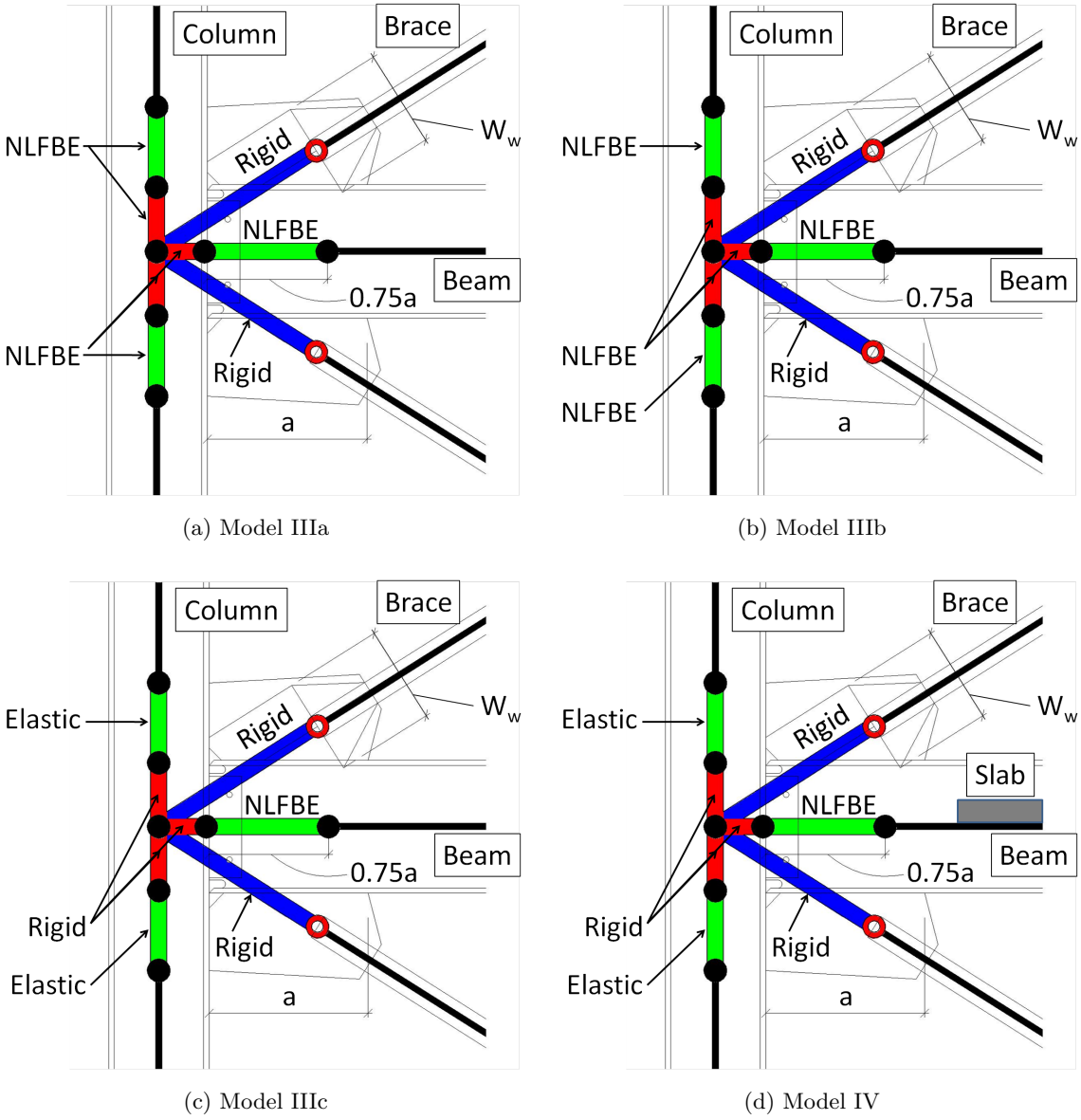

(a) Model IIIa

(b) Model IIIb

(c) Model IIIc

(d) Model IV

Figure 6.8: Beam-column-gusset joint model (Note: NLFBE - Nonlinear forced-based element)

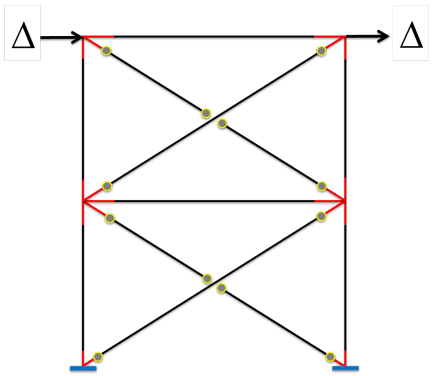

Figure 6.9: Model frame loading for pushover and cyclic analyses

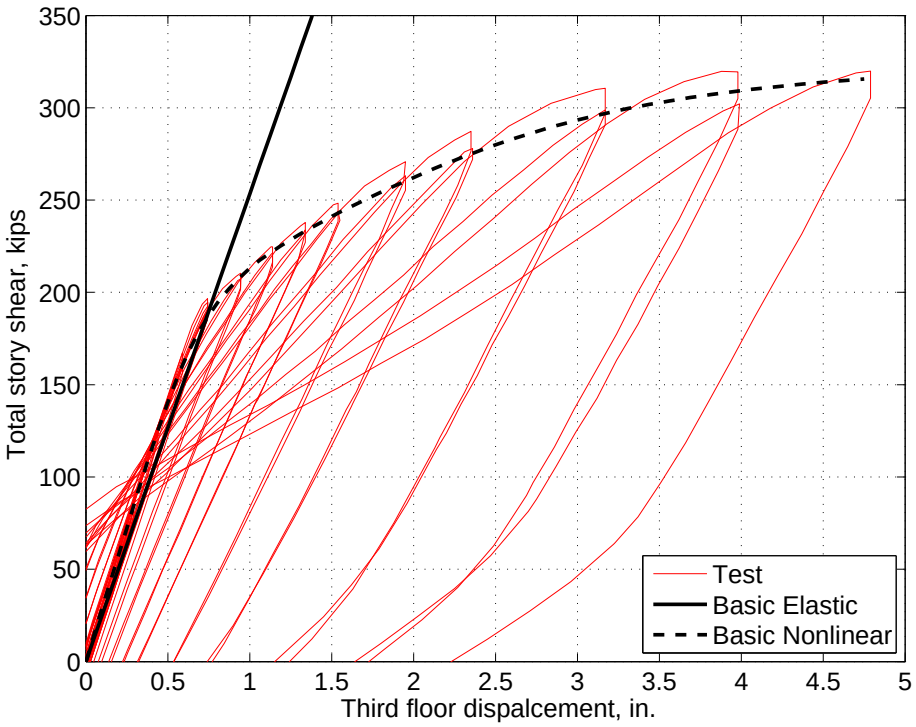

Figure 6.10: Pushover results for Models I (Basic Elastic) and II (Basic Nonlinear)

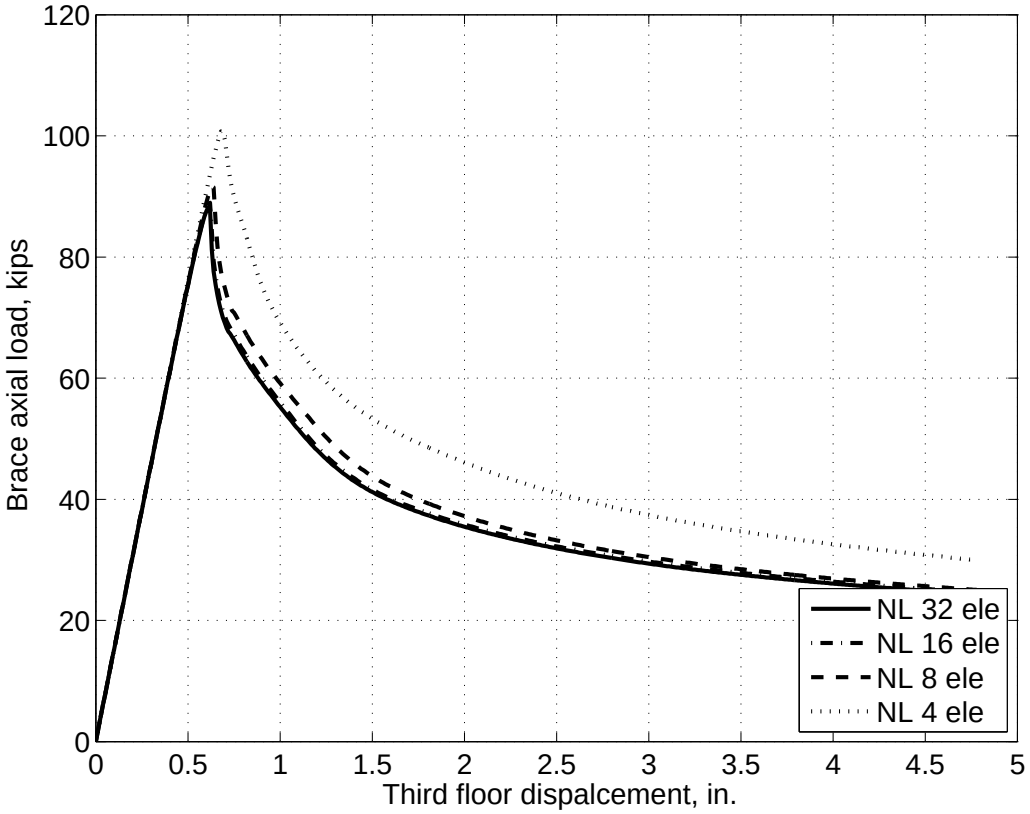

Figure 6.11: Brace discretization study, brace axial load versus third floor drift

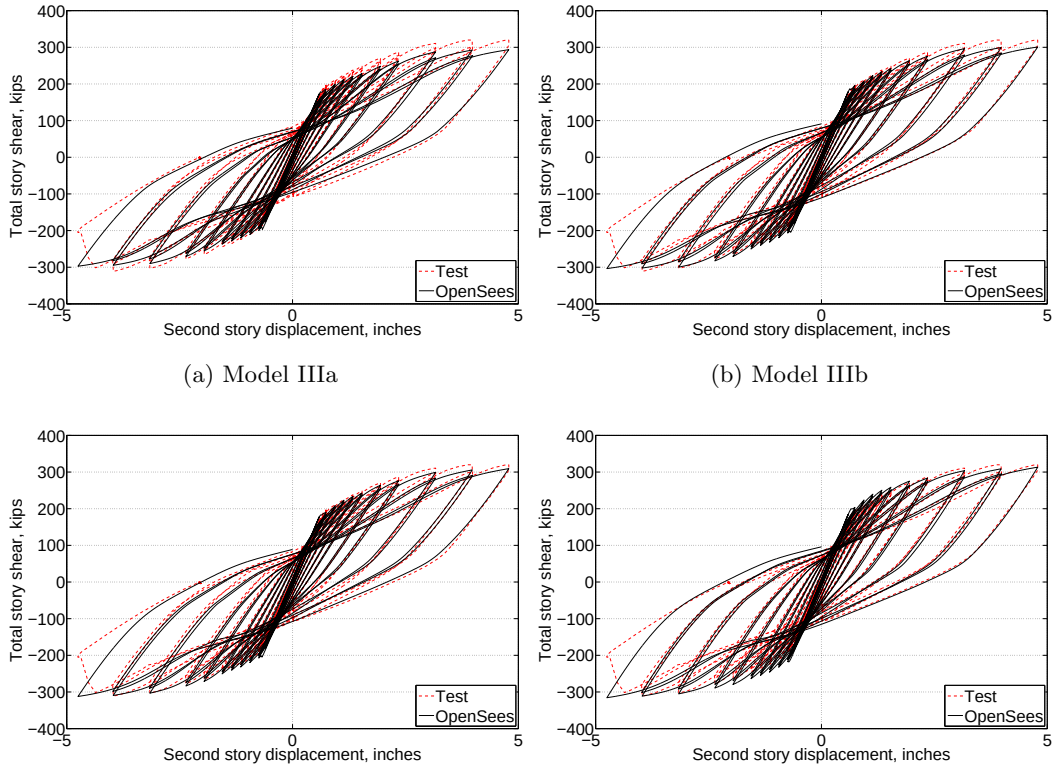

(a) Model IIIa

(b) Model IIIb

(c) Model IIIc

(d) Model IV

Figure 6.12: Global hysteretic response, Models III and IV

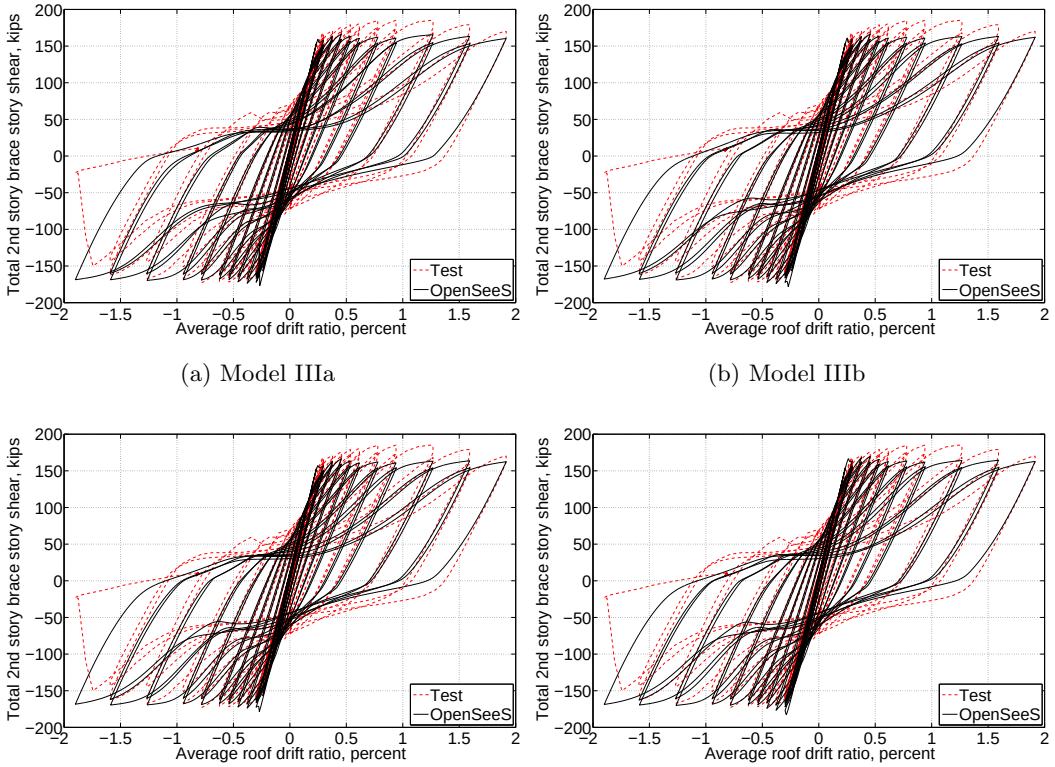

(a) Model IIIa

(b) Model IIIb

(c) Model IIIc

(d) Model IV

Figure 6.13: Second story shear resisted by braces versus average story drift ratio, Models III and IV

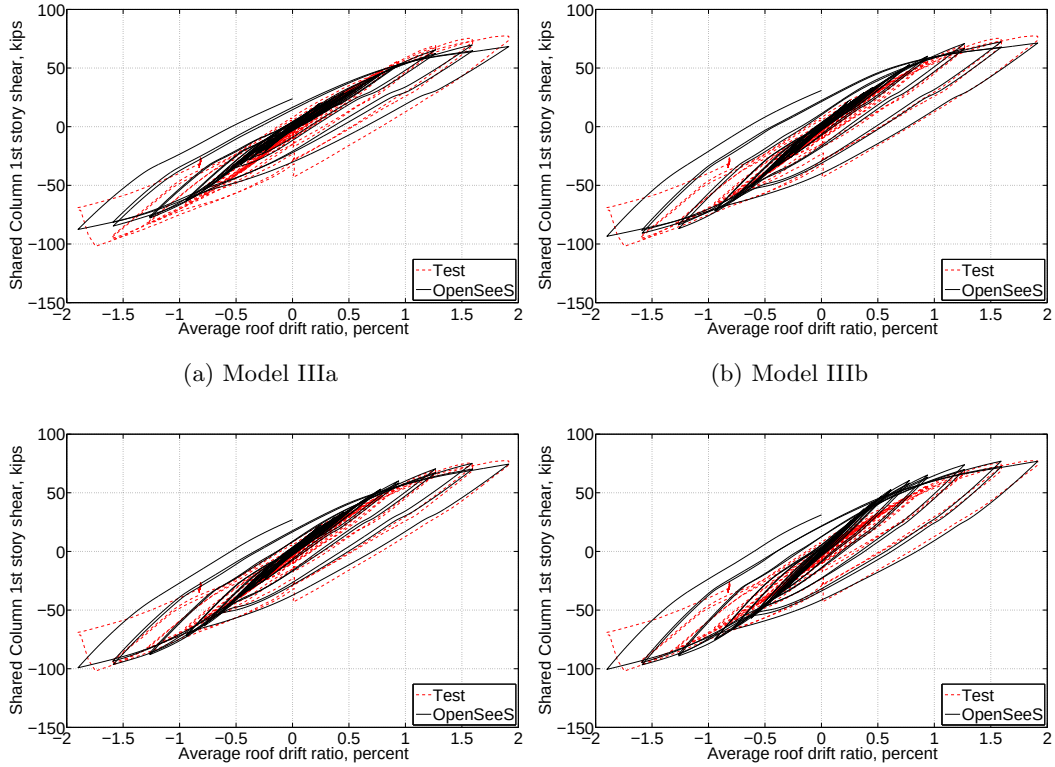

(a) Model IIIa

(b) Model IIIb

(c) Model IIIc

(d) Model IV

Figure 6.14: First story shared column shear versus average story drift ratio, Models III and IV

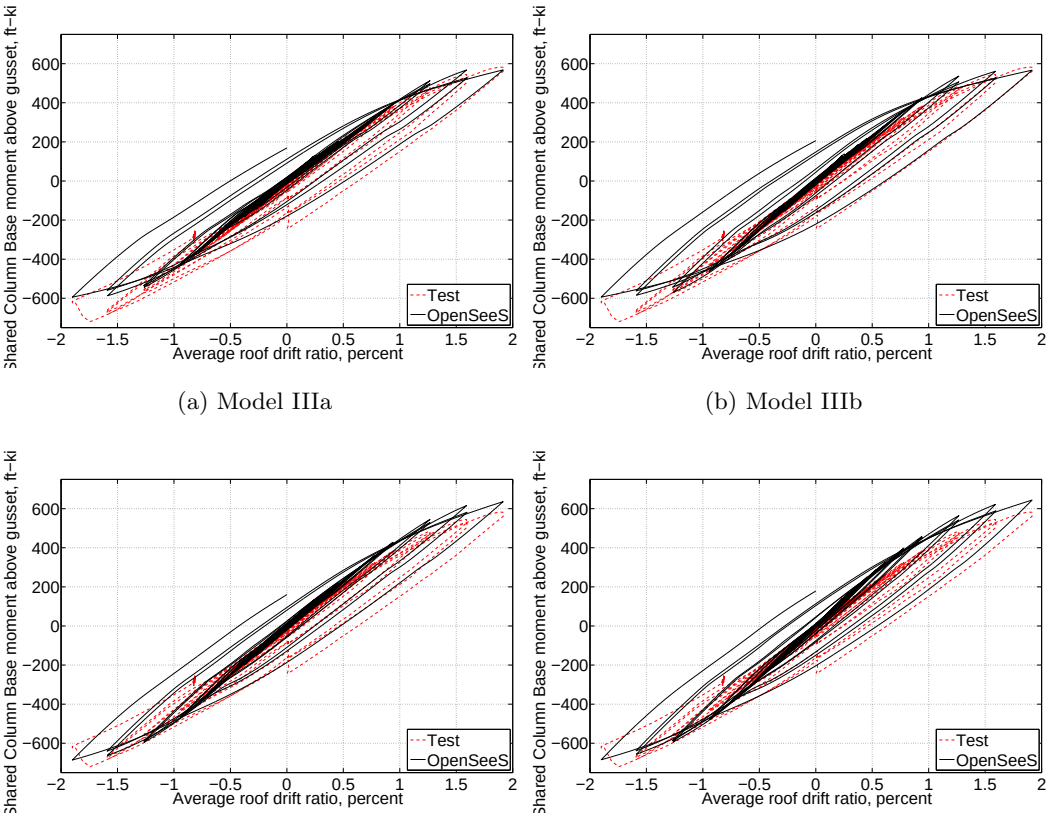

(a) Model IIIa

(b) Model IIIb

(c) Model IIIc

(d) Model IV

Figure 6.15: Moment at shared column base versus average story drift ratio, Models III and IV

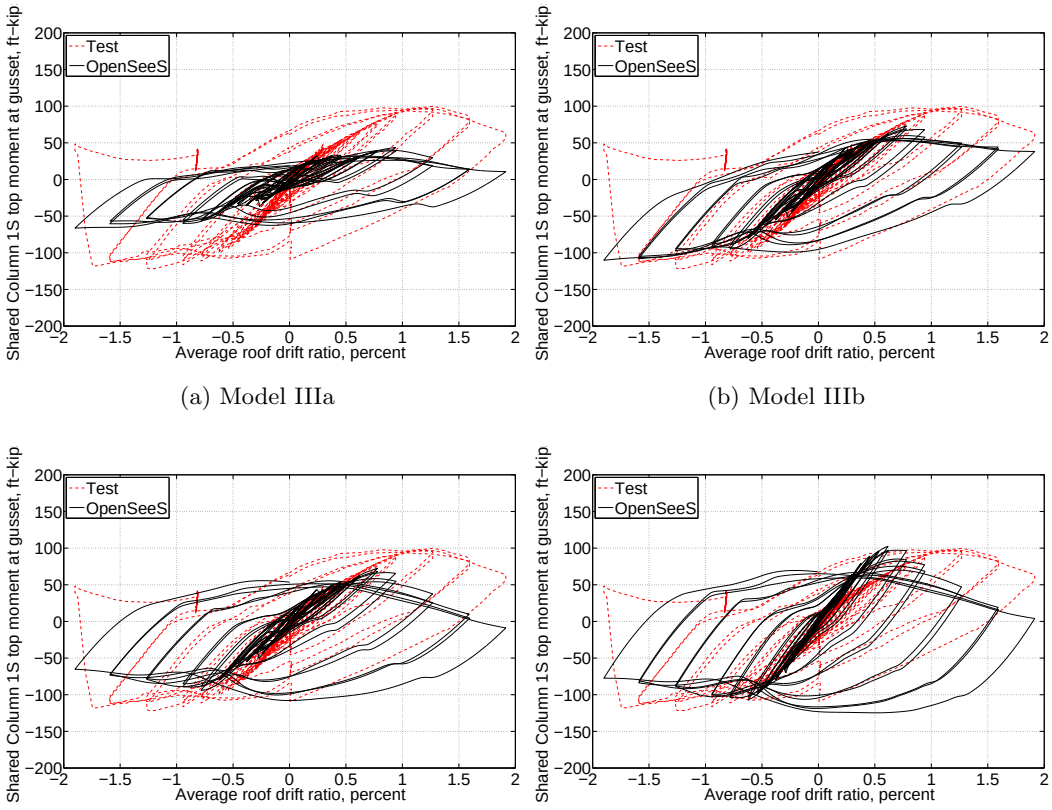

(a) Model IIIa

(b) Model IIIb

(c) Model IIIc

(d) Model IV

Figure 6.16: Moment at top of 1st story shared column versus average story drift ratio, Models III and IV

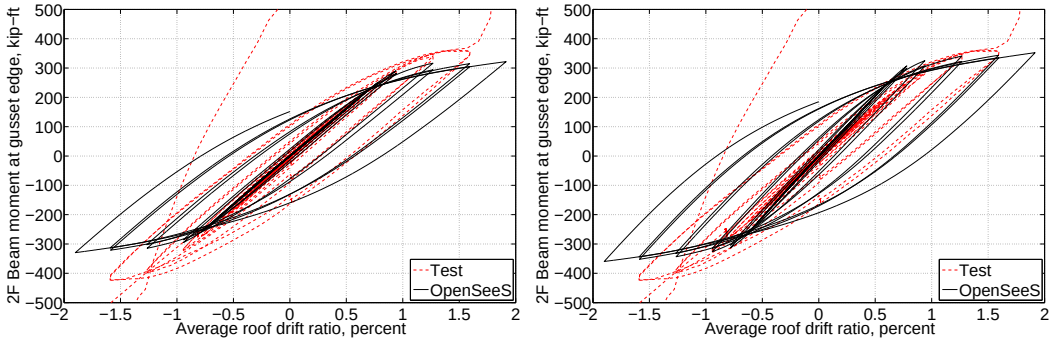

(a) Model IIIa

(b) Model IIIb

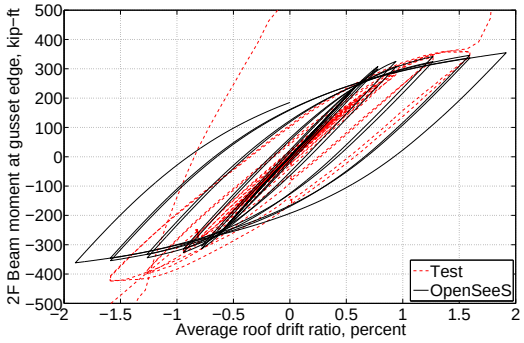

(c) Model IIIc

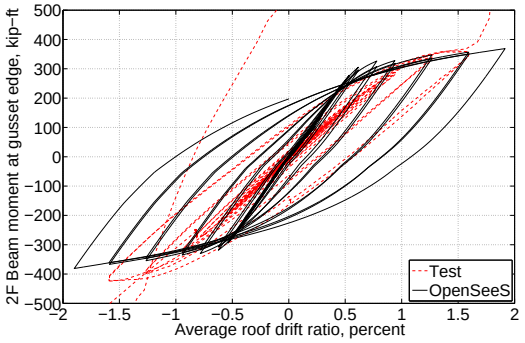

(d) Model IV

Figure 6.17: Second floor beam moment at shared column versus average story drift ratio, Models III and IV

Chapter 7

BRBF CONTINUUM FINITE ELEMENT SIMULATIONS

7.1 Introduction

The behavior of the corner connection region of BRBFs was studied through finite element (FE) simulations. The objective of the study was to extend the experimental portion of this research to further investigate the effect of variables that were not considered in the experiments on the behavior and seismic performance of the members and elements within the connection region. The ultimate goal of this study was to develop design and detailing recommendations that will improve the performance of the system by preventing or minimizing the damage at the connection region that has been shown experimentally to limit the larger drift capacities that BRBFs have relative to conventional buckling-brace systems.

To achieve this, nonlinear FE simulations were performed on Frame 1 of the BRBF test specimen. This frame is highlighted in the foreground in Fig. 7.1. The model of this frame was developed and calibrated and used as the basis for the parametric studies that will be described in the next chapter. The model included the concrete floor slabs, and the same uni-directional, cyclic displacement protocol applied to the test frame was applied in the simulation. Tearing and fracture of the BRBs, welds and base material was not simulated in the analyses but strain and deformation indices were investigated and monitored during the simulations at the locations where fracture occurred during the experiments. These indices were used to estimate the likelihood of tearing or fracture. The reference model was validated by comparing the simulated global and local force-deformation response with those measured in the experiments. The deformed shapes between the two were also compared.

This chapter describes the model development and validation while the parametric studies will be described in Chapter 8. Section 7.2 will describe the BRBF test frame that was simulated in the FE analyses. Sections 7.3 and 7.4 give the basic description of the FE model including element types, boundary conditions and modeling of the frame members.

Section 7.5 through 7.8 describe the finite element models for each member type. The stress and strain and indices that were used to assess the performance and behavior are discussed in Section 7.9. The calibration of the material constitutive models are discussed in Sections 7.10 through 7.12. The mesh refinement study is described in Section 7.13 while the validation of the final model is discussed in Section 7.14.

7.2 BRBF Test Frame Description

The BRBF test frame has been described in Chapter 3; a summary of the frame is provided here. Frame 1, highlighted in Fig. 7.1 and shown in elevation in Fig. 3.6a, was modeled. As shown in the figures, the beams and columns were wide flange shapes and the BRBs were placed in a single-diagonal configuration. The BRBs were attached to the gusset plates with pins that transferred the load through a pair of plates at the ends of the BRBs through a hole in these end plates and the gusset plates. The gusset plates were attached to the beams and columns with fillet welds on each side of the plates. Concrete floor slabs were attached to the beams with shear studs. The slab was blocked out around the columns at the second floor where the gusset plates occur, and were also blocked out around the columns at the top floor with foam insulation. The webs and flanges of the beams were attached to the columns with complete joint penetration welds providing a connection with full fixity.

The columns in the test frame were welded to 3 inch base plates with complete joint penetration welds. These base plates were attached to 4 inch thick plates that were post-tensioned to the strong floor providing a very rigid connection for the column bases. In fact, little-to-no movement was measured at the base during the experiment. Figure 3.3 shows the second and third floor plans of the test specimen. It can be seen that W14x22 beams frame into the braced frame beams of Frame 1 (and Frame B) at midspan of those beams, limiting twist and out-of-plane movement of the beam at that location relative to the plane of the frame.

7.3 Description of FE Model

The simulations were performed with the general-purpose finite element simulation software ABAQUS Version 6.10-2 [ABAQUS, 2010]. The simulations were performed with a

Dell Opltiplex configured with an Intel Core i7 2600 3.4GHz CPU and 8GB of RAM. The ABAQUS Standard module was used which uses an implicit algorithm to solve the nonlinear equations.

All elements except the BRBs, were modeled using 4-node quadrilateral shell elements with reduced integration (defined as S4R by ABAQUS). Three-node shell elements were used for some elements in the gusset plates where geometry prevented the use of 4-node shell elements. The BRBs were modeled as truss elements. Shell elements were used instead of 8-node solid elements to reduce the computational expense time. Figure 7.2 shows a drawing of the FE model with the element types labeled for each main member.

The 4-node shell elements consider finite membrane strains and may be used to model both thin and thick shell problems. These elements have six degrees of freedom per node, three displacement and three rotation components. First-order (linear interpolation functions) elements with reduced integration and hourglass control were used to reduce runtime and prevent locking. The shell sections had five layers through the thickness and were numerically integrated during the analysis using Simpson's rule to calculate cross-section behavior. Transverse shear stiffness was included in the formulation. Geometric nonlinearities were included in the analyses using the updated Lagrangian approach to capture the local buckling of the beam and column flanges and webs that occurred during the experiment. In this approach, the elements are formulated at each step using the nodal coordinates in the current, deformed configuration.

Material nonlinearities were incorporated into the model using the von Mises yield criterion for all materials except the concrete floor slabs. The BRBs, wide flange and gusset plate materials were modeled using a combined, nonlinear kinematic and isotropic hardening law. The concrete material was modeled using a linear elastic material. The stress and strain measures used were the Cauchy ("true") stress and logarithmic strain. A more detailed description of each material's constitutive law is given in Sections 7.10 through 7.12.

7.4 FE Model Boundary Conditions

The base of the columns in the FE model were modeled with fully restrained boundary conditions. This was accomplished by preventing translation of the elements nodes at the

base of the columns in three orthogonal directions as shown in Fig. 7.3. Out-of-plane restraint was provided to the braced frame beams at mid-span where the intermediate floor beams framed into as shown in Fig. 7.3. A rigid node was used to control the displacement history of the frame. This node is shown at the top of the frame in Fig. 7.3 and was restrained in the global X direction shown on the bottom of Fig. 7.3. The imposed displacement, shown as Δ in the figure, was applied in the Y direction to the control node. Movement of the third floor slab was constrained to the control node with a kinematic coupling constraint that tied the slab degrees of freedom to the control node in the X and Y directions. This simulated the portion of the slab that was connected to the crosshead (rigid loading beam) during the experiment. This constraint is shown graphically in Fig. 7.4.

7.5 BRB Model

A physically accurate model of a BRB is difficult to implement in a FE simulation given the number of components in a BRB and the complicated behaviors and interactions between these components. This includes poisson expansion of the core during compression which results in force transfer from the steel core to the infill grout and outer steel casing. Additionally, during compression, the core exhibits higher-mode buckling along its length which transfers additional force to the restraining system. A model capable of capturing these behaviors requires contact and friction elements. The computational cost of this outweighed the need for that degree of accuracy. Therefore, a simple model was used and calibrated to provide a close representation of the measured force-displacement response of the BRBs.

The BRB model implemented in ABAQUS consisted of a single truss member with a constant cross-sectional area. A truss element is capable of transferring load only along the axis of the member. No moments or forces perpendicular to the longitudinal axis can be supported. The end connection of the PowerCat BRB used in the test frame was connected with a pin that allowed rotation in the plane of the frame but provided some level of fixity out-of-plane and torsional fixity along the brace axis. This was ignored in the analyses because it is conservative and the out-of-plane stiffness of the BRB connection will not impact the demands if there are no stability issues in the BRB or gusset plate. The end collars in the BRBs that were used prevent these instabilities.

BRBs do not have a constant cross-section along their length but at least four sections with different areas as shown in Fig. 7.5. For the BRB shown in the figure, these are the clevis area with length L_{CL} and cross-sectional area A_{CL}; the end zone area with length, L_{EZ} and cross-sectional area A_{EZ}; the transition zone with length L_T and cross-sectional area A_T; and the core with length L_C and cross-sectional A_C. The BRB in the FE model was modeled as a truss element with constant cross-sectional area and therefore the BRB cross-sectional area used in the FE model was not the area of the actual core but a derived area, denoted as A_{equiv}, using the brace length, L_{wp} (see Fig. 7.5), that resulted in the same stiffness and force-displacement relationship as the actual BRB.

The stiffness of an axial member with discrete sections in series as shown in Fig. 7.5 may be described by Eqn. 7.1, where K_i is the axial stiffness of each section 'i' and the axial stiffness K_i is defined in Eqn. 7.2. The results of this stiffness calculation was performed for the BRBs used in the test by the BRB manufacturer and was shown in Table 5.4 along with the stiffness measured during the test. The equivalent cross-sectional area of the BRB used in the simulation was found by setting Eqn. 7.2 equal to the measured stiffness and solving for the area. Table 7.1 shows the results of this calibration. The second column of the table lists the value of the equivalent area, A_{equiv}, used in the simulations; the third column lists the length of the BRB, L_{wp}, and fourth column lists the value of the stiffness measured in the experiment. The modulus of elasticity, E, used in the calibration was 29,000 ksi.

$$\frac{1}{K_{total}} = 2\frac{1}{K_{CL}} + 2\frac{1}{K_{EZ}} + 2\frac{1}{K_t} + \frac{1}{K_c} \tag{7.1}$$

where K_i on the right-hand-side is given by Eqn. 7.2

$$K_i = \frac{EA_i}{L_i} \tag{7.2}$$

7.6 BRB Connection to Gusset Plate

The BRBs used in the experiment were attached to the gusset plates with cylindrical pins that joined the clevis pairs at the ends of the BRBs (see Fig. 3.7) to the gusset plates. The cylindrical pin was modeled in the simulation as an elastic circular shell element joined to the gusset plate on all edges as shown in Fig. 7.6. The ends of the BRB truss elements were attached to the center node of the cylindrical pin.

7.7 Modeling of Wide-flange and Plates

The wide flange members used as beams and columns, the gusset plates and the column stiffeners and continuity plates were modeled with the S4R shell elements discussed in Section 7.3. The beams were attached to the columns with tie constraints to simulate the fixity that complete joint penetration welds provide, but the actual welds were not modeled explicitly. ABAQUS tie constraints ensure that each node on one surface have the same values for its degrees of freedom as the corresponding node on the other surface. The gusset plates were attached to the beams and columns with tie constraints also to simulate the welded connection and the welds were not modeled explicitly except for two simulations described at the end of this chapter. The column stiffeners and continuity plates were attached to the columns with tie constraints also.

The gravity beam framing into the web of column A-1 at the second floor was connected to the web with 3/4 inch diameter bolts. The bolt holes in the column web were modeled by removing the material in the web. The material removed was a 13/16 inch circular hole at each bolt location.

7.8 Modeling of Concrete Slab

The concrete floor slabs at the second and third floors were also modeled with the general-purpose shell elements with reduced integration (S4R). The slab width used was based on the effective slab width recommended in AISC [2005b] for beams with a slab on one side only. The width of the effective overhanging flange is defined as the lesser of: 1.) one-twelfth the span length of the beam; 2.) six times the slab thickness; 3.) one-half the clear distance

to the next web. The resulting slab widths was controlled by the first criteria and the total slab widths including the width on the free edge were 28.5 and 37.5" for the second and third floor, respectively.

The second and third floor slabs were attached to the top flanges of the beams with tie constraints. This assumes that no slip occurs between the floor slabs and the beam and measurements recorded during the experiments confirmed that this was the case.

7.9 Stress and Strain Indices

To enable the comparison of the behaviors, damage and potential for fracture in the beams, columns and gusset plates between the different models for the parametric study, a number of stress and strain indices were used at the critical locations in the frames where damage occurred during the experiment. The main indices used were the equivalent plastic strain (PE), the cumulative equivalent plastic strain (PEEQ), and the von Mises stress (σ_{vm}). These variables are defined below in Eqns. 7.3 through 7.5.

$$PE = \sqrt{\frac{2}{3}\epsilon_{ij}^{pl}\epsilon_{ij}^{pl}} \tag{7.3}$$

where ϵ_{ij}^{pl} are the plastic strain components and the summation is applied over i, j = 1, 2, 3.

$$PEEQ = \int_0^t \sqrt{\frac{2}{3}\epsilon_{ij}^{pl}\epsilon_{ij}^{pl}}\mathrm{d}t \tag{7.4}$$

where the integration takes place over the time interval of interest. For the current study, the time interval was the length of the simulation from the start to the drift level of interest used in the comparisons.

$$\sigma_{vm} = \sqrt{\frac{3}{2}S_{ij}S_{ij}} \tag{7.5}$$

where S_{ij} are the deviatoric stress components defined in Eqn. 7.6 below and the summation is applied over i, j = 1, 2, 3.

$$S_{ij} = \sigma_{ij} + p\delta_{ij} \tag{7.6}$$

where σ_{ij} is the stress tensor, p is the pressure defined as the negative of 1/3 of the sum of the normal stresses (see Eqn. 7.7) or first invariant, and δ_{ij} is the Kronecker delta.

$$p = -\frac{1}{3}\sigma_{ii} \tag{7.7}$$

where σ_{ii} is the sum of the normal stress.

7.9.1 Stress and Strain Sampling Points

The above indices were recorded during the simulations at four locations at each floor joint where gusset plates occurred, for a total 12 locations. These locations represent the areas where the bulk of the frame damage occurred during the experiments. These locations are shown in Fig. 7.7 and occur along lines in the beam, columns and gusset plates at the interface between the gussets and the beams and columns. The stresses and strains sampled in the beams and columns at these locations were an average of the two elements on either side of the gusset plate while the gusset plate indices were sampled from the single elements that occurred at the interface as shown in Fig. 7.8. Additionally, these values were sampled at the elements that occurred at the edge of the gusset plates in the beams, columns and gusset plates. These points were the locations where the peak values of PE, PEEQ and σ_{vm} occurred and are shown as dark-filled quadrilaterals in Fig. 7.8. Plots of the stress and strain indices along the gusset interfaces are plotted as a function of the length along the connection with the origin at the intersection of the beam flange and column on the side that the gusset plate is attached to. A diagram of this is shown in Fig. 7.9a for the connection at the second floor of column A-1 and in Fig. 7.9b for the second and third floors of column B-1. All plots will be shown with the origin in the lower left corner as if it were the connection of Fig. 7.9a regardless of which connection is used as explained in Fig. 7.9b.

7.10 BRB Material Modeling and Calibration

The von Mises model was used to model the material inelasticity of the BRB. This model is typically used to simulate the behavior of metals. It is independent of the hydrostatic stress state and depends solely on the deviatoric portion of the stress tensor [Chen and Han,

2007]. The ABAQUS model uses an associative flow rule in which the direction of the rate of inelastic deformation is normal to the yield surface. Temperature and rate dependence were ignored in the model as the experiment was performed quasi-statically at a relatively constant temperature.

A nonlinear, combined isotropic and kinematic hardening model was used to capture the post-yield, cyclic behavior of the BRB. This material model is included in the ABAQUS metal plasticity library and requires a number of parameters and data from cyclic material tests. Much of this cyclic material test data was not available and therefore, a trial-and-error procedure was used to fit the experimentally determined force-displacement behavior of the BRB in the test frame. The FE model used for this calibration consisted of a single truss member with one end pinned; an axial, cyclic displacement protocol was applied at the other end with out-of-plane restraint.

The stress-strain curve shown in Fig. 7.10a was created to model the initial elastic behavior and post-yield kinematic hardening behavior of the BRB material. The curve consists of an initial linear portion with modulus of elasticity, E (29,000 ksi for all simulations). Following the elastic portion, the curve consists of a linear portion with a slope shallower than E, added to an exponential curve to simulate the Bauschinger effect and the gradual yielding that occurs. The adjusted yield stress, $f_{y,adj}$, shown in Fig. 7.10a, was determined from the coupon tests of the BRB core material and adjusted to match the measured yield force of the BRB. These adjusted yield stresses, $f_{y,adj}$ are shown in Table 7.2. Additionally, a lower value, f_{yo}, initiated the exponential transition to the linear hardening region after yield. The equation of the kinematic stress in the post-yield region of the curve is given by Eqn. 7.8.

Figure 7.10b depicts the kinematic plastic stress as a function of plastic strain, ϵ^{pl}, where the plastic strain is the absolute magnitude of strain minus the yield strain, ϵ_y. The dark line indicates the total kinematic plastic stress which is a function of the yield stress, f_y and the two backstresses, α_1 and α_1 labeled in the figure. The backstresses are described by Eqns. 7.9 and 7.10 while the total plastic kinematic stress is given by Eqn. 7.8.

$$f_{KIN} = f_{yo} + \alpha_1 + \alpha_2 \tag{7.8}$$

$$\alpha_1 = E_{sh}\epsilon^{pl} \tag{7.9}$$

where ϵ^{pl} is the plastic strain and E_{sh} is the linear strain hardening modulus.

$$\alpha_2 = C_1(1 - e^{-\eta_k \epsilon^{pl}}) \tag{7.10}$$

where C_1 is the difference between $f_{y,adj}$ and f_{yo}. The constant η_k determines the rate at which the stress in the exponential transition increases.

Isotropic hardening was also modeled using the exponential law shown in Eqn. 7.11 and whose form is identical to Eqn. 7.10 and shown in Fig. 7.10b.

$$f_{ISO} = f_{yo} + Q_\infty(1 - e^{-b\epsilon^{pl}}) \tag{7.11}$$

where Q_∞ is the maximum change in size of the yield surface and b, similar to η_k, determines the rate at which the size of the yield surfaces changes.

In total, five parameters were required to calibrate the kinematic and isotropic hardening models (E_{sh}, C_1, η_k, Q_∞ and b). The initial, elastic modulus, E was assumed to be 29,000 ksi. Accurate modeling of a BRB requires the isotropic hardening and the overstrength of the brace in compression, both of which vary with brace axial deformation. These dependencies are extremely difficult to model with a symmetric constitutive model. The calibration was judged on the basis of the accuracy of the estimate of the initial yield load, total energy dissipated and the difference in measured and simulated tensile and compressive loads at peak story drifts.

The choice of C_1 and η_k values were chosen such that the initial yield load matched the experimental value, and the shape of the simulated post-yield curve matched the shape of the measured post-yield curve. Similarly, E_{sh} was chosen such that the slope of the linear segment of the post-yield portion of the curve matched the measured response. Table 7.2 lists the values chosen for each BRB.

A range of values were investigated for the isotropic parameters Q_∞ and Fig. 7.11 shows a comparison of three models with a b of 25 and a Q_∞ of 20, 12 and 16 for models 1, 2 and 3, respectively. The plots show the force-deformation response at four different levels of brace

axial deformation that corresponded to story drifts of 0.5, 1.6, 2.4 and 4.6%.. In the earlier cycles where the isotropic hardening does not have a significant impact, the yield load is simulated well along with the peak tensile load for all models (see Fig. 7.11a). As the cyclic deformations increase, the measured isotropic hardening and the compression overstrength increases. For all models, the simulated peak compressive load is close to the measured (less than 10% difference) and the peak tensile load is overestimated by approximately 12 to 33% at 1.6% story drift (Fig. 7.11b). At 2.4% story drift, Model-1 predicts the compressive load well but overpredicts the tensile strength by 36% while Model-2 overpredicts the tensile load by less than 10% but underpredicts the compressive load by slightly over 20% (see Fig. 7.11c). The differences for Model-3 are similar to those for Model-1 except they are reversed for tension and compression. At this drift level, there is not a considerable difference between Models 1 and 3 while Model-2 tensile prediction is large. Model-3 is deemed the best at 4.6% story drift (Fig. 7.11d). While it does not provide the least extreme differences for both tension and compression combined (24% in tension and 20% in compression) it does provide the best relative differences in both tension and compression; especially when considering that the difference in peak compressive load for Model-2 is almost 100 kips or over 40% and the same is true for Model-1 in tension with a tensile load at peak that is 40% greater than the measured. Model-3 provides the least extreme differences in tension and compression at the peak drift levels.

Figure 7.12 shows the cumulative energy dissipated by the BRB as a function of cycle number for the experiment and the three different isotropic hardening models. It can be seen that all of the models dissipate a similar amount of energy and the maximum difference between the models at the last cycle is approximately 15%.

7.11 Wide Flange and Gusset Plate Material Modeling and Calibration

The wide flange members used as beams and columns, and the gusset plates were modeled with general-purpose shell elements as discussed in Section 7.3. The von Mises material model was used with a kinematic hardening rule that modeled the plastic, cyclic behavior. The kinematic plastic stress-plastic strain curves for each wide flange member were determined using Eqns. 7.9 through 7.8. Only the magnitude of the yield stress of each shape

was available and therefore, values of the strain-hardening modulus and the exponential parameters required to model the Bauschinger effect (C_1 and η) could not be calibrated. Values provided in Bruneau et al. (2011) for E_{sh} at the onset of strain hardening vary from 1 to 5% of the elastic modulus, E. Values of zero (perfectly plastic), $0.02E$ were investigated. A range of values for C_1 and η were also investigated. It was found that values of 2%, 15 and 1000 provided adequate matching between experimental and simulated response.

A comparison of the cyclic results of the simulations and the test results are shown in Fig. 7.13. Two simulations are shown and the model noted as "0.2E" models the strain hardening modulus of the wide flanges and gusset plates as 2% of the elastic modulus while the model noted as "EPP" models these materials as elastic perfectly plastic. It can be seen in Fig. 7.13a that the base shear versus roof displacement behavior is relatively similar between the models which is expected because the BRB story shear resistance dominates this behavior. The shared column base shear is shown in Fig. 7.13b and it can be seen that model "0.02E" simulates the shear in positive drift range better than the elastic perfectly plastic model while the two nearly match each other in the negative drift range. This is similar to the behavior for the moment at the top of the second story (Fig. 7.13d). The simulated moments are very similar in the negative drift range while the moment in the positive drift range for the elastic perfectly plastic model is significantly less than the moment in model "0.02E" and the measured moment at roof displacements larger than four inches. The simulated values of the moment at the base of the shared column are relatively similar for both models (Fig. 7.13c).

The two material models did not result in drastically different predictions for the most part except at the larger positive drift ranges for two of the local force measurements where the elastic perfectly plastic model underpredicted the loads. Therefore, the model with 2% strain hardening was chosen.

7.12 Slab Material Modeling

No visible damage was observed in the slabs during the experiment and therefore the slab was modeled using a linear elastic material model. A sensitivity study was performed to assess the effect of the concrete modulus of elasticity on the global and local behaviors. The

modulus of elasticity used in the models was of the form $\alpha_c E_{con}$, where E_{con} is the modulus recommend by ACI 318 [2008] given by Eq. 7.12, and α_c was varied between zero and 2. A poisson's ratio of 0.2 was used. Four different models were investigated in the assessment and included models with varying magnitudes of modulus of elasticity of 0, 2500, 5000 and 10000 psi (α_c of 0, 0.5, 1.0 and 2.0). A compressive strength, f'_c, of 8000 psi was used and based on the cylinder tests performed on the slab concrete.

$$E_{con} = 57,000\sqrt{f'_c} \tag{7.12}$$

Figure 7.14a shows the envelope of the base shear versus roof displacement from the FE analysis results using the four concrete models described above. Also shown in the plot is the complete curve of the experimentally measured base shear versus roof displacement. The envelopes for all of the models with the slab are nearly coincident. The maximum difference in base shear was less than 5%. Similar results were observed for the first-story shear in column B-1 and the base moment at column B-1 as Figs. 7.14b and 7.14c show. As these three figures demonstrate, there is very little difference in the global response and local response at the base and first-story in column B-1 between the models with slabs and the model without the slabs.

The most significant difference in the moment at the top of column B-1 (Fig. 7.14d). The models with the slab has an initial flexural stiffness at this joint that is approximately 20% larger than the model without the slab. The measured initial stiffness is less than 5% larger than the initial stiffness of the model without the slab. The moments at the peak drift levels are better matched by the models with the slabs at roof dispalcements exceeding 3.5" (1.5% SDR). Because the main focus of the simulations was the performance at larger drift levels ($> 2\%$), including the slabs was more appropriate. The curves for the models with the slabs are essentially coincident at this frame location.

The purpose of these simulations was to assess the behavior and performance at the joints through an exploration of a range of parameters. These are relative comparisons and as such, rely more on consistency of the slab model between different models than on the actual slab model (as long as the slab model is realistic as the current ones used are). To

further this point, a comparison is made between four models, two of which have E_c=2,500 psi and two of which have E_c=5,000 psi. Two of these models have gusset plate thicknesses of one inch and the other two models have gusset plate thicknesses of 3/4" Otherwise, the models are exactly the same. Table 7.3 lists these models and the parameters. Figure 7.15a shows the PEEQ in column B-1 at the third floor along the gusset interface for the four models. The difference between the maximum PEEQ values for the models with the concrete modulus of 2,500 psi and a one inch and 3/4" gusset is 47%. The difference between the maximum PEEQ values for the models with the concrete modulus of 5,000 psi and a one inch and 3/4" gusset is also 47%. A similar comparison is made in Fig. 7.15b for the maximum values of PEEQ in the gusset plate at this same location. The differences are 71 and 74%, respectively, for this case. This indicates that regardless of the concrete model, the differences between models with different gusset plate thicknesses remains the same and provides confidence in the parameteric studies with the slab model. The slab model with an elastic moduli of 2,500 psi was chosen for the parametric studies as it provided the better prediction to the measured response.

7.13 Mesh Refinement Study

A mesh refinement study was performed to ensure convergence, accurate results and minimize analysis run time. Four models with different mesh densities were analyzed under cyclic loading using the experimental displacement loading protocol. The average element sizes studied here ranged between 0.5 to 2 inches. Figure 7.16 shows the elevation of the four different models and lists the average element size. Mesh 1 (Fig. 7.16a) had an average element size of two inch everywhere. Mesh 2 (Fig. 7.16b) had an average element size in the beam-column-gusset regions (joint regions) of one inch while the average element size away from the joint was two inches. Mesh 3 (Fig. 7.16c) had an average element size of one inch everywhere while Mesh 4 (Fig. 7.16d) had an average element size of 0.5 inches everywhere.

Close-up details of the mesh at the second floor joint of the shared column for each model are shown in Fig. 7.17. The transition of Mesh 2 at the joint from the fine to coarse mesh can be seen in Fig. 7.17b (note that the frame has been rotated such that the beam is vertical to show its underside).

Figures 7.18 and 7.19 display the frame elevation with the von Mises stress contours and PEEQ contours, respectively, for each mesh size. The contours are virtually identical between all of the models. Figures 7.20a shows the peak values of the base reaction at column B-1 corresponding to the positive drift peaks. The results for each mesh are similar and match the measured values. This reaction is also shown in Figs. 7.20b and 7.20c during the experimental cycles 35 and 43 at 1.5 and 3.3% story drift, respectively. Again, the curves from the simulations are nearly identical. The von Mises stress distribution in the beam along the interface with the gusset is shown in Fig. 7.20d and shows that there is some variation between Mesh 1 and Meshes 2, 3 and 4.

Based on the above study, Mesh 2 was chosen. This mesh consisted of elements in the joint region that were approximately 1 inch square and elements away from the joint region that were approximately 2 inches square.

7.14 Test Frame Simulation Validation

The model was validated through a quantitative comparison of the measured and simulated global and local force-displacement behavior. Additionally, qualitative comparisons of selected local deformations and yielding patterns between the two were made.

The quantitative comparisons were made for the following:

- Base shear versus roof displacement
- Column B-1 base shear versus roof displacement
- Column B-1 base moment versus roof displacement
- Column B-1 moment at top of the second story versus roof displacement
- BRB axial force versus roof displacement

The qualitative comparisons were made for the following:

- Beam yielding and local web and flange buckling at the third floor beam at the gusset plate connection region
- Column A-1 panel zone yielding at the second and third floor levels
- Column A-1 yielding and local flange buckling at the base

The loading simulated the experimental testing protocol with the exception that the first 18 cycles of small deformation were not simulated. This limited the computation time of the simulations without compromising accuracy. These initial cycles did not damage the frame and the majority of brace and element yielding occurred in the cycles beyond these initial 18 cycles. Figure 7.21 shows the complete displacement history applied by the crosshead to the test frame and that portion which was applied to the simulations at the control node.

7.14.1 Force-displacement comparisons

Figure 7.22a shows the total base shear as a function of the applied displacement at the top of the frame. It can be seen that there is good agreement between the experimental results and the simulation. The peak loads in compression match very well while the simulated peak loads in tension are approximately 5 to 12% larger than those observed for the experiment. This larger strength difference in tension results from the symmetric BRB material model that was used that did not accurately capture the compression overstrength. The brace model is stronger in tension at brace deformations larger than approximately 3/4 inches. The global frame stiffness prior to and beyond yield was well simulated up to the point of brace fracture. Beyond brace fracture, the model was not able to accurately simulate the response because fracture was not explicitly modeled in the simulation.

Figure 7.22b shows the base reaction of this column as a function of the applied roof displacement. The initial stiffness is simulated well and is less than 5% greater than the measured stiffness. The stiffness immediately following drift reversal is also simulated well but does not soften as rapidly as the measured response does and therefore does not predict the peak shears in the negative drift range as well. The peak shears are well simulated in the positive drift range.

Figure 7.22c shows the moment at the base of column B-1. The initial stiffness is simulated well and is approximately 8% greater than the measured stiffness. As expected, the behavior upon drift reversal is similar to the base shear of this column. The measured response softens more rapidly and smoothly than the simulated response. However, because the simulated response softens more sharply, the peak moments are simulated relatively well

with the maximum differences at peak drifts on the order of no greater than 10%.

Figure 7.22d shows the moment at the top of second story at the gusset plate edge of column B-1 as a function of roof displacement. The initial stiffness is simulated well and is less than 10% of the measured stiffness. The softening response upon drift reversal is not captured as well with the measured response softening more smoothly and rapidly than the simulated and therefore the simulated peak moments are slightly larger the measured but not more than 10%. The large degredation in moment that occurs at roof displacements larger than 7.5" is not captured because this degradation is due to the tearing of the bottom flange of the beam which was not simulated.

The complete force-displacement curves for the second and first story BRBs are shown in Figs. 7.23a and 7.23b, respectively. The curves are identical to the curves that were discussed in Section 7.10. The compression overstrength is not simulated well due to the symmetric material model that was used.

7.14.2 Qualitative comparisons

Qualitative comparisons of local deformations and yielding were also made. Figure 7.24 compares the experimental and simulated third floor beam deformation at column B-1 at approximately 3.8% 2SDRY. The figures show excellent agreement of the local flange buckling and out-of-plane web deformation at this location. Locations of panel zone yielding at the second and third floor of column A-1 were also compared as shown in Fig. 7.25. Figures 7.25a and 7.25b compare the third floor panel zone yielding which are similar and exhibit the concentration of yielding on either side of the vertical web stiffener. Likewise for the second floor, the horizontal and vertical yielding around the bolt holes and at the free edge of the gusset plate and bottom beam flange match very well (Figs. 7.25c and 7.25d). As a final comparison, Fig. 7.26 compares the yielding and deformation at the base of column A-1. Again, the deformation and yield patterns of the experiment and simulation match well.

7.15 Gusset plate weld tearing analysis

Yoo performed nonlinear simulations of the planar UW test frames and investigated the use of strain indices in the shell element models for predicting initial gusset plate weld tearing [Yoo, 2006]. The indices investigated were the equivalent plastic strain (PE) and the cumulative equivalent plastic strain (PEEQ). Yoo found that using PE provided a relatively small range that correlated with the observed instance of gusset plate weld tearing in the experiments. These values ranged between 0.031 and 0.05 for tearing at the beam interface and ranged between 0.054 and 0.065 for tearing at the column interface. The coefficient of variation (COV) for the beam interface tearing values and for the column interface tearing values were 7 and 20%, respectively.

Other researchers have investigated using a stress-modified critical strain model which combines PEEQ, von Mises stress and the hydrostatic stress into one expression [Kanvinde and Deierlein, 2006]. This type of index has been successful with the use of solid elements but require a mesh size in the fracture area equal to 0.2 mm (0.008 inches). The size of the frame simulations and the use of shell elements performed in the current study precluded the use of elements this small and this index. Therefore, the indices investigated by Yoo were investigated in the current study.

Two models were investigated in the current study and compared to the instance of observed gusset plate weld tearing in the BRBF test frame. The first model was described in this chapter and did not consider the weld material at the gusset connection to the beams and columns (denoted as the "reference" model). The second model considered the weld material at the gusset interface. This was done by assigning a weld constitutive model to the shell elements in the gusset plate that connected to the beam and column shell elements at the interface. The length of the weld elements used were the size of the leg of the welds and thickness assigned to the elements was twice the leg size because fillet welds were used on both sides of the gusset plate. The model was calibrated to match the force-deformation response given by Eqn. 7.13 [AISC, 2005b].

$$P = 0.60F_{EXX}(1.0 + 0.50\sin^{1.5}\theta)[p(1.9 - 0.9p)]^{0.3} \tag{7.13}$$

where P is the nominal strength of the weld segment at a deformation Δ, F_{EXX} is the weld electrode strength (70 ksi), θ is the load angle measured relative to the weld longitudinal axis, and p is the ratio of element deformation to its deformation at maximum stress given by Eqn. 7.14. A theta of 50 degrees was used as the simulations showed that the stress perpendicular to the weld was a larger component than shear. This angle results in a weld strength increase of 35%. The strength increase for weld loaded at 90 degrees is 50%.

$$\Delta_{max} = 1.087w(\theta + 6)^{-0.65} \leq 0.17w \tag{7.14}$$

where w is the weld size.

Initial tearing was observed in the gusset plate welds in the test frame at a roof displacement of -5.3 inches at the three locations where this occurred in the frame that was simulated. Three deformation indices were sampled in the elements at the edge of the gusset plates in the simulations at this drift level. These indices were the PEEQ, PE, and the elongation of the element. The last value was only sampled in the model with the weld material. The sampled values from the simulations are listed in Table 7.4. Also listed are the mean values for each index and the standard deviation (Std Dev) and the COV.

It can be seen that the PEEQ index for the simulation with the weld material explicitly modeled provides the best correlation to the observed tearing with a COV of 15%. This falls within the range found by Yoo [2006] discussed above. The models without the weld material modeled provided the worst correlation with COVs of 35 and 46% for the PEEQ and PE indices, respectively.

A simulation was performed for a model with weld sizes designed for the strength of the plate to assess the likelihood of gusset plate weld tearing for the gusset plate geometry and thickness used in the test frame. The results of this simulation are shown in Fig. 7.27 which shows the PEEQ value sampled at the gusset plate edge for each gusset plate as a function of negative roof displacement. The values are shown for the negative roof displacement because the welds tore in the negative drift range due to frame action. Six curves are shown which coincide with the three gusset plates and the two models. The models with the reference welds are shown as dashed while the models with the welds designed for the

strength of the plate are shown as solid lines. It can be seen in the figure that the models with the stronger welds for gusset plates 2FA1 and 3FB1 exceed the lowest value of the correlated PEEQ at weld tearing reported in Table 7.4 at 8 inches of roof displacement which is the displacement at which BRB core fracture occurred in the experiments. The PEEQ in gusset plate 2FB1 never reached this limit. This analysis shows that the likelihood of weld tearing is significantly reduced when the welds are designed for the strength of the plate and not the forces that result from application of the Uniform Force Method.

7.16 Conclusions

The nonlinear behavior of the BRBF was simulated well. The global and local behaviors matched well especially at the peak drift values. Additionally, the simulated local web and flange buckling of the beams and columns that occurred during the larger drifts matched that observed in the experiment. The next chapter describes the parametric studies that were performed using the validated model as the starting point. The gusset plate weld material models were not included in the parametric study simulations.

Table 7.1: Equivalent cross-sectional area parameters for simulated BRBs

BRB	A_{equiv}, in.^{2}	L_{wp}, in.	$K_{experiment}$, k/in. (K_3 Table 5.4)
Story 2	3.5	175	572
Story 1	3.43	188.7	527

Table 7.2: Material Parameters for FE Simulations

Element	$f_{y,coupon}$	$f_{y,adj}$	f_{yo}	$\frac{E_{sh}}{E}$	C_1	η	Q_∞	b
BRB-2S	43.3	36.1	24	0.024	12.1	1500	16	25
BRB-1S	42.1	35	23	0.024	12	1500	16	25
W12x106	56	-	41	0.02	15	1000	10	25
W12x72	57	-	42	0.02	15	1000	10	25
W16x50	53	-	38	0.02	15	1000	10	25
Gussets	55	-	55	0.02	15	1000	10	25

Table 7.3: FE models for slab sensitivity study

Model Name	Slab E, psi	Gusset plate thickness, in.
Slab2500 1-gp	2500	1
Slab5000 1-gp	5000	1
Slab2500 3/4-gp	2500	3/4
Slab5000 3/4-gp	5000	3/4

Table 7.4: Weld tearing analysis results

Gusset plate	with weld model			w/o weld model	
	PEEQ	PE	Elongation	PEEQ	PE
2FA1	3.60	0.230	0.105	0.125	0.011
3FB1	3.04	0.170	0.064	0.149	0.0131
2FB1	2.68	0.134	0.048	0.071	0.005
Mean	3.11	0.178	0.072	0.115	0.001
Std Dev	0.463	0.049	0.029	0.040	0.005
COV (%)	14.9	27.4	40.7	34.8	46.4

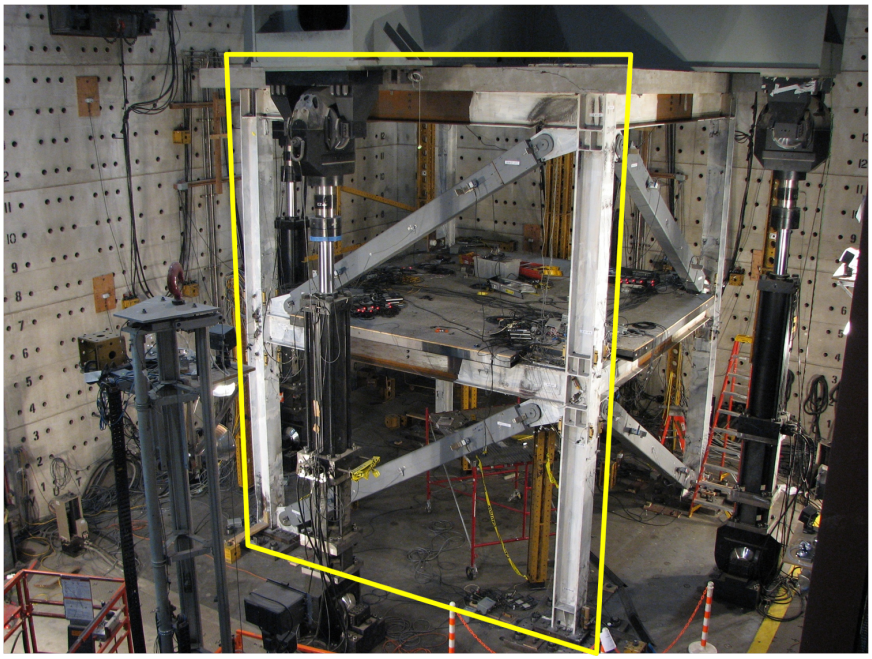

Figure 7.1: BRBF Frame 1 modeled in FE simulation

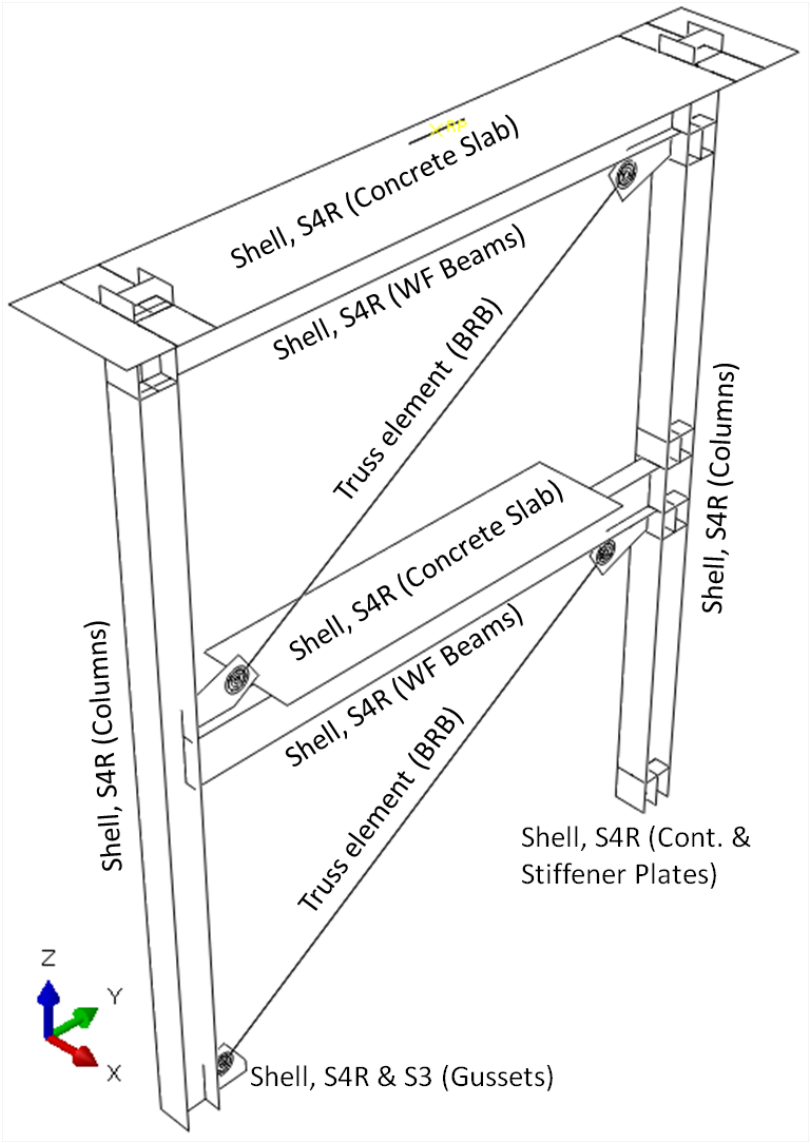

Figure 7.2: Base FE model with element types depicted

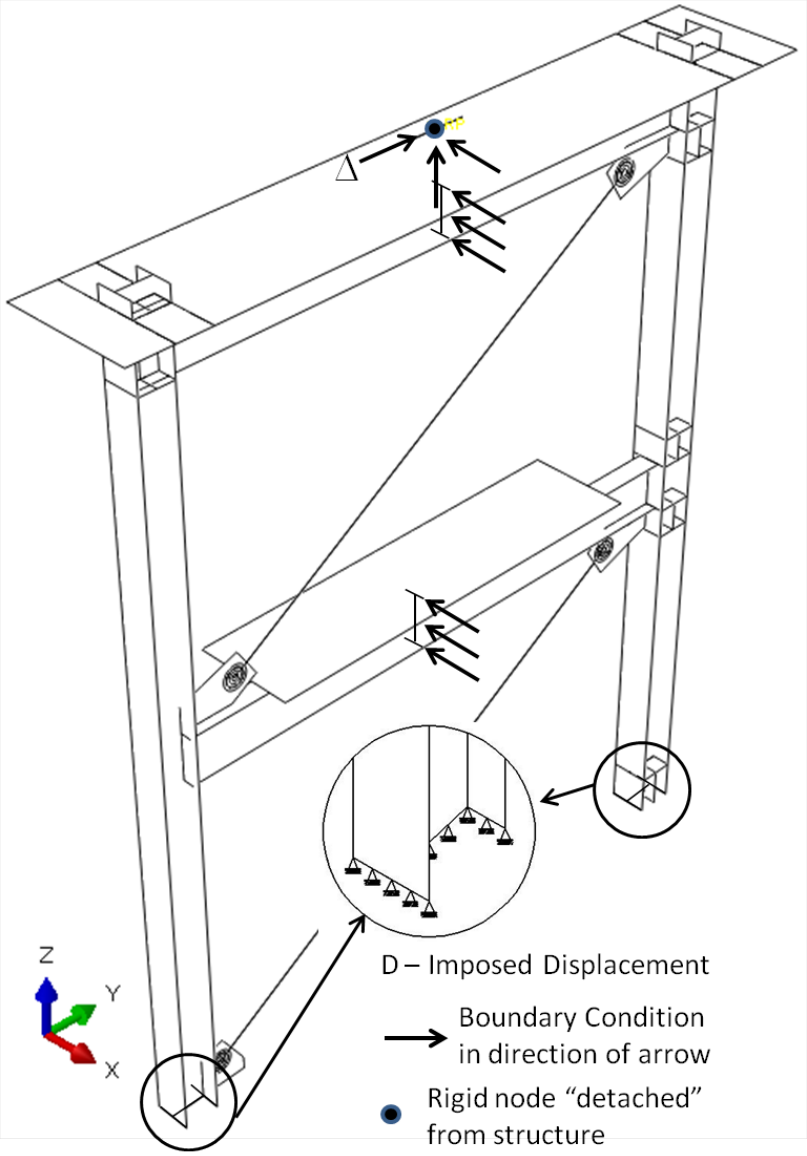

Figure 7.3: FE model nodal boundary conditions

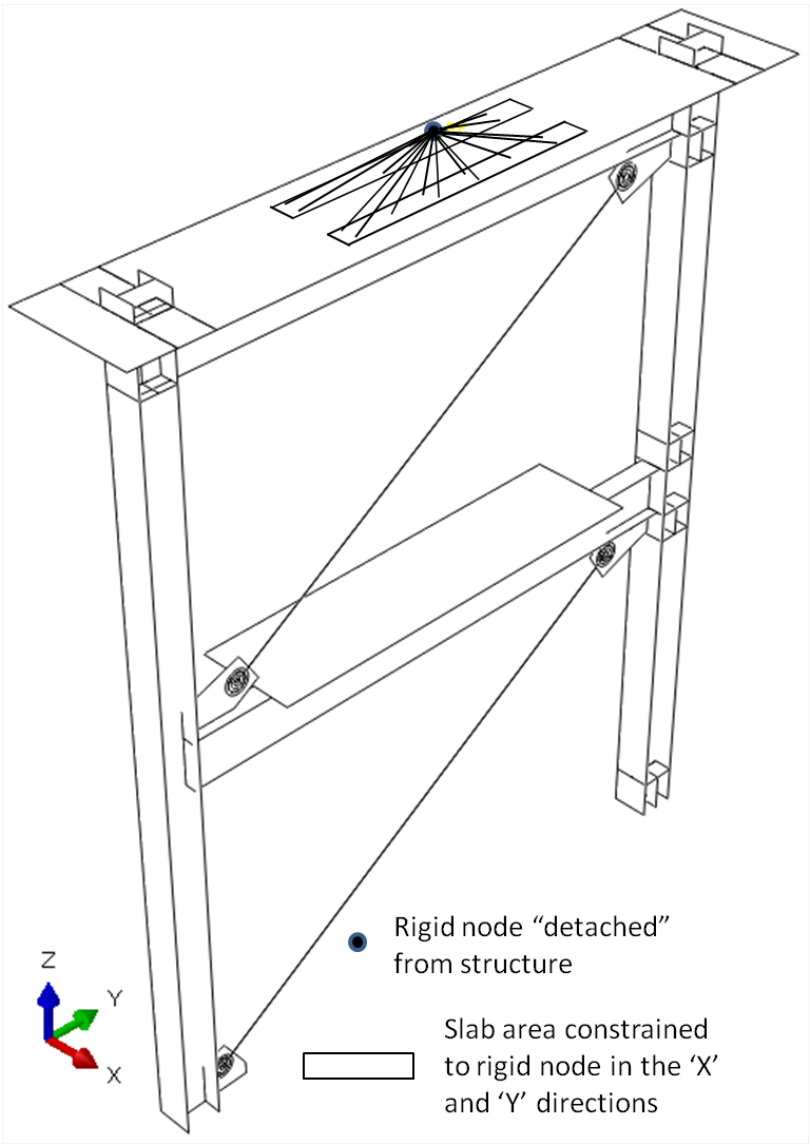

Figure 7.4: FE model third floor slab constraint to rigid “control” node

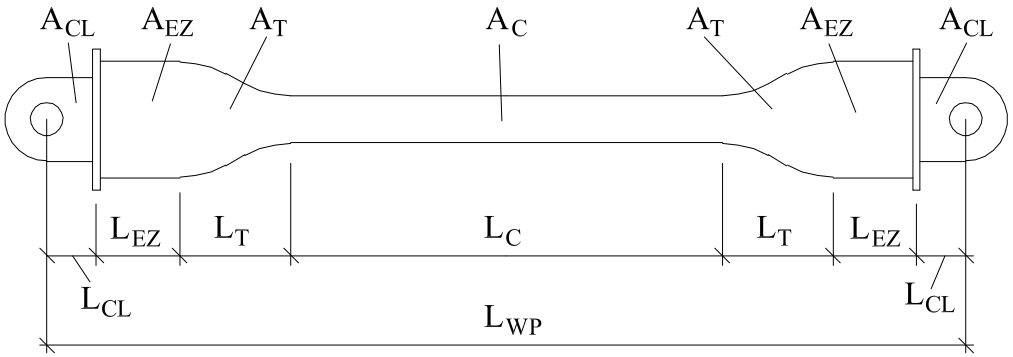

Figure 7.5: BRB sections along length

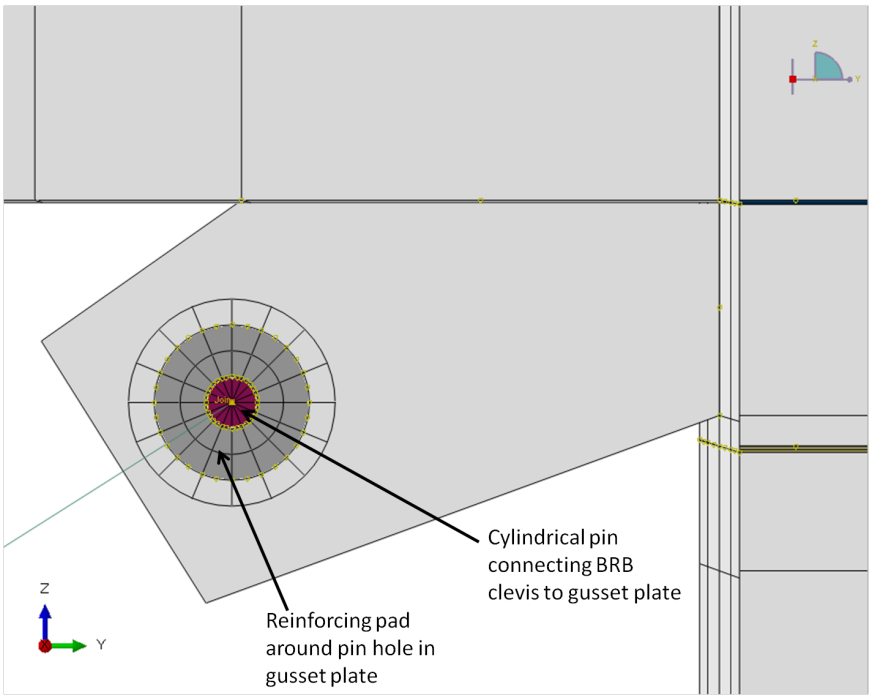

Figure 7.6: FE model detail of gusset plate, reinforcing pad and pin connecting BRB to gusset plate

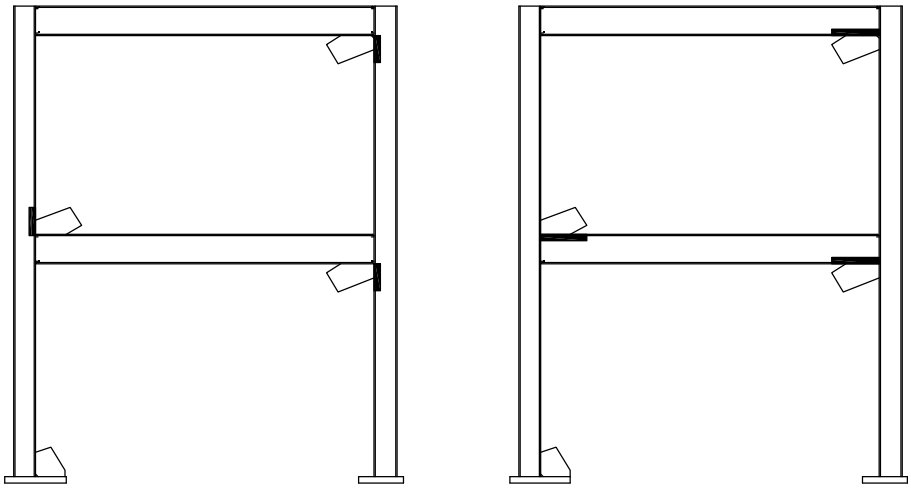

(a) In column along gusset interface

(b) In beam along gusset interface

(c) In gusset along column interface

(d) In gusset along beam interface

Figure 7.7: Stress and strain sampling locations (thick, dark lines) in beams, columns and gusset plates for parametric study.

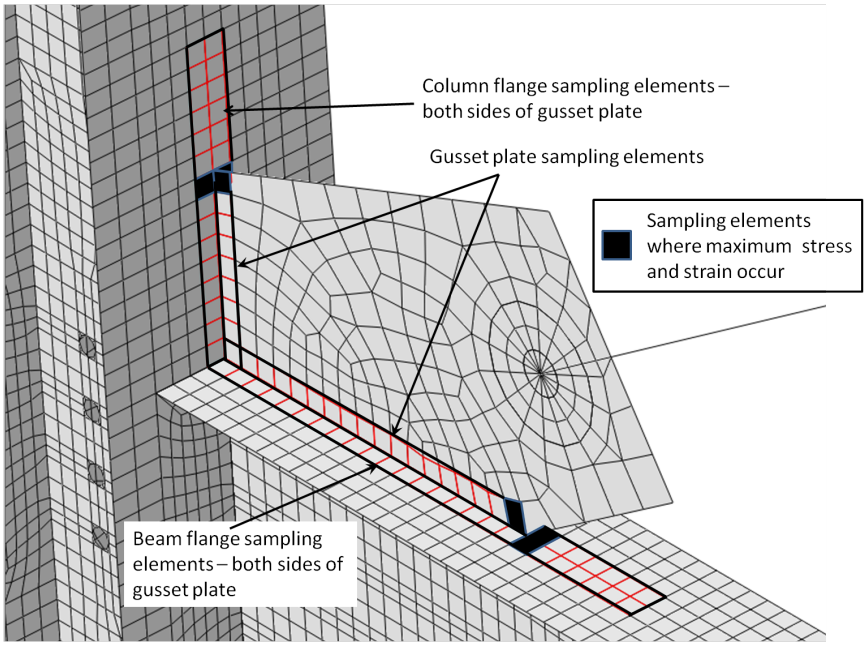

Figure 7.8: Highlighted elements used for sampling maximum stress and strain indices at gusset plate interfaces with beams and columns

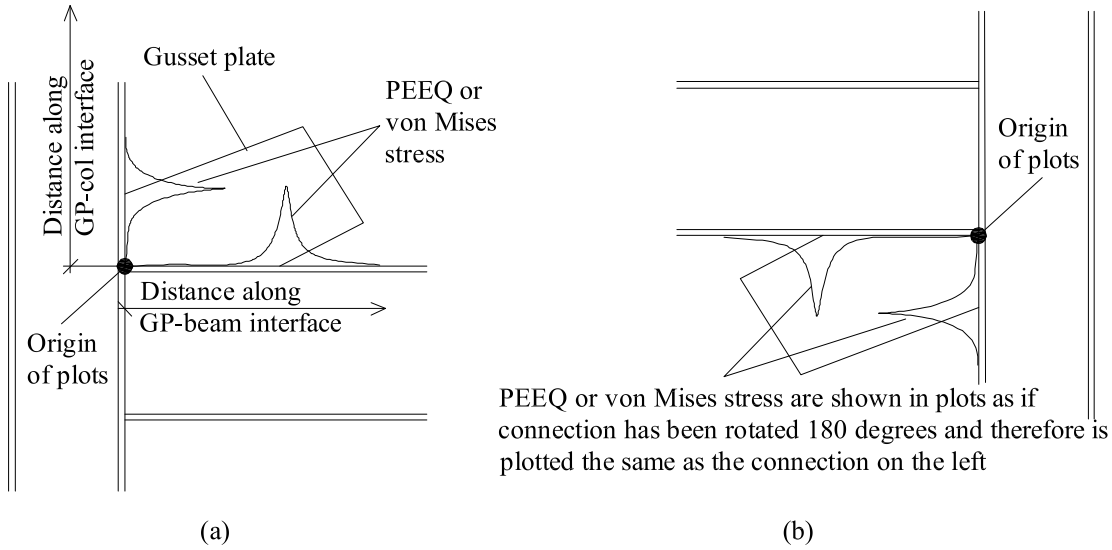

Figure 7.9: Description of plotting method of stress and strain indices along gusset interfaces with beams and columns

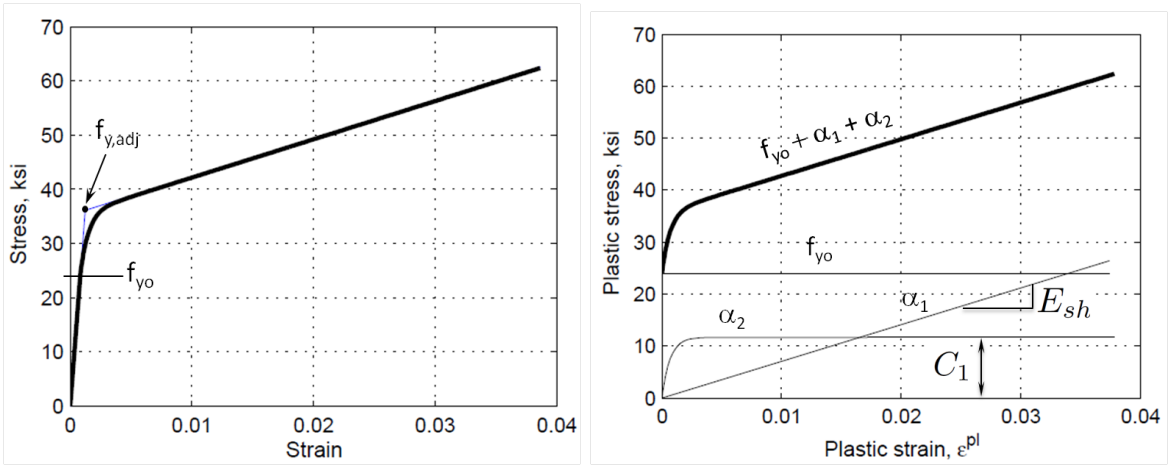

(a) (b)

Figure 7.10: BRB uni-axial material curves: (a) Stress v. strain; (b) Kinematic plastic stress v. plastic strain

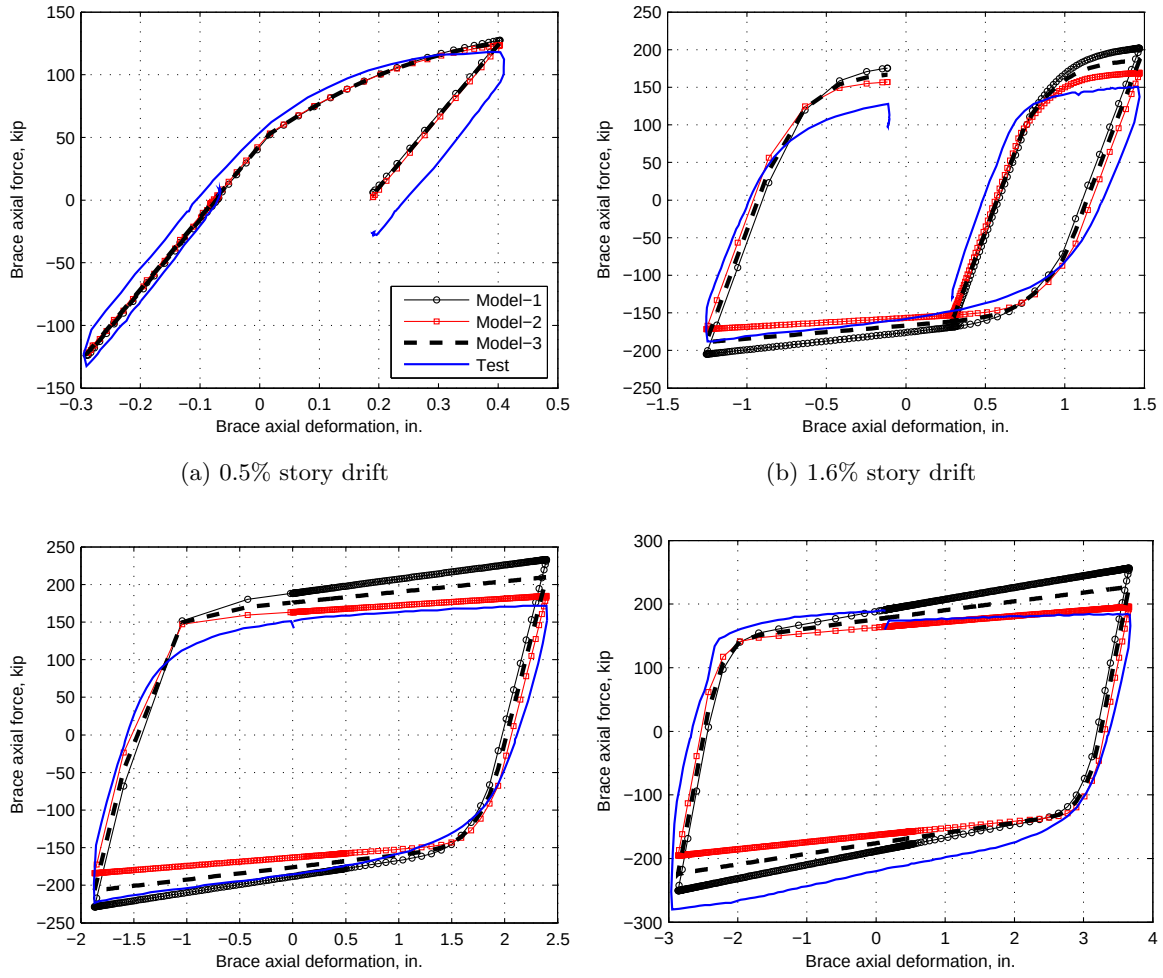

(a) 0.5% story drift

(b) 1.6% story drift

(c) 2.4% story drift

(d) 4.6% story drift

Figure 7.11: BRB force-deformation comparison for BRB material model calibration

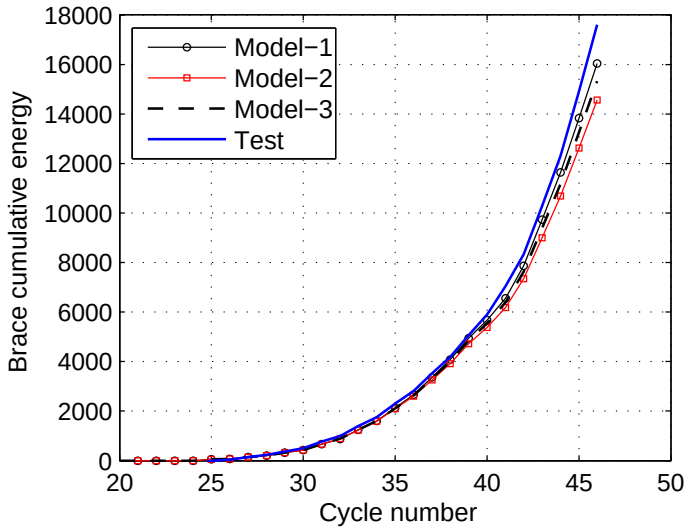

Figure 7.12: BRB dissipated energy comparison between simulation and experiment for BRB material model calibration

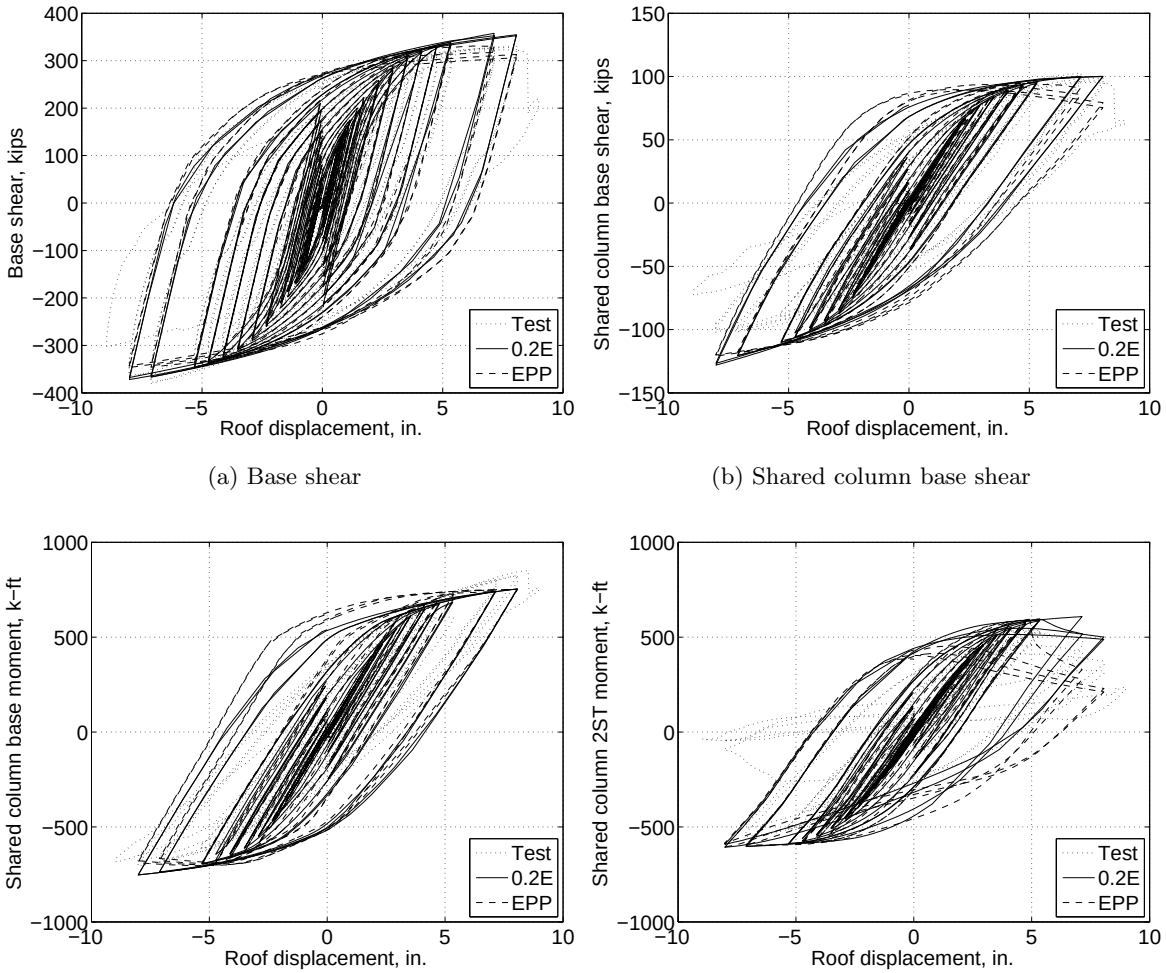

(a) Base shear

(b) Shared column base shear

(c) Shared column base moment

(d) Shared column 2ST moment

Figure 7.13: Wide flange and gusset plate material model calibration comparison plots. (Legend - 0.2E indicates 2% strain hardening modulus; EPP - indicates elastic perfectly plastic)

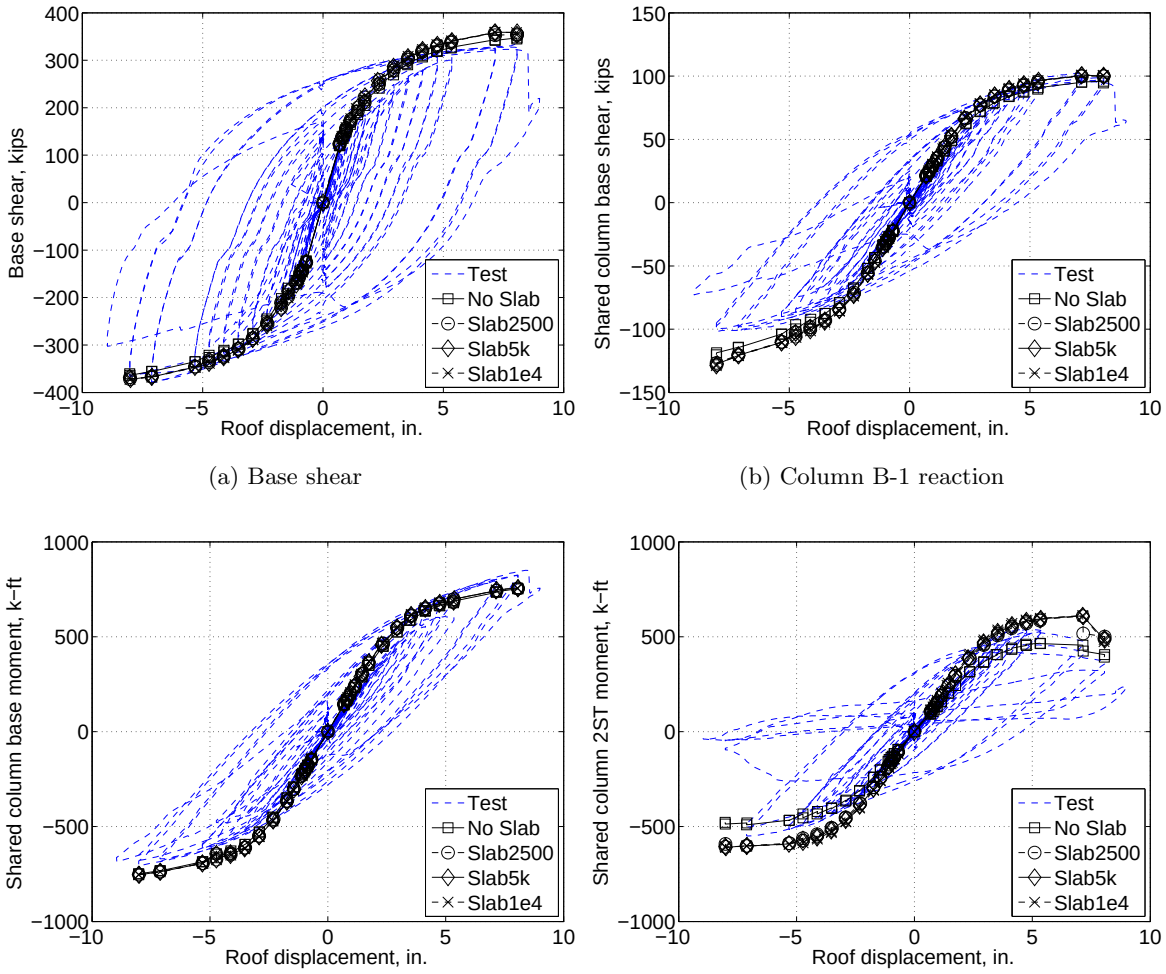

(a) Base shear

(b) Column B-1 reaction

(c) Column B-1 base moment

(d) Column B-1 second story top moment

Figure 7.14: Global force-displacement envelopes for slab sensitivity study

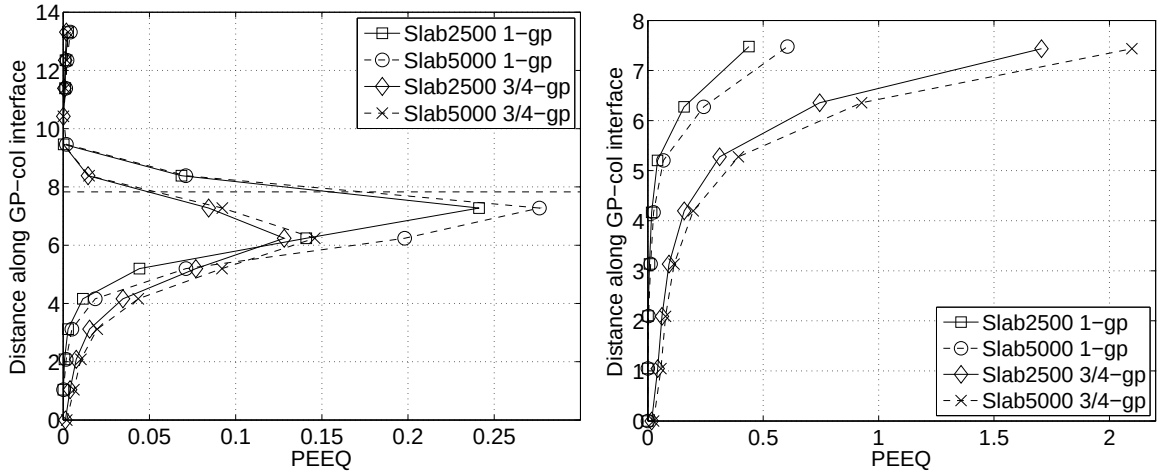

(a) Column PEEQ along gusset interface

(b) Gusset PEEQ along interface with column

Figure 7.15: Comparison of PEEQ values at -3.2% RDR with slab moduli of 2,500 and 5,000 psi with one in. and 3/4 in. gusset plates, column B-1 third floor joint

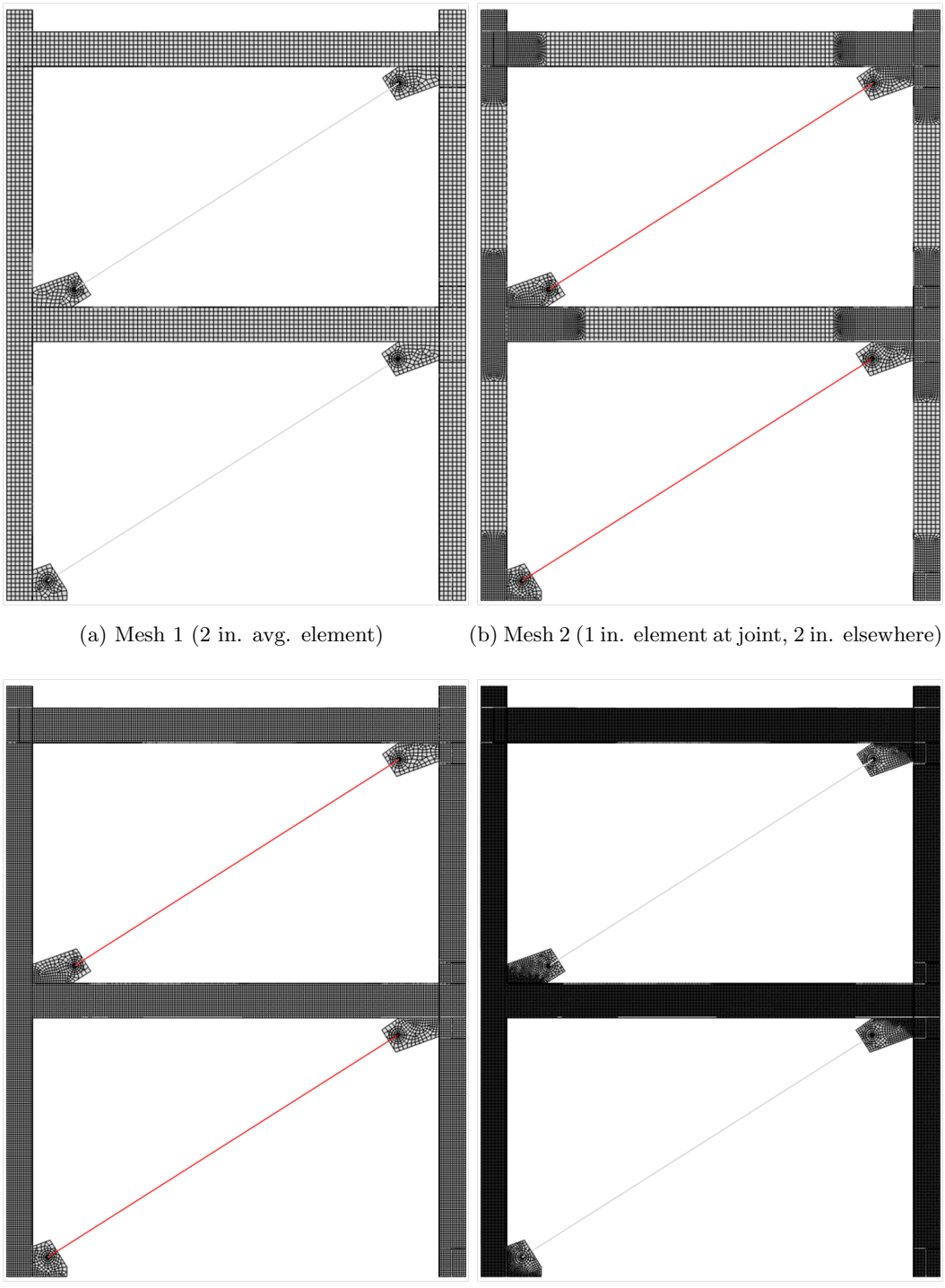

(a) Mesh 1 (2 in. avg. element)

(b) Mesh 2 (1 in. element at joint, 2 in. elsewhere)

(c) Mesh 3 (1 in. avg. element)

(d) Mesh 4 (1/2 in. avg. element)

Figure 7.16: Mesh densities for mesh refinement study

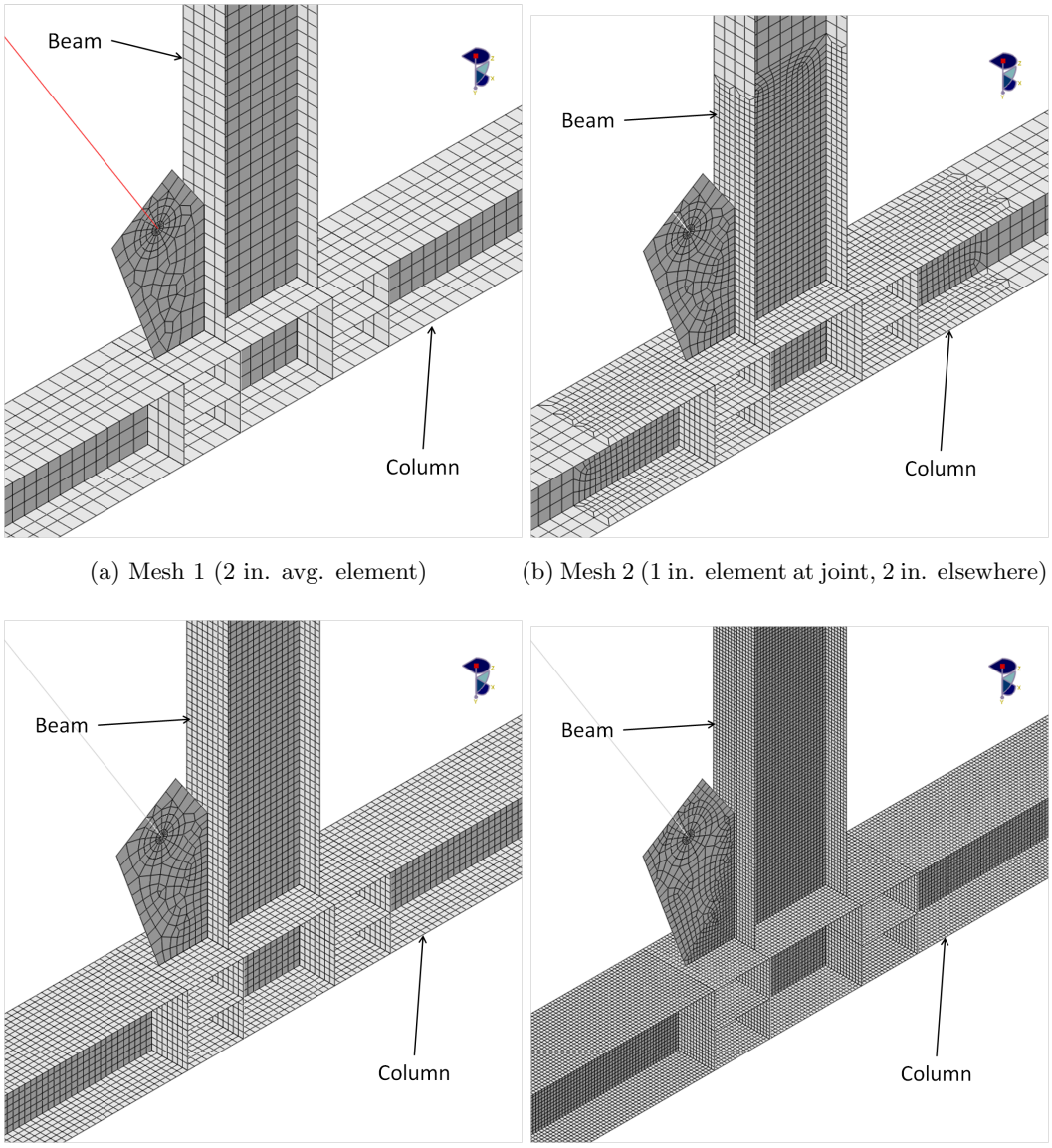

(a) Mesh 1 (2 in. avg. element)

(b) Mesh 2 (1 in. element at joint, 2 in. elsewhere)

(c) Mesh 3 (1 in. avg. element)

(d) Mesh 4 (1/2 in. avg. element)

Figure 7.17: Mesh densities at joint region for mesh refinement study

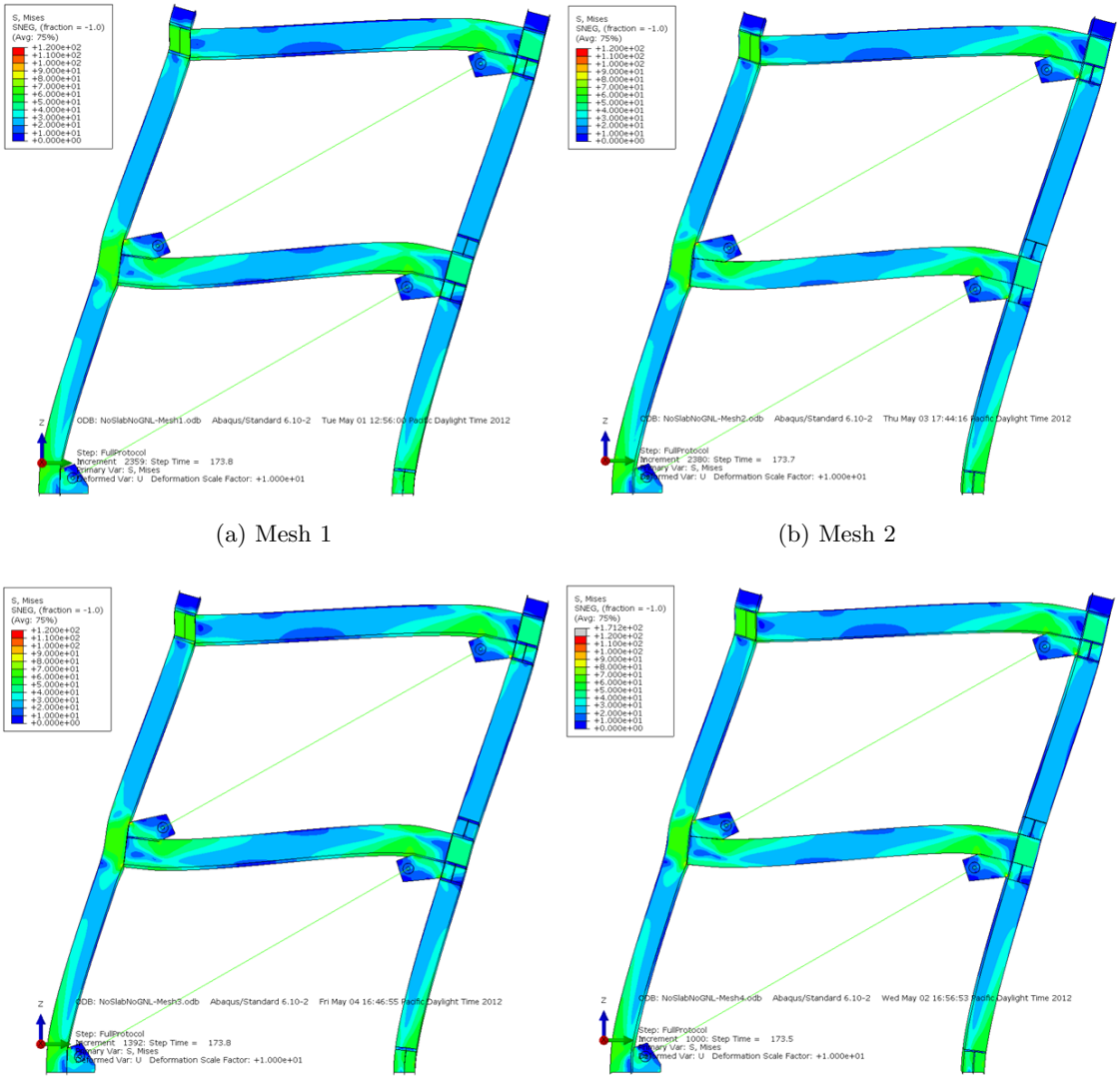

(a) Mesh 1

(b) Mesh 2

(c) Mesh 3

(d) Mesh 4

Figure 7.18: von Mises stress distribution at 3% RDR for mesh refinement study

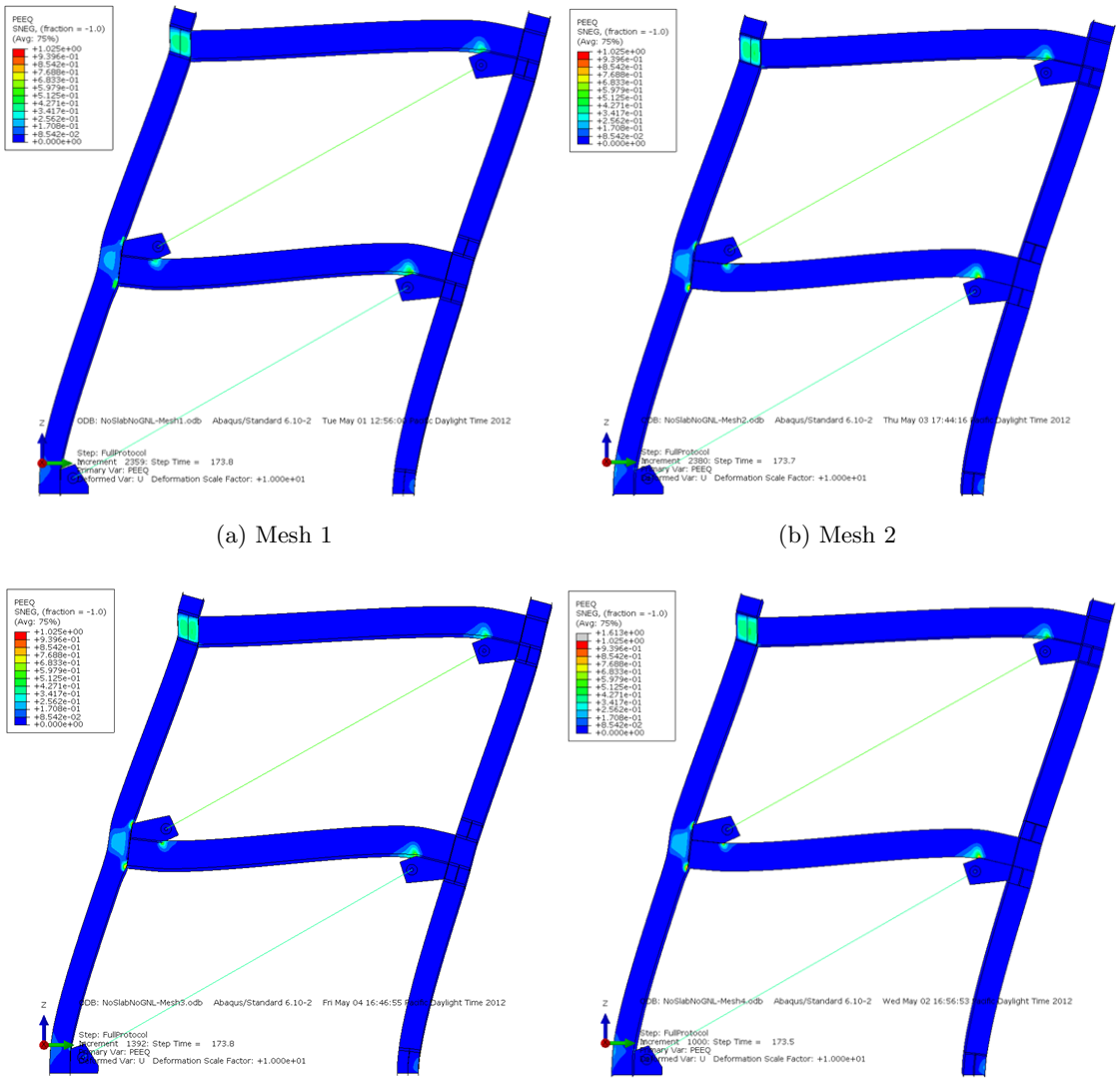

(a) Mesh 1

(b) Mesh 2

(c) Mesh 3

(d) Mesh 4

Figure 7.19: PEEQ stress distribution at 3% RDR for mesh refinement study

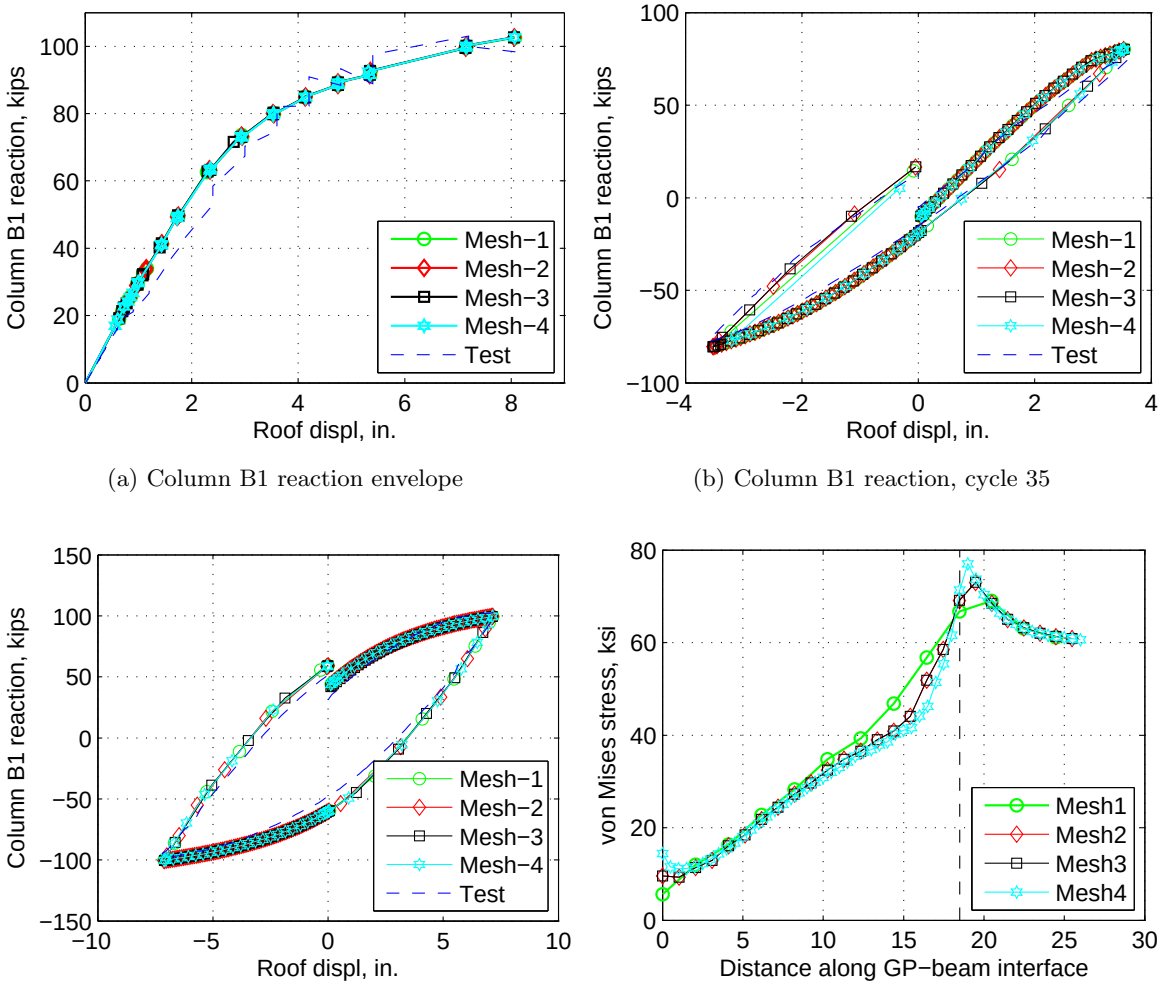

(a) Column B1 reaction envelope

(b) Column B1 reaction, cycle 35

(c) Column B1 reaction, cycle 43

(d) von Mises stress at beam-gusset interface

Figure 7.20: Mesh refinement study analysis results comparison

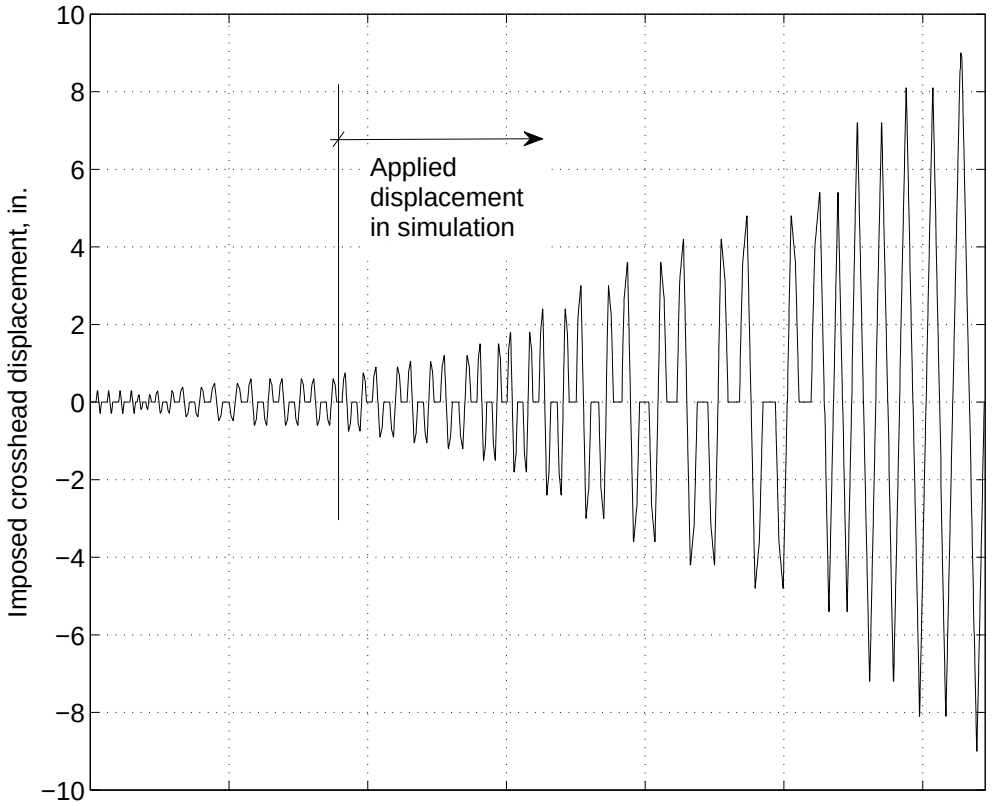

Figure 7.21: Experimental displacement of crosshead and applied displacement in simulations

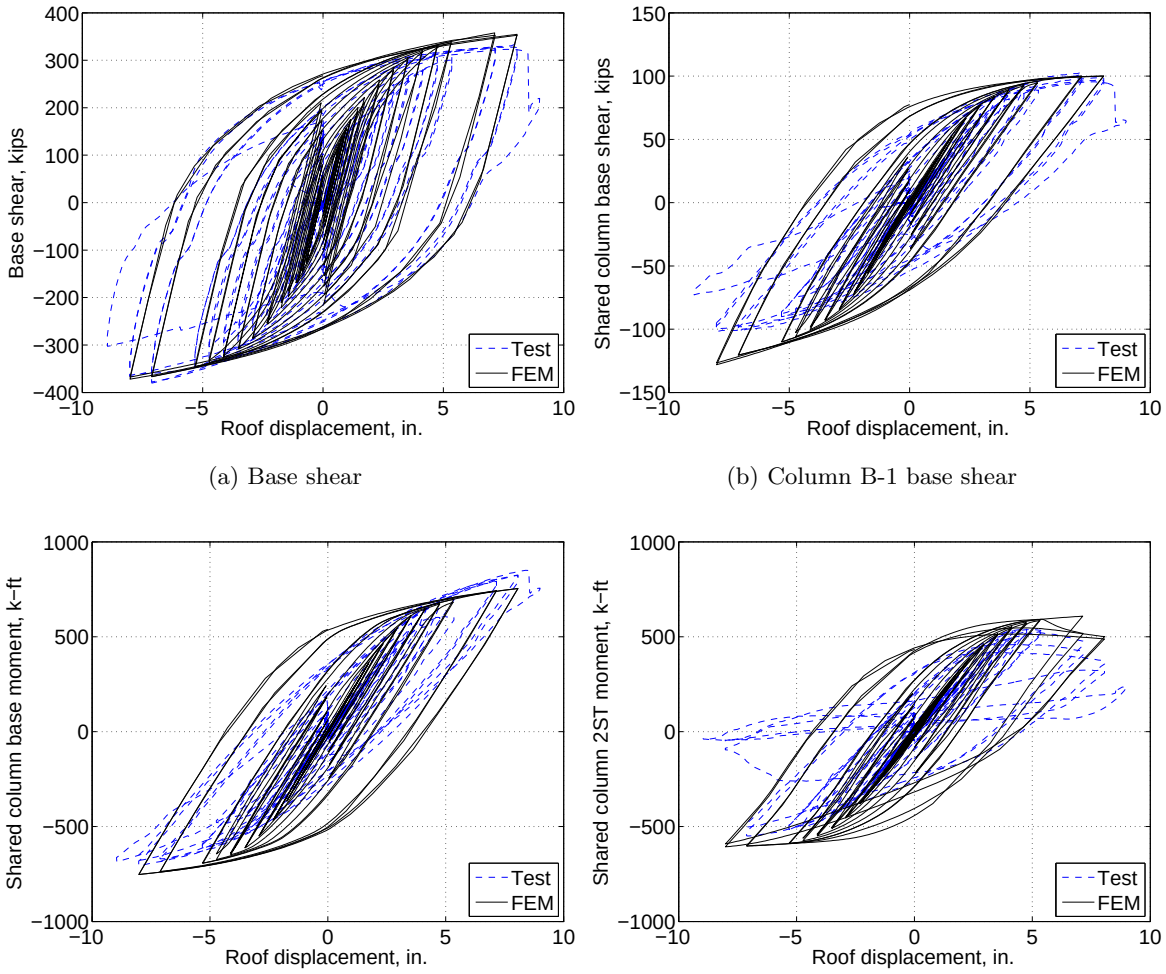

(a) Base shear

(b) Column B-1 base shear

(c) Column B-1 base moment

(d) Column B-1 second story top moment

Figure 7.22: Comparison of test results to simulated results

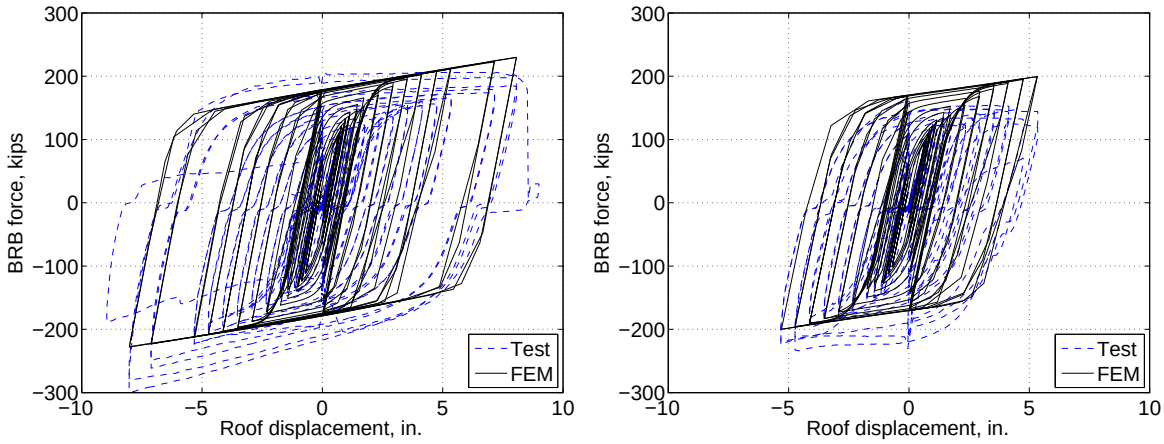

(a) Second story BRB

(b) First story BRB

Figure 7.23: Comparison of test results to simulated results



(a) Experiment

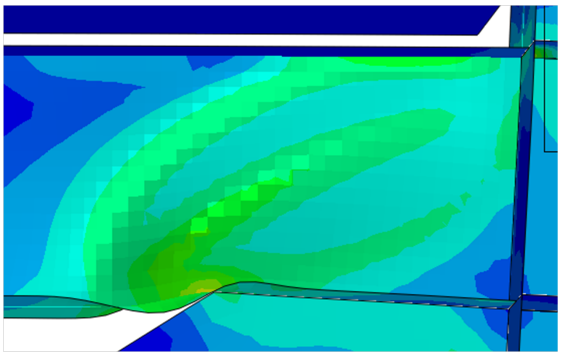

(b) Simulation



(c) Experiment

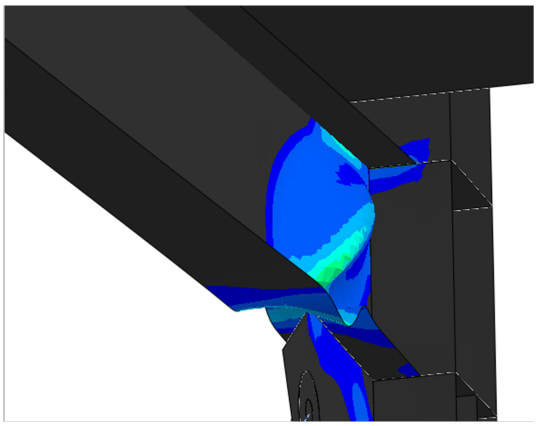

(d) Simulation

Figure 7.24: Comparison of experimental and simulated beam deformation at 3F column B-1



(a) Column A-1 3F experiment

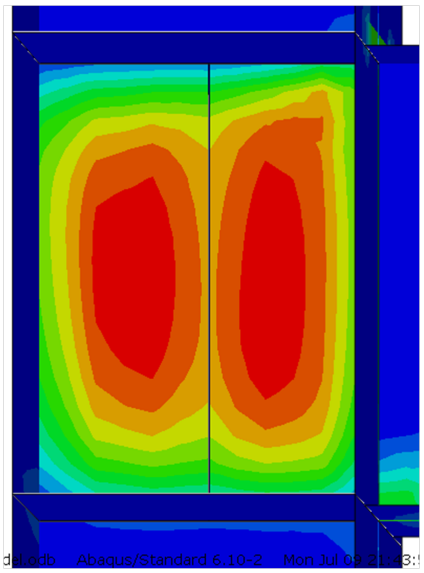

(b) Column A-1 3F simulation

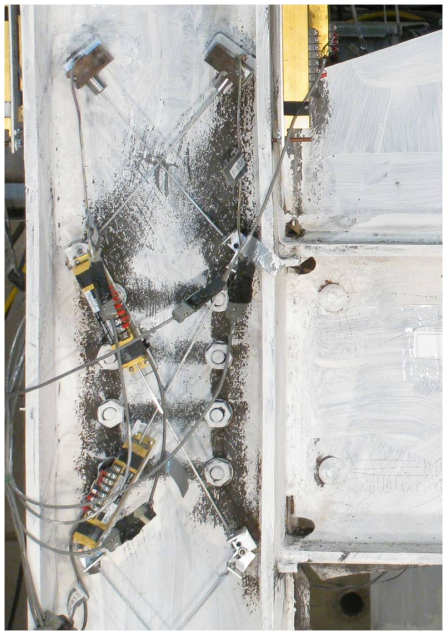

(c) Column A-1 2F experiment

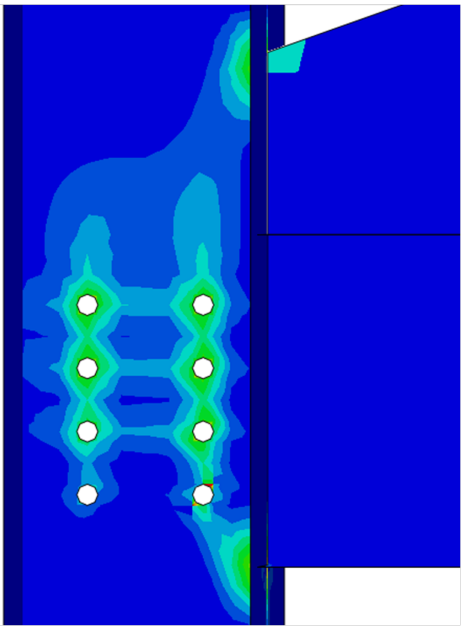

(d) Column A-1 2F simulation

Figure 7.25: Comparison of experimental and simulated panel zone yielding

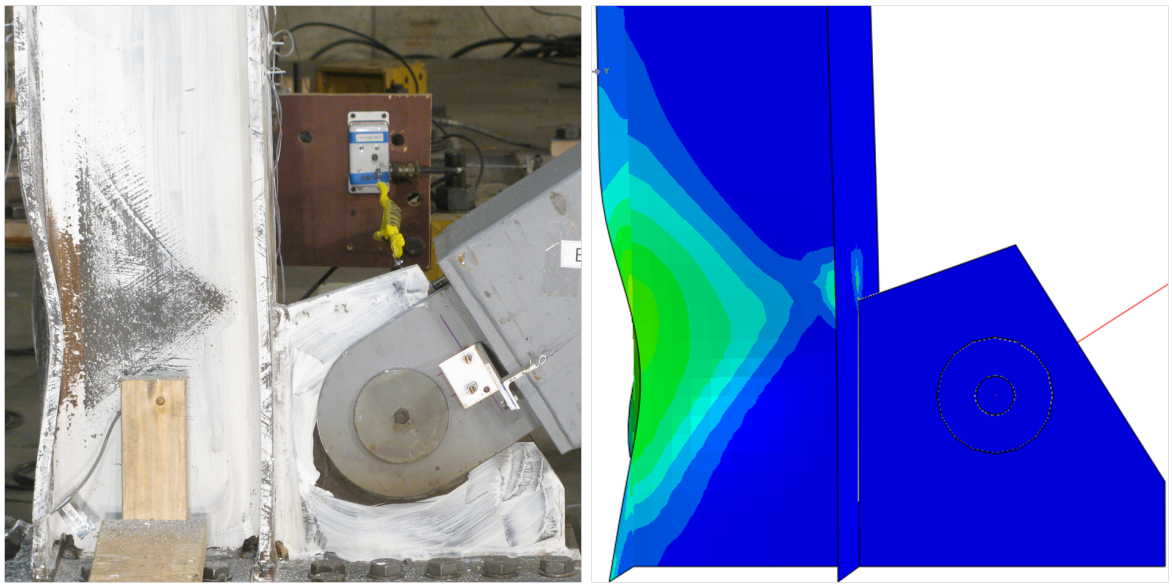

(a) Experiment (b) Simulation

Figure 7.26: Comparison of experimental and simulated column A-1 base deformation

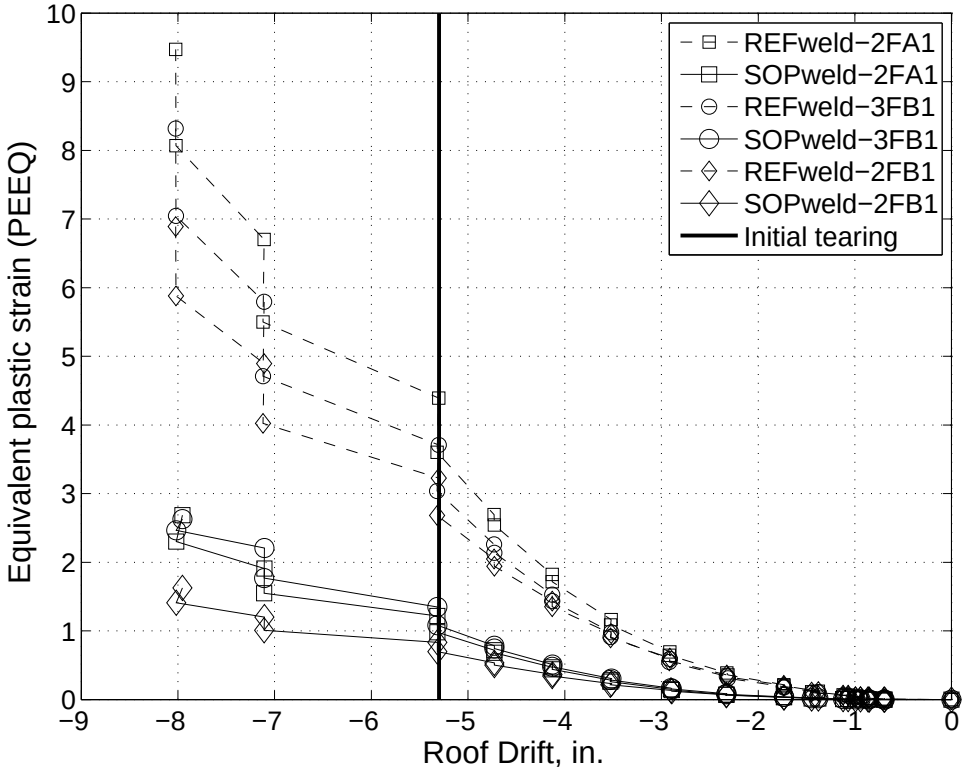

Figure 7.27: PEEQ indices for simulations with gusset plate weld material modeled. (REFweld - indicates the welds sized per UFM, SOPweld - indicates welds designed for the strength of the plate)

Chapter 8

BRBF PARAMETRIC STUDY

8.1 Introduction

This chapter discusses a suite of finite element simulations conducted using the BRBF model described in the previous chapter as the basis. This study was conducted to extend the experiments through a variation of parameters that were not studied experimentally and assess their impact on the frame response, demands and damage. Global frame response was studied but the main focus was on the components at the corner beam-column-gusset connection regions (denoted as "joint" regions) as the most detrimental damage occurred at these locations during the BRBF experiment. This damage included web and flange buckling along with tearing and fracture of the beams, columns and gusset plate welds. The main objective of this study was to gain a deeper understanding of the effects of various parameters on the demands and behaviors of the joint region with the ultimate goal of providing design and detailing recommendations that improve the performance of these systems under the design basis earthquake (DBE) and the maximum considered earthquake (MCE).

This chapter is organized into four main sections. Section 8.2 describes the parameters that were varied and the specific models that were analyzed. This section will also describe the methodology used for assessing and comparing the models. Section 8.3 discusses the results of each parameter variation in greater detail. Section 8.4 will discuss the relationship between the ratio of the gusset plate thickness to the beam web thickness and the simulated demands in the beam and column components. Finally, Section 8.5 summarizes the results of the parametric study.

8.2 Description of Parameters

The following parameters were studied:

1. Gusset plate thickness (GPT)
2. Gusset plate taper - length of gusset at column interface relative to beam interface (GP geom)
3. Gusset plate reinforcement (long-edge stiffeners)
4. Beam reinforcement at gusset plate (web doublers and stiffeners)
5. Column size and reinforcement at joint (web doublers and continuity plates)
6. Beam fixity at gusset plate connection region
7. Strength and stiffness of brace (varies from no brace to brace used in experiment)

Table 8.1 summarizes all of the models analyzed for the parametric study. The first column in the table lists the main parameter that was varied in each particular group of interest. The second column provides the name of the model and this name will be used throughout this section in the text and plots. The remaining columns correspond to the parameters that were varied. When the model contains the same parameter that was used in the reference model, "Ref" is listed in that cell. The reference model is the first model listed and its model name is "REF." The second to last column of the table lists the ratio of the thickness of the beam web, t_w to the thickness of the gusset plate, t_{gp}. The last column lists the ratio of the length of the gusset plate at the beam interface, L_{bw}, to the length of the gusset plate at the column interface, L_{cw}.

For example, in the 11th row of the table within the parameter "GP geom," is model "gpt0.75NT." This model has the same BRB area as the reference model, a more rectangular gusset plate than the reference model with a length of the gusset plate at the beam interface of 18.5" and a length of the gusset plate at the column interface of 15.75," a gusset plate thickness of 0.75" and beam and column sizes matching the reference model. The "NT" in the model name indicates a more rectangular gusset plate geometry and the "NT" means "**N**o **T**aper."

The reference model is listed in the first row and is the same as the experimental frame but does *not* include the beam web doubler that was installed prior to the BRBF test following the first test. However, this doubler was included in the test frame model that

was calibrated to the experimental results but subsequently removed to assess the impact of this.

Comparison among the models will use global and local force-deformation response envelopes along with local stress and strain indices and local deformations of the components at story drifts of 2 and 3.5%. These story drifts were chosen because numerical simulations [Chen et al., 2008] showed that these story drifts can be expected to occur during earthquakes representing hazard levels of 10/50 and 2/50, respectively, which correspond approximately to the code-defined DBE and MCE [ASCE, 2010]. The global and local force-deformation responses used for comparison are shown schematically in Fig. 8.1 and include the total base shear, base shear resisted by column B-1, column B-1 base moment, and the moment in column B-1 at the top of the second story at the edge of the gusset plate. The strain and stress indices used are the cumulative equivalent plastic strain (PEEQ) and the von Mises stress described in Section 7.9. These indices were sampled globally at the joints shown in Fig. 7.7 and locally in the elements in the beams, columns, and gusset plates at the joints as shown in Fig. 7.8. These stress and strain indices will be plotted as described schematically in Fig. 7.9.

Table 8.1: FE Models for Parametric Study

Primary Category	Model Name	BRB Area, in.^{2}	Gusset pl. (GP) size, in.	Gusset pl. thickness (GPT), in.	Beam reinforcement and fixity	Column B-1 size	Column reinf.	$\frac{t_w}{t_{gp}}$	$\frac{L_{bw}}{L_{cw}}$
Reference	REF	3.5 (2S) 3.43 (1S)	18.5 x 8.5	1.0	None Full fixity	W12x106	Same as test frame	0.38	2.2
GPT	gpt1.5	Ref	Ref	1.5	Ref	Ref	Ref	0.25	Ref
	gpt0.75			0.75				0.51	
	gpt0.75stiff			0.75				0.51	
	gpt0.625			0.625				0.61	
	gpt0.625elastic			0.625				0.61	
	gpt0.5			0.5				0.76	
	gpt0.5stiff			0.5				0.76	
GP geom	gpt1.5NT	Ref	18.5 x 15.75	1.5	Ref	Ref	Ref	0.25	1.12
	REFnt			Ref				0.38	
	gpt0.75NT			0.75				0.51	
	gpt0.5NT			0.5				0.76	
Bm reinf.	bmWD076	Ref	Ref	Ref	0.76” thick web doubler	Ref	Ref	0.76	Ref
	bmWD051	Ref	Ref	Ref	0.51” thick web doubler	Ref	Ref	0.51	Ref
	bmFS	Ref	Ref	Ref	Full-depth vert. flange stiffener	Ref	Ref	0.38	Ref
	bmFS05d	Ref	Ref	Ref	Half-depth vert. flange stiffener	Ref	Ref	0.38	Ref
	bmWD076FS	Ref	Ref	Ref	0.76” thick web doubler Full-depth vert. flange stiffener	Ref	Ref	0.76	Ref
	bmWD076FS05d	Ref	Ref	Ref	0.76” thick web doubler Half-depth vert. flange stiffener	Ref	Ref	0.76	Ref
	bmWD0.76NT	Ref	18.5 x 15.75	Ref	0.51” thick web doubler	Ref	Ref	0.76	1.12
	bmWD0.51NT	Ref	18.5 x 15.75	Ref	0.51” thick web doubler	Ref	Ref	0.51	1.12
	bmWDcolWD	Ref	Ref	Ref	0.76” thick web doubler in beam and column	Ref	Ref	0.76	Ref
BRB size	gpt1.5nb	0	Ref	1.5	Ref	Ref	Ref	Ref	Ref
	REFnb	0	Ref	Ref	Ref	Ref	Ref	Ref	Ref
	gpt075nb	0	Ref	0.75	Ref	Ref	Ref	Ref	Ref
	gpt063nb	0	Ref	0.625	Ref	Ref	Ref	Ref	Ref
	gpt05nb	0	Ref	0.5	Ref	Ref	Ref	Ref	Ref
	REFwb	1.75 (2S) 1.72 (1S)	Ref	Ref	Ref	Ref	Ref	Ref	Ref
GPT GP geom	REFntNB	0	18.5 x 15.75	Ref	Ref	Ref	Ref	Ref	1.12
	gpt075NTnb	0	18.5 x 15.75	0.75	Ref	Ref	Ref	0.51	1.12

Table 8.1: FE Models for Parametric Study

Primary Category	Model Name	BRB Area, in.^{2}	Gusset pl. (GP) size, in.	Gusset pl. thickness (GPT), in.	Beam reinforcement and fixity	Column B-1 size	Column reinf.	$\frac{t_w}{t_{gp}}$	$\frac{L_{bw}}{L_{cw}}$
BRB size	gpt05NTnb	0	18.5 x 15.75	0.5	Ref	Ref	Ref	0.76	1.12
Column size and reinf.	REFsc	Ref	Ref	Ref	Ref	W12x50	None	Ref	Ref
	REFscPZD	Ref	Ref	Ref	Ref	W12x50	Panel zone doubler t_{total}=1.0”	Ref	Ref
	REFscCP	Ref	Ref	Ref	Ref	W12x50	Flange cont. plates	Ref	Ref
	REFscWD	Ref	Ref	Ref	Ref	W12x50	Panel zone doubler t_{total}=1.0” in the gusset region	Ref	Ref
Beam fixity	REFbmPin	Ref	Ref	Ref	No reinf. End released	Ref	Ref	Ref	Ref

8.3 Results of Parameteric Study

8.3.1 Gusset plate thickness

Given the large amount of beam and/or column damage relative to the little to no damage that occurred in the gusset plate (very minor yielding at edge at column interface), it is logical to assume that this may a result of the relative thickness between the beam and column webs and the gusset plates. Therefore, five different models with varying gusset plate thickness were analyzed. The gusset plate thicknesses were 0.5, 0.625, 0.75, 1.0, and 1.5," with the same geometry (taper) as the test frame (L_{bw}= 18.5" and L_{cw}= 8.3," see Fig. 8.16a). The 0.625" gusset plates satisfied all design limit states per the current state-of-the-practice LRFD method discussed in Section 3.4. The 0.5" gusset plates did not satisfy the buckling or yielding criteria but were included in the analyses to assess the effect of a very thin gusset plate. The DCRs for each gusset plate for the limit states of yielding and buckling are shown in Table 8.2. The other limit states are not shown because there are reinforcing pads around the hole in the gusset plate that increase the total thickness to 2.0" and this is sufficient to resist these limit states.

A few comments are needed regarding the gusset plate and BRB models. Numerical instabilities were encountered during the analyses in the models with 0.5, 0.625 and 0.75" thick gusset plates. These instabilities were encountered at approximately 1, 2 and 3% RDR, respectively for the 0.5, 0.625 and 0.75 thicknesses. These instabilities were partly due to the BRB end conditions that were modeled as pins without any out-of-plane flexural restraint that in reality were there. As described in the previous chapter, the end conditions of the BRBs in the simulations were pinned to the gusset plates but in reality the BRBs have OOP rotational stiffness at this connection and provide restraint that is not modeled. Buckling for the 0.5" thick gusset plate was expected because it did not pass the buckling limit state check. When the OOP degree of freedom of the gusset plate edges was tied to the node at the centerline of the intersection of the gusset plate and column flange, these instabilities did not occur (tie constraint in ABAQUS, see Fig. 8.2 for detail). Therefore, the demands described below for the 0.5" gusset plate at 2% RDR may not reflect true conditions due to the constraint applied to the long edge of the gusset plate in the model.

However, the values for the 0.625 and 0.75" gussets are realible because the edges did not require any artificial constraint up to RDRs of 2 and 3%, respecitvely, and these are the values that are discussed.

Fig. 8.3a shows the base shear envelope for each model in the positive drift range along with the measured base shear as a function of roof displacement. It can be seen that the impact of the gusset plate thickness on the global base shear-displacement response was negligible. Similarly, the story shear resisted by column B-1 (Fig. 8.3b) and the moment at the base of column B1 (Fig. 8.3c) were unaffected by the gusset plate thickness. However, the moment in column B1 at the top of the second story was affected by the gusset plate thickness as Fig. 8.3d shows. Larger moments occurred in the column at this location for the models with thicker gusset plates. This is logical as a thicker gusset plate creates a stiffer joint, thus attracting more moment for a given deformation. At approximately 5.5" of roof displacement (2.2% story drift), the moment in the model with the 1.5" thick gusset plate is 20% greater than the moment in the model with the 0.5" thick gusset plate. It can also be seen that there is a significant drop in moment in all of the models at a roof displacement of 7.2" (2.9% story drift). This is due to the beam local web and flange buckling that occurs at the joint and is discussed below.

During the experiment, considerable beam damage occurred in the beams where gusset plates occurred especially at column B-1 (see Section 4.5) and the simulation of the experimental frame captured this damage well (Fig. 7.24). A comparison of the von Mises stress contours and beam deformation at the third floor joint of column B-1 at 3.5% RDR for the varying gusset plate thickness models is shown in Fig. 8.4. It can be seen that considerable local flange and web buckling occurrs at this drift level in the models with gusset plate thicknesses of 0.75, 1.0 and 1.5 inches. No web buckling and only slight local flange buckling ($<$ 0.1" of flange deformation) occurs when 0.5 and 0.625" gusset plates are used. None of this beam damage occurred in the models at 2.0% RDR as Fig. 8.5 shows. Unlike the third floor joint, beam damage did occur at the second floor joint at 3.5% RDR regardless of the gusset plate thickness as Fig. 8.7 shows. At 2.0% RDR the local flange buckling that occurred in the reference specimen also occurred in the other models to varying degrees as shown in Fig. 8.6 with the least amount of visible deformation occuring for the model with

the 0.5" gusset plate.

Figures 8.8a through 8.8d show the strain demand (PEEQ) values in the beam, column and gusset plate along the gusset interfaces at the third floor joint at Column B1 at -2% RDR. These locations are described in Fig. 7.7 and 7.8. Fig. 8.8a shows the PEEQ in the column along the gusset interface. The horizontal dashed line at approximately 8" is the location of the edge of the gusset plate and it can be seen that the maximum PEEQ in the column occurs at or near this location for all of the models. The distribution of the column PEEQ is also similar for all models, with zero or nearly zero values near the beam and sharp increases as the gusset edge is approached. There is considerable difference in the maximum PEEQ values in the column for the varying gusset thicknesses with the largest value for the thickest gusset plate and the smallest PEEQ values for the thinnest gusset plate. The maximum PEEQ value in the column for the model with the 1.5" gusset plate is nearly 10 times greater than the PEEQ value in the column for the model with the 0.5" gusset plate.

A similar trend is noted for the strain demand in the beam along the gusset interface as shown in Fig. 8.8c. The vertical dashed line indicates the location of the edge of the gusset plate. The maximum value of PEEQ occurs at the edge of the gusset plate with zero or nearly zero values of PEEQ along the majority of the length of the gusset plate with a sharp increase near the gusset plate edge for all models. Similar to the column, the maximum PEEQ value in the beam for the model with the 1.5" gusset plate is larger than the maximum PEEQ in the beam for the model with the 0.5" gusset plate. However, the difference is not as great, approximately 60% greater.

Figures 8.8b and 8.8d depict the strain demand in the gusset plate at the column B-1 third floor joint at -2% RDR along the column and beam interface, respectively. As expected, the thinner gusset plates have larger PEEQ values than the thicker gusset plates and as Fig. 8.8d shows, no yielding occured in the 1.0 and 1.5" gusset plates along the beam interface. Considerably less yielding occurred along the column interface in the 1.5 and 1.0" gusset plates than the 0.5, 0.625 and 0.75" gusset plates as Fig. 8.8b demonstrates. The maximum PEEQ values occur at the gusset plate edges and the PEEQ values are relatively small along the length of the column interface and increase sharply near the edge. The

PEEQ distribution in the gusset along the beam interface is consistent between different thicknesses with a peak occurring at a couple of inches away from the column face followed by a trough with a sharp increase near the edge.

Figures 8.9a through 8.9d show the distribution of von Mises stress along the gusset plate interfaces in the beam, column, and gussets at the third floor joint of Column B1 at -2% RDR. Similar to the PEEQ index, the maximum values of von Mises stress occur at or near the edge of the gusset plates. The maximum value of the von Mises stress in the column when the gusset plate is 1.5" is 16% larger than that for the 0.5" gusset plate model. In the beam, this difference is 6%. While these differences may seem small, these elements have yielded and therefore the differences in strains are relatively large as the PEEQ indicates. For example, the difference in the maximum von Mises stress in the column at the gusset plate edge between the 0.5" and 1.5" gusset plate models is approximately 9 ksi which corresponds to a difference in strain of approximately 7 times the yield strain because the slope of the stress-strain curve is only 2% of the elastic modulus.

The von Mises stress distribution in the gusset plates at the interface follow the same trend as the PEEQ values in the gusset plates. As Figs. 8.9b and 8.9d demonstrate, thinner gusset plates are highly stressed relative to the thicker gussets. In fact, at this drift level, only the edge of the 1.0 and 1.5" gusset plates has reached yield while the 0.5" gusset plate has yielded nearly along its entire length (Fig. 8.9b). A similar situation occurs in the gusset plate along the beam interface. The 1.5" gusset plate has not yielded at this location while the 0.5" gusset plate has yielded extensively (Fig. 8.9d).

The thinner gusset plates yield considerably more than the thicker ones and this limits the yielding in the beams and columns and limits the local web and flange buckling in the beams. Analyses performed with a linear elastic material model for the gusset plates corroborate this. Figures 8.10a through 8.10d show the strain and stress demands in the beam and column along the gusset plate interface at the third floor of column B-1 at -2% strory drift. Three models are shown, the model with the 0.625" gusset plate with the von Mises material model ("gpt0.625"), the same overall model but with an elastic material model for the gusset plate ("gpt0.625elastic"), and the model with the 1.5" gusset plate with the von Mises material model ("gpt1.5"). It can be seen that the demands in the beams

and columns with the elastic 0.625" gusset plate are larger than those for the 0.625" gusset plate with the von Mises material model. The differences are not trivial with von Mises stresses increasing by approximately 20% in both the beam and column, and the PEEQ increasing by 59 and 430% in the beam and column, respectively. The beam and column demands due to the 0.625" thick elastic gusset plate are comparable to or larger than the demands from the 1.5" gusset plate whose material was modeled with the von Mises yield criterion.

Summary and implications of gusset plate thickness parameter

The following list summarizes the main conclusions from the gusset plate thickness parameter study:

1. The gusset plate thickness has negligible impact on the global force-deformation response of the frame.
2. The gusset plate thickness did impact the amount of moment resisted by the beams and columns at the joints with thicker gusset plates stiffening the joints and attracting larger moments for a given deformation relative to the thinner gusset plates.
3. Thinner gusset plates reduce the potential for beam local web and flange buckling at the DBE drift level but not at the MCE drift level.
4. There is a clear and significant reduction in the beam and column strain demands at the gusset plate interface with a reduction of gusset plate thickness.
5. The reductions in demand are a direct function of the extent of yielding that occurs in the gusset plates.
6. Thinner gusset plates limit the damage in the beams and columns but thinner gusset plates (0.5 and 0.625") were shown to have stability issues which can prevent the BRB from reaching its full capacity and limit the large energy dissipation capacity that BRBs are capable of achieving. The next section investigates the impact of stiffening the longest free edge of the gusset plate to mitigate the gusset plate instabilities.

8.3.2 Gusset plates w/ edge stiffeners

As discussed in the previous section, numerical instabilities occurred in the models with the 0.5, 0.625 and 0.75" thick gusset plates at approximately 1, 2 and 3% RDR, respectively, and were mainly due to gusset plate yielding. This section discusses the analyses of models with stiffeners attached to the long edge of the gusset plates to study if these stiffeners would mitigate the instability issues and also to investigate the effect of these stiffeners on the component demands in the connection region.

Two models with long-edge gusset plate stiffeners and gusset plate thicknesses of 0.5 and 0.75" were analyzed. These models are denoted as "gpt0.5stiff" and "gpt0.75stiff." The stiffener is shown in Fig. 8.11 and had a length equal to the length of the gusset interface with the beam, L_{bw}, and the same thickness as the gusset plate.

The envelope of the global base shear-roof displacement is shown in Fig. 8.12a. There is very little difference between the reference model and the models with and without stiffeners with 0.5 and 0.75" thick gusset plates. A similar trend was noted for the base shear and moment of column B-1 as shown in Figs. 8.12b and 8.12c, respectively. There were differences in the moment at the top of second story of column B-1 as shown in Fig. 8.12d. The response of the model with the stiffened 0.75" gusset plate was nearly identical to the model with the unstiffened 1.0" gusset plate. That is, a larger column moment was developed at a give roof displacement relative to the unstiffened 0.75" thick gusset plate model. The same trend was observed for the 0.5" thick stiffened and unstiffened models.

The stress contours and deformed shape at the second floor joint at 2.0% RDR are shown in Fig. 8.13 for the above models. It can be seen that the countours and local flange buckling of the beam bottom flange are similar regardless of the gusset plate detail. The same is true at 3.5% RDR as shown in Fig. 8.14 where the local flange and web buckling of the beam are significant and similar for all models.

The strain demands in the beam, column and gusset plate along the gusset interfaces at the third floor joint at column B-1 at -2% RDR are shown in Figs. 8.15a through 8.15d. The demands in the column and beam for models gpt0.5stiff and gpt0.75stiff are reduced relative to the reference model as seen in Figs. 8.15a and 8.15c but not as much as they are

reduced for the models without edge stiffeners (gpt0.5 and gpt0.75). The demands in the beam are reduced by less than 5% for model gpt0.75stiff indicating little improvement over the reference model. However, the demand reduction for gpt0.5stiff is nearly the same as the reduction for model gpt0.5. For example, the reduction in strain demand at the beam for model gpt0.5 is 32% while the reduction for gpt0.5stiff is 27% (Fig. 8.15c). Similar behavior occurred at the second floor joint.

The strain demands in the gusset plate along the column interface are reduced by approximately 50% for the models with edge stiffeners relative to those without stiffeners but with the same thickness (Fig. 8.15b). Conversely, the strain demands in the gusset along the beam interface are increased when the gusset plates are detailed with free-edge stiffeners relative to those without. This increase is approximately 10%. The same also holds true at the second floor joint.

Adding the stiffeners to the 0.75" thick gusset plate mitigated the stability issues in this gusset plate at all drift levels. These instabilities did occur in the unstiffened 0.75" thick gusset plate at 3% story drift. The stiffeners also helped mitigate the instabilities in the 0.5" thick gusset plate but only up to 2.3% story drift, whereas instabilities occurred in the 0.5" thick unstiffened gusset plates at 1% story drift.

Summary and implications of gusset plate edge stiffening

The results of the study with stiffeners attached to long edge of the gusset plates are listed below:

1. Adding stiffeners to the long edge of the 0.75" thick gusset plates mitigated the instabilities at all drift levels (these instabilities occurred in this gusset plate without stiffeners at 3% story drift).
2. Unlike adding stiffeners to the 0.5" thick gusset plate, adding stiffeners to the 0.75" gusset plate negated all of the beam and column demand reduction that occurred in the model with the unstiffened 0.75" gusset plate.
3. The beam and column demand reduction was similar for the 0.5" thick gusset plates regardless of whether the edge was stiffened. While the stiffeners did mitigate the

instabilities in this plate at small drift levels, they did not mitigate them at drift levels larger than 2.3%.

4. The above indicates that the advantages gained through reducing the gusset plate thickness come at the cost of gusset plate instabilities. Depending on the gusset plate thickness, these instabilities can be mitigated through the use of edge stiffeners but either the beam and column demand reduction is minimal or the gusset plate instabilities occur at larger story drifts but still at levels that are unacceptable.

5. Therefore, using relatively thin gusset plates is not an efficient way of reducing beam and column demands at the connection region.

8.3.3 Gusset plate taper

Three models without a gusset plate taper on the column side were analyzed. The gusset plate thicknesses of these models were 0.5, 0.75 and 1.0 inches and the gusset plate geometry is shown in Fig. 8.16b. This geometry was chosen to provide nearly equal connection lengths along the gusset plate interfaces with the beam and column. These models were compared to the models with the tapered gusset geometry that was used in the test frame and shown in Fig. 8.16a.

Fig. 8.17a shows the base shear envelope for each model in the positive drift range along with the experimental base shear as a function of roof displacement. It can be seen that global force-displacement response was not influenced very heavily by the gusset plate taper. Similarly, the story shear resisted by the shared column (Fig. 8.17b) and the moment at the base of column B1 (Fig. 8.17c) were unaffected by the gusset plate taper.

The moment in column B1 at the top of the second story was affected by the gusset plate taper as Fig. 8.17d shows. Larger moments occurred in the column at this location up to 4" of roof displacement (1.6% story drift) for the models without the taper relative to the models with the taper for the same gusset thickness. This is logical as a larger gusset plate creates a stiffer joint, thus attracting more moment for a given deformation. The moment degradation for the models without the taper occurs at smaller drifts relative to the models with the taper and the same thickness. For example, the moment in model

“gpt1.0NT” reaches a peak at 4.1” of roof displacement (1.6% story drift) and is reduced considerably beyond this drift level while the moment in model “gpt1.0” reaches a peak at a roof displacement of 7.2.” The same behavior is obersved when comparing “gpt0.75NT” to ”gpt0.75,” and “gpt0.5NT” to ”gpt0.5.”

The above behavior is due to the large amount of beam local flange and web buckling that occurs within the gusset region even at 2.0% RDR in the models without the gusset plate tapers at the column (Fig. 8.18). Fig. 8.18 depicts the von Mises stress contours and any local flange and web buckling at the third floor joint of column B-1. There is local flange and web buckling in the beam for all models without the gusset plate taper regardless of the gusset plate thickness while none of this occurs when the tapered gusset plates are used. This indicates that under the DBE, beam repair may be necessary when the larger gusset plates are used. Figure 8.19 compares the same quantities at 3.5% RDR and it can be seen that there is beam local flange and web buckling regardless of the gusset plate thickness and taper.

Figures 8.20a through 8.20d show the strain demands in the beam, column and gusset plate along the gusset interfaces at the third floor joint at Column B1 at -2% RDR. Fig. 8.20a shows the PEEQ in the column along the gusset interface. It can be seen that removing the taper on the column side reduces the strain demands in the column for all gusset plate thicknesses. The reduction in strain demand is greatest for the 1.0” thick gusset plate and there is only a very small reduction for the 0.5” gusset plate. A similar trend is also noted for the maximum PEEQ in the gusset plate along the column interface as shown in Fig. 8.20b. There is a reduction in the PEEQ values for the 0.5 and 0.75” gussets without a taper relative to those with a taper and essentially no reduction for the 1.0” thick gusset.

The decreases in the PEEQ values in the column noted above coincided with increases in the PEEQ in the beam along the gusset interface. This is shown in Fig. 8.20c and it can be seen that maximum value of PEEQ for the 1.0” gusset plate increased by 100% when the taper was removed. The increases for the 0.75 and 0.5” gussets were 92 and 25%, respectively. Again, the tapers had a smaller impact for the thinner gusset plate models.

Removing the taper resulted in a dramatic increase in the maximum strain demand in the gusset plates along the beam interface as Fig. 8.20d shows. For example, there is a

200% increase in the maximum PEEQ value for the 0.5" gusset plate when there is no taper relative to when there is a taper. The increase is nearly 300% for the 0.75" gusset plate. The 1.0" gusset plate did not yield at this interface when the gusset was tapered and only slightly yielded at the edge when the taper was removed.

The von Mises stress distribution in the column, beam and gusset plates at the interfaces at the third floor joint of column B-1 at -2% RDR are shown in Figs. 8.21a through 8.21d. There was very little change in the maximum values in the column and beam along the interface as shown in Figs. 8.21a and 8.21c, respectively. These differences were less than 5% in the column and approximately 10% in the beams. The distribution of these stresses did vary depending on the thickness and taper with steeper gradients in the columns for the models with tapered gusset. Removing the taper reduced the value of the von Mises stress in the beam at the column face as shown in Fig. 8.21c while the maximum values increased by approximately 10%.

Removing the taper reduced the stress in the gusset plate along the whole length of the column interface except at the edge where yielding still occurred (Fig. 8.21b) no matter the geometry. The reduction in yielding was considerable especially in the mid-region along the length with reductions in stress as high as 44.5% for the 1.0" gusset plates. This reduction in stress along the length in the gusset plate was accompanied by an increase in stress in the column at the same location. The reduction in yielding in the gusset plates was not as large for the 0.5" gusset plates (11% maximum reduction). The effect on the stresses in the gusset plate along the beam interface were not as substantial as Fig. 8.21d shows.

Summary and implications of gusset plate geometry

The results of the study of the effect of the gusset plate taper are summarized below:

1. The taper of the gusset plate has negligible impact on the global force-deformation response of the frame.
2. Removing the taper on the column side increased the demands on the the beam and reduced the demands on the column at the gusset interfaces relative to the reference tapered geometry.

3. The potential for beam local web and flange buckling was increased when the taper was removed and this deformation occurred at 2% story drift regardless of the gusset plate thickness while this deformation did not occur at 2% in the models with tapered gusset plates.
4. Beam local web and flange buckling occurred at 3.5% regardless of gusset plate thickness and taper.
5. The strain demands in the gusset plate along the column interface were reduced when the taper was removed indicating the potential for mitigating the weld tearing that occurred during the experiment in the tapered gusset plates. However, the weld demand analysis discussed in Section 7.15 showed that when the weld is as strong as the gusset plate, the potential for tearing was mitigated for the reference model tapered gusset plates.

8.3.4 Beam Reinforcement

Models with tapered gusset plates

Given the beam damage that occurred at the gusset plate locations during the experiment, a number of models were analyzed with web doublers and/or flange stiffeners at the location of this damage. Web doublers that increased the beam web to gusset plate thickness ratio from 0.38 to 0.51 and 0.76 were added. These models are denoted as "bmWD051" and "bmWD076," respectively and the web area where the doublers were added is shown in Fig. 8.22. The gusset plates in these models were 1.0" thick and therefore the total thickness of the beam webs with the doublers were 0.51 and 0.76" Flange stiffeners were also added at the location where flange local buckling occurred during the experiment slightly away from the gusset plate edge as shown in Fig. 8.22. Full-depth and half-depth stiffeners were both investigated and are denoted as "bmFS" and "bmFS05d," respectively. A model with both web doublers and full-depth stiffeners was also analyzed and is denoted as "bmWD076FS."

The base shear envelope for each model in the positive drift range along with the experimental base shear as a function of roof displacement is shown in Fig. 8.23a. It can be seen that global force-displacement response was not heavily influenced by the addition of beam

reinforcement at roof displacements less than approximately 4" (1.6% story drift). The increase in global strength beyond this level in the models with reinforcement can be seen in the figure along with the reduction in strength at 7.1" of roof displacement (2.8% story drift) in the Reference model but not in the models with reinforcment. This drop in load in the reference model corresponds to the large amount of beam web and flange buckling. This did not occur in the models with beam reinforcement. This deformation resulted in a large softening of the joints and can also be seen in the plots of the shear in column B-1 (Fig. 8.23b) and the moment at the top of the second story in column B-1 (Fig. 8.23d). As expected, the moment at the base of column B-1 was unaffected by the beam reinforcement (Fig. 8.23c).

Adding the 0.76 beam web doubler plates mitigated the web and flange buckling at the MCE drift level as seen by a comparison between Figs. 8.24a, the reference specimen, and Fig. 8.24b, model bmWD076 for the third floor joint at column B-1. The same holds true for the second floor joint (see Figs. 8.25a and 8.25b) for this size doubler plate. It does not hold true for 0.51 doubler plates at the second floor as shown in Fig. 8.25c where the flange has begun to buckle locally. This beam local flange buckling did not occur at the third floor joint as shown in Fig. 8.24c. Adding the full-depth flange stiffener only (no doubler) mitigated this beam deformation at the third floor joint (see Fig. 8.24d) but not at the second floor joint where the flange and web local buckling have migrated away from the stiffeners and doubler as shown in Fig. 8.25d. The combination of web doubler and flange stiffener have essentially the same effect as the doublers alone as a comparison of Fig. 8.24b and 8.24e or 8.25b and 8.25e reveals.

Figures 8.26a through 8.26d show the strain demand in the beam, column and gusset plate along the gusset interfaces at the third floor joint at Column B1 at -2% RDR. Fig. 8.26a shows the PEEQ in the column along the gusset interface. The horizontal dashed line at approximately 8" is the location of the edge of the gusset plate. It can be seen that all of the curves are nearly coincident and the PEEQ values for the models with beam reinforcement are larger than the reference model (no beam reinforcement) but only by at most 8%. As expected, the largest difference between the models with beam reinforcement and that without reinforcement occurs in the beam as shown in Fig. 8.26c. There is a 70%

reduction in the maximum PEEQ in the beam for model bmWD076 and a 40% reduction for model bmWD051. There is actually a slight increase in the maximum PEEQ when the flange stiffeners are added but is only 5% (model bmFS, see Fig. 8.22 for stiffeners). The maximum PEEQ for the model with both doublers and stiffeners (bmWD076FS) is also larger than the model with only doublers (bmWD076) by approximately 20%.

There is minimal effect on the distribution and maximum PEEQ in the gusset plate along the column interface as Fig. 8.26b demonstrates. The largest increase occurs for model bmWD076 and is approximately 10% while the smallest increase in PEEQ occurs for model bmFS and is less than 2%. There is little to no effect on the PEEQ in the gusset plate along the beam interface as Fig. 8.26d shows. Addtion of the 0.76" beam doubler causes a slight amount of yielding at the edge of the gusset but the magnitude of this PEEQ is orders of magnitude less than the magnitudes PEEQ that are seen at the other locations.

Figures 8.27a through 8.27d show the von Mises stress distributions in the column, beam and gusset plate at the interfaces at -2% RDR at the third floor joint in column B-1. There is little to no change in the stress distribtuion in the components and only slight changes in the maximum values (less than 3%). As expected, the largest changes occur in the beam for model bmWD076 with a reduction of approximately 15%. The reduction for model bmWD051 is approximately 10% and there is essentially no change when the flange stiffener is added to the beam.

Models with tapered and untapered gusset plates

Section 8.3.3 demonstrated the negative impact on the beam when the gusset plate taper on the column side is removed. Therefore, the the effect of beam reinforcement on the beam damage when there was no gusset plate taper was investigated. Figures 8.28a through 8.28d show the strain demand in the column, beam and gusset plates at the interface at -2% RDR at the third floor joint in column B-1. Adding the beam doubler plate when the gusset plate did not have a taper on the column side increase the maximum PEEQ in the column by 65% from 0.038 to 0.063 but this is still less than the reference model PEEQ of 0.106 (see Fig. 8.28a). The biggest impact on the maximum PEEQ was in the beam as shown in

Fig. 8.28c. There was 76% reduction in the maximum PEEQ in the beam when a doubler plate was added to the model with no tapers in the gusset plates on the column side. This reduction caused the maximum PEEQ to fall below that in the reference model also.

Adding the doubler plate when no gusset taper occurred on the column side increased the maximum PEEQ at the edge of the gusset plates by 45% to 0.313 (see Fig. 8.28b), which was slightly higher than twice that of the reference model indicating that the potential for tearing at the gusset-column interface is high. The PEEQ in the gusset plate along the beam interface also increased due to the addition of the web doubler for the model without a gusset taper as Fig. 8.29d shows. This increase was approximately 21% but these magnitudes were an order of magnitude less than the PEEQ in the gusset along the column interface.

The impact on the von Mises stress distribution and magnitudes at the interface for the models without tapered gusset plates and with and without beam reinforcement was minimal as Figs. 8.29a through 8.29d show. The largest impact on the maximum value was in the beam as seen in Fig. 8.29c with a 20% reduction for model bmWD076NT relative to gpt1.0NT.

The 0.76 web doublers also mitigated the web and flange buckling at the larger drift levels for the models with the gussets that were not tapered at the column. This can be seen by comparing Figs. 8.30c and 8.30d for the third floor joint and Figs. 8.31c and 8.31d for the second floor joint. However, slight flange buckling is beginning to form at the second floor as seen in Fig. 8.31d but is considerably less than that which occurs for the model without the doubler as seen in Fig. 8.31c. The models with the tapered gussets are shown in Figs. 8.30a and 8.30b for third floor and Figs. 8.43a and 8.31b for the second floor for comparison.

Summary and implications of beam reinforcement

The results of the study with beam reinforcement at the gusset connection region are summarized below:

1. The models with the doublers displayed slightly greater global strength and did not display the strength degradation that occurred in the reference model at 3.2% story

drift.

2. The thicker doubler plate mitigated the local beam deformation at the joint at the DBE and MCE drift levels while the thinner doubler mitigated this deformation only at the DBE drift level. There was local deformation at the MCE drift levels at the second floor joint when the smaller doubler was used but was considerably less than that which occurred in the reference specimen.
3. The addition of beam web doublers decreased the strain demand in the beams at the gusset interface by 50 and 70% for doublers that increased the web thickness to 0.51 and 0.76 times the thickness of the gusset plate, respectively.
4. Little to no change occurred in the strain demands in the tapered gusset plates at the interface with the addition of the doublers. However, the strain demands in the gusset plates without the taper on the column side increased by approximately 45% at the column interface and 20% at the beam interface.
5. Increases in the column strain demands occurred and were less than 10% at the third floor joint but nearly 80% at the second floor which did not have a slab near the column and had a column above and below the joint. However, no detrimental deformation was observed in this column nor was any resistance lost at this joint.
6. There was no observable benefit in adding flange stiffeners at the location where local flange buckling occurred as this flange deformation shifted beyond the point of the stiffeners.

8.3.5 Column Size and Reinforcement

It was observed during the experiment that more beam damage occurred at column B-1 than A-1. Column B-1 (W12x106) was 60% stiffer than column A-1 (W12x72). Addtionally, column A-1 had considerably more panel zone deformation than B-1. To investigate the effect of the column size and panel zone deformation on the beam demands at a joint with a gusset plate, a relatively small column (W12x50) was used in the simulation at column B-1. The column demands and behavior were also investigated. The DCR for this column based on the reference experimental BRB sizes, W16x50 frame beams, and assuming seismic

loading in only one direction was approximately 1.15. This column satisfies the seismic width-thickness ratio limits but is obviously underdesigned.

Five different small column models were analyzed with different column reinforcement details at the beam-column joint. Model "REFsc" is the small column model with no reinforcement; model "REFscPZD" is the small column model with 5/8" panel zone doubler plates at the second and third floor; model "REFscCP" is the small column model with continuity plates at the beam flanges at each floor; model "REFscPZDcp" is the small column model with 5/8" panel zone doubler plates and continuity plates at each floor; and model "REFscWD" is the small column model with 3/8" web doubler plates in the panel zone *and* gusset region as shown in Fig. 8.22. This latter model was analyzed due to the local column web and flange deformation that occurred in the other small column analyses at the edge of the gusset plate. The web thickness of the W12x50 is 0.37" and therefore the models with the 5/8" panel zone web doublers increased the total web thickness to one inch and the model with the 3/8" web doublers increased the total web thickness to 3/4." The thickness of the continuity plates used in the models was 0.375" which was half the thickness of the beam flanges. The increase in web thickness due to the doublers was modeled by increasing the thickness of the shell elements in the web.

The base shear envelope for each model in the positive drift range along with the experimentally measured base shear as a function of roof displacement is shown in Fig. 8.32a. It can be seen that reducing the size of column B-1 reduced the strength of the system due to the strength and stiffness reduction of this column. The base shear resisted by this column is shown in Fig. 8.32b and the reduction in shear ranged between 40 and 50%. The base moment and moment at the top of the second story are shown in Figs. 8.32c and 8.32d, respectively and it can be seen that the moments were reduced by approximately 40 to 50%. The drop in load and moment in the figures at approximately 7" of roof displacement (3.2% story drift) is due to the large amounts of column and beam local deformation that occurred at each floor. This deformation can be seen in Figs. 8.33a through 8.33d. The smaller column mitigated the beam local flange and web buckling that occurred with the larger column (Fig. 8.33a) but this damage was transferred to the smaller column (Figs. 8.33b and 8.33c). However, when the column web doubler extended into the gusset region (Fig. 8.33d) both

the beam and column damage was mitigated.

The distribution of strain demand in the beams and column B-1 at the second and third floor at -2% RDR are shown in Figs. 8.34a through 8.34d. As expected, the PEEQ in the columns for the models with the smaller column increased and the size of the increase was dependent on the model and the location. For example, at the third floor, the increase ranged between 2.8 (model REFsc) to 3.2 (model REFscPZDcp) times the PEEQ value for the reference model (see Fig. 8.34a). At the second floor (see Fig. 8.34c), the increase ranged from 7.5 (model REFscPZDcp) to 10 (model REFsc) times the PEEQ value for the reference model. However, the demands for the model with the column web doublers that extended into the gusset region did not increase as much. The increase at the second floor was 3 times the reference model and at the third floor was only 1.2 times the reference model indicating the significant advantage of extending the column web doublers into the gusset region.

The increases in the column PEEQ coincided with considerable reductions in the beam PEEQ as demonstrated by Figs. 8.34b and 8.34d for the third and second floors, respectively. At the second floor, this reduction varied between 45 to 75% of the PEEQ in the reference model and depended on the column reinforcement details. The reduction at the third floor was more uniform between the models and ranged between 76 and 86%. There are obvious differences between the second and third floor joints with the main ones being the concrete floor slab at the second floor does not extend all the way to the columns because of the blockouts required for the gusset plates. Additionally, there is a column above and below the beam at the second floor while there is only a column below the third floor beam. This later condition results in a stiffer joint which places greater demands on the beam and this is reflected in the results of the analyses. There was a larger reduction in the second floor beam PEEQ when the columns were not reinforced and this may be seen in Fig. 8.34d; a 75% reduction when the column webs were not reinforced in the panel zone compared to a 45% reduction when the column panel zones were reinforced. As such, the maximum PEEQ demands in the beam are twice as large when the column panel zone is reinforced relative to no column web reinforcement. Conversely, the PEEQ in the column was larger in the models with the weaker panel zones (see Fig. 8.34c). The demands in the beam are

slightly larger when the column web doublers extended into the gusset region but are not significant. The addition of continuity plates had minimal impact and served to increase the PEEQ only slightly in the beams and slightly reduce the column demands.

The von Mises stress distribution in the column and beams at the gusset interface at each floor at column B-1 at -2% RDR are shown in Figs. 8.35a through 8.35d. The stress increased at the column interface and was reduced at the beam interfaces for the models with the small column. The magnitudes and distribution were all very similar in the columns and in the beam at the third floor for all of the small column models. There was a difference in magnitudes in the beam at the second floor between the small column models with and without panel zone reinforcement as can be seen in Fig. 8.35d with maximum stress being 16% less for the models without panel zone reinforcement.

Models with column A-1 web reinforcement

The angle of the brace was not varied in this study but it is logical that a steeper brace angle may impose large demands on the columns relative to the beams. This would be the reverse behavior of what has been observed and discussed for the shallow brace angle used in the current study. Therefore, an analysis was performed with column web doublers in the panel zone and within the gusset plate region as shown in Fig. 8.22 in column A-1 (W12x72). This model is denoted as "bmWDcolWD." This was done to assess the impact on the beam demands through mitigating potential column damage. The discussion will center around the second floor joints of both columns A-1 (W12x72) and B-1 (W12x106) because other than the size of the column and web doublers in column A-1, the conditions at this joint are similar. The web doublers used in column A-1 increased the total web thickness from 0.43 to 0.76 to match the total thickness of the beam web plus web doubler at the joint. The thickness of the web of the W12x106 is 0.61.

The PEEQ demands in column A-1 along the gusset interface are shown in Fig. 8.36a and it can be seen that adding the beam web doublers without adding column web doublers (model "bmWD076") increased the column strain demand by 26%. When column web doublers are added, the strain demand is significantly decreased by 75%. However, adding

the column web doublers increases the strain demand in the beam relative to the model with no column doublers as Fig. 8.36c shows but this strain demand is approximately the same as the strain demand in the beam on the column B-1 side for the model with the beam web doublers ("bmWD076") as Fig. 8.36d shows (0.429 for "bmWDcolWD" at column A-1 versus 0.394 for "bmWD076" at column B-1). In other words, the W12x72 column with web doublers and the W12x106 without web doublers produce similar demands in the beam. It was discussed in the previous section that adding the beam web doublers mitigated the damage that was observed at the DBE and MCE drift levels and this remains the case even when web doublers were added to the W12x72 column and increased the beam demands; but did not increase them so much as to negate the positive influence of the beam web doubler.

Summary and implications of column size and reinforcement

The results of the study on the impact of column size and reinforcement are summarized below:

1. Smaller column sizes resulted in reduced strain demand in the beam along the gusset interfaces and also resulted in mitigating the local flange and web buckling at MCE drift levels. However, this damage was transferred to the column web and flanges except for the case when the column web doublers extended into the gusset region.

2. Weaker and more flexible panel zones (t_{pz}=0.38") produced less demand on the beam at the interface relative to stronger panel zones (t_{pz}=1.0"). However, weaker panel zones coincided with more column damage outside the panel zone as discussed in Item 1.

3. Adding web doublers to column A-1 (W12x72) decreased the column demands along the gusset interface with a corresponding increase in the beam demands but not so much as to negate the performance improvement of the beam with added web doublers.

8.3.6 Beam Release

Given the beam damage that occurred during the experiment and the lack of beam damage during the BRBF experiment performed by Fahnestock (2006), a model was analyzed with the beam fixity released just beyond the gusset plate away from each column at the second floor level. This was accomplished through a shear plate attached at mid-depth of the beam on either side of the web as shown in Fig. 8.37. All other details remained the same as those of the reference model.

The base shear envelope for the reference model (Ref), model with 0.5" gusset plate (gpt0.5), the model with the beam web doublers (bmWD0.76), and the model with the second floor beam released (REFbmPin) is shown in Fig. 8.38a. Models gpt0.5 and bmWD0.76 are included in this comparison as these models placed the smallest demands on the beams and columns relative to the reference model. It can be seen that the system strength with the beam release is approximately 15% lower than the strength of the other two models. This is obviously due to the loss of the moment frame action at the second floor and it can be seen that the shared column base shear is reduced (Fig. 8.38b). The base moment of column B-1 is relatively unchanged as shown in Fig. 8.38c. The moment in column B-1 at the top of second story is also relatively unchanged (Fig. 8.38d) because the beam fixity was released only at the second floor.

The stress contours and deformed shape at the second floor joint at column B-1 at 3.5% RDR of the four models discussed above are shown in Figs. 8.39a through 8.39d. As discussed in previous sections, the beam in the reference model displayed considerable local flange and web buckling while gpt05 and bmWD076 displayed very limited local buckling. Fig. 8.39c shows the deformation for the model with the beam released and it can be seen that the beam has rotated due to the release but that no web or flange buckling has taken place. The deformation scale of the plot make it appear that the bottom flanges of the beams at the splice are in contact but in reality they are not. Engineers should ensure that the gap is large enough to prevent contact.

The strain demand in the column along the gusset interface at the second floor of column B-1 is shown in Fig. 8.40a. As shown previously, the PEEQ was increased as a result of

adding beam web doublers while it was reduced to near zero when the 0.5" gusset plate was used and when the beam fixity was released. The PEEQ in the beam was reduced as a result of the addition of web doublers and using the 0.5" gusset plate by 46 and 35%, respectively (see Fig. 8.40c). Most remarkably, the plastic strain demands on the beam flange were completely removed through the use of the beam release. Similarly, the plastic strain demands in the gusset plates along the column and beam interfaces were also completely removed as Figs. 8.40b and 8.40d demonstrate.

Figures 8.41a through 8.41d show the von Mises stress in the column, beam and gusset plates along the interfaces at the second floor of column B-1 at -2% RDR. At all locations, the von Mises stress distribution for the model with the beam released was nearly constant and the maximum values were considerably less than the maximum values for the other models. The stress in the gusset plates for the model with the beam released is only from the brace action because the moment frame action has been eliminated. A comparison between the stresses of this model with the others indicates that frame action contributes the most significant part of the stresses.

Summary and design implications of beam release

The results of the study on the impact of releasing the fixity of the braced frame beams are summarized below:

1. Releasing the fixity of the beam resulted in a reduction of the resistance of the frame due to the loss of moment frame action.
2. Complete removal of strain demands in the beams and columns at the gusset plate interfaces was observed at the DBE drift levels and a ten-fold reduction was observed at the MCE level relative to the reference model.
3. No local flange and web buckling occurred in the beams with the release as was observed in the experiment and the simulations for many of the other models.
4. A dramatic reduction in the von Mises stresses were observed in all elements at the connection interfaces along with the distribution changing to a constant, nearly linear

value from the distribution with a high gradient that was observed in the models with the beam fixed.

8.3.7 BRB Strength

The strength, stiffness and hardening behaviors of BRBs vary between brace manufacturers and brace types and therefore a number of analyses were performed with varying BRB strength and stiffness. Additionally, different engineers may approach column design differently and some may prefer to design columns with significantly more strength than is necessary while others may design them with DCRs closer to unity. Changing the BRB strength also changed the DCR of the columns.

The strength and stiffness of the BRBs were varied by changing the area of the BRB relative to the reference model but keeping the same physical and constitutive model. A brace model with a BRB of half of the reference BRB area (REFwb) and a model with no BRB (REFnb) were investigated. All other parameters in these models remained the same as the reference model. Additionally, a model with 0.75" thick gusset plates and no BRB (REFgpt075nb) was also analyzed to determine the effect of changing both of these parameters on the demands at the joint.

The base shear envelopes for the above models are shown in Fig. 8.42a and as expected, the models with the weak or no BRB have strengths less than the reference model with the 1.0 and 0.75" gusset plates. The base shear resisted by column B-1 is approximately 5 to 10% larger for the models with a weak BRB or without a BRB that those with the reference BRB (see Fig. 8.42b). This is attributed to smaller axial demand in the column when a weak BRB or no BRB is included in the model and therefore less yielding occurs in the column. This is also reflected in the column base moment as seen in Fig. 8.38c. The moment at the top of the second story is larger for the models with the weak braces up until approximately 4" of roof displacement after which the moment magnitude plateuas in the weak brace models. More flexural column yielding occurs at this point in the models with the weak braces. The moments for the weak and no BRB models are also on the order of 5 to 10% larger than the models with the reference BRB.

The von Mises stress contours and deformed shape at the second floor joint at 3.5% RDR are shown in Figs. 8.43a through 8.43e. It can be seen that the beam local buckling was reduced as the brace strength was reduced. For example, the local flange buckling for the model without braces shown in Fig. 8.43c and it is clearly less than that which occurred in the reference model shown in Fig. 8.43a. The same behavior was observed for the models with the 0.75" gusset plates as a comparison of Figs. 8.43d and 8.43e shows.

Figures 8.44a through 8.44d show the strain demand in the beam, column and gusset plate along the gusset interfaces at the third floor joint at Column B1 at -2% RDR. As shown in Fig. 8.44a the maximum strain demands in the column are nearly unchanged between the models with the reference BRB and the weak BRB and no BRB with the differences being less than 5% for the models with the 1.0" thick gusset plates and approximately 15% for the models with the 0.75" thick gusset plates. This indicates that for this gusset plate geometry, frame action, not brace action, had the dominant effect on the column demands.

The converse was true for the strain demands in the beam as Fig. 8.44c demonstrates. For the models with 1.0" gusset plates, the beam strain demand was reduced by 37 and 62% for models REFwb and REFnb relative to the reference model. Similarly, the strain demand was reduced by 67% for the model with the 0.75" gusset plate. This indicates that for this gusset plate geometry, brace action had a significant effect on the interface demands.

The strain demands in the gusset plate along the column interface increased when weaker BRBs were used as Fig. 8.44b shows. The increase depended on the gusset plate thickness and the brace strength and ranged between 35 and 80%. Again, this indicates that at this location, frame action contributes more to the strain demands than the brace action and that these two have opposite effects. Frame action opens the joint causing a tensile stress when the BRB is in compression which cause a compressive effect. Hence, the strain is increased when the BRB is removed or a weaker brace is used.

There was no plastic strain demand in the gusset plate along the beam interface for the 1.0" thick gusset plates but there was for the 0.75" gusset plates as see in Fig. 8.44d. The strain demands decrease considerably when only frame action contributes as comparison between REFgpt075 and REFgpt075nb in Fig. 8.44d shows. This indicates that for this location (the beam interface), the brace contributes more to the demand in the gusset plate

than frame action.

The trends discussed above for the third floor joint were consistent with those at the second floor except for the strain demands in the column and the relative difference in the beam strain demands between the reference model and those with weaker braces. For example, there was a reduction in column demands at the gusset interface as the strength of the brace decreased as shown in Fig. 8.45a. The reduction was 24% and 47% for models REFwb and REFnb, respectively, relative to the demands in the reference model. It is also noted that the column strain demands at this location were an order of magnitude less than those at the third floor column.

The beam strain demands at the second floor joint at the gusset interface are shown in Fig. 8.45c and the demands in models REFwb and REFnb were 14 and 26% less than the demands in the reference model. The beam strain demands at the gusset interface at the second floor were higher than those at the third floor as was the case in all analyses (compare Fig. 8.44c with 8.45c for this group of analyses). The trends discussed above for the gusset plate demands were the same at each floor joint (see Figs 8.44b, 8.44d, 8.45b and 8.45d).

Similar to the beam deformation at the second floor, this was reduced at the third floor as the strength of the brace was reduced. Interestingly, at this level there was no beam deformation in the models with the weak braces as Fig. 8.46b, 8.46c and 8.46e demonstrate. This was due to the brace influence on the gusset plate yielding behavior and the resultant force transfer to the beams and columns. Table 8.3 lists the gusset plate interface forces in the vertical and horizontal direction at the beam and column interfaces for the gusset plate at the third floor at column B-1. These are the forces due to the force in the BRB in the reference model and were determined by integrating the shear and normal stresses at each interface at the positive roof drifts listed in the table. This was performed for models "Ref" and "REFnb" and the values listed in the table were calcualted by subtracting the interface forces calculated in model "Ref" from those calculated in model "REFnb." Also listed in the table are the forces that result from application of the UFM.

The distribution of the horizontal component of the brace force at 0.9% approximately matches the distribution estimated from the UFM while the distribution from the vertical

component of the brace force does not (Table 8.3). At this drift level, no part of the gusset plate had yielded. Approximately half of the elements in the gusset plate along the column interface had yielded by 2% story drift but not along the beam interface. There is a drop in load at the column interface of 50% of the horizontal brace component at 2% story drift (relative to load at 0.9%) due to this gusset plate yielding along the column interface. The drop in vertical load at the column interface at 2% is 15%.

The force distribution is similar at story drifts of 2 and 2.7% but change at 3%, and drastically change at 3.5% drift. At 3.5% drift, the column interface resists 85% of the horizontal brace load while at 2% drift it resists only 16% of the horizontal brace load. This large shift in force transfer is due to the gusset plate yielding that begins to occur at the beam interface at 3% drift.

This load shedding to the column interface explains the reason for the difference in the local and global frame deformation shown in Fig. 8.47a and 8.47b. The reference model with the brace is shown in Fig. 8.47a while the model without the brace is shown in Fig. 8.47b. Besides the obvious difference in beam local web and flange deformation, there is much more column deformation due to frame action in the model without the brace, which relieves the demands on the beam. This column yielding and deformation does not occur in the model with the brace because of the large increase in horizontal force at the gusset plate interface at the column which creates a moment at the joint in the opposite direction of the frame action moment.

Summary and implications of BRB strength

The results of the study on the impact of the BRB strength and stiffness are summarized below:

1. The global strength of the system was obviously impacted by the use of weaker and more flexible braces as this is the dominant component in force resistance and stiffness of the frames.
2. For this relatively shallow brace angle (32.3 degrees from the horizontal), frame action has a more dominant effect on the demands in the gusset plate at the column interface.

The demands at this location increase when the BRB is removed from the analysis.

3. The opposite is true at the beam interface, the demands in the beam and gusset plate at this location decrease when the BRB is removed.

4. The distribution of interface forces in the gusset plate in the vertical direction estimated from the Uniform Force Method did not match those predicted by the simulations at any drift levels. The distribution of interface forces in the horizontal direction estimated from the Uniform Force Method did match those predicted by the simulations at 0.9% story drift but diverged considerably at story drifts greater than 2%.

5. The distribution of forces in the gusset plates at the interface are highly dependent on the yielding that occurs in the gusset plate.

8.4 Further Analysis

The above analyses clearly illustrate that beam demands and the potential for local deformation in the beams are larger for connection regions with relatively thin beam webs and thick gusset plates. The results of the BRBF experiment corroborate this as the gusset plate thickness of the test frame (1.0") was 2.6 times thicker than the beam webs (0.38"). By the end of the test, the beams had considerable damage in the form of yielding and local buckling in the beams at the gusset plates, while little to no yielding or observable deformation occurred in the gusset plates.

The above observations suggest that beam damage may be related to the ratio of the beam web thickness (t_{bw}) to the gusset plate thickness (t_{gp}). To assess this relationship and provide guidance in recommending the best performing connection details, plots of the maximum strain (PEEQ) demands in the elements are compared for 14 different connection details from the parametric study discussed in the previous sections.

Figures 8.49b through 8.49d show the maximum, normalized strain demand in the beams at the gusset plate interface for the regions at the second floor of columns A-1 and B-1 and at the third floor of column B-1 as described in Fig. 8.49a. Plotted on the horizontal axis is the ratio of the beam web thickness to the gusset plate thickness and is defined as BGR as shown in Eqn. 8.1.

$$BGR = \frac{t_{bw}}{t_{gp}} \tag{8.1}$$

The location of the maximum PEEQ demand is at the gusset plate edge as shown in Fig. 8.49f. The reference model which matched the experimental frame is shown as the filled triangle. The plots are all normalized with respect to the PEEQ value of the reference model at each location. Each symbol in the plots coincide with one particular parameter that was varied in the simulations and a line connects these points to help identify the trend. For example, the left-facing triangles are used for the gusset plate thickness parameter and the decreasing size of the triangles indicating decreasing gusset plate thickness. Similarly, the stars indicate the models with the beam doubler plates and a larger star indicates a thicker doubler plate.

Observation of the figures show that the maximum strain demands in the beam are inversely proportional to the BGR and the relationship is nearly linear for each parameter group. It is obvious that while the strain demand is related to the BGR, the demand varies between parameter groups for a given BGR. Detailing the gusset plates with nearly equal connection lengths at the beam and column interfaces ("nt" models, square symbol in plots) increases the beam demand significantly relative to the gusset plates with tapers and no other reinforcement (left-facing triangles). The relative size of these larger demands vary depending on the location in the frame but they are consistently larger and up to twice as large. Likewise, when free-edge stiffeners are added to the gusset plate ('+' symbol in plots), the beam strain demands are increased relative to the models without gusset plate stiffeners. However, the increase in demand is not nearly as large as the increase when the gusset plates are not tapered at the column (square symbol in plots), and as Section 8.3.2 discusses, the beam deformations at 2 and 3.5% are no larger for the models with gusset plate edge stiffeners than those without.

The largest reduction in beam strain demand occurs as a result of providing the beam with web doubler plates (the model with the beam fixity released notwithstanding). The models with beam web doublers are shown as stars in Figs. 8.49b through 8.49d for these models with the tapered gusset plates and as circles for these models with the gusset plates

without tapers at the column. Using doubler plates with a BGR of 0.76 reduces the beam demand by more than half relative to the reference model for the models with the tapered gusset plates. The reduction is also significant for the models without the gusset tapers when doublers are provided and varies depending on the BGR and the location of the frame. As discussed in Section 8.3.4, the doublers prevented the beam local web and flange buckling from occurring in the simulations at MCE drift levels regardless of the gusset plate geometry.

The advantage of adding beam web doublers over reducing the gusset plate thickness is obvious from these figures but is also apparent when considering that gusset plate stability issues occurred in the models with 0.5 and 0.625" gusset plates at RDRs greater than 1% and 2% (DBE) RDR. Using thicker gusset plates with beam web doublers mitigates the gusset plate stability issue of thinner gusset plates and reduces the demands in the beams.

The model with the beam release removed the strain demands in the beam completely at the gusset interface in this study at the DBE drift level and is clearly the best detail from this standpoint. Deformation and yielding is shifted to the splice connecting the beam elements but this can be designed for and is easier to repair than beam web and flange buckling as the design of the splice can limit the damage to the connectors as was done in the experiments performed by Fahnestock (2006).

The same analysis discussed above for the beams is also shown for the columns in Figs. 8.50b through 8.50d. The inverse relationship between the column demands and the BGR are the same as it was for the beam except for the models with the beam doubler plates. As discussed in Section 8.3.4, addition of the beam doubler plates increases the strain demand in the columns. These models are indicated by the stars (beam doublers and tapered gussets) and the circle symbols (beam web doublers and gussets without taper on the column side) in Figs. 8.50b through 8.50d. The increase in column strain demand for the models with beam doublers and tapered gusset plates relative to the reference model (filled triangle) varied between 8% at the third floor joint (Fig. 8.50b), to 78% at the second floor joint at column B-1 (Fig. 8.50d). No detrimental local column deformation or loss of column resistance was observed in the simulations in these models. When beam web doublers were used with gusset plates that were not tapered, the column demands were less

than the demands from the reference model as seen in Figs. 8.50b through 8.50d (compare the circle symbols with the filled triangle).

8.5 Summary of Parametric Study

Finite element simulations of modifications of Frame 1 of the BRBF test were performed to identify the main parameters that influence the damage observed at the beam-column-gusset connection region. The validated frame model described in Chapter 7 was used as the starting point for all of the models used for the parametric study. Seven main parameters were varied and more than 30 different models were analyzed. The key observations from this study are summarized below:

- Reducing the gusset plate thickness reduced the demands in the beam and column at the gusset interface and reduced the potential for local web and flange buckling at the DBE drift level but not at the MCE drift level even for the 0.5" gusset plates. However, thinner gusset plates become unstable as yielding progresses and the 0.5 and 0.625" thick gusset plates required long-edge stiffeners to prevent these instabilities at DBE and MCE drift levels, respectively. Therefore, the advantages gained in reducing component demand through the use of thin gusset plates are offset by the instabilities that may occur in the gusset plates and therefore this is not an effective way of reducing component demands in the connection region.
- Rectangular gusset plates increased the beam demands at the connection interface and increased the likelihood of local web and flange buckling at DBE drift levels. The increased demands were not as significant for thinner gusset plates. The gusset plate demands at the column were reduced significantly for the rectangular gusset plate relative to the tapered gusset plate indicating less potential for the tearing that occurred during the experiment. However, analyses showed that designing the weld for the strength of the plate in the tapered case would potentially have mitigated that problem as the properly designed weld reduced the strain demand to below the strain that occurred in the simulations at the instance of weld tearing.
- The addition of beam web doublers significantly reduced the demands in the beam at

the gusset interface. Adding beam web doublers that increased the web thickness to 75% of the gusset thickness within the gusset plate region mitigated the local web and flange buckling that occurred at MCE drift levels regardless of the shape of the gusset plate (taper, no taper). Doublers that increased the beam web thickness to 50% of the the gusset thickness mitigated this deformation at DBE but not at MCE drift levels. Little to no change was observed in the demands in the tapered gusset plates along the interface when beam web doublers were added. There was however, a 45% increase in gusset plate strain demands at the column interface when the gusset plates were not tapered indicating the importance of designing the weld for the strength of the plate. The demands in the columns at the gusset interface did increase as a result of the doublers but no loss of resistance or local deformation was observed at MCE drift levels and the addition of column web doublers mitigates this demand increase with a negligible increase in beam demands (see next bullet point). The global strength of the frame increased between 5 and 10% with the addition of doublers as a result of the increased local beam stiffness and strength.

- A smaller column resulted in significant reductions in beam demands and local web and flange deformation at all drift levels. However, this demand and deformation was transferred to the column. Adding column web doublers within the gusset region mitigated these demands and deformations and while this caused an increase in beam demands, this increase resulted in beam demands that were considerably less than those seen in the reference model and had negligible impact on the behavior and performance.

- Relative impacts of frame and brace action were shown to be dependent on the gusset plate geometry. Removing the BRB from the frame had little effect on the column demands at the gusset interface for the models with the tapered gusset plates indicating that frame action contributed the most to the column demands for this gusset geometry. The demands in the beam at the gusset interface were reduced by up to 70% with the removal of the brace for the tapered gusset plate models indicating frame action had less of an impact at this location. When rectangular gusset plates were

employed, there was only a 10% reduction in the demands at each interface indicating frame action contributed a large part to both the beam and column demands at the connection interfaces for this gusset geometry. Similar trends were observed in the gusset plate demands at the interface when the brace was removed from the analysis.

- Releasing the beam fixity just inboard of the gusset plate edge had the most significant impact on the demand reduction in all components at the gusset interfaces. Additionally, no detrimental beam local flange or web buckling occurred in the connection region at MCE drift levels.
- The strain demands in the beam along the gusset plate interface were clearly shown to be inversely proportional to the ratio of the beam web thickness to the thickness of the gusset plate. Additionally, the reduction in demands depends not only the magnitude of this ratio but also on the way the ratio is changed. For example, reducing the gusset plate thickness by 50% does not have the same impact as doubling the beam web thickness. Doubling the beam web thickness provides a better improvement of beam performance than decreasing the gusset plate thickness.
- The strain demands in the column along the gusset plate interface were also shown to be inversely proportional to the ratio of the beam web thickness to the thickness of the gusset plate except when the ratio was increased by providing beam web doubler plates in the gusset region. In the latter case, the column demands at the interface increased.

Table 8.2: Gusset plate demand-capacity ratios for parametric study

Limit State	Gusset plate thickness, in.				
	1.5	1.0	0.75	0.625	0.5
Whitemore Yielding	0.41	0.61	0.81	0.98	1.22
Buckling	0.41	0.61	0.83	1.0	1.3

Table 8.3: Gusset plate interface force ratios from brace force only in FE simulations at third floor, column B-1 (see Fig. 8.48 for nomenclature)

Roof drift (%)	V_b/V	V_c/V	H_b/H	H_c/H
0.9	0.56	0.44	0.68	0.32
2	0.63	0.37	0.84	0.16
2.7	0.62	0.38	0.82	0.18
3	0.52	0.48	0.58	0.42
3.5	0.43	0.57	0.15	0.85
UFM	0.72	0.28	0.65	0.35

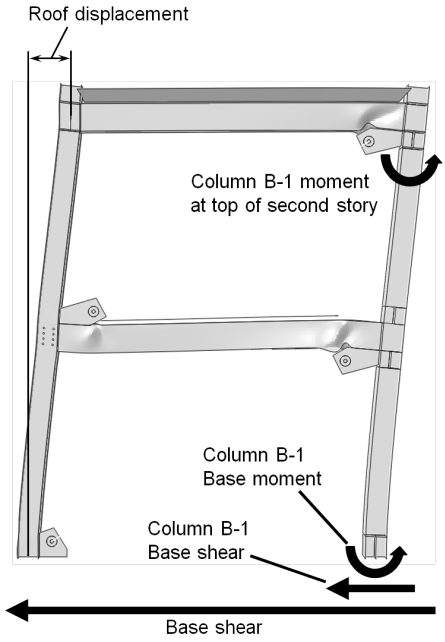

Figure 8.1: Global and local force-deformation responses used for comparisons in parametric study

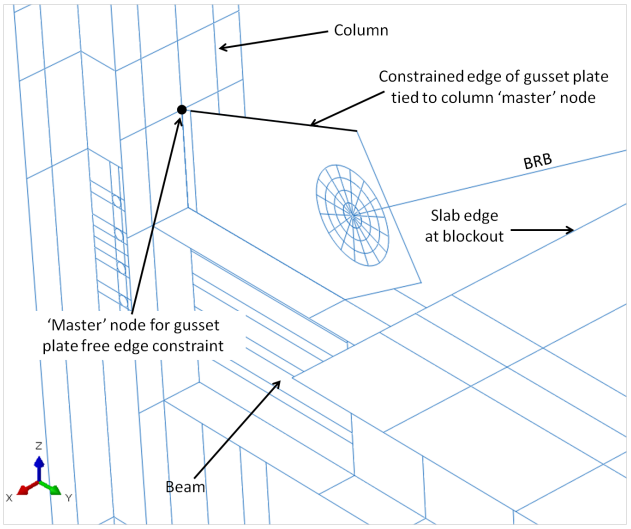

Figure 8.2: Gusset plate long-edge tie constraint

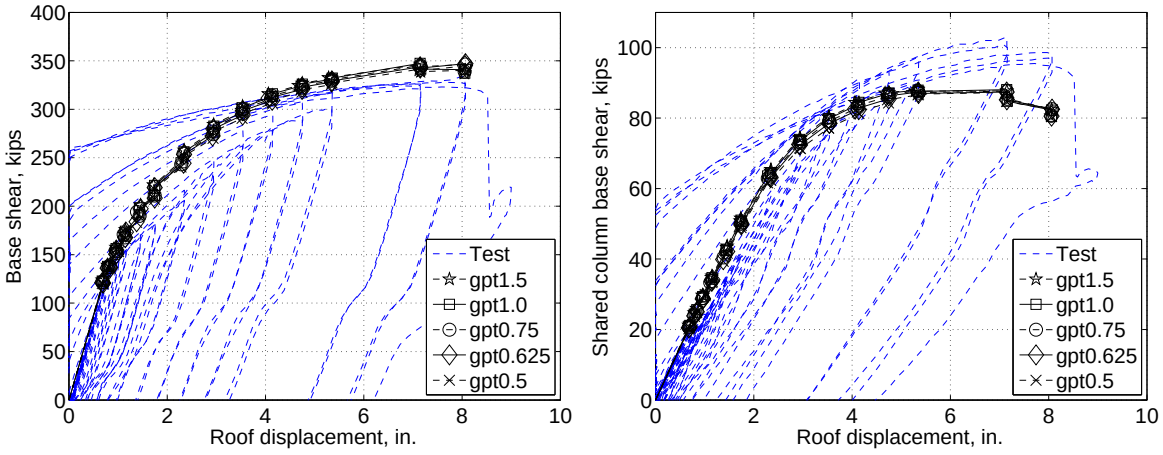

(a) Base shear

(b) Shared column base shear

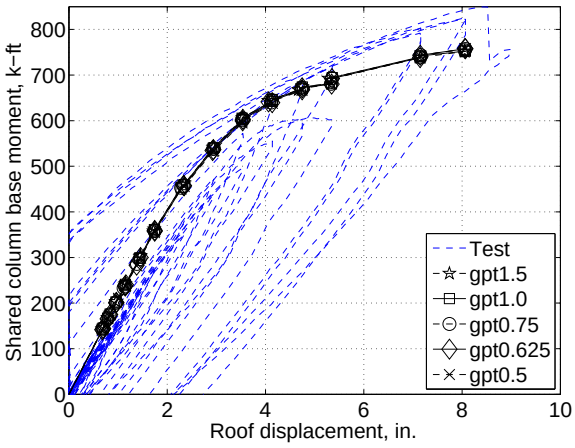

(c) Shared column base moment

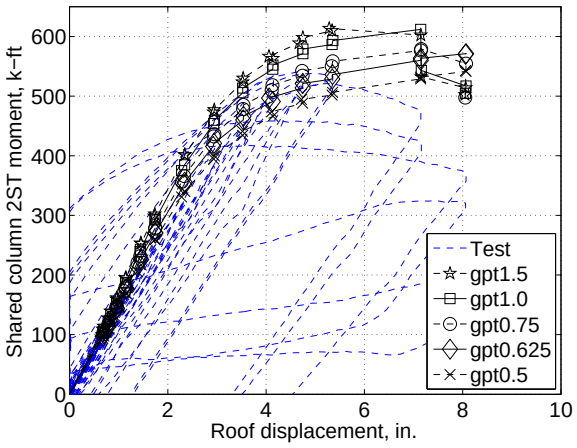

(d) Shared column 2ST moment

Figure 8.3: Global behavior comparison (Parameter - gusset plate thickness)

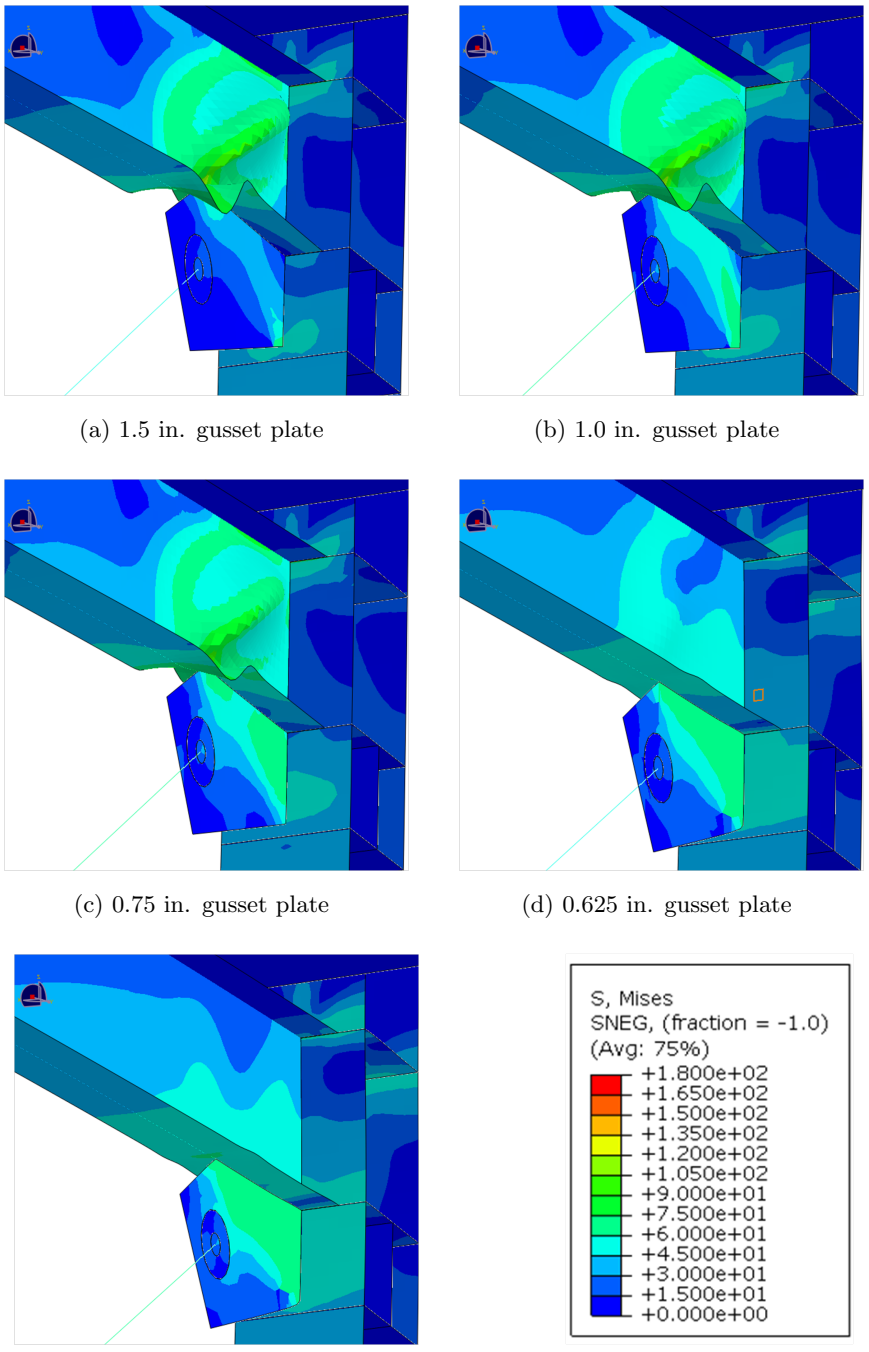

(a) 1.5 in. gusset plate

(b) 1.0 in. gusset plate

(c) 0.75 in. gusset plate

(d) 0.625 in. gusset plate

(e) 0.5 in. gusset plate

(f) Contour legend

Figure 8.4: Stress contours and beam deformation at third floor joint at column B-1 at 3.5% RDR (Parameter - gusset plate thickness)

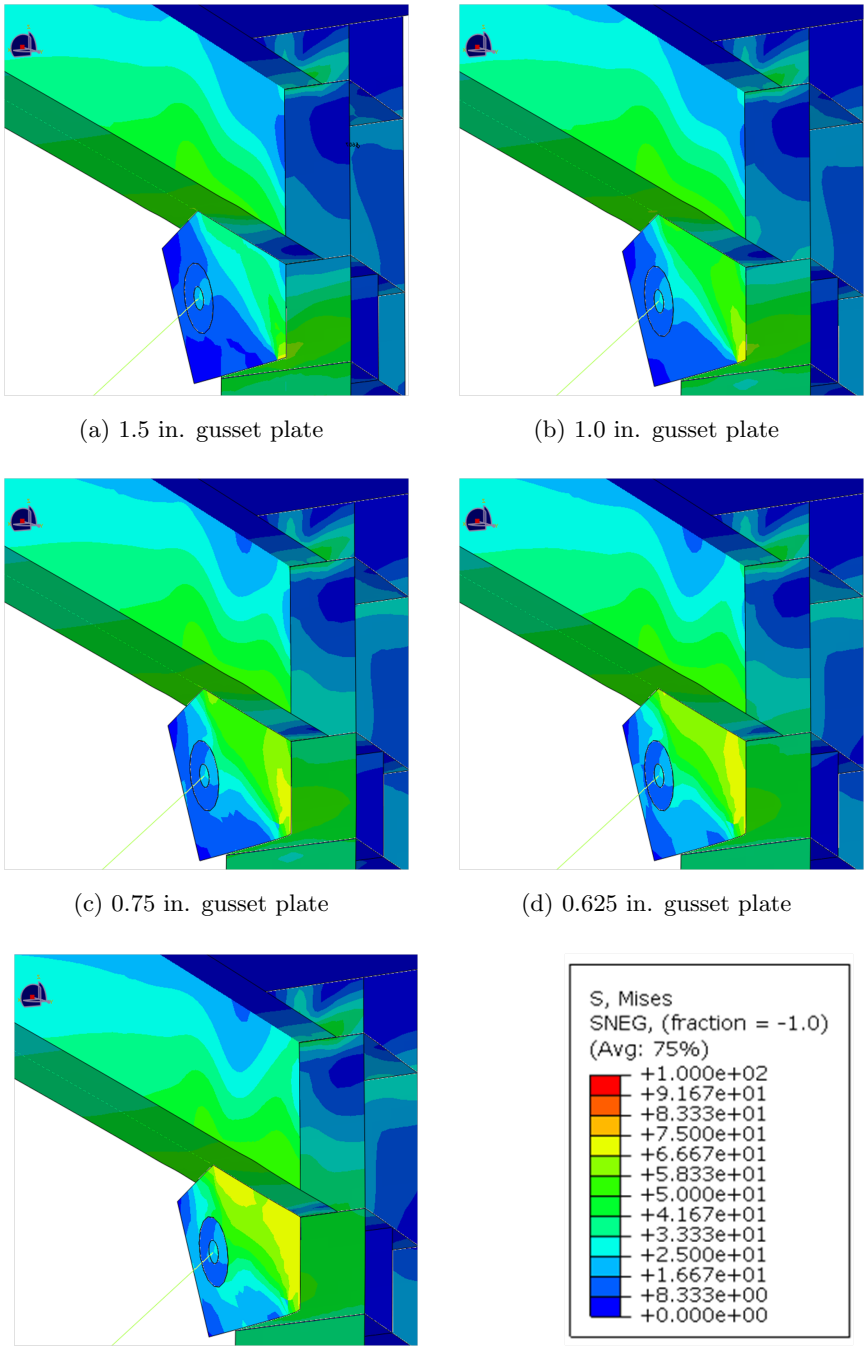

(a) 1.5 in. gusset plate

(b) 1.0 in. gusset plate

(c) 0.75 in. gusset plate

(d) 0.625 in. gusset plate

(e) 0.5 in. gusset plate

(f) Contour legend

Figure 8.5: Stress contours and beam deformation at third floor joint at column B-1 at 2.0% RDR (Parameter - gusset plate thickness)

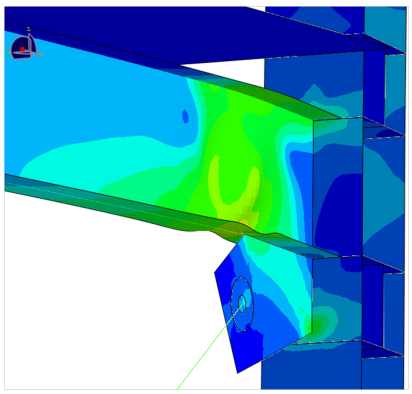

(a) 1.5 in. gusset plate

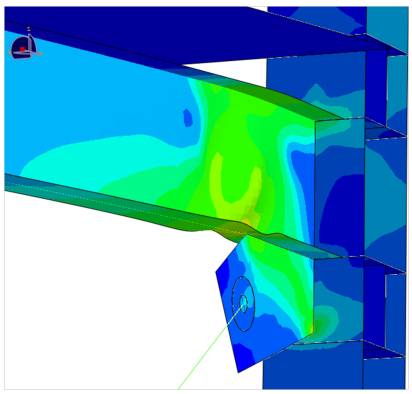

(b) 1.0 in. gusset plate

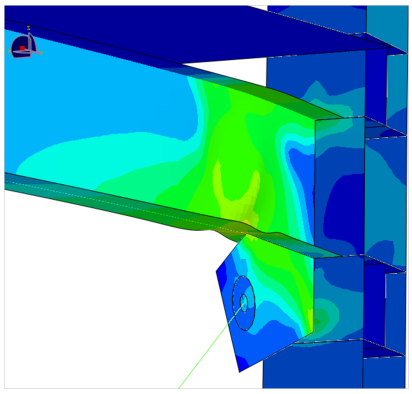

(c) 0.75 in. gusset plate

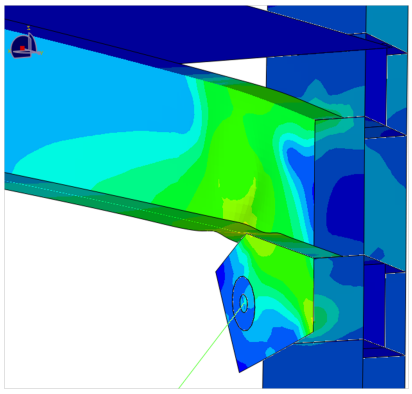

(d) 0.625 in. gusset plate

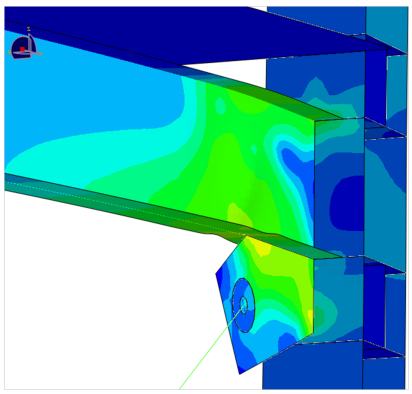

(e) 0.5 in. gusset plate

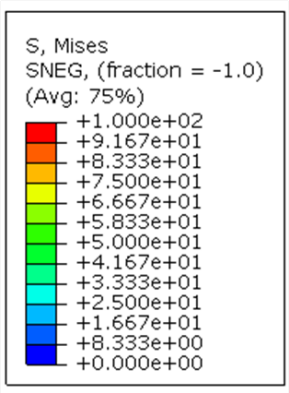

(f) Contour legend

Figure 8.6: Stress contours and beam deformation at second floor joint at column B-1 at 2.0% RDR (Parameter - gusset plate thickness)

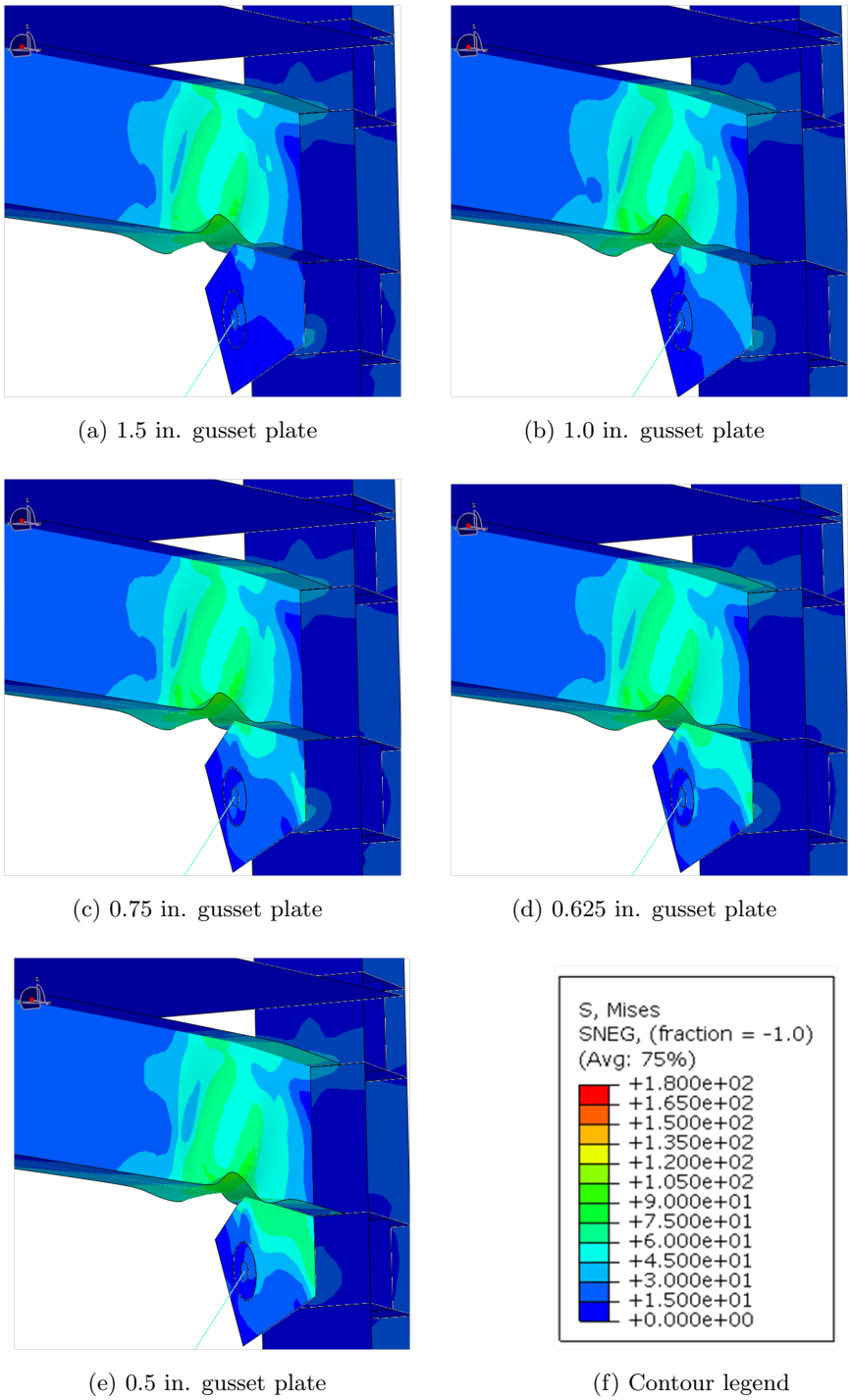

(a) 1.5 in. gusset plate

(b) 1.0 in. gusset plate

(c) 0.75 in. gusset plate

(d) 0.625 in. gusset plate

(e) 0.5 in. gusset plate

(f) Contour legend

Figure 8.7: Stress contours and beam deformation at second floor joint at column B-1 at 3.5% RDR (Parameter - gusset plate thickness)

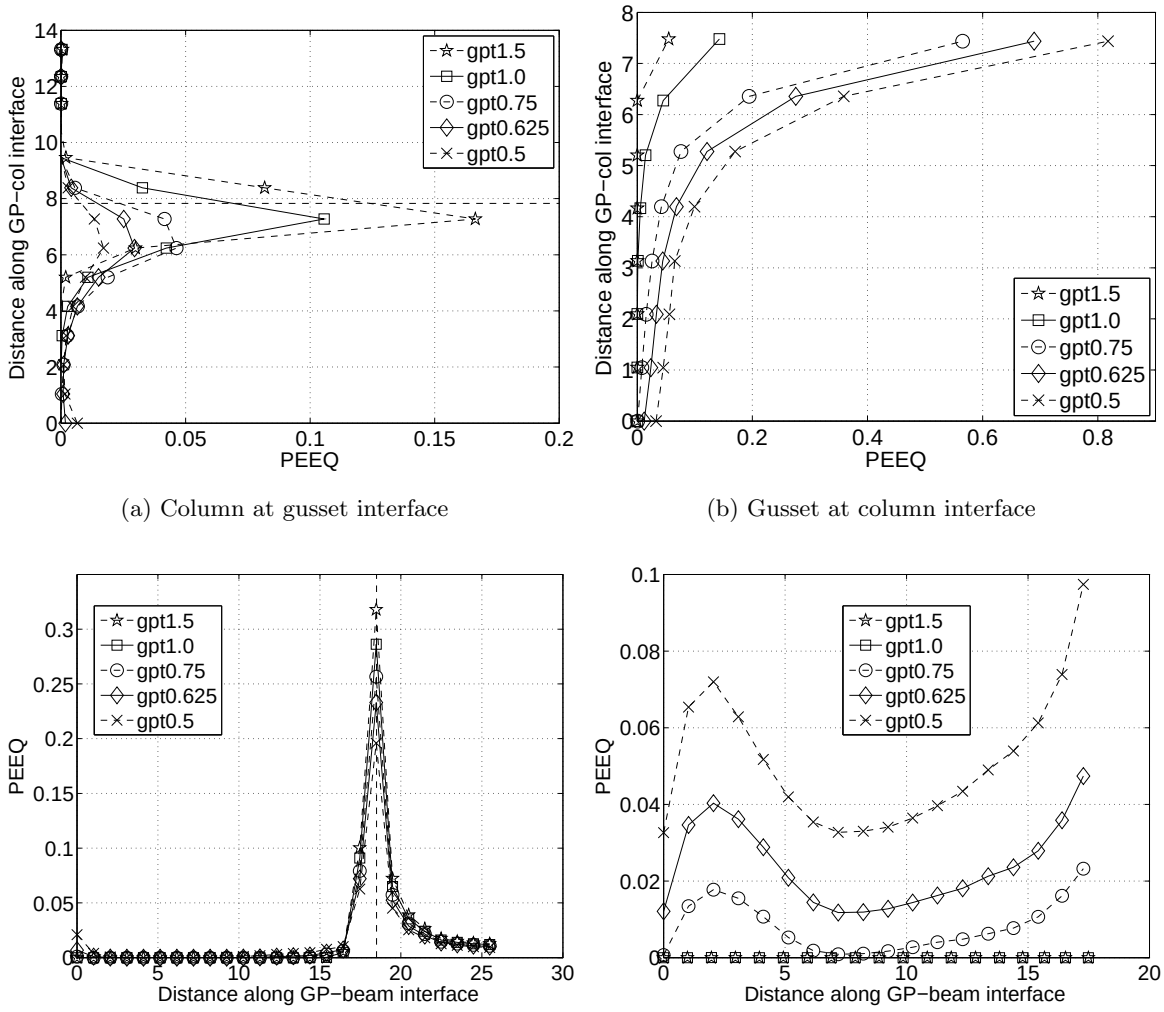

(a) Column at gusset interface

(b) Gusset at column interface

(c) Beam at gusset interface

(d) Gusset at beam interface

Figure 8.8: PEEQ comparison at column B-1 third floor joint at -2% RDR (Parameter - gusset plate thickness)

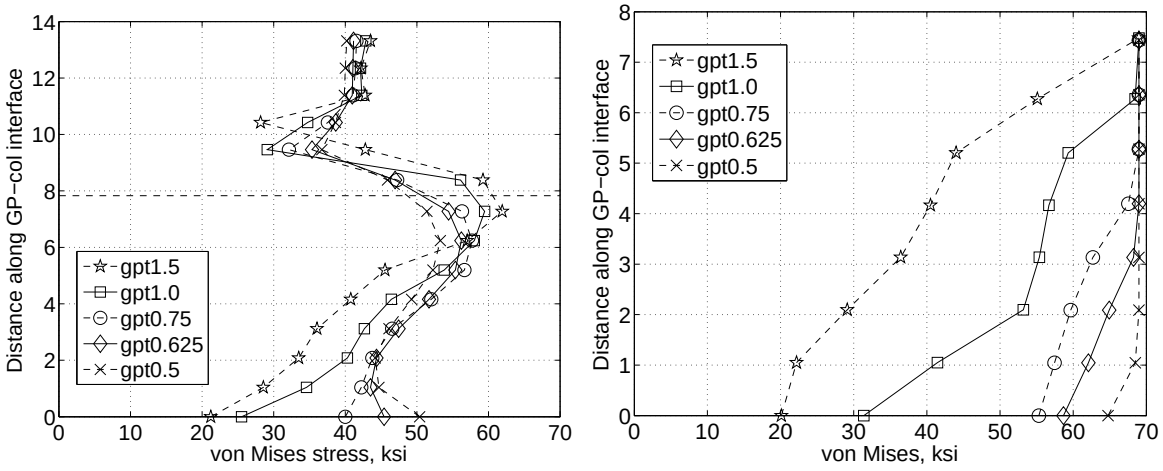

(a) Column at gusset interface

(b) Gusset at column interface

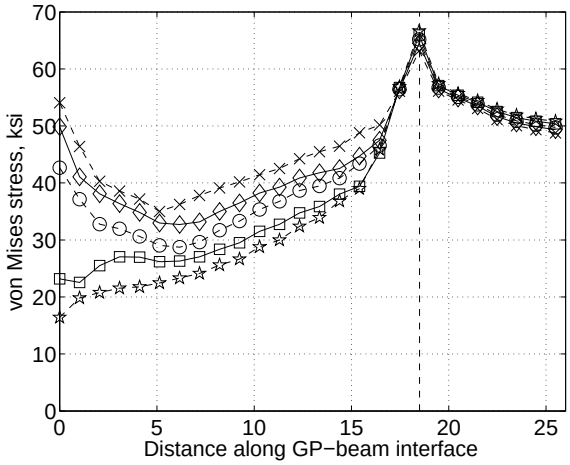

(c) Beam at gusset interface

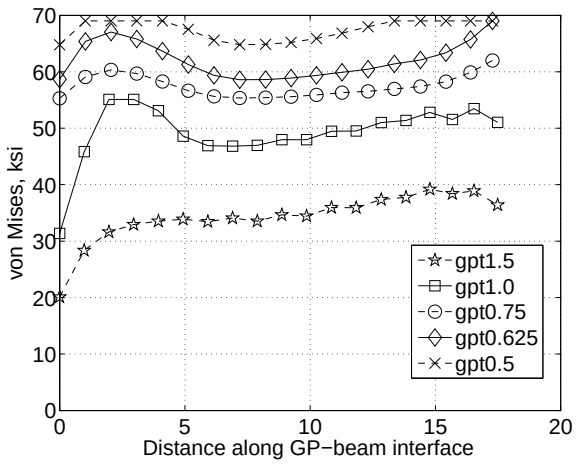

(d) Gusset at beam interface

Figure 8.9: Von Mises stress comparison at column B-1 third floor joint at -2% RDR (Parameter - gusset plate thickness)

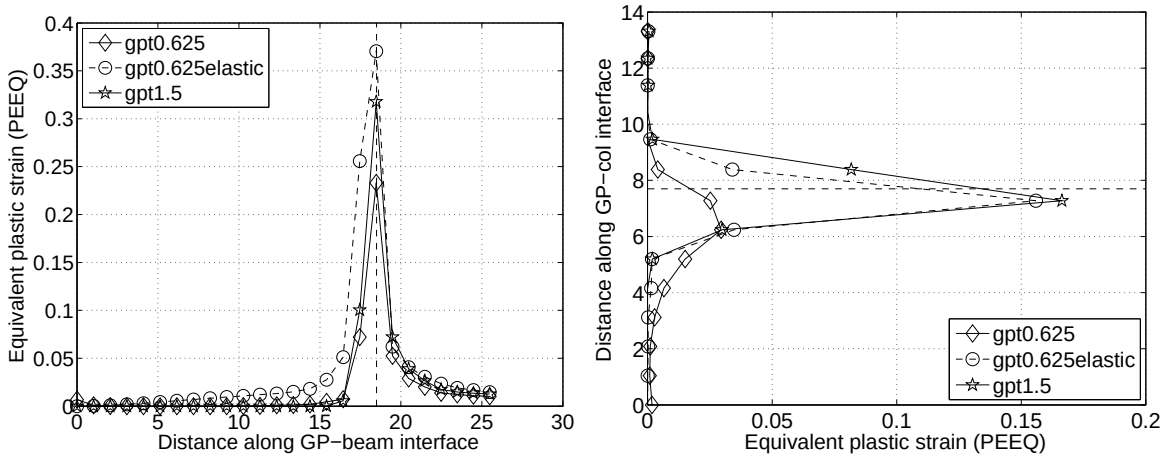

(a) Beam at gusset interface

(b) Column at gusset interface

(c) Beam at gusset interface

(d) Column at gusset interface

Figure 8.10: PEEQ and Von Mises stress comparison at column B-1 third floor joint at -2% RDR (Parameter - gusset plate thickness)

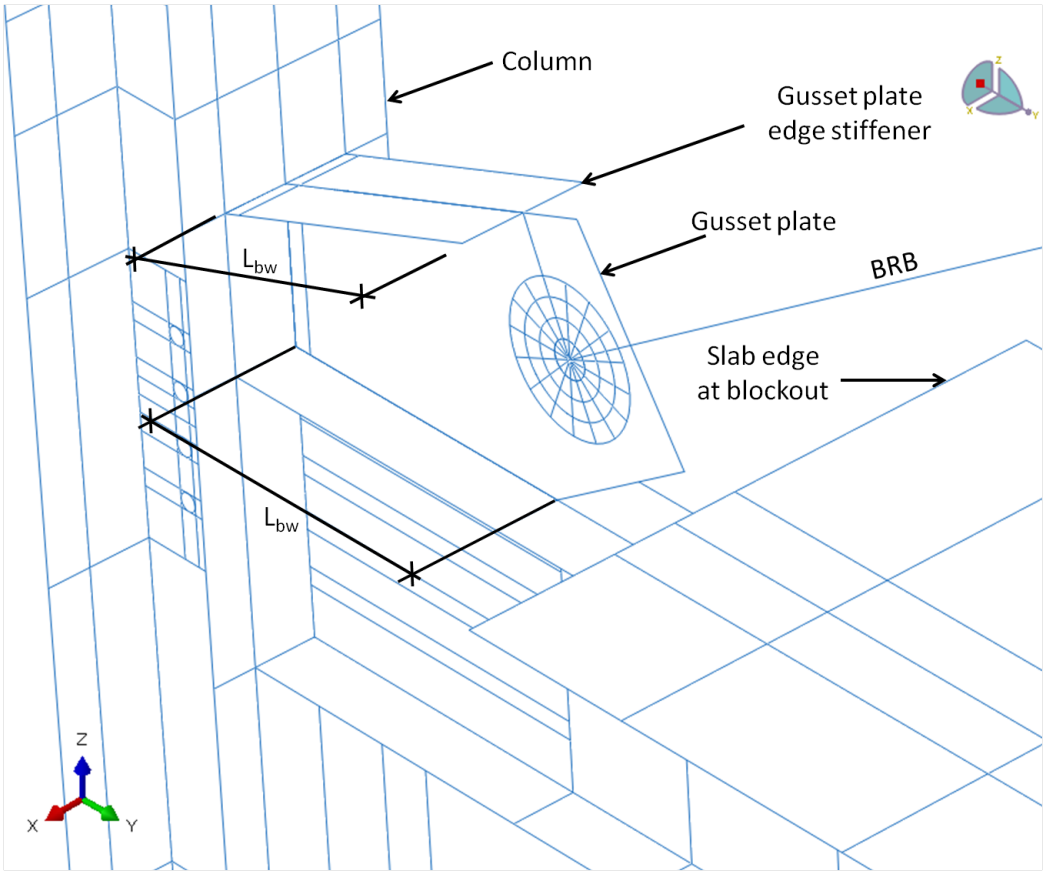

Figure 8.11: Gusset plate long-edge stiffener detail

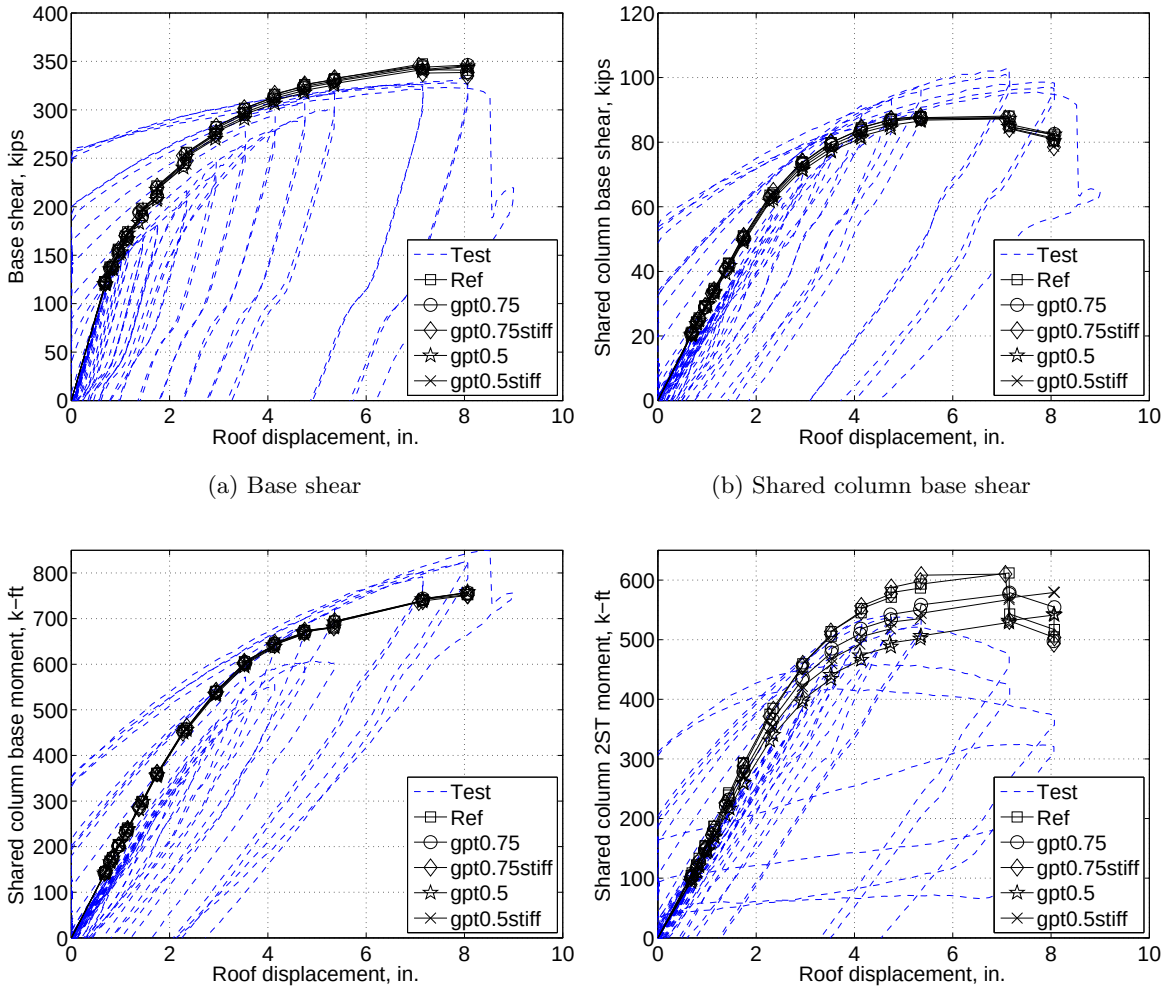

(a) Base shear

(b) Shared column base shear

(c) Shared column base moment

(d) Shared column 2ST moment

Figure 8.12: Global behavior comparison (Parameter - gusset plate edge stiffeners)

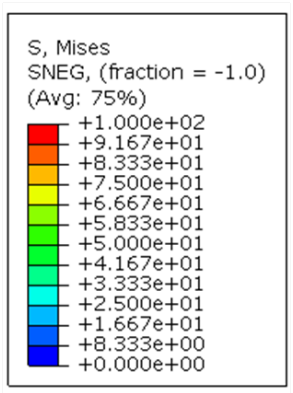

(a) Legend

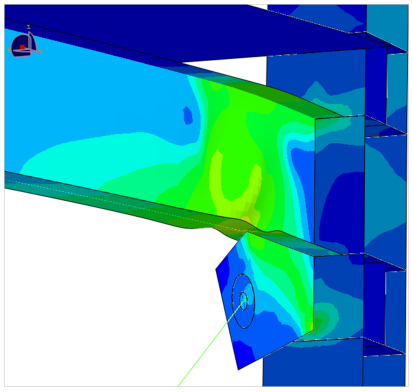

(b) Ref

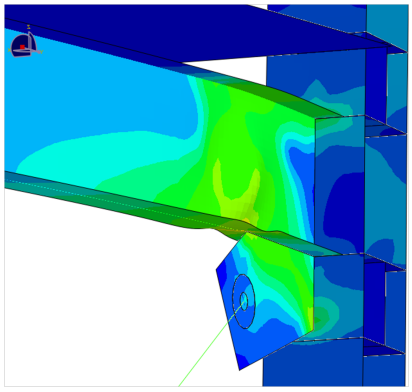

(c) gpt0.75

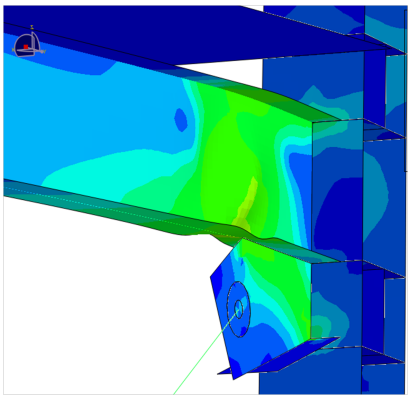

(d) gpt0.75stiff

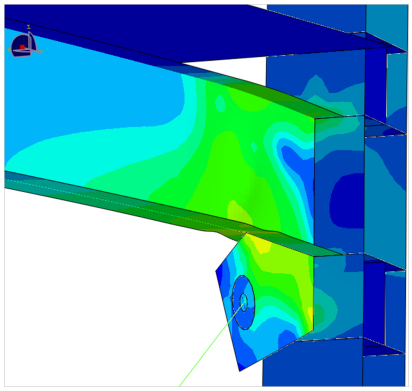

(e) gpt0.5

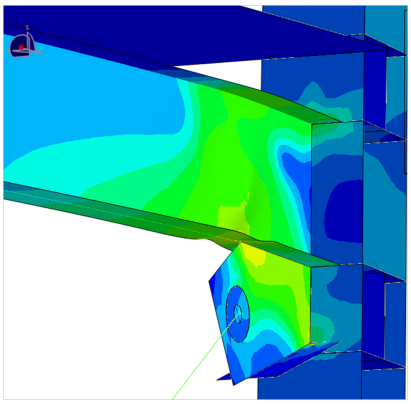

(f) gpt0.5stiff

Figure 8.13: Stress contours and beam deformation at second floor joint at column B-1 at 2.0% RDR (Parameter - gusset plate edge stiffeners)

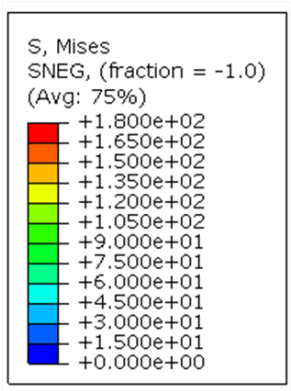

(a) Legend

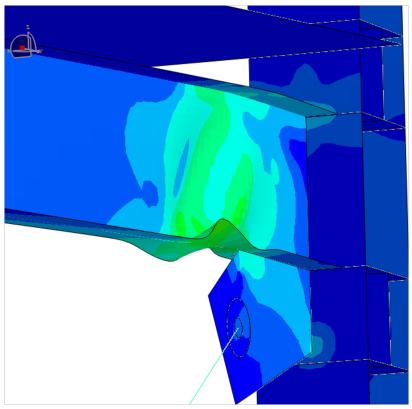

(b) Ref

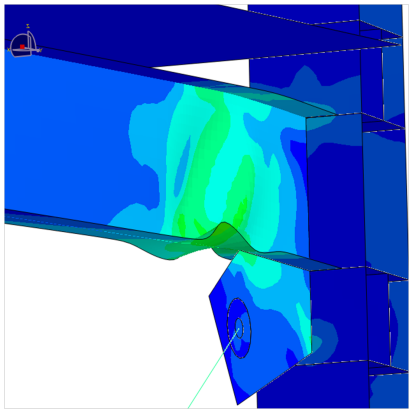

(c) gpt0.75

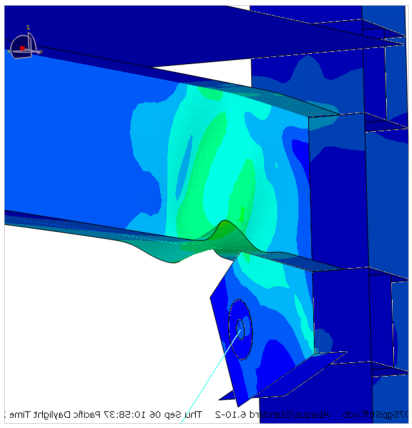

(d) gpt0.75stiff

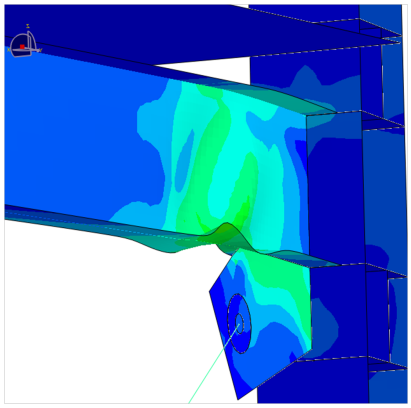

(e) gpt0.5

Figure 8.14: Stress contours and beam deformation at second floor joint at column B-1 at 3.5% RDR (Parameter - gusset plate edge stiffeners)

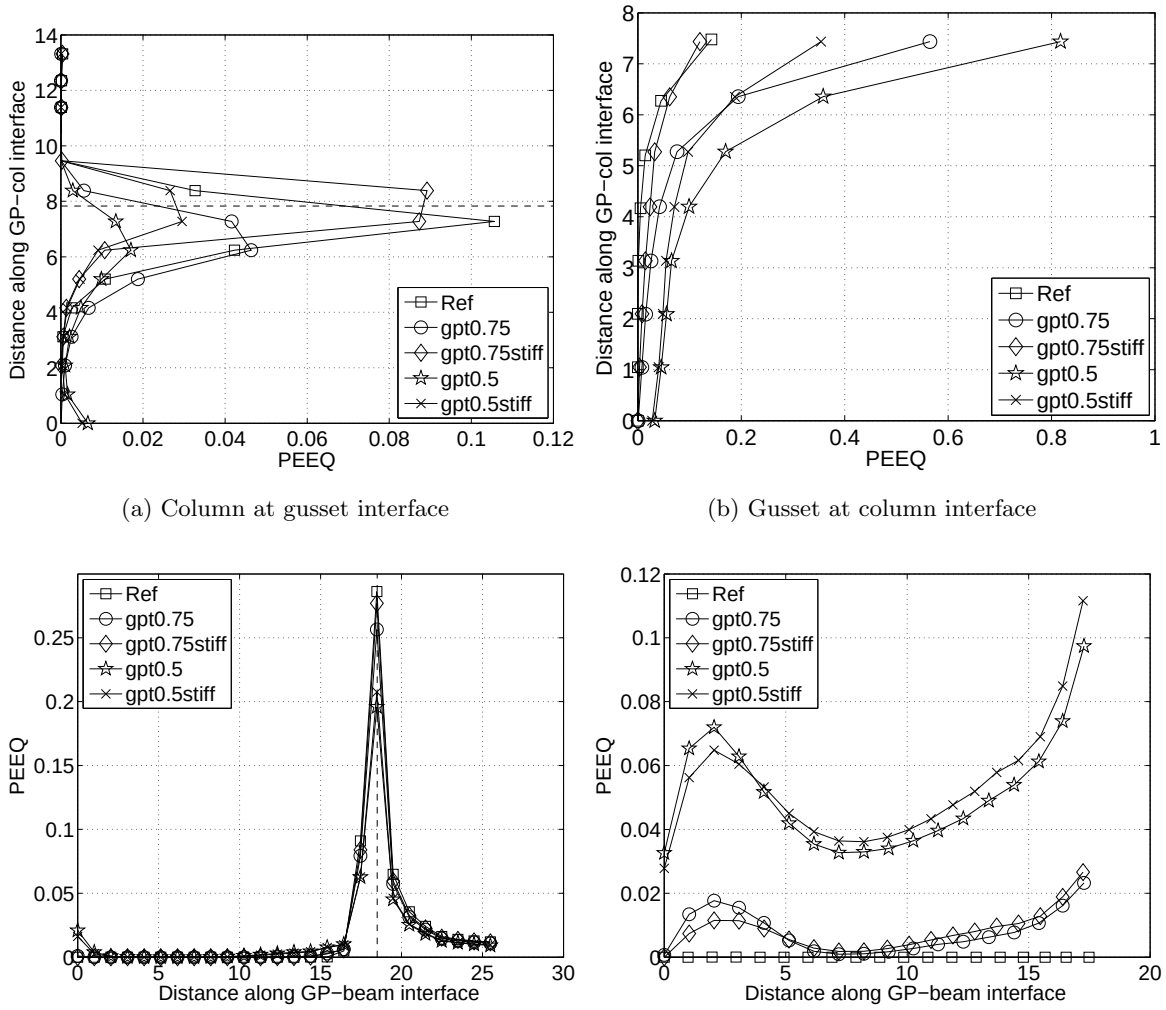

(a) Column at gusset interface

(b) Gusset at column interface

(c) Beam at gusset interface

(d) Gusset at beam interface

Figure 8.15: PEEQ comparison at column B-1 third floor joint at -2% RDR (Parameter - gusset plate edge stiffeners)

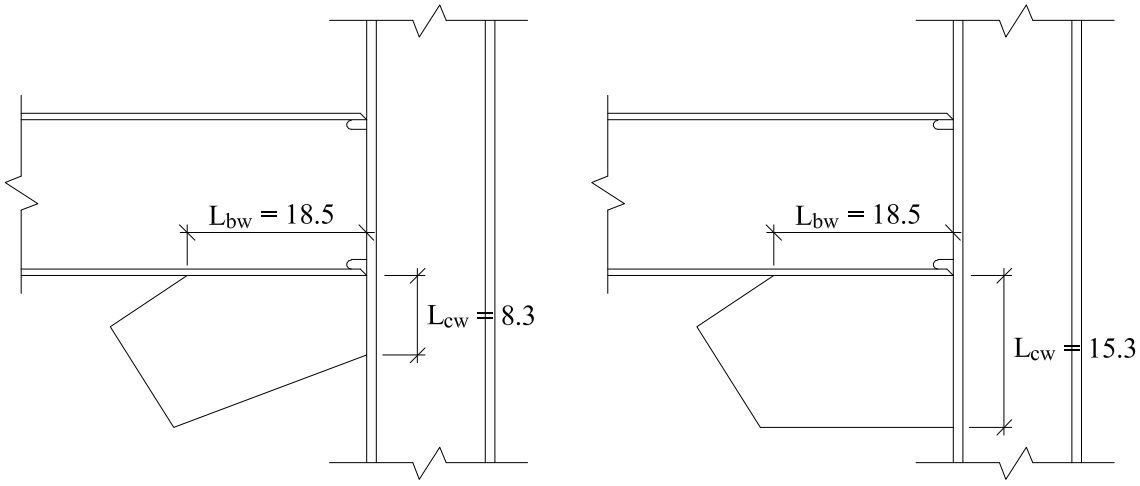

(a) (b)

Figure 8.16: Gusset plate geometry: (a) with taper at column; (b) without taper at column (models with "NT" in their designation)

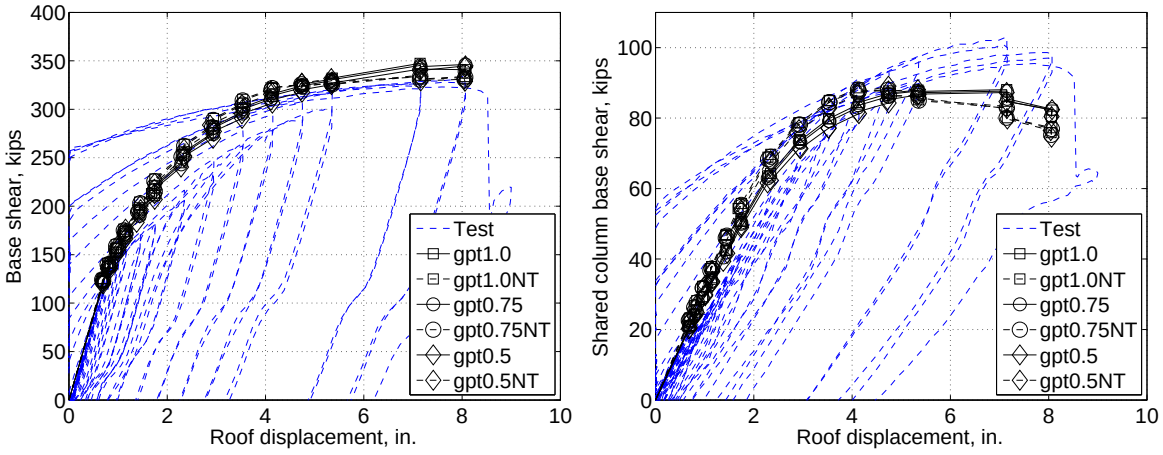

(a) Base shear

(b) Shared column base shear

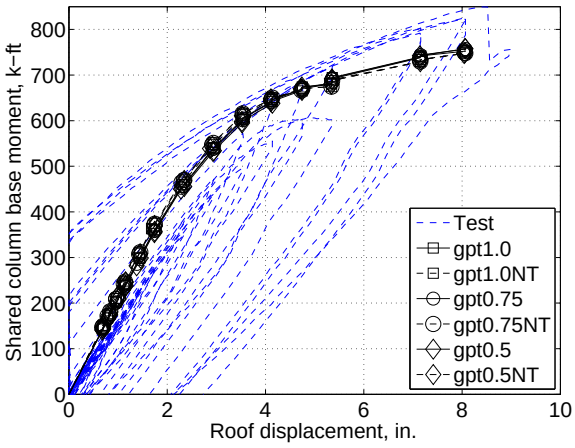

(c) Shared column base moment

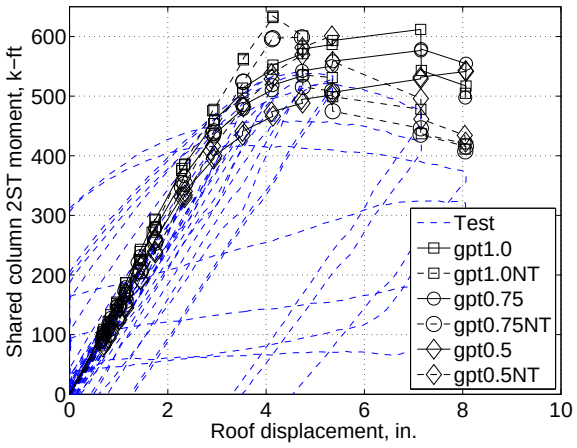

(d) Shared column 2ST moment

Figure 8.17: Global behavior comparison (Parameter - gusset plate taper)

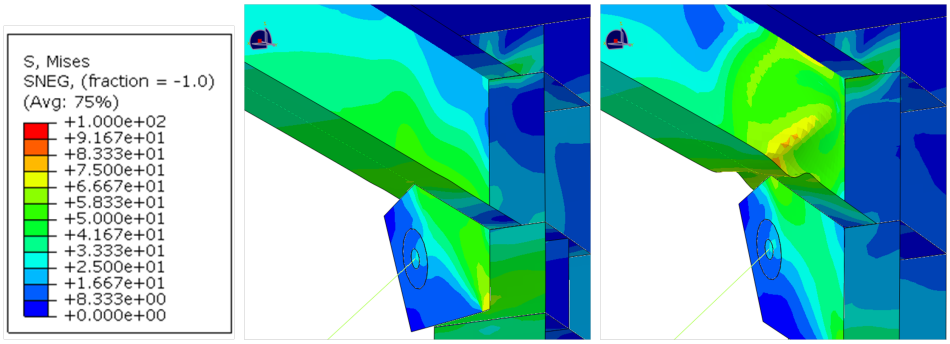

(a) Legend (b) 1.0 in. tapered gusset plate (c) 1.0 in. gusset plate w/o taper

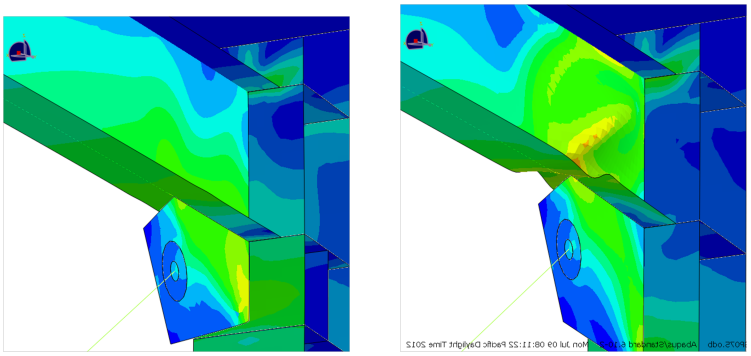

(d) 0.75 in. tapered gusset plate (e) 0.75 in. gusset plate w/o taper

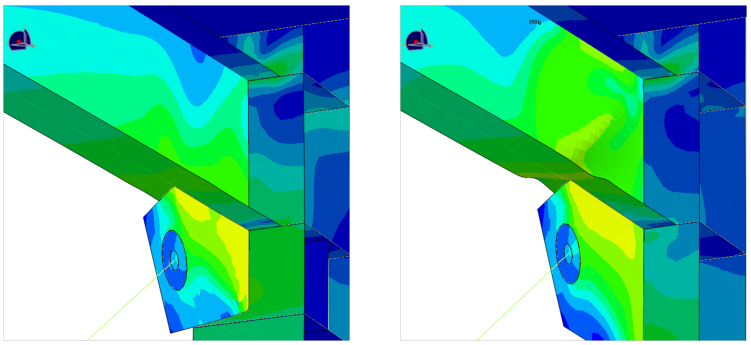

(f) 0.5 in. tapered gusset plate (g) 0.5 in. gusset plate w/o taper

Figure 8.18: Stress contours and beam deformation at third floor joint at column B-1 at 2.0% RDR (Parameter - gusset plate taper)

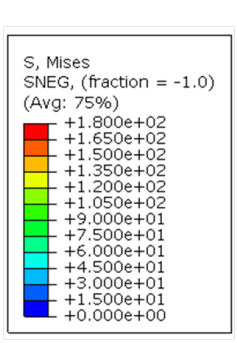

(a) Legend

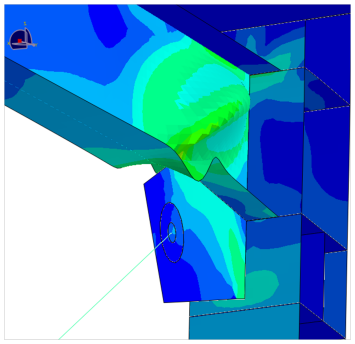

(b) 1.0 in. tapered gusset plate

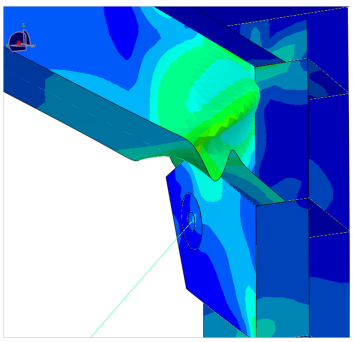

(c) 1.0 in. gusset plate w/o taper

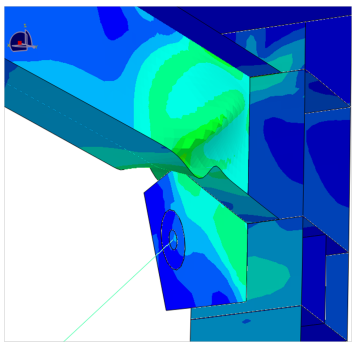

(d) 0.75 in. tapered gusset plate

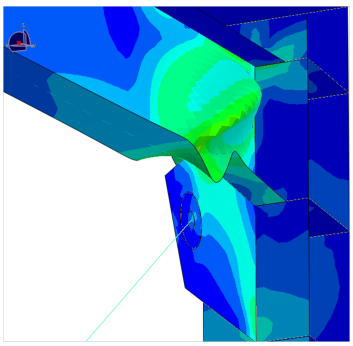

(e) 0.75 in. gusset plate w/o taper

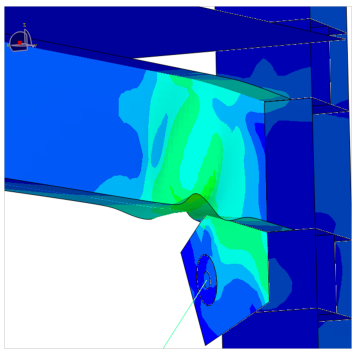

(f) 0.5 in. tapered gusset plate

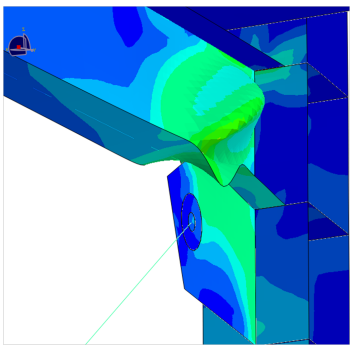

(g) 0.5 in. gusset plate w/o taper

Figure 8.19: Stress contours and beam deformation at third floor joint at column B-1 at 3.5% RDR (Parameter - gusset plate taper)

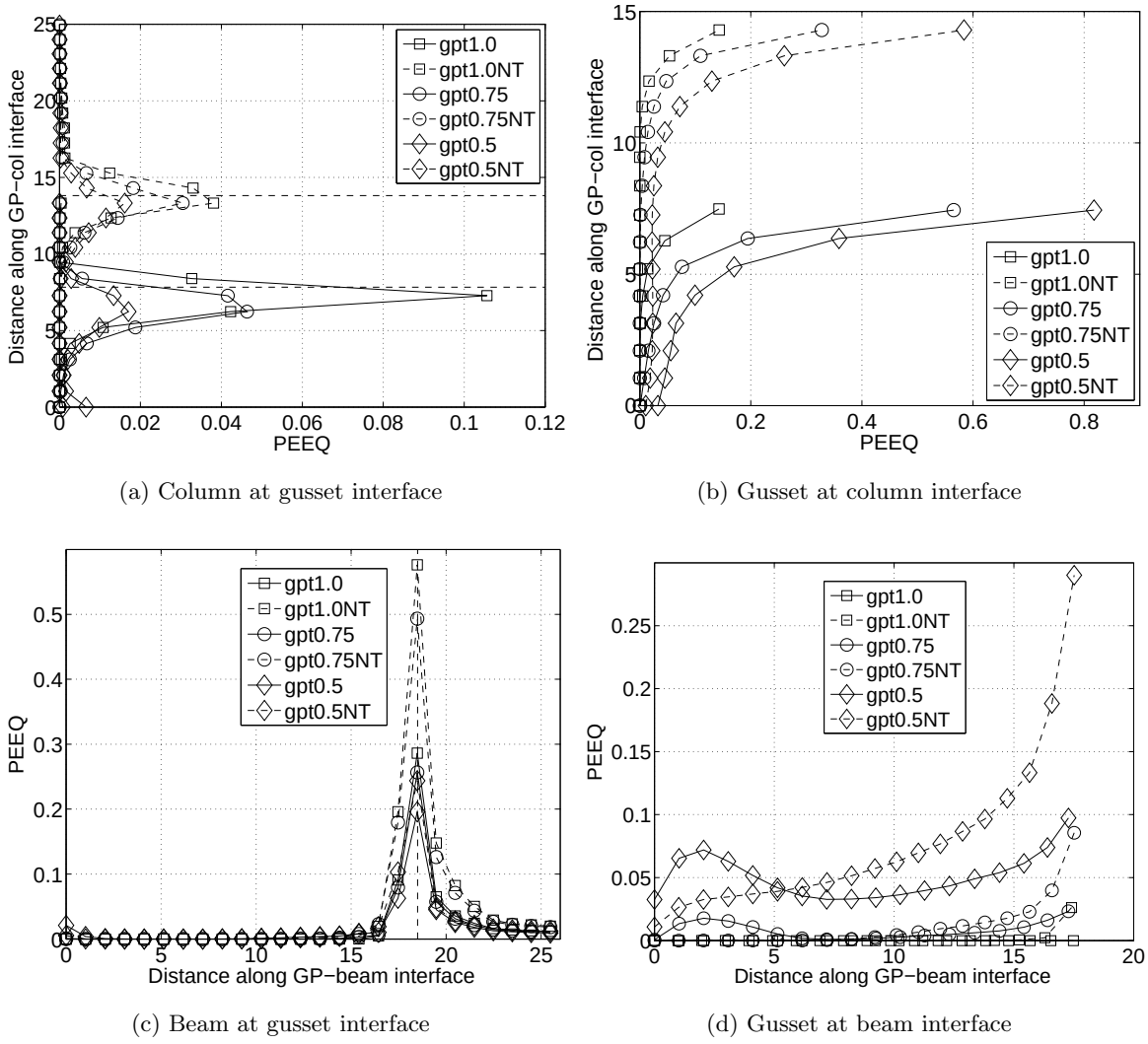

(a) Column at gusset interface

(b) Gusset at column interface

(c) Beam at gusset interface

(d) Gusset at beam interface

Figure 8.20: PEEQ comparison at column B-1 third floor joint at -2% RDR (Parameter - gusset plate taper)

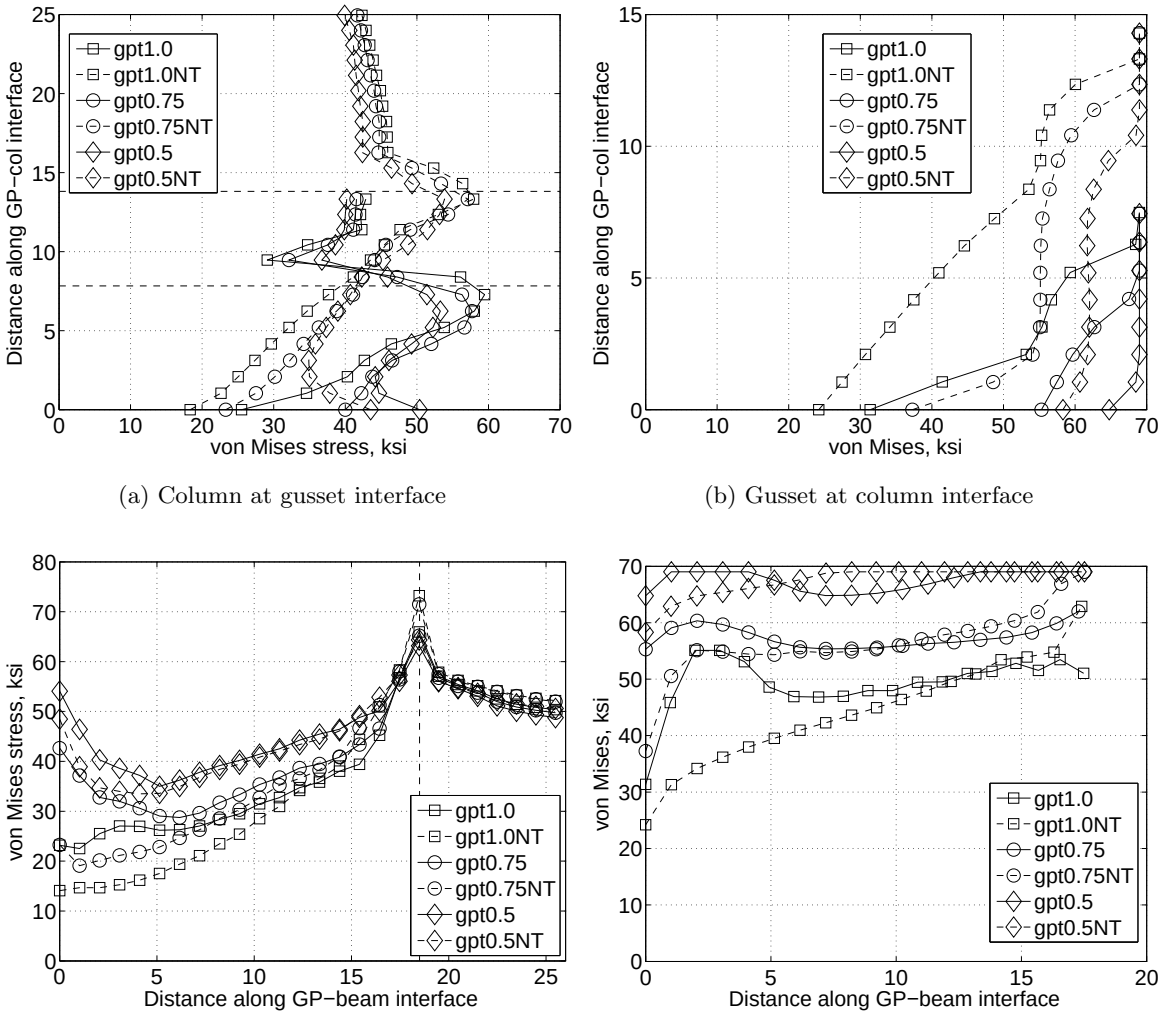

(a) Column at gusset interface

(b) Gusset at column interface

(c) Beam at gusset interface

(d) Gusset at beam interface

Figure 8.21: Von Mises stress comparison at column B-1 third floor joint at -2% RDR (Parameter - gusset plate taper)

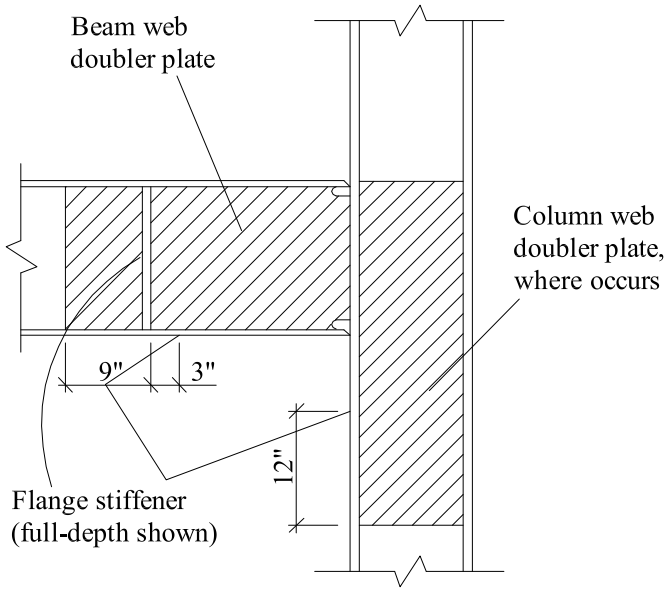

Figure 8.22: Location of beam web doubler and flange stiffeners at beam-column-gusset joint

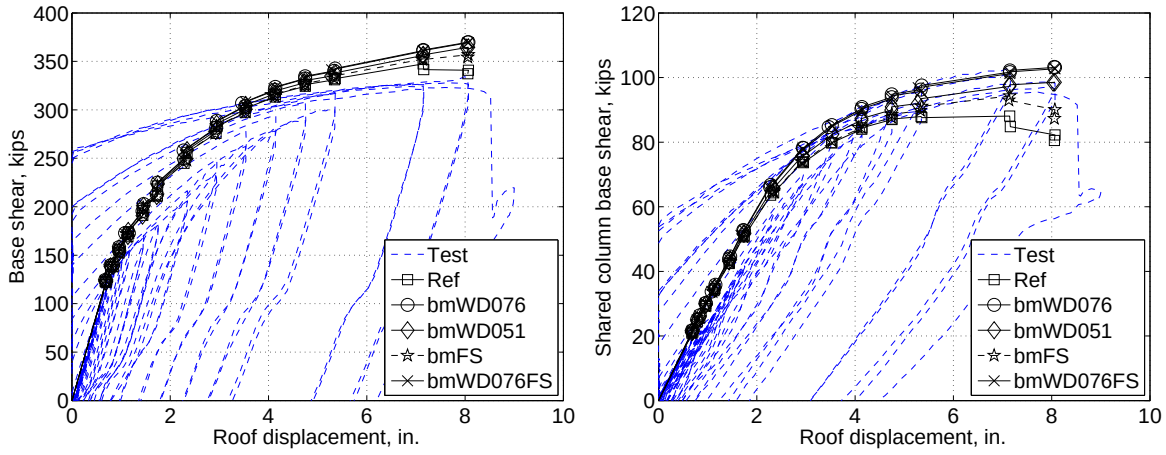

(a) Base shear

(b) Shared column base shear

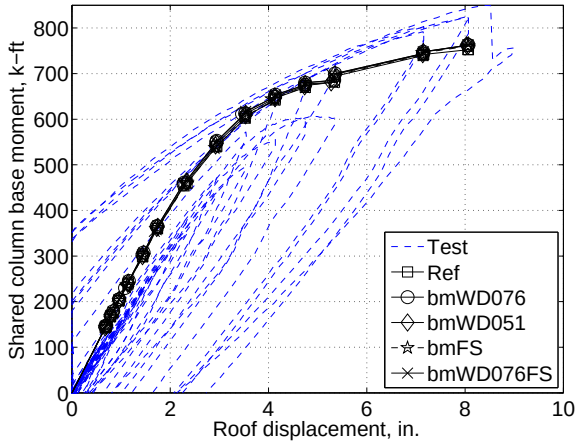

(c) Shared column base moment

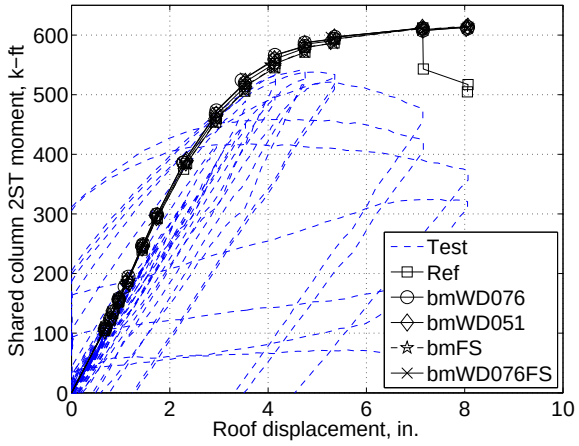

(d) Shared column 2ST moment

Figure 8.23: Global behavior comparison (Parameter - beam reinforcement)

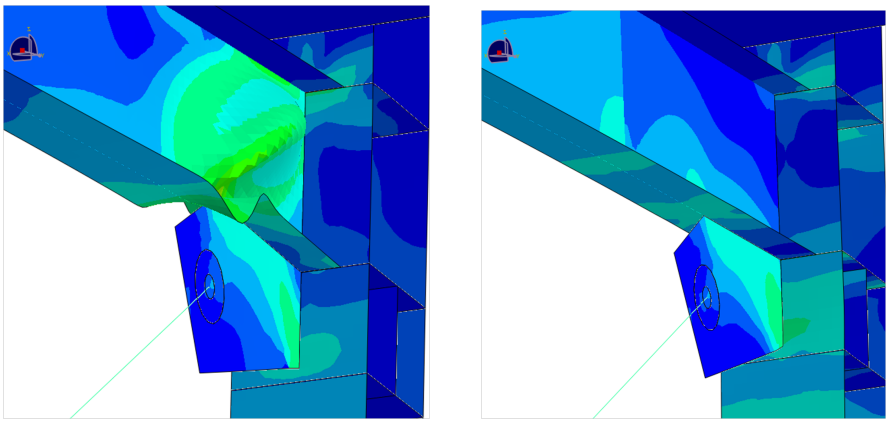

(a) Ref

(b) bmWD076

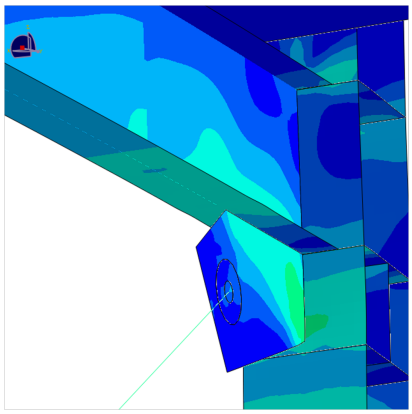

(c) bmWD051

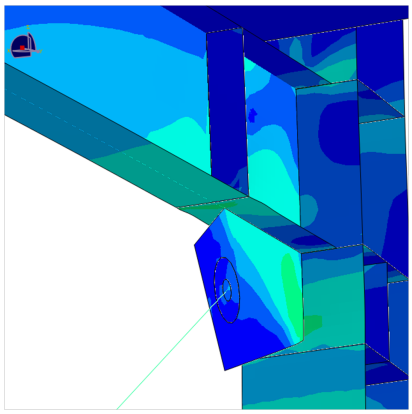

(d) bmFS

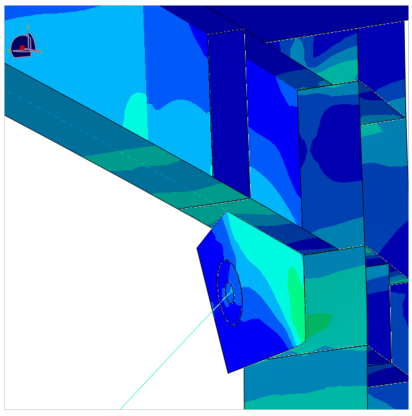

(e) bmWD076FS

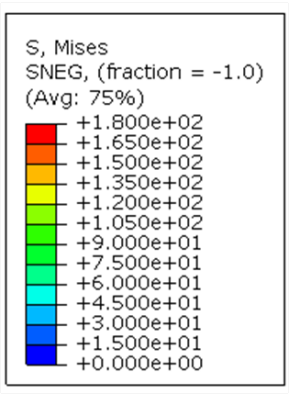

(f) Legend

Figure 8.24: Stress contours and beam deformation at third floor joint at column B-1 at 3.5% RDR (Parameter - beam reinforcement)

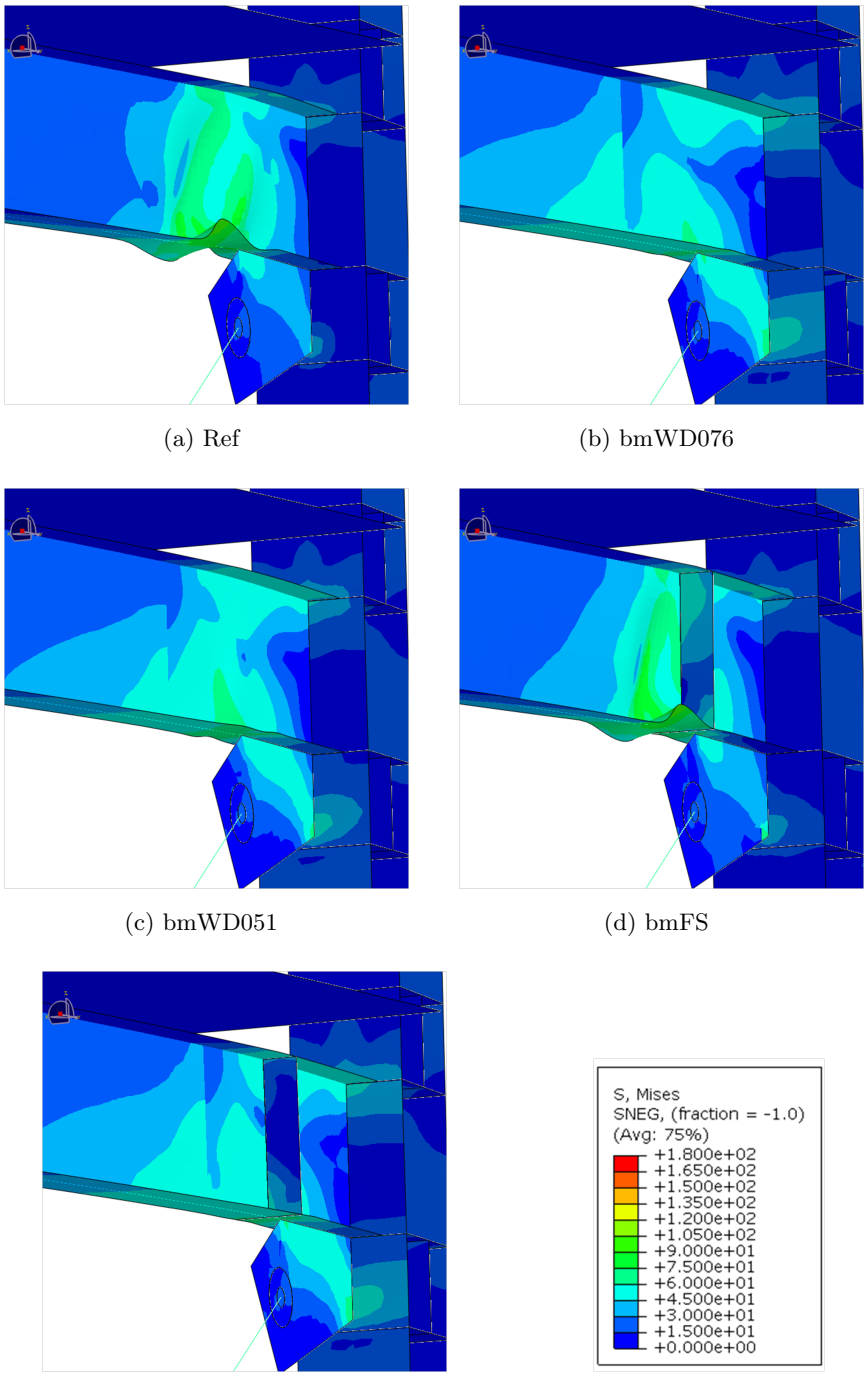

(a) Ref (b) bmWD076

(c) bmWD051 (d) bmFS

(e) bmWD076FS (f) Legend

Figure 8.25: Stress contours and beam deformation at second floor joint at column B-1 at 3.5% RDR (Parameter - beam reinforcement)

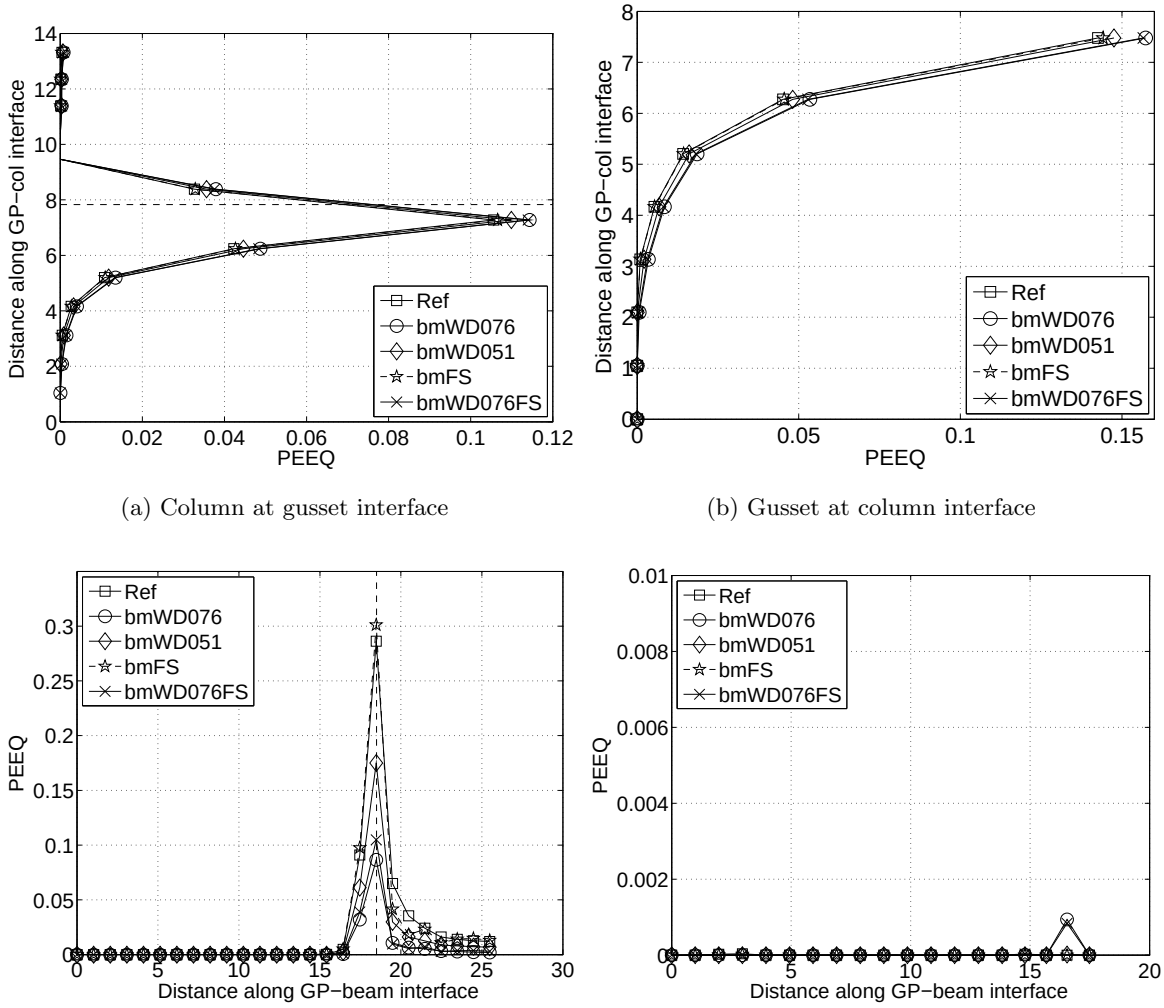

(a) Column at gusset interface

(b) Gusset at column interface

(c) Beam at gusset interface

(d) Gusset at beam interface

Figure 8.26: PEEQ comparison at column B-1 third floor joint at -2% RDR (Parameter - beam reinforcement)

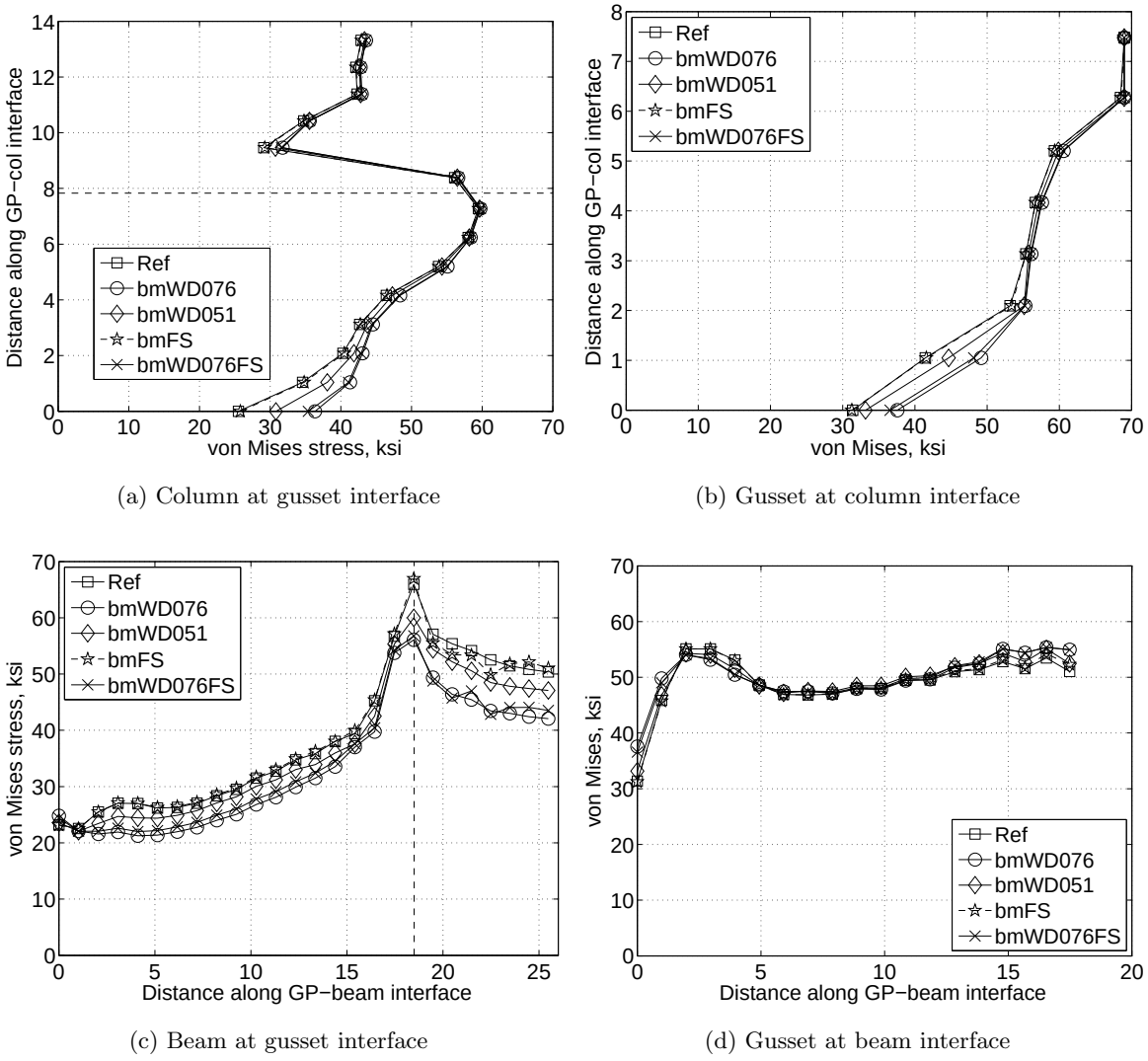

(a) Column at gusset interface

(b) Gusset at column interface

(c) Beam at gusset interface

(d) Gusset at beam interface

Figure 8.27: Von Mises stress comparison at column B-1 third floor joint at -2% RDR (Parameter - beam reinforcement)

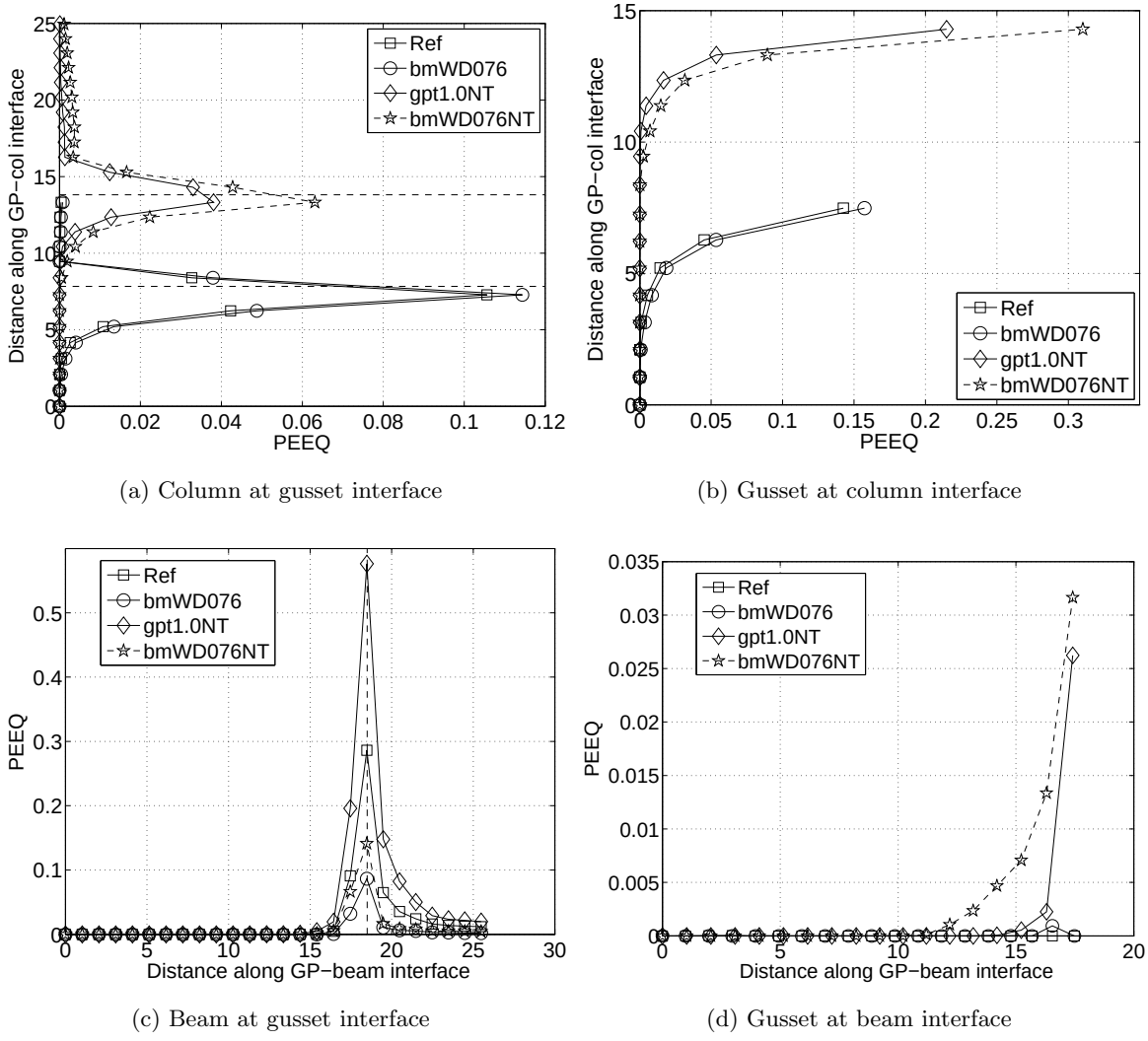

(a) Column at gusset interface

(b) Gusset at column interface

(c) Beam at gusset interface

(d) Gusset at beam interface

Figure 8.28: PEEQ comparison at column B-1 third floor joint at -2% RDR (Parameter - beam reinforcement)

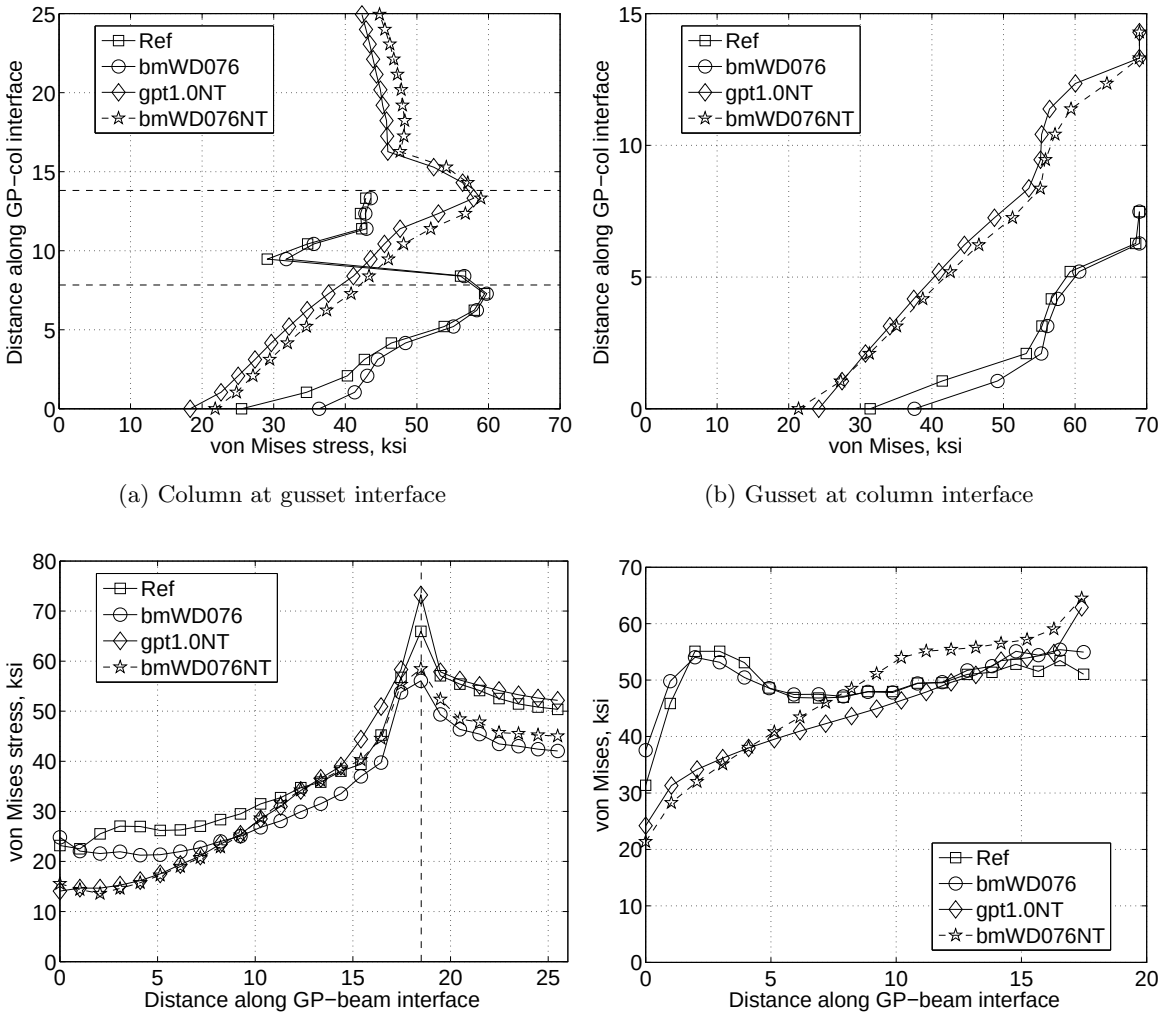

(a) Column at gusset interface

(b) Gusset at column interface

(c) Beam at gusset interface

(d) Gusset at beam interface

Figure 8.29: Von Mises stress comparison at column B-1 third floor joint at -2% RDR (Parameter - beam reinforcement)

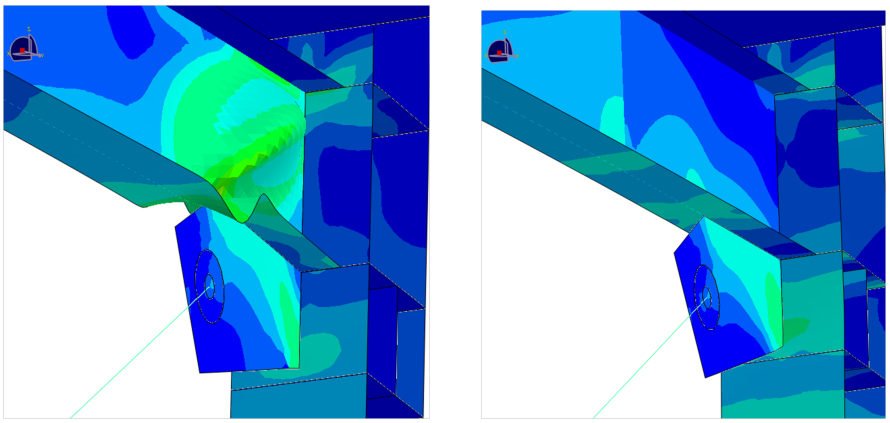

(a) Ref

(b) bmWD076

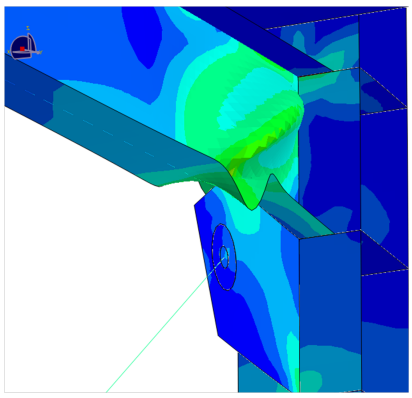

(c) gpt1.0NT

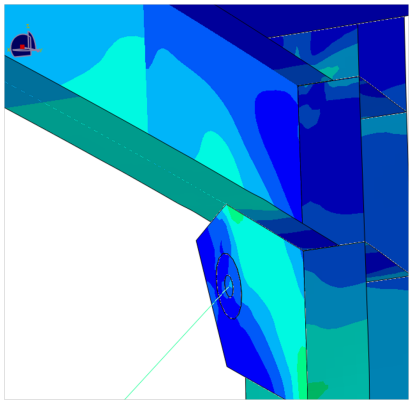

(d) bmWD076NT

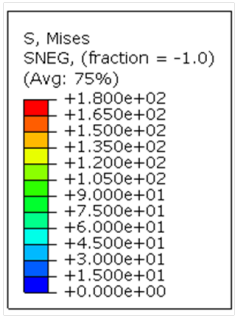

(e) Legend

Figure 8.30: Stress contours and beam deformation at third floor joint at column B-1 at 3.5% RDR (Parameter - beam reinforcement)

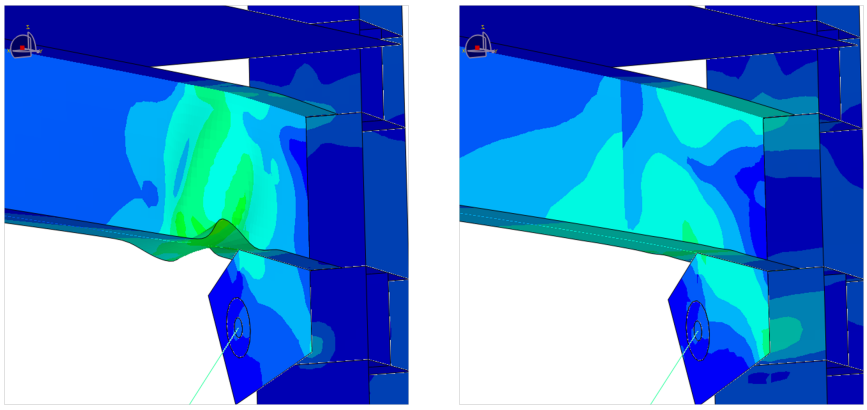

(a) Ref

(b) bmWD076

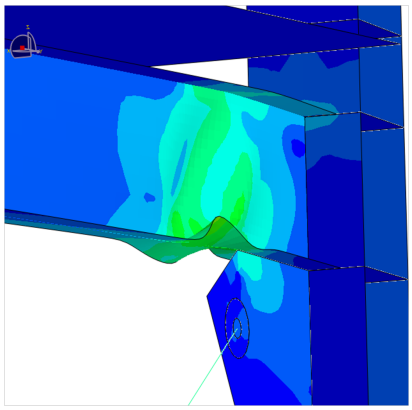

(c) gpt1.0NT

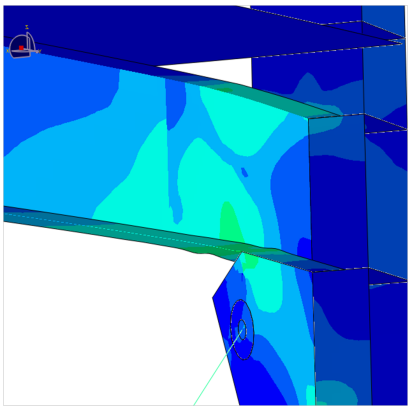

(d) bmWD076NT

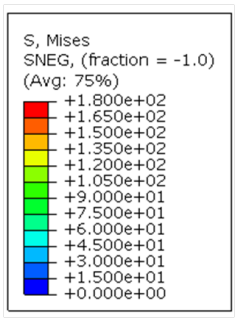

(e) Legend

Figure 8.31: Stress contours and beam deformation at second floor joint at column B-1 at 3.5% RDR (Parameter - beam reinforcement)

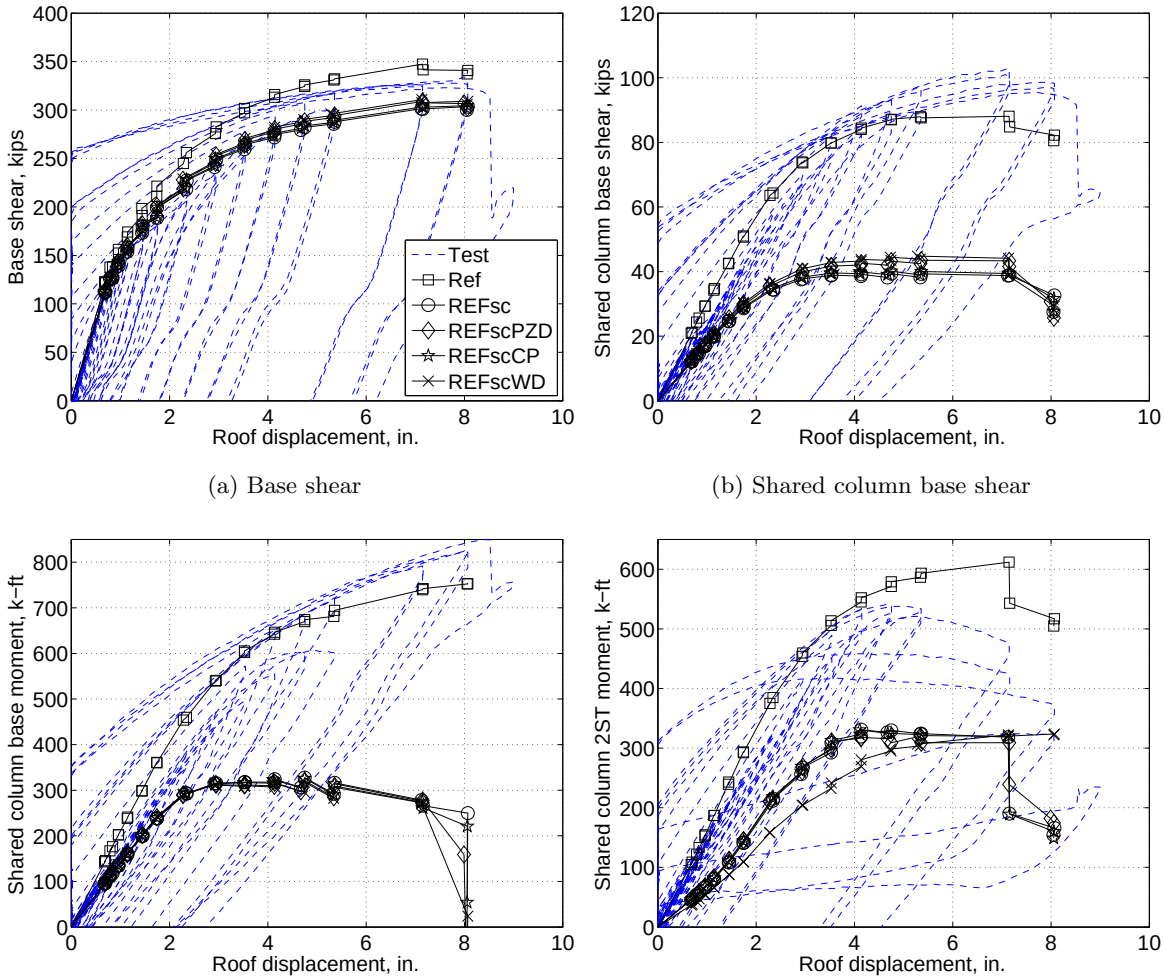

(a) Base shear

(b) Shared column base shear

(c) Shared column base moment

(d) Shared column 2ST moment

Figure 8.32: Global behavior comparison (Parameter - Column size and reinforcement)

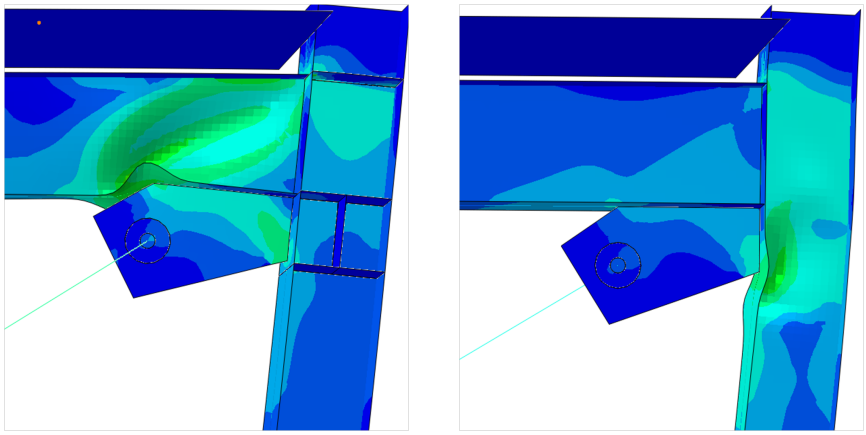

(a) Ref

(b) REFsc

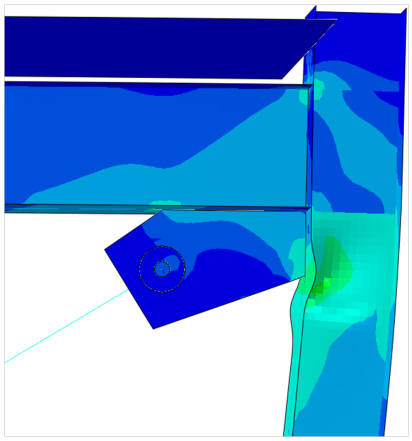

(c) REFscPZD

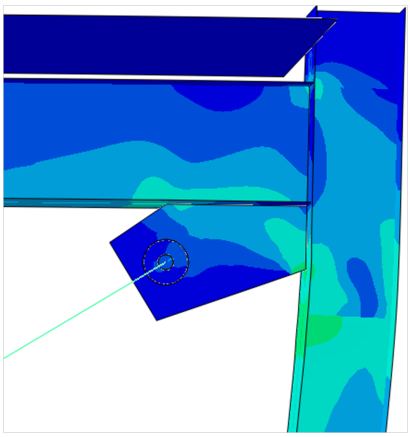

(d) REFscWD

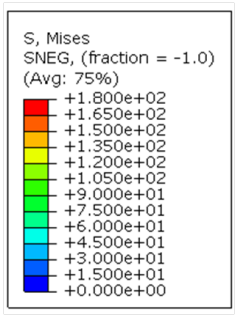

(e) Legend

Figure 8.33: Stress contours and beam deformation at third floor joint at column B-1 at 3.5% RDR (Parameter - Column size and reinforcement)

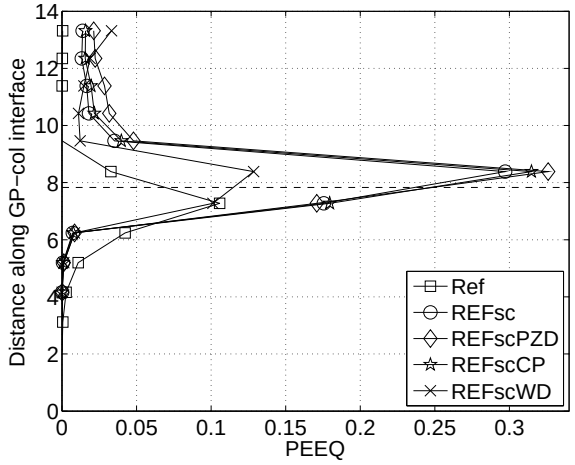

(a) Column at gusset interface 3rd floor column B-1

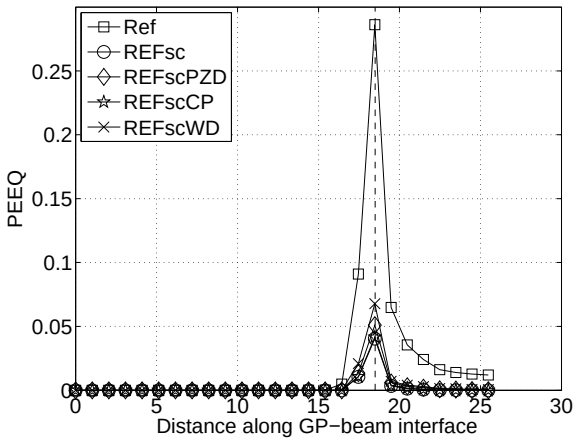

(b) Beam at gusset interface 3rd floor column B-1

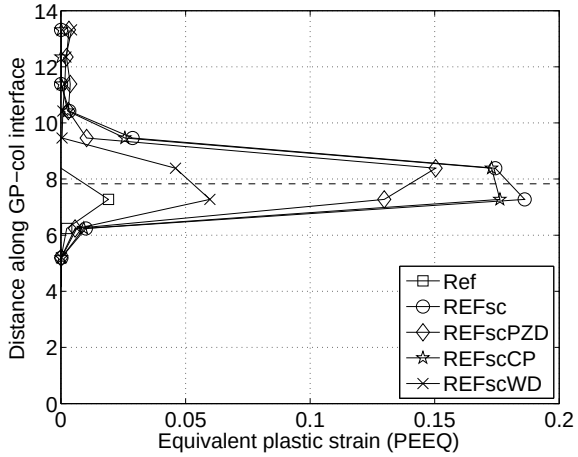

(c) Column at gusset interface 2nd floor column B-1

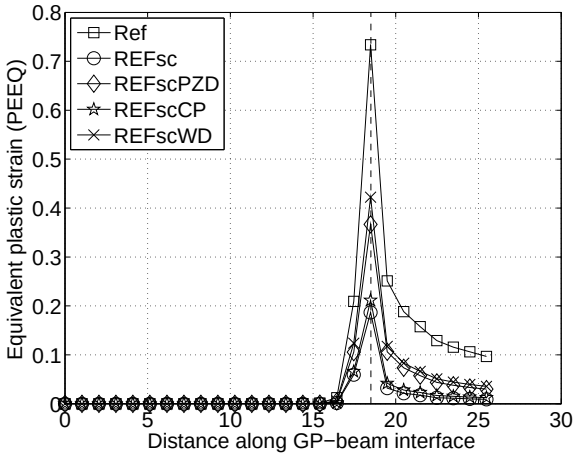

(d) Beam at gusset interface 2nd floor column B-1

Figure 8.34: PEEQ comparison at column B-1 joints at -2% RDR (Parameter - Column size and reinforcement)

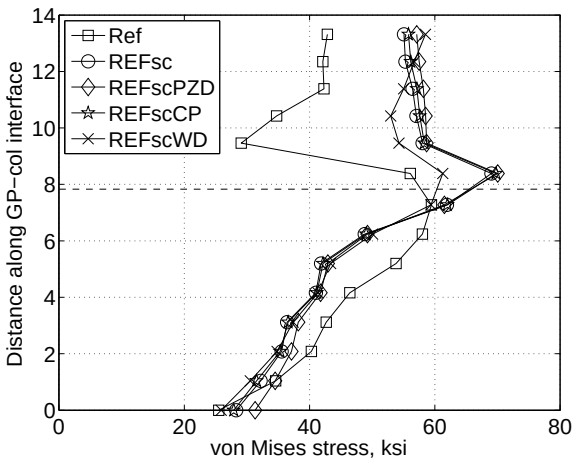

(a) Column at gusset interface 3rd floor column B-1

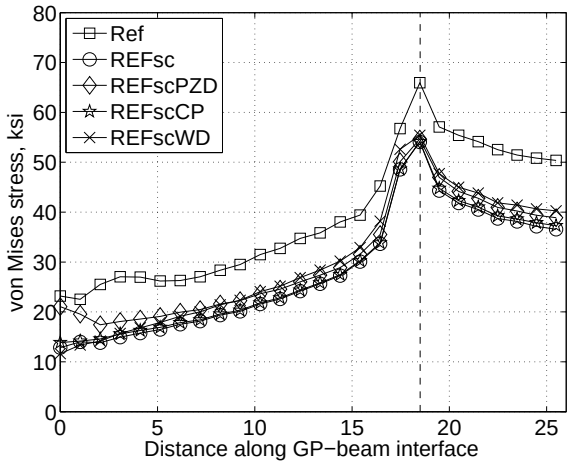

(b) Beam at gusset interface 3rd floor column B-1

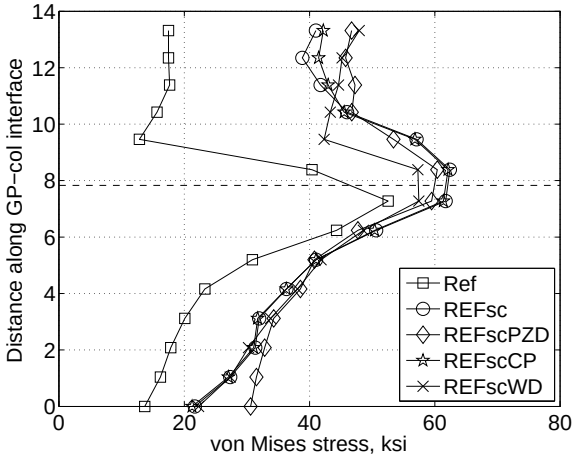

(c) Column at gusset interface 2nd floor column B-1

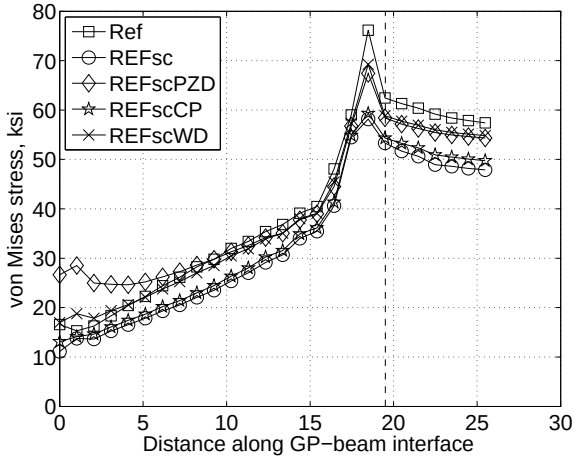

(d) Beam at gusset interface 2nd floor column B-1

Figure 8.35: Von Mises stress comparison at column B-1 joint at -2% RDR (Parameter - Column size and reinforcement)

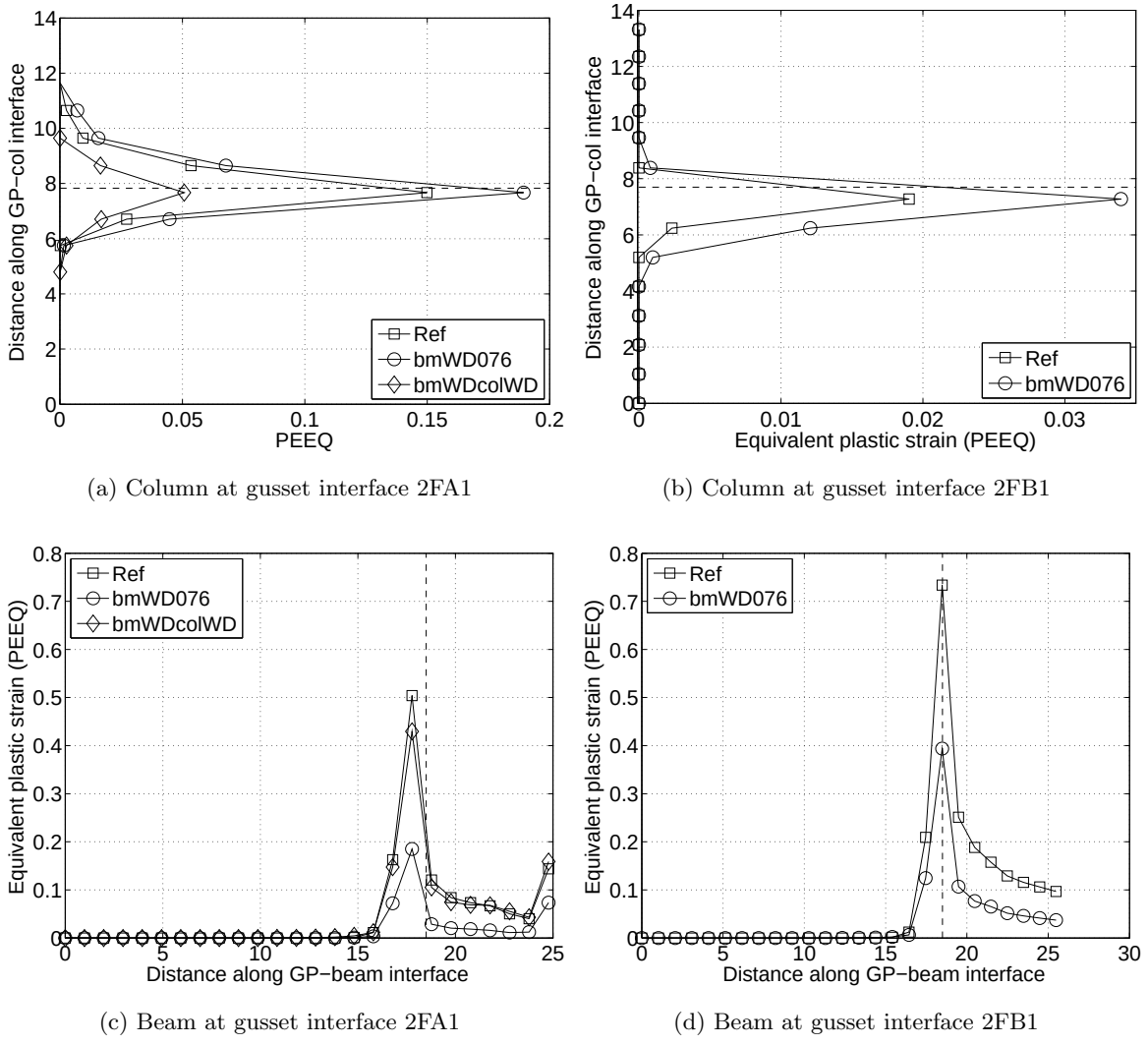

(a) Column at gusset interface 2FA1

(b) Column at gusset interface 2FB1

(c) Beam at gusset interface 2FA1

(d) Beam at gusset interface 2FB1

Figure 8.36: PEEQ comparison at columns A-1 and B-1 second floor joint at -2% RDR (Parameter - beam and column reinforcement)

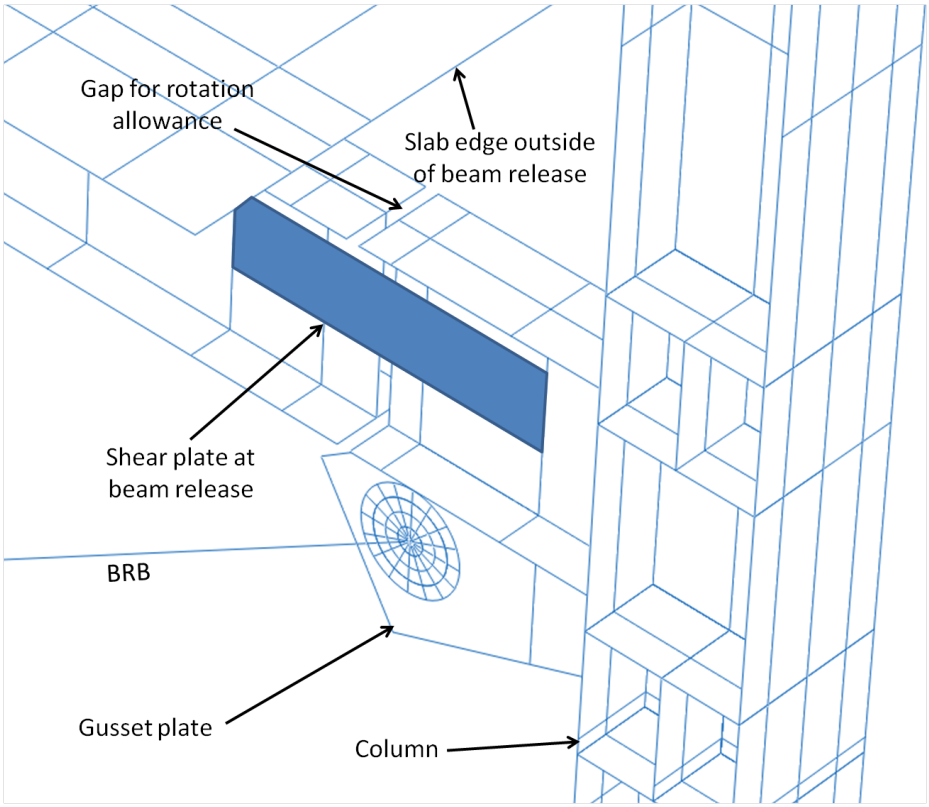

Figure 8.37: Beam fixity release detail at second floor beam outside of gusset plate

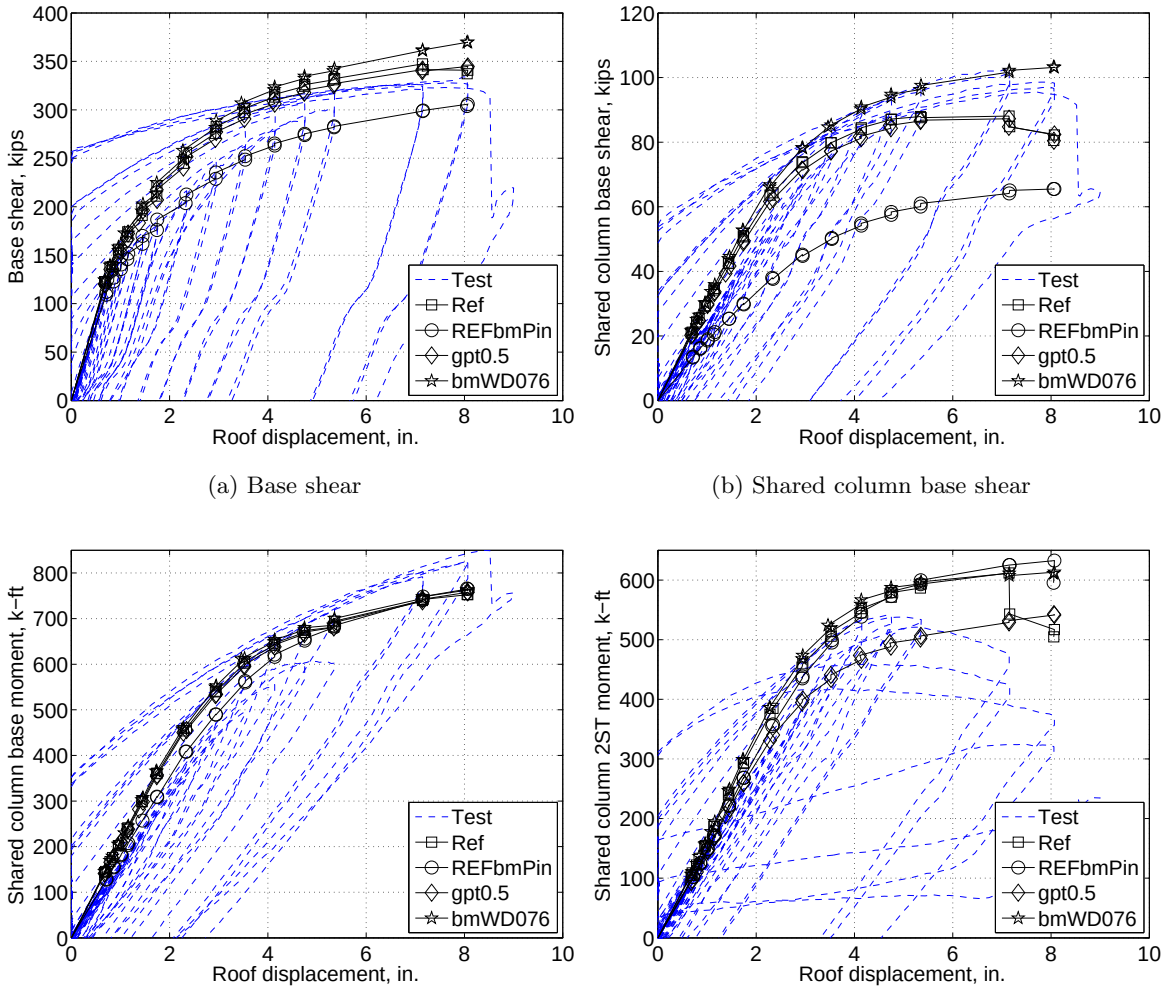

(a) Base shear

(b) Shared column base shear

(c) Shared column base moment

(d) Shared column 2ST moment

Figure 8.38: Global behavior comparison (Parameter - Beam fixity)

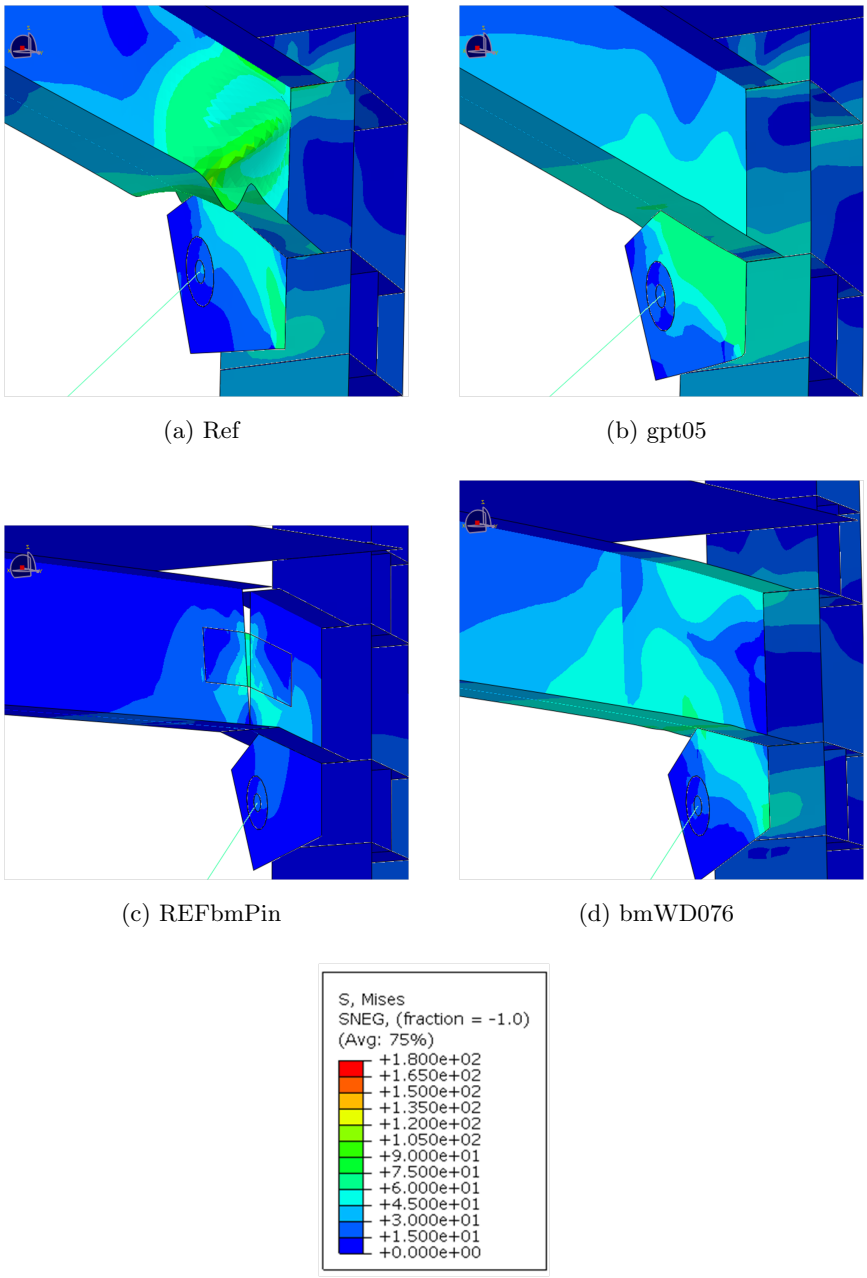

(a) Ref

(b) gpt05

(c) REFbmPin

(d) bmWD076

(e) Legend

Figure 8.39: Stress contours and beam deformation at second floor joint at column B-1 at 3.5% RDR (Parameter - Beam fixity)

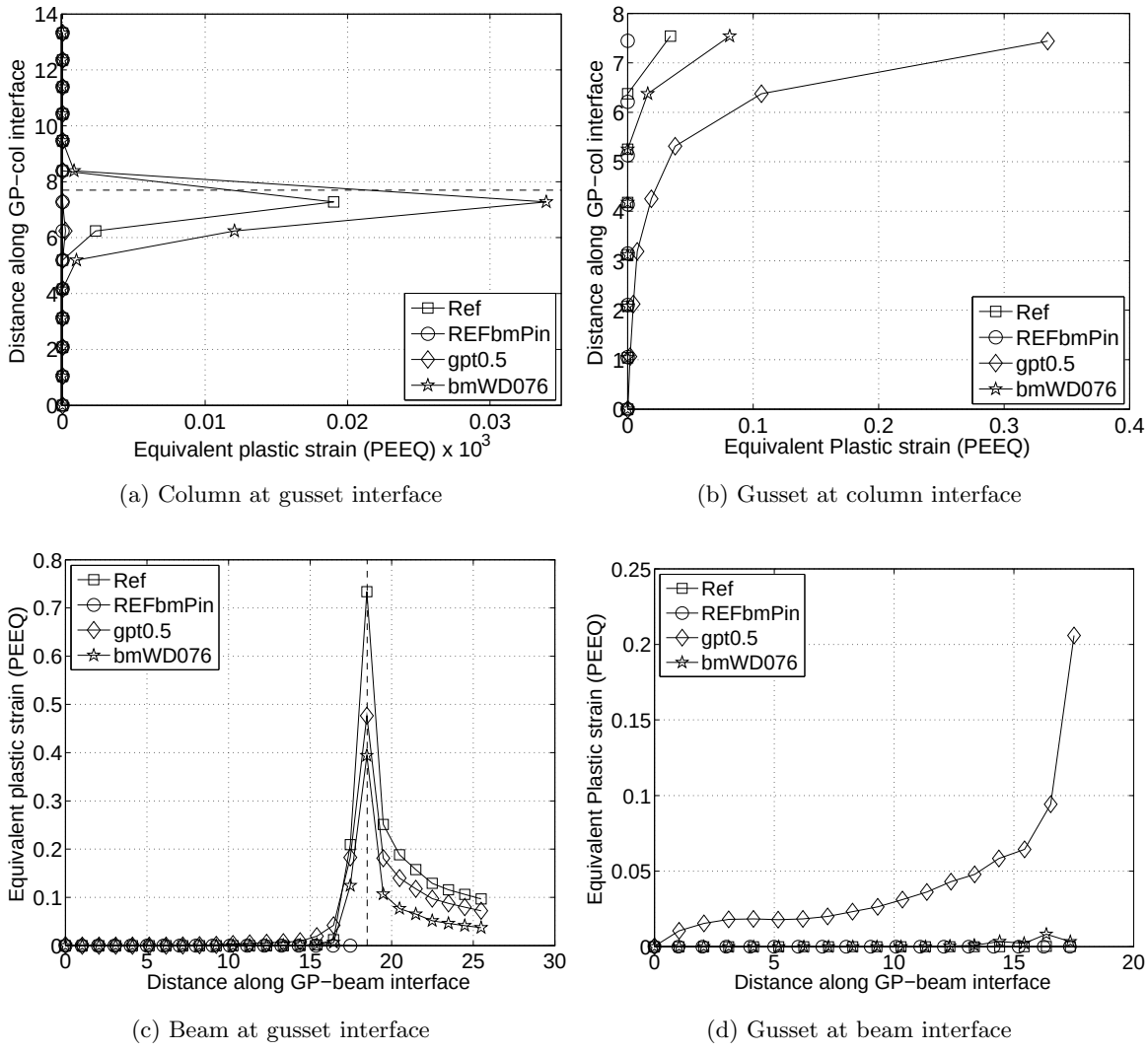

(a) Column at gusset interface

(b) Gusset at column interface

(c) Beam at gusset interface

(d) Gusset at beam interface

Figure 8.40: PEEQ comparison at column B-1 second floor joint at -2% RDR (Parameter - Beam fixity)

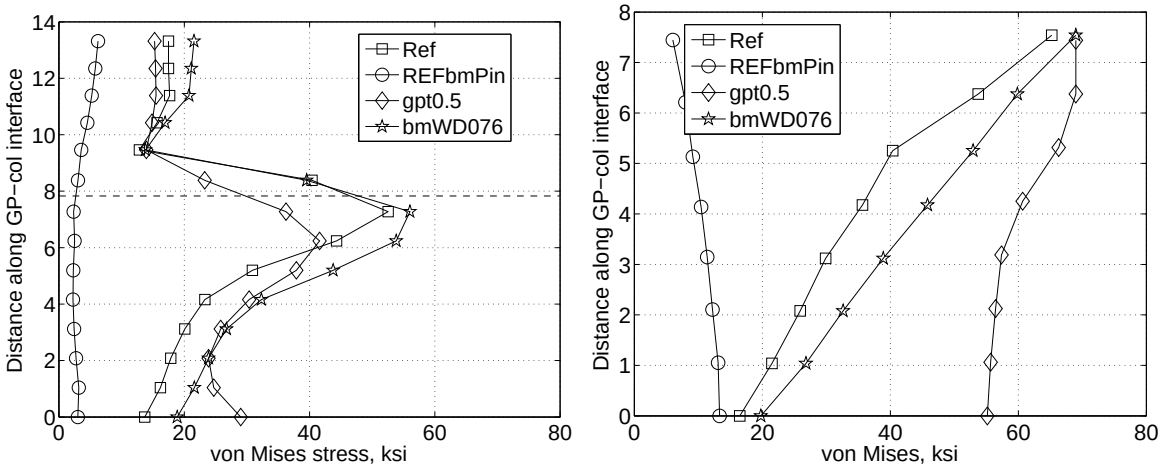

(a) Column at gusset interface

(b) Gusset at column interface

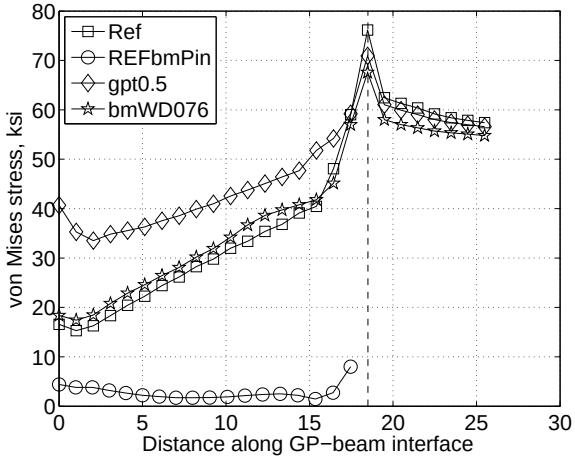

(c) Beam at gusset interface

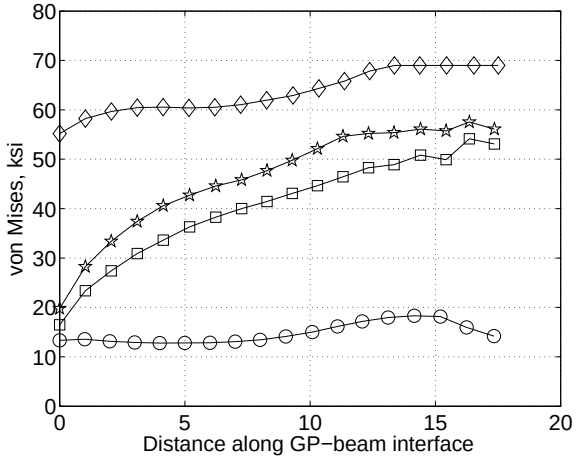

(d) Gusset at beam interface

Figure 8.41: Von Mises stress comparison at column B-1 second floor joint at -2% RDR (Parameter - Beam fixity)

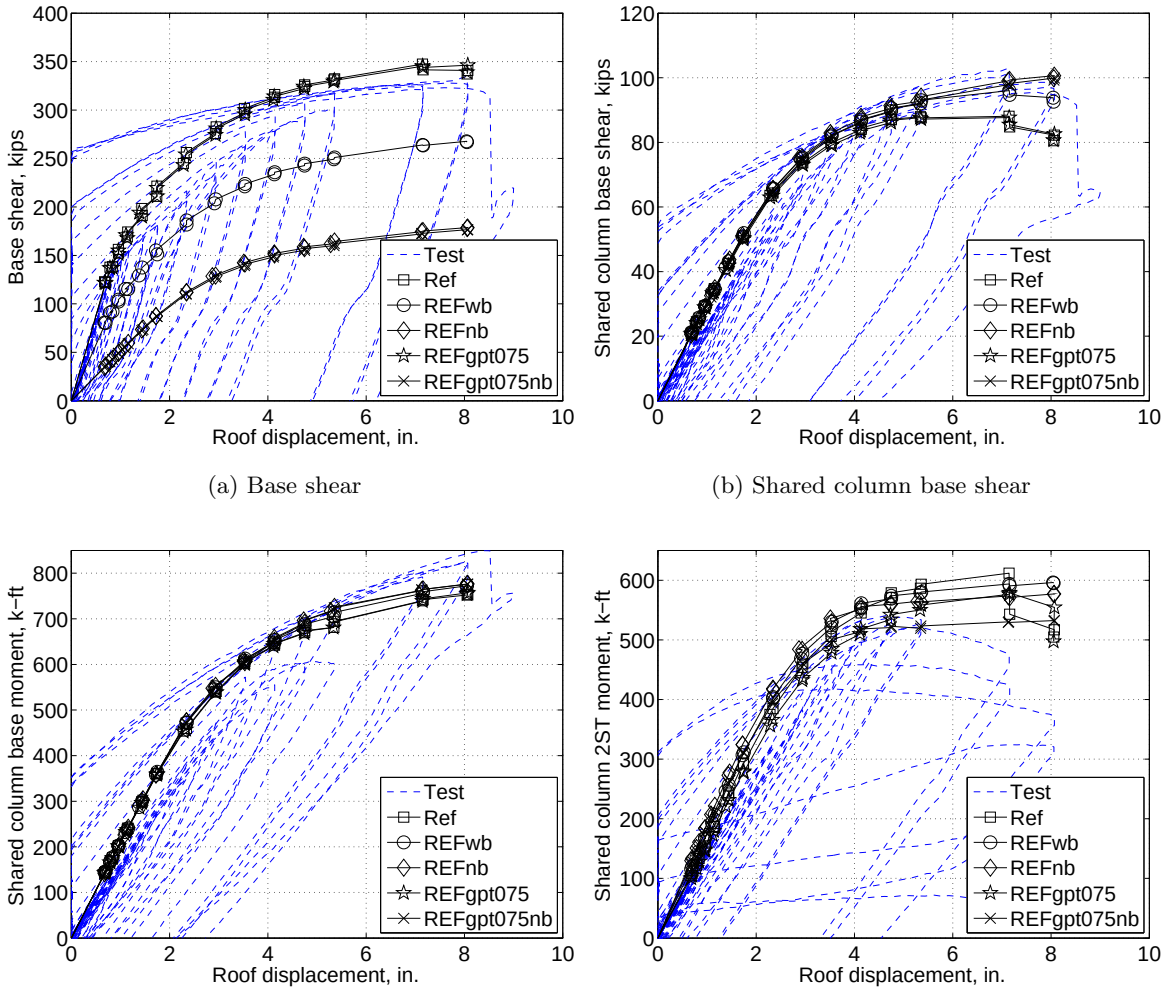

(a) Base shear

(b) Shared column base shear

(c) Shared column base moment

(d) Shared column 2ST moment

Figure 8.42: Global behavior comparison (Parameter - BRB strength)

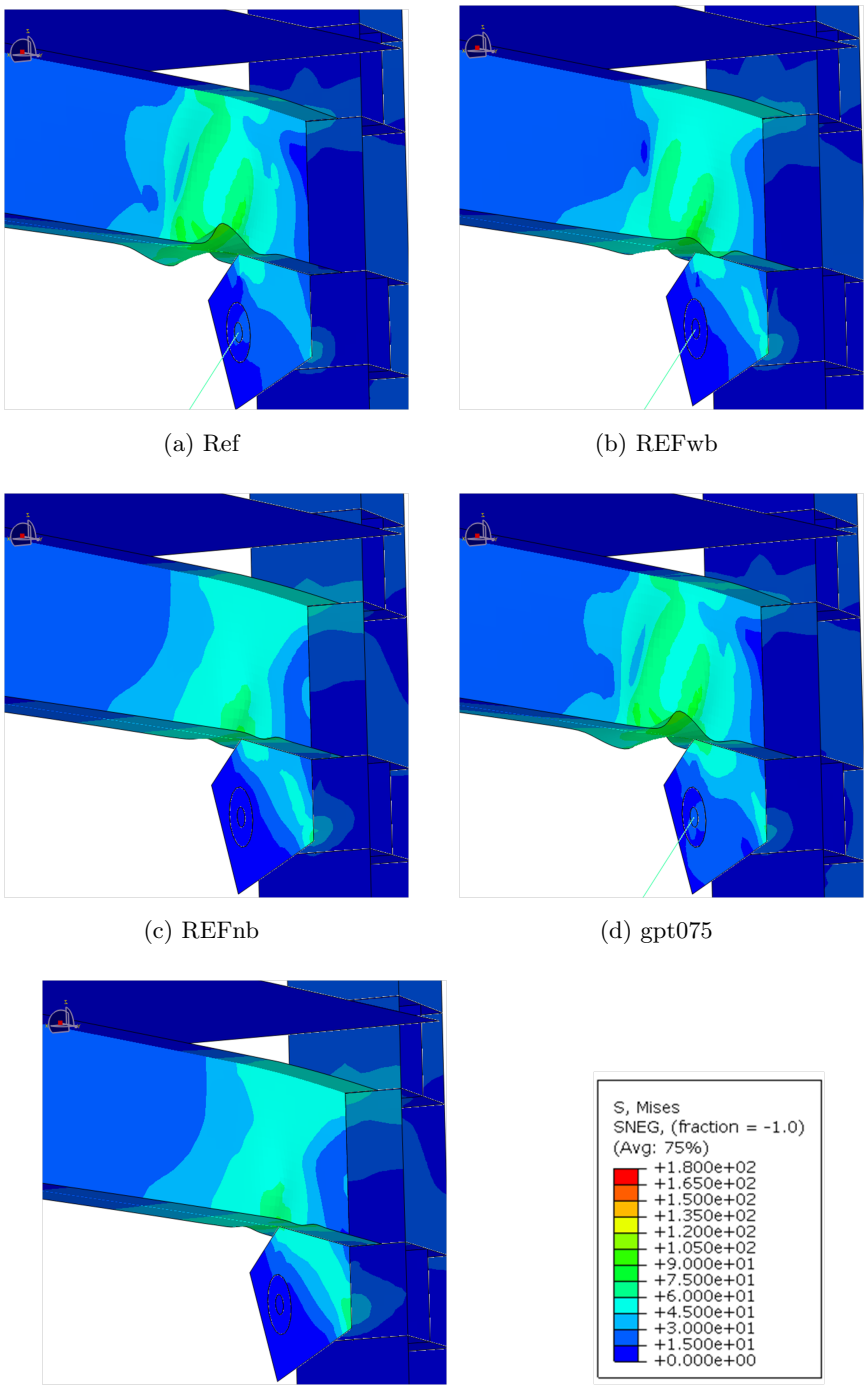

(a) Ref (b) REFwb

(c) REFnb (d) gpt075

(e) gpt075nb (f) Legend

Figure 8.43: Stress contours and beam deformation at second floor joint at column B-1 at 3.5% RDR (Parameter - BRB strength)

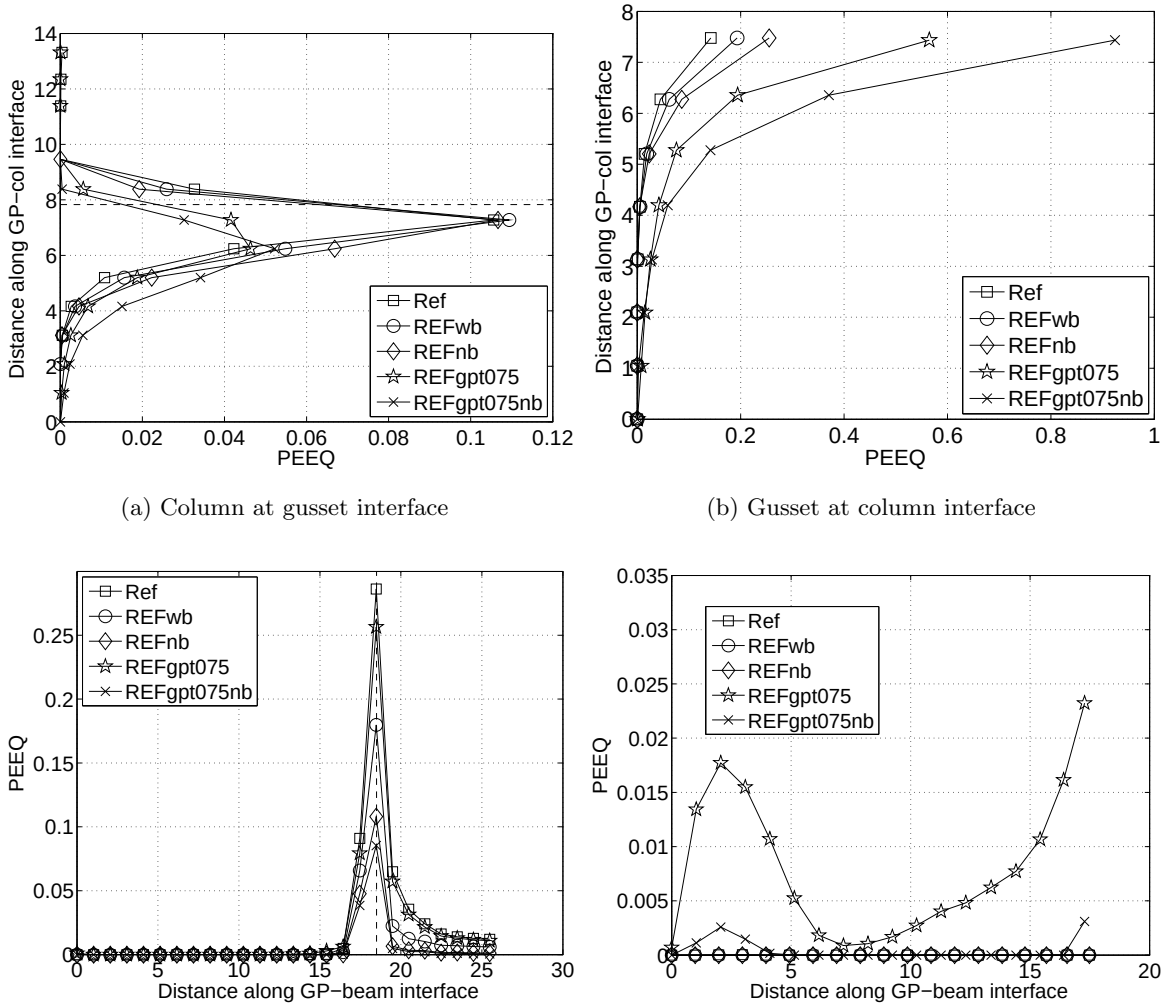

(a) Column at gusset interface

(b) Gusset at column interface

(c) Beam at gusset interface

(d) Gusset at beam interface

Figure 8.44: PEEQ comparison at column B-1 third floor joint at -2% RDR (Parameter - BRB strength)

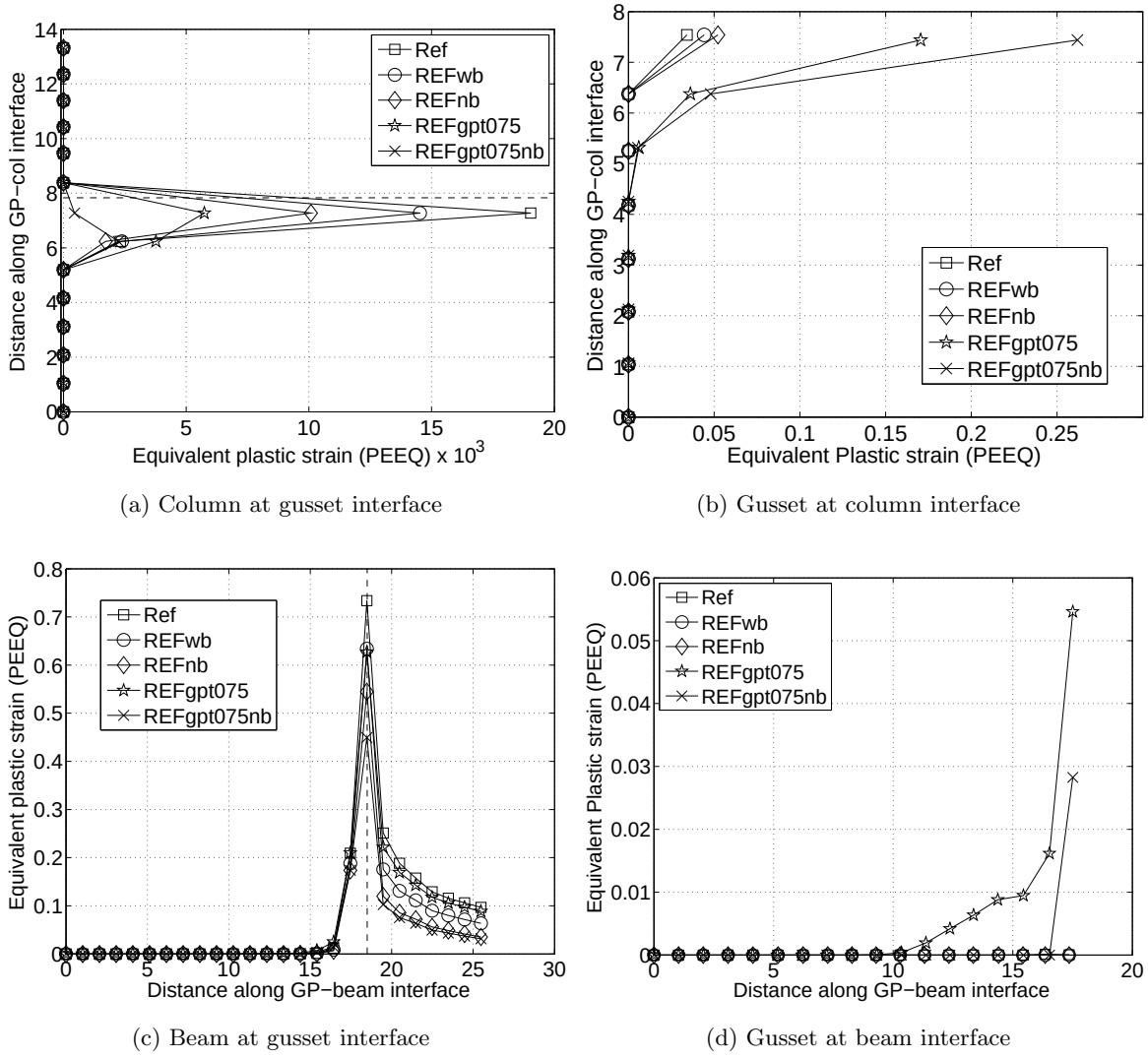

(a) Column at gusset interface

(b) Gusset at column interface

(c) Beam at gusset interface

(d) Gusset at beam interface

Figure 8.45: PEEQ comparison at column B-1 second floor joint at -2% RDR (Parameter - BRB strength)

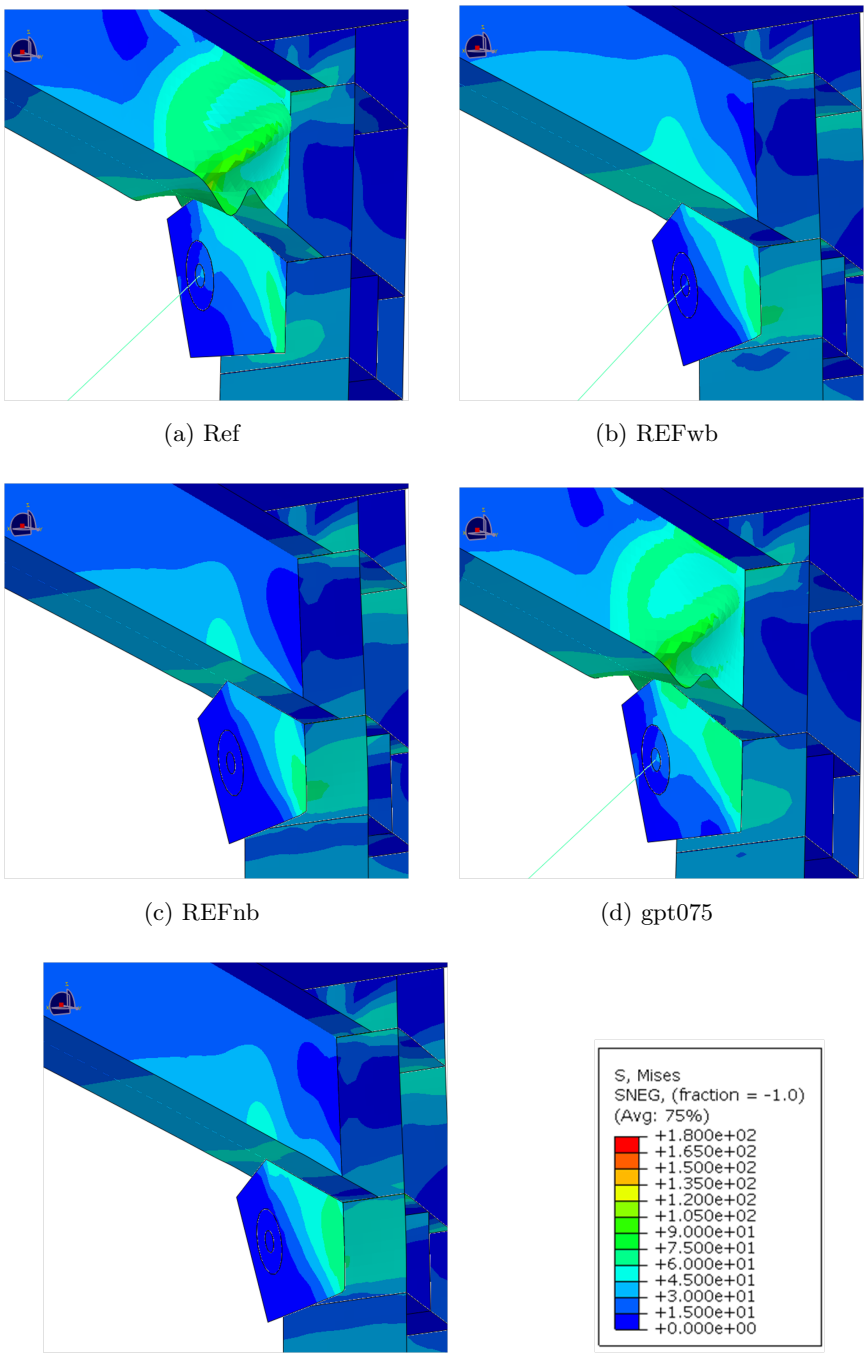

(a) Ref (b) REFwb

(c) REFnb (d) gpt075

(e) gpt075nb (f) Legend

Figure 8.46: Stress contours and beam deformation at third floor joint at column B-1 at 3.5% RDR (Parameter - BRB strength)

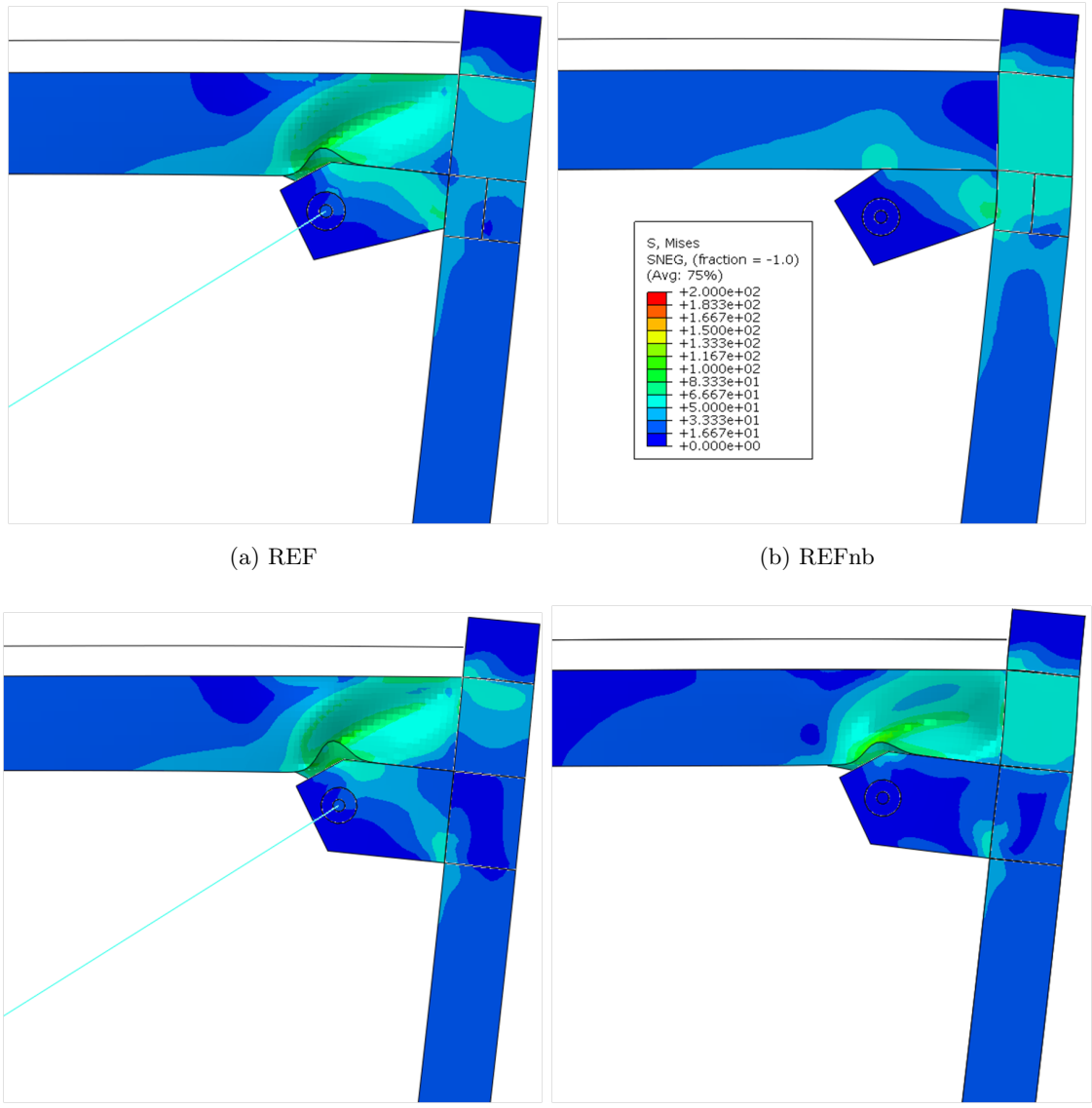

(a) REF

(b) REFnb

(c) REFnt

(d) REFntNB

Figure 8.47: Stress contours and beam deformation at third floor joint at column B-1 at 3.5% RDR (Parameter - BRB strength)

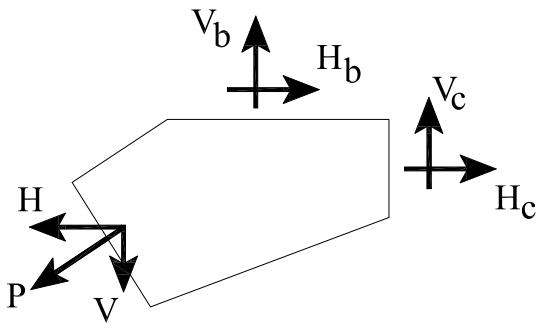

Figure 8.48: Gusset plate interface force resultant nomenclature

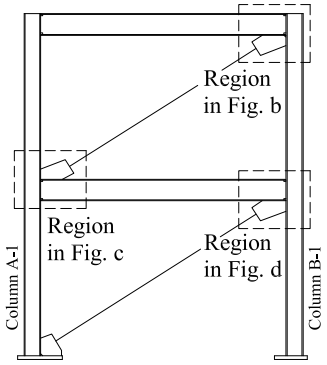

(a) Connection location of figures

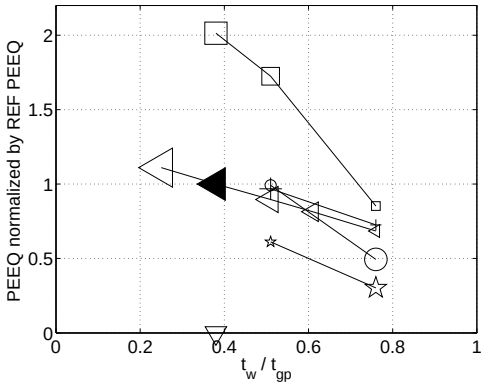

(b) 3rd floor column B-1

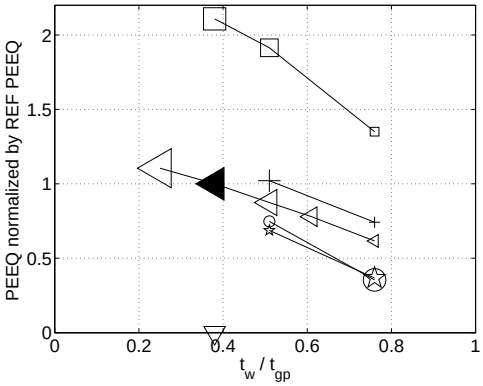

(c) 2nd floor column A-1

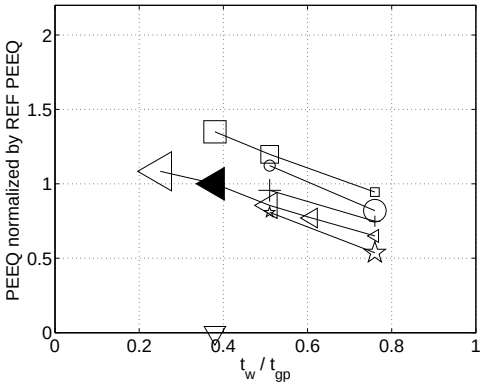

(d) 2nd floor column B-1

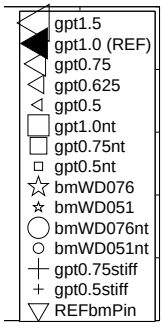

(e) Legend

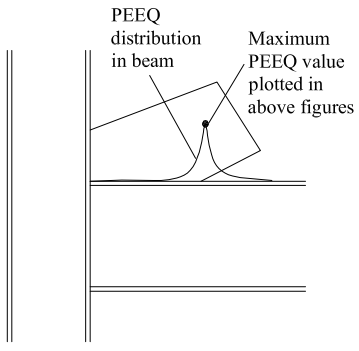

(f) Description of PEEQ demand in beam

Figure 8.49: Normalized, maximum PEEQ demands in the beam at the edge of the gusset plate at -2% RDR from FE simulations as a function of the ratio of the beam web thickness to gusset plate thickness.

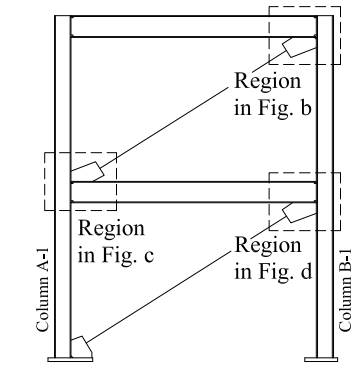

(a) Connection location of figures

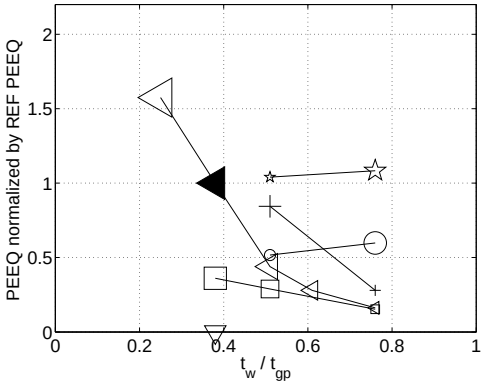

(b) 3rd floor column B-1

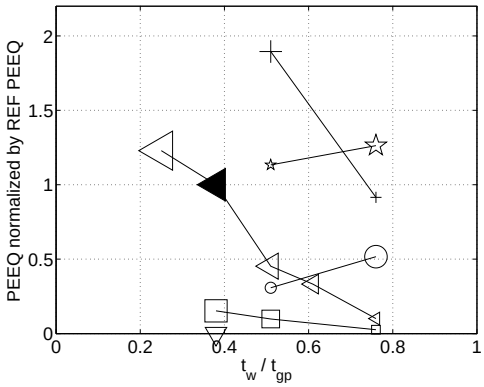

(c) 2nd floor column A-1

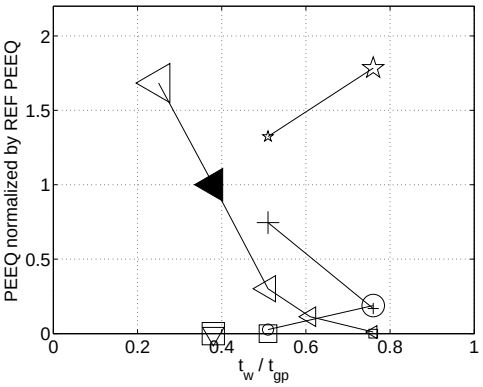

(d) 2nd floor column B-1

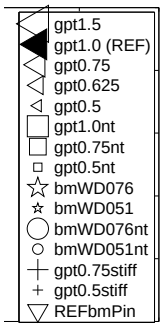

(e) Legend

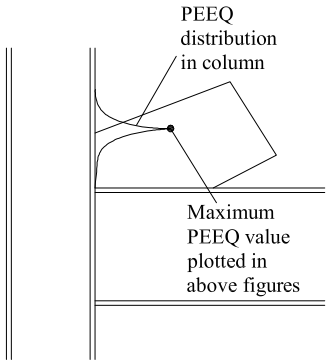

(f) Description of PEEQ demand in column

Figure 8.50: Normalized, maximum PEEQ demands in the column at the edge of the gusset plate at -2% RDR from FE simulations as a function of the ratio of the beam web thickness to gusset plate thickness.

Chapter 9
DESIGN RECOMMENDATIONS

9.1 Introduction

This chapter presents a design guide for assisting structural engineers in the design of connections used at the brace splice in a single-story, X-configured concentrically braced frame and also at the corner gusset plate connection region for BRBFs. The first section of this chapter will cover the two connection types for the single-story, X-configured SCBF. Effective length factors to be used in the design of the compression braces are also recommended. The second section of this chapter will cover design and detailing recommendations for the corner gusset plate connection region of BRBFs. These recommendations are based on the experiments and parametric study described in the previous chapters, and are designed to mitigate the damage that occurred in the connection region during the experiments.

9.2 SCBF Design Recommendations

9.2.1 Connection descriptions and behaviors

Single-story X-configured bracing systems (Fig. 9.1) require at least one brace to be spliced at the intersection of the opposing braces if the opposing braces are to be in the same plane. Two splice connections for the single-story, X-configured SCBFs are shown in Figs. 9.2a and b. These are denoted as the "sandwich plate" connection (Fig. 9.2a) and the "through-plate" connection (Fig. 9.2b). The layout and behavior of each connection will first be discussed followed by a comparison of the the two. Design recommendations will follow this discussion.

Sandwich plate splice connection

The sandwich plate connection shown in Fig. 9.2a provides full continuity at the splice between each half of the discontinuous braces. This is accomplished by attaching a plate to

each side of the outer faces of the HSS and welding these plates at each tube corner with flare bevel groove welds. As shown in the figure, a gap between the end of the discontinuous brace and the side of the continuous brace, B_g, equal to at least four times the thickness of the plate is recommended for erection tolerances. If a larger gap is desired, it must be ensured that the sandwich plates satisfy the buckling limit state (see Eq. 9.12). Additionally, the sandwich plate must be wide enough to ensure that the weld can be made. If reasonably thick plates are used in the design, this will be easily satisfied.

The tension braces act as an OOP support for the compression braces at the splice location and therefore, it is recommended that the sandwich plates be fillet-welded to the continuous brace also as shown in Fig. 9.2a. These welds can also aid in erection as one sandwich plate can be shop-welded to the continuous brace with an erection bolt attached to this sandwich plate that can receive the spliced brace with a hole in it at the correct location (Fig. 9.2a). The second sandwich plate will have a hole in it and then be bolted to the setup using the erection bolt on the sandwich plate shop-welded to the continuous brace. Welding may then take place with the braces in their design configuration.

The sandwich plate connection results in similar behavior between each opposing brace. That is, both buckle in a mode-2 type pattern as shown in Fig. 9.3a for the continuous brace and Fig. 9.3b for the spliced brace. Additionally, the sandwich plate caused a relatively large amount of twisting in the tension brace and its gusset plates which appeared to cause earlier gusset tearing along the interface with the beams and columns (see Section 2.5.1).

Through-plate splice connection

The through-plate connection shown in Fig. 9.2b provides very little continuity at the splice between each half of the discontinuous braces. For this connection, a slot is cut through the continuous brace at mid-face for the through-plate to slide through. The plate is then welded on each side of the continuous brace for a length matching the width of the plate using a fillet weld. A size of 1/16" less than the tube wall thickness is adequate. This weld is not designed to transfer brace axial load but is necessary to ensure that the tension brace acts as an OOP support for the compression brace. The through-plate is ideally attached

to the continuous brace in the shop and erection bolts may be attached to receive the discontinuous braces (Fig. 9.2b). The discontinuous braces are slotted and fillet-welded on all four sides. The spliced braces should be offset from the face of the continuous braces to ensure no binding occurs when the spliced braces deform OOP and potentially bear on the wall of the continuous brace. An offset, B_g, of four times the thickness of the through-plate is recommended.

The through-plate connection results in different behaviors between each opposing brace. The continuous brace buckles in an S-shape as shown in Fig. 9.4a but only one-half of the spliced brace buckles as shown in Fig. 9.4b.

Connection comparison

There are advantages and disadvantages to each connection type although the drift range at which fracture of the brace occurred was the same for each one in Powell's tests (3.83%). The disadvantage of the through-plate connection is that brace OOP deformation due to buckling is concentrated in only one half of the spliced brace while it is distributed between both halves of the brace when the sandwich connection is used. This concentration of deformation should lead to a shorter fracture life but this was not observed experimentally [Tremblay et al., 2003]. A disadvantage of the sandwich plate detail is that it was shown to cause more twisting of the brace in tension and its gusset plate which appeared to cause earlier gusset tearing along the interface, although the final length of tearing was comparable between the two details (see Section 2.5.1). The weld length required for the sandwich plate will be slightly longer due to the use of flare bevel groove welds as opposed to fillet welds used for the through-plate but otherwise the ease of erection is the same. There appears to be no clear advantage between the two details and therefore both will be discussed.

9.2.2 Connection Design

The design of the splice connection presented here will follow the Balanced Design Procedure (BDP) [Roeder et al., 2011]. This method makes use of balance factors which are used similarly to LRFD ϕ factors but are fundamentally different. Resistance factors account

for uncertainties in the capacity, whereas the balance factors are used to maximize system ductility while ensuring that that failure limit states are suppressed. The connections used in the author's and Powell's experiments were designed using the BDP and performed exceptionally well with no failures occurring in the splice region.

The equations that must be satisfied for the BDP for each tensile limit state are given by Eqn. 9.1 and those for the compressive limit state of gusset plate buckling is given by Eqn. 9.2. The connection design forces to be used are those currently prescribed by the Seismic Provisions [AISC, 2010], which are the expected strength of the brace in tension and compression given by the right-hand side of Eqn. 9.1 and Eqn. 9.2, respectively.

$$\beta R_n \geq R_y F_y A_g \tag{9.1}$$

$$\beta R_n \geq 1.1 R_y P_n \tag{9.2}$$

where β is the balance factor described above and in more detail in Section 3.4.2.

The limit states are essentially the same as those used for the design of corner gusset plates and include the following:

1. Brace-to-splice plate weld
2. Base metal at brace-to-splice plate weld
3. Brace net section fracture
4. Gusset plate yielding
5. Gusset plate fracture
6. Gusset plate block shear rupture
7. Gusset plate buckling

Brace-to-splice plate welds

For the sandwich plate connection, the spliced braces are attached to the plates using flare bevel groove welds at each corner of the brace as shown in Fig. 9.2a. This is a prequalified

welded joint and the design requirements can be found in the Steel Construction Manual [AISC, 2005b].

The fillet welds attaching the slotted brace to the through-plate must be designed to satisfy Eqn. 9.1. The nominal strength of the weld is given by Eqn. 9.3. In this case, β=0.75.

$$R_n = 0.6 F_{EXX} N_w L_w t_{eff} \tag{9.3}$$

where F_{EXX} is nominal electrode strength, N_w is the number of welds used, L_w is the length of the welds and t_{eff} is the effective throat of the fillet weld.

The base metal for each connection must also be checked where the connecting welds occur. This design expression for the nominal strength is given by Eqn. 9.4 and β=0.75.

$$R_n = 0.6 F_u N_w L_w t_{bm} \tag{9.4}$$

where F_u is the tensile strength of the base metal and t_{bm} is the thickness of the base metal.

Brace net section fracture

Fracture on the net section of both the continuous and the spliced braces must be checked because of the slots required for the through-plate. The nominal strength for this limit state is given by Eqn. 9.5. For this mode, β=0.9.

$$R_n = R_{tb} F_u A_n U \tag{9.5}$$

where A_n is the net area of the section where material was removed, and U is the factor accounting for shear lag of the force transfer from the weld to the brace and is given by Equation 9.6.

$$U = 1 - \frac{x}{L_w} \tag{9.6}$$

where x is given by Equation 9.7 for a HSS brace attached to a single concentric gusset plate.

$$x = \frac{B^2}{4(B+H)} \tag{9.7}$$

where B and H are the dimensions of the HSS shown in Figure 9.5a. If net section reinforcement is used, Equation 9.5 becomes Equation 9.8

$$R_n = U\left(R_{tb}F_{ub}A_{nb} + F_{urp}A_{rp}\right) \tag{9.8}$$

where $R_{tb}F_{ub}$ is the expected tensile strength of the brace, A_{nb} is the net area of the brace where the material has been removed, F_{urp} is the tensile strength of the net section reinforcement and A_{rp} is the area of the net section reinforcement.

Splice plate yielding

Rectangular plates would typically be used for the sandwich plate connection with a width larger than the tube to allow for adequate welding but not much larger. Therefore, the total width of the plate may be used to resist the tensile load. If the plate is relatively wide, the Whitmore width may be used to calculate the area of resistance. The through-plate connection will most likely be wider than the sandwich plates because only one through-plate is used. Therefore, the yield resistance of the through-plate may be calculated using the Whitmore width according to Eqn. 9.9. For this mode, β=1.0.

$$R_n = F_y B t \tag{9.9}$$

where t is the thickness of the gusset plate and B is the lesser of the width of the plate or the Whitmore width.

Gusset plate fracture

Fracture in tension of the sandwich or through-plates is also a possibility and the nominal expression governing this limit state is given by Eqn. 9.10, where the total width of the plate may be used in the sandwich plate if it is not wide enough to warrant using the Whitmore width. For this mode, β=0.85.

$$R_n = F_u B t \tag{9.10}$$

Splice plate block shear rupture

Block shear rupture in the gusset plate along the tube profile must be checked in both cases (see Fig. 9.5b for tube profile area for block shear). The design expression is given by Eqn. 9.11 and β=0.85.

$$R_n = 0.6 F_u A_{nv} + U_{bs} F_u A_{nt} \tag{9.11}$$

where A_{nv} is the net area subject to shear, U_{bs} is a factor that accounts for the uniformity of the tensile stress in the plate at the end of the bracing member,A_{nt} is the net area subject to tension, A_{gv} is the gross area subject to shear. U_{bs} is generally unity for brace connections used in typical construction.

Splice plate buckling

Gusset plate buckling when the brace is in compression must be checked for both connection details. Although it is unlikely that it will govern in either case if the recommended $4t$ brace offset is used. The buckling length for each type of splice is shown in Figs. 9.2c and 9.2d. The length for the sandwich plate is simply the average of the three lengths as shown in Fig. 9.2c. Similarly, the length for the through-plate is the average of the three lengths as shown in Figs. 9.2d and depends on whether the width of the plate is larger or smaller than the Whitmore width. In the figure, the plate width is shown larger than the Whitmore width for the plate above the continuous brace while it is shown as smaller below the continuous brace. An effective length factor of 1.4 is recommended and is similar to that recommended for gusset plates in Chevron configuration (Roeder et al. 2011). The nominal buckling strength of the plate(s) is given by Eqn. 9.12 and β=0.9.

$$R_n = F_{cr} B_w t_g \tag{9.12}$$

where F_{cr} is the critical load defined by Equations 9.13 or 9.14.

When $KL/r \leq 4.71\sqrt{E/F_y}$ (or $F_e \geq 0.44F_y$)

$$F_{cr} = \left[0.658^{\frac{F_y}{F_e}}\right] F_y \tag{9.13}$$

When $KL/r > 4.71\sqrt{E/F_y}$ (or $F_e < 0.44F_y$)

$$F_{cr} = 0.877F_e \tag{9.14}$$

where F_e is the Euler buckling load defined by Equation 9.15.

$$F_e = \frac{\pi^2 E}{\left(\frac{KL}{r}\right)^2} \tag{9.15}$$

9.2.3 Brace Effective Length

Section 5.4.1 discussed the results of the experimentally determined effective length factors for the braces in the single-story X-configuration. Tests by Powell and the author show that the tension brace acts as an OOP support at the splice location and this is reflected in the effective length of the brace which is one-half of the total brace length for both the continuous brace and the spliced braces (twice the length of each spliced brace). As a result, the recommended effective length factor, K, for this type of brace is 0.5. This brace length is defined as the actual length of the braces from each corner gusset plate as shown in Fig. 9.1. This ability of the tension brace to act as an OOP support agrees with the experimental findings of Tremblay [2003] and numerical work performed by Moon [2007].

9.3 BRBF Design Recommendations

This section provides design and detailing recommendations for the beams, columns and gusset plates at a corner connection region of a BRBF. The first four sections provide a summary and brief background of the reasons behind the recommendations. The recommendations are given in the last section in a concise list.

9.3.1 Column detailing remarks

Column flange tearing occurred in column B-2 at the location of the beam flange CJP welded connections and was similar to those that occurred during the 1994 Northridge earthquake.

Continuity plates were not provided at this location although if this were a moment frame, they would be required. This column flange tearing did not occur in column A-1 which had nearly the exact same conditions as B-2. The loading histories were different between the two but the cumulative deformation was approximately the same in both cases when the story drift at which the divot formed was reached. Therefore, the slightly different loading histories are likely not the reason for this difference in performance. The beam CJP backing bar was not removed in either case nor was the weld inspected through ultrasonic means. It is possible that a defect was present at the location where tearing occurred in column B-2 and not in column A-1 which could have acted as a notch-like condition with a greater potential for crack initiation.

Extensive local web and flange buckling occurred in the simulations when a relatively small column was used with thin webs. This damage was mitigated with the addition of web doublers that increased the thickness of the web to 75% of the gusset plate thickness. This coincided with only a minor increase in the beam demands. Additionally, it is logical to expect that more column damage would occur with a steeper brace angle as extensive beam damage occurred with a shallow brace angle.

9.3.2 Beam detailing remarks

Extensive damage occurred in the test frame in the beams at the location of the gusset plates including extensive yielding, local web and flange buckling and ultimately tearing of the flange up through the web. Yielding was extensive in the beam webs by approximately 1.5% story drift which is below the DBE drift level of 2%. The local web and flange buckling was first observed at approximately 2.5% story drift and flange tearing was first observed at 3.7% story drift.

This beam yielding and local web and flange buckling was accurately captured in the finite element simulations. It was found that by attaching doubler plates to the web of the beam within the gusset plate connection region, there was a significant reduction in beam demands at this location. Additionally, when doubler plates were used that increased the total beam web thickness to one-half the thickness of the gusset plates, the beam local

buckling was mitigated at DBE level drifts, but not at the MCE level drifts. These were mitigated at the MCE level drifts by using beam web doublers that increased the total web thickness to three-quarters of the gusset plate thickness.

Another viable option of reducing the demands on the beam and the potential for local buckling and fracture at the connection region is to release the fixity of the beam just beyond the gusset plate edge (away from the column). This detail was tested by Fahnestock (2006) and performed well with no beam damage at the gusset connection region and negligible damage at the beam splice.

9.3.3 Gusset plate remarks

The gusset plate welds at the column interface began tearing in four of the eight locations at 2% story drift and propagated the total length of the weld in all but one location by 3% story drift. The beam damage was more extensive at the location where the weld tear did not propagate the total length and this beam damage appeared to relieve the demands on the weld at this location. This tearing did not cause BRB instabilities nor was a reduction in strength observed. The welds were designed according to the force demands that result from application of the Uniform Force Method using the maximum adjusted BRB strength. As is common practice no attention was paid to the joint moments or the deformation demands. The finite element analyses indicated that had the welds been designed for the strength of the gusset plate, the potential for weld tearing was dramatically reduced.

The Balanced Design Procedure works well for the conventional buckling brace system as gusset plate yielding has been shown to be advantageous in that system. While gusset plate yielding was shown in the parametric study to reduce the demands on the beams and column, there are negative side effects such as gusset plate instabilities which can negatively impact the performance of BRBs and potentially cause a plastic hinge to form in the BRB at the connection region like those observed in the frame experiments at UCB [Uriz, 2005] and UW [Christopolus, 2005]. Therefore, the current LRFD methodology should still be employed when checking BRB gusset plate limit states, particularly buckling and yielding. Supplying beam web doublers is more reliable than providing thin gusset plates.

9.3.4 Gravity system remarks

The gravity system performed well through all drift ranges in both experiments. However, during the BRBF experiment, tears formed in the braced frame column webs at the second floor locations where the gravity beams were connected to the webs with bolted, double-angle connections. These tears were first observed at 2% story drift and propagated through the length of the connection by the end of the test. While this damage did not cause any apparent loss of load-carrying ability by the beam, there was also very little gravity load on the system. This type of damage did not occur at the third floor where the gravity beams were connected to the column webs with extended shear tab connections.

9.3.5 BRBF recommendations

Based on the discussions and evidence in the previous chapters and the summary above, the following recommendations are made for the corner connection region of BRBF systems:

Column

1. Provide continuity plates at the beam flange location in the column (Fig. 9.6) according to the Seismic Provision recommendations for special moment frames [AISC, 2010]. This applies to "fixed" beam connections.

2. Until further studies are performed on the effect of the brace angle on column demands at the gusset-beam-column connection region, it is recommended that column web doublers be installed in the panel zone and within the gusset region that increases the total web thickness to at least 75% of the gusset plate thickness or that columns with web thicknesses satisfying this criteria be used. The web doublers should extend at least 12 inches beyond the gusset plate as shown in Fig. 9.6.

Beam

3. It is recommended that backing bars are removed at the beam bottom flange CJP connections to the column at the corner gusset plate locations as they are required in special moment frames per the Seismic Provisions [AISC, 2010].

4. It is recommended that beam web doubler(s) be installed in beams at gusset plate locations that will increase the web thickness to at least 75% of the gusset plate thickness or speicfy beams with web thicknesses satisfying this ratio. The web doubler(s) should extend beyond the edge of the gusset plate by at least 12 inches as shown in Fig. 9.6.

5. In lieu of providing beam and column web doubler plates, splice the braced frame beam at or just beyond the gusset plate edge (away from the column) with a connection to the web only. This limits the moment resisted by the beam and the amount of frame action that can develop. This connection must be designed to transfer shear from gravity load, shear due to flexure due to frame action, and axial load due to seismic action that must be transferred through the beam. Until further study is done, it is recommended that the floor slab continuity be interrupted directly above the splice. This can be accomplished by a blockout above the splice and interrupting any reinforcing steel in the slab and should extend for at least the width of effective width of the composite slab as defined by AISC [2005b]. An example detail is shown in Fig. 9.7. This is done to ensure that no moment will developed due to the force couple developed between the splice plate and the composite slab. Additionally, it is recommended that fixed connections that were removed with the beam release be installed elsewhere in the building frame to ensure that the lost redundancy is replaced.

Gusset plate

6. The current LRFD gusset plate design limit states be used excepting that all welds connecting the gusset plate to the beams and columns should be complete joint penetration welds (CJP) or fillet welds with a strength equal to the yield capacity of the gusset plate. The expected strength of the plate should be used and is given by $R_y F_y t$, and the nominal fillet weld strength is given by Eqn. 9.3 where an L_w of unity should be used when comparing it to expected strength of the plate.

Gravity system

7. Gravity beams framing into the web of braced frame columns should be connected with a welded connection and not a bolted connection.

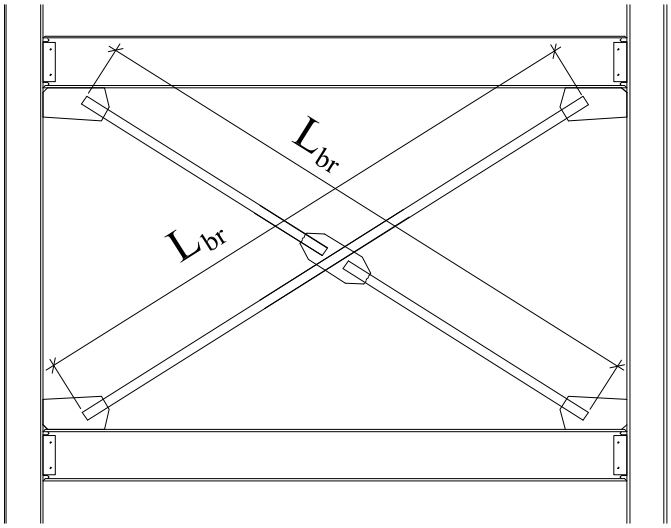

Figure 9.1: Recommended brace length for buckling strength calculations

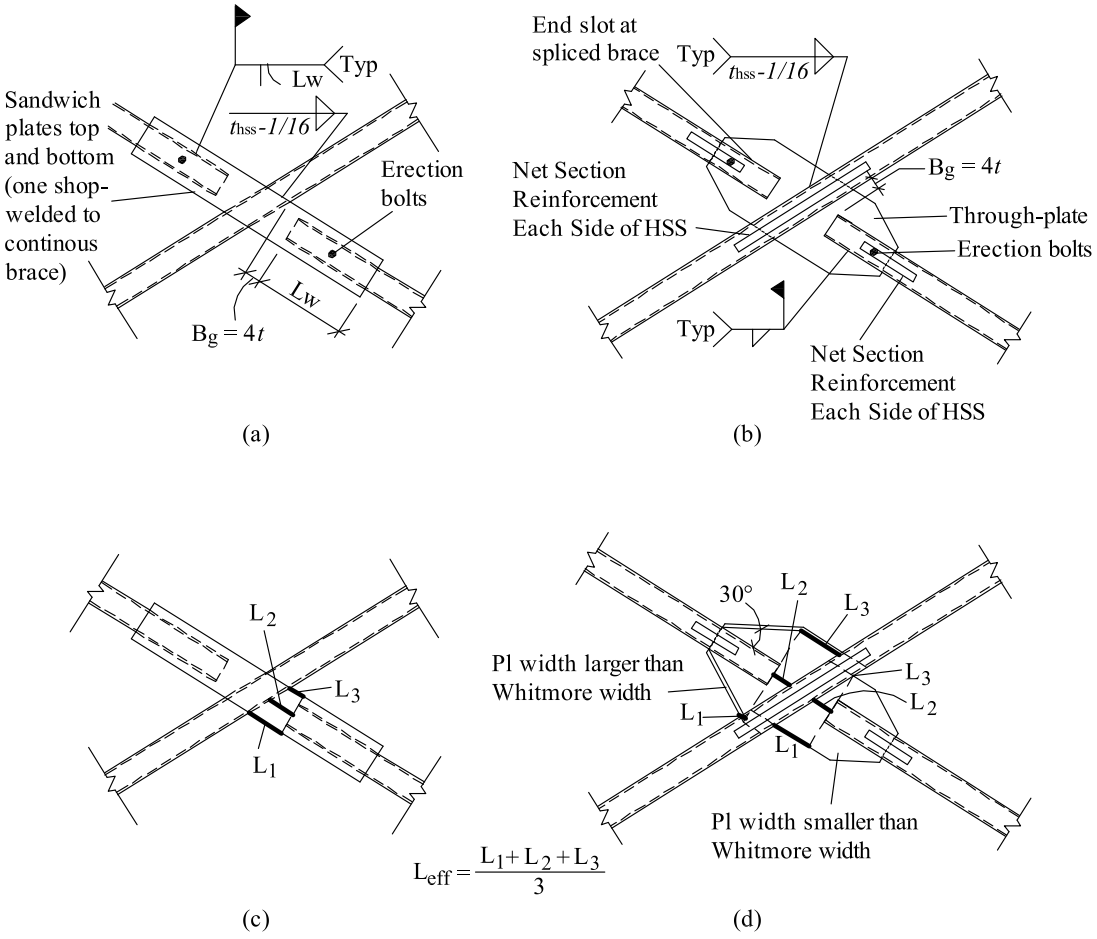

Figure 9.2: Brace splice detail at center of single-story, X-configuration: (a) sandwich plate detail; (b) through-plate detail; (c) buckling length for sandwich plate; (d) buckling lengths for through-plate.



(a) Buckled continuous brace (b) Buckled spliced brace

Figure 9.3: Comparison of buckled brace shapes with sandwich plate splice detail



(a) Buckled continuous brace (b) Buckled spliced brace

Figure 9.4: Comparison of buckled brace shapes with through-plate splice detail

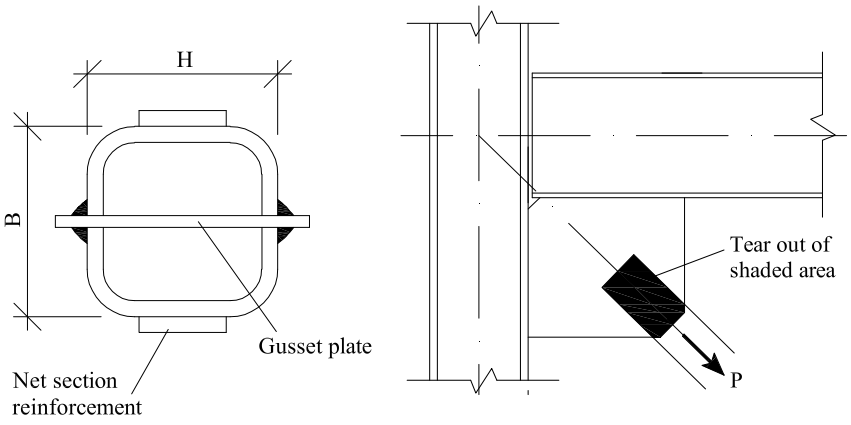

(a) HSS brace net section dimension nomenclature

(b) Block shear rupture area

Figure 9.5: Gusset plate schematics

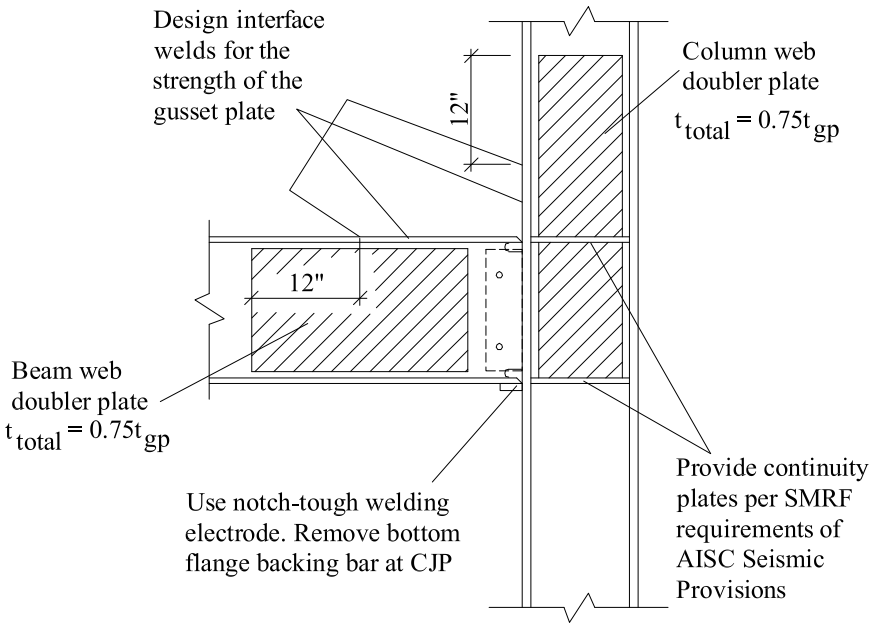

Figure 9.6: Recommended detailing at corner beam-column-gusset connection region.

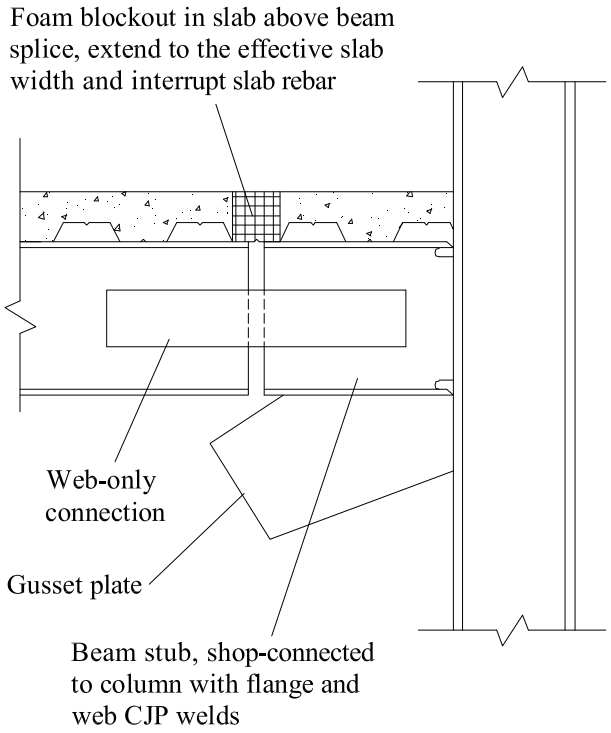

Figure 9.7: Beam fixity release detail at BRB gusset plate

Chapter 10

SUMMARY, CONCLUSIONS AND RECOMMENDATIONS

10.1 Summary

Special concentrically braced frames (SCBF) are relatively stiff, strong lateral force resisting systems commonly used in earthquake-prone areas. An SCBF ***system*** is composed of the brace, gusset plate, beam and column ***components***, and "conventional" SCBF bracing systems often employ square and round HSS braces that buckle in compression and yield in tension. A relatively new bracing system, the buckling-restrained brace (BRB), has been developed that prevents brace buckling and is gaining popularity due its symmetric hysteretic behavior caused by yielding in both tension and compression.

Advances have been made recently toward an improved design philosophy and a better understanding of SCBF and BRBF system performance since braced frame system performance issues first came to light. These advances include improved design methods and details for SCBF connection regions [Roeder et al., 2011] and improved numerical models that more accurately capture degrading behavior such as brace fracture [Hsiao et al., 2012b]. However, a number of aspects required further study and understanding. These include but are not limited to the need for a better understanding of 3D loading and deformation effects on the ductility of the system, and a better understanding of the parameters that influence the behavior and performance at corner gusset plate connections in BRBFs.

A research program was undertaken to address the above issues and the program included one large-scale SCBF experiment and one large-scale BRBF experiment. Both were performed at the Multi-Axial Subassemblage Testing Facility at the University of Minnesota. Additionally, analyses were performed which included a large suite of finite element simulations of a two-story BRBF. This research was part of the last phase of a Network for Earthquake Engineering Simulation Research-funded (NEESR) project entitled "International Hybrid Simulation of Tomorrow's Braced Frame Systems."

10.2 Summary of Experimental Program

10.2.1 General

Two frames were tested and were one-bay by one-bay, two-story frame with braces in two orthogonal bays which framed in a "shared" column. The floor system included typical wide flange beam sizes supporting a concrete slab cast on metal deck similar to that used in modern construction. Both test frames were instrumented with more than 400 sensors which included strain gauges, string potentiometers and linear variable displacement transducers. Lateral loads in two orthogonal directions were applied to the top slab of the test specimen in displacement control. The magnitude of deformation for the primary direction was the deformation history used in planar frame tests of NEESR research program. The bi-directional loading pattern was a "cloverleaf" pattern with the magnitude of the maximum displacement in the secondary direction being two-thirds of that in the primary direction. The bi-directional loading protocol development was based on nonlinear simulations of 3, 6 and 9-story prototype buildings subjected to bi-directional ground motions.

10.2.2 Summary of SCBF Test

The first test specimen was configured with HSS buckling braces in a single-story X with one continuous diagonal brace and the opposing diagonal brace split into two pieces and spliced at the intersection of the X. The braced frame beams were rigidly connected to the columns. The other two frames were designed as "gravity" frames with beam to column connections designed and detailed for shear forces only. Brace connection design followed the newly-developed Balanced Design Procedure (BDP) [Roeder et al., 2011], and the braces were offset at the corner gusset plates using the 8t elliptical offset method. The results of the SCBF test are summarized below.

1. Brace behavior was dependent on the continuity of the brace. The continuous braces buckled in an S-shape and spread out the inelastic action between the two halves of the brace. The braces that were spliced at the intersection with the knife plate tended to concentrate damage in one-half of the brace because only one-half of the brace

buckled while the other half remained straight.

2. The corner gusset plates were designed using the BDP and offset from the framing elements using the $8t$ elliptical offset method. The BDP encourages secondary yielding in the gusset plate rather than isolating inelastic action to just the brace and the gusset plates exhibited this expected performance by yielding extensively. The square gusset plates at the base rotated and yielded along an elliptical yield line. However, for the rectangular gusset plate with different edge lengths at the beam-column connection regions, the elliptical yield line was not as apparent and yielding was concentrated along the beam and column interfaces. Frame action also caused the longer edge of these gusset plates to deform out-of-plane when the joint moments tended to close the joint when the braces were in tension. This occurred at story drifts of 1.5% and larger and there was no observable detrimental impact on the frame resistance or deformation capacity from this edge deformation.

3. The gusset plate interface welds were fillet welds designed to match the strength of the plate and not the force demands that result from application of the Uniform Force Method. Only one weld tear was observed during the experiment and this occurred at approximately 1.8% SDR and propagated a maximum of one inch by the end of the test. The total weld length at this location was 18 inches. The gusset plate base material at the interface also tore in three locations but was stable and did not propagate longer than two inches at any of these locations.

4. Beam yielding and damage was minimal, with the majority of yielding occurring in the beam flanges near the CJP connection to the columns. However, significant yielding and ultimately out-of-plane web deformation occurred at brace fracture at the second floor beam connected to the strong axis of the W12x106. The W12x106 column is 60% flexurally stiffer than the W12x72 and therefore deformed less than the W12x72 which transferred more of the deformation to the beam at a given story drift. Additionally, panel zone shear strains of up to 4.5 times the yield strain were measured in the W12x72 while no shear yielding was measured in the W12x106 panel zone.

5. Contribution of the frame to the stiffness and strength of the system was not negligible. At a story drift of 1%, the braces resisted 60% of the story shear while the rest was resisted by column shear. At a story drift of 2%, the braces and the frames each resisted 50% of the total shear. This distribution is of course dependent on the frame design and could be less or more depending on the relative stiffness and strength of each element.

10.2.3 Summary of BRBF test

Following the SCBF test, the braces and gusset plates were removed from the frame to prepare for the second test frame. PowerCat BRBs manufactured by Star Seismic were installed in the frame in a single-diagonal configuration in the same two orthogonal bays that the SCBF braces were installed. The BRBs were connected to the gusset plates using a true pin through a reinforced hole in the gusset plates. The design of the gusset plates and welds connecting the plates to the frame elements followed the current state-of-the-practice method using LRFD [AISC, 2005b] for the plate limit states and the Uniform Force Method for the weld design. The results of the BRBF test are summarized below.

1. Good BRB performance was observed with no instabilities occurring in the BRBs and no strength degradation prior to core fracture.

2. Bulging in the BRB casing was not observed until fracture occurred although the fracture BRBs were in the second story and the casing was not as easily observed. Therefore, bulging may have taken place prior to fracture. However, the dimensions of the steel casing were such that this should not have limited the strength of the BRB according to a study by Lin et al. [2012].

3. The BRBs yielded in tension at story drifts ranging from 0.29 to 0.33%. The cores fractured in two of the four BRBs and occurred in the second story of both Frames 1 and B at drift ratios of 4.2% and 3.6%, respectively. The total drift capacity, defined as the sum of the largest absolute value of the negative and positive drifts achieved

prior to or during the last complete cycle before brace fracture, for Frames 1 and B was 7.5% and 7.1%, respectively.

4. The maximum ductility of the braces that fractured were 20 and 17 inches/inch for the BRBs in Frames 1 and B, respectively. The cumulative ductility capacity of the braces that fractured were 611 and 597 inches/inch for the BRBs in Frames 1 and B, respectively. These are three times as large as the pre-qualification requirements of the Seismic Provisions (AISC 2010). The maximum ductilities were comparable to the ductilities of the BRBs in the system tests performed by Christopolus [2005] and slightly less than those in the system tests performed by Fahnestock [2006]. The cumulative ductility capacities were 35% larger than the maximum achieved in the Fahnestock's system tests, which was the maximum achieved in any system tests prior to the author's system tests.

5. The analytically-predicted elastic axial tensile stiffness of the BRBs differed from the experimentally measured stiffness by less than 1% in the best case and 7% in the worst case.

6. Average measured values (between the four tested BRBs) of hardening and overstrength factors ω and β at 2% story drift were 1.36 and 1.43, respectively, and the product of these two, $\omega\beta$, is 1.95. The value of $\omega\beta$ is consistent with that typically assumed at the beginning of design [Bruneau et al., 2011] while the value of ω is slightly more and β slightly less than that typically assumed.

7. Gusset plates welds at the column interface tore in four locations at 2% story drift. Initial tearing lengths were approximately 0.75 inches for all cases. The welds tore when the BRBs were in compression indicating that the tears were a result of frame action opening the joint. The tears propagated the total length of the connection in three of the four cases and no greater than 1.5 inches in the other. The gusset plates were designed according to the BRB force demands calculated according to the

Uniform Force Method which does not take frame action into account. This tearing was not accompanied by BRB instability or an observable reduction in resistance.

8. The damage to the beams and columns was extensive at the locations where gusset plate connections occurred while very little damage to these components occurred at the joints where there were no gussets. This damage included considerable web and flange yielding followed by local buckling, tearing and fracture. Beam flange tearing occurred in two connection regions at MCE level drifts but not at DBE drift levels but local web and flange buckling did occur at DBE drift levels.

9. Tearing of the flange and web of column B-2 occurred at the bottom beam flange at the second floor. Formation of a divot in the column flange just outside the K-region was first observed at 2.8% story drift and initial tearing was observed in the second excursion at 2.8% story drift. This tearing was similar to the tearing that occurred in moment frames during the 1994 Northridge earthquake [Bruneau et al., 2011]. The gusset plate was attached to the top of the beam at this location. The backing bar for the beam flange CJP connecting it to the column was not removed at this location and therefore a potential stress concentration occurred at this location. Notch-tough weld metal was used but inspection of the welds was not performed. Column continuity plates were not used and column tearing did not occur in column A-1 which had the exact same conditions as column B-2. Column continuity plates would have been required had this been a moment frame [AISC, 2010].

10. Similar to the SCBF test, more damage occurred in the beams that were connected to the strong axis of the W12x106 column than those connected to the strong axis of the W12x72 column.

11. Panel zone shear strains of up to eight times the yield strain were measured in the W12x72 while no shear yielding was measured in the W12x106 panel zone. At the second floor panel zones in the W12x72, gravity beams were framed into the web with

bolts which caused the panel zone yielding to concentrate around the holes and tears eventually formed at 2% in column B-2 and at 3.7% in column A-1.

12. Local flange buckling occurred at the base of columns A-1 and B-1 (W12x72) at story drifts of approximately 3%. These columns did not satisfy seismic b/t ratio limits. This local buckling did not occurr at the base of column B-1 (W12x106) which did satisfy seismic b/t ratio limits.

13. No damage or distress was observed in any part of the gravity framing system. This is concerting as the system sustained story drifts larger than 4.5%.

14. Similar to the SCBF test frame, the columns resisted a relatively large portion of the story shear after brace yielding. At story drifts greater than 1.0 to 1.5%, the column shears due to frame action were at least 50% of the story shear.

10.3 Summary of Analytical Program

10.3.1 Summary of SCBF analytical work

The analytical work for the SCBF consisted of three main tasks, the first of which compared the 3D tests with similar planar frame tests to assess the impact of bi-directional loading on the ductility of these systems. The second task analyzed the results of the 3D and planar frame tests to determine the appropriate effective length factor for the compression design of single-story, X-configured braces.

The third task consisted of developing and analyzing nonlinear models of one frame of the X-configured SCBF test frame using the OpenSees finite element program. The purpose of these analyses was to assess the effectiveness of this program in simulating the complex nonlinear behavior of this type of system for future studies to help determine system seismic performance factors. Displacement-based fiber elements were used for the brace while force-based fiber elements were used for the beams and columns. Rotational springs at the ends of the braces were included and a corotational formulation was used to capture brace buckling behavior. A number of element types within the beam-column-gusset region were studied.

The OpenSees simulations captured the global and brace response of the frame very well. Local responses in the columns at some locations were not predicted as well but these had a small influence on the global response and no influence on the brace response.

10.3.2 Summary of BRBF analytical work

The largest part of the analytical program consisted of parametric studies performed to provide insights into the parameters influencing the behavior, performance and damage that occurs in the corner gusset plate connection regions of BRBFs. The ultimate goal of these simulations was to provide design recommendations that improve the system performance. More than 30 nonlinear finite element simulations were performed in ABAQUS with the validated model of Frame 1 of the BRBF experimental frame used as the basis for all simulation models. The beams, columns, gusset plates and concrete floor slabs were modeled with shell elements while the BRBs were modeled with truss elements. Material and geometric nonlinearities were incorporated into the analysis. The results of the BRBF simulations are summarized below.

1. The simulated global and local force-displacement behavior matched the experimentally measured force-displacement behaviors very well except that the asymmetric BRB force-displacement behavior was not captured accurately at all drift levels. The yielding patterns and local beam and column web and flange local buckling that occurred in the experiments were simulated well.

2. Due to the difficulty and complexity of modeling the BRB components (core, infill grout, restrainer, bond between these elements, etc.), a truss element was used that was calibrated to the measured axial force-deformation behavior of the BRB but lacked the compression overstrength. The lack of asymmetry in the BRB model was deemed acceptable because the purpose of the parametric studies was to assess the behavior and performance at the joints by comparing the demands at the connection interfaces. These studies were relative comparisons and as such, consistency between the models (other than the parameter being varied) is most important. Additionally,

as the strength, stiffness, hardening and overstrength characteristics vary between brace manufacturers and brace types, there was no reason to favor the behavior of one BRB over another. The analysis in Section 8.3.7 showed that BRBs of varying strengths still resulted in the same or similar relative differences in the demand indices used for comparison between the different parameter models.

3. The parametric study demonstrated the complexity of the behavior of the beam-column-gusset connection region and the trade-off in most cases of improving the behavior in one element which causes more demands or less desirable behavior in other elements.

10.4 Conclusions from SCBF Experimental Investigation

1. The out-of-plane loading and deformation that was imposed on the three-dimensional SCBF test frame had negligible effect on the system ductility and strength. Brace buckling occurred at the expected story drift ratios and force levels, and the braces reached their expected strength in tension and compression. The story drifts at which buckling occurred ranged between 0.23 and 0.34%. The system deformation capacity of the three-dimensional frame in the principal direction was a story drift range of 3.61% which was only 6% less than the drift capactiy of the two planar frames with the same braces and similar frame sizes tested by Powell.

2. The tension brace in a single-story X-configuration acts as an out-of-plane support for the compression brace.

3. Assessment and detailing for column panel zone yielding is not required in the Seismic Provisions [AISC, 2010] for braced frame columns. However, the experiments demonstrated that panel zone yielding can indeed occur in the columns with gusset plates at the joint. It appears though that the panel zone yielding helped distribute the deformation at the joints instead of concentrating it in the beam.

4. The BDP used for the design of the center brace splice detail worked well and no fail-

ures or detrimental behaviors were observed at this location. Formal design guidelines were provided in Section 9.2.2 for the splice connection in this type of bracing system.

10.5 Conclusions from the BRBF Experimental Investigation

1. Similar to the SCBF test frame, the out-of-plane deformation and loading had no negative impact on the ductility and drift capacities of the system relative to similar planar frame experiments. The ductilities exceeded those observed in many of the other BRBF system tests and the cumulative ductility capacities exceeded those observed in all other system tests.

2. Given the observed column damage at the bottom beam flange at the CJP connection to the column flange, it is recommended that backing bars be removed from CJP beam flange connections to columns in braced frames and column continuity plates be installed as currently required for moment frames.

3. Tearing occurred in the braced frame column webs at the holes connecting the in-framing gravity beams but did not occur at the locations utilizing an extended shear plate connection for the gravity beam. It is recommended that gravity beams framing into the webs of braced frame columns be connected with welded and not bolted connections.

10.6 Conclusions from the SCBF Analytical Investigations

1. Analyses of the experimental results from the SCBF test and the two planar frame tests performed by Powell were used to estimate the effective length used to predict brace buckling strength in a single-story X-configured frame. It was shown that effective length of 0.5 may be used when the length of the brace is defined as the total out-to-out length of the brace regardless of the center splice connection types investigated (sandwich plate connection or through-plate connection).

2. The OpenSees simulation results show that this model may be extrapolated to analyze multi-story model buildings designs with the single-story X-configuration to assess

their performance under earthquake hazard. These analyses should include the brace fracture model developed by Hsiao [2012b] in order to assess the brace fracture potential which was not done in the work described here. Additionally, assessment of the seismic performance factors may be made which has not yet been done for this system.

10.7 Conclusions from BRBF Simulations and Parametric Study

1. Tearing and fracture at the beam flanges and at the gusset plate column welds that occurred in the test were not simulated in the model. Studies were performed to find a correlation between three different demand indices and the occurrence of weld tearing at the gusset plate interface with the column. It was found that when the elements at the interface were modeled using a constitutive model for the weld material, the PEEQ demands in the gusset plate element at the edge correlated well in the three locations at which weld tearing occurred with a coefficient of variation of less than 15%.

2. Increasing the weld sizes in the simulation to match the weld strength to the gusset plate strength resulted in PEEQ demands that were less than the demands that occurred in the reference model simulation at initial weld tearing. This suggests that providing a weld with the same strength as the gusset plate would have mitigated the weld tearing that occurred in the experiment.

3. Reducing the thickness of the gusset plates can significantly reduce the demands in the beams and columns at the beam-column-gusset connection interfaces and is a result of gusset plate yielding. However, this is not an effective way of reducing beam and column demands as thinner gusset plates exhibited stability issues that were not efficiently resolved through attachment of long-edge stiffeners.

4. Beam web doublers providing a total web thickness of at least 75% of the gusset plate thickness reduced the beam demands at the connection interfaces considerably and mitigated all of the local web and flange buckling at the MCE drift level. Web doublers

providing a total web thickness of 50% of the gusset plate thickness also reduced the demands considerably and mitigated the local web and flange buckling at the DBE drift level but not the MCE drift level. It is therefore recommended that beam web doublers be provided within the gusset plate connection region providing a total web thickness equal to 75% of the gusset plate thickness. This requirement may be relaxed if the fixity of the beam is released as discussed in Item 7.

5. Rectangular gusset plates increased the potential for beam damage relative to tapered gusset plates even at DBE drift levels. However, the addition of beam web doublers mitigated this damage to levels observed in the models with tapered gusset plates.

6. Column web doublers in the panel zone and extending into the gusset region reduced the column demands considerably without increasing the beam demands markedly. The local web and flange local buckling that occurred in the underdesigned column was completely eliminated at the MCE drift level through the use of doublers. Additionally, given the significant beam damage that occurred with a brace angle of 32 degrees from the horizontal, it is reasonable to assume that significant column damage would occur with a relatively steep brace angle. Therefore, it is recommended that column web doublers be installed in the panel zone and gusset region that increases the total web thickness to at least 75% of the gusset plate thickness. This requirement may be relaxed if the fixity of the beam is released as discussed in Item 7.

7. Releasing the beam fixity just outside the gusset plate edge (away from the column) had the most significant impact on the demand reduction at the gusset interfaces. This detail essentially removed all plastic strain demands and significantly reduced the stress demands in the beams, columns and gusset plates.

8. Frame action contributes a significant amount to the demands at the connection interfaces and is dependent on the taper of the gusset plates. For the brace angle studied, removal of the brace *increased* the demands at the column interface by 10% and *decreased* the demands at the beam interface by 60%. When rectangular gusset plates

were employed, removal of the BRB *reduced* the strain demands at both interfacess by 10%.

9. The strain demands in the beam at the gusset interface are inversely proportional to the ratio of the beam web thickness to the thickness of the gusset plate. However, the demands are not a unique function of this ratio but depend on the details of the specific thicknesses that make up this ratio. Reducing the gusset plate thickness by 50% is not as advantageous as doubling the beam web thickness.

10. The strain demands in the column are also inversely proportional to the ratio of the beam web thickness to the thickness of the gusset plate except for when the ratio is increased by increasing the beam web thickness with doubler plates. In this case, the column demands are increased at the interface.

10.8 Recommendations for Future Research

The work described in this dissertation included the first 3D, large-scale experiments performed on SCBFs and BRBFs and a large number of numerical simulations. More work is needed to advance the state-of-the-art design for SCBFs and in particular, BRBFs.

Releasing the fixity of the beam in a BRBF outside the gusset plate region is a very promising detail but a number of aspects of this connection need further study. This includes the impact of a concrete floor slab that would typically occur in an actual building. It is expected that this will influence the behavior as a force couple between the concrete slab and the web plate has the possibility of providing flexural rigidity and negate the intended effect of releasing this. Various details such as a slab blockout above the beam release should be investigated. Additionally, a number of different connection details should be investigated to determine which one provides the best performance and limits the beam damage within this connection region.

Recent simulations on monotonically loaded braces attached to gusset plates have shown that the gusset plate demands were influenced by the location of the brace axis relative to the corner of the gusset plate [Cui et al., 2012]. Frame action was not accounted for in

these simulations because the gusset plates attached to rigid supports at the location of the interface with the beams and columns. Validated simulations of BRBF systems with varying brace angles are needed to determine the effect of the angle on the demands and performance of the members at the connection region.

The gusset plate weld tearing that occurred during the experiment at the column was not accompanied by BRB instability or an observable reduction in resistance. Promising experimental work has been done by Berman and Bruneau [2009] on a connection detail in which the BRB is connected to a gusset plate that is only connected to the beam. More studies are required to further understand the behavior of this connection and to develop details that adequately address the demands at this location.

The addition of beam and column web doublers was shown to improve the performance of the connection region and mitigate the damage that was observed in this region during the experiment.

To date, the behavior of single-story, X-configured SCBFs under strong ground motion has not been adequately studied. In particular, the system seismic performance factors, R, Ω and C_d are needed along with an understanding of their susceptibility to brace fracture relative to other SCBF systems. The validated OpenSees model of this system was discussed in Chapter 6 and the modeling details may be used along with the brace fracture model developed by Hsaio [2012b] to implement the analyses required to assess the performance of this system.

REFERENCES

ABAQUS, *ABAQUS version 6.10 documentation*. Simulia, 2010.

ACI, *Building Code Requirements for Structural Concrete (ACI 318-08) and Commentary (ACI 318R-08)*, American Concrete Institute, Committe 318, Farmington Hills, MI, 2008.

AISC, *Seismic Provisions for Structural Steel Buildings, ANSI/AISC 341-97*, American Institute of Steel Construction, Chicago, IL, 1997.

——, *Steel Construction Manual, 13th Edition*, 13th ed., American Institute of Steel Construction, Chicago, IL, 2005.

——, *Seismic Provisions for Structural Steel Buildings, ANSI/AISC 341-05*, American Institute of Steel Construction, Chicago, IL, 2005.

——, *Seismic Provisions for Structural Steel Buildings, ANSI/AISC 341-10*, American Institute of Steel Construction, Chicago, IL, 2010.

——, *Code of Standard Practice for Steel Buildings and Bridges, ANSI/AISC 303-05*, American Institute of Steel Construction, Chicago, IL, 2005.

ASCE, *Minimum Design Loads for Buildings and Other Structures*, A. S. of Civil Engineers, Ed. Reston, VA: ASCE/SEI 7-10, 2010.

A. Astaneh-Asl, S. C. Goel, and R. D. Hanson, "Cyclic out-of-plane buckling of double-angle bracing," *Journal of Structural Engineering*, vol. 111, no. 5, pp. 1135–1153, 1985.

ASTM, "1049-85, standard practices for cycle counting in fatigue analysis," *Annual book of ASTM standards*, 1985.

ATC, "Guidelines for cyclic seismic testing of components of steel structures, ATC-24," Applied Technology Council, Redwood City, CA, Tech. Rep., 1992.

J. Berman and M. Bruneau, "Cyclic testing of a buckling restrained braced frame with unconstrained gusset connections," *Journal of Structural Engineering*, vol. 135, no. 12, pp. 1499–1510, 2009.

R. Bjorhovde and S. Chakrabarti, "Tests of full-size gusset plate connections," *Journal of Structural Engineering*, vol. 111, no. 3, pp. 667–684, 1985.

C. Black, N. Makris, and I. Aiken, "Component testing, stability analysis and characterization of buckling restrained braces," Pacific Earthquake Engineering Research Center, Berkeley, CA, Tech. Rep. No. 2002/08, 2002.

R. G. Black, W. Wenger, and E. P. Popov, "Inelastic buckling of steel struts under cyclic load reversals," Earthquake Engineering Research Center, University of California, Berkeley, CA, Tech. Rep. UCB/EERC Report No. 80/40, 1980.

M. Bruneau, C. Uang, and R. Sabelli, *Ductile Design of STEEL STRUCTURES*, 2nd ed. McGraw Hill, 2011.

J. Chambers and C. Ernst, "Braced Frame Gusset Plate Research," University of Utah, Salt Lake City, UT, Tech. Rep. Report to AISC, 2005.

C. Chen, J. Lai, and S. Mahin, "Seismic performance assessment of concentrically braced steel frame buildings," in *The 14th World Conference on Earthquake Engineering*, October, 2008 2008.

W. Chen and D. Han, *Plasticity for Structural Engineers*. J. Ross Publishing, 2007.

A. S. Christopolus, "Improved seismic performance of buckling restrained braced frames," MS thesis, Civil and Environmental Engineering Dept., University of Washington, Seattle, WA, 2005.

K. Clark, "Experimental performance of multi-story x-braced scbf systems," MS thesis, Civil and Environmental Engineering Dept., University of Washington, Seattle, WA, 2009.

CSI, *Perform 3D. Nonlinear Analysis and Performance Assessment for 3D Structures User Guide Version 4*. Berkeley, CA: Computers and Structures Inc., 2007.

——, *Structural Analysis Program, SAP-2000: Integrated Finite Element Analysis and Design of Structures.* Berkeley, CA: Computers and Structures Inc., 2010.

Y. Cui, H. Asada, S. Kishiki, and S. Yamada, "Ultimate strength of gusset plate connections with fillet welds," *Journal of Constructional Steel Research*, vol. 75, pp. 104–115, 2012.

M. Engelhardt, *Seismic Provisions Educational Series*, A. I. of Steel Construction, Ed. Chicago, IL: AISC, 2008.

L. A. Fahnestock, R. Sause, and J. M. Ricles, "Analytical and large-scale experimental studies of earthquake-resistant buckling-restrained braced frame systems," Lehigh University, Tech. Rep. No. 06-01 ATLSS, 2006.

B. Fell, A. Kanvinde, G. Deierlein, and A. Myers, "Experimental investigation of inelastic cyclic buckling and fracture of steel braces," *Journal of Structural Engineering*, vol. 135, pp. 19–32, 2009.

FEMA, "Quantification of building seismic performance factors," Federal Emergency Management Agency, Washington, D.C., Tech. Rep. No. FEMA P-695, 2009.

J. Gross and G. Check, "Experimental study of gusseted connections for laterally braced steel buildings," National Institute of Standards and Technology, Gaithersburg, MD, Tech. Rep., 1988.

I. Gunnarsson, "Numerical performance evaluation of braced frame systems," MS thesis, Civil and Environmental Engineering Dept., University of Washington, Seattle, WA, 2004.

D. Herman, "Further improvements on and understanding of special concentrically braced frame systems," MS thesis, Civil and Environmental Engineering Dept., University of Washington, Seattle, WA, 2007.

C. M. Hewitt and W. A. Thornton, "Rationale behind and proper application of the ductility factor for bracing connections subjected to shear and transverse loading," *Engineering Journal*, vol. 41, no. 1, pp. 3–6, 2004.

P. Hsiao, "Seismic Performance Evaluation of Concentrically Braced Frames," Ph.D. dissertation, Civil and Environmental Engineering Dept., University of Washington, Seattle, WA, 2012.

P. Hsiao, D. Lehman, and C. Roeder, "A model to simulate special concentrically braced frames beyond brace fracture," *Earthquake Engineering & Structural Dynamics*, 2012. [Online]. Available: http://dx.doi.org/10.1002/eqe.2202

——, "Improved analytical model for special concentrically braced frames," *Journal of Constructional Steel Research*, vol. 73, pp. 80–94, 2012.

S. Johnson, "Improved seismic performance of special concentrically braced frames," MS thesis, Civil and Environmental Engineering Dept., University of Washington, Seattle, WA, 2005.

A. Kanvinde and G. Deierlein, "Void growth model and stress modified critical strain model to predict ductile fracture in structural steels," *Journal of Structural Engineering*, vol. 132, no. 12, pp. 1907–1918, 2006.

B. Kotulka, "Analysis for a design guide on gusset plates used in special concentrically braced frames," MS thesis, Civil and Environmental Engineering Dept., University of Washington, Seattle, WA, 2007.

D. Lehman, C. Roeder, D. Herman, S. Johnson, and B. Kotulka, "Improved seismic performance of gusset plate connections," *Journal of Structural Engineering*, vol. 134, no. 6, pp. 890–901, 2008.

P. Lin, K. Tsai, K. Wang, Y. Yu, C. Wei, A. Wu, C. Tsai, C. Lin, J. Chen, A. Shellenberg, S. Mahin, and C. Roeder, "Seismic design and hybrid tests of a full-scale three-story buckling-restrained braced frame using welded end connections and thin profile," *Earthquake Engineering & Structural Dynamics*, vol. 41, no. 5, 2012.

E. Lumpkin, "Seismic performance of multi-story special concentrically brace frames using a balanced design procedure," MS thesis, Civil and Environmental Engineering Dept., University of Washington, Seattle, WA, 2009.

F. McKenna, "Object-oriented finite element programming," Ph.D. dissertation, Civil and Environmental Engineering Dept., University of California, Berkeley, Berkeley, CA, 1997.

S. Merritt, C. Uang, and G. Benzoni, "Subassemblage testing of star seismic buckling-restrained braces," University of California, San Diego, La Jolla, CA, Tech. Rep. No. TR-2003/04, 2003.

J. Moon, K. Yoon, T. Han, and H. Lee, "Out-of-plane buckling and design of x-bracing systems with discontinuous diagonals," *Journal of Constructional Steel Research*, vol. 64, pp. 285–294, 2007.

R. Ozcelik and T. Okazaki, "Summary of Finite Element Simulation of BRBF," *personal correspondence*, 2010.

J. Powell, "Evaluation of special concentrically braced frames for improved seismic performance and constructability," MS thesis, Civil and Environmental Engineering Dept., University of Washington, Seattle, WA, 2010.

D. Rabern, "Stress, strain, and force distributions in gusset plate connections," MS thesis, Dept. of Civil Engineering and Engineering Mechanics, University of Arizona, Tucson, AZ, 1983.

C. Roeder, D. Lehman, and E. Lumpkin, "Fragility curves for concentrically braced steel frames with buckling braces, ATC-58," Applied Technology Council, Redwood City, CA, Tech. Rep., 2009.

C. Roeder, E. Lumpkin, and D. Lehman, "A balanced design procedure for special concentrically braced frame connections," *Journal of Constructional Steel Research*, vol. 67, pp. 1760–1772, 2011.

P. Romero, L. Reaveley, P. Miller, and T. Okahashi, "Full Scale Testing of WC Series Buckling-Restrained Braces," University of Utah, Salt Lake City, UT, Tech. Rep. Final Report to Star Seismic, 2007.

SAC, "Protocol for Fabrication, Inspection, Testing and Documentation of Beam-Column Connection Tests and Other Experiments," SAC Joint Venture, Sacramento, CA, Tech. Rep., 1997.

SEAOC-AISC, "Recommended provisions for buckling-restrained braced frames, proposed," 2001.

J. Sherman, "Bidirectional loading behavior of buckling-restrained braced frames," MS thesis, Civil and Environmental Engineering Dept., University of Minnesota, Minnesota, MN, 2009.

W. Thornton, "On the analysis and design of bracing connections," in *Proceedings, National Steel Construction Conference*, 1991, pp. 26–33.

R. Tremblay, "Inelastic seismic response of steel bracing members," *Journal of Constructional Steel Research*, vol. 58, no. 5-8, pp. 665–701, 2002.

R. Tremblay, M. H. Archambault, and A. Filiatrault, "Seismic response of concentrically braced steel frames made with rectangular hollow bracing members," *Journal of Structural Engineering*, vol. 129, pp. 1626–1636, 2003.

P. Uriz, "Towards earthquake resistant design of concentrically braced steel structures," Ph.D. dissertation, Civil and Environmental Engineering Dept., University of California, Berkeley, Berkeley, CA, 2005.

S. Walbridge, G. Grondin, and J. Cheng, "Gusset plate connections under monotonic and cyclic loading," *Canadian Journal of Civil Engineering*, vol. 32, no. 5, pp. 981–995, 2005.

R. Whitmore, "Experimental Investigation of Stresses in Gusset Plates," University of Tennessee, Tech. Rep. No. 16, 1952.

V. R. Wigle and L. A. Fahnestock, "Buckling-restrained braced frame connection performance," *Journal of Constructional Steel Research*, vol. 66, no. 1, pp. 65–74, 2010.

G. Williams, "Steel connection designs based on inelastic finite element analysis," The University of Arizona, Tucson, AZ, Tech. Rep., 1986.

M. Yam and J. Cheng, "Behavior and design of gusset plate connections in compression," *Journal of Constructional Steel Research*, vol. 58, no. 5-8, pp. 1143–1159, 2002.

J. Yoo, "Analytical investigation on the seismic performance of special concentrically braced frames," Ph.D. dissertation, Civil and Environmental Engineering Dept., University of Washington, Seattle, WA, 2006.

J. Yoo, D. Lehman, and C. Roeder, "Influence of connection design parameters on the seismic performance of braced frames," *Journal of Constructional Steel Research*, vol. 64, no. 6, pp. 607–623, 2008.

Appendix A

SPECIMEN DESIGN

A.1 SCBF Gusset Plate Design

This section will discuss and show the calculations for the design of the gusset plates of the SCBF specimen with buckling braces. Full calculations are shown for two of the gusset plates: one at the second floor beam framing into the shared column and the other at the base of column A-1 (or B-2). The calculations shown are based on either the Balanced Design Procedure (BDP) or the AISC limit states as described in Chapter 3.

A.1.1 Brace Slenderness Limit Check

HSS3x3x1/4 were used in this frame and satisfy the local and global slenderness ratios per the Seismic Provisions [AISC, 2010] as shown below.

Local compactness criteria:

$\frac{b}{t} \leq \lambda_{ps} = 0.55\sqrt{\frac{E}{F_y}}$

$\frac{b}{t} = 9.88 \leq \lambda_{ps} = 0.55\sqrt{\frac{29000}{46}} = 13.8$ **O.K.**

Global compactness criteria [AISC, 2005a]:

$\frac{KL}{r} \leq 4\sqrt{\frac{E}{F_y}}$

$\frac{KL}{r} = \frac{0.5(101.8)}{1.11} = 91 \leq 4\sqrt{\frac{E}{F_y}} = 4\sqrt{\frac{29000}{46}} = 100.4$ **O.K.**

In reality, since the columns were designed using capacity principles, the brace slenderness need only be less than 200. The effective length factor of 0.5 was used because the tension brace acts as an out-of-place lateral support. The length used was the distance defined by the intersection of the brace axis and the beam or column flange interface with the gusset plate.

A.1.2 Design Brace Forces

The brace forces for connection design are as follows:

In tension:

$P_t = R_y F_y A_g = 1.4(46)(2.44) = 157$ kips

In compression:

$\frac{KL}{r} = 91 \leq 4.71\sqrt{\frac{E}{F_y}} = 4.71\sqrt{\frac{29000}{46}} = 118.3.$

Therefore use Equation 3.19 repeated below.

$$F_{cr} = \left[0.658^{\frac{F_y}{F_e}}\right] F_y$$

Need to find the Euler buckling stress first

$$F_e = \frac{\pi^2 E}{\left(\frac{KL}{r}\right)^2} = \frac{(3.14159)^2(29000)}{(91)^2} = 34.6 \text{ ksi}$$

Then

$$F_{cr} = \left[0.658^{\frac{F_y}{F_e}}\right] F_y = \left[0.658^{\frac{46}{34.6}}\right] 46 = 26.4 \text{ ksi}$$

Finally, the design brace force in compression

$$1.1P_c = 1.1R_yP_n = 1.1(1.4)(26.4)(2.44) = 99 \text{ kips}$$

A.1.3 Brace to Gusset Connection

Brace to gusset weld

Assume 1/4 in. fillet welds on four sides of the brace.

$\phi R_n = (4sides)1.392Dl_w = 157$ kips

Then

$l_w = \frac{157}{4(1.392)(4)} = 7.0$ in.

Note that the 1.392 in the above equation comes from:

$1.392 = \phi(0.6F_{EXX})\frac{\sqrt{2}}{2}\frac{1}{16}$ with ϕ=0.75 and F_{EXX}=70 ksi

Use 1/4" fillet weld 8 in. long

Rupture strength of base brace material

HSS3x3x1/4 wall thickness = 0.233 in.

Weld strength:

$\phi R_n = 1.392(4 \text{ sixteenths})(1 \text{ in.}) = 5.6$ k/in.

HSS rupture strength:

$\phi R_n = 0.75(0.6F_u)t = 0.75(0.6)(58)(0.233) = 6.1$ k/in. > 5.6 k/in. **O.K.**

A.1.4 Gusset Plate Limit States (all gussets)

Yielding on the Whitmore width

Whitmore width:

$$B_w = b_{HSS} + 2l_w(\tan 30) = 3 + 2(8)(0.577) = 12.24 \text{ in.}$$

Yielding:

$$\beta R_n = \beta R_y F_y B_w t_g \geq 157$$

$$t_g = \frac{157}{1.0(1.1)(50)(12.24)} = 0.23 \text{ in.}$$

Fracture on the Whitmore width

$$\beta R_n = \beta F_u B_w t_g$$

$$t_g = \frac{157}{0.85(65)(12.24)} = 0.23 \text{ in.}$$

Block shear rupture

$$\beta R_n = \beta(0.6F_u A_{nv} + U_{bs} F_u A_{nt})$$

$$\beta R_n = \beta\left[0.6F_u(2l_w)t_g + U_{bs}F_u(b_{HSS}t_g)\right]$$

$$t_g = \frac{157}{0.6(65)(2)(8)+1.0(65)(3)} = 0.19 \text{ in.}$$

Try 1/4" thick gusset plates for all gussets except the brace splice

A.1.5 Brace Splice Gusset Plate Limit States

Yielding on the Whitmore width

As mentioned in Chapter 3, the gusset plate width, B_w' at this location was less wide than the Whitmore width.

Gusset width:

$$B_w\text{'} = 9.81 \text{ in.}$$

Yielding:

$$\beta R_n = \beta R_y F_y B'_w t_g \geq 157$$

$$t_g = \frac{157}{1.0(1.1)(50)(9.81)} = 0.29 \text{ in.}$$

Fracture on the width

$\beta R_n = \beta F_u B'_w t_g$

$t_g = \frac{157}{0.85(65)(9.81)} = 0.29$ in.

Block shear rupture

$\beta R_n = \beta(0.6F_u A_{nv} + U_{bs} F_u A_{nt})$

$\beta R_n = \beta\left[0.6F_u(2l_w)t_g + U_{bs}F_u(b_{HSS}t_g)\right]$

$t_g = \frac{157}{0.6(65)(2)(8)+1.0(65)(3)} = 0.19$ in.

Try 3/8" thick gusset plate at brace splice.

A.1.6 Gusset plate buckling limit state

Based on the previous limit states, a gusset plate thickness of 1/4 in. will be checked for buckling on the Whitmore width for all of the gussets except at the brace splice where a 3/8 in. thick gusset will be checked. Figure A.1 shows the four conditions for which buckling needs to be checked. Shown in the figure is the three buckling lengths that are averaged to determine the buckling length to be used in the calculations per the Thornton method. Note in Figures A.1a and A.1c that the lengths were calculated ignoring the stiffening effect of the continuity plates used to transfer the brace force into the column web and flanges. An example calculation is shown for the gusset plate framing into the flange of the column at the floor level and the results for all gussets are shown in Table A.1. The buckling demand-capacity ratios for the gusset plates framing into the webs of the shared columns are slightly larger than unity. It was felt that this was reasonable as the effective length is less than that calculated due to the stiffeners noted previously.

Calculate the average buckling length:

$l_{b,ave} = \frac{\sum l_i}{3} = \frac{11.54+7.77-1.92}{3} = 5.8$ in.

Note that when one of the buckling lengths begins within the beam or column the length is taken as negative.

The slenderness ratio is evaluated using an effective length factor of 0.65:

$\frac{Kl}{r} = \frac{0.65(5.8)}{0.25}\sqrt{12} = 52.2$

Table A.1: SCBF Gusset plate buckling limit state parameters

Mark	l_{ave} (in.)	Kl_{ave} (in.)	$\frac{Kl_{ave}}{r}$	F_{cr} (ksi)	$\beta\ P_{cr}$ (kips)	$\frac{P_c}{\beta P_{cr}}$
GP-1	2.7	1.8	24.3	47.8	132	0.75
GP-2	5.8	3.8	52.8	40.8	113	0.88
GP-3	7.7	5.0	69.5	35.1	97	1.02
GP-4	7.8	5.1	70.9	34.6	95	1.04
GP-5	2.4	2.8	26.2	42.7	157	0.63

Note that the effective length factor used for the brace splice was 1.2.

This is less than $4.71\sqrt{\frac{E}{F_y}} = 4.71\sqrt{\frac{29000}{50}} = 113.4$, therefore use Equation 3.19.

$$F_{cr} = \left[0.658^{\frac{F_y}{F_e}}\right] F_y$$

Need to find the Euler buckling stress first

$$F_e = \frac{\pi^2 E}{\left(\frac{KL}{r}\right)^2} = \frac{(3.14159)^2(29000)}{(52.2)^2} = 105 \text{ ksi}$$

Then

$$F_{cr} = \left[0.658^{\frac{F_y}{F_e}}\right] F_y = \left[0.658^{\frac{50}{105}}\right] 50 = 41 \text{ ksi}$$

Finally, the gusset plate buckling resistance is:

$$\beta P_{cr} = \beta F_{cr} A_g = \beta F_{cr} B_w t_g = 0.9(41)(12.24)(0.25) = 113 \text{ kips} > 99 \text{ kips } \textbf{O.K.}$$

A.1.7 Gusset interface weld design

The gusset interface welds are designed for the strength of the gusset plate per Equation 3.36 to ensure stable and ductile performance of the connection region prior to brace fracture [Roeder et al., 2011]. $2(1.5)\beta(0.6)F_{EXX}t_{eff} \geq R_y F_y t_g = 1.1(50)(0.25) = 13.75$ k/in. Rearranging for D: $D = \frac{2(16)(13.75)}{2(1.5)(0.75)(0.6)(70)sqrt2} = 3.3$ sixteenths

Use 1/4" weld each side of gusset plates

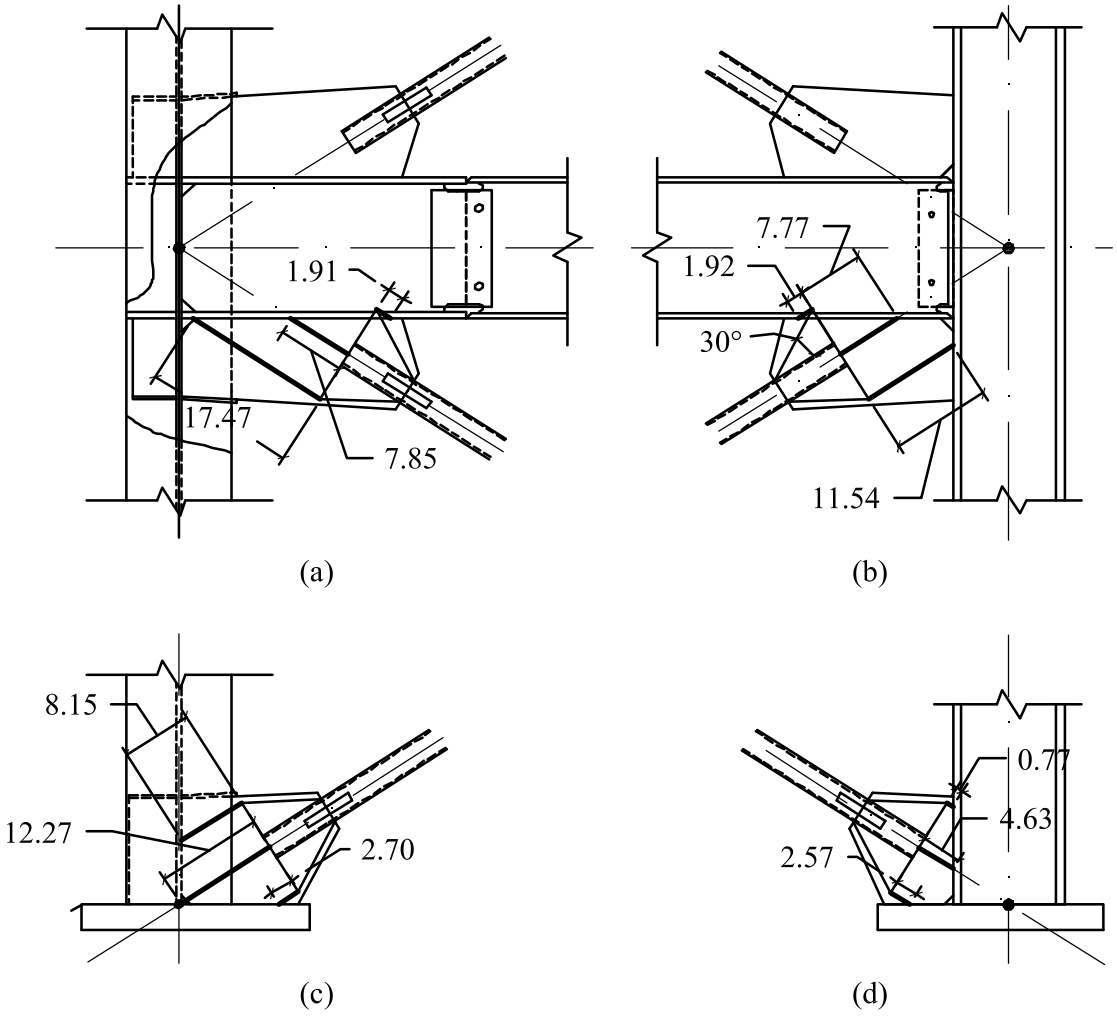

Figure A.1: Gusset plate buckling lengths per the Thornton method: (a) gussets framing into the shared column web (GP-4); (b) gussets framing into the flanges of all braced frame columns at floor levels (GP-2); (c) gusset framing into web at base of shared column (GP-3); (d) gussets framing into column flange at base of shared column and columns A-1 and B-2 (GP-1). (See Figure 3.13 for gusset plate mark locations)

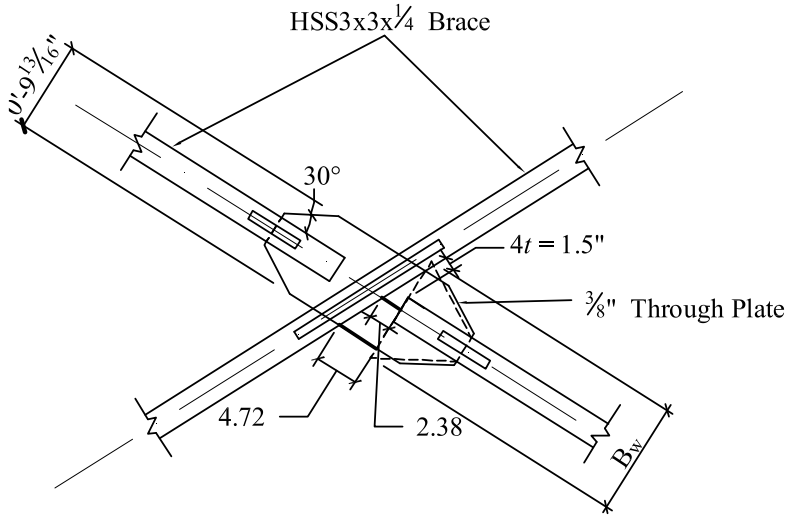

Figure A.2: Gusset plate buckling length at brace splice per the Thornton method)

A.2 Column Panel Zone Calculations

The panel zones of the braced frame columns were analyzed to determine if the webs were adequately sized to prevent yielding according to the current philosophy used for moment frames [AISC, 2010]. This check is typically not performed by practicing engineers during the design of braced frame columns and is not required by AISC [2010]. This check was performed for the test frame columns however web doublers were not installed in columns A-1 and B-2 at the WFWW beam connections where the calculations showed that the webs would be inadequate if this provision were followed. The check was performed as a basis for assessing the behavior of panel zones in braced frame systems where gussets plate occur above, below or at both locations on a beam at the joint.

The forces on the panel zones were determined according to the forces shown in Figure A.3. It was assumed that the beams formed plastic hinges at a distance of $d/2$ from the gusset plate reentrant corners and the column moments were determined from equilibrium and assuming plastic hinges formed at joints away from the joint in question.

The plastic moment at the beam face was determined ignoring axial load in the beam and calculated from Equation A.1 below.

$$M_b = 1.1 Z_x R_y F_y \tag{A.1}$$

The beam shear is calculated from the equation below

$$V_b = \frac{2M_b}{L'} \tag{A.2}$$

The moment at the column face is found from

$$M_{cf} = M_b + V_b \left(L_g + 0.5 d_b\right) \tag{A.3}$$

where L_g is the horizontal gusset plate dimension and d_b is the beam depth.

This moment is assumed to be transfered to the column solely through the beam flanges and therefore the flange force is:

$$P_f = \frac{M_{cf}}{d_m} \tag{A.4}$$

where d_m is the distance between the flange centroids.

Finally, the panel zone shear is the difference between the above beam flange force and the column shears as shown in Equation A.5.

$$V_{pz} = P_f - V_c \tag{A.5}$$

The capacity of the column web is determined according to [2005b] and is given by the Equation A.6 when the column axial load is less that 75% of the squash load as it is in this case.

$$R_v = 0.6 F_y d_c t_w \left(1 + \frac{3 b_f t_f^2}{d_b d_c t_w}\right) \tag{A.6}$$

The demands, capacities, demand to capacity ratios and shape properties for the W12x72 (column A-1) and W12x106 (column B-1) are listed in Table 3.11. The capacities are based on the measured material strengths.

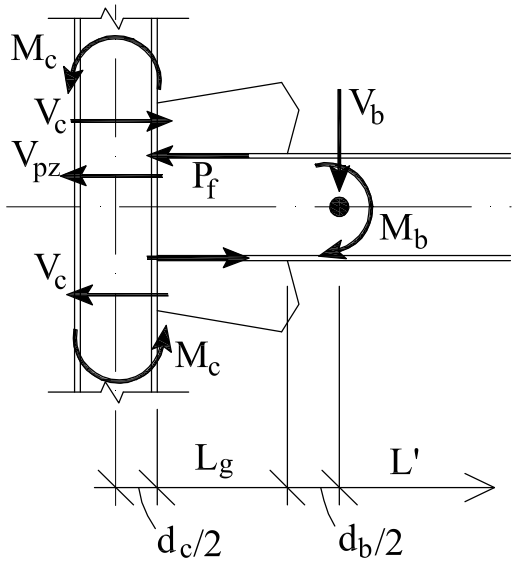

Figure A.3: Column panel zone force diagram

Appendix B

SPECIMEN DRAWINGS

All of the structural steel drawings that were supplied to the steel fabricator, LeJeune Steel Company based in Minneapolis, MN, are provided in this appendix along with the BRBF shop drawings prepared by Star Seismic.

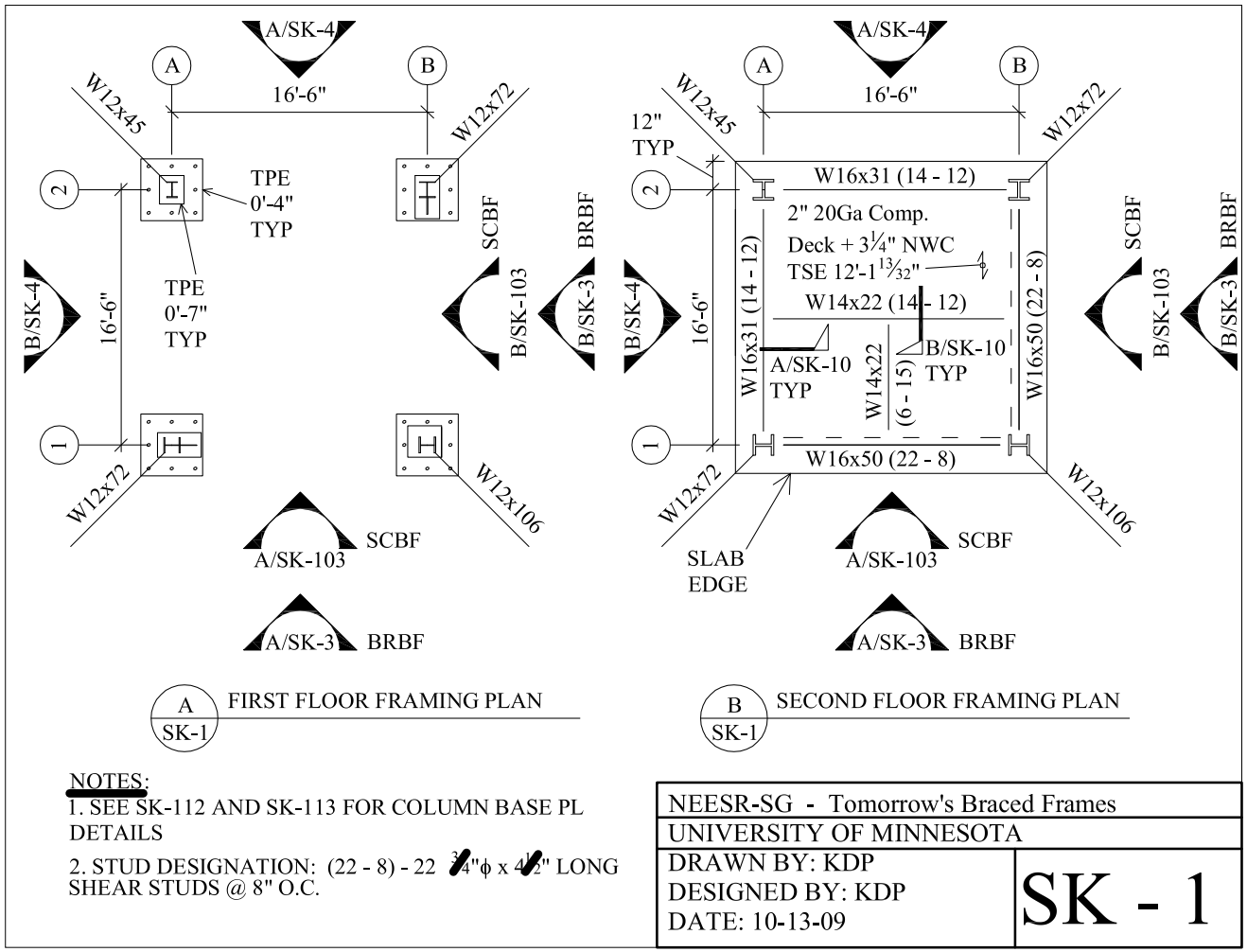

Figure B.1: Specimen floor plans

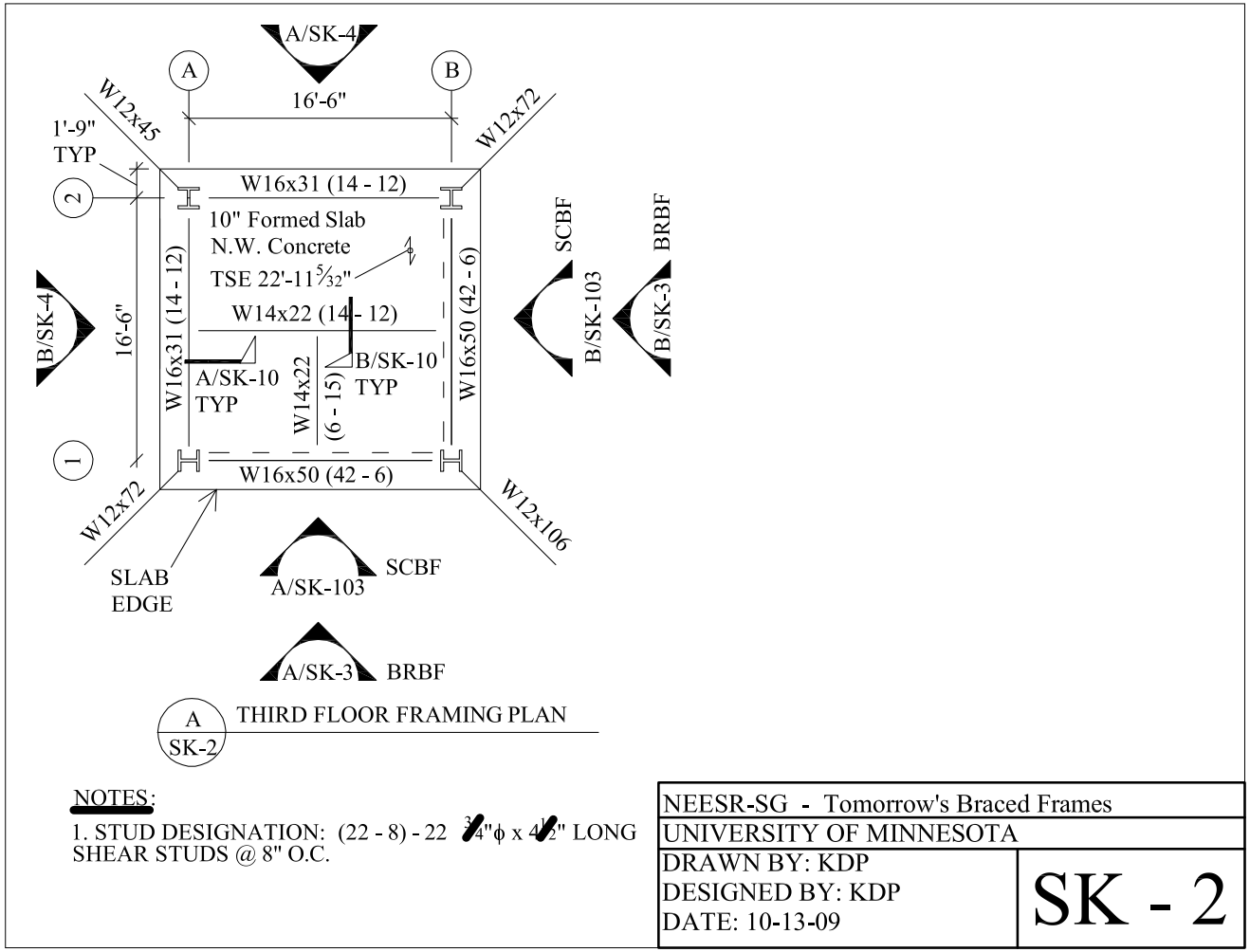

Figure B.2: Specimen floor plan

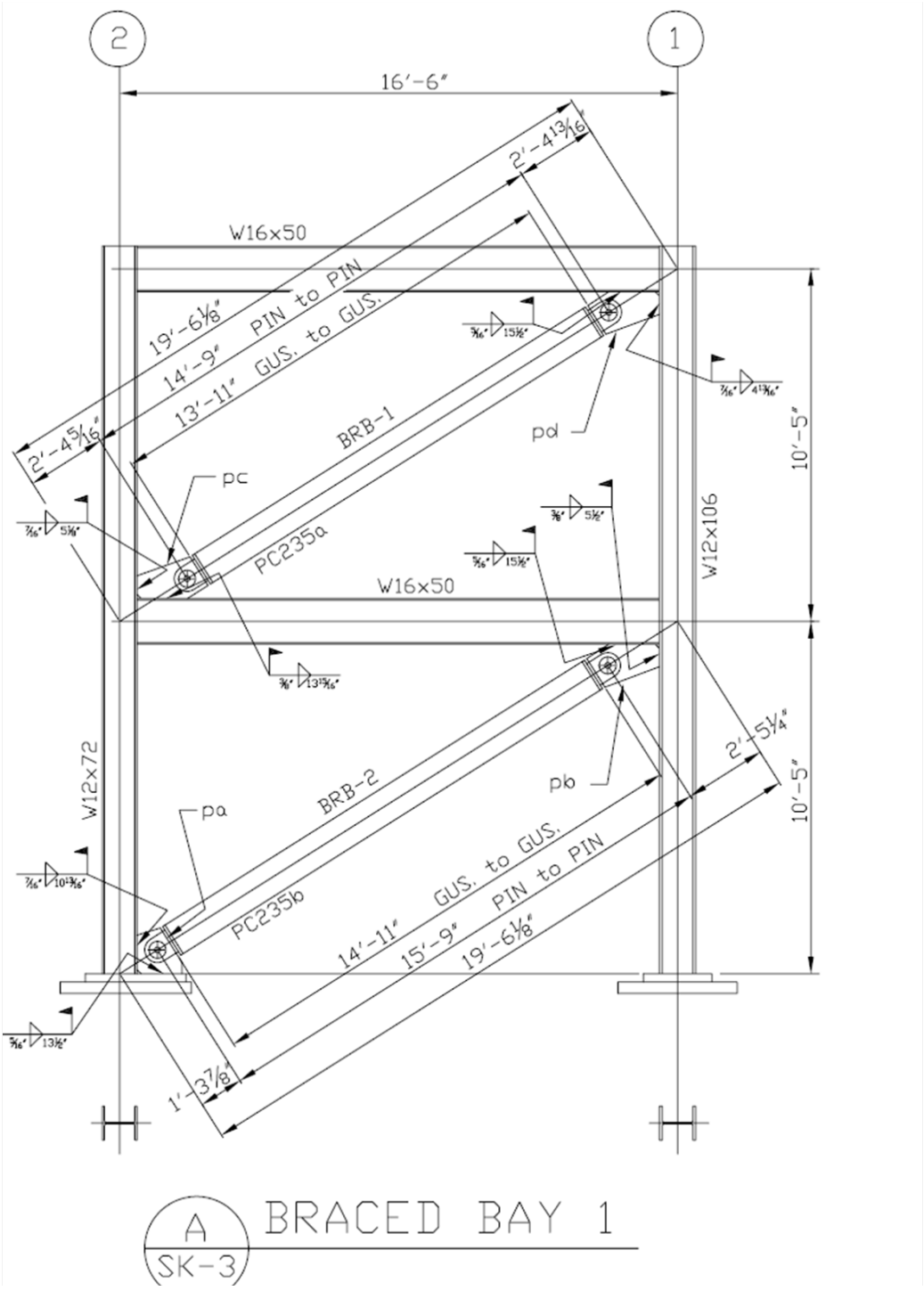

Figure B.3: BRBF Frame 1 elevation

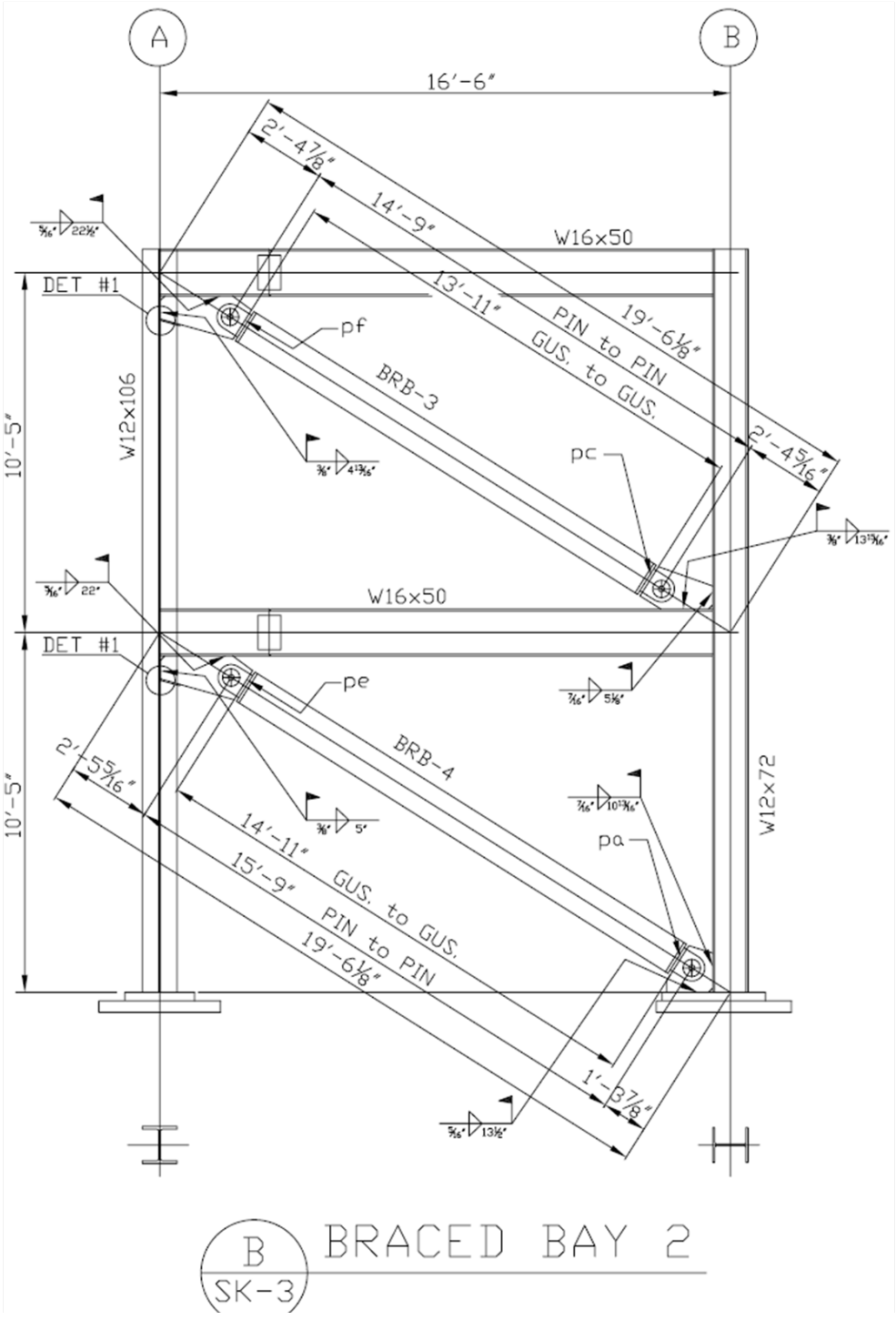

Figure B.4: BRBF Frame B elevation

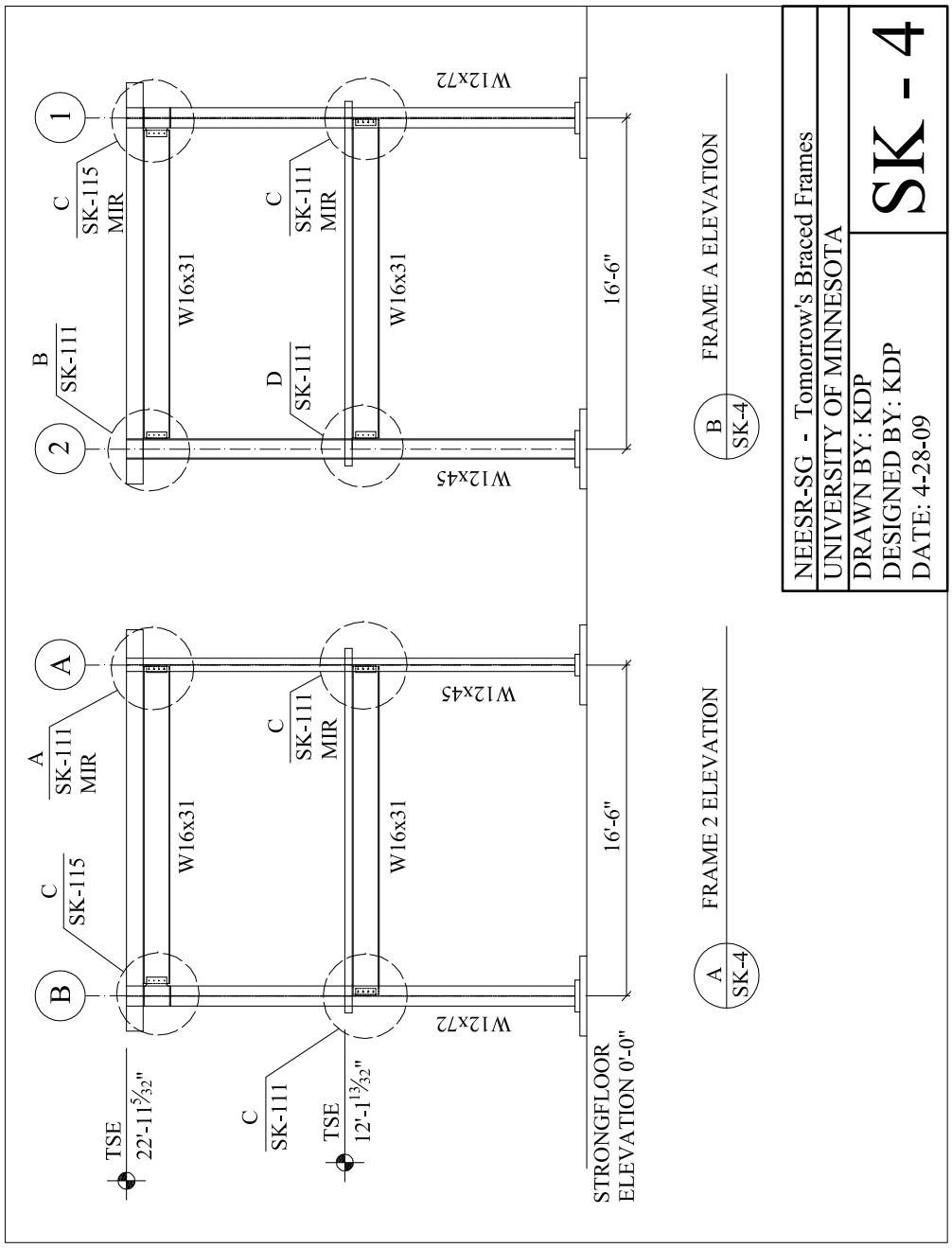

Figure B.5: Gravity frame elevations

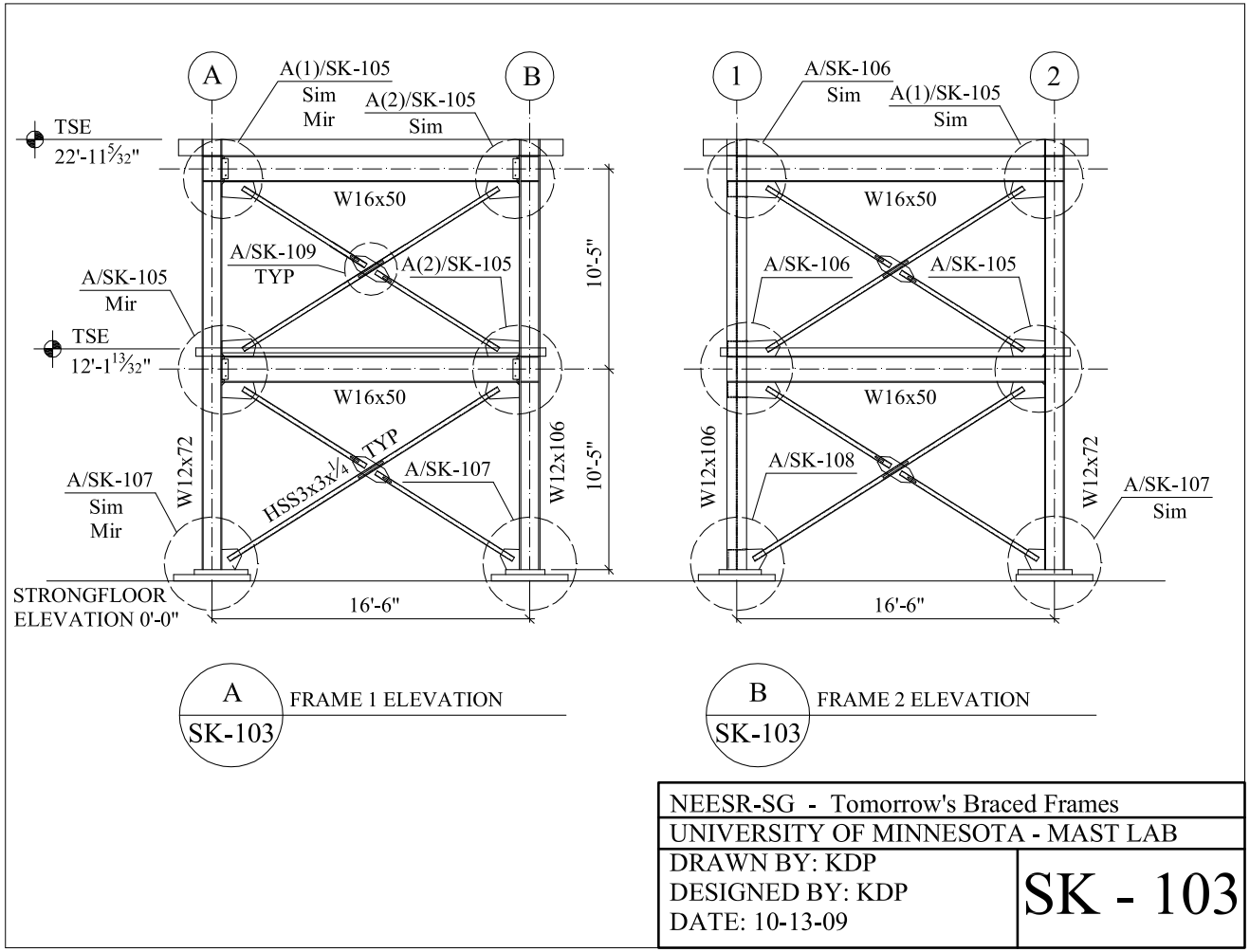

Figure B.6: SCBF frame elevations

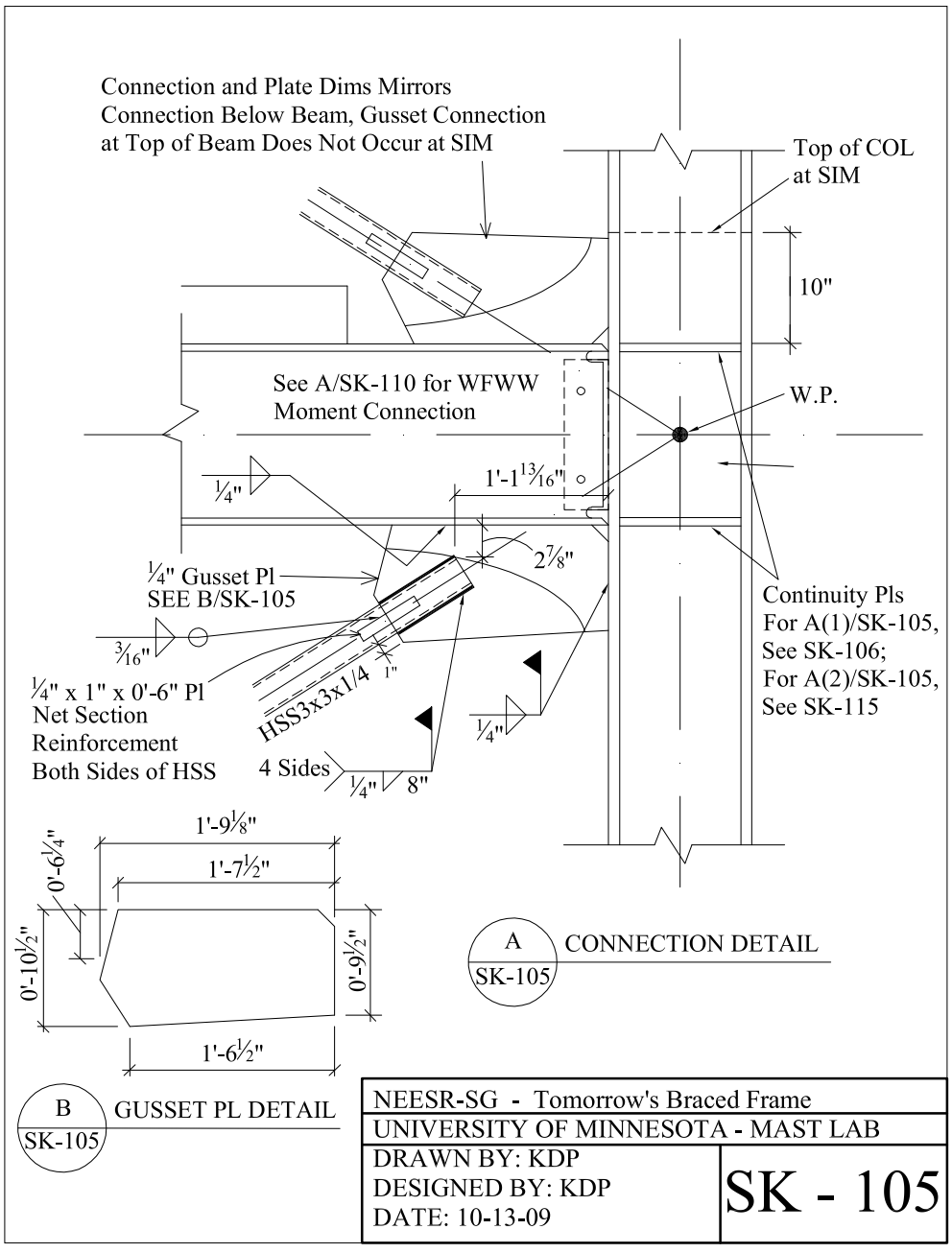

Figure B.7: SCBF gusset plate connection detail

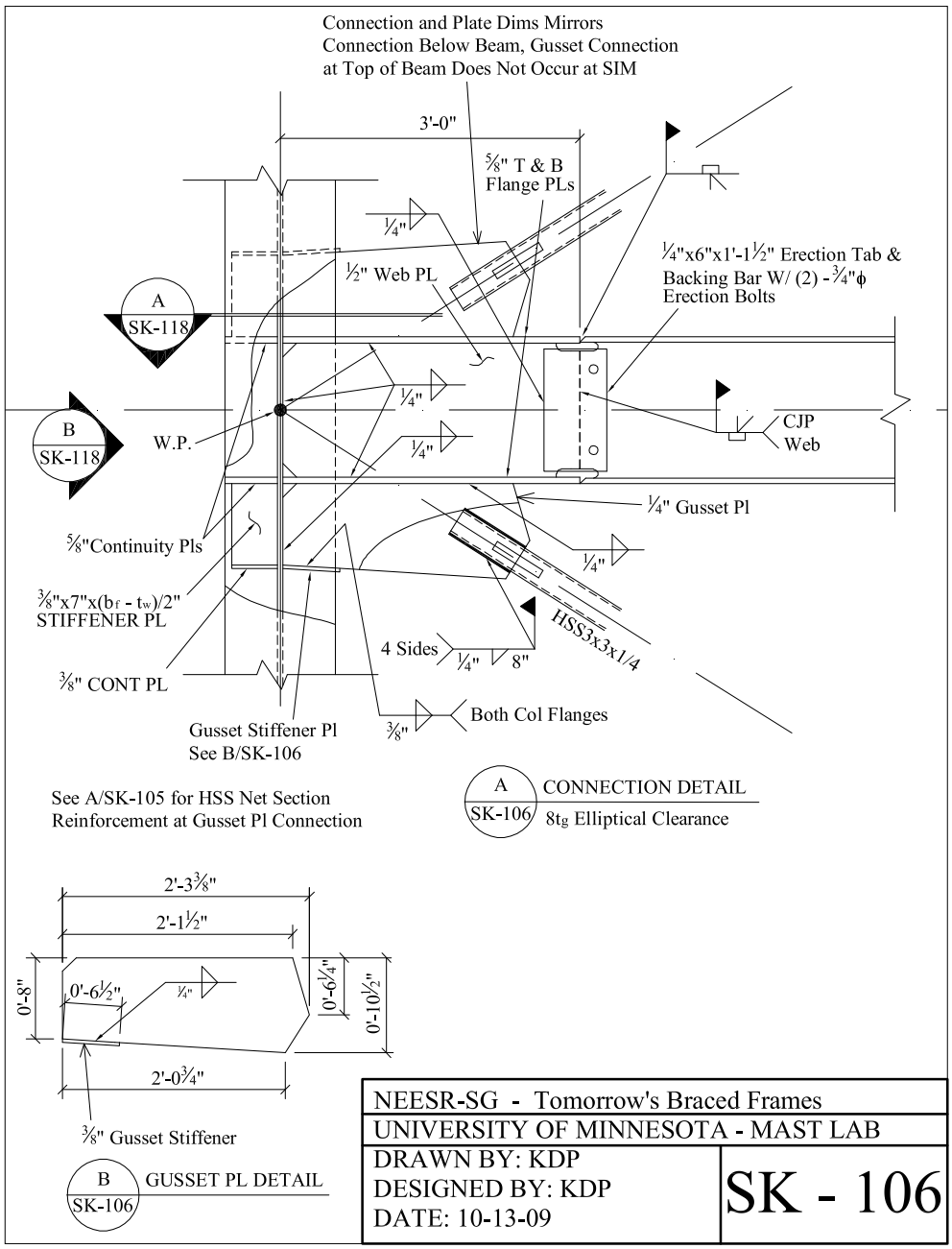

Figure B.8: SCBF gusset plate connection detail

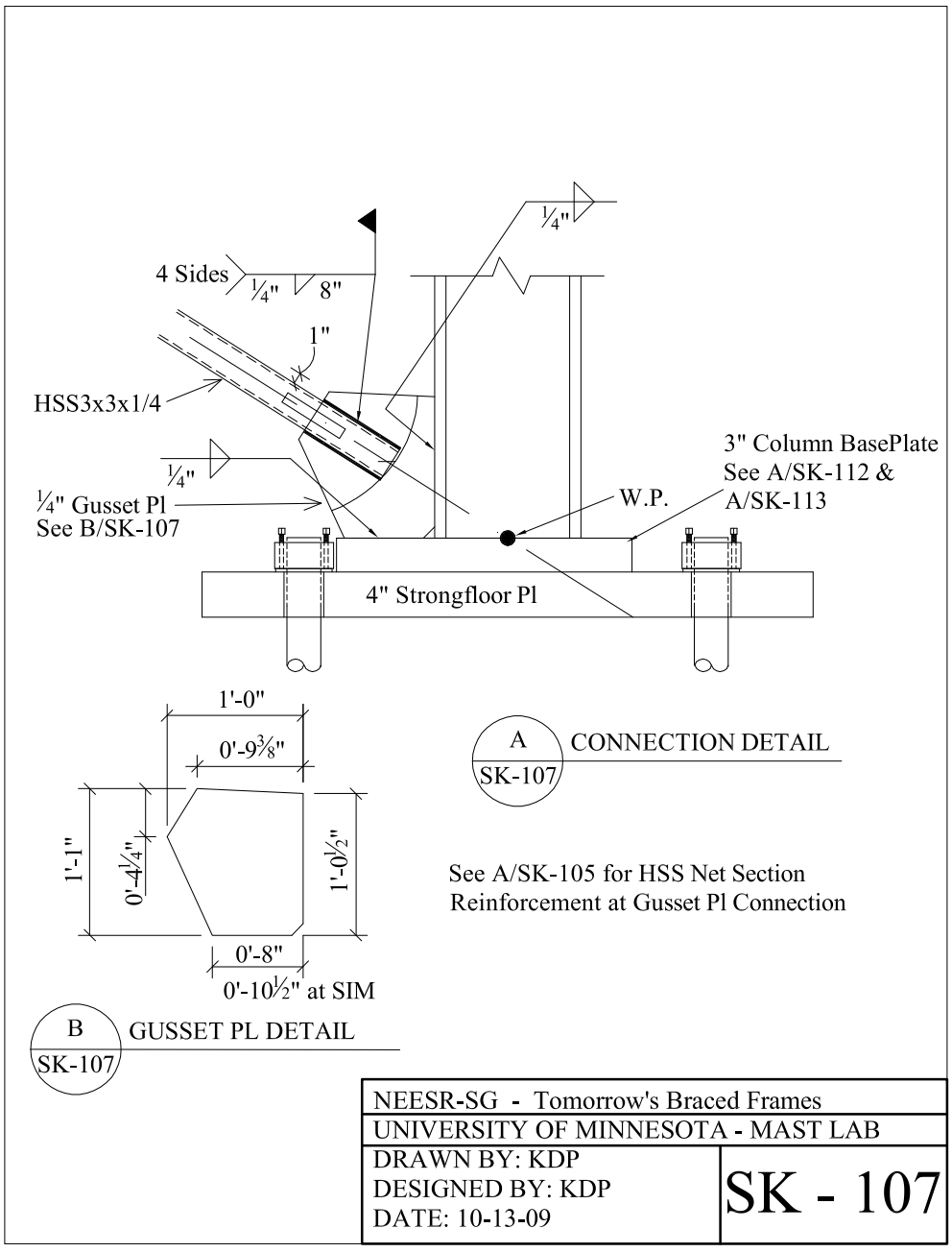

Figure B.9: SCBF gusset plate connection detail

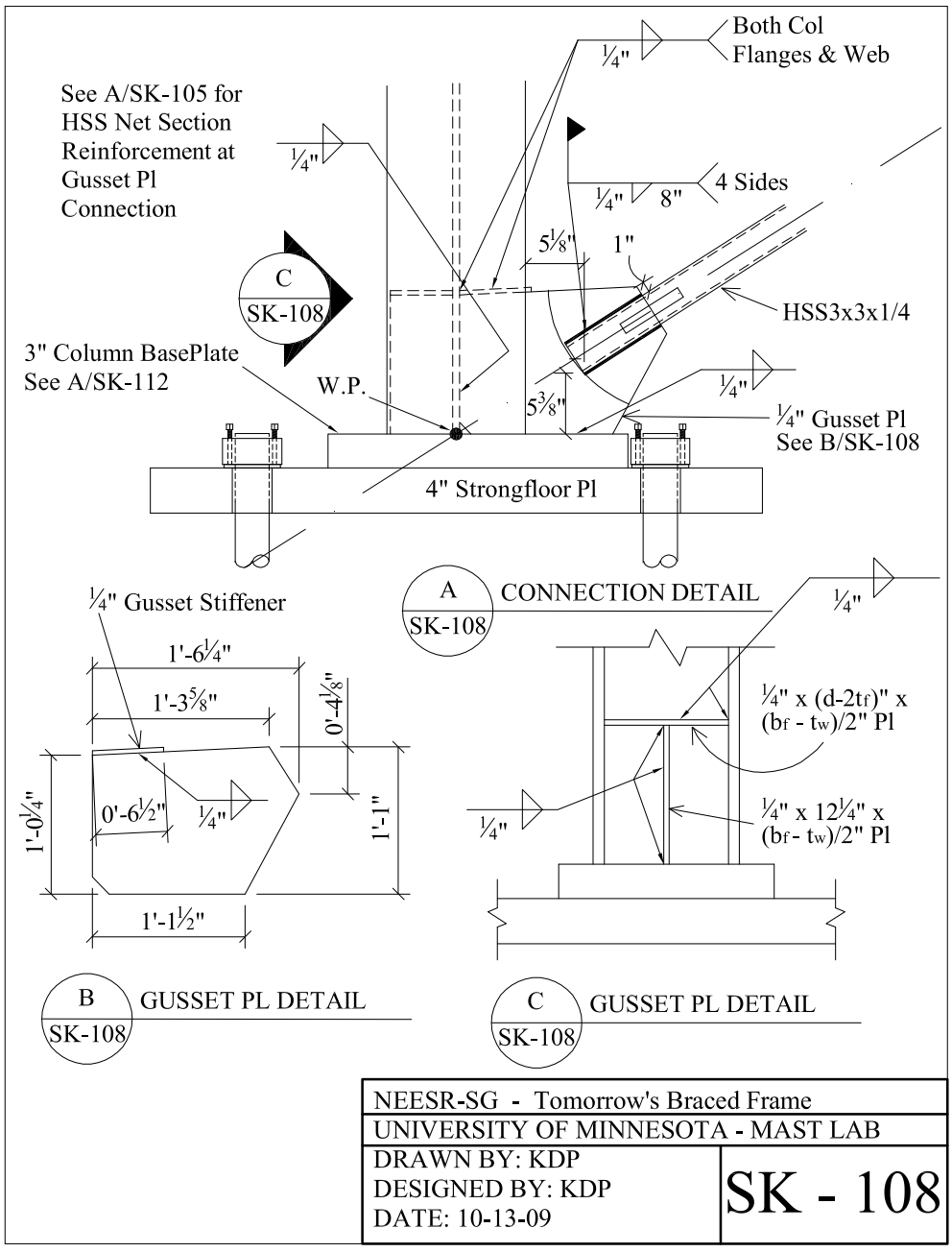

Figure B.10: SCBF gusset plate connection detail

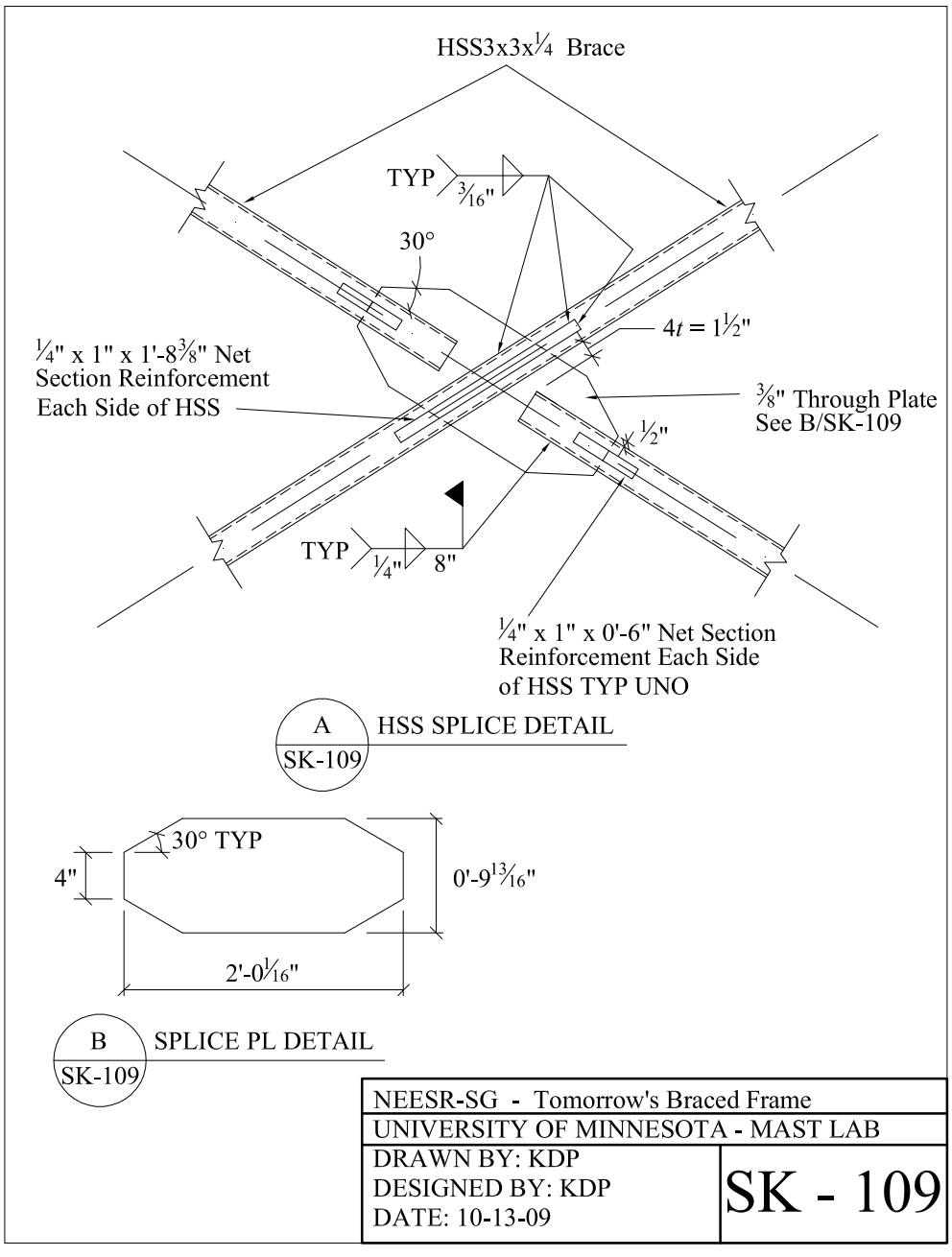

Figure B.11: SCBF gusset plate connection detail

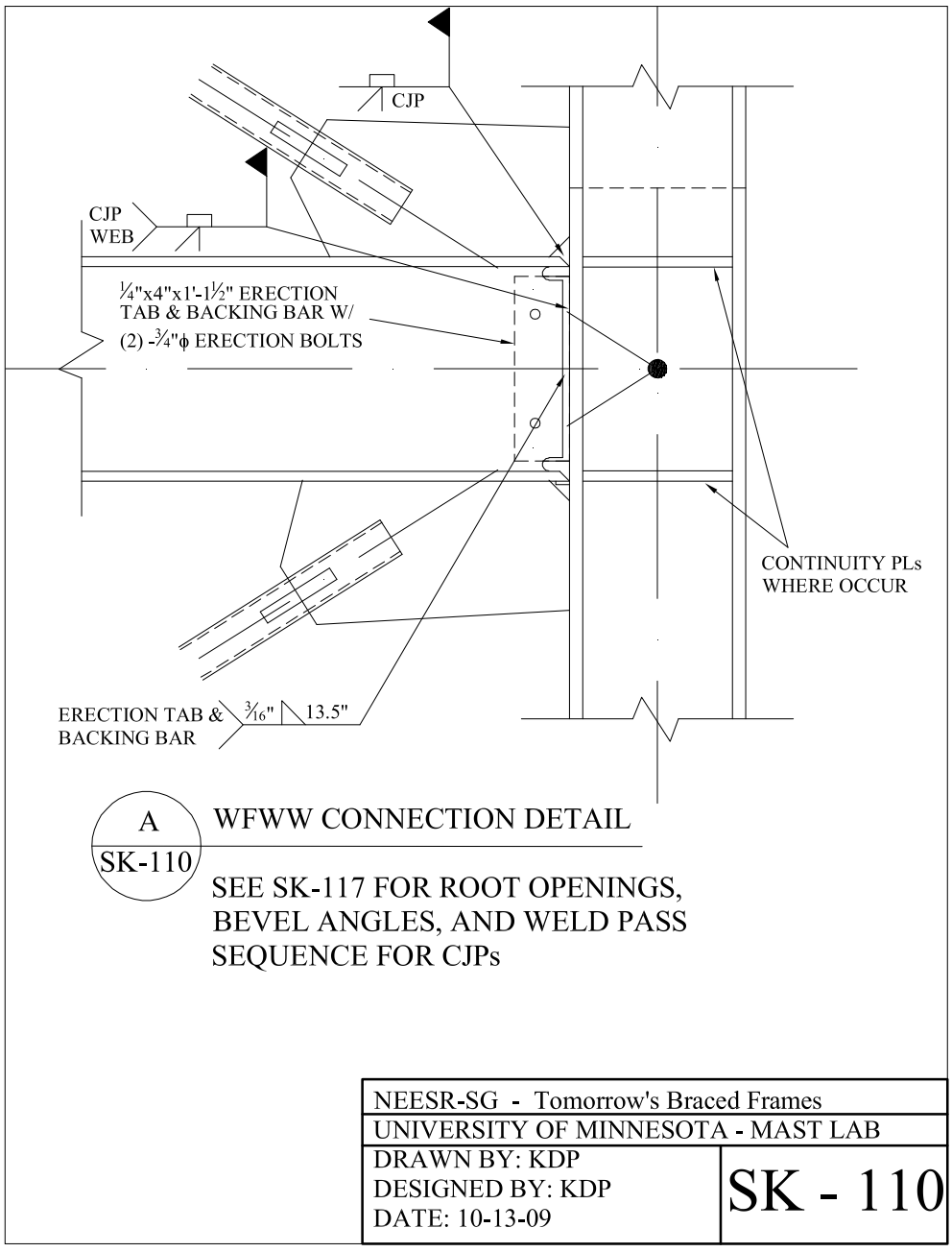

Figure B.12: WFWW beam-to-column connection detail

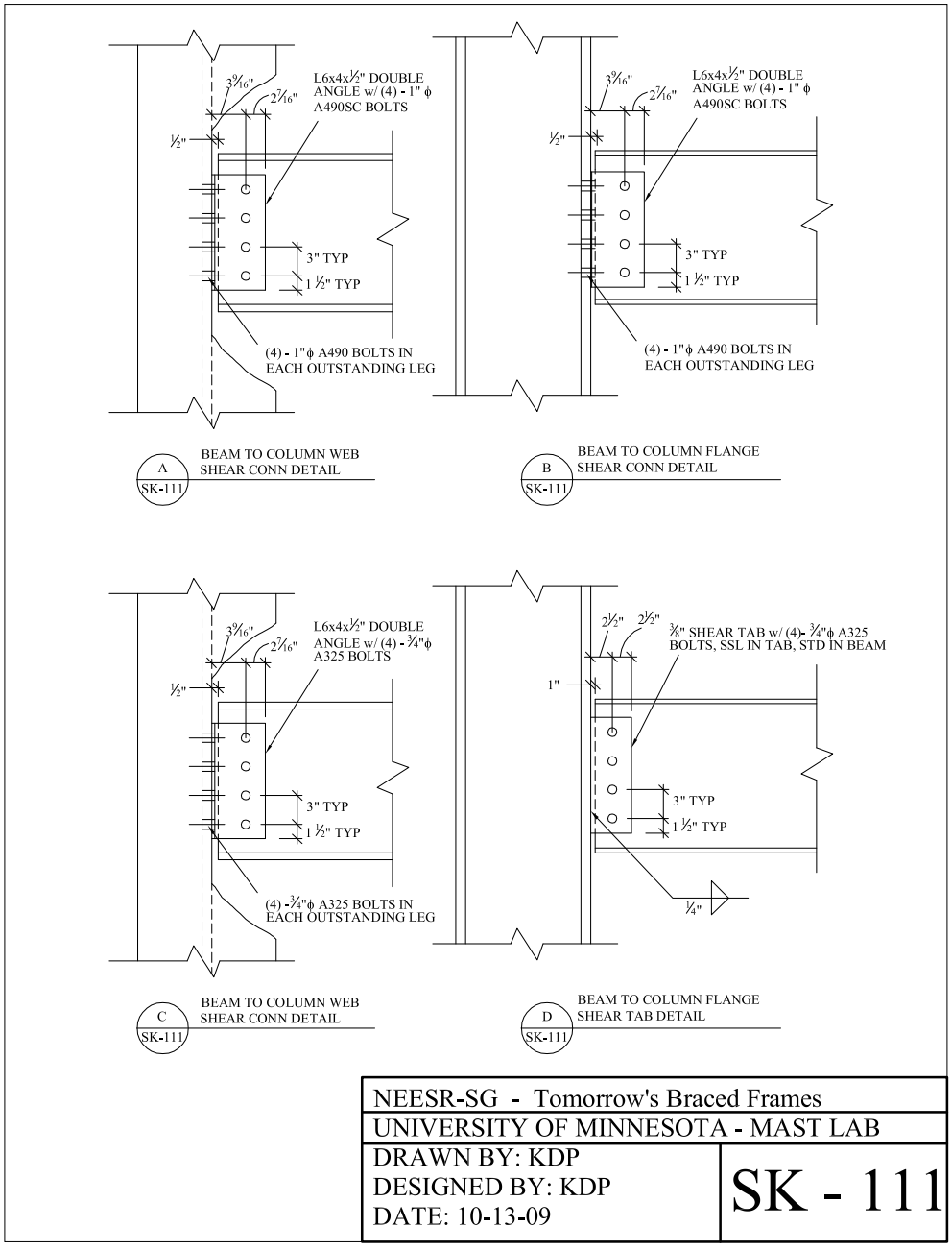

Figure B.13: Shear connection details

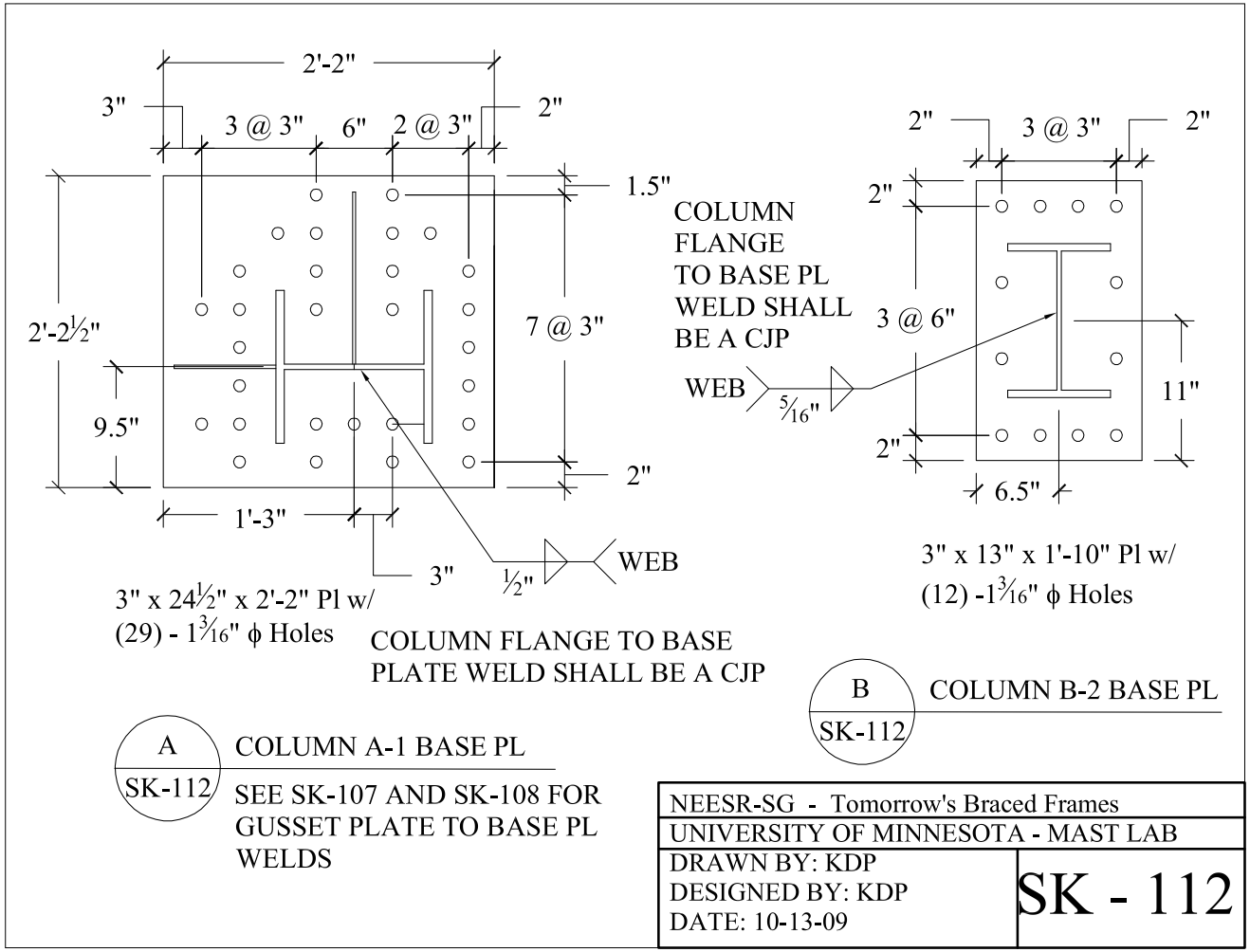

Figure B.14: Base plate details

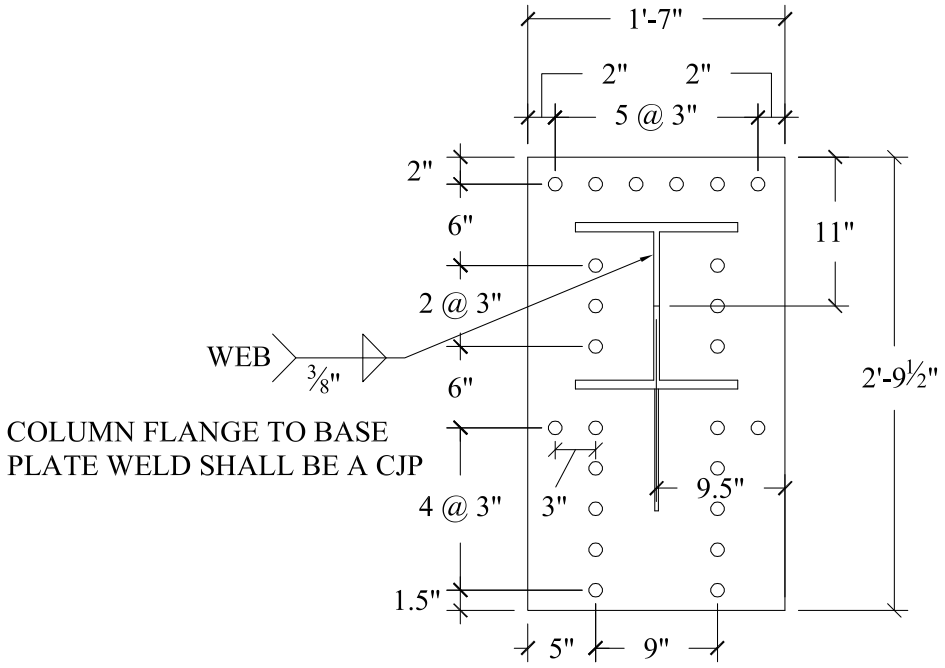

Figure B.15: Base plate detail

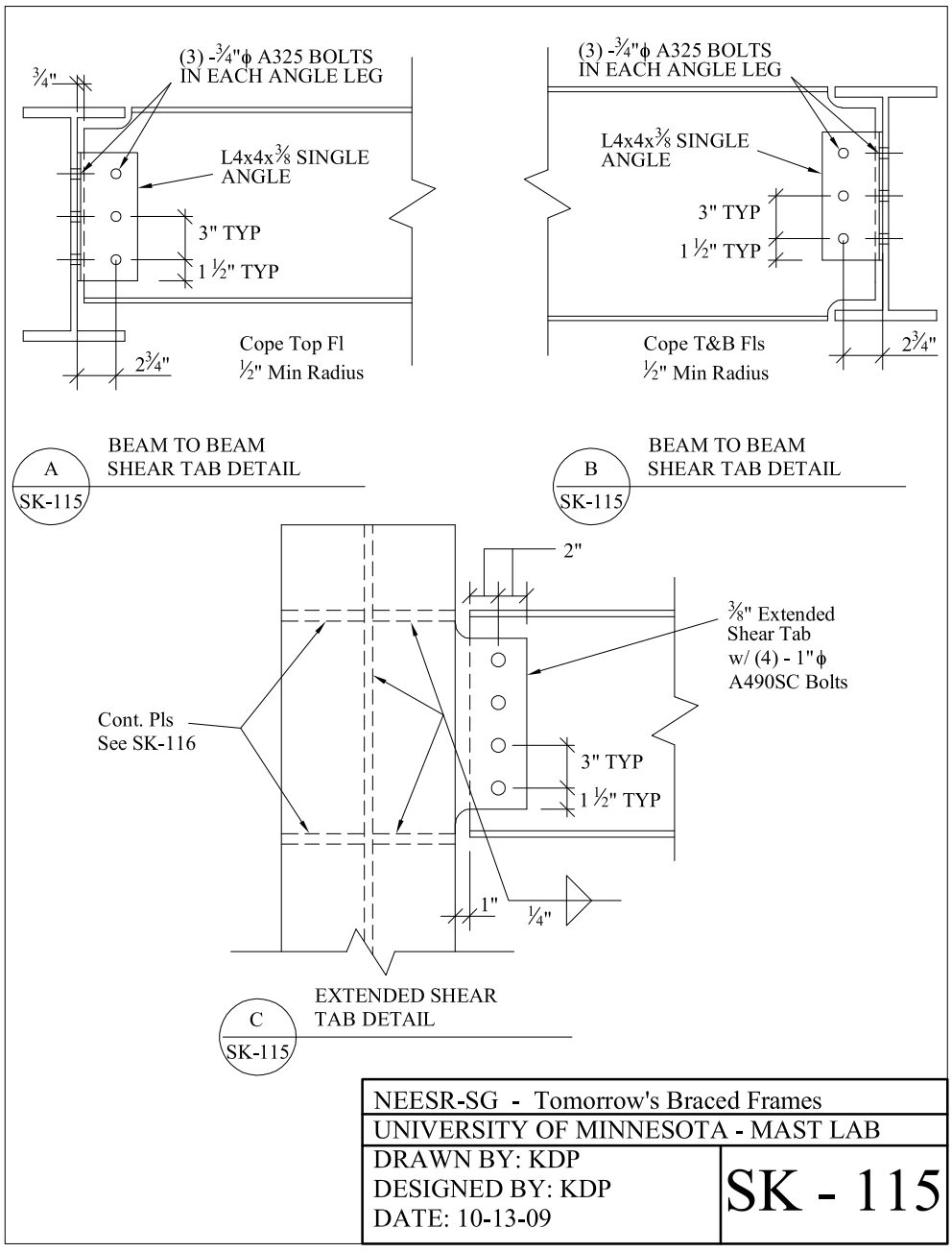

Figure B.16: Shear connection details

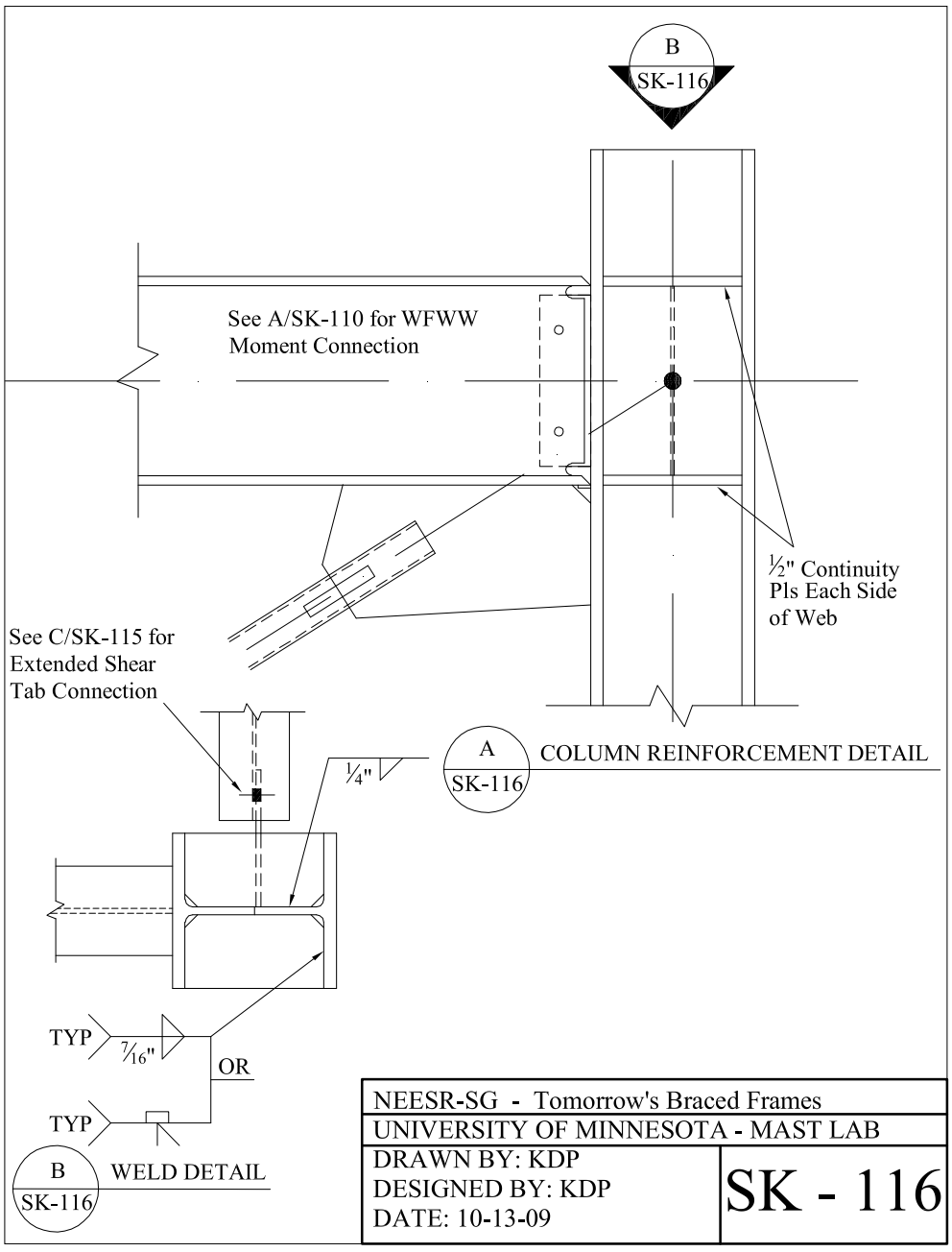

Figure B.17: Column reinforcement details

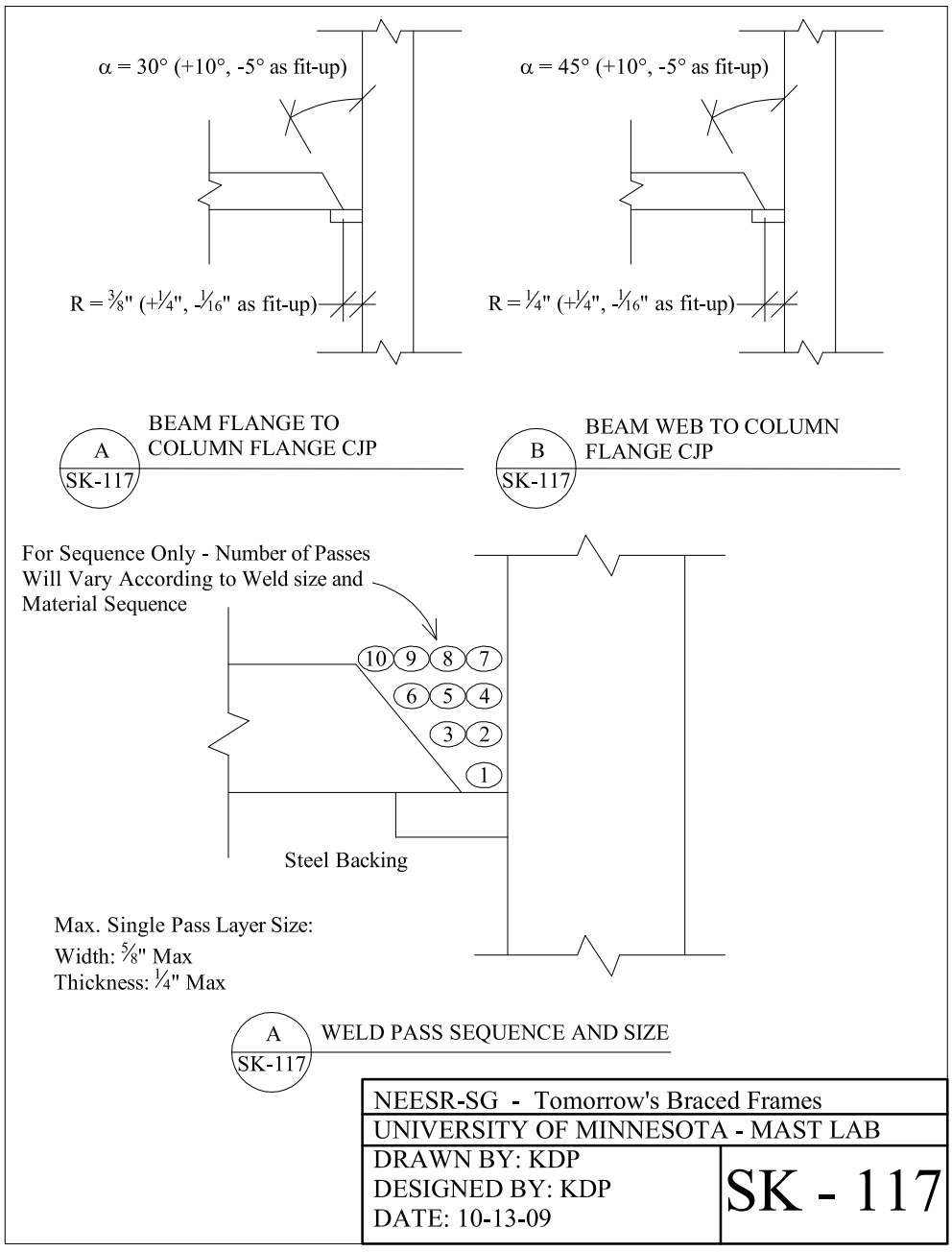

Figure B.18: CJP weld details

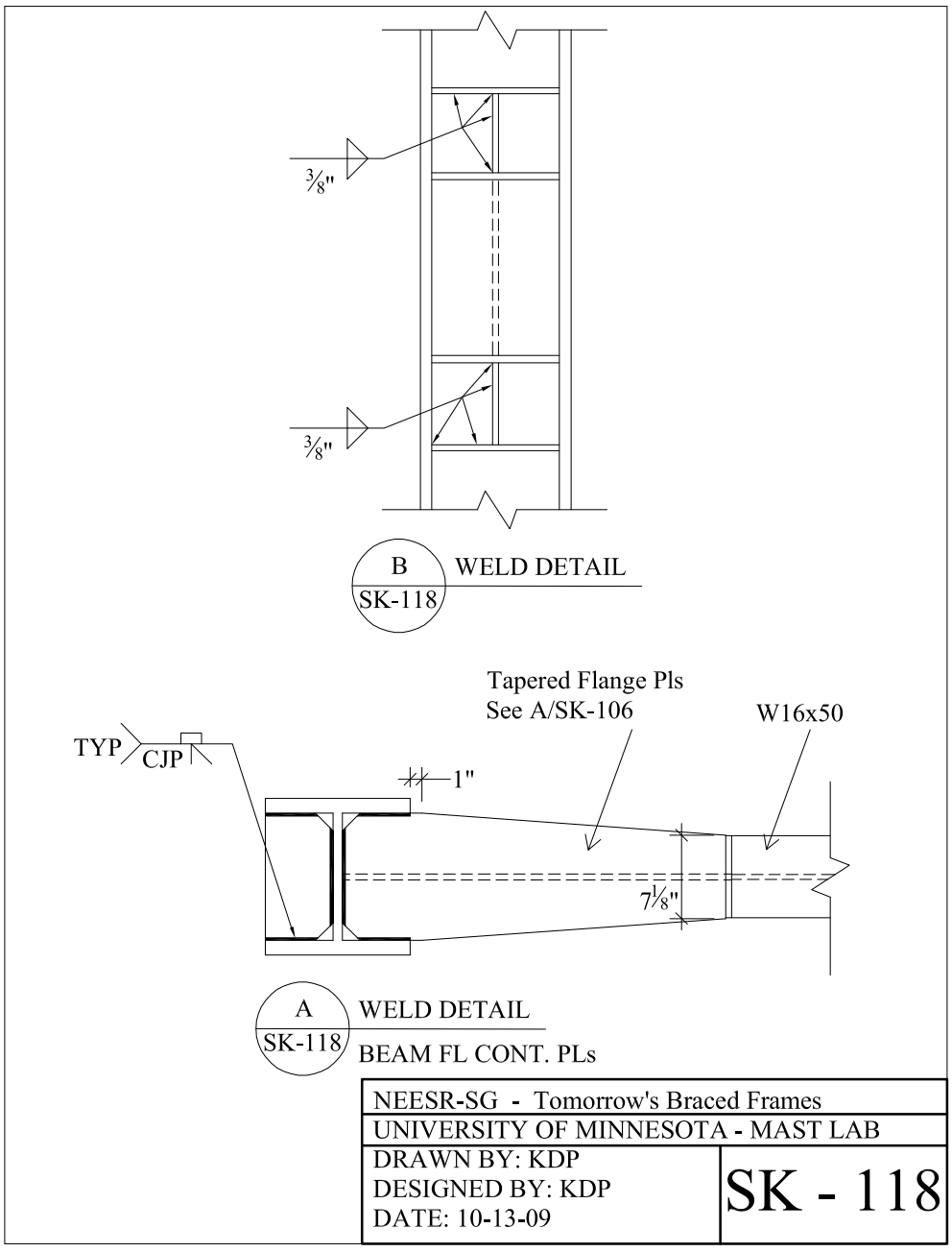

Figure B.19: Beam splice detail

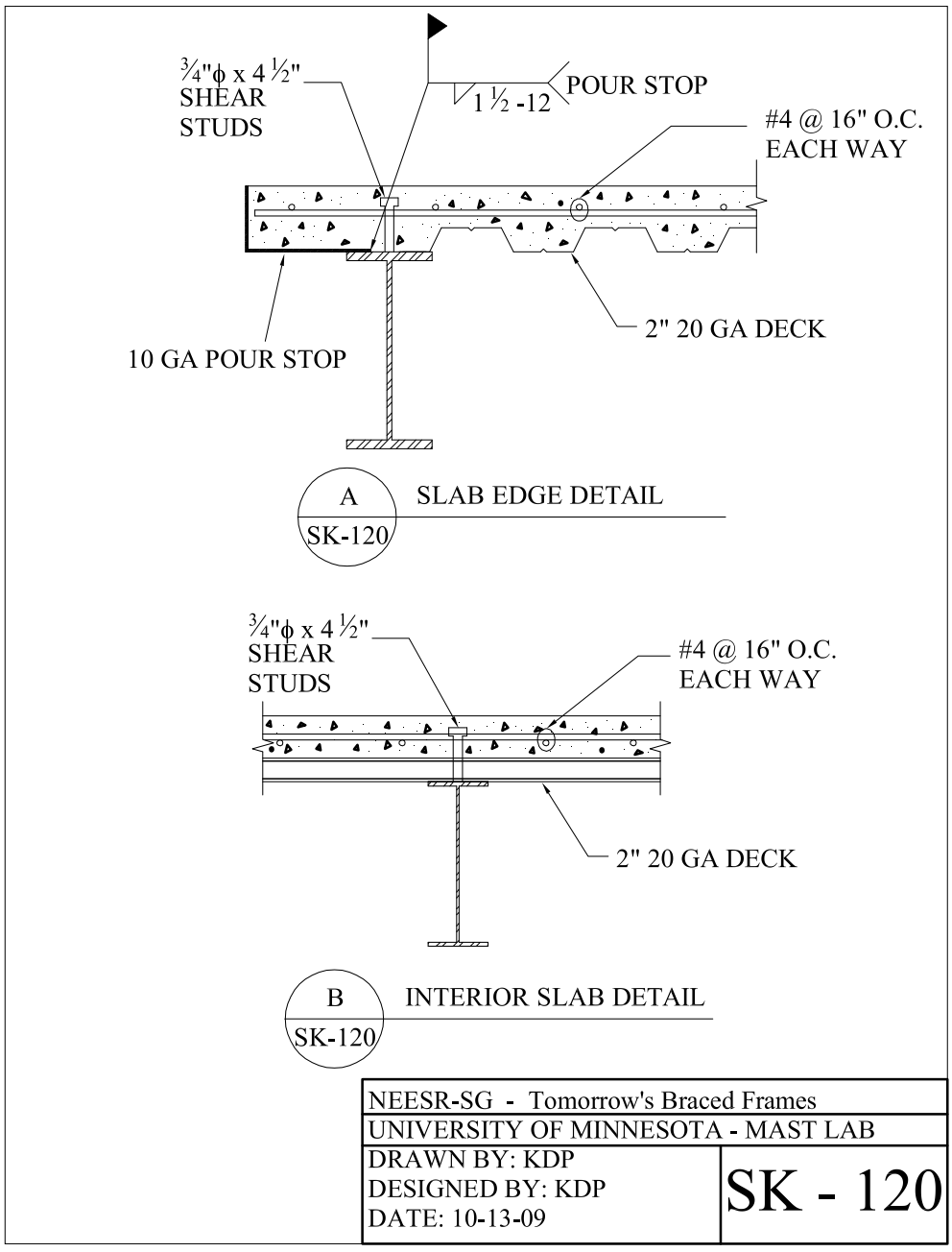

Figure B.20: Floor slab details

The following drawings are the BRB gusset plate details. See A/SK-3 and B/SK-3 for plate locations in elevation.

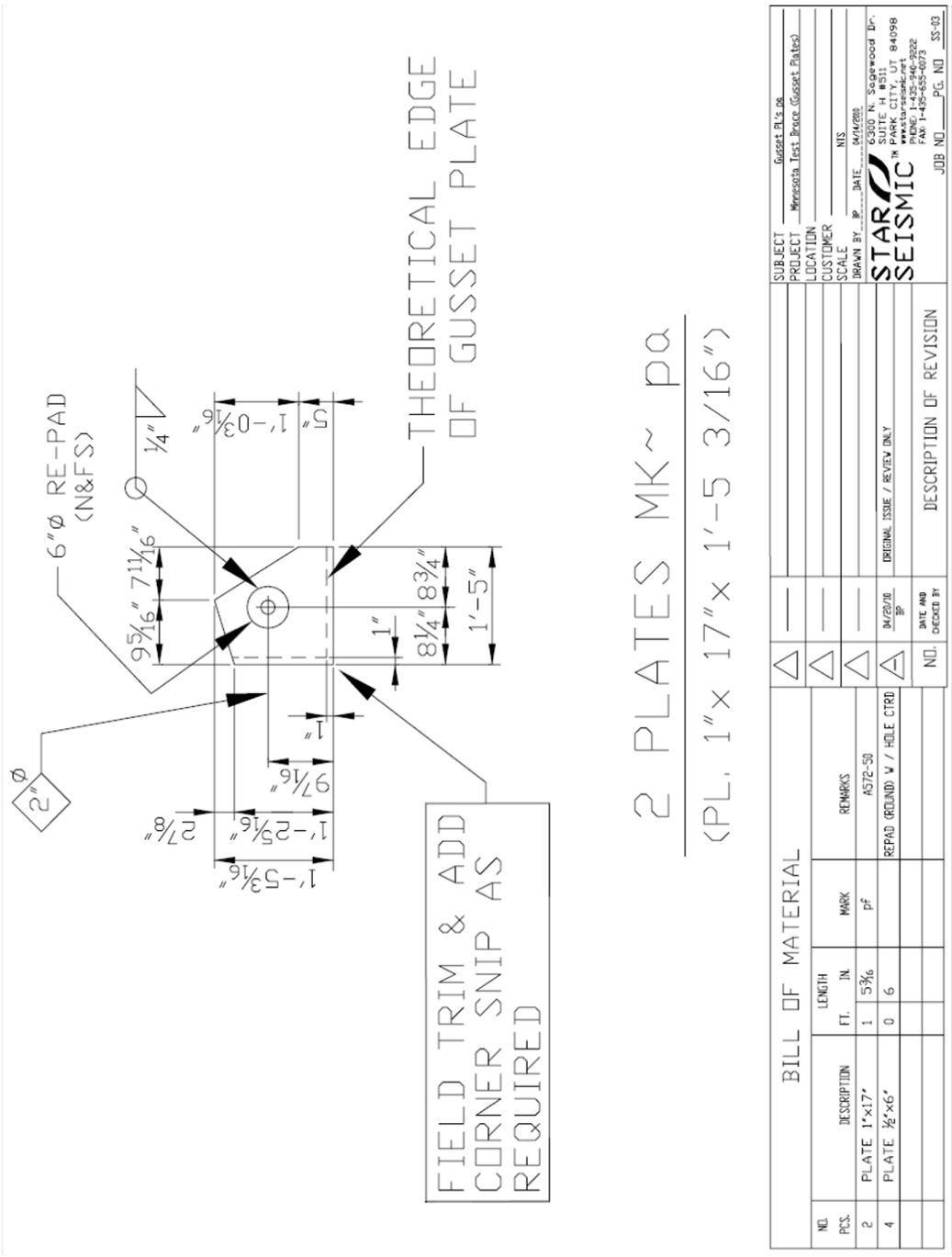

Figure B.21: BRBF gusset plate detail

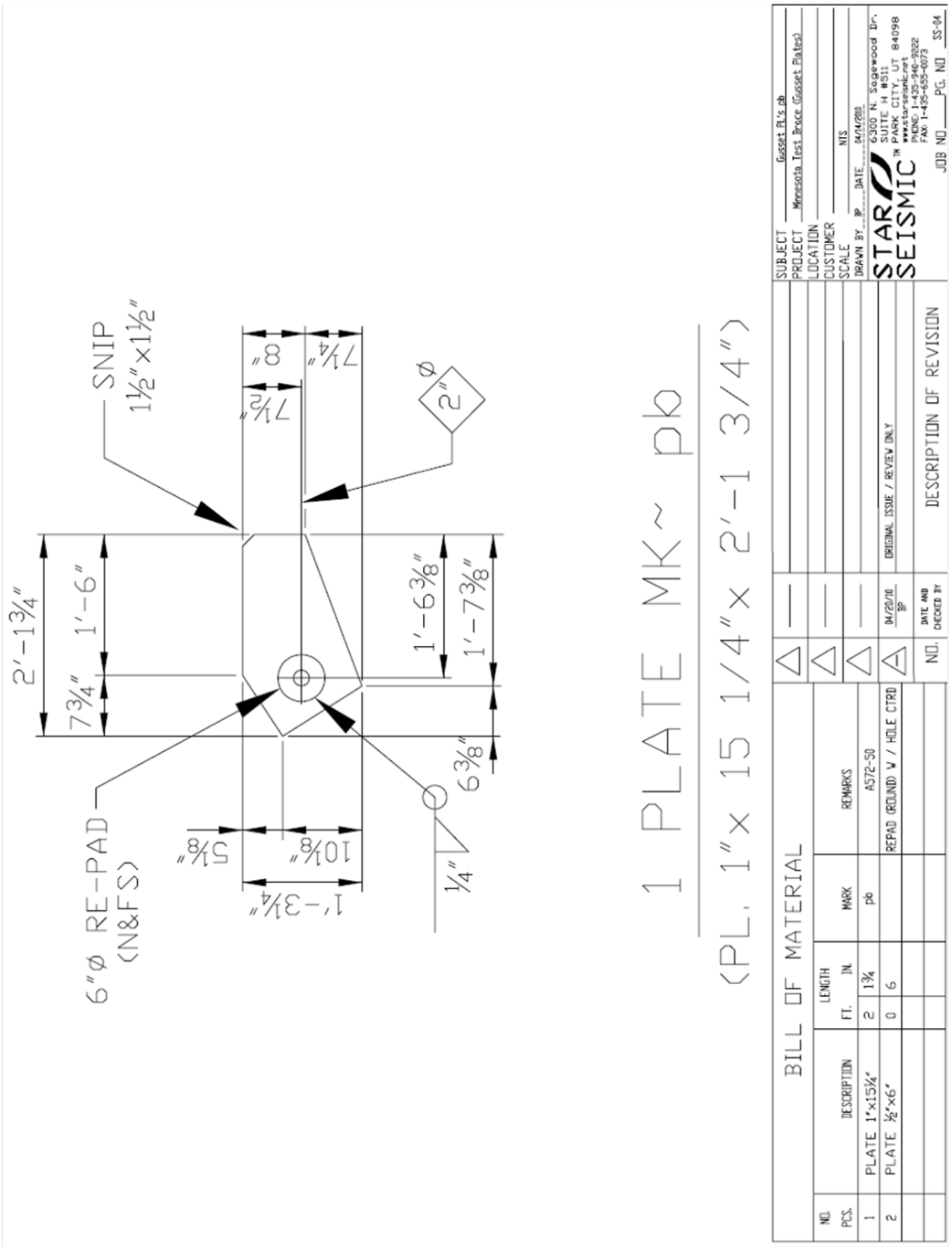

Figure B.22: BRBF gusset plate detail

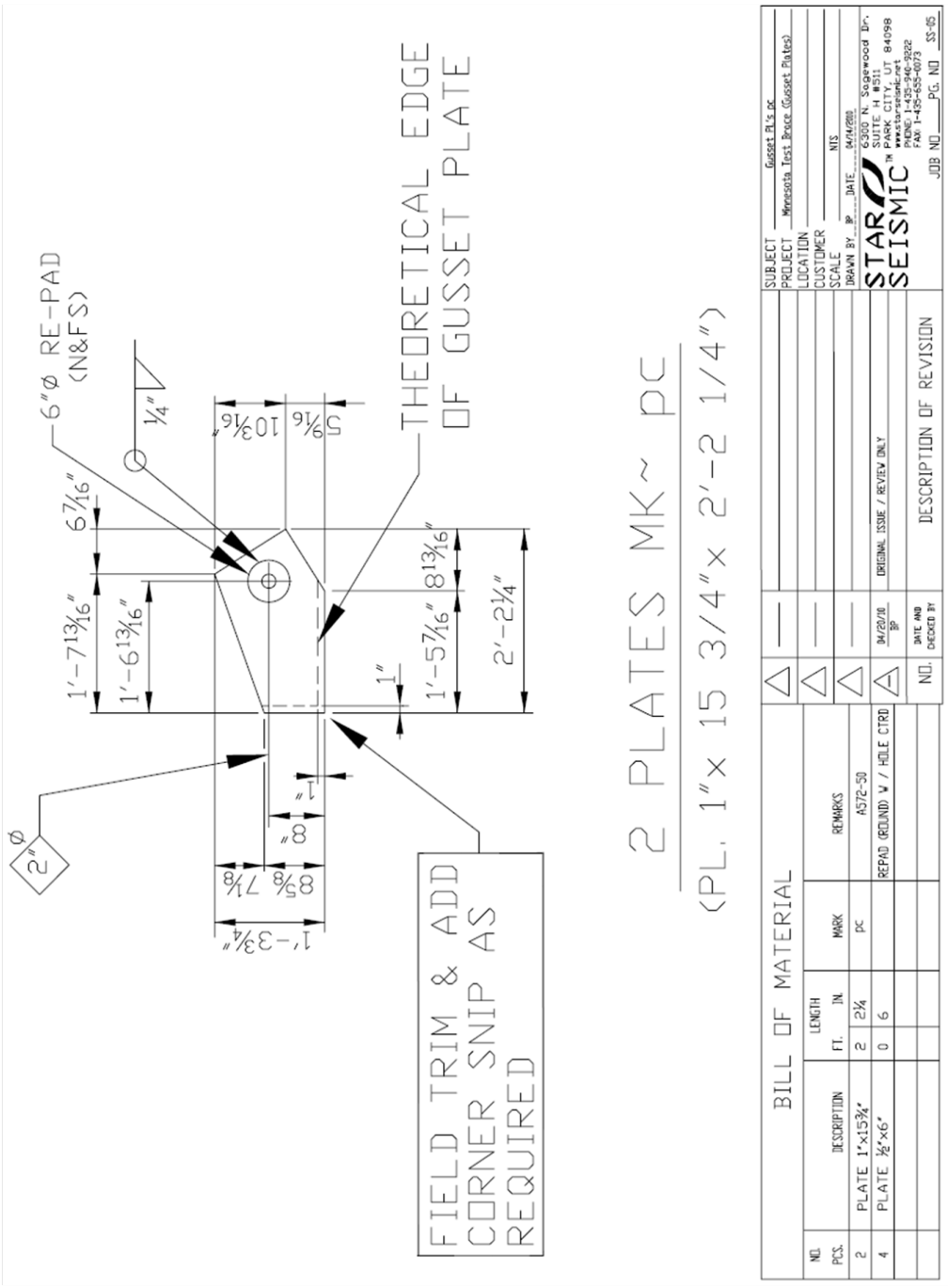

Figure B.23: BRBF gusset plate detail

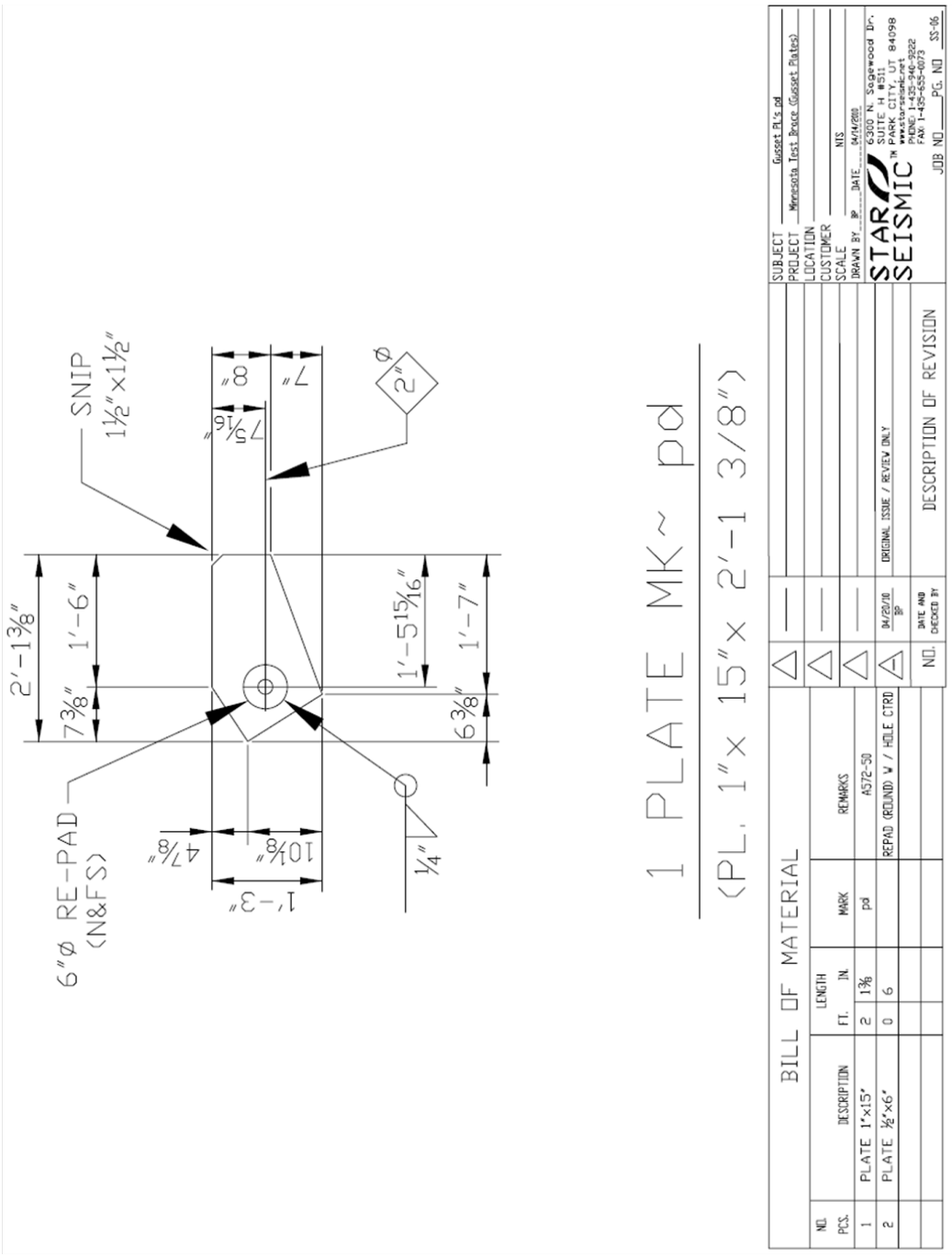

Figure B.24: BRBF gusset plate detail

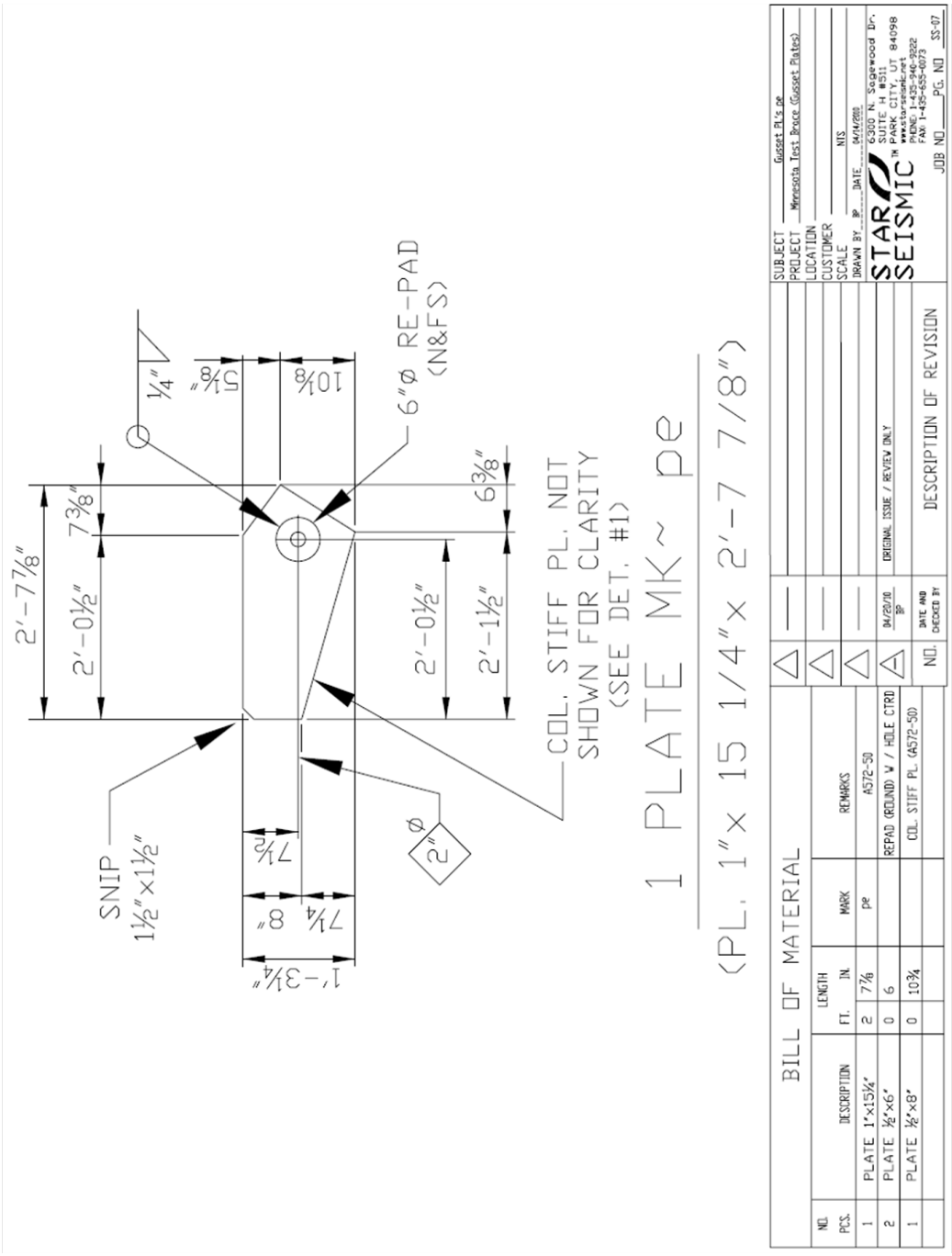

Figure B.25: BRBF gusset plate detail

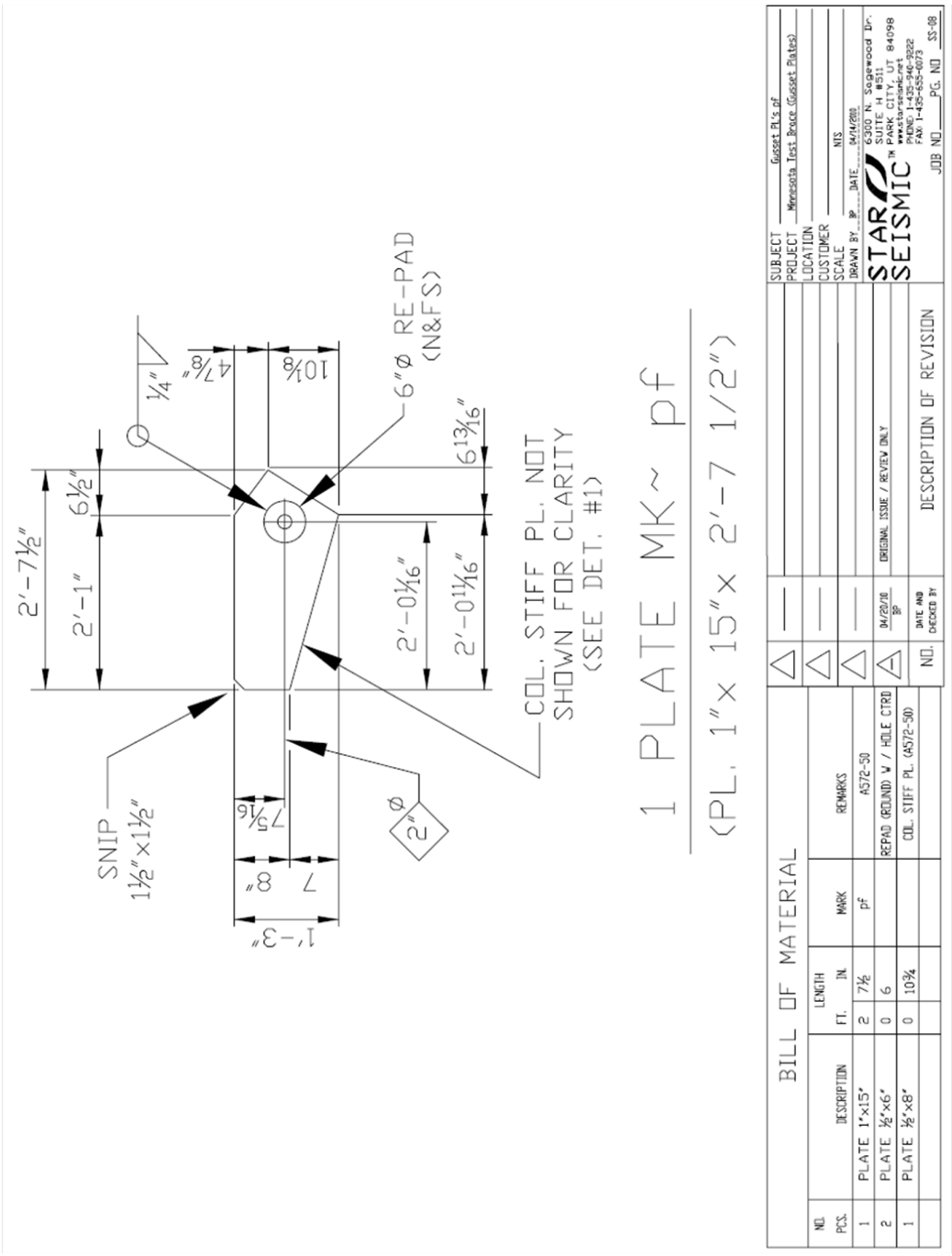

Figure B.26: BRBF gusset plate detail

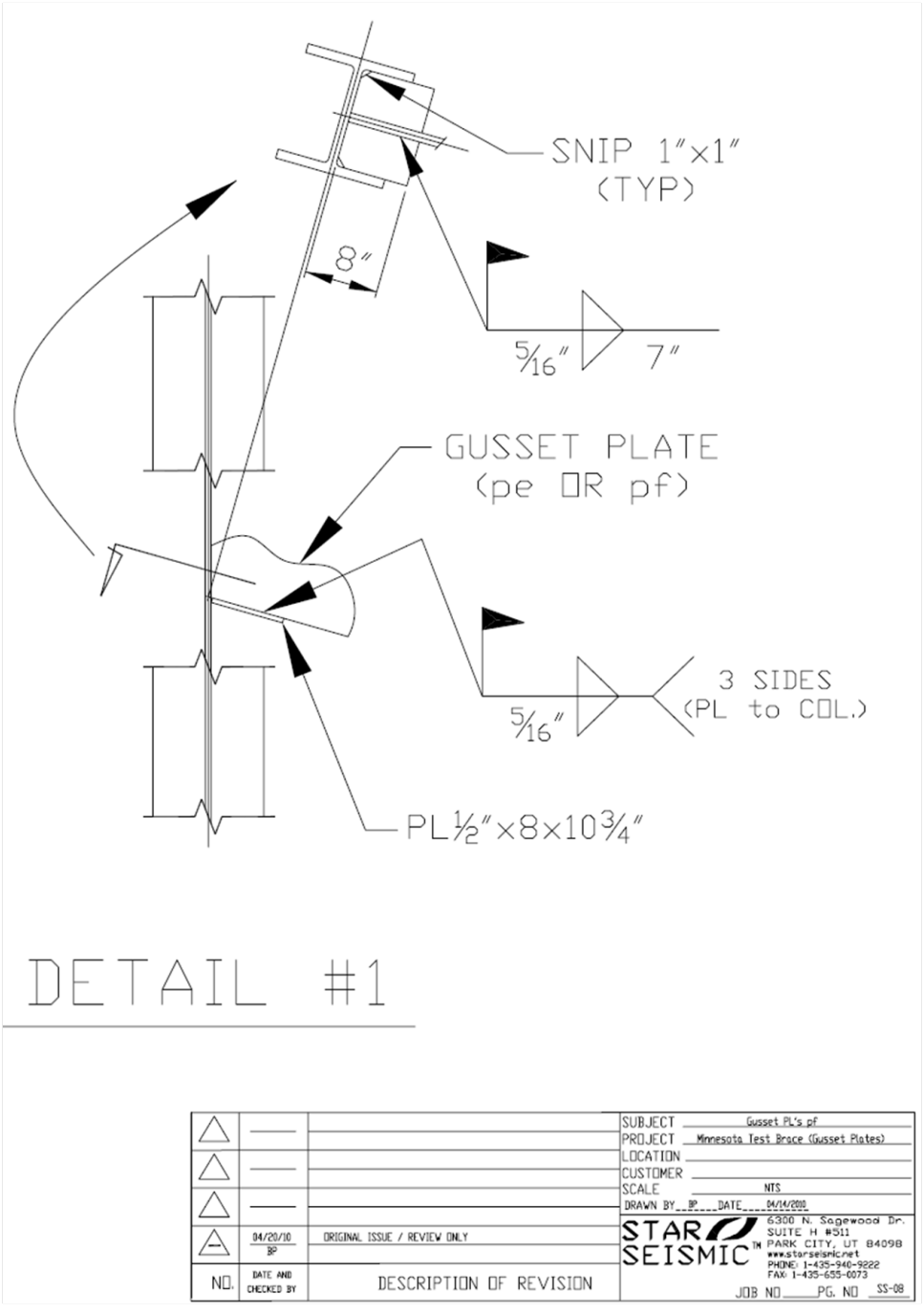

Figure B.27: BRBF gusset plate detail

The following drawings are the shop drawings for the individual BRBs produced by Star Seismic.

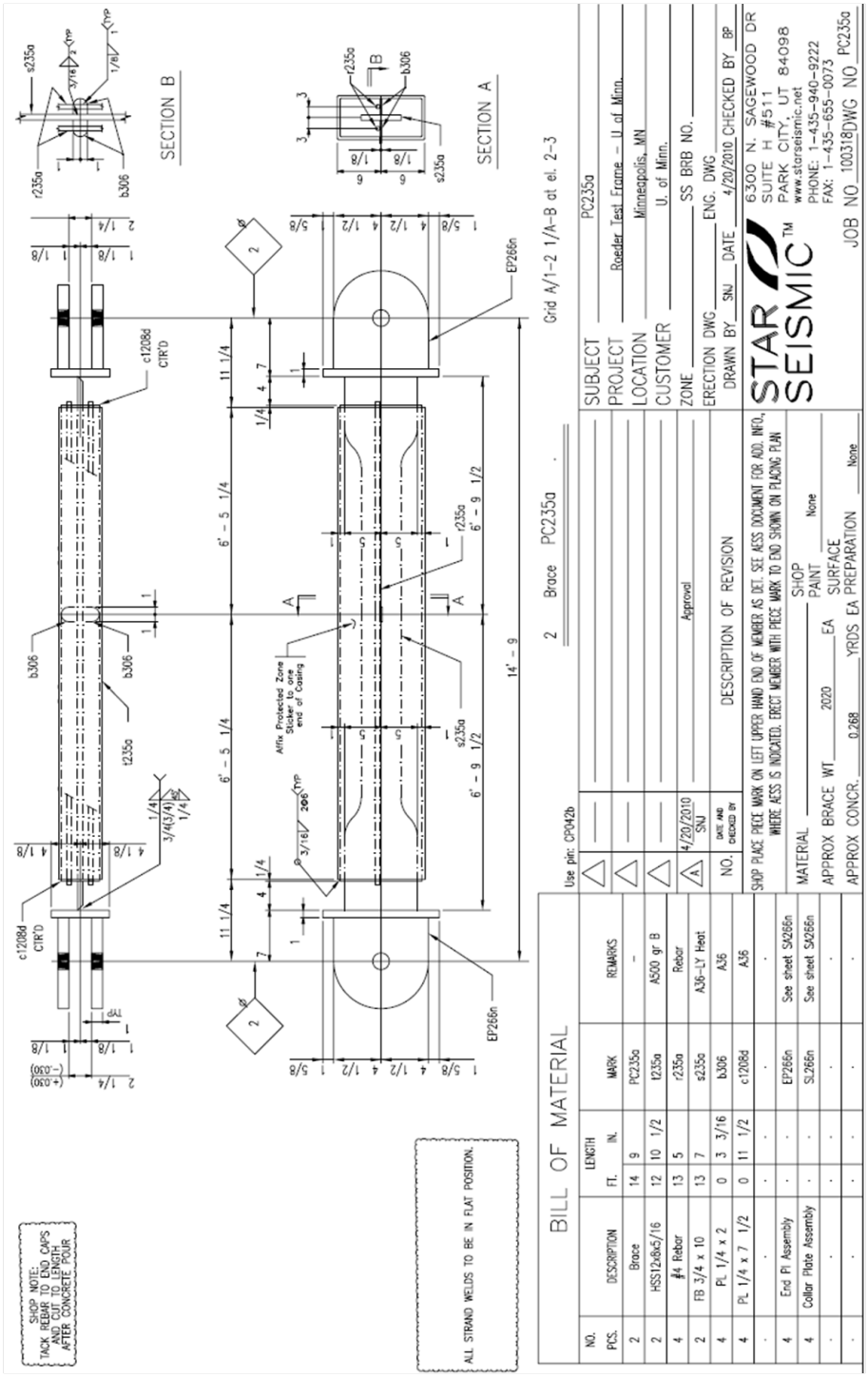

NO. PCS.	DESCRIPTION	LENGTH FT.	LENGTH IN.	MARK	REMARKS
2	Brace	14	9	PC235a	-
2	HSS12x8x5/16	12	10 1/2	t235a	A500 gr B
4	#4 Rebar	13	5	r235a	Rebar
2	FB 3/4 x 10	13	7	s235a	A36-LY Heat
4	PL 1/4 x 2	0	3 3/16	b306	A36
4	PL 1/4 x 7 1/2	0	11 1/2	c12084	A36
.	.	.	.	.	.
4	End Pl Assembly	.	.	EP266n	See sheet SA266n
4	Collar Plate Assembly	.	.	SL266n	See sheet SA266n
.	.	.	.	.	.
.	.	.	.	.	.

Figure B.28: BRBF shop drawings

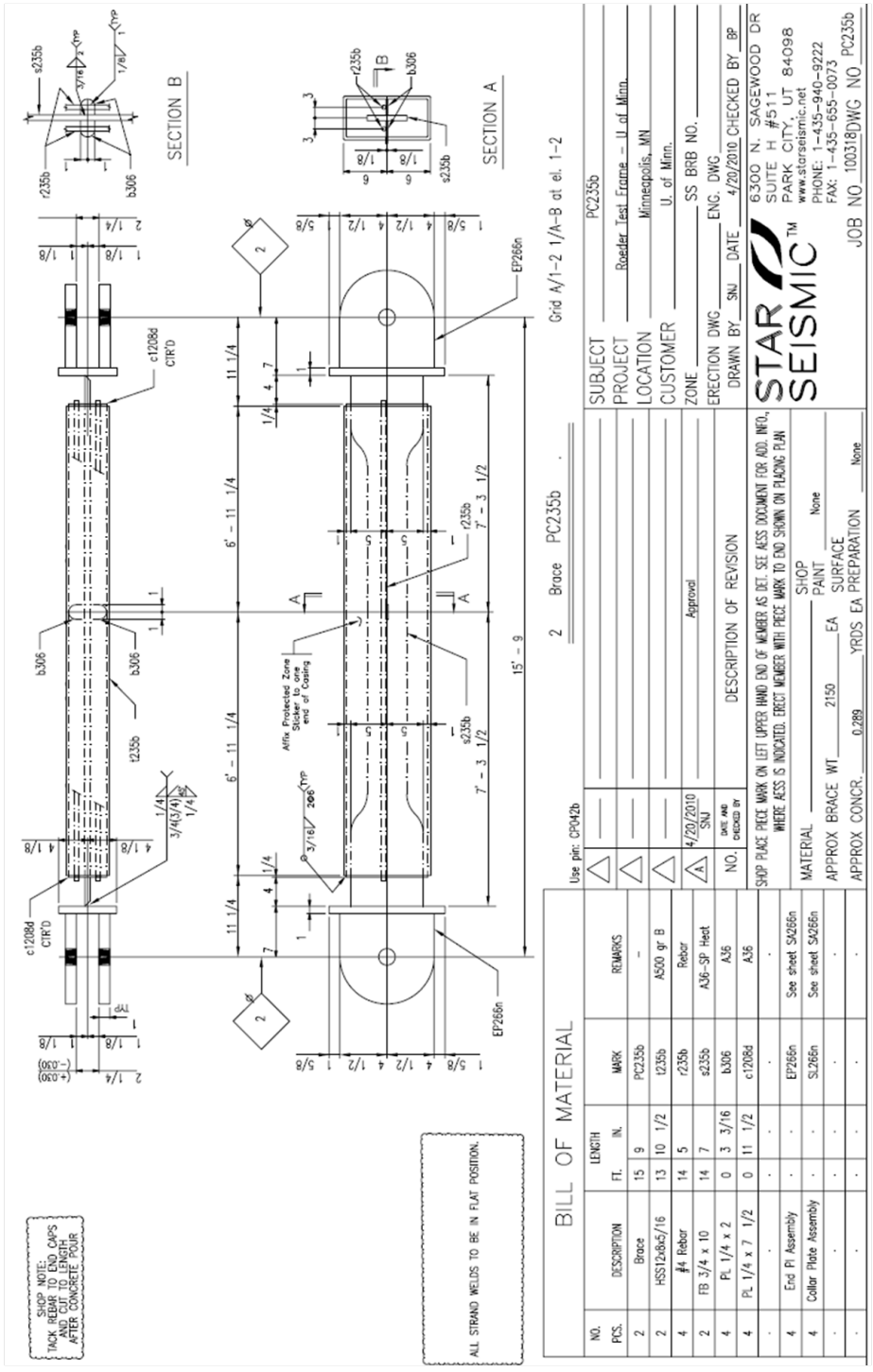

NO. PCS.	DESCRIPTION	LENGTH FT.	LENGTH IN.	MARK	REMARKS
2	Brace	15	9	PC235b	-
2	HSS12x8x5/16	13	10 1/2	t235b	A500 gr B
4	#4 Rebar	14	5	r235b	Rebar
2	FB 3/4 x 10	14	7	s235b	A36-SP Heat
4	PL 1/4 x 2	0	3 3/16	b306	A36
4	PL 1/4 x 7 1/2	0	11 1/2	c12086	A36
.	.	.	.	.	.
4	End Pl Assembly	.	.	EP266n	See sheet SA266n
4	Collar Plate Assembly	.	.	SL266n	See sheet SA266n
.	.	.	.	.	.
.	.	.	.	.	.

MATERIAL	SHOP	
APPROX BRACE WT 2150	PAINT	None
APPROX CONCR. 0.289 YRDS EA	SURFACE PREPARATION	None

Figure B.29: BRBF shop drawings

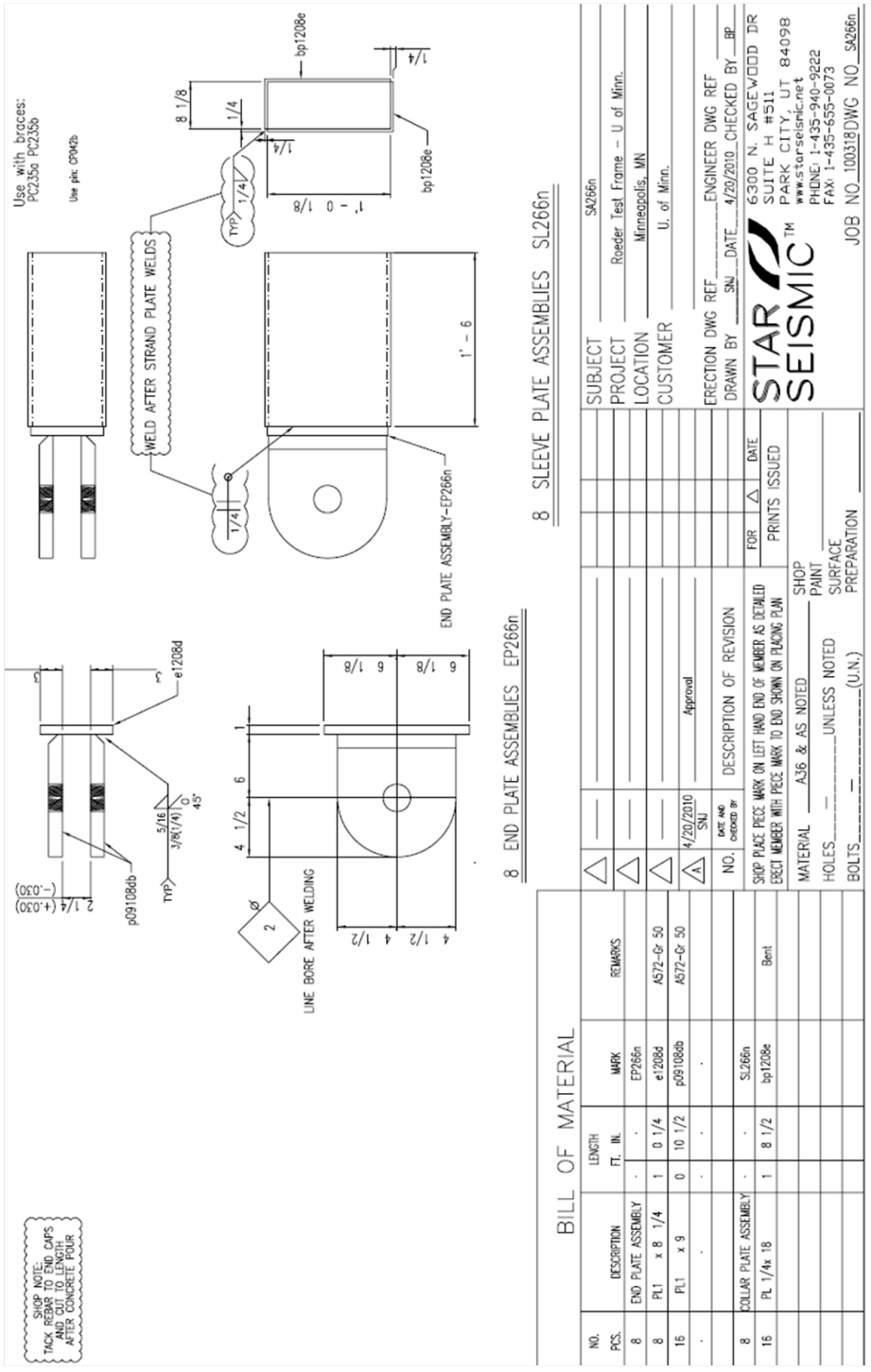

Figure B.30: BRBF shop drawings

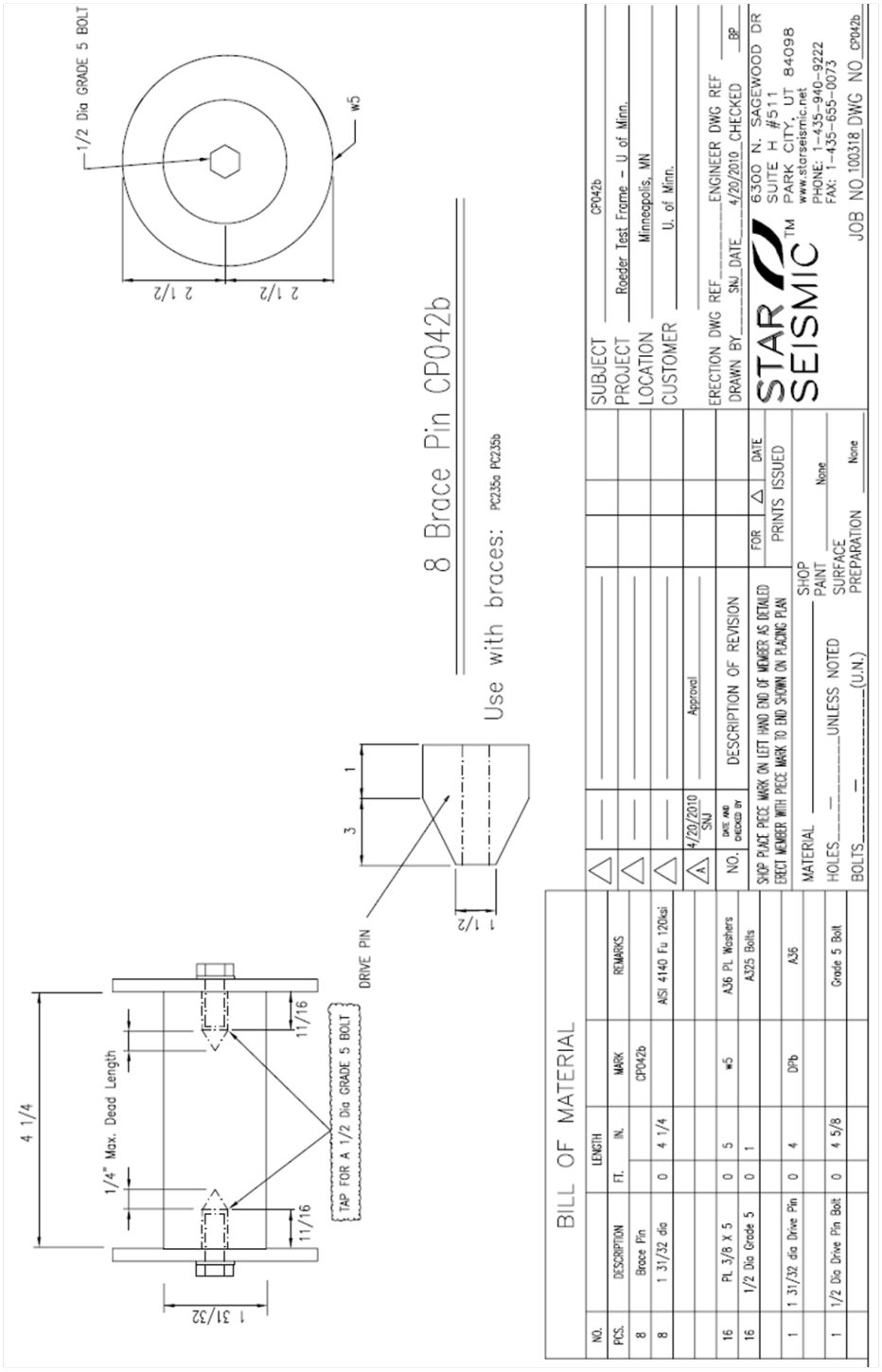

Figure B.31: BRBF shop drawings

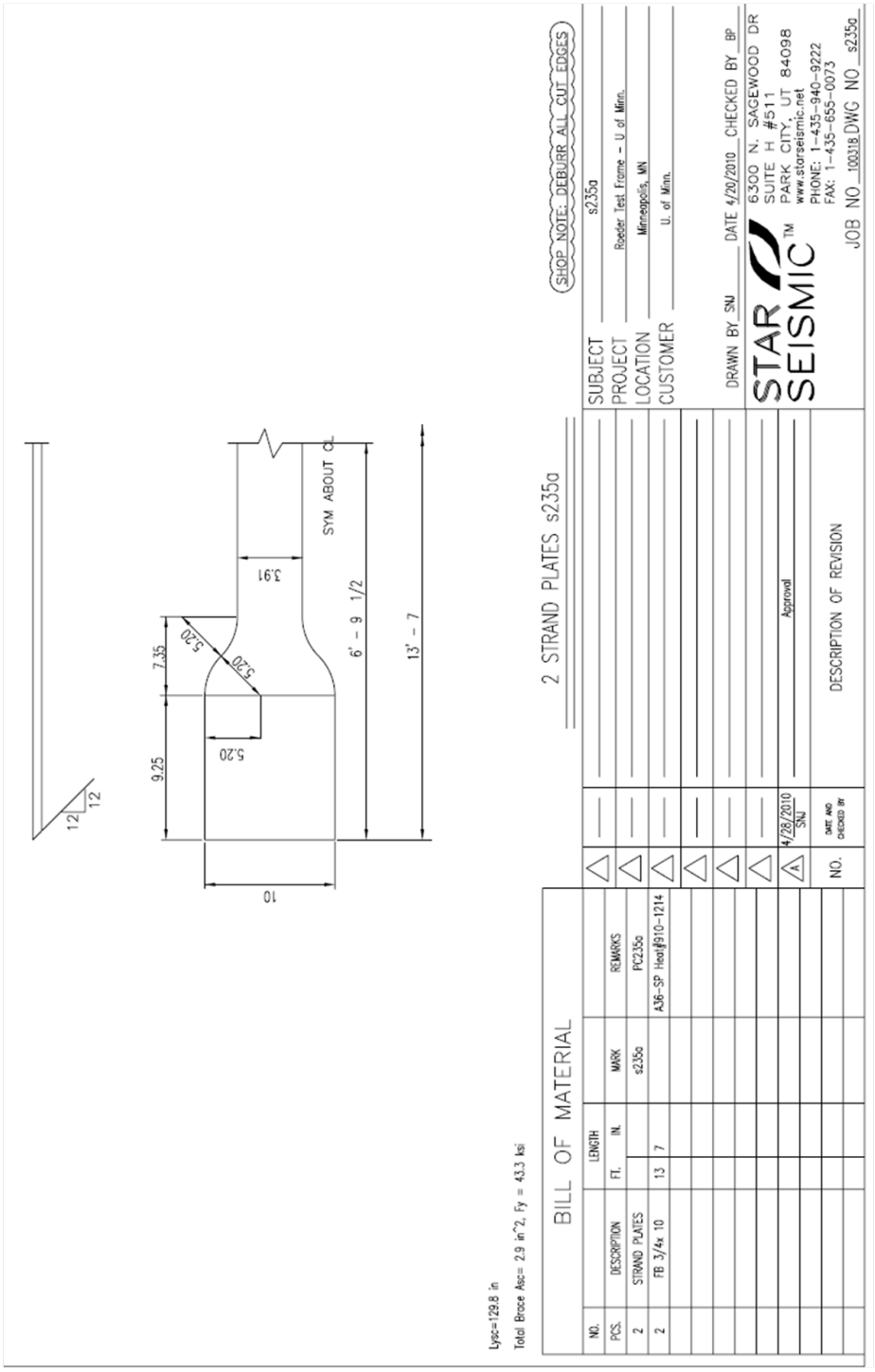

Figure B.32: BRBF shop drawings

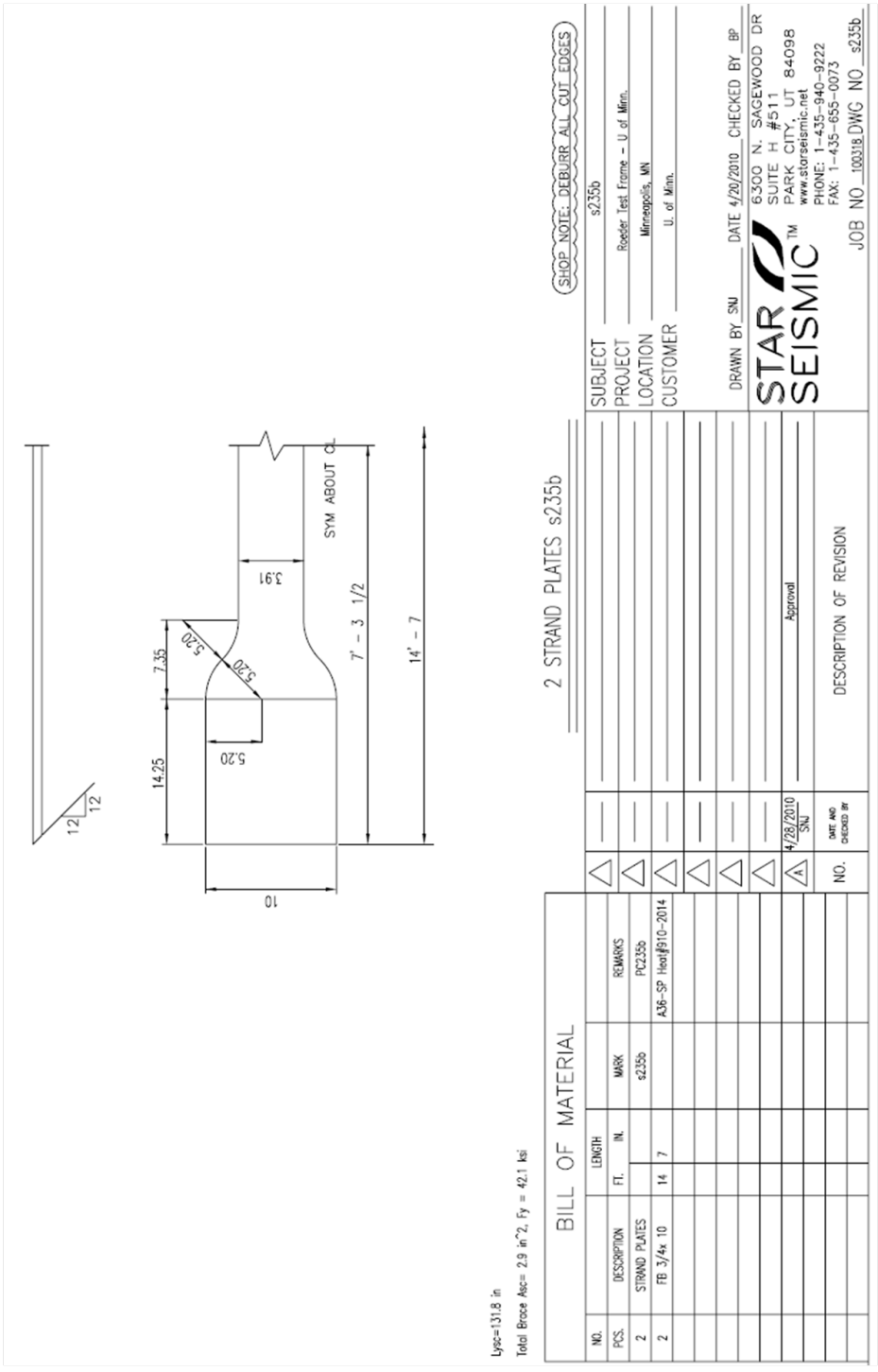

Figure B.33: BRBF shop drawings

Appendix C

DATA REDUCTION

The raw data obtained during each test was processed upon completion of the test. During the experiments, the data was typically saved in a new file every two cycles resulting in 20 to 25 individual data files for each test. The processing consisted of the following:

1. Reorganizing the data files into a file for each individual cycle for ease of processing.

2. Removing the pauses that occurred during observations and overnight after ensuring no large jumps occurred during these pauses.

3. Sampling the data since it was recorded at 1 Hz and resulted in unmanageable file sizes. The sampling rate varied depending on the number of data points per cycle with larger sampling rates being used for larger cycles. It was ensured that no loss of fidelity occurred during sampling.

4. Removing data points where measurements spiked as a result of an unknown malfunction. These spikes occurred in four to six stringpots during each test and occurred infrequently and lasted no longer than one second.

5. Calculating those quantities from the raw instrumentation data that are needed to quantify the response of the systems.

Negligible shifts were observed in the data during the observational pauses and no corrections were made. Some strain gauge drift was observed during the weekend pause after the first day of testing for the conventional braced frame. These strains were adjusted by subtracting the recorded shift from the subsequent data. The following sections of this appendix describe how key response parameters, such as forces and drifts, were calculated from the recorded data.

C.1 Member Forces

C.1.1 Column Forces

A minimum of four strain gauges were placed on the columns at the bottom and the top of each story. These were used to estimate the column axial, moment and shear forces as

outlined below.

Column axial force

The column axial forces were estimated from the average of the strain gauges at each cross-section where the gauges were installed multiplied by the modulus of elasticity and the cross-sectional area. The result is given by Equation C.1 below. Reference Figure C.1 for the strain gauge designations.

$$P_{col} = \frac{\epsilon_{1a} + \epsilon_{2a} + \epsilon_{3a} + \epsilon_{4a}}{4} EA \tag{C.1}$$

where E is the modulus of elasticity and A is the cross-sectional area of the column section. A modulus of elasticity of 29,000 ksi was used in all calculations.

Column moments

The curvatures were estimated as the difference between the average of the extreme fiber strains divided by the distance between the strain gauges. Curvatures about the strong and weak axis of the cross-sections were calculated as moments about each axis were required. The curvatures were calculated as shown below in Equations C.2 and C.3.

$$\phi_x = \frac{\left(\frac{\epsilon_{1a}+\epsilon_{2a}}{2}\right) - \left(\frac{\epsilon_{3a}+\epsilon_{4a}}{2}\right)}{d} \tag{C.2}$$

$$\phi_y = \frac{\left(\frac{\epsilon_{1a}+\epsilon_{3a}}{2}\right) - \left(\frac{\epsilon_{2a}+\epsilon_{4a}}{2}\right)}{b_{sg}} \tag{C.3}$$

where d is the depth of the section and b_{sg} is the distance between strain gauges across the flange width and the strain gauge nomenclature follows that shown in Figure C.1.

The moments about the strong (x) and weak (y) axis of the columns are then given by Equations C.4 and C.5 below.

$$M_x = EI\phi_x \tag{C.4}$$

$$M_y = EI\phi_y \tag{C.5}$$

where I_x and I_y are moments of inertia about the x and y axes of the cross section.

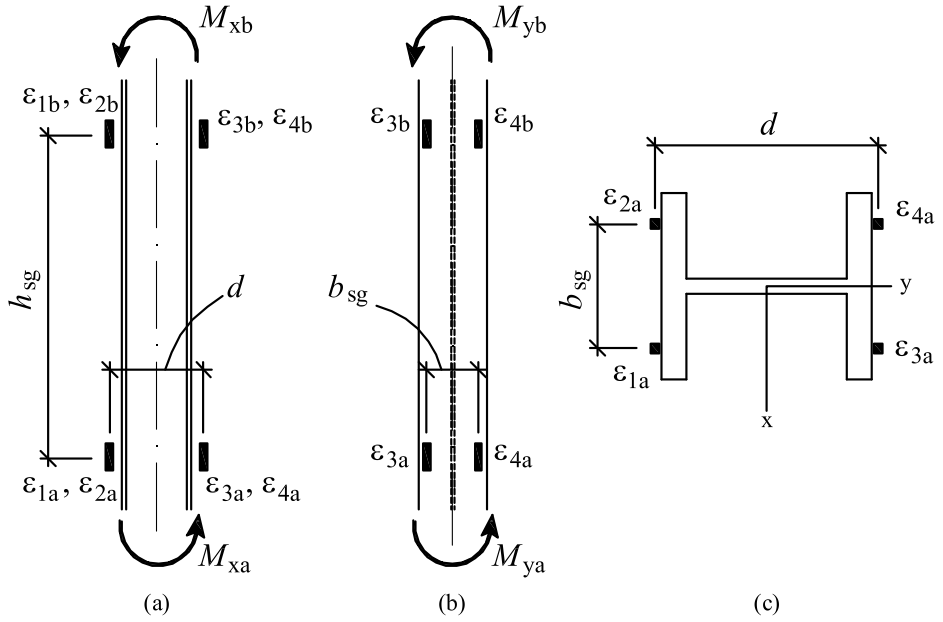

Figure C.1: Column strain gauge and moment nomenclature for curvature, moment and shear calculations

Column shears

The column story shears were found through equilibrium of the column with the known moments at the top and bottom of the story. This story shear is given by Equations C.6 and C.7.

$$V_y = \frac{M_{xa} + M_{xb}}{h_{sg}} \tag{C.6}$$

$$V_x = \frac{M_{ya} + M_{yb}}{h_{sg}} \tag{C.7}$$

C.1.2 Beams

The calculation of the beam forces and moments followed a similar procedure as that used for the column forces and moments except that only the moment about the strong axis of the beam was used along with the corresponding shear.

Beam axial force

The axial force in the beam was calculated as the average strain in the cross section multiplied by EA as shown in Equation C.8.

$$P_{beam} = \frac{\sum_{i=1}^{n} \epsilon_i}{n} EA \tag{C.8}$$

where i is the strain gauge number and n is the total number of strain gauges at the cross section of interest.

Beam moments

The beam curvatures were calculated from the two strain gauges attached to the flanges and given by Equation C.9 below.

$$\phi_x = \frac{\epsilon_b - \epsilon_t}{d_{sg}} \tag{C.9}$$

where d_{sg} is the distance between strain gauges and ϵ_t is the strain at the top of the section while ϵ_b is the strain at the bottom of the section. The moment at the beam cross section is then found from Equation C.10 shown below.

$$M_x = EI_x\phi_x \tag{C.10}$$

Beam shears

The beam shears were calculated from moment equilibrium based on the moments at each of the beam calculated per the previous discussion. These shears are given by Equation C.11 below.

$$V = \frac{M_1 + M_2}{l_{sg}} \tag{C.11}$$

where l_{sg} is the horizontal distance between beam strain gauge locations.

C.1.3 Braces

HSS brace axial force

Prior to yielding, the HSS brace axial force was estimated based on the average strains measured from four strain gauges placed at each end of the brace. This force is given by Equation C.12 below.

$$P_{brace} = \frac{\epsilon_1 + \epsilon_2 + \epsilon_3 + \epsilon_4}{4} EA \tag{C.12}$$

where E is the modulus of elasticity and A is the cross-sectional area of the brace. A modulus of elasticity of 29,000 ksi was used in all calculations.

Prior to and following brace yielding, the sum of the tensile and compressive brace force was estimated by subtracting the column story shears from the actuator forces in the global direction of interest.

BRB axial force

Prior to yielding, the BRB axial force was estimated from the average axial deformations measured by the string pots at each end of the BRB. The axial deformation, Δ_{BRB}, was calcualted per Equation C.13 below.

$$\Delta_{BRB} = \frac{\delta_{1a} + \delta_{2a}}{2} + \frac{\delta_{1b} + \delta_{2b}}{2} \tag{C.13}$$

where δ_{ij} is the string pot measurement of one pot at the end of the BRB.

The BRB axial force was then estimated per Equation C.14 below.

$$P_{BRB} = K_{eff} \Delta_{BRB} \tag{C.14}$$

where K_{eff} is the effective axial stiffness of the BRB accounting for the combination of the smaller area of the yielding portion of the core and the larger area at the ends of the core. This effective stiffness is calculated according to Equation C.15, which is just the stiffness of three elements in series.

$$K_{eff} = \frac{1}{\frac{L_1}{EA_1} + \frac{L_1}{EA_1} + \frac{L_{ysc}}{EA_{ysc}}} \tag{C.15}$$

where L_1 and L_2 are the lengths of the steel core in the elastic region, L_{ysc} is the length of yielding zone of the steel core, and A_i are the cross-sectional areas of the respective regions of the steel core.

Prior to and following brace yielding, the sum of the tensile and compressive brace force was estimated by subtracting the column story shears from the actuator forces in the global direction of interest.

C.2 Frame and Story Drifts

Frame and story drifts were calculated using the eight string pots shown in Figure 3.45. Due to the roof displacements being applied in two horizontal directions, triangulation was required to located the frame in space. It was assumed that the floor slabs behaved rigidly in plane (i.e. no elongation or shear deformations). Figure C.2 shows a plan view of the outline of the test frame with the corners labeled as A, B, C and D, and the middle of the specimen labeled as M. Also shown in the figure is the strongwall and coordinate system used in the triangulation calculations, which occurs on the inside of the intersection of the strongwalls and is labeled as point O. Two string pots at right angles to each other were attached to the frame at point D. Circles C2 and C3 result, with original radii L_{o2} and L_{o3}. As the frame moves in space, both of the string pots extend or contract and result in new circles C2 and C3 with radii L_2 and L_3. The difference between the new radii and the old radii are simply the measured extension or contraction of the respective string pots. The new coordinates of point D were found by solving the equation of each circle for Y_D, equating the two and solving for the numerical value of X_D. Y_D is then found by plugging in X_D into the equation of either circle. The resulting formulas for X_D and Y_D are shown below as Equations C.16 and C.17.

$$\left[1+\left(\frac{L_{o3}}{L_{o2}}^2\right)\right]X_D^2+2L_{o3}\left(\frac{k_1}{L_{o2}}-1\right)X_D+k_1^2+L_{o3}^2-(L_{o2}+\Delta_2)^2=0 \tag{C.16}$$

$$Y_D=\sqrt{L_{o2}^2+2\Delta_2L_{o2}+\Delta_2^2-X_D^2+2X_DL_{o3}-L_{o3}^2} \tag{C.17}$$

where k_1 is given by Equation C.18 below

$$k_1=\frac{L_{o2}^2-L_{o3}^2+(L_{o2}+\Delta_2)^2-(L_{o3}+\Delta_3)^2}{2L_{o2}} \tag{C.18}$$

where Δ_2 and Δ_3 are the string pot measurements at point D in the Y and X directions, respectively.

Finally, the displacements of point D from its original position, δ_{DY} and δ_{DX}, is shown in Figure C.2 and are calculated according to Equations C.19 and C.20.

$$\delta_{DY}=Y_D-L_{o2} \tag{C.19}$$

$$\delta_{DX}=X_D-L_{o3} \tag{C.20}$$

Similar calculations were performed for points A and C shown in Figure C.2. Three, story displacement quantities for each global direction (X and Y) were then determined from the displacements of the frame corners: 1.) displacement of the braced frames, 2.) displacement of the gravity frames, and 3.) displacement of the center of the frame. During the test, the floor twisted slightly and therefore the above three quantities are not the same. Figure C.3a shows the deformation quantities at points A, C, D and M that were used to calculate the three story displacement quantities shown in Equations C.21 through C.26.

The displacements in Y direction for Frames 1 and 2 and the center of the frame are given by the following three equations.

$$\Delta_{F2Y}=\frac{\delta_{DY}+\delta_{CY}}{2} \tag{C.21}$$

$$\Delta_{F1Y}=\frac{\delta_{AY}+Y_A+L\cos\theta_{story}-(L_{o2}+L)}{2} \tag{C.22}$$

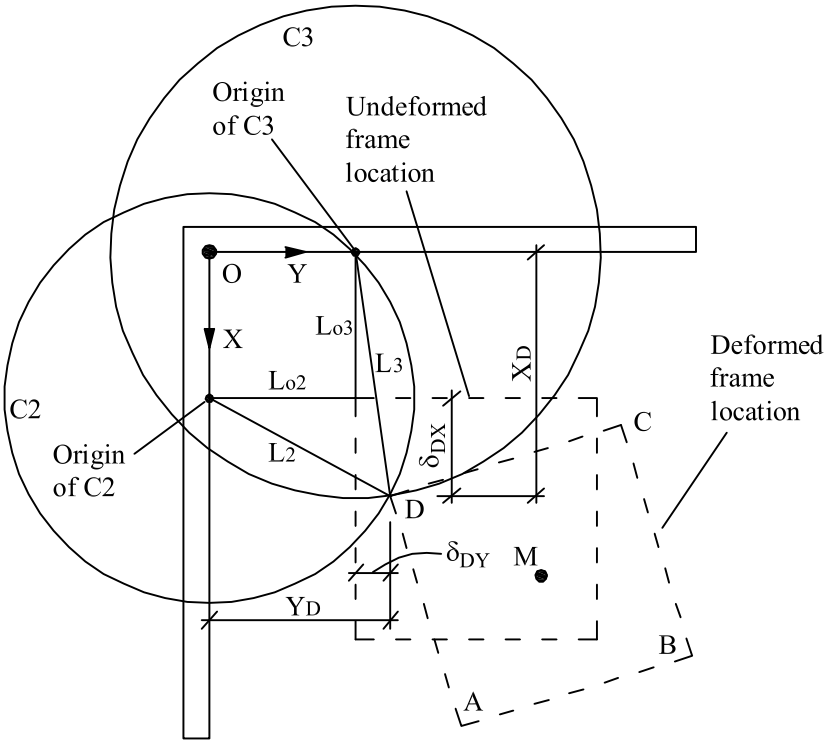

Figure C.2: Triangulation of point D on test frame

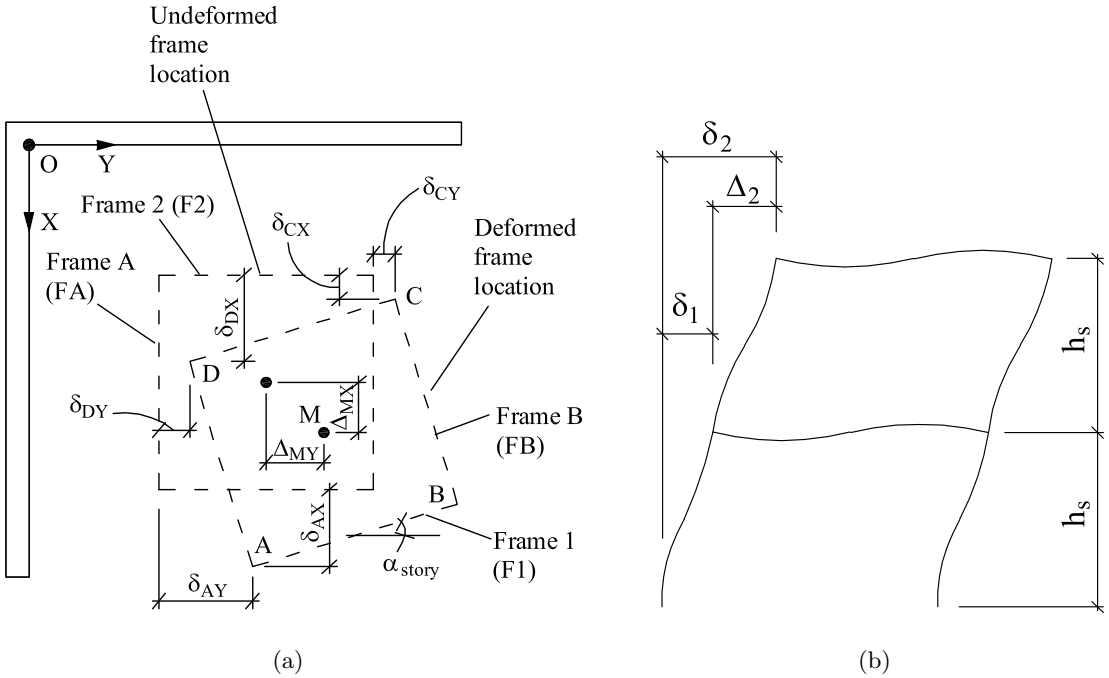

Figure C.3: Story displacement and drift quantities: (a) plan view; (b) elevation

$$\Delta_{MY} = \frac{\Delta_{F2Y} + \Delta_{F1Y}}{2} \tag{C.23}$$

The displacements in X direction for Frames A and B and the center of the frame are given by the following three equations.

$$\Delta_{FAX} = \frac{\delta_{DX} + \delta_{AX}}{2} \tag{C.24}$$

$$\Delta_{FBX} = \frac{\delta_{CX} + X_C + L\cos\theta_{story} - (L_{o3} + L)}{2} \tag{C.25}$$

$$\Delta_{MX} = \frac{\Delta_{FAX} + \Delta_{FBX}}{2} \tag{C.26}$$

These calculations were performed at the second and third stories which allowed the determination of the first and second story drift ratios for each frame. The story drift ratios

are defined as the relative displacement between the top and bottom of the story divided by the story height as shown in Figure C.3b and Equations C.27 and C.28.

$$SDR_{1S} = \frac{\delta_1}{h_s} \tag{C.27}$$

$$SDR_{2S} = \frac{\Delta_2}{h_s} \tag{C.28}$$

where

$$\Delta_2 = \delta_2 - \delta_1 \tag{C.29}$$

The story twist was calculated from the X and Y coordinates of points A and D and is given by Equation C.30 below.

$$\alpha_{story} = \tan^{-1}\left(\frac{Y_A - Y_D}{X_A - X_D}\right) \tag{C.30}$$

Corrections to the story drift displacements due to base slip or uplift were unnecessary as there was little to no slip during the course of the test.

C.3 Gusset Plate Rotations

The gusset plate rotations were estimated using a string pot located at the edge of the gusset plate and assuming that the plate rotated about the intersection of the elliptical clearance line and the brace centerline as shown in Figure C.4a. The rotation is described by Equation C.31 below.

$$\theta_{gp} = \frac{\delta_{gp,oop}}{l_{gp}} \tag{C.31}$$

C.4 Column Panel Zone Deformations

Two LVDTs were placed within the panel zones of the three braced frame columns at the second floor as shown in Figure C.4b, where the panel zone is defined as the area between the column flanges and the beam flanges. The law of sines was used to calculate the change in angle of the panel for each LVDT and the shear deformation of the panel was taken as the average of these two. The equations used to calculate this are shown below, and the variables are defined in Figure C.4b.

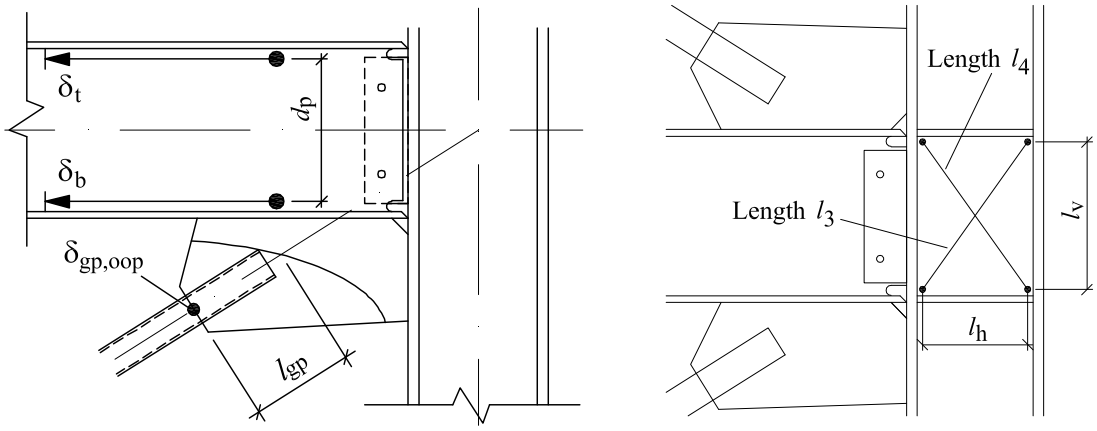

(a) (b)

Figure C.4: Parameters used to calculate deformations: (a) OOP gusset rotation and beam rotation; (b) panel zone shear deformation

$$\gamma_3 = \sin^{-1}\left(\frac{L_{N3}^2 - L_{o3}^2}{2l_h l_v}\right) \tag{C.32}$$

$$\gamma_4 = \sin^{-1}\left(\frac{L_{N4}^2 - L_{o4}^2}{2l_h l_v}\right) \tag{C.33}$$

where

$$L_{o3} = L_{o4} = \sqrt{l_h^2 + l_v^2} \tag{C.34}$$

and

$$L_{N3} = L_{o3} + \Delta_{3,lvdt} \tag{C.35}$$

and

$$L_{N4} = L_{o4} + \Delta_{4,lvdt} \tag{C.36}$$

where $\Delta_{3,lvdt}$ and $\Delta_{4,lvdt}$ are LVDT measurements for the LVDTs marked 3 and 4 in Figure C.4b.

C.5 Member Rotations

The beam average rotations at the ends of each braced frame beam at the second floor were calculated using the measurements of two LVDTs, each mounted on the top and bottom flanges of the beam. This rotation is calculated as the difference between LVDT measurements divided by the distance between the LVDT cores as described by Equation C.37 and Figure C.4a.

$$\theta_{bm} = \frac{\delta_t - \delta_b}{d_p} \tag{C.37}$$

The rotations about the strong (x) and weak (y) axes of the column were calculated in a manner similar to that described above for the beams and are given by Equations C.38 and C.39. The parameters in these equations are shown in Figure C.5.

$$\theta_{x,col} = \frac{\left(\frac{\delta_1+\delta_2}{2}\right) - \left(\frac{\delta_3+\delta_4}{2}\right)}{d_{cr}} \tag{C.38}$$

$$\theta_{y,col} = \frac{\left(\frac{\delta_1+\delta_3}{2}\right) - \left(\frac{\delta_2+\delta_4}{2}\right)}{b_{cr}} \tag{C.39}$$

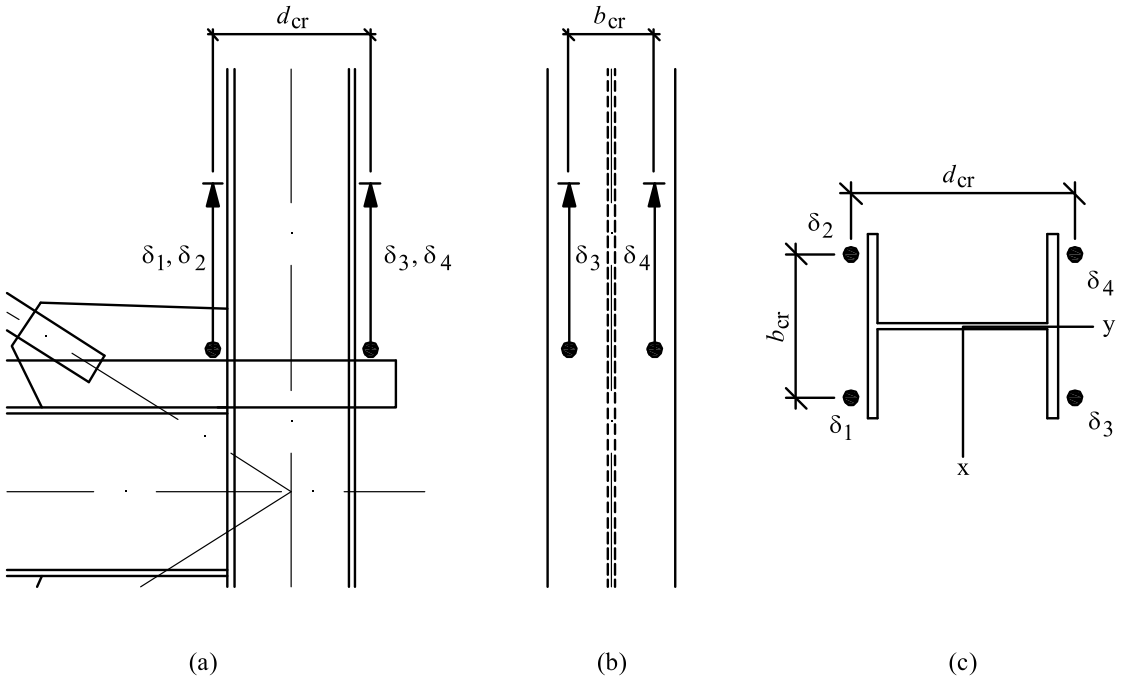

Figure C.5: Column rotation calculation parameters: (a) side view; (b) rear view; (c) cross-sectional view

Appendix D

SCBF EXPERIMENTAL PLOTS AND TABLES

This appendix provides additional tables, figures and plots to supplement the SCBF test results discussed in Section 4.4.

D.1 SCBF Displacement and Loading Protocol Information

Figure D.1 shows the displacement imposed on the specimen in the X and Y directions by the crosshead, as measured by the LVDTs in crosshead actuators. The histories of story drift ratios for each story in each direction are shown in Figures D.2 and D.3.

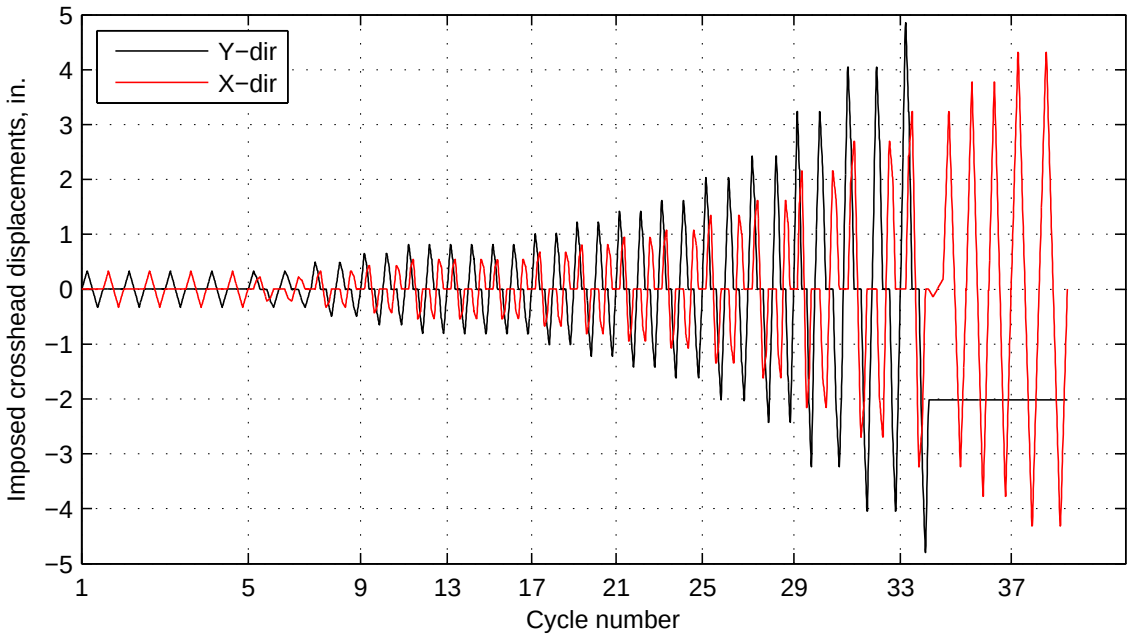

Figure D.1: Imposed Crosshead Displacements (SCBF test)

Figures D.4a and D.4b show the cloverleaf SDR traces for the second and first story, respectively. These were obtained from the four horizontal string pots at the centerline of each floor shown in Fig. 3.45. It can be seen that at larger SDRs, more deformation was concentrated in the second-story than in the first. This is mainly due to the increased stiffness of the first story due to the fixity of the column bases.

Figure D.5 shows the forces in the actuators in the X and Y directions as a function of the cycle number. It can be seen from the figure that the peak positive force in the

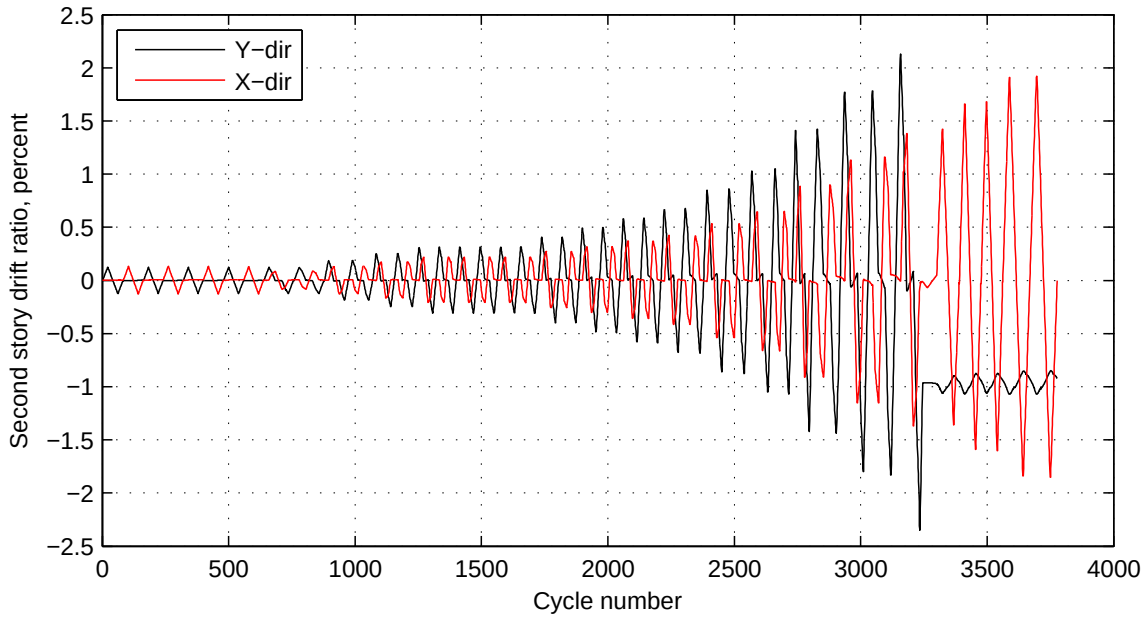

Figure D.2: Measured second-story drift ratios, percent (SCBF test)

Y-direction was 335 kips while the peak positive force in the X-direction was 321 kips. The peak negative force in the Y-direction was 325 kips while the peak negative in the X-direction was 313 kips. The difference between the peak forces between the X and Y directions is due to the fact that peak displacement in the Y-direction was larger than the peak displacement in the X-direction. Additionally, the frame is slightly stiffer in the Y-direction due to the shared column being bent about its major axis. Tables D.1 and D.2 list the peak negative and positive shear forces and roof and story drift ratios for each cycle.

Table D.1: Maximum frame resistances and average roof drifts in each cycle (SCBF test)

Cycle	Maximum Shear (kips)				Maximum ave. RDR, percent			
	Y-direction		X-direction		Y-direction		X-direction	
	Pos	Neg	Pos	Neg	Pos	Neg	Pos	Neg
1	83	-86	82	-87	0.117	-0.119	0.121	-0.119
2	86	-86	84	-87	0.116	-0.119	0.121	-0.119
3	86	-85	84	-87	0.117	-0.119	0.121	-0.119

Table D.1: Maximum frame resistances and average roof drifts in each cycle (SCBF test)

Cycle	Maximum Shear (kips)				Maximum ave. RDR, percent			
	Y-direction		X-direction		Y-direction		X-direction	
	Pos	Neg	Pos	Neg	Pos	Neg	Pos	Neg
4	86	-85	85	-87	0.116	-0.119	0.120	-0.119
5	86	-85	55	-58	0.117	-0.119	0.078	-0.077
6	87	-84	56	-57	0.117	-0.119	0.079	-0.077
7	126	-125	84	-87	0.176	-0.179	0.120	-0.119
8	127	-126	85	-86	0.176	-0.178	0.121	-0.118
9	165	-168	109	-114	0.237	-0.238	0.158	-0.156
10	170	-165	111	-112	0.236	-0.238	0.159	-0.156
11	200	-198	136	-143	0.298	-0.299	0.200	-0.197
12	198	-193	139	-140	0.298	-0.299	0.201	-0.196
13	196	-195	137	-142	0.298	-0.299	0.200	-0.197
14	195	-194	139	-140	0.298	-0.299	0.201	-0.196
15	194	-194	137	-142	0.298	-0.299	0.200	-0.197
16	193	-193	139	-140	0.299	-0.299	0.202	-0.196
17	215	-216	168	-174	0.378	-0.379	0.252	-0.248
18	212	-209	172	-169	0.378	-0.380	0.253	-0.247
19	230	-230	192	-196	0.456	-0.460	0.304	-0.300
20	227	-225	194	-190	0.456	-0.460	0.306	-0.299
21	244	-242	209	-209	0.536	-0.540	0.357	-0.352
22	240	-236	210	-201	0.536	-0.544	0.359	-0.352
23	255	-252	222	-217	0.616	-0.624	0.412	-0.404
24	251	-245	221	-211	0.620	-0.624	0.412	-0.404
25	279	-274	243	-236	0.780	-0.784	0.516	-0.512
26	272	-263	239	-229	0.780	-0.784	0.520	-0.508
27	297	-288	259	-252	0.940	-0.944	0.624	-0.620
28	288	-274	253	-243	0.944	-0.948	0.628	-0.620
29	323	-315	286	-281	1.268	-1.264	0.844	-0.836
30	311	-294	275	-269	1.268	-1.268	0.848	-0.836
31	334	-325	302	-299	1.592	-1.588	1.064	-1.056

Table D.1: Maximum frame resistances and average roof drifts in each cycle (SCBF test)

Cycle	Maximum Shear (kips)				Maximum ave. RDR, percent			
	Y-direction		X-direction		Y-direction		X-direction	
	Pos	Neg	Pos	Neg	Pos	Neg	Pos	Neg
32	316	-305	291	-284	1.596	-1.592	1.064	-1.056
33	335	-315	311	-308	1.916	-1.900	1.280	-1.272
34	-4	-7	299	-291	-0.828	-0.812	1.280	-1.272
35	-8	-4	320	-311	-0.828	-0.812	1.496	-1.488
36	-7	-3	301	-295	-0.828	-0.812	1.496	-1.488
37	-7	-3	321	-313	-0.832	-0.812	1.708	-1.708
38	-6	-2	303	-296	-0.832	-0.812	1.712	-1.708

Table D.2: Maximum frame story drift ratios in each cycle (SCBF test)

Cycle	Max 2nd SDR, percent				Max 1st SDR, percent			
	Y-direction		X-direction		Y-direction		X-direction	
	Pos	Neg	Pos	Neg	Pos	Neg	Pos	Neg
1	0.123	-0.125	0.131	-0.127	0.111	-0.113	0.113	-0.111
2	0.123	-0.125	0.131	-0.127	0.110	-0.113	0.111	-0.111
3	0.123	-0.126	0.132	-0.129	0.110	-0.113	0.111	-0.111
4	0.123	-0.126	0.130	-0.127	0.110	-0.113	0.110	-0.111
5	0.124	-0.124	0.086	-0.084	0.110	-0.113	0.071	-0.072
6	0.124	-0.125	0.088	-0.083	0.110	-0.113	0.072	-0.072
7	0.187	-0.187	0.130	-0.128	0.166	-0.170	0.109	-0.112
8	0.187	-0.187	0.133	-0.125	0.166	-0.170	0.111	-0.111
9	0.251	-0.249	0.172	-0.167	0.223	-0.228	0.144	-0.147
10	0.251	-0.249	0.174	-0.165	0.222	-0.227	0.145	-0.146
11	0.310	-0.307	0.218	-0.208	0.284	-0.291	0.184	-0.186
12	0.313	-0.308	0.219	-0.207	0.283	-0.291	0.184	-0.185
13	0.314	-0.307	0.217	-0.208	0.282	-0.292	0.183	-0.186
14	0.315	-0.307	0.219	-0.207	0.281	-0.291	0.184	-0.185
15	0.315	-0.306	0.217	-0.208	0.281	-0.291	0.182	-0.186

Table D.2: Maximum frame story drift ratios in each cycle (SCBF test)

Cycle	Max 2nd SDR, percent				Max 1st SDR, percent			
	Y-direction		X-direction		Y-direction		X-direction	
	Pos	Neg	Pos	Neg	Pos	Neg	Pos	Neg
16	0.317	-0.307	0.219	-0.209	0.281	-0.291	0.184	-0.185
17	0.406	-0.397	0.272	-0.257	0.350	-0.361	0.233	-0.239
18	0.407	-0.400	0.272	-0.257	0.349	-0.358	0.235	-0.238
19	0.492	-0.485	0.319	-0.301	0.422	-0.431	0.290	-0.298
20	0.497	-0.491	0.319	-0.301	0.419	-0.427	0.292	-0.297
21	0.581	-0.581	0.371	-0.356	0.493	-0.502	0.343	-0.351
22	0.587	-0.589	0.370	-0.357	0.488	-0.495	0.348	-0.347
23	0.671	-0.676	0.424	-0.416	0.564	-0.570	0.398	-0.394
24	0.677	-0.685	0.421	-0.417	0.559	-0.559	0.403	-0.391
25	0.849	-0.860	0.532	-0.538	0.707	-0.704	0.502	-0.485
26	0.860	-0.876	0.532	-0.539	0.700	-0.692	0.506	-0.481
27	1.030	-1.050	0.646	-0.661	0.847	-0.837	0.604	-0.578
28	1.050	-1.070	0.649	-0.664	0.839	-0.826	0.607	-0.574
29	1.410	-1.420	0.886	-0.911	1.130	-1.110	0.801	-0.765
30	1.420	-1.440	0.899	-0.910	1.120	-1.090	0.795	-0.764
31	1.770	-1.800	1.130	-1.150	1.410	-1.380	0.992	-0.959
32	1.780	-1.830	1.160	-1.150	1.410	-1.350	0.972	-0.966
33	2.130	-2.350	1.380	-1.370	1.710	-1.530	1.180	-1.170
34	-1.060	-0.896	1.420	-1.360	-0.591	-0.734	1.140	-1.190
35	-1.070	-0.874	1.660	-1.590	-0.588	-0.756	1.330	-1.380
36	-1.060	-0.873	1.680	-1.600	-0.593	-0.757	1.320	-1.380
37	-1.070	-0.852	1.910	-1.840	-0.587	-0.779	1.510	-1.570
38	-1.070	-0.850	1.920	-1.850	-0.589	-0.781	1.500	-1.570

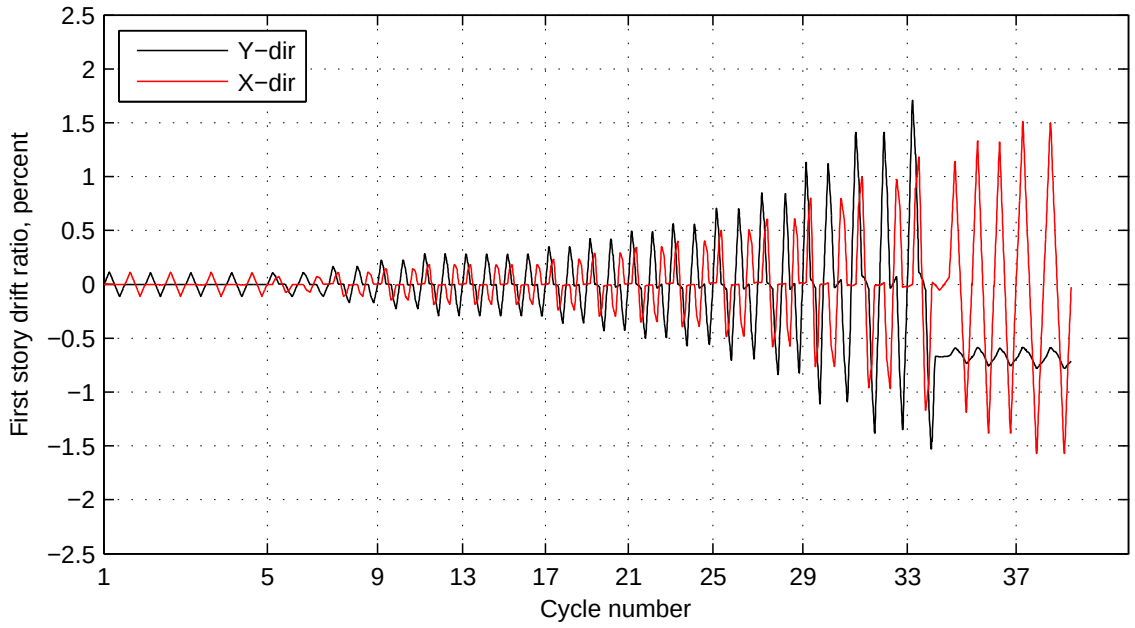

Figure D.3: Measured first-story drift ratios, percent (SCBF test)

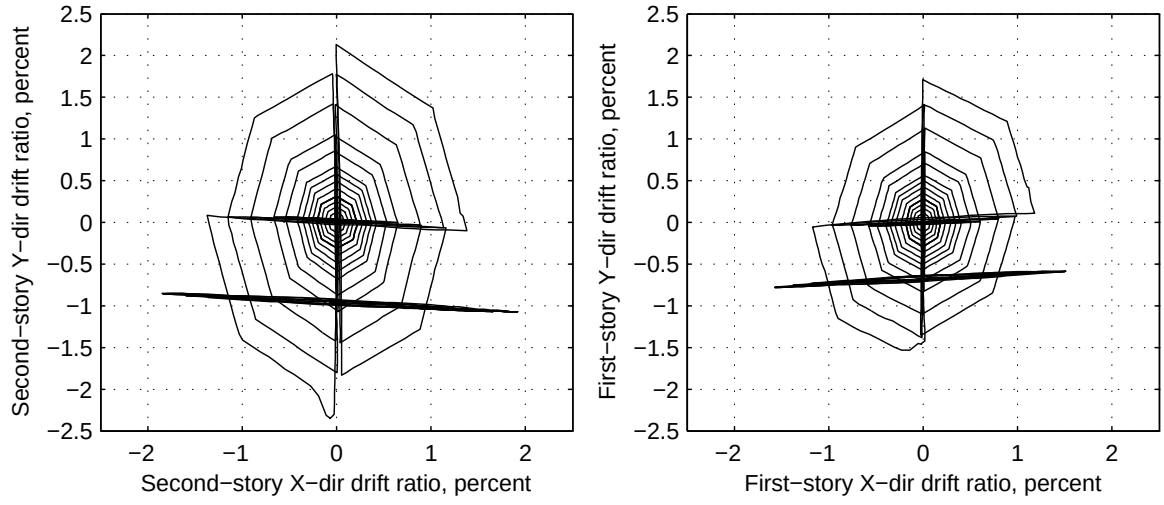

(a) Second-story SDR

(b) First-story SDR

Figure D.4: SDR cloverleaf traces, percent (SCBF test)

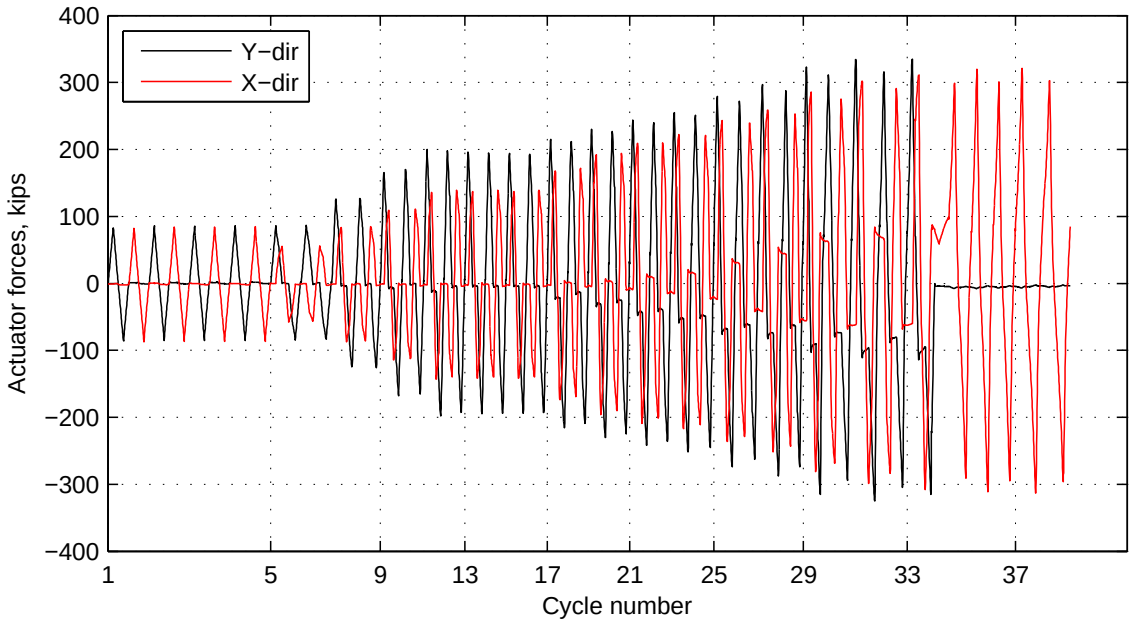

Figure D.5: Actuator forces in X and Y directions, kips (SCBF test)

D.2 SCBF Damage Tables

Tables D.3 through D.10 describe the damage states that were observed during the SCBF experiment at the end of each cycle. The descriptors follow the nomenclature defined in Section 4.2 and Figs. 4.6e and 4.6f.

Table D.3: Brace Performance State Progression Table (SCBF test)

	Y-dir SDR		X-dir SDR		Frame 1 (Y-Dir)						Frame B (X-Dir)					
Cycles	RDR	Story 2 Story 1	RDR	Story 2 Story 1	Story 1			Story 2			Story 1			Story 2		
					C	Dt	Db	C	Dt	Db	C	Dt	Db	C	Dt	Db
1-10	No observable damage during these cycles.															
11-16	0.298 -0.299	0.314 0.284 -0.307 -0.291	0.2 -0.197	0.218 0.184 -0.208 -0.186	B1		B1	B1	B1							
17-18	0.378 -0.379	0.406 0.35 -0.4 -0.361	0.253 -0.248	0.272 0.233 -0.257 -0.239							B1		B1			
19-20	0.456 -0.46	0.497 0.422 -0.491 -0.431	0.304 -0.3	0.319 0.29 -0.301 -0.298										B1	B1	
21-22	0.536 -0.54	0.587 0.493 -0.589 -0.502	0.357 -0.352	0.371 0.343 -0.356 -0.351	B2		B2	B2	B2							
23-24	0.616 -0.624	0.677 0.564 -0.685 -0.57	0.412 -0.404	0.424 0.398 -0.416 -0.394												
25-26	0.78 -0.784	0.86 0.707 -0.876 -0.704	0.516 -0.512	0.532 0.502 -0.538 -0.485							B2		B2	B2	B2	
27-28	0.94 -0.944	1.05 0.847 -1.07 -0.837	0.624 -0.62	0.646 0.604 -0.661 -0.578	B3		B3	B3	B3							
29-30	1.268 -1.264	1.42 1.13 -1.44 -1.11	0.844 -0.836	0.886 0.801 -0.911 -0.765												
31-32	1.592 -1.588	1.78 1.41 -1.83 -1.38	1.064 -1.056	1.13 0.992 -1.15 -0.959					BC		B3		B3	B3	B3	
33	1.916	2.13 1.71	1.28	1.38 1.18												

Continued on next page

Table D.3 – continued from previous page

	Y-dir SDR		X-dir SDR		Frame 1 (Y-Dir)						Frame B (X-Dir)					
Cycles	RDR	Story 2 Story 1	RDR	Story 2 Story 1	Story 1			Story 2			Story 1			Story 2		
					C	Dt	Db	C	Dt	Db	C	Dt	Db	C	Dt	Db
	-1.9	-2.35 -1.53	-1.272	-1.37 -1.17					BF							
34	-0.828	-1.07 -0.591	1.28	1.42 1.14	No loading in this direction following brace fracture. Uni-directional loading in X-direction only.											
	-0.812	-0.873 -0.734	-1.272	-1.36 -1.19												
35-36	-0.828	-1.07 -0.593	1.496	1.66 1.33												
	-0.812	-0.873 -0.757	-1.488	-1.59 -1.38												
37-38	-0.828	-1.07 -0.589	1.712	1.92 1.5												
	-0.812	-0.873 -0.781	-1.708	-1.85 -1.57												

Table D.4: Frame 1 Gusset Plate Performance State Progression Table (SCBF test)

	Y-dir SDR		X-dir SDR		Frame 1 (Y-Dir)									
Cycles	RDR	Story 2 Story 1	RDR	Story 2 Story 1	Story 1					Story 2				
					A1-base	B1-base	m	2F-A1-b	2F-B1-b	2F-A1-a	2F-B1-a	m	3F-A1	3F-B1
1-6	No observable damage during these cycles.													
7-8	0.176	0.187 0.166	0.12	0.13 0.109				Y1		Y1				
	-0.179	-0.187 -0.17	-0.119	-0.128 -0.112										
9-10	0.237	0.251 0.223	0.158	0.172 0.144	Y1				Y1		Y1		Y1	Y1
	-0.238	-0.249 -0.228	-0.156	-0.167 -0.147										
11-16	0.298	0.314 0.284	0.2	0.218 0.184										
	-0.299	-0.307 -0.291	-0.197	-0.208 -0.186										
17-18	0.378	0.406 0.35	0.253	0.272 0.233		Y1								
	-0.379	-0.4 -0.361	-0.248	-0.257 -0.239										
19-20	0.456	0.497 0.422	0.304	0.319 0.29			Y1					Y1		
	-0.46	-0.491 -0.431	-0.3	-0.301 -0.298										
21-22	0.536	0.587 0.493	0.357	0.371 0.343										
	-0.54	-0.589 -0.502	-0.352	-0.356 -0.351										
23-24	0.616	0.677 0.564	0.412	0.424 0.398			Y2						Y2	
	-0.624	-0.685 -0.57	-0.404	-0.416 -0.394										
25-26	0.78	0.86 0.707	0.516	0.532 0.502	Y2			Y2	Y2	Y2	Y2	Y2		
	-0.784	-0.876 -0.704	-0.512	-0.538 -0.485										Y2

Continued on next page

Table D.4 – continued from previous page

	Y-dir SDR		X-dir SDR		Frame 1 (Y-Dir)									
Cycles	RDR	Story 2 Story 1	RDR	Story 2 Story 1	Story 1					Story 2				
					A1-base	B1-base	m	2F-A1-b	2F-B1-b	2F-A1-a	2F-B1-a	m	3F-A1	3F-B1
27-28	0.94 0.847 -1.07 -0.837	1.05 0.847 -1.07 -0.837	0.624 -0.62	0.646 0.604 -0.661 -0.578		Y2	Y3		Y3			Y3	Y3	
29-30	1.268 1.13 -1.44 -1.264	1.42 1.13 -1.44 -1.11	0.844 -0.836	0.886 0.801 -0.911 -0.765	Y3	Y3		B3,Y3		B3,Y3	Y3			Y3
31-32	1.592 1.41 -1.83 -1.588	1.78 1.41 -1.83 -1.38	1.064 -1.056	1.13 0.992 -1.15 -0.959				WBc					B3, Wb	WBc
33	1.916 1.71 -2.35 -1.9	2.13 1.71 -2.35 -1.53	1.28 -1.272	1.38 1.18 -1.37 -1.17					B3		B3			
34-38	No loading in the Y-direction following brace fracture. Uni-directionl loading in X-direction only.													

Table D.5: Frame B Gusset Plate Performance State Progression Table (SCBF test)

	Y-dir SDR		X-dir SDR		Frame B (X-Dir)									
Cycles	RDR	Story 2 Story 1	RDR	Story 2 Story 1	Story 1					Story 2				
					B1-base	B2-base	m	2F-B1-b	2F-B2-b	2F-B1-a	2F-B2-a	m	3F-B1	3F-B2
1-10	No observable damage during these cycles.													
11-16	0.298	0.314 0.284	0.2	0.218 0.184				Y1	Y1	Y1	Y1			Y1
	-0.299	-0.307 -0.291	-0.197	-0.208 -0.186										
17-18	0.378	0.406 0.35	0.253	0.272 0.233									Y1	
	-0.379	-0.4 -0.361	-0.248	-0.257 -0.239										
19-20	0.456	0.497 0.422	0.304	0.319 0.29	Y1									
	-0.46	-0.491 -0.431	-0.3	-0.301 -0.298										
21-22	0.536	0.587 0.493	0.357	0.371 0.343			Y1					Y1		
	-0.54	-0.589 -0.502	-0.352	-0.356 -0.351										
23-24	0.616	0.677 0.564	0.412	0.424 0.398										
	-0.624	-0.685 -0.57	-0.404	-0.416 -0.394										
25-26	0.78	0.86 0.707	0.516	0.532 0.502		Y1								
	-0.784	-0.876 -0.704	-0.512	-0.538 -0.485										
27-28	0.94	1.05 0.847	0.624	0.646 0.604	Y2	Y2	Y2	Y2				Y2	Y2	
	-0.944	-1.07 -0.837	-0.62	-0.661 -0.578										
29-30	1.268	1.42 1.13	0.844	0.886 0.801				Y3						
	-1.264	-1.44 -1.11	-0.836	-0.911 -0.765	Y3	Y3	Y3		Y2		Y2	Y3		

Continued on next page

Table D.5 – continued from previous page

	Y-dir SDR		X-dir SDR		Frame B (X-Dir)									
Cycles	RDR	Story 2 Story 1	RDR	Story 2 Story 1	Story 1					Story 2				
					B1-base	B2-base	m	2F-B1-b	2F-B2-b	2F-B1-a	2F-B2-a	m	3F-B1	3F-B2
31-32	1.592 -1.588	1.78 1.41 -1.83 -1.38	1.064 -1.056	1.13 0.992 -1.15 -0.959					Y3	Y2	Y3			Y2
33	1.916 -1.9	2.13 1.71 -2.35 -1.53	1.28 -1.272	1.38 1.18 -1.37 -1.17						Y3				
34	-0.828 -0.812	-1.07 -0.591 -0.873 -0.734	1.28 -1.272	1.42 1.14 -1.36 -1.19										
35-36	-0.828 -0.812	-1.07 -0.593 -0.873 -0.757	1.496 -1.488	1.66 1.33 -1.59 -1.38									Y3	B3
37-38	-0.828 -0.812	-1.07 -0.589 -0.873 -0.781	1.712 -1.708	1.92 1.5 -1.85 -1.57									WBb	Y3

Table D.6: Column A-1 Performance State Progression Table (SCBF test)

Cycles	Y-dir SDR		X-dir SDR		Column A-1					
	RDR	Story 2 Story 1	RDR	Story 2 Story 1	1Sb	1St	2F panel zone	2Sb	2St	3F panel zone
1-22	No observable damage during these cycles.									
23-24	0.616	0.677 0.564	0.412	0.424 0.398						Y1
	-0.624	-0.685 -0.57	-0.404	-0.416 -0.394						
25-26	0.78	0.86 0.707	0.516	0.532 0.502	Y1				Y1	
	-0.784	-0.876 -0.704	-0.512	-0.538 -0.485						
27-28	0.94	1.05 0.847	0.624	0.646 0.604		Y1				
	-0.944	-1.07 -0.837	-0.62	-0.661 -0.578						
29-30	1.268	1.42 1.13	0.844	0.886 0.801	Y2		Y1			Y2
	-1.264	-1.44 -1.11	-0.836	-0.911 -0.765						
31-32	1.592	1.78 1.41	1.064	1.13 0.992	Y3		Y2	Y1		Y3
	-1.588	-1.83 -1.38	-1.056	-1.15 -0.959						
33	1.916	2.13 1.71	1.28	1.38 1.18		Y2	Y3		Y2	
	-1.9	-2.35 -1.53	-1.272	-1.37 -1.17						
34-38	No loading in the Y-direction following brace fracture. Uni-directionl loading in X-direction only.									

Table D.7: Column B-1 Performance State Progression Table (SCBF test)

Cycles	Y-dir SDR		X-dir SDR		Column B-1					
	RDR	Story 2 Story 1	RDR	Story 2 Story 1	1Sb	1St	2F panel zone	2Sb	2St	3F panel zone
1-18	No observable damage during these cycles.									
19-20	0.456	0.497 0.422	0.304	0.319 0.29	Y1					
	-0.46	-0.491 -0.431	-0.3	-0.301 -0.298				Y1		
21-22	0.536	0.587 0.493	0.357	0.371 0.343						
	-0.54	-0.589 -0.502	-0.352	-0.356 -0.351						
23-24	0.616	0.677 0.564	0.412	0.424 0.398					Y1	
	-0.624	-0.685 -0.57	-0.404	-0.416 -0.394						
25-26	0.78	0.86 0.707	0.516	0.532 0.502			Y1			Y1
	-0.784	-0.876 -0.704	-0.512	-0.538 -0.485						
27-28	0.94	1.05 0.847	0.624	0.646 0.604	Y2					
	-0.944	-1.07 -0.837	-0.62	-0.661 -0.578						
29-30	1.268	1.42 1.13	0.844	0.886 0.801	Y3				Y2	Y2
	-1.264	-1.44 -1.11	-0.836	-0.911 -0.765						
31-32	1.592	1.78 1.41	1.064	1.13 0.992		Y1				Y3
	-1.588	-1.83 -1.38	-1.056	-1.15 -0.959						
33	1.916	2.13 1.71	1.28	1.38 1.18					Y3	
	-1.9	-2.35 -1.53	-1.272	-1.37 -1.17						
34-38	No loading in the Y-direction following brace fracture. Uni-directionl loading in X-direction only.									

Table D.8: Column B-2 Performance State Progression Table (SCBF test)

Cycles	Y-dir SDR		X-dir SDR		Column B-2					
	RDR	Story 2 Story 1	RDR	Story 2 Story 1	1Sb	1St	2F panel zone	2Sb	2St	3F panel zone
1-26	No observable damage during these cycles.									
27-28	0.94 -0.944	1.05 0.847 -1.07 -0.837	0.624 -0.62	0.646 0.604 -0.661 -0.578	Y1				Y1	Y1
29-30	1.268 -1.264	1.42 1.13 -1.44 -1.11	0.844 -0.836	0.886 0.801 -0.911 -0.765	Y2	Y1				Y2
31-32	1.592 -1.588	1.78 1.41 -1.83 -1.38	1.064 -1.056	1.13 0.992 -1.15 -0.959	Y3					
33	1.916 -1.9	2.13 1.71 -2.35 -1.53	1.28 -1.272	1.38 1.18 -1.37 -1.17						
34	-0.828 -0.812	-1.07 -0.591 -0.873 -0.734	1.28 -1.272	1.42 1.14 -1.36 -1.19						
35-36	-0.828 -0.812	-1.07 -0.593 -0.873 -0.757	1.496 -1.488	1.66 1.33 -1.59 -1.38						Y3
37-38	-0.828 -0.812	-1.07 -0.589 -0.873 -0.781	1.712 -1.708	1.92 1.5 -1.85 -1.57		Y2				

Table D.9: Frame 1 Beams Performance State Progression Table (SCBF test)

Cycles	Y-dir SDR		X-dir SDR		2nd Floor		3rd Floor	
	RDR	Story 2 Story 1	RDR	Story 2 Story 1	A-1	B-1	A-1	B-1
1-20	No observable damage during these cycles.							
21-22	0.536	0.587 0.493	0.357	0.371 0.343	Y1	Y1		
	-0.54	-0.589 -0.502	-0.352	-0.356 -0.351				
23-24	0.616	0.677 0.564	0.412	0.424 0.398				Y1
	-0.624	-0.685 -0.57	-0.404	-0.416 -0.394				
25-26	0.78	0.86 0.707	0.516	0.532 0.502				
	-0.784	-0.876 -0.704	-0.512	-0.538 -0.485				
27-28	0.94	1.05 0.847	0.624	0.646 0.604				
	-0.944	-1.07 -0.837	-0.62	-0.661 -0.578			Y1	
29-30	1.268	1.42 1.13	0.844	0.886 0.801		Y2		Y2
	-1.264	-1.44 -1.11	-0.836	-0.911 -0.765				
31-32	1.592	1.78 1.41	1.064	1.13 0.992		Y3		
	-1.588	-1.83 -1.38	-1.056	-1.15 -0.959			Y2	Y3
33	1.916	2.13 1.71	1.28	1.38 1.18		B1 Web		
	-1.9	-2.35 -1.53	-1.272	-1.37 -1.17				
34-38	No loading in the Y-direction following brace fracture. Uni-directionl loading in X-direction only.							

Table D.10: Frame B Beams Performance State Progression Table (SCBF test)

Cycles	Y-dir SDR		X-dir SDR		2nd Floor		3rd Floor	
	RDR	Story 2 Story 1	RDR	Story 2 Story 1	B-1	B-2	B-1	B-2
1-22	No observable damage during these cycles.							
23-24	0.616	0.677 0.564	0.412	0.424 0.398				
	-0.624	-0.685 -0.57	-0.404	-0.416 -0.394				Y1
25-26	0.78	0.86 0.707	0.516	0.532 0.502	Y1			
	-0.784	-0.876 -0.704	-0.512	-0.538 -0.485				
27-28	0.94	1.05 0.847	0.624	0.646 0.604				
	-0.944	-1.07 -0.837	-0.62	-0.661 -0.578		Y1		
29-30	1.268	1.42 1.13	0.844	0.886 0.801			Y1	
	-1.264	-1.44 -1.11	-0.836	-0.911 -0.765				
31-32	1.592	1.78 1.41	1.064	1.13 0.992				
	-1.588	-1.83 -1.38	-1.056	-1.15 -0.959				
33	1.916	2.13 1.71	1.28	1.38 1.18				
	-1.9	-2.35 -1.53	-1.272	-1.37 -1.17				
34	-0.828	-1.07 -0.591	1.28	1.42 1.14	Y3			
	-0.812	-0.873 -0.734	-1.272	-1.36 -1.19				
35-36	-0.828	-1.07 -0.593	1.496	1.66 1.33				
	-0.812	-0.873 -0.757	-1.488	-1.59 -1.38				
37-38	-0.828	-1.07 -0.589	1.712	1.92 1.5				
	-0.812	-0.873 -0.781	-1.708	-1.85 -1.57				

D.3 SCBF energy dissipation

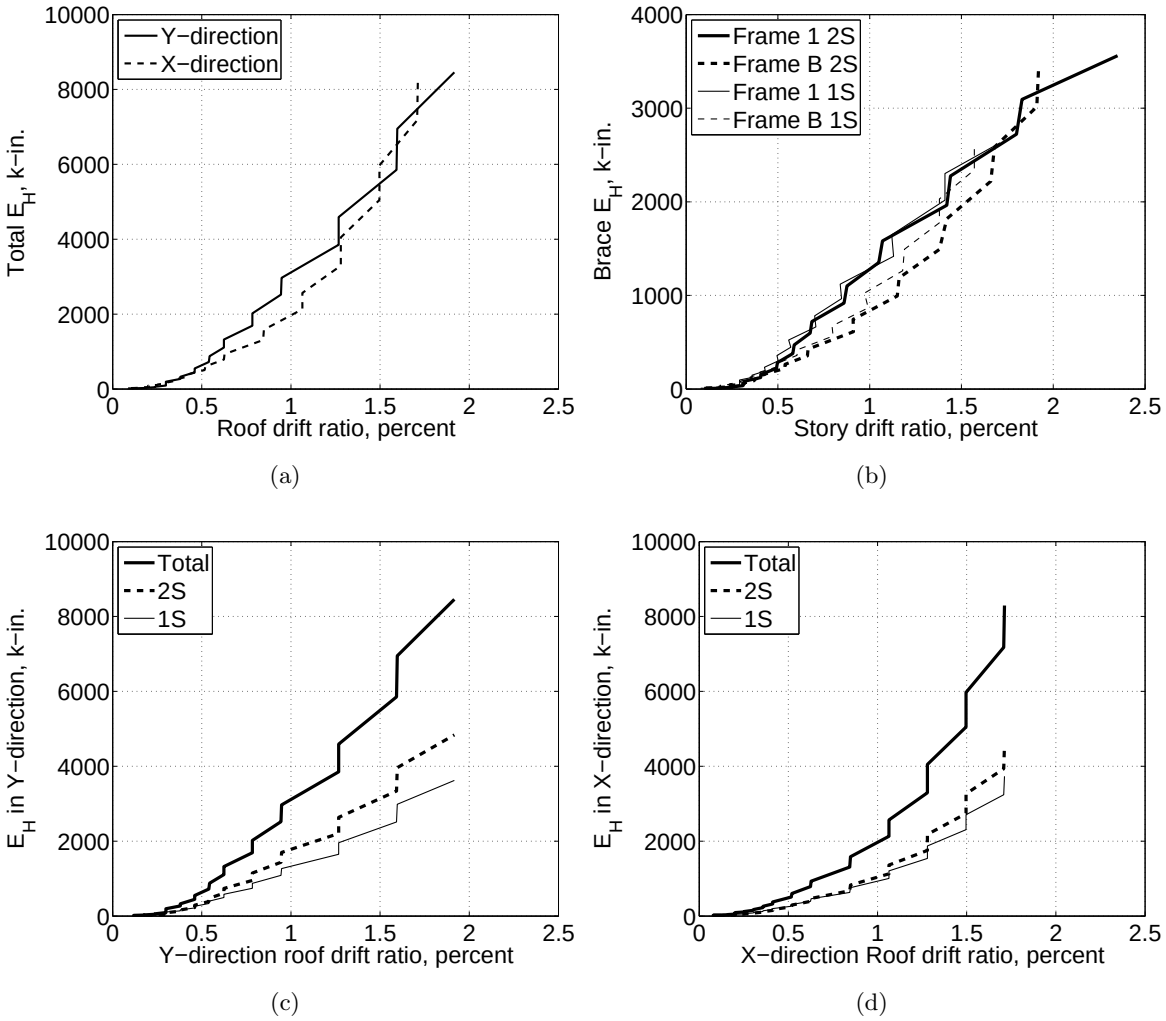

Figure D.6: Energy dissipation comparison: (a) total energy dissipated in each principal direction; (b) energy dissipated by braces in each frame and story; (c) energy dissipated in the Y-directions frames; (d) energy dissipated in the X-direction frames.

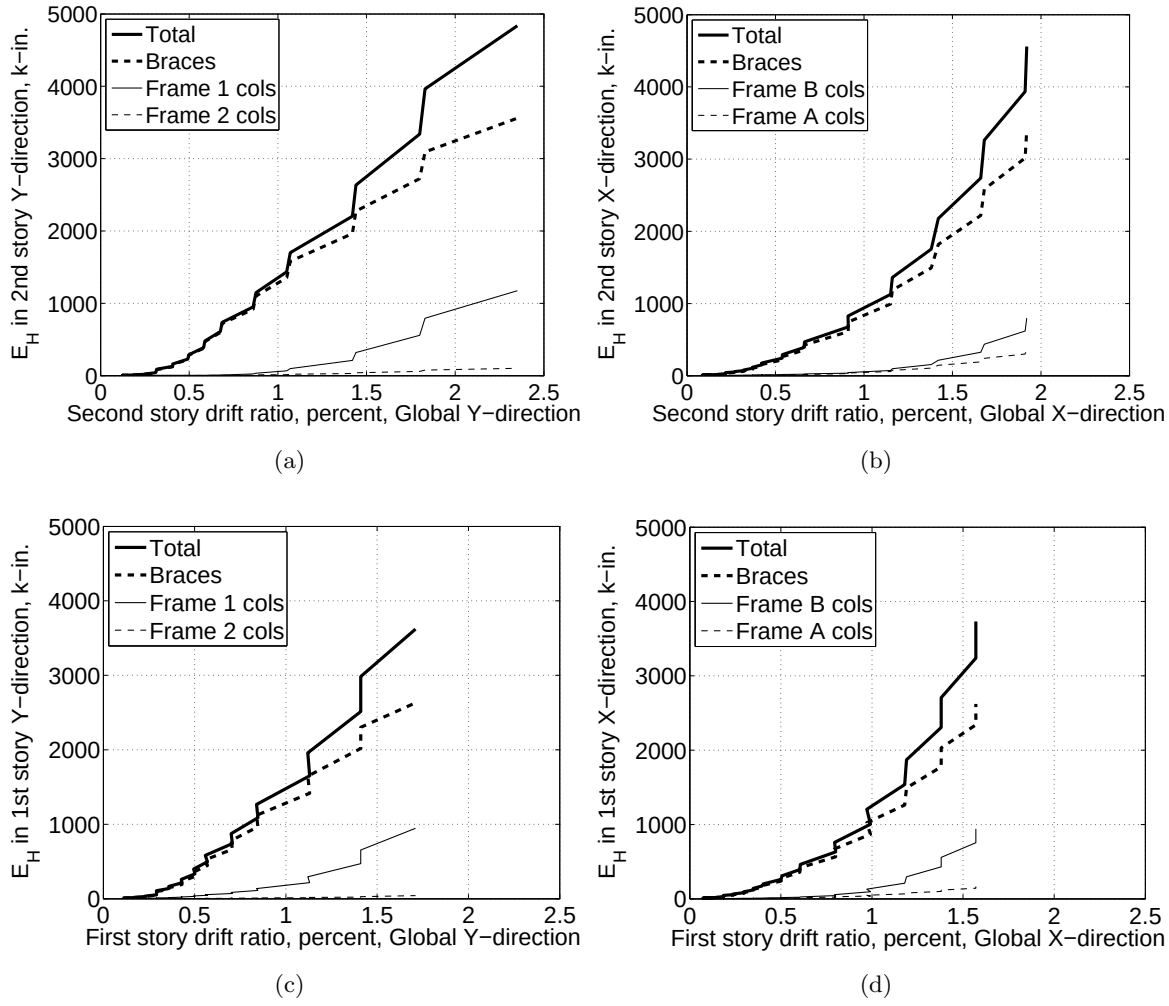

Figure D.7: Energy dissipation comparison: (a) second story frames in Y-direction; (b) second story frames in X-direction; (c) first story frames in Y-direction; (d) first story frames in X-direction.

Appendix E

BRBF EXPERIMENTAL PLOTS AND TABLES

This appendix provides additional tables, figures and plots to supplement the BRBF test results discussed in Section 4.5.

E.1 BRBF Displacement and Loading Protocol Information

Figure E.1 shows the displacement imposed on the specimen in the X and Y directions by the crosshead, as measured by the LVDTs in crosshead actuators. The histories of story drift ratios for each story in each direction are shown in Figures E.2 and E.3. Five points are noted in Fig. E.1 and correspond to the occurrence of major damage and these are listed in Table E.1.

Figures E.4a and E.4b show the cloverleaf SDR traces for the second and first story, respectively.

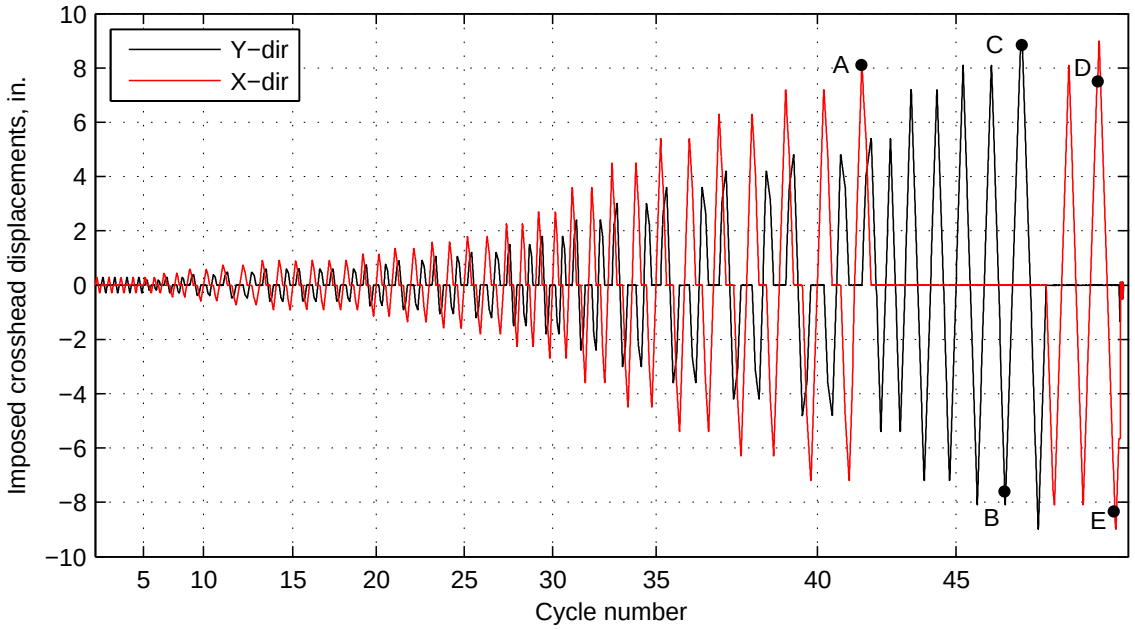

Figure E.1: Imposed Crosshead Displacements (BRBF test)

Figure E.5 shows the forces in the actuators in the X and Y directions as a function of cycle number. The peak positive force in the Y-direction was 348 kips while the peak positive force in the X-direction was 354 kips. The peak negative force in the Y-direction

Table E.1: BRBF experimental damage description (Fig. E.1)

Mark	Damage Description
A	Divot in column B-2 flange observed
B	Frame 1 third floor beam bottom flange tearing at column B-2 side
C	Frame 1 BRB core fracture
D	Frame B BRB core fracture
E	Frame B second floor beam bottom flange fracture at column B-2 side

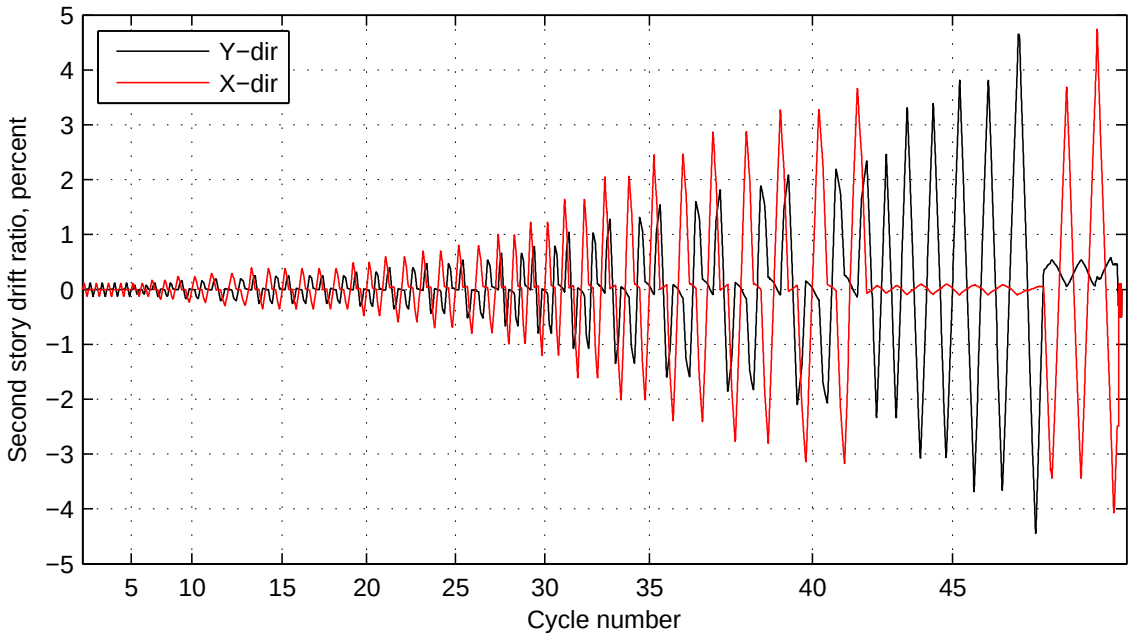

Figure E.2: Measured second-story drift ratios, percent (BRBF test)

was -400 kips while the peak negative force in the X-direction was -403 kips. The difference in peak positive and negative forces was mainly due to the BRB compression overstrength. Tables E.2 and E.3 list the peak negative and positive shear forces and roof and story drift ratios for each cycle.

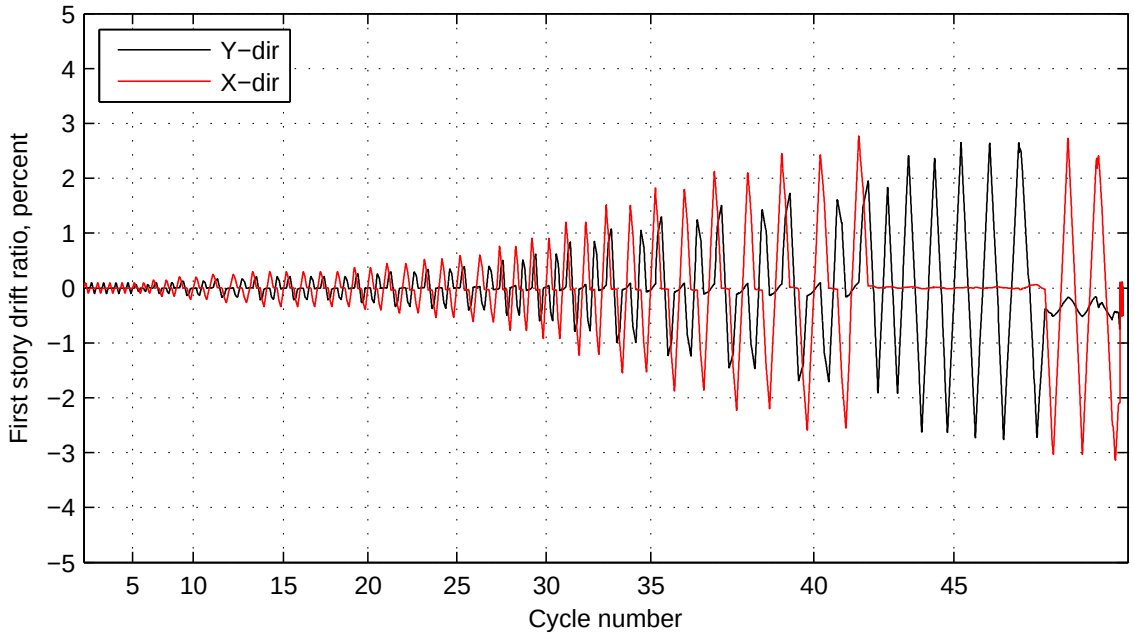

Figure E.3: Measured first-story drift ratios, percent (BRBF test)

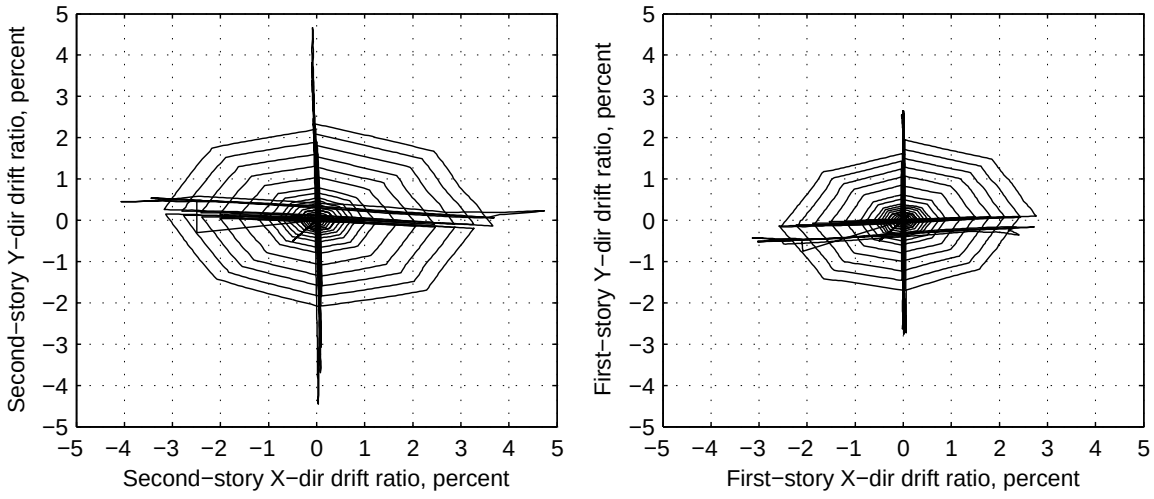

(a) Second-story SDR

(b) First-story SDR

Figure E.4: SDR cloverleaf traces, percent (BRBF test)

Table E.2: Maximum frame resistances and average roof drifts in each cycle (BRBF test)

Cycle	Maximum Shear (kips)				Maximum ave. RDR, percent			
	Y-direction		X-direction		Y-direction		X-direction	
	Pos	Neg	Pos	Neg	Pos	Neg	Pos	Neg

Table E.2: Maximum frame resistances and average roof drifts in each cycle (BRBF test)

Cycle	Maximum Shear (kips)				Maximum ave. RDR, percent			
	Y-direction		X-direction		Y-direction		X-direction	
	Pos	Neg	Pos	Neg	Pos	Neg	Pos	Neg
1	47	-27	48	-29	0.107	-0.114	0.104	-0.112
2	46	-27	48	-28	0.107	-0.114	0.104	-0.112
3	46	-27	47	-28	0.107	-0.114	0.104	-0.112
4	46	-27	47	-28	0.107	-0.114	0.104	-0.112
5	27	-20	47	-28	0.068	-0.075	0.104	-0.112
6	-19	27	-28	47	-0.074	0.069	-0.112	0.104
7	45	-27	72	-42	0.106	-0.114	0.156	-0.166
8	-26	46	-41	71	-0.114	0.107	-0.166	0.156
9	61	-39	98	-66	0.142	-0.150	0.215	-0.223
10	-38	62	-66	98	-0.149	0.143	-0.224	0.216
11	79	-56	122	-94	0.181	-0.187	0.270	-0.278
12	-55	79	-93	121	-0.186	0.182	-0.278	0.270
13	99	-79	140	-137	0.227	-0.234	0.340	-0.346
14	-78	100	-137	137	-0.233	0.228	-0.347	0.340
15	98	-79	137	-136	0.227	-0.234	0.340	-0.347
16	-77	100	-136	138	-0.233	0.228	-0.346	0.340
17	98	-79	137	-136	0.227	-0.234	0.341	-0.347
18	-77	100	-136	137	-0.232	0.228	-0.347	0.341
19	125	-109	152	-171	0.286	-0.290	0.432	-0.436
20	-107	126	-170	150	-0.289	0.287	-0.436	0.432
21	141	-146	161	-188	0.345	-0.347	0.520	-0.524
22	-143	142	-188	160	-0.346	0.347	-0.524	0.520
23	150	-170	172	-200	0.404	-0.404	0.612	-0.616

Table E.2: Maximum frame resistances and average roof drifts in each cycle (BRBF test)

Cycle	Maximum Shear (kips)				Maximum ave. RDR, percent			
	Y-direction		X-direction		Y-direction		X-direction	
	Pos	Neg	Pos	Neg	Pos	Neg	Pos	Neg
24	-164	152	-200	171	-0.404	0.408	-0.616	0.612
25	157	-183	181	-213	0.464	-0.464	0.700	-0.704
26	-176	160	-213	183	-0.460	0.468	-0.704	0.700
27	171	-201	203	-243	0.580	-0.580	0.876	-0.880
28	-194	174	-241	204	-0.580	0.584	-0.880	0.876
29	185	-220	226	-269	0.700	-0.700	1.060	-1.060
30	-214	189	-267	229	-0.696	0.704	-1.056	1.060
31	210	-263	260	-304	0.940	-0.936	1.424	-1.416
32	-253	221	-302	266	-0.932	0.940	-1.412	1.420
33	237	-295	291	-327	1.180	-1.168	1.780	-1.772
34	-280	255	295	-324	-1.168	1.180	1.780	-1.772
35	268	-319	318	-349	1.416	-1.412	2.132	-2.136
36	-297	286	319	-346	-1.408	1.420	2.132	-2.136
37	285	-334	331	-364	1.656	-1.652	2.492	-2.500
38	-308	304	333	-363	-1.652	1.660	2.488	-2.500
39	297	-347	344	-380	1.900	-1.892	2.852	-2.864
40	-319	318	344	-378	-1.892	1.904	2.852	-2.864
41	309	-366	354	-258	2.140	-2.128	-0.027	3.212
42	329	-366	-210	-163	2.144	-2.128	-0.027	0.036
43	340	-398	-209	-148	2.860	-2.848	-0.041	0.042
44	342	-400	-201	-145	2.864	-2.844	-0.042	0.042
45	345	-389	-200	-141	3.228	-3.208	-0.050	0.047
46	348	-395	-197	-139	3.224	-3.212	-0.050	0.047
47	335	-343	-196	-138	3.600	-3.584	-0.060	0.051
48	160	106	-403	344	0.011	-0.055	3.208	-3.236
49	126	1	318	-335	0.011	-0.528	3.572	-3.604

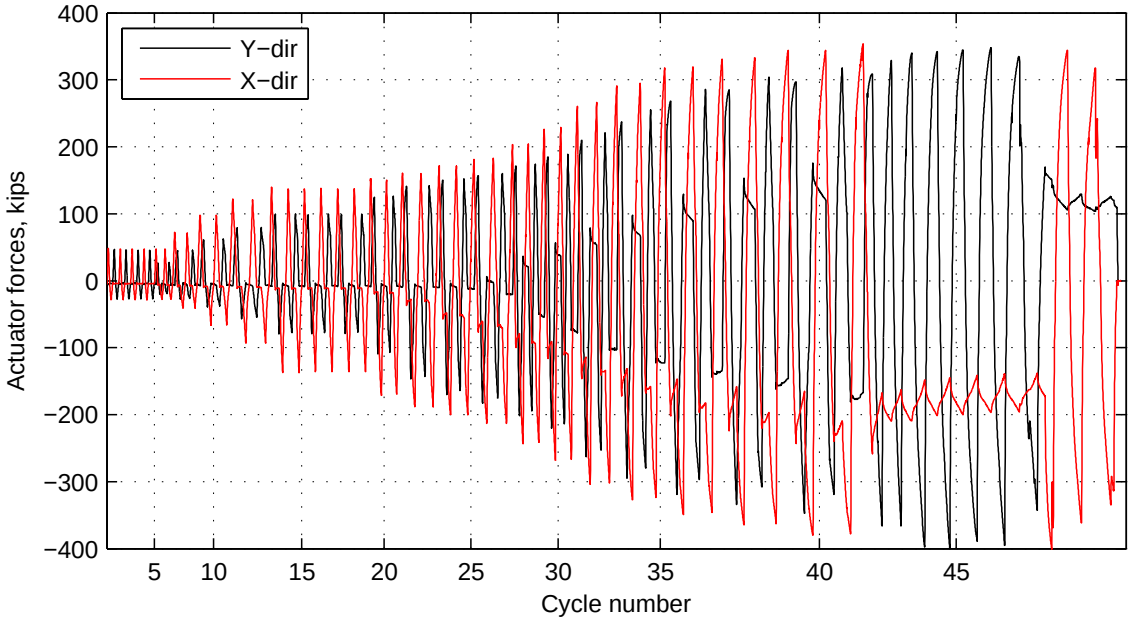

Figure E.5: Actuator forces in X and Y directions, kips (BRBF test)

Table E.3: Maximum frame story drift ratios in each cycle (BRBF test)

Cycle	Max 2nd SDR, percent				Max 1st SDR, percent			
	Y-direction		X-direction		Y-direction		X-direction	
	Pos	Neg	Pos	Neg	Pos	Neg	Pos	Neg
1	0.117	-0.129	0.111	-0.126	0.097	-0.100	0.096	-0.098
2	0.117	-0.129	0.111	-0.127	0.097	-0.100	0.096	-0.098
3	0.117	-0.129	0.111	-0.127	0.097	-0.100	0.096	-0.098
4	0.117	-0.129	0.111	-0.127	0.097	-0.100	0.096	-0.098
5	0.075	-0.085	0.111	-0.127	0.062	-0.064	0.097	-0.097
6	-0.085	0.076	-0.127	0.111	-0.064	0.062	-0.097	0.096
7	0.117	-0.129	0.169	-0.178	0.096	-0.100	0.146	-0.155
8	-0.129	0.117	-0.177	0.169	-0.099	0.097	-0.155	0.146
9	0.156	-0.165	0.233	-0.236	0.129	-0.135	0.199	-0.211
10	-0.165	0.156	-0.238	0.232	-0.133	0.130	-0.211	0.200
11	0.196	-0.205	0.290	-0.295	0.165	-0.169	0.249	-0.264

Table E.3: Maximum frame story drift ratios in each cycle (BRBF test)

Cycle	Max 2nd SDR, percent				Max 1st SDR, percent			
	Y-direction		X-direction		Y-direction		X-direction	
	Pos	Neg	Pos	Neg	Pos	Neg	Pos	Neg
12	-0.205	0.197	-0.293	0.291	-0.168	0.167	-0.263	0.249
13	0.248	-0.254	0.386	-0.356	0.206	-0.213	0.298	-0.337
14	-0.254	0.248	-0.358	0.382	-0.212	0.209	-0.337	0.299
15	0.248	-0.254	0.384	-0.356	0.206	-0.214	0.298	-0.337
16	-0.254	0.248	-0.356	0.382	-0.212	0.209	-0.337	0.300
17	0.248	-0.254	0.384	-0.357	0.207	-0.213	0.300	-0.337
18	-0.253	0.248	-0.358	0.382	-0.212	0.209	-0.337	0.300
19	0.314	-0.310	0.490	-0.482	0.258	-0.270	0.373	-0.392
20	-0.309	0.318	-0.481	0.495	-0.270	0.257	-0.394	0.371
21	0.400	-0.355	0.596	-0.592	0.291	-0.338	0.442	-0.458
22	-0.356	0.400	-0.592	0.597	-0.336	0.294	-0.456	0.443
23	0.470	-0.436	0.699	-0.698	0.337	-0.374	0.522	-0.537
24	-0.438	0.469	-0.695	0.699	-0.369	0.344	-0.537	0.524
25	0.535	-0.523	0.804	-0.799	0.392	-0.403	0.594	-0.611
26	-0.522	0.538	-0.790	0.796	-0.400	0.394	-0.621	0.601
27	0.656	-0.664	1.000	-0.991	0.508	-0.498	0.753	-0.774
28	-0.664	0.661	-0.988	0.997	-0.497	0.509	-0.775	0.760
29	0.785	-0.800	1.220	-1.200	0.618	-0.598	0.902	-0.922
30	-0.799	0.789	-1.200	1.220	-0.595	0.618	-0.917	0.902
31	1.040	-1.080	1.640	-1.610	0.837	-0.788	1.200	-1.220
32	-1.080	1.030	-1.610	1.640	-0.783	0.850	-1.210	1.200
33	1.280	-1.350	2.050	-2.010	1.080	-0.992	1.510	-1.540
34	-1.350	1.310	2.060	-2.010	-0.994	1.050	1.500	-1.530
35	1.540	-1.600	2.450	-2.390	1.300	-1.230	1.820	-1.880
36	-1.590	1.600	2.470	-2.410	-1.240	1.240	1.800	-1.860
37	1.810	-1.850	2.870	-2.770	1.500	-1.450	2.120	-2.230
38	-1.830	1.890	2.880	-2.800	-1.470	1.430	2.100	-2.200
39	2.080	-2.100	3.270	-3.140	1.720	-1.690	2.440	-2.590

Table E.3: Maximum frame story drift ratios in each cycle (BRBF test)

Cycle	Max 2nd SDR, percent				Max 1st SDR, percent			
	Y-direction		X-direction		Y-direction		X-direction	
	Pos	Neg	Pos	Neg	Pos	Neg	Pos	Neg
40	-2.070	2.190	3.280	-3.170	-1.710	1.610	2.430	-2.550
41	2.340	-2.340	3.660	-0.073	1.950	-1.910	-0.134	2.770
42	2.460	-2.340	-0.072	0.073	1.830	-1.920	0.024	-0.002
43	3.310	-3.070	-0.097	0.094	2.410	-2.620	0.021	-0.012
44	3.380	-3.070	-0.093	0.096	2.360	-2.630	0.014	-0.014
45	3.810	-3.690	-0.105	0.082	2.650	-2.730	-0.004	0.012
46	3.810	-3.660	-0.104	0.085	2.640	-2.760	-0.007	0.021
47	4.660	-4.450	-0.101	0.058	2.650	-2.720	-0.032	0.064
48	0.056	0.540	-3.440	3.690	-0.165	-0.523	-3.030	2.730
49	0.578	-0.303	4.740	-4.070	-0.162	-0.749	2.410	-3.140

E.2 BRBF Damage Tables

Tables E.4 through E.9 describe the damage states that were observed during the SCBF experiment at the end of each cycle. The descriptors follow the nomenclature defined in Section 4.2.

Table E.4: Gusset Plate Performance State Progression Table (BRBF test)

	Y-dir SDR		X-dir SDR		Frame 1 (Y-Dir)				Frame B (X-Dir)			
Cycles	RDR	Story 2 Story 1	RDR	Story 2 Story 1	B1-base	2F-B1-b	2F-A1-t	3F-B1-b	B2-base	2F-A1-b	2F-B2-t	3F-B1-b
1-30	No observable damage during these cycles.											
31-32	0.94	1.04 0.84	1.42	1.64 1.20						Y1		
	-0.93	-1.08 -0.79	-1.42	-1.61 -1.22								
33-34	1.18	1.28 1.08	1.78	2.05 1.51							Y1	
	-1.17	-1.35 -0.99	-1.78	-2.01 -1.54								
35-36	1.42	1.54 1.3	2.14	2.45 1.82							Wc (0.75")	
	-1.42	-1.60 -1.23	-2.14	-2.39 -1.88								
37-38	1.66	1.81 1.50	2.50	2.87 2.12								
	-1.65	-1.85 -1.45	-2.5	-2.77 -2.23				Y1				
39-40	1.9	2.08 1.72	2.86	3.27 2.44			Y1		Y1		Wc L_w	
	-1.90	-1.69 -1.69	-2.87	-3.14 -2.59								
41-42	2.15	2.34 1.95	3.22	3.66 2.77		Y1						
	-2.13	-2.34 -1.91	-0.10	-0.07 -0.13	Y1	Wc (0.75")	Wc (0.75")	Wc (L_w)				
43-44	2.86	3.31 2.41	0.06	0.09 0.02								
	-2.85	-3.07 -2.62	-0.05	-0.1 -0.01		Wc (1.5")	Wc (L_w)					
45-46	3.23	3.81 2.65	0.045	0.08 0.01								
	-3.21	-3.69 -2.73	-0.05	-0.1 -0.01								

Continued on next page

Table E.4 – continued from previous page

	Y-dir SDR		X-dir SDR		Frame 1 (Y-Dir)				Frame B (X-Dir)			
Cycles	RDR	Story 2 Story 1	RDR	Story 2 Story 1	B1-base	2F-B1-b	2F-A1-t	3F-B1-b	B2-base	2F-A1-b	2F-B2-t	3F-B1-b
47	3.66	4.66 2.65	0.05	0.06 0.06								
	-3.59	-4.45 -2.72	-0.06	-0.10 -0.03								
48	0.01	0.54 -0.53	3.21	3.69 2.73								
	-0.06	0.056 -0.17	-3.24	-3.44 -3.303								
49	0.21	0.58 -0.16	3.58	4.74 2.41								
	-0.53	-0.313 -0.75	-3.61	-4.07 -3.14								

Table E.5: Column A-1 Performance State Progression Table (BRBF test)

Cycles	Y-dir SDR		X-dir SDR		Column A-1					
	RDR	Story 2 Story 1	RDR	Story 2 Story 1	1Sb	1St	2F panel zone	2Sb	2St	3F panel zone
1-36	No observable damage during these cycles. Damage from first test not marked, see Table D.6.									
37-38	1.66	1.81 1.50	2.50	2.87 2.12	Y1, web near gusset reentrant			Y1, web w/in gusset region		
	-1.65	-1.85 -1.45	-2.5	-2.77 -2.23						
39-40	1.9	2.08 1.72	2.86	3.27 2.44						
	-1.90	-1.69 -1.69	-2.87	-3.14 -2.59						
41-42	2.15	2.34 1.95	3.22	3.66 2.77	Y2, web near gusset reentrant			Y2, web w/in gusset region		
	-2.13	-2.34 -1.91	-0.10	-0.07 -0.13						
43-44	2.86	3.31 2.41	0.06	0.09 0.02	Y3, web near gusset reentrant B2, flange			Y3, web w/in gusset region	Y3, flanges Y3, flanges at beam bot fl	
	-2.85	-3.07 -2.62	-0.05	-0.1 -0.01						
45-46	3.23	3.81 2.65	0.045	0.08 0.01	opposite gusset pl					
	-3.21	-3.69 -2.73	-0.05	-0.1 -0.01	B3, flange opposite					
47	3.66	4.66 2.65	0.05	0.06 0.06	gusset pl		Tear at bottom bolt hole			
	-3.59	-4.45 -2.72	-0.06	-0.10 -0.03						
48	0.01	0.54 -0.53	3.21	3.69 2.73						
	-0.06	0.056 -0.17	-3.24	-3.44 -3.303						
49	0.21	0.58 -0.16	3.58	4.74 2.41						
	-0.53	-0.313 -0.75	-3.61	-4.07 -3.14						

Table E.6: Column B-1 Performance State Progression Table (BRBF test)

Cycles	Y-dir SDR		X-dir SDR		Column A-1					
	RDR	Story 2 Story 1	RDR	Story 2 Story 1	1Sb	1St	2F PZ	2Sb	2St	3F PZ
This column reached level Y3 during the first test. Yielding did increase during the BRBF experiment but technically did not exceed Y3. See remaining chapter for discussion of Column B-1 damage and yielding.										

Table E.7: Column B-2 Performance State Progression Table (BRBF test)

Cycles	Y-dir SDR		X-dir SDR		Column A-1					
	RDR	Story 2 Story 1	RDR	Story 2 Story 1	1Sb	1St	2F panel zone	2Sb	2St	3F panel zone
1-32	No observable damage during these cycles. Damage from first test not marked, see Table D.8.									
33-34	1.18 -1.17	1.28 1.08 -1.35 -0.99	1.78 -1.78	2.05 1.51 -2.01 -1.54	Y1, web w/in gusset region					
35-36	1.42 -1.42	1.54 1.3 -1.60 -1.23	2.14 -2.14	2.45 1.82 -2.39 -1.88	Y2, web w/in gusset region			Y1, web w/in gusset region		
37-38	1.66 -1.65	1.81 1.50 -1.85 -1.45	2.50 -2.5	2.87 2.12 -2.77 -2.23				Y2, web w/in gusset region		
39-40	1.9 -1.90	2.08 1.72 -1.69 -1.69	2.86 -2.87	3.27 2.44 -3.14 -2.59			Tear at bottom bolt hole	Y3, web w/in gusset region		
41-42	2.15 -2.13	2.34 1.95 -2.34 -1.91	3.22 -0.10	3.66 2.77 -0.07 -0.13	Y3, web w/in gusset region	Divot in flange at bm bot flange	Tear thru whole bolt lines			
43-44	2.86 -2.85	3.31 2.41 -3.07 -2.62	0.06 -0.05	0.09 0.02 -0.1 -0.01						
45-46	3.23 -3.21	3.81 2.65 -3.69 -2.73	0.045 -0.05	0.08 0.01 -0.1 -0.01						
47	3.66 -3.59	4.66 2.65 -4.45	0.05 -0.06	0.06 0.06 -0.10						

Continued on next page

Table E.7 – continued from previous page

Cycles	Y-dir SDR		X-dir SDR		Column A-1					
	RDR	Story 2 Story 1	RDR	Story 2 Story 1	1Sb	1St	2F panel zone	2Sb	2St	3F panel zone
		-2.72		-0.03						
48	0.01	0.54 -0.53	3.21	3.69 2.73		Tear penetrates thru entire				
	-0.06	0.056 -0.17	-3.24	-3.44 -3.303	B3, flange opposite	flange				
49	0.21	0.58 -0.16	3.58	4.74 2.41	gusset pl	Flange tear connects w/ web tear				
	-0.53	-0.313 -0.75	-3.61	-4.07 -3.14						

Table E.8: Frame 1 Beams Performance State Progression Table (BRBF test)

Cycles	Y-dir SDR		X-dir SDR		2nd Floor		3rd Floor	
	RDR	Story 2 Story 1	RDR	Story 2 Story 1	A-1	B-1	A-1	B-1
1-34	No observable damage during these cycles. Damage from first test not marked, see Table D.9.							
35-36	1.42	1.54 1.3	2.14	2.45 1.82	Y1, top flange and web w/in slab blockout			
	-1.42	-1.60 -1.23	-2.14	-2.39 -1.88				
37-38	1.66	1.81 1.50	2.50	2.87 2.12				
	-1.65	-1.85 -1.45	-2.5	-2.77 -2.23				
39-40	1.9	2.08 1.72	2.86	3.27 2.44				
	-1.90	-1.69 -1.69	-2.87	-3.14 -2.59				
41-42	2.15	2.34 1.95	3.22	3.66 2.77				B1, web and bot flange just outside of gusset reentrant
	-2.13	-2.34 -1.91	-0.10	-0.07 -0.13				
43-44	2.86	3.31 2.41	0.06	0.09 0.02	Y3, top flange and	B1, bot flange just outside		Y2, web and flange w/in
	-2.85	-3.07 -2.62	-0.05	-0.1 -0.01	web w/in slab blockout	of gusset reentrant		gusset region
45-46	3.23	3.81 2.65	0.045	0.08 0.01	B1, top flange w/in slab blockout	B3, bot flange just outside of gusset reentrant		Y3, B3, web and bot flange
	-3.21	-3.69 -2.73	-0.05	-0.1 -0.01				WBb, bot fl and 3"' into web
47	3.66	4.66 2.65	0.05	0.06 0.06				
	-3.59	-4.45 -2.72	-0.06	-0.10 -0.03				WBb, half of beam depth
48	0.01	0.54 -0.53	3.21	3.69 2.73				
	-0.06	0.056 -0.17	-3.24	-3.44 -3.303				
49	0.21	0.58 -0.16	3.58	4.74 2.41				
	-0.53	-0.313 -0.75	-3.61	-4.07 -3.14				

Table E.9: Frame B Beams Performance State Progression Table (BRBF test)

Cycles	Y-dir SDR		X-dir SDR		2nd Floor		3rd Floor	
	RDR	Story 2 Story 1	RDR	Story 2 Story 1	B-1	B-2	B-1	B-2
1-30	No observable damage during these cycles. Damage from first test not marked, see Table D.10.							
31-32	0.94	1.04 0.84	1.42	1.64 1.20		Y1, top flange and web w/in slab blockout		
	-0.93	-1.08 -0.79	-1.42	-1.61 -1.22				
33-34	1.18	1.28 1.08	1.78	2.05 1.51				
	-1.17	-1.35 -0.99	-1.78	-2.01 -1.54				
35-36	1.42	1.54 1.3	2.14	2.45 1.82				
	-1.42	-1.60 -1.23	-2.14	-2.39 -1.88				
37-38	1.66	1.81 1.50	2.50	2.87 2.12	Y3, web at splice			
	-1.65	-1.85 -1.45	-2.5	-2.77 -2.23				
39-40	1.9	2.08 1.72	2.86	3.27 2.44		Y2, top flange and web w/in slab blockout		
	-1.90	-1.69 -1.69	-2.87	-3.14 -2.59	Tear in web at bottom			
41-42	2.15	2.34 1.95	3.22	3.66 2.77	erection bolt			
	-2.13	-2.34 -1.91	-0.10	-0.07 -0.13				
43-44	2.86	3.31 2.41	0.06	0.09 0.02				
	-2.85	-3.07 -2.62	-0.05	-0.1 -0.01				
45-46	3.23	3.81 2.65	0.045	0.08 0.01				
	-3.21	-3.69 -2.73	-0.05	-0.1 -0.01				
47	3.66	4.66 2.65	0.05	0.06 0.06				
	-3.59	-4.45 -2.72	-0.06	-0.10 -0.03				
48	0.01	0.54 -0.53	3.21	3.69 2.73				
	-0.06	0.056 -0.17	-3.24	-3.44 -3.303	Web tear propagates			
49	0.21	0.58 -0.16	3.58	4.74 2.41	to 1/4 beam depth			
	-0.53	-0.313 -0.75	-3.61	-4.07 -3.14	Bottom flange fractures			

E.3 BRB axial force-axial deformation envelopes

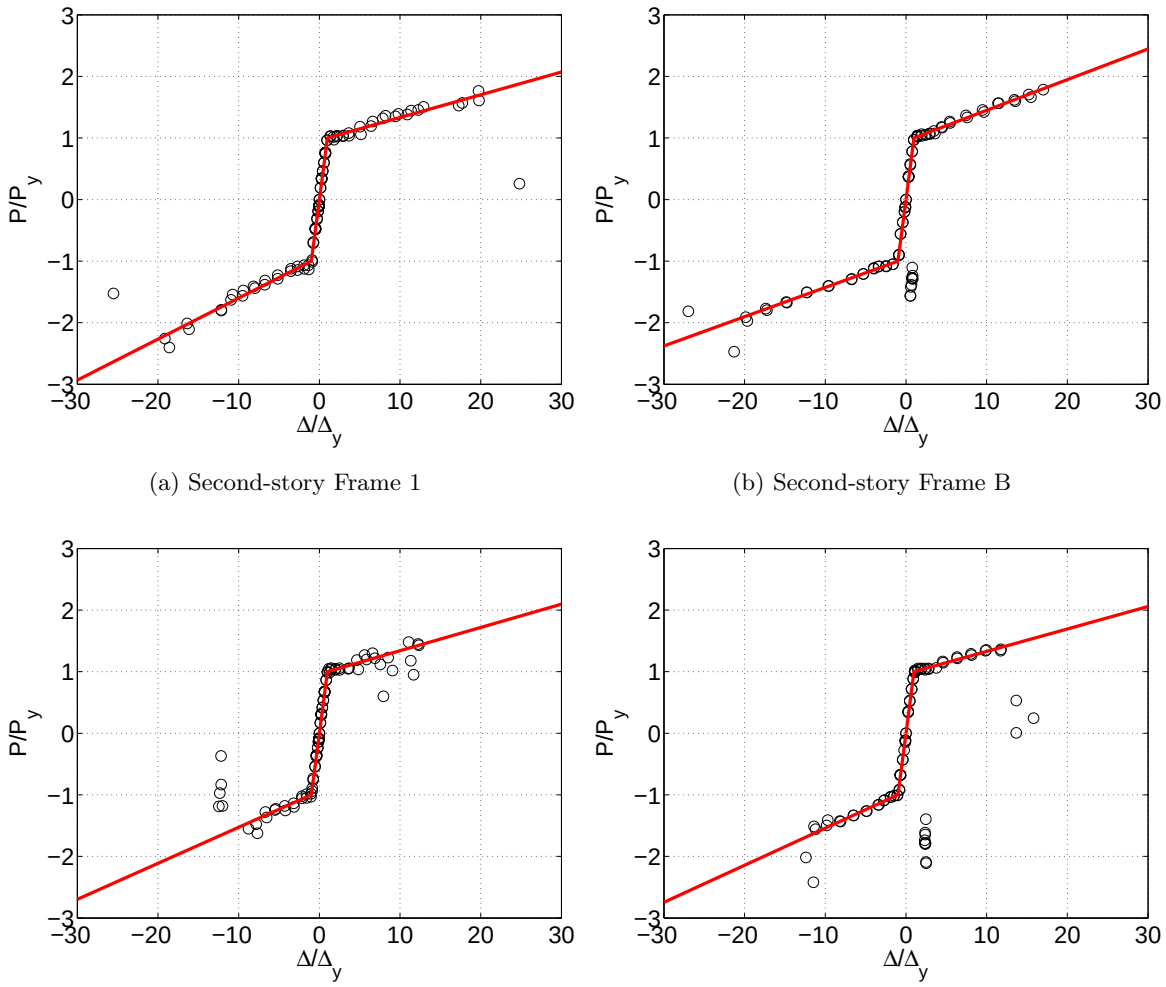

(a) Second-story Frame 1

(b) Second-story Frame B

(c) Fisrt-story Frame 1

(d) First-story Frame B

Figure E.6: Normalized brace axial load vs. normalized brace axial deformation (BRBF test). Note that the yield load in tension is not equal to the yield load in compression.

E.4 BRB core elongation stringpot measurements

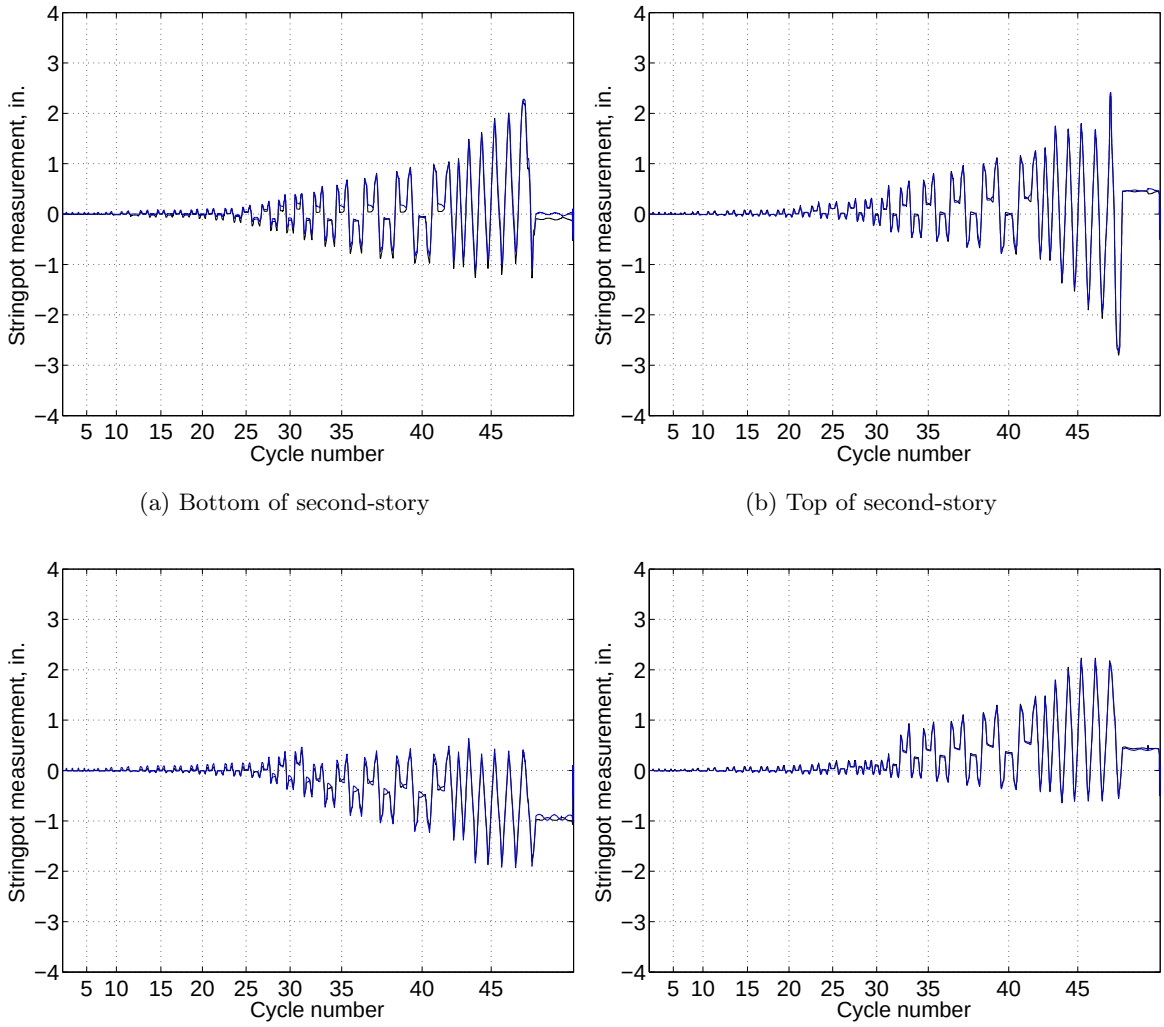

(a) Bottom of second-story

(b) Top of second-story

(c) Bottom of first-story

(d) Top of first-story

Figure E.7: BRB elongation stringpot measurements at each BRB end (two pots at each end in each plot), Frame 1

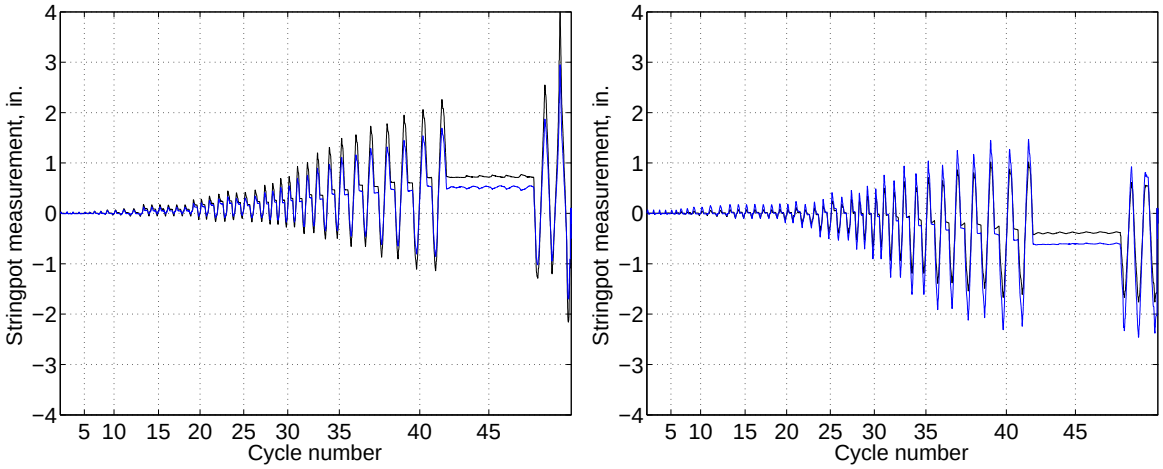

(a) Bottom of second-story

(b) Top of second-story

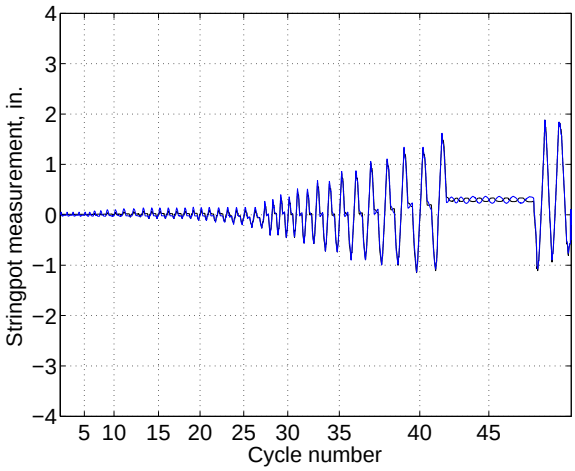

(c) Bottom of first-story

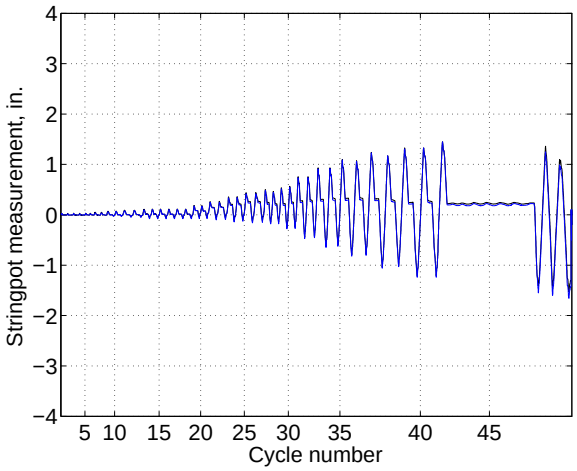

(d) Top of first-story

Figure E.8: BRB elongation stringpot measurements at each BRB end (two pots at each end in each plot), Frame B

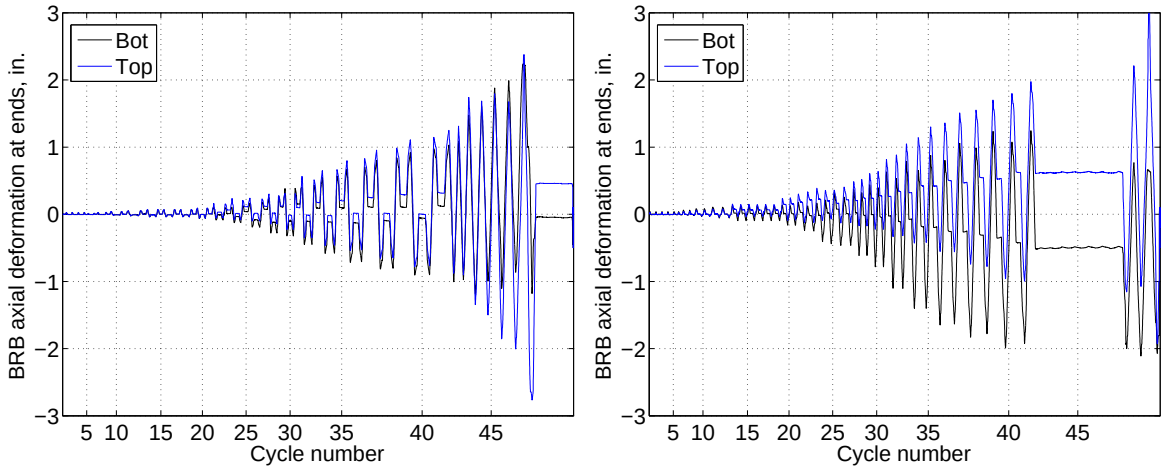

(a) Second story, Frame 1

(b) Second story, Frame B

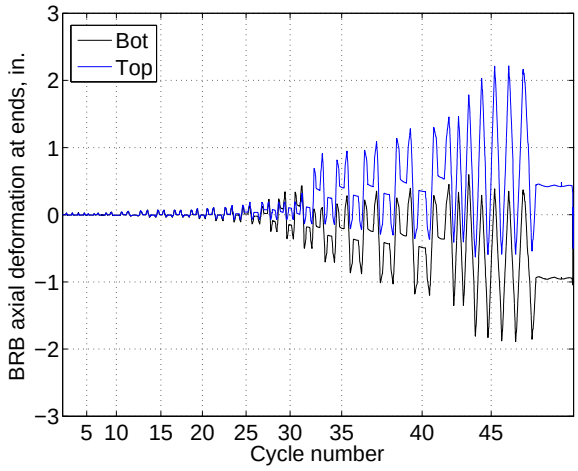

(c) First story, Frame 1

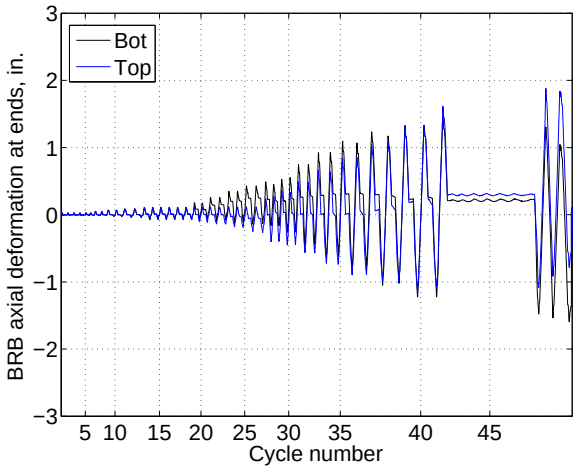

(d) First story, Frame B

Figure E.9: BRB axial deformations at ends of braces ('Bot' indicates the average of the two stringpot measurements at the bottom of the BRB, 'Top' indicates the average of the two stringpot measurements at the top of the BRB), Frames 1 and B

E.5 BRB casing strains

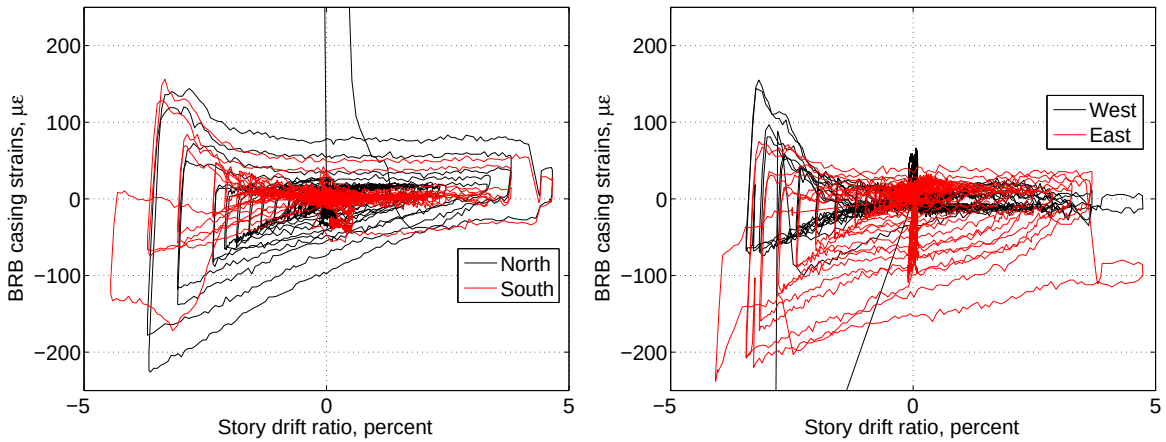

(a) Second story Frame 1

(b) Second story Frame B

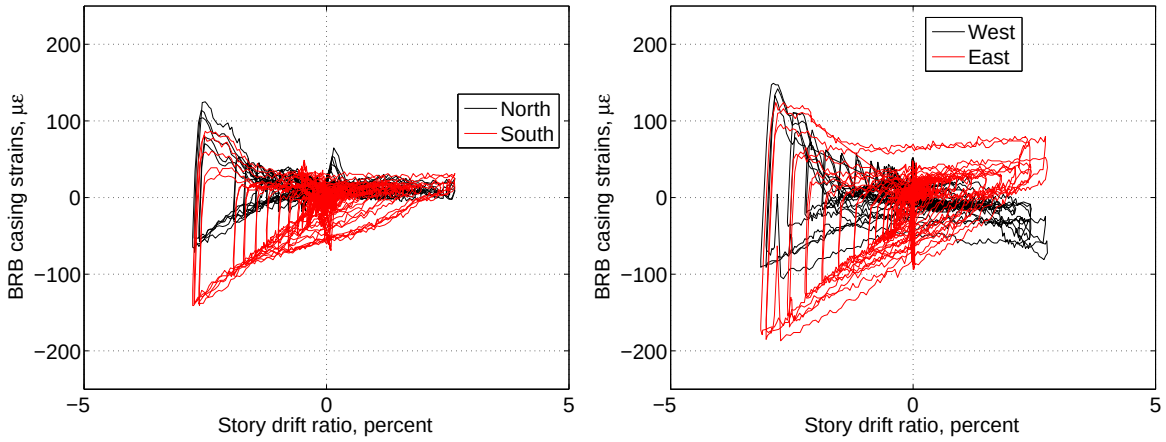

(c) First story Frame 1

(d) First story Frame B

Figure E.10: BRB casing strains (BRBF)

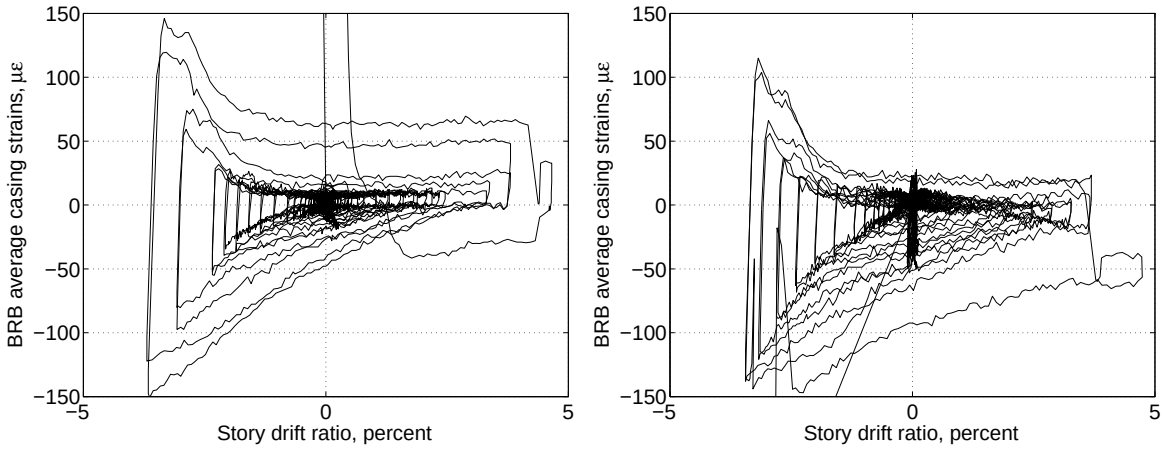

(a) Second story Frame 1

(b) Second story Frame B

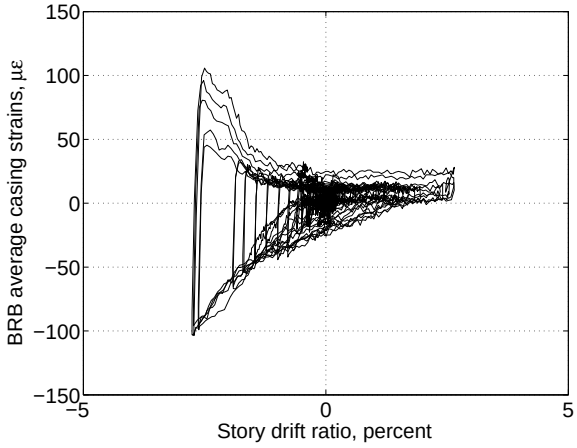

(c) First story Frame 1

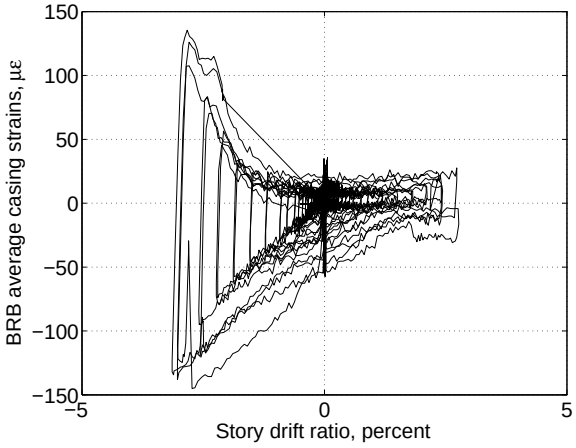

(d) First story Frame B

Figure E.11: Average BRB casing strains (BRBF)

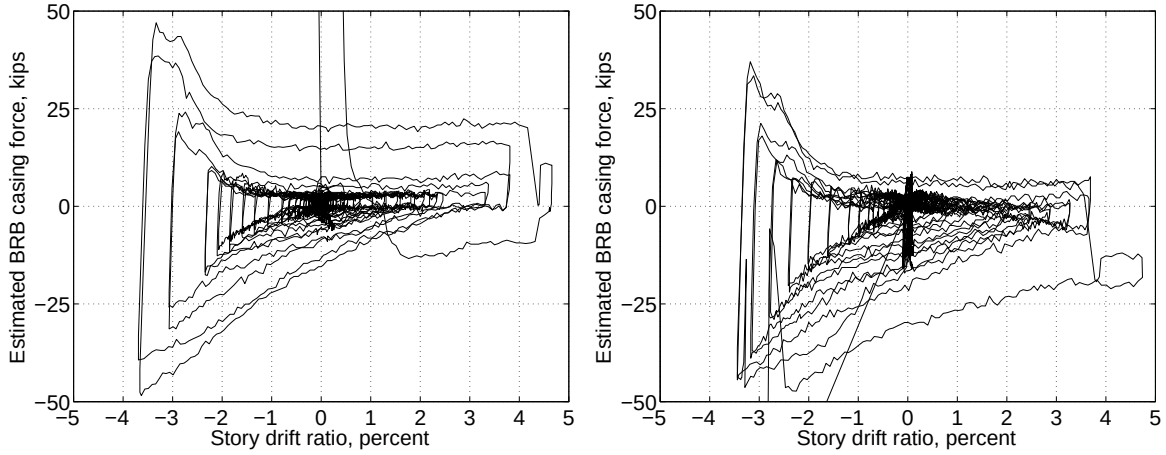

(a) Second-story Frame 1

(b) Second-story Frame B

(c) First-story Frame 1

(d) First-story Frame B

Figure E.12: Estimated BRB casing forces from casing strain gauges (BRBF)

E.6 BRBF energy dissipation

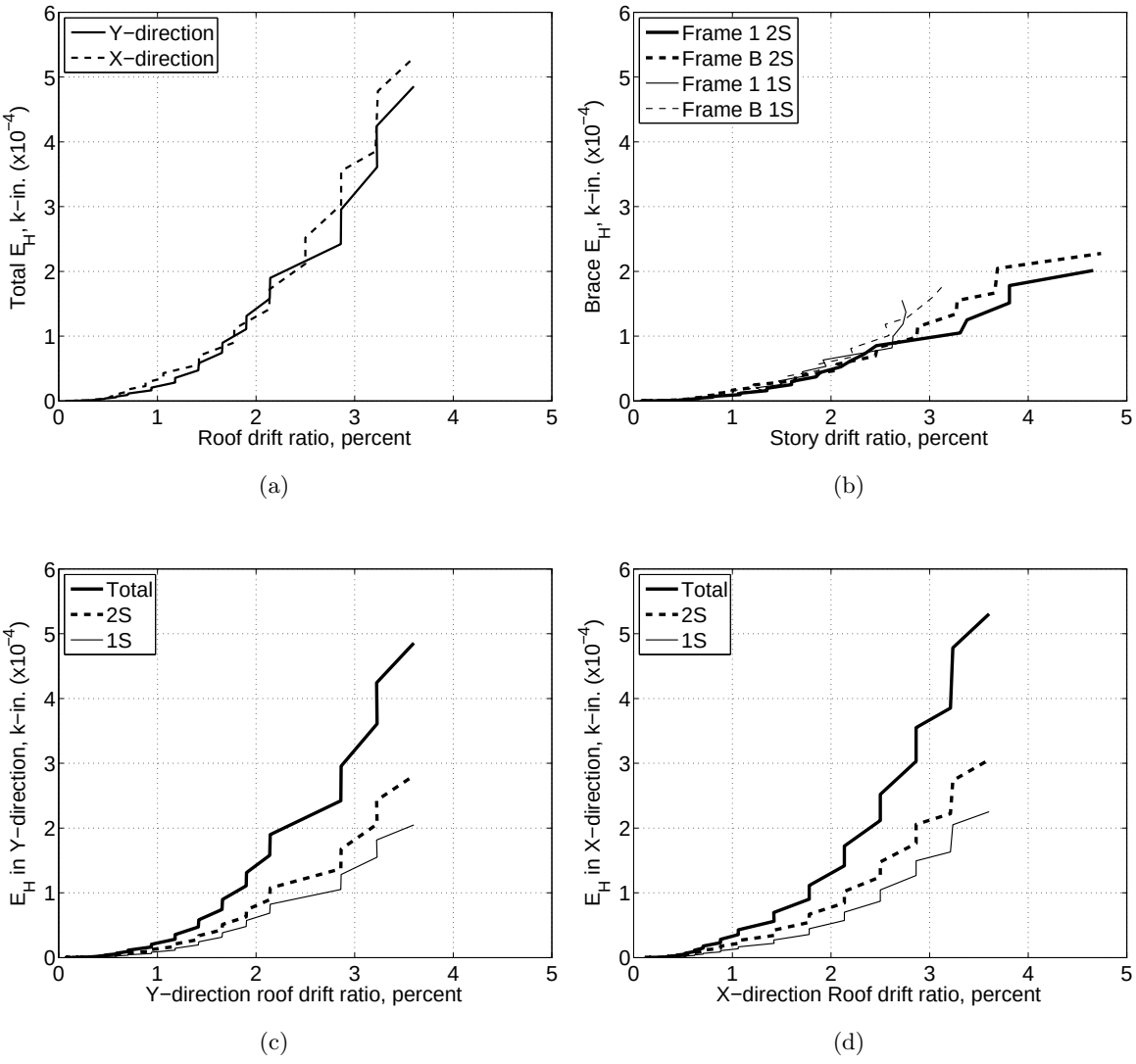

Figure E.13: BRBF energy dissipation comparison: (a) total energy dissipated in each principal direction; (b) energy dissipated by braces in each frame and story; (c) energy dissipated in the Y-directions frames; (d) energy disspiated in the X-direction frames.

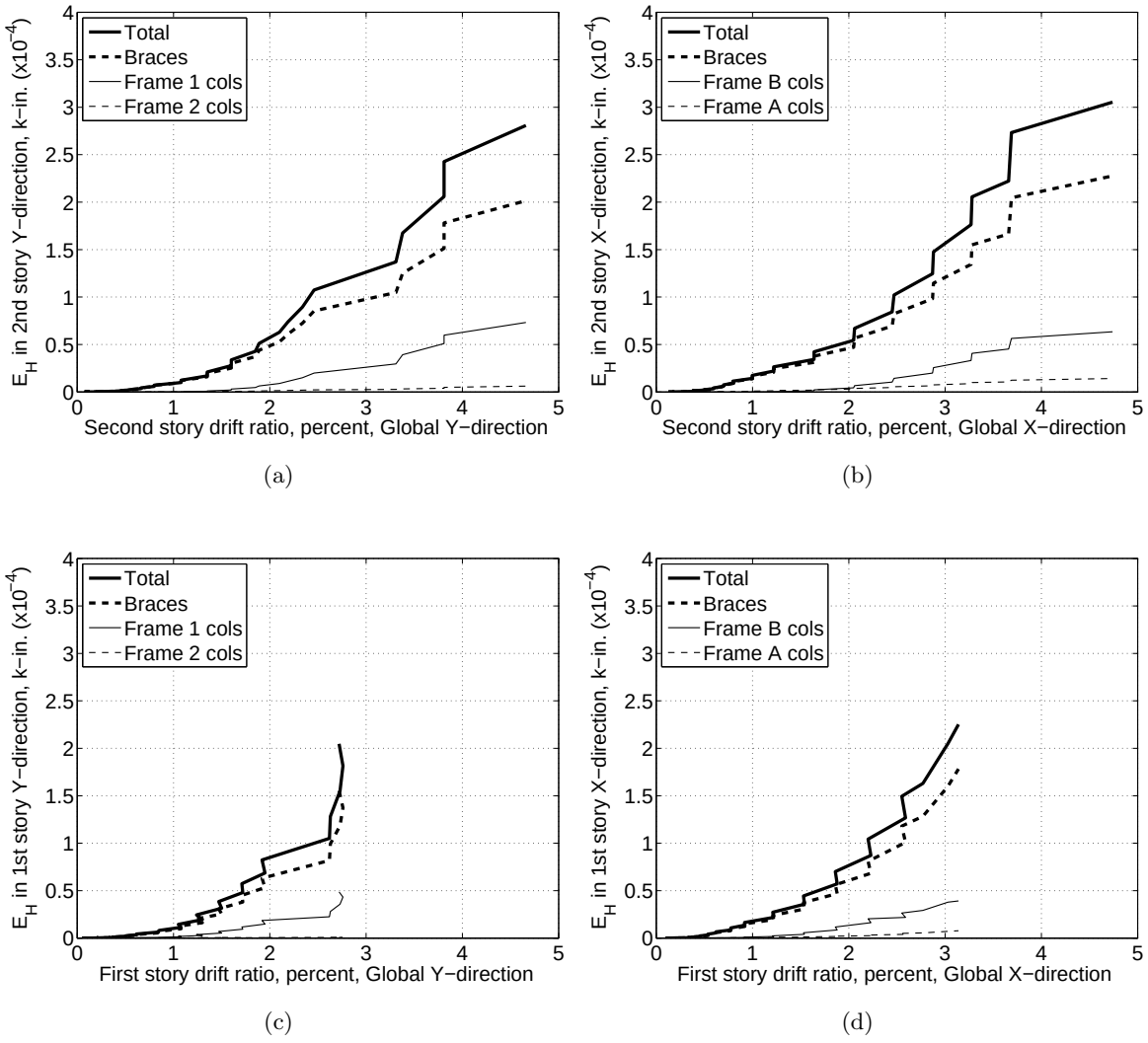

Figure E.14: BRBF energy dissipation comparison: (a) second story frames in Y-direction; (b) second story frames in X-direction; (c) first story frames in Y-direction; (d) first story frames in X-direction.

Appendix F

MATERIAL CERTIFICATES

This appendix provides the certificates of material testing for the wide flange shapes, HSS braces and BRB core plate steel as supplied by the testing agencies.

F.1 Wide flange mill certs

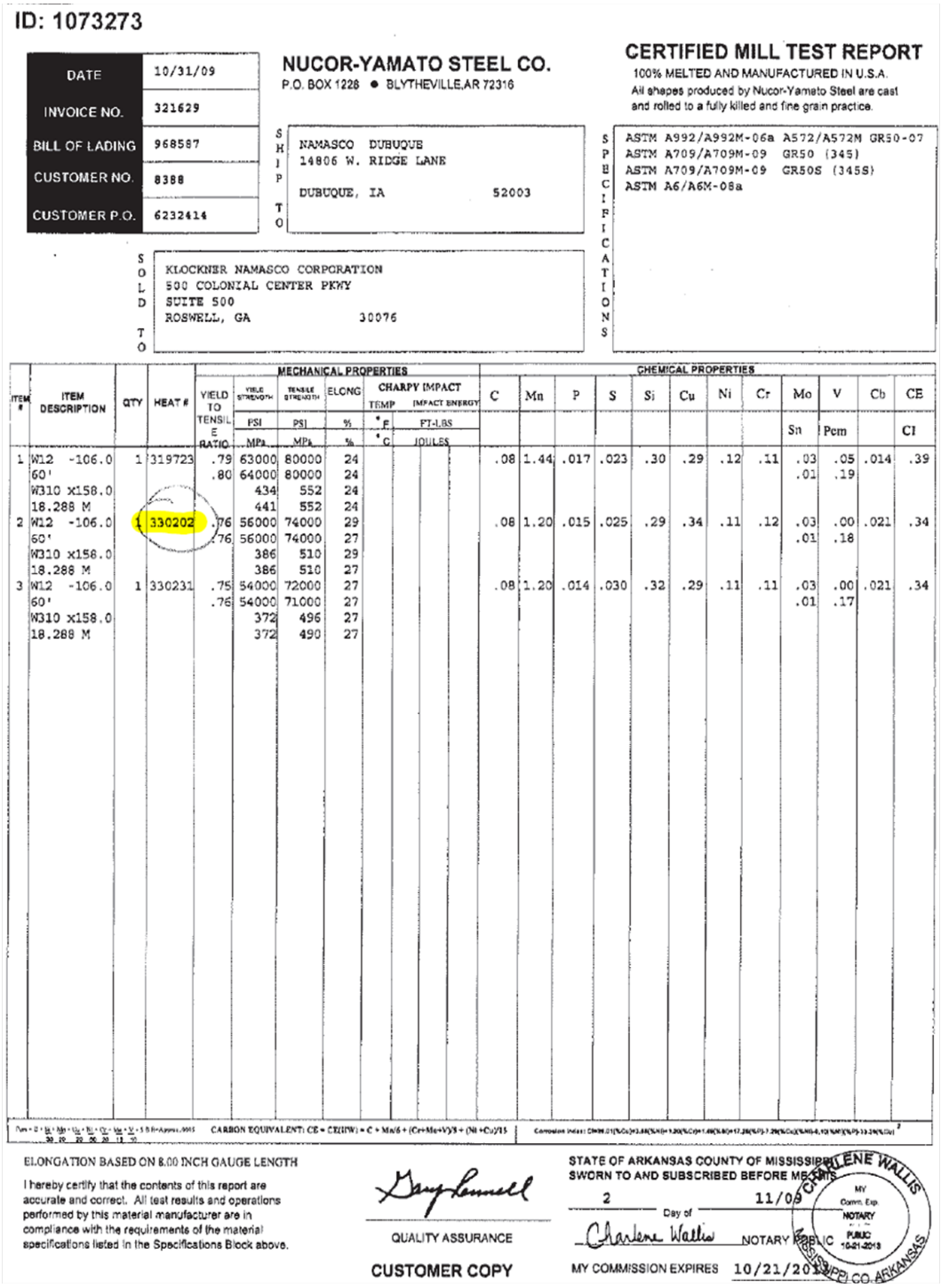

ID: 1073273

DATE	10/31/09
INVOICE NO.	321629
BILL OF LADING	968587
CUSTOMER NO.	8388
CUSTOMER P.O.	6232414

NUCOR-YAMATO STEEL CO.
P.O. BOX 1228 • BLYTHEVILLE,AR 72316

CERTIFIED MILL TEST REPORT
100% MELTED AND MANUFACTURED IN U.S.A.
All shapes produced by Nucor-Yamato Steel are cast and rolled to a fully killed and fine grain practice.

SHIP TO:
NAMASCO DUBUQUE
14806 W. RIDGE LANE
DUBUQUE, IA 52003

SOLD TO:
KLOCKNER NAMASCO CORPORATION
500 COLONIAL CENTER PKWY
SUITE 500
ROSWELL, GA 30076

SPECIFICATIONS:
ASTM A992/A992M-06a A572/A572M GR50-07
ASTM A709/A709M-09 GR50 (345)
ASTM A709/A709M-09 GR50S (345S)
ASTM A6/A6M-08a

ITEM #	ITEM DESCRIPTION	QTY	HEAT #	MECHANICAL PROPERTIES						CHEMICAL PROPERTIES											
				YIELD TO TENSILE RATIO	YIELD STRENGTH PSI / MPa	TENSILE STRENGTH PSI / MPa	ELONG %	CHARPY IMPACT TEMP °F / °C	CHARPY IMPACT ENERGY FT-LBS / JOULES	C	Mn	P	S	Si	Cu	Ni	Cr	Mo / Sn	V / Pcm	Cb	CE / CI
1	W12 -106.0	1	319723	.79	63000	80000	24			.08	1.44	.017	.023	.30	.29	.12	.11	.03	.05	.014	.39
	60'			.80	64000	80000	24											.01	.19		
	W310 x158.0				434	552	24														
	18.288 M				441	552	24														
2	W12 -106.0	1	330202	.76	56000	74000	29			.08	1.20	.015	.025	.29	.34	.11	.12	.03	.00	.021	.34
	60'			.76	56000	74000	27											.01	.18		
	W310 x158.0				386	510	29														
	18.288 M				386	510	27														
3	W12 -106.0	1	330231	.75	54000	72000	27			.08	1.20	.014	.030	.32	.29	.11	.11	.03	.00	.021	.34
	60'			.76	54000	71000	27											.01	.17		
	W310 x158.0				372	496	27														
	18.288 M				372	490	27														

CARBON EQUIVALENT: CE = CE(IIW) = C + Mn/6 + (Cr+Mo+V)/5 + (Ni +Cu)/15

ELONGATION BASED ON 8.00 INCH GAUGE LENGTH

I hereby certify that the contents of this report are accurate and correct. All test results and operations performed by this material manufacturer are in compliance with the requirements of the material specifications listed in the Specifications Block above.

QUALITY ASSURANCE

CUSTOMER COPY

STATE OF ARKANSAS COUNTY OF MISSISSIPPI
SWORN TO AND SUBSCRIBED BEFORE ME THIS 2 Day of 11/09

Charlene Wallis NOTARY PUBLIC

MY COMMISSION EXPIRES 10/21/2018

CHARLENE WALLIS NOTARY PUBLIC MISSISSIPPI CO. ARKANSAS MY Comm. Exp. 10-21-2018

Figure F.1: Mill certification

ID: 1024295

DATE	6/19/09
INVOICE NO.	299475
BILL OF LADING	954962
CUSTOMER NO.	8388
CUSTOMER P.O.	6205885

NUCOR-YAMATO STEEL CO.
P.O. BOX 1228 ● BLYTHEVILLE,AR 72316

CERTIFIED MILL TEST REPORT
100% MELTED AND MANUFACTURED IN U.S.A.
All shapes produced by Nucor-Yamato Steel are cast and rolled to a fully killed and fine grain practice.

SHIP TO
NAMASCO DUBUQUE
14806 W. RIDGE LANE
DUBUQUE, IA 52003

SPECIFICATIONS
ASTM A992/A992M-06a A572/A572M GR50-06
ASTM A709/A709M-07 GR50 (345)
ASTM A709/A709M-07 GR50S (345S)
ASTM A6/A6M-07

SOLD TO
KLOCKNER NAMASCO CORPORATION
500 COLONIAL CENTER PKWY
SUITE 500
ROSWELL, GA 30076

ITEM #	ITEM DESCRIPTION	QTY	HEAT #	MECHANICAL PROPERTIES						CHEMICAL PROPERTIES											
				YIELD TO TENSILE RATIO	YIELD STRENGTH PSI / MPa	TENSILE STRENGTH PSI / MPa	ELONG %	CHARPY IMPACT TEMP °F / °C	CHARPY IMPACT IMPACT ENERGY FT-LBS / JOULES	C	Mn	P	S	Si	Cu	Ni	Cr	Mo	V	Cb	CE
																		Sn	Pcm		CI
1	W16 - 26.0	12	335017	.81	60000	74000	24			.07	.80	.012	.028	.26	.32	.11	.11	.03	.00	.011	.26
	50'			.81	59000	73000	24											.01	.15		
	W410 x 38.8				414	510	24														
	15.240 M				407	503	24														
2	W16 - 26.0	2	335018	.82	59000	72000	24			.07	.80	.011	.032	.26	.32	.11	.09	.03	.00	.011	.25
	50'			.82	59000	72000	25											.01	.14		
	W410 x 38.8				407	496	24														
	15.240 M				407	496	25														
3	W16 - 31.0	14	335015	.80	55000	69000	26			.07	.80	.015	.026	.21	.30	.11	.14	.03	.00	.012	.26
	40'			.78	53000	68000	25											.01	.15		
	W410 x 46.1				379	476	26														
	12.192 M				365	469	25														
4	W16 - 31.0	4	335028	.86	62000	72000	23			.08	.82	.014	.034	.23	.31	.12	.12	.03	.00	.011	.28
	40'			.86	62000	72000	21											.01	.16		
	W410 x 46.1				427	496	23														
	12.192 M				427	496	21														
5	W16 - 31.0	3	335030	.80	53000	66000	25			.07	.80	.016	.032	.27	.30	.10	.12	.03	.00	.011	.26
	40'			.81	54000	67000	26											.01	.15		
	W410 x 46.1				365	455	25														
	12.192 M				372	462	26														

CARBON EQUIVALENT: CE = C+(Mn/6) + (Cr+Mo+V)/5 + (Ni +Cu)/15

ELONGATION BASED ON 8.00 INCH GAUGE LENGTH

I hereby certify that the contents of this report are accurate and correct. All test results and operations performed by this material manufacturer are in compliance with the requirements of the material specifications listed in the Specifications Block above.

QUALITY ASSURANCE

CUSTOMER COPY

STATE OF ARKANSAS COUNTY OF MISSISSIPPI
SWORN TO AND SUBSCRIBED BEFORE ME THIS
19 Day of 06/09

Charlene Wallis NOTARY PUBLIC

MY COMMISSION EXPIRES 10/21/2018

CHARLENE WALLIS NOTARY PUBLIC MISSISSIPPI CO. ARKANSAS MY Comm. Exp. 10-21-2018

Figure F.2: Mill certification

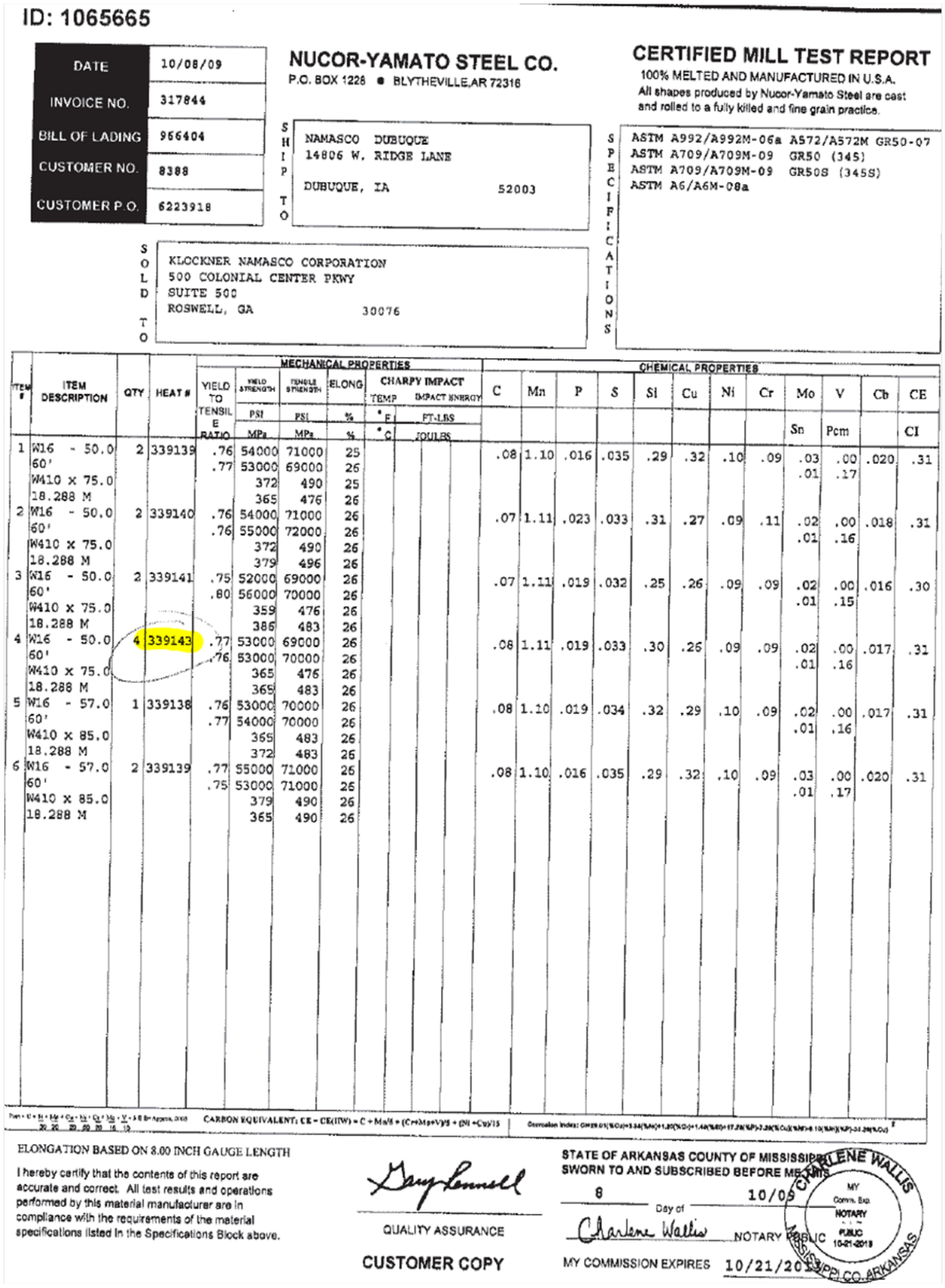

ID: 1065665

DATE	10/08/09
INVOICE NO.	317844
BILL OF LADING	956404
CUSTOMER NO.	8388
CUSTOMER P.O.	6223918

NUCOR-YAMATO STEEL CO.
P.O. BOX 1228 ● BLYTHEVILLE,AR 72316

CERTIFIED MILL TEST REPORT
100% MELTED AND MANUFACTURED IN U.S.A.
All shapes produced by Nucor-Yamato Steel are cast and rolled to a fully killed and fine grain practice.

SHIP TO
NAMASCO DUBUQUE
14806 W. RIDGE LANE
DUBUQUE, IA 52003

SOLD TO
KLOCKNER NAMASCO CORPORATION
500 COLONIAL CENTER PKWY
SUITE 500
ROSWELL, GA 30076

SPECIFICATIONS
ASTM A992/A992M-06a A572/A572M GR50-07
ASTM A709/A709M-09 GR50 (345)
ASTM A709/A709M-09 GR50S (345S)
ASTM A6/A6M-08a

ITEM #	ITEM DESCRIPTION	QTY	HEAT #	MECHANICAL PROPERTIES: YIELD TO TENSILE RATIO	YIELD STRENGTH PSI / MPa	TENSILE STRENGTH PSI / MPa	ELONG %	CHARPY IMPACT TEMP °F / °C	CHARPY IMPACT ENERGY FT-LBS / JOULES	C	Mn	P	S	Si	Cu	Ni	Cr	Mo	V	Cb	CE
																		Sn	Pcm		CI
1	W16 - 50.0 60' W410 X 75.0 18.288 M	2	339139	.76 .77	54000 53000 372 365	71000 69000 490 476	25 26 25 26			.08	1.10	.016	.035	.29	.32	.10	.09	.03 .01	.00 .17	.020	.31
2	W16 - 50.0 60' W410 X 75.0 18.288 M	2	339140	.76 .76	54000 55000 372 379	71000 72000 490 496	26 26 26 26			.07	1.11	.023	.033	.31	.27	.09	.11	.02 .01	.00 .16	.018	.31
3	W16 - 50.0 60' W410 X 75.0 18.288 M	2	339141	.75 .80	52000 56000 359 386	69000 70000 476 483	26 26 26 26			.07	1.11	.019	.032	.25	.26	.09	.09	.02 .01	.00 .15	.016	.30
4	W16 - 50.0 60' W410 X 75.0 18.288 M	4	339143	.77 .76	53000 53000 365 365	69000 70000 476 483	26 26 26 26			.08	1.11	.019	.033	.30	.25	.09	.09	.02 .01	.00 .16	.017	.31
5	W16 - 57.0 60' W410 X 85.0 18.288 M	1	339138	.76 .77	53000 54000 365 372	70000 70000 483 483	26 26 26 26			.08	1.10	.019	.034	.32	.29	.10	.09	.02 .01	.00 .16	.017	.31
6	W16 - 57.0 60' W410 X 85.0 18.288 M	2	339139	.77 .75	55000 53000 379 365	71000 71000 490 490	26 25 26 26			.08	1.10	.016	.035	.29	.32	.10	.09	.03 .01	.00 .17	.020	.31

CHEMICAL PROPERTIES

CARBON EQUIVALENT: CE = CE(IIW) = C + Mn/6 + (Cr+Mo+V)/5 + (Ni +Cu)/15

ELONGATION BASED ON 8.00 INCH GAUGE LENGTH

I hereby certify that the contents of this report are accurate and correct. All test results and operations performed by this material manufacturer are in compliance with the requirements of the material specifications listed in the Specifications Block above.

QUALITY ASSURANCE

CUSTOMER COPY

STATE OF ARKANSAS COUNTY OF MISSISSIPPI
SWORN TO AND SUBSCRIBED BEFORE ME THIS
8 Day of 10/09
Charlene Wallis NOTARY PUBLIC
MY COMMISSION EXPIRES 10/21/2013

CHARLENE WALLIS
NOTARY PUBLIC
MISSISSIPPI CO. ARKANSAS
MY Comm. Exp. 10-21-2013

Figure F.3: Mill certification

ID: 1079946

DATE	11/19/09
INVOICE NO.	324081
BILL OF LADING	970143
CUSTOMER NO.	8388
CUSTOMER P.O.	6227171

NUCOR-YAMATO STEEL CO.
P.O. BOX 1228 • BLYTHEVILLE,AR 72316

CERTIFIED MILL TEST REPORT
100% MELTED AND MANUFACTURED IN U.S.A.
All shapes produced by Nucor-Yamato Steel are cast and rolled to a fully killed and fine grain practice.

SHIP TO
NAMASCO DUBUQUE
14806 W. RIDGE LANE
DUBUQUE, IA 52003

SPECIFICATIONS
ASTM A992/A992M-06a A572/A572M GR50-07
ASTM A709/A709M-09 GR50 (345)
ASTM A709/A709M-09 GR50S (345S)
ASTM A6/A6M-08a

SOLD TO
KLOCKNER NAMASCO CORPORATION
500 COLONIAL CENTER PKWY
SUITE 500
ROSWELL, GA 30076

ITEM #	ITEM DESCRIPTION	QTY	HEAT #	MECHANICAL PROPERTIES: YIELD TO TENSILE RATIO	YIELD STRENGTH PSI / MPa	TENSILE STRENGTH PSI / MPa	ELONG %	CHARPY IMPACT TEMP °F / °C	CHARPY IMPACT ENERGY FT-LBS / JOULES	CHEMICAL PROPERTIES: C	Mn	P	S	Si	Cu	Ni	Cr	Mo	V	Cb	CE
																		Sn	Pcm		CI
1	W12 - 72.0	3	340349	.78	57000	73000	26			.07	1.21	.013	.022	.24	.30	.10	.09	.03	.00	.023	.32
	55'			.78	57000	73000	26											.01	.16		
	W310 x107.0				393	503	26														
	16.764 M				393	503	26														
2	W12 - 79.0	1	340339	.76	54000	71000	27			.07	1.10	.018	.018	.23	.30	.11	.13	.03	.00	.019	.31
	60'			.76	55000	72000	28											.01	.17		
	W310 x117.0				372	490	27														
	18.288 M				379	496	28														
3	W12 - 79.0	1	340340	.77	55000	71000	28			.08	1.03	.016	.027	.25	.29	.10	.11	.03	.00	.021	.31
	60'			.76	54000	71000	27											.01	.16		
	W310 x117.0				379	490	28														
	18.288 M				372	490	27														
4	W12 - 79.0	1	340580	.75	55000	73000	27			.08	1.10	.018	.027	.27	.31	.11	.13	.03	.00	.020	.32
	60'			.78	56000	72000	27											.01	.18		
	W310 x117.0				379	503	27														
	18.288 M				386	496	27														

CARBON EQUIVALENT: CE = CE(IIW) = C + Mn/6 + (Cr+Mo+V)/5 + (Ni +Cu)/15

ELONGATION BASED ON 8.00 INCH GAUGE LENGTH

I hereby certify that the contents of this report are accurate and correct. All test results and operations performed by this material manufacturer are in compliance with the requirements of the material specifications listed in the Specifications Block above.

QUALITY ASSURANCE

CUSTOMER COPY

STATE OF ARKANSAS COUNTY OF MISSISSIPPI
SWORN TO AND SUBSCRIBED BEFORE ME THIS
19 Day of 11/09
Charlene Wallis NOTARY PUBLIC
MY COMMISSION EXPIRES 10/21/2018

CHARLENE WALLIS NOTARY PUBLIC MISSISSIPPI CO. ARKANSAS MY Comm. Exp. 10-21-2018

Figure F.4: Mill certification

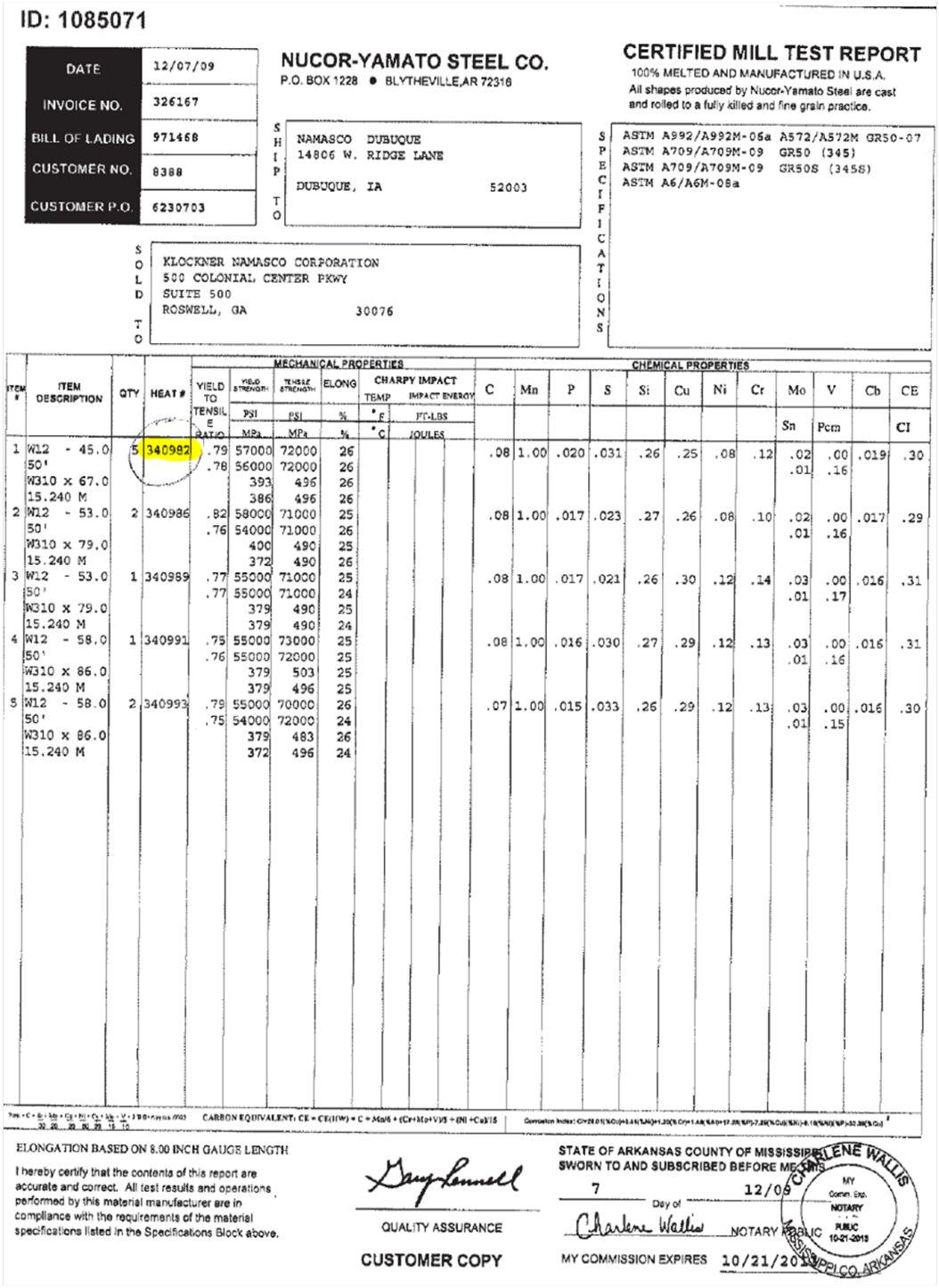

ID: 1085071

DATE	12/07/09
INVOICE NO.	326167
BILL OF LADING	971468
CUSTOMER NO.	8388
CUSTOMER P.O.	6230703

NUCOR-YAMATO STEEL CO.
P.O. BOX 1228 • BLYTHEVILLE,AR 72316

CERTIFIED MILL TEST REPORT
100% MELTED AND MANUFACTURED IN U.S.A.
All shapes produced by Nucor-Yamato Steel are cast and rolled to a fully killed and fine grain practice.

SHIP TO: NAMASCO DUBUQUE
14806 W. RIDGE LANE
DUBUQUE, IA 52003

SOLD TO: KLOCKNER NAMASCO CORPORATION
500 COLONIAL CENTER PKWY
SUITE 500
ROSWELL, GA 30076

SPECIFICATIONS:
ASTM A992/A992M-06a A572/A572M GR50-07
ASTM A709/A709M-09 GR50 (345)
ASTM A709/A709M-09 GR50S (345S)
ASTM A6/A6M-08a

ITEM #	ITEM DESCRIPTION	QTY	HEAT #	MECHANICAL PROPERTIES: YIELD TO TENSILE RATIO	YIELD STRENGTH PSI / MPa	TENSILE STRENGTH PSI / MPa	ELONG % / %	CHARPY IMPACT TEMP °F / °C	CHARPY IMPACT ENERGY FT-LBS / JOULES	CHEMICAL PROPERTIES: C	Mn	P	S	Si	Cu	Ni	Cr	Mo / Sn	V / Pcm	Cb	CE / CI
1	W12 - 45.0	5	340982	.79	57000	72000	26			.08	1.00	.020	.031	.26	.25	.08	.12	.02	.00	.019	.30
	50'			.78	56000	72000	26											.01	.16		
	W310 x 67.0				393	496	26														
	15.240 M				386	496	26														
2	W12 - 53.0	2	340986	.82	58000	71000	25			.08	1.00	.017	.023	.27	.26	.08	.10	.02	.00	.017	.29
	50'			.76	54000	71000	26											.01	.16		
	W310 x 79.0				400	490	25														
	15.240 M				372	490	26														
3	W12 - 53.0	1	340989	.77	55000	71000	25			.08	1.00	.017	.021	.26	.30	.12	.14	.03	.00	.016	.31
	50'			.77	55000	71000	24											.01	.17		
	W310 x 79.0				379	490	25														
	15.240 M				379	490	24														
4	W12 - 58.0	1	340991	.75	55000	73000	25			.08	1.00	.016	.030	.27	.29	.12	.13	.03	.00	.016	.31
	50'			.76	55000	72000	25											.01	.16		
	W310 x 86.0				379	503	25														
	15.240 M				379	496	25														
5	W12 - 58.0	2	340993	.79	55000	70000	26			.07	1.00	.015	.033	.26	.29	.12	.13	.03	.00	.016	.30
	50'			.75	54000	72000	24											.01	.15		
	W310 x 86.0				379	483	26														
	15.240 M				372	496	24														

CARBON EQUIVALENT: CE = CE(IIW) = C + Mn/6 + (Cr+Mo+V)/5 + (Ni +Cu)/15

ELONGATION BASED ON 8.00 INCH GAUGE LENGTH

I hereby certify that the contents of this report are accurate and correct. All test results and operations performed by this material manufacturer are in compliance with the requirements of the material specifications listed in the Specifications Block above.

QUALITY ASSURANCE

CUSTOMER COPY

STATE OF ARKANSAS COUNTY OF MISSISSIPPI
SWORN TO AND SUBSCRIBED BEFORE ME THIS 7 Day of 12/09

Charlene Wallis NOTARY PUBLIC

MY COMMISSION EXPIRES 10/21/2013

CHARLENE WALLIS NOTARY PUBLIC MISSISSIPPI CO. ARKANSAS MY Comm. Exp. 10-21-2013

Figure F.5: Mill certification

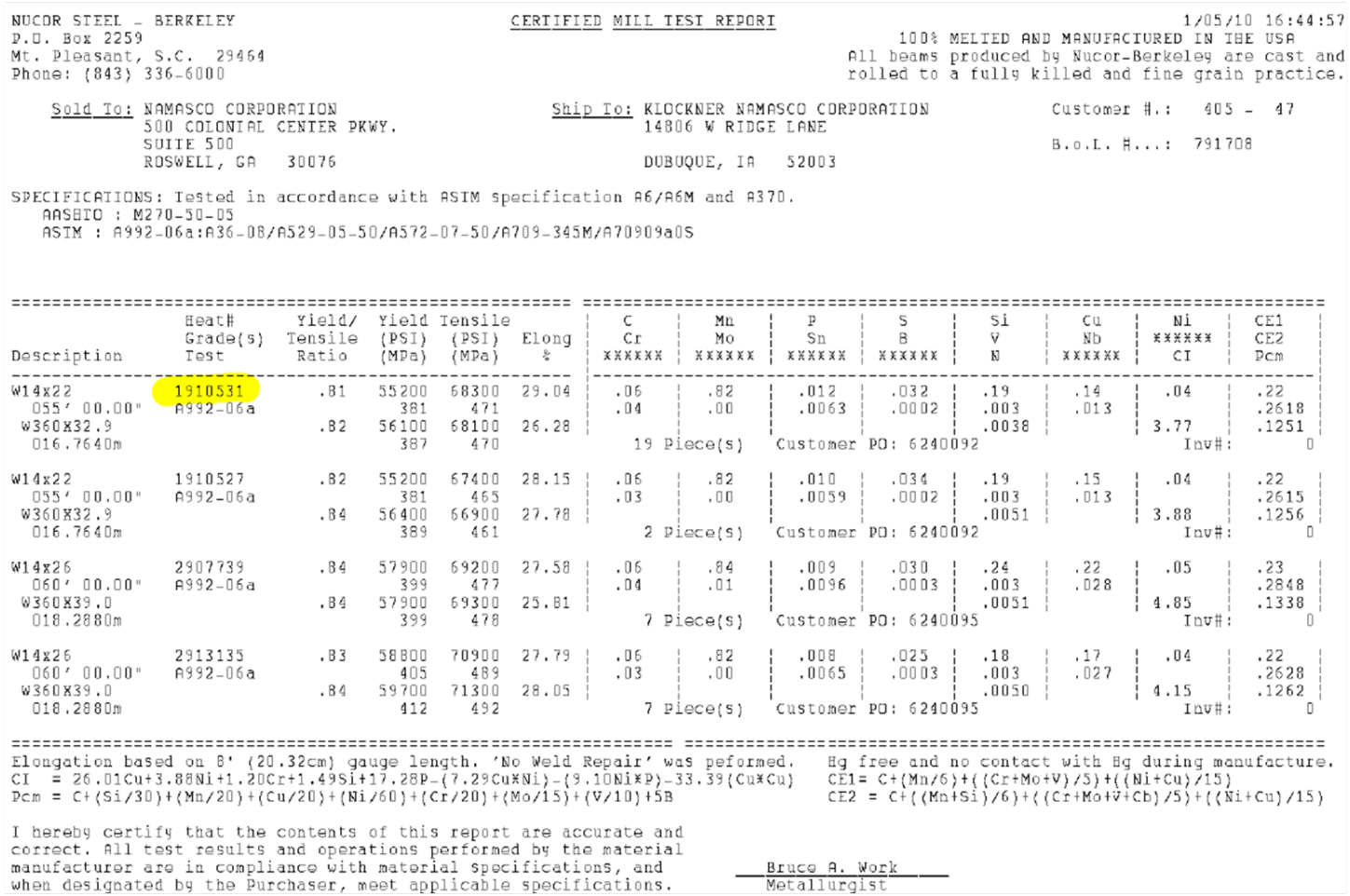

NUCOR STEEL - BERKELEY
P.O. Box 2259
Mt. Pleasant, S.C. 29464
Phone: (843) 336-6000

CERTIFIED MILL TEST REPORT

1/05/10 16:44:57
100% MELTED AND MANUFACTURED IN THE USA
All beams produced by Nucor-Berkeley are cast and rolled to a fully killed and fine grain practice.

Sold To: NAMASCO CORPORATION
500 COLONIAL CENTER PKWY.
SUITE 500
ROSWELL, GA 30076

Ship To: KLOCKNER NAMASCO CORPORATION
14806 W RIDGE LANE
DUBUQUE, IA 52003

Customer #.: 405 - 47
B.o.L. #...: 791708

SPECIFICATIONS: Tested in accordance with ASTM specification A6/A6M and A370.
AASHTO : M270-50-05
ASTM : A992-06a:A36-08/A529-05-50/A572-07-50/A709-345M/A70909a0S

Description	Heat# / Grade(s) / Test	Yield/ Tensile Ratio	Yield (PSI) (MPa)	Tensile (PSI) (MPa)	Elong %	C / Cr / xxxxxx	Mn / Mo / xxxxxx	P / Sn / xxxxxx	S / B / xxxxxx	Si / V / N	Cu / Nb / xxxxxx	Ni / xxxxxx / CI	CE1 / CE2 / Pcm
W14x22	1910531	.81	55200	68300	29.04	.06	.82	.012	.032	.19	.14	.04	.22
055' 00.00"	A992-06a		381	471		.04	.00	.0063	.0002	.003	.013		.2618
W360X32.9		.82	56100	68100	26.28					.0038		3.77	.1251
016.7640m			387	470		19 Piece(s)		Customer PO: 6240092				Inv#:	0
W14x22	1910527	.82	55200	67400	28.15	.06	.82	.010	.034	.19	.15	.04	.22
055' 00.00"	A992-06a		381	465		.03	.00	.0059	.0002	.003	.013		.2615
W360X32.9		.84	56400	66900	27.78					.0051		3.88	.1256
016.7640m			389	461		2 Piece(s)		Customer PO: 6240092				Inv#:	0
W14x26	2907739	.84	57900	69200	27.58	.06	.84	.009	.030	.24	.22	.05	.23
060' 00.00"	A992-06a		399	477		.04	.01	.0096	.0003	.003	.028		.2848
W360X39.0		.84	57900	69300	25.81					.0051		4.85	.1338
018.2880m			399	478		7 Piece(s)		Customer PO: 6240095				Inv#:	0
W14x26	2913135	.83	58800	70900	27.79	.06	.82	.008	.025	.18	.17	.04	.22
060' 00.00"	A992-06a		405	489		.03	.00	.0065	.0003	.003	.027		.2628
W360X39.0		.84	59700	71300	28.05					.0050		4.15	.1262
018.2880m			412	492		7 Piece(s)		Customer PO: 6240095				Inv#:	0

Elongation based on 8' (20.32cm) gauge length. 'No Weld Repair' was peformed. Hg free and no contact with Hg during manufacture.
CI = 26.01Cu+3.88Ni+1.20Cr+1.49Si+17.28P-(7.29Cu*Ni)-(9.10Ni*P)-33.39(Cu*Cu) CE1= C+(Mn/6)+((Cr+Mo+V)/5)+((Ni+Cu)/15)
Pcm = C+(Si/30)+(Mn/20)+(Cu/20)+(Ni/60)+(Cr/20)+(Mo/15)+(V/10)+5B CE2 = C+((Mn+Si)/6)+((Cr+Mo+V+Cb)/5)+((Ni+Cu)/15)

I hereby certify that the contents of this report are accurate and correct. All test results and operations performed by the material manufacturer are in compliance with material specifications, and when designated by the Purchaser, meet applicable specifications.

Bruce A. Work
Metallurgist

Figure F.6: Mill certification

F.2 HSS mill certs

10-05-'09 13:41 FROM-ITC 708-563-1950 T-899 P030/030 F-235

ID: 1063475

05Oct09 11:11 T E S T C E R T I F I C A T E No: MAR 626363

Sold By:
INDEPENDENCE TUBE CORPORATION
6226 W. 74TH STREET
CHICAGO, IL 60638
Tel: 708-496-0380 Fax: 708-563-1950

P/O No 6228071
Rel
S/O No MAR 159160-002
B/L No MAR 95216-002 Shp 02Oct09
Inv No Inv

Sold To: (144)
NAMASCO-EAST
500 COLONIAL PARKWAY
SUITE 500
ROSWELL, GA 30076

Ship To: (7)
NAMASCO-HOUSTON
14200 ALMEDA ROAD
713-433-7211
HOUSTON, TX

Tel: 678-259-8845 Fax: 571 323-0613

CERTIFICATE of ANALYSIS and TESTS Cert. No: MAR 626363
02Oct09

Part No 002
TUBING A500 GRADE B(C)
3" SQ X 1/4" X 40'

		Pcs	Wgt
		25	8,810

Heat Number	Tag No	Pcs	Wgt
Y85562	433560	25	8,810
	YLD=64790/TEN=79050/ELG=33.5		

Heat Number *** Chemical Analysis ***
Y85562 C=0.2200 Mn=0.8100 P=0.0090 S=0.0080 Si=0.0180 Al=0.0460
Cu=0.0100

T/R FAX

Test Report Clerk
MELTED IN U.S.A.

WE PROUDLY MANUFACTURE ALL OF OUR HSS IN THE USA.
INDEPENDENCE TUBE PRODUCT IS MANUFACTURED, TESTED,
AND INSPECTED IN ACCORDANCE WITH ASTM STANDARDS.
****

CURRENT STANDARDS:
..... A500/A500M-07
..... A513-07
..... A252-98 (2002)

Page: 1 .... Last

Figure F.7: Mill certification

F.3 BRB core plate mill certs

MSI TESTING, INC.

"SERVING THE INDUSTRY FOR 30 YEARS"
50 WEST LOUISE AVE. • SALT LAKE CITY, UT 84115
TELEPHONE (801) 484-1789

REPORT of ANALYSIS

Star Seismic
3070 Rassmussen Road Suite 260
Park City , Utah 84098

April 20, 2009
Project # 09-113
P.O. # Verbal Carter
Page 1 of 2

Attn : Carter Mickey

The following are the results of the testing done on the sample(s) you provided:

Sample #	Description :	
1	910-1216	1" Plate
2	910-1214	3/4" Plate
3	910-1210	3/4" Plate
4	910-1213	1" Plate
5	910-1212	3/4" Plate
6	910-1214	1" Plate

Longitudinal Tensile Test: Test Method in accordance with ASTM A370 .

Sample	Dia-meter	Area	Tensile Load (LBS)	Tensile Strength (PSI)	Yield Load (LBS)	Yield Strength (PSI)	Elong. %	Reduction of Area
1-1	.501	.1971	12,588	64,000	8,150	41,400	34	68
1-2	.498	.1948	12,242	63,000	7,600	39,000	32	68
1-3	.490	.1886	12,729	67,500	7,426	39,400	31.5	64
2-1	.494	.1917	12,920	67,500	7,984	41,700	32.5	68
2-2	.499	.1956	12,.801	65,500	8,267	42,300	34.5	65
2-3	.498	.1948	12,872	66,000	8,905	45,700	32	68
3-1	.491	.1893	11,.961	63,000	7,232	38,200	29.5	66
3-2	.497	.1940	12,408	64,000	8,696	44,800	32	66
3-3	.498	.1948	12,415	63,500	7,462	43,400	34	64

Star Seismic Note:

Average Fysc of mill and MSI testing = 43.3 ksi. Use 43.3 ksi in design.

Figure F.8: Mill certification

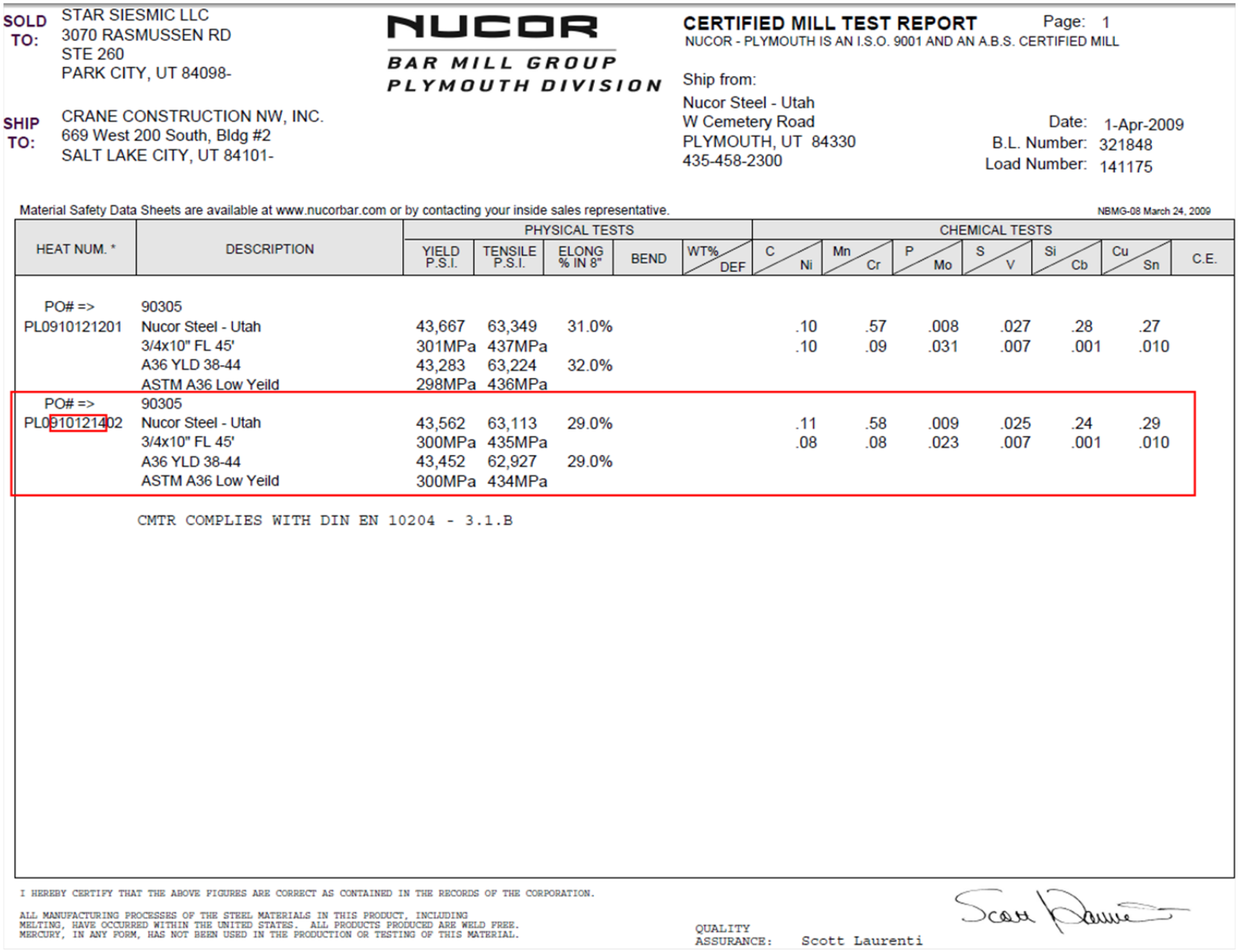

SOLD TO: STAR SIESMIC LLC
3070 RASMUSSEN RD
STE 260
PARK CITY, UT 84098-

SHIP TO: CRANE CONSTRUCTION NW, INC.
669 West 200 South, Bldg #2
SALT LAKE CITY, UT 84101-

NUCOR
BAR MILL GROUP
PLYMOUTH DIVISION

CERTIFIED MILL TEST REPORT Page: 1
NUCOR - PLYMOUTH IS AN I.S.O. 9001 AND AN A.B.S. CERTIFIED MILL

Ship from:
Nucor Steel - Utah
W Cemetery Road
PLYMOUTH, UT 84330
435-458-2300

Date: 1-Apr-2009
B.L. Number: 321848
Load Number: 141175

Material Safety Data Sheets are available at www.nucorbar.com or by contacting your inside sales representative. NBMG-08 March 24, 2009

HEAT NUM. *	DESCRIPTION	PHYSICAL TESTS					CHEMICAL TESTS						
		YIELD P.S.I.	TENSILE P.S.I.	ELONG % IN 8"	BEND	WT% DEF	C Ni	Mn Cr	P Mo	S V	Si Cb	Cu Sn	C.E.
PO# =>	90305												
PL0910121201	Nucor Steel - Utah	43,667	63,349	31.0%			.10	.57	.008	.027	.28	.27	
	3/4x10" FL 45'	301MPa	437MPa				.10	.09	.031	.007	.001	.010	
	A36 YLD 38-44	43,283	63,224	32.0%									
	ASTM A36 Low Yeild	298MPa	436MPa										
PO# =>	90305												
PL0910121402	Nucor Steel - Utah	43,562	63,113	29.0%			.11	.58	.009	.025	.24	.29	
	3/4x10" FL 45'	300MPa	435MPa				.08	.08	.023	.007	.001	.010	
	A36 YLD 38-44	43,452	62,927	29.0%									
	ASTM A36 Low Yeild	300MPa	434MPa										

CMTR COMPLIES WITH DIN EN 10204 - 3.1.B

I HEREBY CERTIFY THAT THE ABOVE FIGURES ARE CORRECT AS CONTAINED IN THE RECORDS OF THE CORPORATION.

ALL MANUFACTURING PROCESSES OF THE STEEL MATERIALS IN THIS PRODUCT, INCLUDING MELTING, HAVE OCCURRED WITHIN THE UNITED STATES. ALL PRODUCTS PRODUCED ARE WELD FREE. MERCURY, IN ANY FORM, HAS NOT BEEN USED IN THE PRODUCTION OR TESTING OF THIS MATERIAL.

QUALITY ASSURANCE: Scott Laurenti

Figure F.9: Mill certification

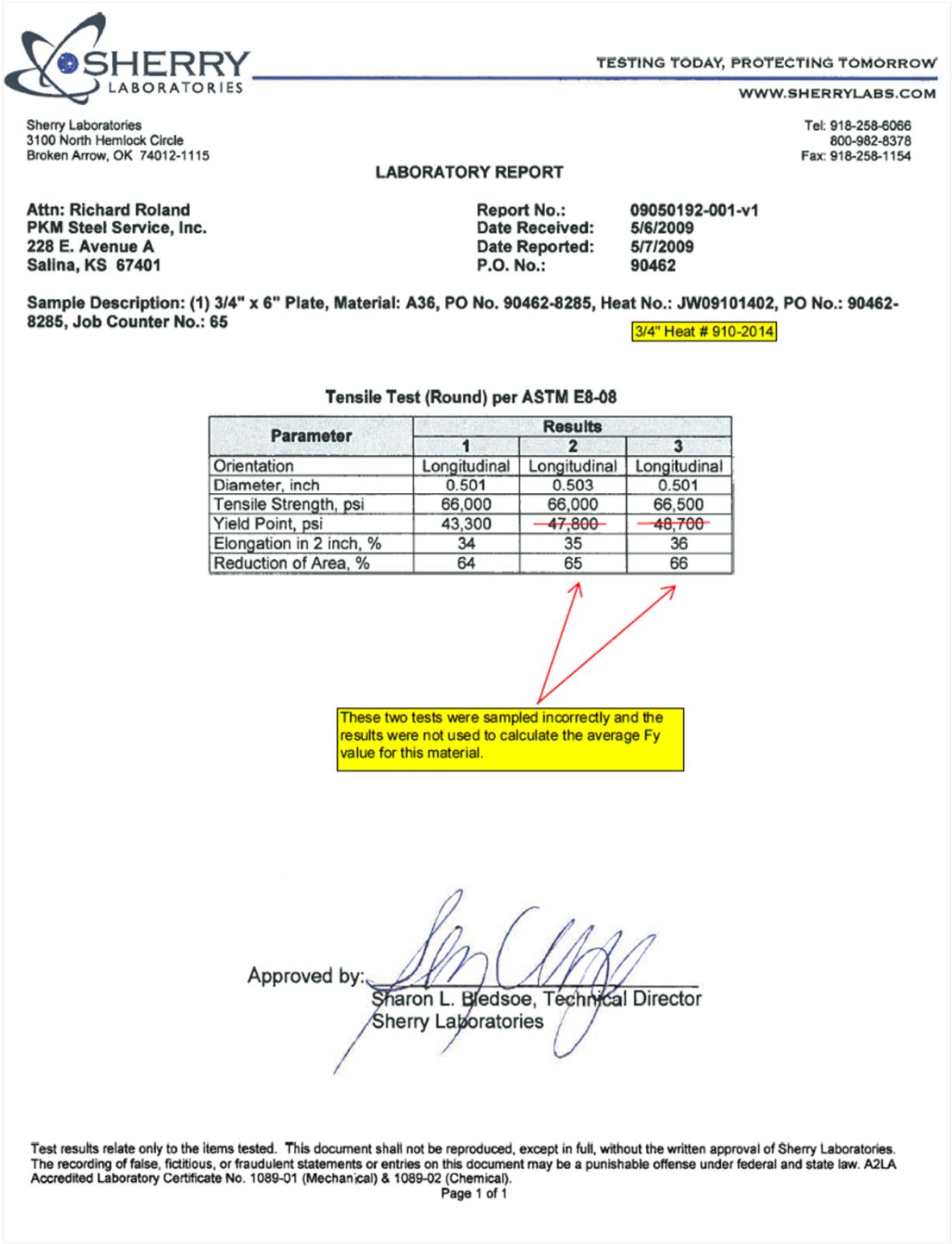

SHERRY LABORATORIES

TESTING TODAY, PROTECTING TOMORROW

WWW.SHERRYLABS.COM

Sherry Laboratories
3100 North Hemlock Circle
Broken Arrow, OK 74012-1115

Tel: 918-258-6066
800-982-8378
Fax: 918-258-1154

LABORATORY REPORT

Attn: Richard Roland
PKM Steel Service, Inc.
228 E. Avenue A
Salina, KS 67401

Report No.: 09050192-001-v1
Date Received: 5/6/2009
Date Reported: 5/7/2009
P.O. No.: 90462

Sample Description: (1) 3/4" x 6" Plate, Material: A36, PO No. 90462-8285, Heat No.: JW09101402, PO No.: 90462-8285, Job Counter No.: 65

3/4" Heat # 910-2014

Tensile Test (Round) per ASTM E8-08

Parameter	Results		
	1	2	3
Orientation	Longitudinal	Longitudinal	Longitudinal
Diameter, inch	0.501	0.503	0.501
Tensile Strength, psi	66,000	66,000	66,500
Yield Point, psi	43,300	~~47,800~~	~~48,700~~
Elongation in 2 inch, %	34	35	36
Reduction of Area, %	64	65	66

These two tests were sampled incorrectly and the results were not used to calculate the average Fy value for this material.

Approved by:
Sharon L. Bledsoe, Technical Director
Sherry Laboratories

Test results relate only to the items tested. This document shall not be reproduced, except in full, without the written approval of Sherry Laboratories. The recording of false, fictitious, or fraudulent statements or entries on this document may be a punishable offense under federal and state law. A2LA Accredited Laboratory Certificate No. 1089-01 (Mechanical) & 1089-02 (Chemical).

Page 1 of 1

Figure F.10: Mill certification

SHERRY LABORATORIES

TESTING TODAY, PROTECTING TOMORROW

WWW.SHERRYLABS.COM

Sherry Laboratories
3100 North Hemlock Circle
Broken Arrow, OK 74012-1115

Tel: 918-258-6066
800-982-8378
Fax: 918-258-1154

LABORATORY REPORT

Attn: Richard Roland
PKM Steel Service, Inc.
228 E. Avenue A
Salina, KS 67401

Report No.: 09050524-001-v1
Date Received: 5/14/2009
Date Reported: 5/15/2009
P.O. No.: 90462

Sample Description: (1) Sample, 3/4" Plate, Material: A36, Heat No.: 910-2014

Tensile Test (Rectangular) per ASTM E8-08

Parameter	Results		
	1	2	3
Orientation	Longitudinal	Longitudinal	Longitudinal
Thickness, inch	0.719	0.721	0.720
Width, inch	0.502	0.503	0.502
Tensile Strength, psi	65,000	65,000	65,000
Yield Point, psi	42,800	43,200	42,700
Elongation in 2 inch, %	42	43	43

Star Seismic Note:
Second and third test from 5/6/2009 test taken incorrectly, so three additional tests were pulled (shown on this sheet). The average of the first test from 5/6, the mill tests, and these three tests is 42.1. Use Fysc= 42.1 ksi

Approved by:
Sharon L. Bledsoe, Technical Director
Sherry Laboratories

Test results relate only to the items tested. This document shall not be reproduced, except in full, without the written approval of Sherry Laboratories. The recording of false, fictitious, or fraudulent statements or entries on this document may be a punishable offense under federal and state law. A2LA Accredited Laboratory Certificate No. 1089-01 (Mechanical) & 1089-02 (Chemical).

Figure F.11: Mill certification

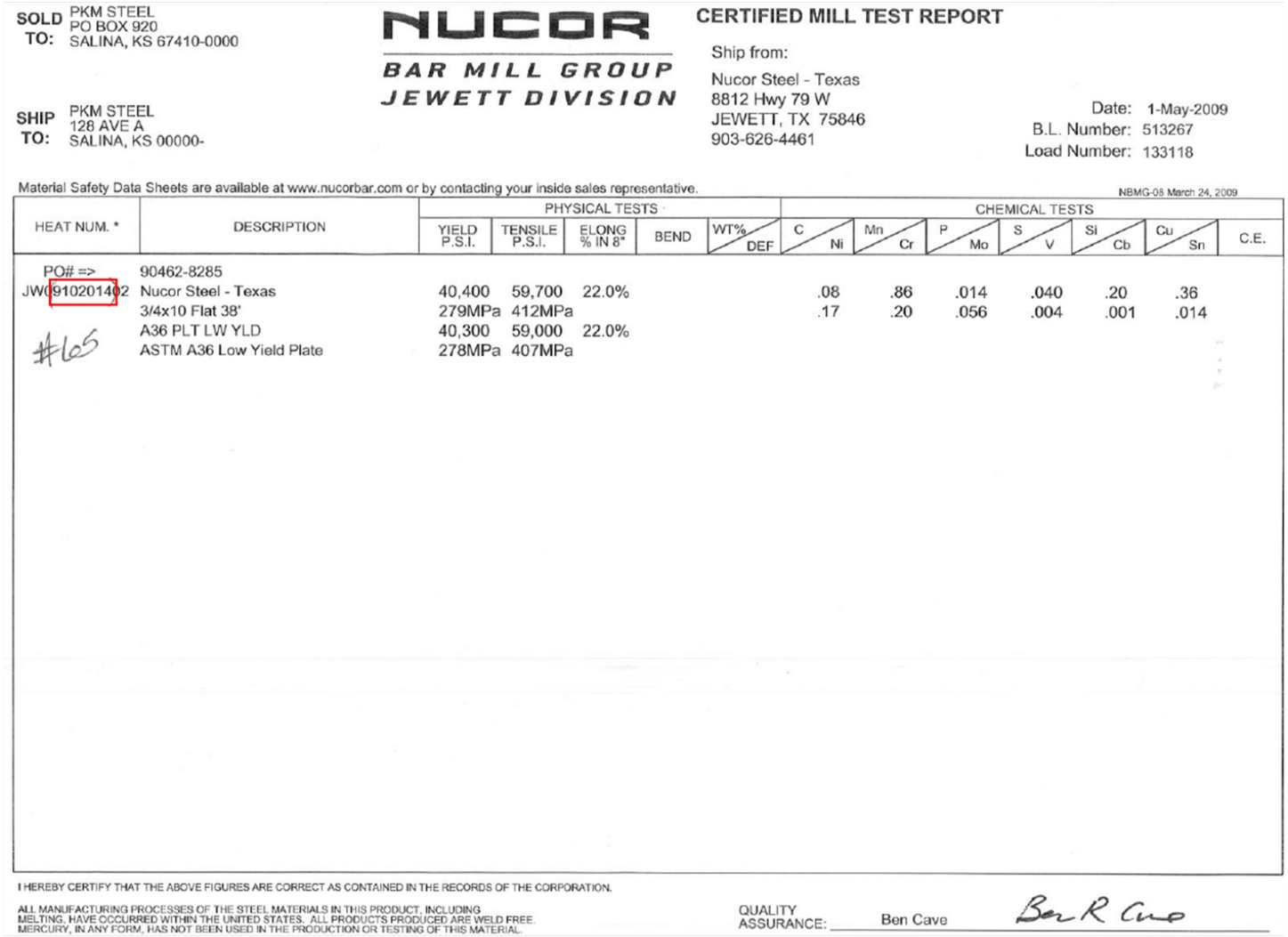

SOLD TO: PKM STEEL
PO BOX 920
SALINA, KS 67410-0000

SHIP TO: PKM STEEL
128 AVE A
SALINA, KS 00000-

NUCOR
BAR MILL GROUP
JEWETT DIVISION

CERTIFIED MILL TEST REPORT

Ship from:
Nucor Steel - Texas
8812 Hwy 79 W
JEWETT, TX 75846
903-626-4461

Date: 1-May-2009
B.L. Number: 513267
Load Number: 133118

Material Safety Data Sheets are available at www.nucorbar.com or by contacting your inside sales representative.

NBMG-08 March 24, 2009

HEAT NUM. *	DESCRIPTION	PHYSICAL TESTS					CHEMICAL TESTS							
		YIELD P.S.I.	TENSILE P.S.I.	ELONG % IN 8"	BEND	WT% DEF	C / Ni	Mn / Cr	P / Mo	S / V	Si / Cb	Cu / Sn	C.E.
PO# =>	90462-8285												
JW0910201402	Nucor Steel - Texas	40,400	59,700	22.0%			.08	.86	.014	.040	.20	.36	
	3/4x10 Flat 38'	279MPa	412MPa				.17	.20	.056	.004	.001	.014	
#165	A36 PLT LW YLD	40,300	59,000	22.0%									
	ASTM A36 Low Yield Plate	278MPa	407MPa										

I HEREBY CERTIFY THAT THE ABOVE FIGURES ARE CORRECT AS CONTAINED IN THE RECORDS OF THE CORPORATION.

ALL MANUFACTURING PROCESSES OF THE STEEL MATERIALS IN THIS PRODUCT, INCLUDING MELTING, HAVE OCCURRED WITHIN THE UNITED STATES. ALL PRODUCTS PRODUCED ARE WELD FREE. MERCURY, IN ANY FORM, HAS NOT BEEN USED IN THE PRODUCTION OR TESTING OF THIS MATERIAL.

QUALITY ASSURANCE: Ben Cave Ben R Cave

Figure F.12: Mill certification

VITA

Keith Palmer was born on April 17, 1973 in Champagne-Urbana, Illinois to Howard J. and Patricia A. Palmer. He attended The Pennsylvania State University and graduated in 1999 with a Bachelor of Architectural Engineering with a focus in structural engineering. He practiced structural engineering for an architectural and engineering firm in Minneapolis, MN from 1999 to 2006 and is a licensed professional engineer. In 2006, he returned to graduate school full-time at the University of Minnesota and received a Master of Science in Civil Engineering in 2008. He began work on his doctorate immediately thereafter.